

ABSTRACT ADMINISTRATION
2017 JUL 11 AM 9:31

ANALYSIS OF CHANNEL MORPHOLOGY AND HYDRAULICS OF
SELECT REACHES ALONG THE LOWER SAN ANTONIO RIVER,
TEXAS

TWDB Contract Number 1004831023

İnci Güneralp¹, Billy Hales²

¹ Associate Professor, Department of Geography, Texas A&M University

² Ph.D. Student, Department of Geography, Texas A&M University

**ANALYSIS OF CHANNEL MORPHOLOGY AND HYDRAULICS OF
SELECT REACHES ALONG THE LOWER SAN ANTONIO RIVER,
TEXAS**

TWDB Contract Number 1004831023

İnci Güneralp¹, Billy Hales²

¹ Associate Professor, Department of Geography, Texas A&M University

² Ph.D. Student, Department of Geography, Texas A&M University

<u>CONTENT</u>	<u>Page</u>
1. BACKGROUND	1
1.1. RIVER MORPHOLOGY, HYDROLOGY, AND AQUATIC HABITAT INTERACTION	1
1.1.1. <i>Geomorphology</i>	2
1.1.2. <i>Hydrology</i>	4
1.1.3. <i>Natural and Human Disturbance</i>	7
2. SPECIFIC OBJECTIVES OF THE STUDY	9
3. STUDY SITES ON THE LOWER SAN ANTONIO RIVER (LSAR)	9
3.1. CRITERIA FOR SITE SELECTION ON THE <i>LSAR</i> AND ITS TRIBUTARY LOWER CIBOLO CREEK (<i>LCC</i>)	9
3.2. THE STUDY SITES ON THE <i>LSAR</i> AND THE <i>LCC</i>	11
4. METHODS	12
4.1. DETRENDING TOPOGRAPHY	12
4.2. GEOMORPHIC CLASSIFICATION	13
4.3. RIVER2D® MODELS AND INPUT AND OUTPUT DATA FOR HYDROGEOMORPHIC ANALYSIS	14
4.4. PREPROCESSING OF RIVER2D® MODEL OUTPUTS	16
4.5. ANALYSIS OF MODEL OUTPUT PARAMETERS	19
5. THE GOLIAD STUDY REACH	21
5.1. GEOMORPHIC CHARACTERISTICS	21
5.2. RELATIONSHIPS BETWEEN GEOMORPHIC UNITS AND HYDRAULIC PROPERTIES	23
5.3. WATER DEPTH AND FROUDE NUMBER DISTRIBUTIONS	25
5.4. VELOCITY MAGNITUDE	27
5.4.1. <i>Velocity Magnitude Distribution</i>	27
5.4.2. <i>Velocity Magnitude Spatial Distribution</i>	27
5.4.3. <i>Velocity Magnitude Relationships</i>	27
5.4.4. <i>Summary on Velocity Magnitude Distribution</i>	29
5.5. STREAMWISE VELOCITY DISTRIBUTION	29
5.5.1. <i>Streamwise Velocity Distribution</i>	29
5.5.2. <i>Streamwise Velocity Spatial Distribution</i>	30
5.5.3. <i>Streamwise Velocity Relationships</i>	30
5.5.4. <i>Summary on Streamwise Velocity Distribution</i>	31
5.6. NORMAL VELOCITY DISTRIBUTION	32
5.6.1. <i>Normal Velocity Distribution</i>	32
5.6.2. <i>Normal Velocity Spatial Distribution</i>	32
5.6.3. <i>Normal Velocity Relationships</i>	32
5.6.4. <i>Summary on Normal Velocity Distribution</i>	33
5.7. SHEAR STRESS DISTRIBUTION	33
5.7.1. <i>Shear Stress Distribution</i>	33
5.7.2. <i>Shear Stress Spatial Distribution</i>	34
5.7.3. <i>Shear Stress Relationships</i>	34

5.7.4.	<i>Summary on Shear Stress Distribution</i>	35
5.8.	SUMMARY ON THE GOLIAD STUDY REACH	35
6.	THE FALLS CITY STUDY REACH	85
6.1.	GEOMORPHIC CHARACTERISTICS	85
6.2.	RELATIONSHIPS BETWEEN GEOMORPHIC UNITS AND HYDRAULIC PROPERTIES	88
6.3.	WATER DEPTH AND FROUDE NUMBER DISTRIBUTIONS	90
6.4.	VELOCITY MAGNITUDE	90
6.4.1.	<i>Velocity Magnitude Distribution</i>	90
6.4.2.	<i>Velocity Magnitude Spatial Distribution</i>	91
6.4.3.	<i>Velocity Magnitude Relationships</i>	92
6.4.4.	<i>Summary on Velocity Magnitude Distribution</i>	93
6.5.	STREAMWISE VELOCITY DISTRIBUTION	93
6.5.1.	<i>Streamwise Velocity Distribution</i>	93
6.5.2.	<i>Streamwise Velocity Spatial Distribution</i>	93
6.5.3.	<i>Streamwise Velocity Relationships</i>	94
6.5.4.	<i>Summary on Streamwise Velocity Distribution</i>	94
6.6.	NORMAL VELOCITY DISTRIBUTION	95
6.6.1.	<i>Normal Velocity Distribution</i>	95
6.6.2.	<i>Normal Velocity Spatial Distribution</i>	95
6.6.3.	<i>Normal Velocity Relationships</i>	95
6.6.4.	<i>Summary on Normal Velocity Distribution</i>	96
6.7.	SHEAR STRESS DISTRIBUTION	96
6.7.1.	<i>Shear Stress Distribution</i>	96
6.7.2.	<i>Shear Stress Spatial Distribution</i>	96
6.7.3.	<i>Shear Stress Relationships</i>	97
6.7.4.	<i>Summary on Shear Stress Distribution</i>	97
6.8.	SUMMARY ON THE FALLS CITY STUDY REACH	97
7.	THE CALAVERAS STUDY REACH	148
7.1.	GEOMORPHIC CHARACTERISTICS	148
7.2.	RELATIONSHIPS BETWEEN GEOMORPHIC UNITS AND HYDRAULIC PROPERTIES	151
7.3.	WATER DEPTH AND FROUDE NUMBER DISTRIBUTIONS	153
7.4.	VELOCITY MAGNITUDE	154
7.4.1.	<i>Velocity Magnitude Distribution</i>	154
7.4.2.	<i>Velocity Magnitude Spatial Distribution</i>	155
7.4.3.	<i>Velocity Magnitude Relationships</i>	155
7.4.4.	<i>Summary on Velocity Magnitude Distribution</i>	156
7.5.	STREAMWISE VELOCITY DISTRIBUTION	157
7.5.1.	<i>Streamwise Velocity Distribution</i>	157
7.5.2.	<i>Streamwise Velocity Spatial Distribution</i>	157
7.5.3.	<i>Streamwise Velocity Relationships</i>	158

7.5.4.	<i>Summary on Streamwise Velocity Distribution</i>	159
7.6.	NORMAL VELOCITY DISTRIBUTION	159
7.6.1.	<i>Normal Velocity Distribution</i>	159
7.6.2.	<i>Normal Velocity Spatial Distribution</i>	159
7.6.3.	<i>Normal Velocity Relationships</i>	160
7.6.4.	<i>Summary on Normal Velocity Distribution</i>	161
7.7.	SHEAR STRESS DISTRIBUTION	161
7.7.1.	<i>Shear Stress Distribution</i>	161
7.7.2.	<i>Shear Stress Spatial Distribution</i>	162
7.7.3.	<i>Shear Stress Relationships</i>	162
7.7.4.	<i>Summary on Shear Stress Distribution</i>	163
7.8.	SUMMARY ON THE CALAVERAS STUDY REACH	163
8.	THE CIBOLO STUDY REACH	214
8.1.	GEOMORPHIC CHARACTERISTICS	214
8.2.	RELATIONSHIPS BETWEEN GEOMORPHIC UNITS AND HYDRAULIC PROPERTIES	217
8.3.	WATER DEPTH AND FROUDE NUMBER DISTRIBUTIONS	219
8.4.	VELOCITY MAGNITUDE	220
8.4.1.	<i>Velocity Magnitude Distribution</i>	220
8.4.2.	<i>Velocity Magnitude Spatial Distribution</i>	221
8.4.3.	<i>Velocity Magnitude Relationships</i>	221
8.4.4.	<i>Summary on Velocity Magnitude Distribution</i>	222
8.5.	STREAMWISE VELOCITY DISTRIBUTION	222
8.5.1.	<i>Streamwise Velocity Distribution</i>	222
8.5.2.	<i>Streamwise Velocity Spatial Distribution</i>	223
8.5.3.	<i>Streamwise Velocity Relationships</i>	223
8.5.4.	<i>Summary on Streamwise Velocity Distribution</i>	224
8.6.	NORMAL VELOCITY DISTRIBUTION	224
8.6.1.	<i>Normal Velocity Distribution</i>	224
8.6.2.	<i>Normal Velocity Spatial Distribution</i>	224
8.6.3.	<i>Normal Velocity Relationships</i>	229
8.6.4.	<i>Summary on Normal Velocity Distribution</i>	226
8.7.	SHEAR STRESS DISTRIBUTION	226
8.7.1.	<i>Shear Stress Distribution</i>	226
8.7.2.	<i>Shear Stress Spatial Distribution</i>	226
8.7.3.	<i>Shear Stress Relationships</i>	227
8.7.4.	<i>Summary on Shear Stress Distribution</i>	228
8.8.	SUMMARY ON THE CIBOLO CREEK STUDY REACH	228
9.	DISCUSSION AND CONCLUSIONS	279
10.	REFERENCES	284

<u>LIST OF FIGURES</u>	<u>Page</u>
Figure 3.1. Map of Tier 1 Study Segments, regional geology (Brown et al. 2000) and valley edge (Engel and Curran 2008); <i>after</i> TIFP and SARA (2012).	10
Figure 3.2. Map of the Tier 1 Study Segments and the Gould Ecoregions of Texas (Gould et al. 1960), <i>after</i> TIFP and SARA (2012).	10
Figure 3.3. Location map showing the location of all study reaches on the lower San Antonio River (LSAR) and the lower Cibolo Creek: Goliad (19036), LSAR Segment 2, Reach 3, Falls City (19090), LSAR Segment 3, Reach 5, Calaveras (19107), LSAR Segment 3, Reach 8, and Cibolo Creek (19071), LCC Segment 2, Reach 10 (Table 1). Inset Courtesy of ArcGIS Online, Elevation data from National Elevation Dataset, Map features from www.NationalAtlas.gov.	11
Figure 4.1. Sampled locations for detrending in a section of the Calaveras study reach. Background imagery from Texas Orthoimagery Program.	13
Figure 4.2. Geomorphic classes extracted on an example reach for Calaveras Creek. (+) and (-) represent topographic highs and lows, respectively. Hot colors represent positive residuals or topographic highs referring to riffles/sediment bars (i.e., non-margin or mid-channel units) and channel edges (i.e., margin units). Cool colors represent negative residuals or topographic lows referring to pool units. <i>Legend:</i> Class ± 1 : 0-25 th percentiles, Class ± 2 : 25-50 th percentiles, Class ± 3 : 50-75 th percentiles, and Class ± 4 : 75-100 th percentiles, determined based on the minima and maxima of the pools and sediment bars/riffle/edges.	14
Figure 4.3. Rasterized surface from TIN and binned at one meter, Goliad reach at high discharge (Q5) condition. Background imagery is obtained from Texas Orthoimagery Program.	16
Figure 4.4. Rasterized surface from TIN and binned at one meter clipped with water extent for high discharge condition. Background imagery is obtained from Texas Orthoimagery Program.	17
Figure 4.5. Angles derived from Cartesian vector components of discharge intensity. Elevation information used in this example comes from the low discharge (Q1) condition of the Goliad study reach.	17
Figure 4.6. Component velocity for Cibolo Creek that consists of stream normal velocity (left) and streamwise velocity (right). Background imagery is obtained from Texas Orthoimagery Program.	18
Figure 5.1. The Goliad study reach and its bathymetric distribution.	21
Figure 5.2. Geomorphic unit classes for the Goliad study reach based on the topographic residuals. The (+) classes represent the topographic highs and (-) classes represent topographic lows. Detailed class descriptions are given in Figure 4.2. Flow direction is from left to right.	22
Figure 5.3. Percent coverage of geomorphic unit classes for the Goliad study reach. The (+) classes represent the topographic highs and (-) classes represent topographic lows. Detailed class descriptions are given in Figure 4.2.	22

Figure 5.4. Inundated area (m ²) vs. modeled discharge (m ³ /s) for the Goliad study reach.	25
Figure 5.5. Water depth distribution for Q1–Q6 (rows, top to bottom) for topographic highs (marked as T. High) corresponding to the classes (+1)–(+4), topographic lows (marked as T. Lows) corresponding to the classes (-1)–(-4), and combined (columns, left to right). Horizontal and vertical axes correspond to water depth (m) and the percent values of topographic classes, respectively.	37
Figure 5.6. Froude number (Fr) distribution for Q1–Q6 (rows, top to bottom) for topographic highs (marked as T. High) corresponding to the classes (+1)–(+4), topographic lows (marked as T. Lows) corresponding to the classes (-1)–(-4), and combined (columns, left to right). Horizontal and vertical axes correspond to Fr and the percent values of topographic classes, respectively.	39
Figure 5.7. Distribution of velocity magnitude for Q1–Q6 (rows, top to bottom) for topographic highs (marked as T. High) corresponding to the classes (+1)–(+4), topographic lows (marked as T. Lows) corresponding to the classes (-1)–(-4), and combined (columns, left to right). Horizontal and vertical axes correspond to velocity magnitude (m/s) and the percent values of topographic classes, respectively.	41
Figure 5.8. Spatial distribution of velocity magnitude (m/s) for Q1–Q6 for topographic highs (red colors) and lows (blue colors).	43
Figure 5.9. Distribution of velocity magnitude in relation to water depth for Q1–Q6 classified by topographic highs marked as T. Highs (brown colors), topographic lows marked as T. Lows (blue colors), and Froude number (Fr).	46
Figure 5.10. Distribution of velocity magnitude for topographic high (T. Highs)/low (T. Lows) subclasses (Figure 4.2) and Q1–Q6, classified by Froude number (Fr).	49
Figure 5.11. Distribution of streamwise velocity component for Q1–Q6 (rows, top to bottom) for topographic highs (marked as T. High) corresponding to the classes (+1)–(+4), topographic lows (marked as T. Lows) corresponding to the classes (-1)–(-4), and combined (columns, left to right). Horizontal and vertical axes correspond to streamwise velocity (m/s) and the percent values of topographic classes, respectively.	52
Figure 5.12. Spatial distribution of streamwise velocity (m/s) for Q1–Q6 for topographic highs (red colors) and lows (blue colors).	54
Figure 5.13. Distribution of streamwise velocity in relation to water depth for Q1–Q6 classified by topographic highs marked as T. Highs (brown colors), topographic lows marked as T. Lows (blue colors), and Froude number (Fr).	57
Figure 5.14. Distribution of streamwise velocity for topographic high (T. Highs)/low (T. Lows) subclasses (Figure 4.2) and Q1–Q6, classified by Froude number (Fr).	60

Figure 5.15. Distribution of normal velocity component for Q1–Q6 (rows, top to bottom) for topographic highs (marked as T. High) corresponding to the classes (+1)–(+4), topographic lows (marked as T. Lows) corresponding to the classes (-1)–(-4), and combined (columns, left to right). Horizontal and vertical axes correspond to normal velocity (m/s) and the percent values of topographic classes, respectively.	63
Figure 5.16. Spatial distribution of normal velocity (m/s) for Q1–Q6 for topographic highs (red colors) and lows (blue colors).	65
Figure 5.17. Distribution of normal velocity in relation to water depth for Q1–Q6 classified by topographic highs marked as T. Highs (brown colors), topographic lows marked as T. Lows (blue colors), and Froude number (Fr).	68
Figure 5.18. Distribution of normal velocity for topographic high (T. Highs)/low (T. Lows) subclasses (Figure 4.2) and Q1–Q6, classified by Froude number (Fr).	71
Figure 5.19. Distribution of shear stress for Q1–Q6 (rows, top to bottom) for topographic highs (marked as T. High) corresponding to the classes (+1)–(+4), topographic lows (marked as T. Lows) corresponding to the classes (-1)–(-4), and combined (columns, left to right). Horizontal and vertical axes correspond to shear stress ($\text{kg} \times \text{m}/\text{s}^2$) and the percent values of topographic classes, respectively.	74
Figure 5.20. Spatial distribution of shear stress ($\text{kg} \times \text{m}/\text{s}^2$) for Q1–Q6 for topographic highs (red colors) and lows (blue colors).	76
Figure 5.21. Distribution of shear stress in relation to water depth for Q1–Q6 classified by topographic highs marked as T. Highs (brown colors) and topographic lows marked as T. Lows (blue colors) and Froude number (Fr).	79
Figure 5.22. Distribution of shear stress for topographic high (T. Highs)/low (T. Lows) subclasses (Figure 4.2) and Q1–Q6, classified by Froude number (Fr).	82
Figure 6.1. The Falls City study reach and its bathymetric distribution.	85
Figure 6.2. Geomorphic unit classes for the Falls City study reach based on the topographic residuals. The (+) classes represent the topographic highs and (-) classes represent topographic lows. Detailed class descriptions are given in Figure 4.2. Flow direction is from left to right.	86
Figure 6.3. Percent coverage of geomorphic classes for the Falls City study reach. The (+) classes represent the topographic highs and (-) classes represent topographic lows. Detailed class descriptions are given in Figure 4.2.	87
Figure 6.4. Inundated area (m^2) vs. modeled discharge (m^3/s) for the Falls City study reach.	89
Figure 6.5. Water depth distribution for Q1–Q5 (rows, top to bottom) for topographic highs (marked as T. High) corresponding to the classes (+1)–(+4), topographic lows (marked as T. Lows) corresponding to the classes (-1)–(-4), and combined (columns, left to right). Horizontal and vertical axes correspond to water depth (m) and the percent values of topographic classes, respectively.	100

Figure 6.6. Froude number (Fr) distribution for Q1–Q5 (rows, top to bottom) for topographic highs (marked as T. High) corresponding to the classes (+1)–(+4), topographic lows (marked as T. Lows) corresponding to the classes (-1)–(-4), and combined (columns, left to right). Horizontal and vertical axes correspond to Fr and the percent values of topographic classes, respectively.	102
Figure 6.7. Distribution of velocity magnitude for Q1–Q5 (rows, top to bottom) for topographic highs (marked as T. High) corresponding to the classes (+1)–(+4), topographic lows (marked as T. Lows) corresponding to the classes (-1)–(-4), and combined (columns, left to right). Horizontal and vertical axes correspond to velocity magnitude (m/s) and the percent values of topographic classes, respectively.	104
Figure 6.8. Spatial distribution of velocity magnitude (m/s) for Q1–Q5 for topographic highs (red colors) and lows (blue colors).	106
Figure 6.9. Distribution of velocity magnitude in relation to water depth for Q1–Q5 classified by topographic highs marked as T. Highs (brown colors), topographic lows marked as T. Lows (blue colors), and Froude number (Fr).	109
Figure 6.10. Distribution of velocity magnitude for topographic high (T. Highs)/low (T. Lows) subclasses (Figure 4.2) and Q1–Q5, classified by Froude number (Fr).	112
Figure 6.11. Distribution of streamwise velocity component for Q1–Q5 (rows, top to bottom) for topographic highs (marked as T. High) corresponding to the classes (+1)–(+4), topographic lows (marked as T. Lows) corresponding to the classes (-1)–(-4), and combined (columns, left to right). Horizontal and vertical axes correspond to streamwise velocity (m/s) and the percent values of topographic classes, respectively.	115
Figure 6.12. Spatial distribution of streamwise velocity (m/s) for Q1–Q5 for topographic highs (red colors) and lows (blue colors).	117
Figure 6.13. Distribution of streamwise velocity in relation to water depth for Q1–Q5 classified by topographic highs marked as T. Highs (brown colors), topographic lows marked as T. Lows (blue colors), and Froude number (Fr).	120
Figure 6.14. Distribution of streamwise velocity for topographic high (T. Highs)/low (T. Lows) subclasses (Figure 4.2) and Q1–Q5, classified by Froude number (Fr).	123
Figure 6.15. Distribution of normal velocity component for Q1–Q5 (rows, top to bottom) for topographic highs (marked as T. High) corresponding to the classes (+1)–(+4), topographic lows (marked as T. Lows) corresponding to the classes (-1)–(-4), and combined (columns, left to right). Horizontal and vertical axes correspond to normal velocity (m/s) and the percent values of topographic classes, respectively.	126
Figure 6.16. Spatial distribution of normal velocity (m/s) for Q1–Q5 for topographic highs (red colors) and lows (blue colors).	128
Figure 6.17. Distribution of normal velocity in relation to water depth for Q1–Q5 classified by topographic highs marked as T. Highs (brown colors), topographic lows marked as T. Lows (blue colors), and Froude number (Fr).	131

Figure 6.18. Distribution of normal velocity for topographic high (T. Highs)/low (T. Lows) subclasses (Figure 4.2) and Q1–Q5, classified by Froude number (Fr).	134
Figure 6.19. Distribution of shear stress for Q1–Q5 (rows, top to bottom) for topographic highs (marked as T. High) corresponding to the classes (+1)–(+4), topographic lows (marked as T. Lows) corresponding to the classes (-1)–(-4), and combined (columns, left to right). Horizontal and vertical axes correspond to shear stress ($\text{kg} \times \text{m}/\text{s}^2$) and the percent values of topographic classes, respectively.	137
Figure 6.20. Spatial distribution of shear stress ($\text{kg} \times \text{m}/\text{s}^2$) for Q1–Q5 for topographic highs (red colors) and lows (blue colors).	139
Figure 6.21. Distribution of shear stress in relation to water depth for Q1–Q5 classified by topographic highs marked as T. Highs (brown colors) and topographic lows marked as T. Lows (blue colors) and Froude number (Fr).	142
Figure 6.22. Distribution of shear stress for topographic high (T. Highs)/low (T. Lows) subclasses (Figure 4.2) and Q1–Q5, classified by Froude number (Fr).	145
Figure 7.1. The Calaveras study reach and its bathymetric distribution.	148
Figure 7.2. Geomorphic unit classes for the Calaveras study reach based on the topographic residuals. The (+) classes represent the topographic highs and (-) classes represent topographic lows. Detailed class descriptions are given in Figure 4.2. Flow direction is from left to right.	149
Figure 7.3. Percent coverage of geomorphic unit classes for the Calaveras study reach. The (+) classes represent the topographic highs and (-) classes represent topographic lows. Detailed class descriptions are given in Figure 4.2.	150
Figure 7.4. Inundated area (m^2) vs. modeled discharge (m^3/s) for the Calaveras study reach.	152
Figure 7.5. Water depth distribution for Q1–Q5 (rows, top to bottom) for topographic highs (marked as T. High) corresponding to the classes (+1)–(+4), topographic lows (marked as T. Lows) corresponding to the classes (-1)–(-4), and combined (columns, left to right). Horizontal and vertical axes correspond to water depth (m) and the percent values of topographic classes, respectively.	166
Figure 7.6. Froude number (Fr) distribution for Q1–Q5 (rows, top to bottom) for topographic highs (marked as T. High) corresponding to the classes (+1)–(+4), topographic lows (marked as T. Lows) corresponding to the classes (-1)–(-4), and combined (columns, left to right). Horizontal and vertical axes correspond to Fr and the percent values of topographic classes, respectively.	168
Figure 7.7. Distribution of velocity magnitude for Q1–Q5 (rows, top to bottom) for topographic highs (marked as T. High) corresponding to the classes (+1)–(+4), topographic lows (marked as T. Lows) corresponding to the classes (-1)–(-4), and combined (columns, left to right). Horizontal and vertical axes correspond to velocity magnitude (m/s) and the percent values of topographic classes, respectively.	170

Figure 7.8. Spatial distribution of velocity magnitude (m/s) for Q1–Q5 for topographic highs (red colors) and lows (blue colors).	172
Figure 7.9. Distribution of velocity magnitude in relation to water depth for $Q1–Q5$ classified by topographic highs marked as T. Highs (brown colors), topographic lows marked as T. Lows (blue colors), and Froude number (Fr).	175
Figure 7.10. Distribution of velocity magnitude for topographic high (T. Highs)/low (T. Lows) subclasses (Figure 4.2) and $Q1–Q5$, classified by Froude number (Fr).	178
Figure 7.11. Distribution of streamwise velocity component for Q1–Q5 (rows, top to bottom) for topographic highs (marked as T. High) corresponding to the classes (+1)–(+4), topographic lows (marked as T. Lows) corresponding to the classes (-1)–(-4), and combined (columns, left to right). Horizontal and vertical axes correspond to streamwise velocity (m/s) and the percent values of topographic classes, respectively.	181
Figure 7.12. Spatial distribution of streamwise velocity (m/s) for Q1–Q5 for topographic highs (red colors) and lows (blue colors).	183
Figure 7.13. Distribution of streamwise velocity in relation to water depth for Q1–Q5 classified by topographic highs marked as T. Highs (brown colors), topographic lows marked as T. Lows (blue colors), and Froude number (Fr).	186
Figure 7.14. Distribution of streamwise velocity for topographic high (T. Highs)/low (T. Lows) subclasses (Figure 4.2) and Q1–Q5, classified by Froude number (Fr).	189
Figure 7.15. Distribution of normal velocity component for Q1–Q5 (rows, top to bottom) for topographic highs (marked as T. High) corresponding to the classes (+1)–(+4), topographic lows (marked as T. Lows) corresponding to the classes (-1)–(-4), and combined (columns, left to right). Horizontal and vertical axes correspond to normal velocity (m/s) and the percent values of topographic classes, respectively.	192
Figure 7.16. Spatial distribution of normal velocity (m/s) for Q1–Q5 for topographic highs (red colors) and lows (blue colors).	194
Figure 7.17. Distribution of normal velocity in relation to water depth for Q1–Q5 classified by topographic highs marked as T. Highs (brown colors), topographic lows marked as T. Lows (blue colors), and Froude number (Fr).	197
Figure 7.18. Distribution of normal velocity for topographic high (T. Highs)/low (T. Lows) subclasses (Figure 4.2) and Q1–Q5, classified by Froude number (Fr).	200
Figure 7.19. Distribution of shear stress for Q1–Q5 (rows, top to bottom) for topographic highs (marked as T. High) corresponding to the classes (+1)–(+4), topographic lows (marked as T. Lows) corresponding to the classes (-1)–(-4), and combined (columns, left to right). Horizontal and vertical axes correspond to shear stress ($\text{kg} \times \text{m}/\text{s}^2$) and the percent values of topographic classes, respectively.	203
Figure 7.20. Spatial distribution of shear stress ($\text{kg} \times \text{m}/\text{s}^2$) for Q1–Q5 for topographic highs (red colors) and lows (blue colors).	205

Figure 7.21. Distribution of shear stress in relation to water depth for Q1–Q5 classified by topographic highs marked as T. Highs (brown colors) and topographic lows marked as T. Lows (blue colors) and Froude number (Fr).	208
Figure 7.22. Distribution of shear stress for topographic high (T. Highs)/low (T. Lows) subclasses (Figure 4.2) and Q1–Q5, classified by Froude number (Fr).	211
Figure 8.1. The Cibolo study reach on the LCC and its bathymetric distribution.	218
Figure 8.2. Geomorphic unit classes for the Cibolo study reach based on the topographic residuals. The (+) classes represent the topographic highs and (-) classes represent topographic lows. Detailed class descriptions are given in Figure 4.2. Flow direction is from top to bottom.	219
Figure 8.3. Percent coverage of geomorphic unit classes for the Cibolo study reach. The (+) classes represent the topographic highs and (-) classes represent topographic lows. Detailed class descriptions are given in Figure 4.2.	220
Figure 8.4. Inundated area (m ²) vs. modeled discharge (m ³ /s) for the Cibolo study reach.	222
Figure 8.5. Water depth distribution for Q1–Q5 (rows, top to bottom) for topographic highs (marked as T. High) corresponding to the classes (+1)–(+4), topographic lows (marked as T. Lows) corresponding to the classes (-1)–(-4), and combined (columns, left to right). Horizontal and vertical axes correspond to water depth (m) and the percent values of topographic classes, respectively.	235
Figure 8.6. Froude number (Fr) distribution for Q1–Q5 (rows, top to bottom) for topographic highs (marked as T. High) corresponding to the classes (+1)–(+4), topographic lows (marked as T. Lows) corresponding to the classes (-1)–(-4), and combined (columns, left to right). Horizontal and vertical axes correspond to Fr and the percent values of topographic classes, respectively.	237
Figure 8.7. Distribution of velocity magnitude for Q1–Q5 (rows, top to bottom) for topographic highs (marked as T. High) corresponding to the classes (+1)–(+4), topographic lows (marked as T. Lows) corresponding to the classes (-1)–(-4), and combined (columns, left to right). Horizontal and vertical axes correspond to velocity magnitude (m/s) and the percent values of topographic classes, respectively.	239
Figure 8.8. Spatial distribution of velocity magnitude (m/s) for Q1–Q5 for topographic highs (red colors) and lows (blue colors).	241
Figure 8.9. Distribution of velocity magnitude in relation to water depth for Q1–Q5 classified by topographic highs marked as T. Highs (brown colors), topographic lows marked as T. Lows (blue colors), and Froude number (Fr).	244
Figure 8.10. Distribution of velocity magnitude for topographic high (T. Highs)/low (T. Lows) subclasses (Figure 4.2) and Q1–Q5, classified by Froude number (Fr).	247

Figure 8.11. Distribution of streamwise velocity component for Q1–Q5 (rows, top to bottom) for topographic highs (marked as T. High) corresponding to the classes (+1)–(+4), topographic lows (marked as T. Lows) corresponding to the classes (-1)–(-4), and combined (columns, left to right). Horizontal and vertical axes correspond to streamwise velocity (m/s) and the percent values of topographic classes, respectively.	250
Figure 8.12. Spatial distribution of streamwise velocity (m/s) for Q1–Q5 for topographic highs (red colors) and lows (blue colors).	252
Figure 8.13. Distribution of streamwise velocity in relation to water depth for Q1–Q5 classified by topographic highs marked as T. Highs (brown colors), topographic lows marked as T. Lows (blue colors), and Froude number (Fr).	255
Figure 8.14. Distribution of streamwise velocity for topographic high (T. Highs)/low (T. Lows) subclasses (Figure 4.2) and Q1–Q5, classified by Froude number (Fr).	258
Figure 8.15. Distribution of normal velocity component for Q1–Q5 (rows, top to bottom) for topographic highs (marked as T. High) corresponding to the classes (+1)–(+4), topographic lows (marked as T. Lows) corresponding to the classes (-1)–(-4), and combined (columns, left to right). Horizontal and vertical axes correspond to normal velocity (m/s) and the percent values of topographic classes, respectively.	261
Figure 8.16. Spatial distribution of normal velocity (m/s) for Q1–Q5 for topographic highs (red colors) and lows (blue colors).	263
Figure 8.17. Distribution of normal velocity in relation to water depth for Q1–Q5 classified by topographic highs marked as T. Highs (brown colors), topographic lows marked as T. Lows (blue colors), and Froude number (Fr).	266
Figure 8.18. Distribution of normal velocity for topographic high (T. Highs)/low (T. Lows) subclasses (Figure 4.2) and Q1–Q5, classified by Froude number (Fr).	269
Figure 8.19. Distribution of shear stress for Q1–Q5 (rows, top to bottom) for topographic highs (marked as T. High) corresponding to the classes (+1)–(+4), topographic lows (marked as T. Lows) corresponding to the classes (-1)–(-4), and combined (columns, left to right). Horizontal and vertical axes correspond to shear stress ($\text{kg} \times \text{m}/\text{s}^2$) and the percent values of topographic classes, respectively.	272
Figure 8.20. Spatial distribution of shear stress ($\text{kg} \times \text{m}/\text{s}^2$) for Q1–Q5 for topographic highs (red colors) and lows (blue colors).	274
Figure 8.21. Distribution of shear stress in relation to water depth for Q1–Q5 classified by topographic highs marked as T. Highs (brown colors) and topographic lows marked as T. Lows (blue colors) and Froude number (Fr).	277
Figure 8.22. Distribution of shear stress for topographic high (T. Highs)/low (T. Lows) subclasses (Figure 4.2) and Q1–Q5, classified by Froude number (Fr).	280

<u>LIST OF TABLES</u>	<u>Page</u>
Table 3.1. Properties of the study reaches based on the evaluation criteria defined by TIFP and SARA (2012). A more detailed description of segments and reaches can be found in TIFP and SARA (2012).	11
Table 3.2. Base flow levels Identified by aquatic modeling results by TIFP and SARA (2011).	12
Table 4.1. Hydraulic variables used in the hydrogeomorphic analysis of the study reaches (Goliad, Falls City, Calaveras, and Cibolo Creek), output by River2D® or derived from the outputs.	15
Table 5.1. Areal distribution of geomorphic unit classes in the Goliad study reach.	23
Table 5.2. Information on the Goliad study reach and model input parameters for River2D® model.	24
Table 5.3. Summary of River2D® model output parameters and min-max values for modeled discharges, Q1–Q6 for the Goliad study reach (Table 5.2).	24
Table 6.1. Areal distribution of geomorphic unit classes in the Falls City study reach.	87
Table 6.2. Information on the Falls City study reach and model input parameters for River2D® model.	88
Table 6.3. Summary of River2D® model output parameters and min-max values for modeled discharges, Q1-Q5 (Table 6.2).	89
Table 7.1. Areal distribution of geomorphic unit classes in the Calaveras study reach.	150
Table 7.2. Information on the Calaveras study reach and model input parameters for River2D® model.	151
Table 7.3. Summary of River2D® model output parameters for Calaveras and min-max values for modeled discharges, Q1-Q5 (Table 7.2).	152

1. BACKGROUND

1.1. RIVER MORPHOLOGY, HYDROLOGY, AND AQUATIC HABITAT INTERACTION

The spatiotemporal distribution of fish habitats is largely dependent upon the coupled dynamics between stream geomorphology and hydrology (Frissell et al., 1986; Gregory et al., 1991; Braaten and Berry Jr, 1997; Moir and Pasternack, 2008; Schmitt et al., 2011); Gregory et al., 1991; Braat7; Moir and Pasternack, 2008; Schmitt et al., 2011). The distribution of fish habitats is a function of the interaction between hydrologic flow regimes, which shape channel morphology, and the geomorphic features in the channel driving flow hydraulics. This process-form relationship between flow hydraulics and geomorphic resistance, generate features, or geomorphic units, such as pools, riffles, waterfalls, cascades, gravel bars, runs, and large woody debris.

The geomorphic units serve as habitats for aquatic species to progressively use for daily needs (*i.e.*, feeding, resting and refugia from predation), during specific life cycles (*i.e.*, spawning, acquiring juvenile and adult resources) and as refugia during periods of disturbance (*i.e.*, extreme low or high flows, significant temperature change, human modification) (Hart and Finelli, 1999; Thomson et al., 2001; Schwartz, 2002; Moir et al., 2004; Moir and Pasternack, 2008; Schneider and Winemiller, 2008). Fish habitats are dependent upon the geomorphology and hydrology of a reach to distribute the necessary resources, refugia and spatial availability to nurture a healthy aquatic community (Frissell et al., 1986; Gorecki et al., 2006); because a healthy aquatic community within a habitat is largely dependent upon the ability of species to fulfill their niche and to acquire the necessary resources to cultivate to the aquatic community.

It has become of utmost concern to maintain habitats necessary to sustain fish populations amidst the ever-increasing effects of human modifications to fluvial environments and relating stress added to fish populations. The physical structure of fish habitats change in space and time and their form is dependent upon flow conditions, sediment transport and channel stability (Frothingham et al., 2001). Yet, in order to define the boundaries of a particular habitat, along with ecological parameters, quantifying the physical properties of fish habitats, which are based on fluvial geomorphology and hydrology, is necessary. The geomorphic and hydraulic units of a channel need to be adequately identified or classified in order to measure the state and health of individual habitats, to subsequently quantify the affect of human modification on river ecosystems.

Recently, collaboration efforts between geomorphology, hydrology and ecology have been recognized. Frothingham et al. (2001: page 106) proposes:

“The potential linkage between geomorphology and ecology centers on a common interest in the physical properties of streams where geomorphological conditions define the amount, diversity and structure of the physical habitat. Ecologists recognize that spatial variability of physical properties, such as mean velocity, flow depth and substrate characteristics, has a strong influence on relationships between habitat and community structure and function...Fluvial geomorphologists, on the other hand, have developed theories and techniques related to the dynamic interaction between fluvial forms and processes. The theories provide a foundation for an improved understanding of physical habitat and time-related changes in habitat conditions.”

1.1.1. Geomorphology

There are a number of physical properties of river systems that have been used to define habitat boundaries and conditions relative to fish habitats. The physical characteristics of water depth, channel and flow widths, flow-current velocity, substrate size and type, channel slope, bed morphological stability, sediment transport, stream widths, and vegetation cover, determine the suitability of certain species for habitat utilization (Dent et al., 2001). The type of habitats fish occupy is largely controlled by the life cycle stage of particular species including larval, juvenile, and adult.

Hesse et al. (1937) use channel slope and bed stability to define a “longitudinal zonation” of benthic invertebrates. Statzner and Higler (1986) found the highest number of fish to be located in bank vegetation transition zones where coniferous forest was replaced by hardwood forest and the floodplain transitioned to debris cone zone. Additionally, they suggest that changes in the substrate of a stream segment induce changes in macroinvertebrate assemblage, while stony substrates tend to have more stable populations of species.

In large sand-bed rivers, Statzner and Higler (1986) suggest habitats have a greater “richness” as hydro-morphodynamics create more biologically diverse habitats. Frothingham et al. (2001) found that an increase in the spatial variability of channel morphology resulted in more rich individual habitats. They also found that a more diverse collection of fish habitats within a stream provides higher abundance and biomass of fish communities. Findings of Fischer et al.

(2003) illustrated sediment turnover (sediment transport and active work on substrate within the habitat) positively effects the health of fish habitats. Fischer et al. (2003) states sediment turnover was a major mechanism in the supply of oxygen and nitrogen to sediment bacteria. This provides more resources to support community structure in habitats where the sediment turnover and transport is high. Substrate supply distributes particulate organic carbon deeper into the sediment with faster flows, which begins a positive feedback between stream hydraulics and microbial activity (Fischer et al., 2003).

Meander bends tend to have great temporal variability of habitats, which produces a higher abundance and biomass concentration due to the erosion-deposition dynamics within bends, or sediment turnover. Frothingham et al. (2001) reported that fish in meander bends were twice as large as those in a channelized reach. Marchese et al. (2005) also found a higher turnover of species and higher landscape diversity in meander bends.

Fish habitats serve as temporary refugia from predation for smaller fish or temporary habitation: gravel bars serve as spawning grounds or nurseries for fish (Baras et al., 1996); pools and riffles provide necessary food resources and community structure (Brown and Brussock, 1991); while, waterfalls, cascades and bedrock steps form discrete habitats for particular species (Thomson et al., 2001). Pools, riffles, floodplains, gravel bars, runs, and secondary channels form discrete habitats for transient or resident aquatic organisms and are a function of basin substrate characteristics, hydrology, valley configuration and catchment processes.

Pools often serve as refuge from high flows, turbulent conditions, and predation, while providing an adequate food source without significant energy expenditure (Saffel and Scarnecchia, 1995). On a smaller geomorphic scale, substrate and bedform type become increasingly important for habitat preference based on hydraulic conditions, substrate material and resource distribution. Bedform type creates zones of similar hydraulic conditions, hydraulic biotypes, that can serve as an area where particular species thrive and others do not. Amsler et al. (2009) demonstrates these hydraulic biotypes within dunes, finding troughs of dunes provide refuge and specific food resources for benthic invertebrates, while reattachment zones were not preferred as there was a significant amount of sediment movement. Additionally, large scale dunes migrate very slowly allowing for benthic organisms to migrate as well (Amsler et al., 2009), yet migration rate is dependent upon the substrate material and grain size.

At the bedform/grain scale, substrate particles arrange themselves to make-up bedforms such as ripples, dunes, plane beds, or antidunes. As sediment transport is largely a function of

grain size, the migration and sustainability of these bedforms is dependent on the substrate they are comprised of. Coarse grains and gravel can act as armor and be sustained during high shear stress conditions; therefore, supplying an area for fish spawning to occur that enhances the population of macroinvertebrates within channel reaches (Frothingham et al., 2002). Marchese et al. (2005) note patches with silt and clay had richer biodiversity than sandy sediments and habitat patchiness developed dependent on grain size and substrate characteristics. Floodplain and riverine habitats are distinctly different habitats as the food quality for benthic invertebrates is richer in silt and clay substrate habitats than sandy substrate habitats. In sand-bed rivers, Marchese et al. (2005) suggest logs and snags to be more important as they contribute significantly to benthic productivity due to the absence of silt and clay substratum. Substrate gradation enhances the distribution of microhabitats within a reach and provides a positive feedback between spatial biodiversity within a channel reach.

However, these physical characteristics of fish habitats are protean and difficult to classify as stages or structures change with flow conditions, and consequently, alter microhabitat development. For instance, pools will not serve as a specific habitat-type throughout a river system, but rather, pool microhabitats are determined based on flow conditions in conjunction with substrate characteristics as these properties support different aquatic organisms. Therefore, understanding these geomorphic characteristics and their relation to hydraulic flow conditions is vital for adequately quantifying the spatial and temporal evolution of fish habitats.

1.1.2. Hydrology

The hydrodynamic conditions within a stream are a major determinant for habitat selection by fish, and consequently, a number of conceptual studies to relate flow conditions and channel morphology relative to benthic invertebrate habitat use have been conducted (Statzner and Higler, 1986; Statzner et al., 1988; Lancaster and Hildrew, 1993; Wadeson and Rowntree, 1998; Rhoads et al., 2003; Brooks et al., 2005; Schwartz and Herricks, 2005; Moir and Pasternack, 2008). Early formulations describing the physical structure of fish habitats based on hydraulic parameters within a stream were identified by the zonation concept (Hesse et al., 1937; Huet, 1949). Huet (1949) used the slope and width of a stream segment to calculate drag coefficients to describe the physical hydraulic conditions of zonation. Statzner and Higler (1986) found distinct changes in stream hydraulics produced a distinct change in species assemblage. For instance, salinity gradients show a distinct habitat where freshwater species are absent and

marine species are present. Hart and Finelli (1999) related the local boundary layer conditions of the water column to the spatial and temporal zonation of benthic invertebrates.

Comparing frequency distributions of local hydraulics, bed elevations over channels with different morphology and bank vegetation characteristics, Rhoads et al. (2003) show the relationship between fish habitat, bank vegetation and stream hydraulics. They found large woody debris (LWD) and bank vegetation (dense grass) produced flow separation along the banks and a decrease in flow velocities and adult fish typically inhabited deep pools, but the distribution of fish were also found to coincide with secondary flows within pools.

Wadson and Rowntree (1998) classify hydraulic conditions in a stream into “hydraulic biotopes” based on flow measurements of mean velocity, depth and bed roughness. From these measurements a series of flow parameters based on the aforementioned flow measurements can be used to characterize the hydraulic conditions, including Reynolds number (Re) and Froude number (Fr), shear velocity (V^*), and ‘roughness’ Reynolds number (Re^*). Re and Fr numbers are commonly used to characterize the stream hydraulics of fish habitats (Wadson and Rowntree, 1998; Kemp et al., 1999; Brooks et al., 2005).

In an attempt to relate the complexity of hydraulic parameters at a particular location to fish habitats, the Froude number (Fr) is used to determine the flow type. The Fr is the ratio of the inertial forces to gravitational forces. $Fr < 1$, classifies the flow as subcritical, $F = 1$ critical, and $F > 1$ supercritical. The Fr is scale independent, and therefore can be used as an indicator of hydraulic biotype. In backwater and pool units, the Fr is relatively low in comparison to run, riffle and rapid units where the Fr number is larger (Wadson and Rowntree, 1998).

Hydraulic complexity in a stream has also been used to characterize flow conditions (*i.e.*, whether the flow is laminar, transitional or turbulent). The Reynolds number (Re) is the ratio of the inertial forces to viscous forces within the stream and is dependent on scale. The Re is a measure of forces acting on the stream bed and therefore, experienced by the organisms within a habitat or biotype. Wadson and Rowntree (1998) advise that the use of just the Re and/or Fr numbers is impractical in shallow/rocky or boulder streams. The Re is also lower in backwaters and pools, while progressively higher from runs, riffles, cascades, glides and chutes to rapids.

Shear stress is exerted on the surface from the boundary layer conditions and bed roughness. This is ultimately the mechanism which moves sediment and the flow conditions which are experienced by benthic invertebrate. However, shear stress cannot be directly measured in the field and shear velocity, proportional to shear stress, is used as a surrogate to

describe the conditions at the surface. Shear velocity (U^*) is defined as (Wadeson and Rowntree, 1998).

$$U^* = v / [5.75 + \log (12.3d/k)]$$

where v denotes mean velocity; d denotes depth, and, k denotes bed roughness.

The ‘roughness’ Reynolds number (Re^*) determines whether the boundary layer is hydraulically smooth or hydraulically rough (Wadeson and Rowntree, 1998) and incorporates the shear velocity (V^*) and bed roughness (k):

$$Re^* = V^*k / v$$

David and Barmuta (1989) found that Re^* is an excellent habitat indicator which uses both velocity and substrate characteristics (Wadeson and Rowntree, 1998). Wadeson and Rowntree (1998) found Fr , V^* , and Re^* to be the most useful in classifying habitat biotypes. In studying riffle habitats specifically, Brooks et al. (2005) successfully demonstrates how these invertebrates prefer particular types of hydraulic conditions.

A negative correlation with Re^* a significant indicator of species abundance and community composition was found by Brooks et al. (2005). This suggests that where there are rough-flow conditions, species are less likely to be found. In areas of high roughness, organisms require higher metabolic needs as they are exposed to increase drag, and therefore, increased movement and attachment (Brooks et al., 2005). This concept is incredibly significant as only particular species will inhabit areas where hydraulic roughness is large at the surface, creating a species delineation of habitat preference. This implies that the areas of low Re^* are hotspots for species that have a lower metabolic processing rate. With this basic understanding, we can begin to elucidate between particular environments based on species type, and health.

Brooks et al. (2005) found velocity to be the best explanatory variable for the spatial distribution and patterns of invertebrates within riffle habitats, while Re^* best explained macroinvertebrate abundance, taxonomic richness and community composition. Amsler et al. (2009) found shear stresses associated with dune morphology to be a significant factor in the distribution of fish. Troughs of the dunes had lower shear velocity values, and therefore decreased suspended sediment concentrations than at the crests and reattachment zones.

Troughs served as refuge from high suspended sediment concentrations located at the reattachment zones and crests of dunes (Amsler et al., 2009).

1.1.3. Natural and Human Disturbance

A disturbance is a disruption in an aquatic habitat that alters the state of the system and can be natural or human induced. Natural disturbances include floods, high and low flows, droughts, climatic change, or wildfires, while human-induced disturbances are the construction of dams, stream naturalization or channelization, installation of reservoirs, diverting natural flow, redistributing water to cities, or land use/land cover change.

In differentiating between perturbation, disturbance and response, Lake (2000) proposes that a disturbance is the “cause of a perturbation” and the response of a system is the “effect of the disturbance.” Lake (2000) delineates three types of disturbances in river systems based on temporal patterns: (1) pulses, (2) presses, and (3) ramps.

A pulse disturbance is a short-lived deviation from normal conditions but ultimately returns to normal conditions, such as floods. Floods increase stream power, in turn, producing scour of substrate material, changing the channel morphology, and therefore alters fish habitats. Floods are not entirely a negative impact on fish habitats, as habitats migrate downstream or new habitats are developed in response to floods. During floods, fish utilize floodplain habitats as refugia (Schwartz and Herricks, 2005). Presses are disturbances that are marked by an abrupt change in stream conditions, and the altered conditions are sustained. For example, increased heavy metal concentration, dam construction and channelization are a form of press disturbances (Lake, 2000).

On the other hand, ramp disturbances gradually stress the environment to a point of negatively impacting the river system. Droughts and sedimentation are examples of ramp disturbances. Droughts provide an added complexity to the river systems and increases stress on fish habitats. With droughts, the water level of the river is dropped, consequently reducing the space for habitats (Lake, 2000). Flow conditions are dependent upon local synoptic conditions, and the prediction of the temporal distribution of flood or drought events becomes difficult. However, Richter et al. (2003) suggests using baseflows during these periods for reference to the most severe conditions the river should experience.

In each of these cases, the first process to be affected is the hydraulic conditions, which ultimately changes the morphology of the river and subsequently alters habitat development,

migration and distribution of macroinvertebrate resources. Lancaster and Hildrew (1993) relate macroinvertebrate response and habitat selection to hydraulic conditions as the hydraulic conditions distribute the litter mass and resources needed by the invertebrates. They found that after periods of high and fluctuating flows, a higher abundance of invertebrates were found in flow refugia. This is one example of the response of fish to extreme conditions. Shallow pool habitats will diminish during high flows, as deeper pool-riffle units are more pronounced during low flows (Frothingham et al., 2001).

Furthermore, with decreased flow velocities and sustained increase in temperatures during summer months, the potential for variability from reference conditions is high (Rivers-Moore and Jewitt, 2007). This introduces another aspect of disturbance as the invertebrates have to sustain their population under the limits of the biology. Saffel and Scarnecchia (1995) reported higher temperatures for juvenile Bull Trout constrained productivity and seasonal temperatures controlled the growth rate. This indicates habitat preference along with temperature changes as the hydraulic properties within a channel change.

All disturbances to a system are not negative. Moir et al. (2004) demonstrate fish spawning occurred during high flows in an upland Scottish stream. Moir et al. (2004) demonstrate geomorphic and hydraulic controls on spawning activity of Atlantic salmon (*Salmo salar* L.). Schneider and Winemiller (2008) found large woody debris patches in the Brazos River served as both refuge from predation, an area of high food resource for macroinvertebrates, and protection from high velocity flows.

2. SPECIFIC OBJECTIVES OF THE STUDY

The purpose of this study is to characterize the channel morphology and flow hydraulics of select reaches on the lower San Antonio River (*LSAR*) and its tributary the lower Cibolo Creek (*LCC*), Texas, to inform fish habitat mapping and assessment. For this purpose, we had two major objectives:

- 1) Examine the spatial distribution of channel morphology (*i.e.*, channel-bed geomorphic units),
- 2) Examine the spatial distribution of the hydraulics in the study reaches in relation to channel morphology, and under different discharge conditions.

3. STUDY SITES ON THE LOWER SAN ANTONIO RIVER (LSAR)

3.1. CRITERIA FOR SITE SELECTION ON THE *LSAR* AND ITS TRIBUTARY LOWER CIBOLO CREEK (*LCC*)

The study sites were selected using the criteria discussed in detailed in Texas Instream Flow Program (TIFP) and San Antonio River Authority (SARA) (TIFP and SARA, 2012). Specifically, three-tier criteria were used. According to these criteria, specific divisions of the sub-basin will be referred to as “Study Segments,” “Study Reaches,” and “Study Sites” (TIFP and SARA (2012), pg 37).

To identify the Study Sites on the lower San Antonio River and a tributary, lower Cibolo Creek, the TIFP used a three-tier evaluation: Tier 1, Tier 2, and Tier 3. According to TIFP and SARA (2012), Tier 1 evaluation was high-level and based primarily on basin geology, valley shape, and Texas ecoregions, resulting in the designation of three large-scale Study Segments (TIFP and SARA, 2012; Figures 3.1–3.2).

Tier 2 evaluation was more detailed and focused on “specific parameters relative to the hydrology, biology, physical processes, and water quality supported within those Reaches”. Thus Tier 2 evaluation resulted in Study Reaches selected within the Study Segments primarily on major hydrological and geomorphological features and conditions. Finally, Tier 3 evaluation examined shorter stretches of the Study Sites in much finer detail, including the authorized site access, to be used in this study as Study Sites (TIFP and SARA, 2012; Figure 12).

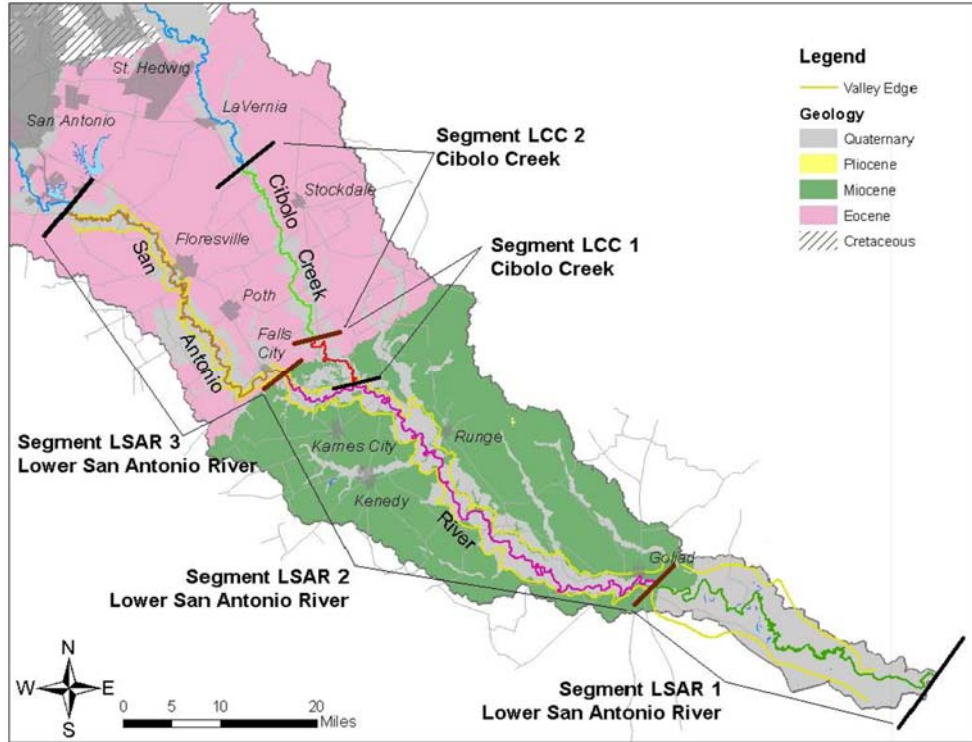


Figure 3.1. Map of Tier 1 Study Segments, regional geology (Brown et al. 2000) and valley edge (Engel and Curran 2008); *after* TIFP and SARA (2012).

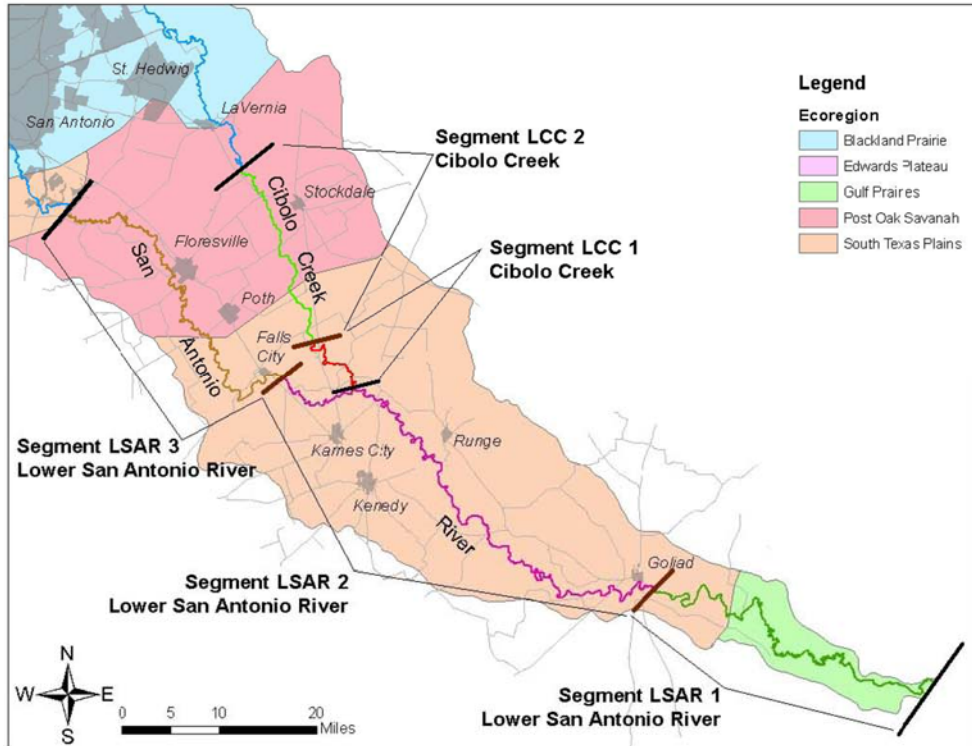


Figure 3.2. Map of the Tier 1 Study Segments and the Gould Ecoregions of Texas (Gould et al. 1960), *after* TIFP and SARA (2012).

3.2. THE STUDY SITES ON THE *LSAR* AND *LCC*

Figure 3.3 shows the location of the study sites investigated in this study. The study sites include Goliad (19036), LSAR Segment 2, Reach 3, Falls City (19090), LSAR Segment 3, Reach 5, Calaveras (19107), LSAR Segment 3, Reach 8, and Cibolo (19071), LCC Segment 2, Reach 10 (Table 3.1).

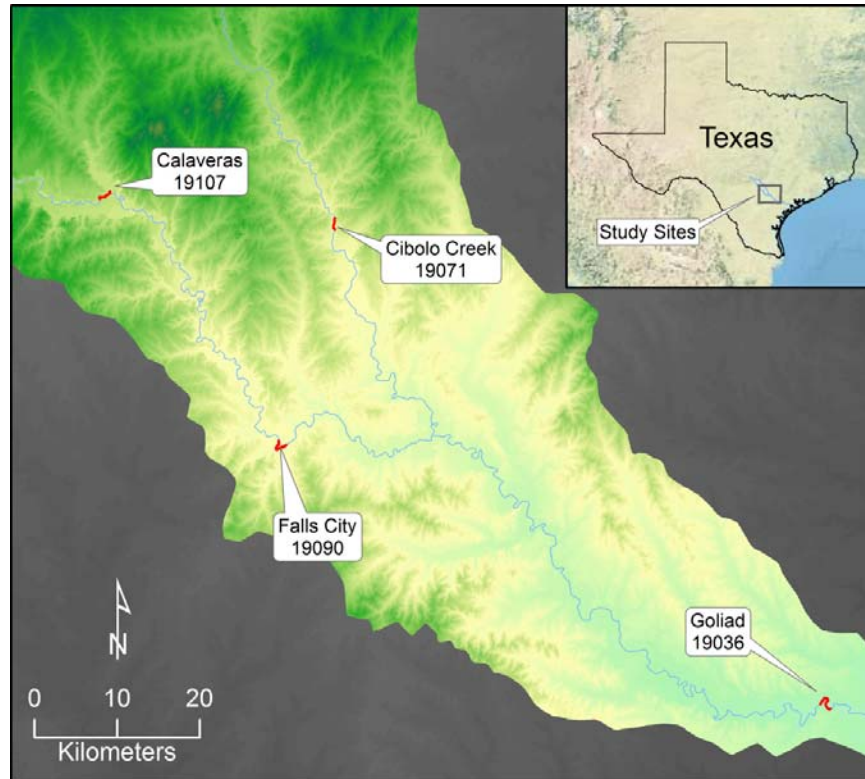


Figure 3.3. Location map showing the location of all study reaches on the lower San Antonio River (LSAR) and the lower Cibolo Creek: Goliad (19036), LSAR Segment 2, Reach 3, Falls City (19090), LSAR Segment 3, Reach 5, Calaveras (19107), LSAR Segment 3, Reach 8, and Cibolo Creek (19071), LCC Segment 2, Reach 10 (Table 1). Inset Courtesy of ArcGIS Online, Elevation data from National Elevation Dataset, Map features from www.NationalAtlas.gov.

Table 3.1. Properties of the study reaches based on the evaluation criteria defined by TIFP and SARA (2012). A more detailed description of segments and reaches can be found in TIFP and SARA (2012).

River	Study Site	Segment	Reach
Lower San Antonio River (LSAR)	Goliad (19036)	LSAR Segment 2	Reach 3
	Falls City (19090)	LSAR Segment 3	Reach 5
	Calaveras (19107)	LSAR Segment 3	Reach 8
Lower Cibolo Creek (LCC)	Cibolo (19071)	LCC Segment 2	Reach 10

Based on the aquatic modeling results they obtained, TIFP and SARA (2011) determined the base flow levels for each site (Table 3.2). Base flow recommendations were focused on maintaining a desirable range of aquatic habitat conditions. To ensure inter-annual variability in base flow conditions, recommendations were made for dry, average/normal, and wet conditions as proposed in TIFP Technical Overview (TPWD et al., 2008). The detailed discussions on the selection of base levels can be found in TIFP and SARA (2011). The study sites and their geomorphological and hydrological characteristics are discussed in more detail in the specific study site sections (*see* Study Sites: Goliad, Falls City, Calaveras, and Cibolo).

Table 3.2. Base flow levels Identified by aquatic modeling results by TIFP and SARA (2011).

River	Study Site	Dry		Normal		Wet	
		(m3/s)	(cfs)	(m3/s)	(cfs)	(m3/s)	(cfs)
LSAR	Goliad (19036)	4.81	170	8.21	290	14.16	500
	Falls City (19090)	3.68	130	7.08	250	12.74	450
	Calaveras (19107)	2.83	100	6.37	225	9.91	350
LCC	Cibolo (19071)	0.42	15	0.71	25	1.13	40

4. METHODS

4.1. DETRENDING TOPOGRAPHY

To delineate between habitat types, flow conditions relative to common morphology of habitats must be considered. In general, no general consensus on the depth for each habitat type has been reached because habitat depth is dependent on the scale of the river (which is commonly why flow type is used for habitat distinction). For instance, Rabeni and Jacobson (1993) define pools as the depth range of 1–5 meters, whereas Rhoads et al. (2003) have depths with a range of 1–2 meters on the Embarrass River as being pools.

Clifford et al. (2006) uses detrended bathymetry data to distinguish between pools and riffles. By detrending the centerline bathymetry, Clifford et al. (2006) classify positive values as riffles and negative as pools. Detrending depth relates the hydraulic state to bathymetry and provides an objective way to quantitatively differentiate among topographic influences on flow in a river. In this study, we detrended the channel bathymetry following an approach similar to that used by Clifford et al. (2006). The approach is discussed as follows.

Different geomorphic unit classes are calculated as pools and sediment bars/riffles/edges based on residual from a detrended elevation. To obtain residuals, the

subaqueous elevation for each reach must be detrended. We conducted the detrending with the channel centerline that we extracted using the method by Güneralp and Rhoads (2008). We also used the same channel centerline in various other steps of data preprocessing (see *Section 4.4* for the other preprocessing steps). We sampled the elevation values along the channel centerline, and calculated a simple linear regression from these elevations along the centerline. We plotted the regression equation along the centerline, and projected the line in a manner that covers the entire reach along two meter intervals (Figure 4.1).

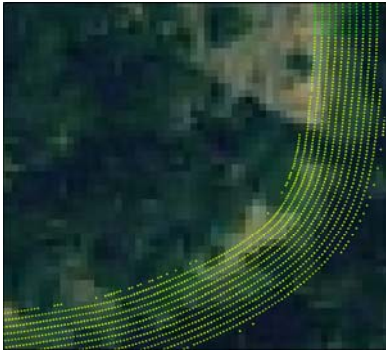


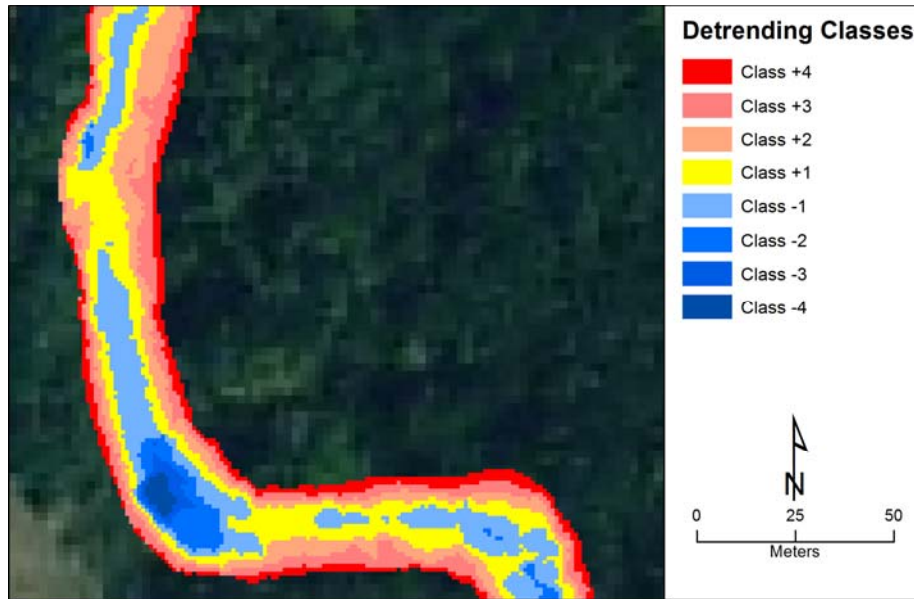
Figure 4.1. Sampled locations for detrending in a section of the Calaveras study reach. Background imagery from Texas Orthoimagery Program.

With the entire reach covered, we transformed the points and sampled the elevation values at each point associated with the detrended surface. We also processed these detrended values into a raster. The result is a trended surface along the reach. We generated the detrended elevation by subtracting this trended surface from the sampled elevation.

4.2. GEOMORPHIC CLASSIFICATION

We resolved the detrended elevations into geomorphic regions based on a classification that defines each negative residual (i.e., detrended elevation) as a topographic low (i.e., pool) and each positive residual as a topographic high (i.e., sediment bar/riffle/edge). We further stratified the pool and sediment bar/riffle/edge classes by dividing each of them into four unique regions based on the quartiles of the minima and maxima of the pools and sediment bars/riffles, respectively. These new classes correspond to the 0-25th, 25-50th, 50-75th, 75-100th percentiles of the detrended (+) and (-) elevations (i.e., classes named as (+1)–(+4) for topographic highs and (-1)–(-4) for topographic lows, respectively; Figure 4.2).

We obtained the results in the form of ArcView® polygon shapefiles that represent these regions (Figure 4.2). River2D® model outputs are extracted in each region (Steffler and Blackburn, 2002). With these classified model outputs, it is possible to analyze and visualize parameters in each region.



Class	Description	Class	Description
-4 – -1:	Topographic lows: Topographic residuals representing pools	1 – 4 :	Topographic highs: Topographic residuals representing bars/riffles/edges
-4 :	Above 75th percentile of maximum topographic low depth	1 :	Below 25th percentile of maximum topographic high height
-3 :	Between 50 and 75th percentile of maximum topographic low depth	2 :	Between 25 and 50th percentile of maximum topographic high height
-2 :	Between 25 and 50th percentile of maximum topographic low depth	3 :	Between 50 and 75th percentile of maximum topographic high height
-1 :	Between 0 and 25th percentile of maximum topographic low depth	4 :	Above 75th percentile of maximum topographic high height

Figure 4.2. Geomorphic classes extracted on an example reach for Calaveras Creek. (+) and (-) represent topographic highs and lows, respectively. Hot colors represent positive residuals or topographic highs referring to riffles/sediment bars (i.e., non-margin or mid-channel units) and channel edges (i.e., margin units). Cool colors represent negative residuals or topographic lows referring to pool units. *Legend:* Class ± 1 : 0-25th percentiles, Class ± 2 : 25-50th percentiles, Class ± 3 : 50-75th percentiles, and Class ± 4 : 75-100th percentiles, determined based on the minima and maxima of the pools and sediment bars/riffle/edges.

4.3. RIVER2D® MODELS AND INPUT AND OUTPUT DATA FOR HYDROGEOMORPHIC ANALYSIS

River2D® (Steffler and Blackburn, 2002) models of the study reaches –three *LSAR* reaches, Goliad, Falls City Crossing, and Calaveras Creek, and one *LCC* reach, Cibolo (Figure 4.3, Tables 3.1–3.2)– were developed by the RPS Group (IIFP and SARA, 2011). For each of these sites, five/six discharge conditions are studied. The specific discharge conditions

considered can be found in the sections on the specific study sites (*see* Study Sites: Goliad, Falls City, Calaveras, and Cibolo).

The discharge conditions consist of a low flow (Q1), high flow (Q5/Q6), and three/four) intermediate flows (Q2-Q4/Q5) that match discharge conditions related to habitat mapping (i.e., base flow levels of dry, normal, and wet, identified by aquatic modeling results by TIFP and SARA (2011); Table 3.2). Outputs for each River2D® model consists of a series of hydraulic variables, including cumulative discharge, water depth, elevation, water surface elevation, shear velocity, discharge intensity components in the Cartesian coordinates (i.e., discharge intensity components in the Cartesian *X* and *Y* directions, roughness, Froude number (Fr), and velocity magnitude. In the hydrogeomorphic analysis, we used seven hydraulic variables either output by the River2D® or derived from these outputs (Table 4.1).

Table 4.1. Hydraulic variables used in the hydrogeomorphic analysis of the study reaches (Goliad, Falls City, Calaveras, and Cibolo Creek), output by River2D® or derived from the outputs.

Hydraulic Variable	Output/ Derived	Description (Unit)
Water depth (Depth)	Output	Height of inundation (meters)
Froude number (Fr)	Output	Froude number to indicate the ratio of inertial to gravitational forces (unitless). For Froude number < 1, flow is subcritical; for Froude number = 1, the flow is critical, for Froude number > 1, then the flow is supercritical.
Velocity magnitude (VMag)	Output	Depth average velocity magnitude (meters/second)
Streamwise velocity (SVel)	Derived	Depth-averaged flow velocity in downstream direction (meters/second). (+) values indicate net velocity along flow; (-) values indicate net velocity against flow, <i>calculated from</i> discharge intensity, velocity magnitude, and centerline
Normal velocity (NVel)	Derived	Depth-averaged velocity normal to streamwise direction (meters/second). (+) values correspond to the flow toward left bank; (-) values correspond to the flow toward right bank, <i>calculated from</i> discharge intensity, velocity magnitude, and centerline.
Shear stress (Stress)	Derived	Shear stress magnitude near the river bed, calculated from shear velocity (kilograms / (meters × second ²))
Water Surface Elevation (WSE)	Output	Topographic elevation plus water depth (meters)

4.4. PREPROCESSING OF RIVER2D® MODEL OUTPUTS

The first step in preprocessing was to turn the tabular model outputs into ArcView® point shapefiles with model outputs as attributes. As point data, model outputs were used to form a Triangulated Irregular Network (TIN). Once depicted as a TIN surface, the output was rasterized to tagged image file format (TIFF) with the ArcGIS® 3D Analyst ‘TINToRaster’ command. Outputs then are one meter in x-y resolution, an example depicted in (Figure 4.3). This TIFF image has an extent matching the TIN, and therefore it was necessary to extract the water boundary.

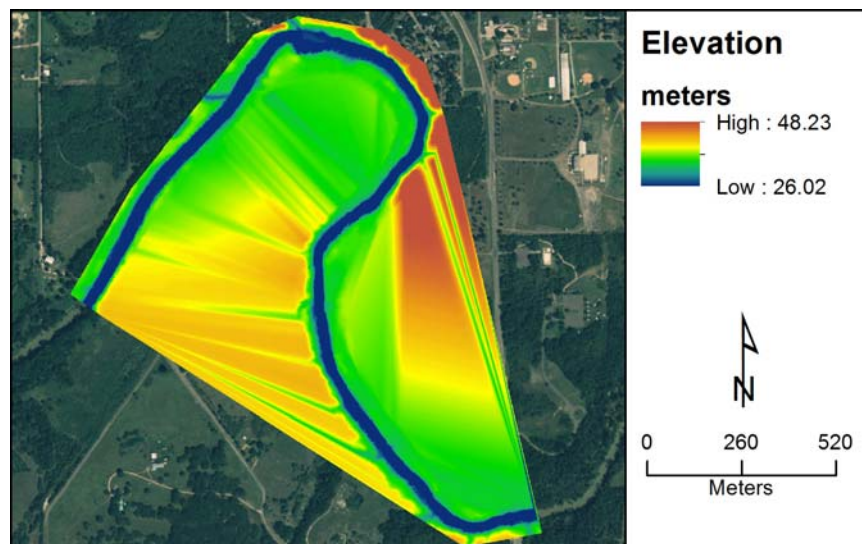


Figure 4.3. Rasterized surface from TIN and binned at one meter, Goliad reach at high discharge (Q5) condition. Background imagery is obtained from Texas Orthoimagery Program.

Then, the water edge outputs from River2D® model were translated into an ArcView® polyline shapefile format. To define the extent, the ‘polylines’ were transformed into a polygon geometry and then the resulting ArcView® polygon shapefile was used to clip each raster output. The final results were sets of TIFF images that represent the output parameters for River2D® and have boundaries coincident with the water extent at each given reach and flow level (Figure 4.4).

To further inform velocity, velocity magnitude was resolved into stream-wise and normal directions. River2D® discharge intensity outputs are in X and Y Cartesian scalars. With the assumption that discharge intensity and velocity should have the same bearing, the discharge intensity vector can be used to inform an angle of flow for velocity magnitude. The process of

resolving stream-wise and normal velocities had several sub-steps, including: 1) calculating arithmetic angels, 2) using centerline to resolve stream angles, and 3) using stream angles to calculate stream vectors.

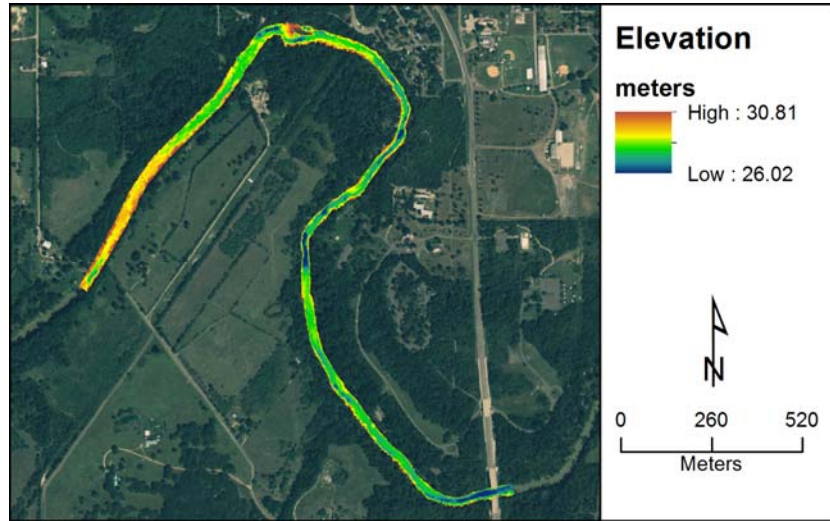


Figure 4.4. Rasterized surface from TIN and binned at one meter clipped with water extent for high discharge condition. Background imagery is obtained from Texas Orthoimagery Program.

We transformed the Cartesian vectors of discharge intensity into ArcView® point shapefiles. Together, we used these Cartesian vectors to generate angles. The outputs (Figure 4.5) are in radians in an arithmetic arrangement (90 degrees face north) that range from $-\pi$ to $+\pi$ (Python, 2010).

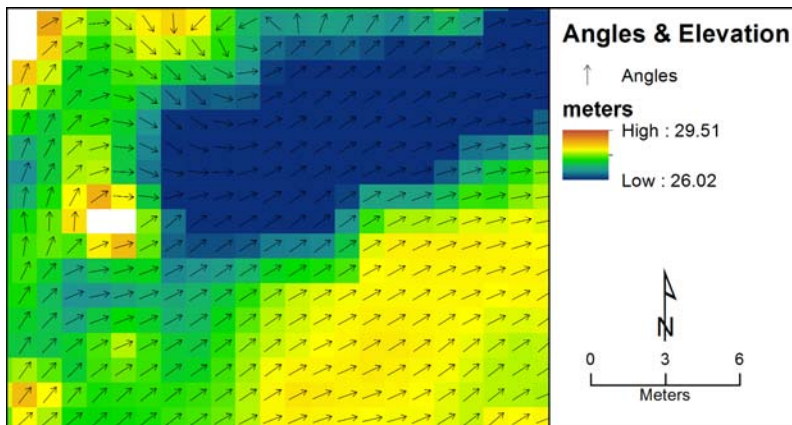


Figure 4.5. Angles derived from Cartesian vector components of discharge intensity. Elevation information used in this example comes from the low discharge (Q1) condition of the Goliad study reach.

This stream coordinate system was informed by a centerline of water extent that corresponds to the highest flow condition studied for a particular reach. This centerline was

densified and split at one meter increments to yield points spaced at one meter. These points were given distance along the centerline from upstream to downstream by using linear referencing in ArcGIS® Desktop. With distance and position, the tangent angle of each point along the centerline was derived.

The angle of the closest point on the point-centerline was associated with each data point. As a result, there is the angle associated with the discharge intensity of each point and the angle of the closest centerline point. With two angles, an arithmetic angle and centerline angle, a minimum difference between these angles was calculated for each point and then a new fixed angle was created from this difference. Fixed angles were then resolved into component vectors of velocity magnitude. The final step was to convert the points back into TIFF images for each component of velocity magnitude (Figure 4.6).

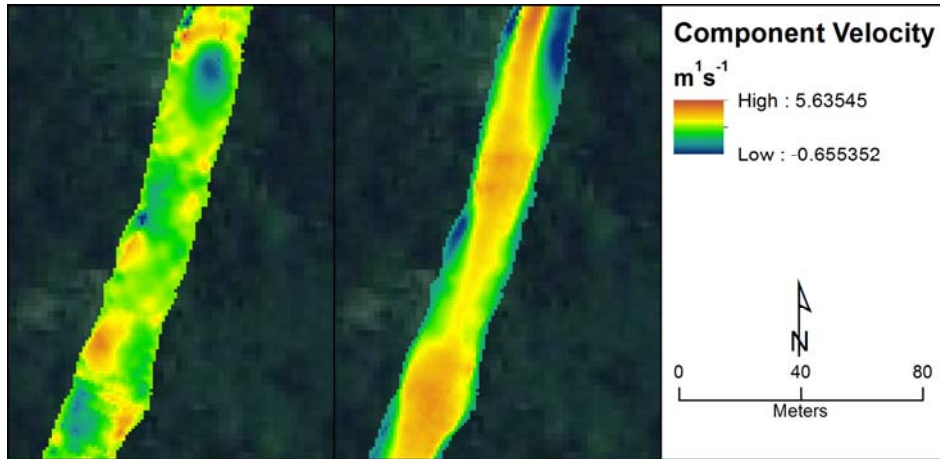


Figure 4.6. Component velocity for Cibolo Creek that consists of stream normal velocity (left) and streamwise velocity (right). Background imagery is obtained from Texas Orthoimagery Program.

To make findings of River2D® relatable to other results, shear stress (τ_B) was calculated from shear velocity (U^*) as $\tau_B = (U^*)^2 \times \rho$, where ρ is the mass density of water at 20°C and 1 atmosphere (i.e., 998.2067 kg/m^3). In addition, the extreme values of shear stress, which were observed at particular locations near roughness features, were filtered out.

4.5. ANALYSIS OF MODEL OUTPUT PARAMETERS

We first segregated model results into topographic highs (i.e., Classes (1)–(4)), representing riffles/sediment bars (i.e., non-margin or mid-channel units) and channel edges (i.e., margin units) and lows (i.e., classes (-4)–(-1)), representing pool units (see *Sections* 4.1–4.2 on the detrending and geomorphic classification procedures). Then, we considered hydraulic variables obtained directly or derived from River2D® (see *Section* 4.4 for a detailed discussion) as collections of point observations at resolution equivalent to the rasters discussed earlier (one meter) in *Section* 4.4.

We examined the distribution of hydraulic variable values (Table 4.1) obtained from River2D® models in relation to geomorphic properties of the study reach and also for the modeled discharges. For this purpose, we analyzed these distributions using 1) histograms, 2) 2D plots, and 3) 3D plots.

We presented the distribution of the model output parameter values using the histograms of the distribution of 1) topographic highs (riffles/bars/edges), 2) topographic lows (pools), and 3) all point observations (where topographic highs and lows were stacked together). Histograms for certain model output parameters, such as Froude number, were observed to have very large ranges that caused the resulting histograms to become artificially leptokurtic for a reasonable amount of bins. To address this issue, we selectively filtered model outputs for both topographic highs and lows according to an extreme outlier criterion (Ott and Longnecker, 2010). According to this criterion, the data are filtered by finding the interquartile range (IQR) value that is found by subtracting value at 25% of sorted data from the value at 75% and excluding values below the first quartile (value at 25% of sorted data) minus a quantity three times the IQR and values above the third quartile (value at 75% of sorted data) plus a quantity three times the IQR. If the minima of the data are higher than the low extreme outlier criterion, then no values were removed, and likewise if the maxima of the data are lower than the high extreme outlier criterion.

We calculated the lowest and highest filtered value that would be applied as common constraint between the topographic high and low model output as the lowest filtered value between the two outputs at all flow stages and the highest filtered value, respectively. We partitioned the range of the highest and lowest filtered values into 20 sections represented by 21 bin edges. Centers for these bins were found by calculating the midpoint for all partitions. The result was 20 common bin centers that we used in the topographic low, high, and combined (i.e.,

topographic high and low stacked) histograms for each model output parameter at each flow regime (*i.e.*, Q1–Q5/Q6).

Plots of water depth and velocity are among the most universally used tools used to understand the hydraulic environment for a given reach. We developed 2D plots to describe the relationships between water depth and velocity for different discharges; and thus, analyze the hydraulic characteristics of the reach in relation to channel morphology in the study sites. Specifically, we aimed to visualize the distribution of the values of modeled hydraulic variables along the geomorphic classes in relation to the water depth and also as categorized for critical hydraulic variable, Froude number (Fr). In addition to 2D plots, we also developed 3D version of these plots where we partitioned the information presented in 2D plots (for the whole channel morphological classes, *i.e.*, geomorphic units) to finer geomorphic classes. For this purpose, we specifically used topographic residual classes (Figure 4.2). We generated the 3D plots for Froude number (Fr). The 3D plots can be seen as the visualizations of the spatial distribution of hydraulic variable values within the finer geomorphic units. The visualization plots, including histograms, 2D, and 3D plots, are also accompanied by maps presenting the spatial distribution of the values of hydraulic variables under examination. We also evaluated the spatial distributions, arrangement of these hydraulic variables, and their relation to channel morphology and to discharge conditions.

5. THE GOLIAD STUDY REACH

The Goliad study reach (Figure 5.1) is one of the study sites on the LSAR (Figure 3.3). This reach is located on LSAR Segment 2 and Reach 3 (Figures 3.1–3.2; TIFP and SARA (2011, 2012)).

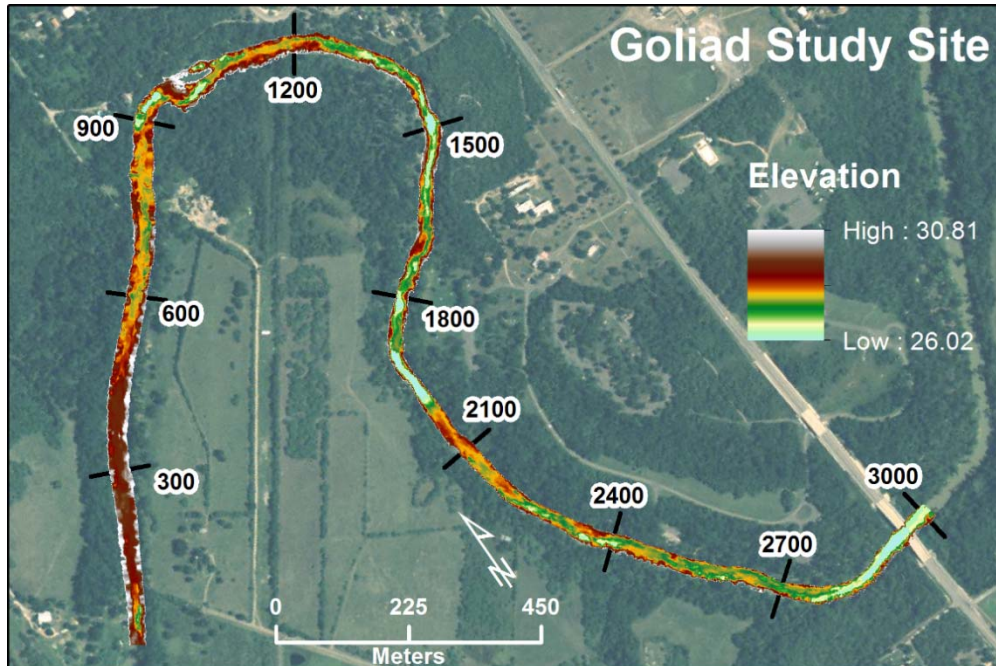


Figure 5.1. The Goliad study reach and its bathymetric distribution.

5.1. GEOMORPHIC CHARACTERISTICS

To determine the geomorphic characteristics of the river channel at the Goliad study reach, first we detrended channel topography using the approach discussed in *Section 4.1* (Figure 4.2). Then, we determined the geomorphic unit classes as topographic highs (sediment bars/riffles/edges) and topographic lows (pools) from the topographic residuals. We subclassified the topographic highs and lows according to the quartiles of the detrended topographic elevations (i.e., geomorphic unit classes named as (+1)–(+4) for topographic highs and (-1)–(-4) for topographic lows, respectively; Figures 4.2 and 5.2).

The distribution of geomorphic unit classes indicates that topographic highs (sediment bars/riffles/edges, corresponding to the classes (+1)–(+4)) account for roughly 72% of the total channel area. The remaining (28%) of the channel is composed of topographic lows (pools, corresponding to the classes (-1)–(-4); Table 5.2, Figures 5.2 and 5.3).

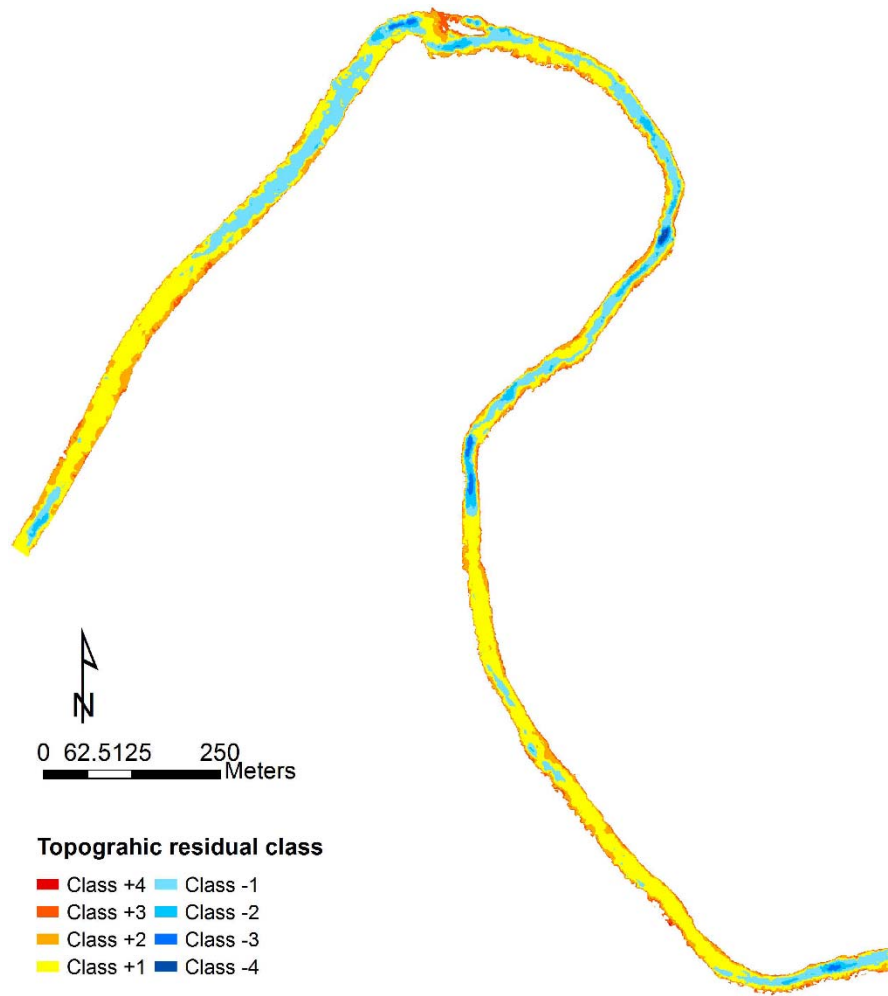


Figure 5.2. Geomorphic unit classes for the Goliad study reach based on the topographic residuals. The (+) classes represent the topographic highs and (-) classes represent topographic lows. Detailed class descriptions are given in Figure 4.2. Flow direction is from left to right.

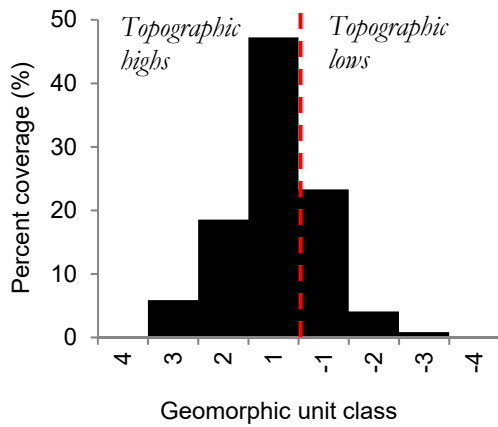


Figure 5.3. Percent coverage of geomorphic unit classes for the Goliad study reach. The (+) classes represent the topographic highs and (-) classes represent topographic lows. Detailed class descriptions are given in Figure 4.2.

Table 5.1. Areal distribution of geomorphic unit classes in the Goliad study reach.

Geomorphic Unit Class (Topographic residual percentile)	Total area (m ²)	Percent coverage (%)	Patch Statistics					
			Mean area (m ²)	Min area (m ²)	Max area (m ²)	StDev (m ²)	Patches (Number)	
Topo Highs (bars/riffles/ edges)	+4 (75-100th)	20	0.02	3.33	1	14	4.78	6
	+3 (50-75th)	5393	5.86	4.22	1	480	15.51	1278
	+2 (25-50th)	17060	18.54	26.29	1	1126	85.65	649
	+1 (0-25th)	43431	47.21	248.18	1	16233	1581.54	175
Topo Lows (pools)	-1 (0-25th)	21437	23.30	186.41	1	7094	809.65	115
	-2 (25-50th)	3766	4.09	66.07	1	693	129.36	57
	-3 (50-75th)	768	0.83	69.82	1	182	65.60	11
	-4 (75-100th)	130	0.14	65.00	2	128	63.00	2

Total area: Total area of a specific class (m²).

Percent (%) coverage: Percentage of the area of a specific class within the total area (%).

Geomorphic Unit Class Patch statistics:

Mean area: Average patch area of individual patches within a class (m²).

Minimum area: Minimum patch area within a specific class (m²).

Maximum area: Maximum patch area within a specific class (m²).

STDev: Standard deviation of patch areas around the mean within a specific class (m²).

Patches: Number of separate patches for each class (Number).

Spatially, the distributions of topographic highs and lows are somewhat patchy (Figure 5.2). Overall, the topographic highs classes +3 and +4 correspond to the channel margins/edges throughout the study reach (Figure 5.2, Table 5.1). However, slightly downstream of the channel entrance and also within the second half of the reach, topographic high class (+1) is dominant (Figure 5.2). The spatial distribution of the topographic lows (pools) indicates that pools are more localized than sediment bars and riffles; especially in the river sections where the channel curvature is high. The deepest pools (i.e., classes -3 and -4) cover less than 1% of the study area (Table 5.1).

Basic patch statistics show that while the lowest portion of the topographic highs (i.e., class +1) has the highest range of patch areas (1–2719 m²), with a mean of 248.18 m² and a STDev of 1581.54 m², the highest portion of topographic lows (i.e., class -1) has the greatest range of patch sizes (1–7094 m²), with a mean of 186.41 m² and STDev of 809.65 m² (Table 5.1).

5.2. RELATIONSHIPS BETWEEN GEOMORPHIC UNITS AND HYDRAULIC PROPERTIES

We examined the relationships between geomorphic units (Figure 4.2) and the hydraulic properties of the reach. We obtained these hydraulic properties from the simulations performed using River2D® model developed for the study reach (TIFP and SARA, 2011) at six different discharge conditions, Q1–Q6. Three of these modeled discharges, low, medium, and high

discharges (Q2, Q3, and Q5, respectively) correspond to the base level discharges defined as dry, normal, and wet conditions (Table 5.2). Table 5.2 presents the information on the study reach and model input parameters for River2D® models.

Table 5.2. Information on the Goliad study reach and model input parameters for River2D® model.

Class	Discharge for base levels		Modeled discharge		Field reported discharge		Assessment of field Q	Field data collection date	Type of field data
	(m3/s)	(cfs)	(m3/s)	(cfs)	(m3/s)	(cfs)			
Dry	4.81	170	0.85	30	–	–	Q1 (<Q2)	–	–
			3.40	120	3.371	119	Low (Q2)	6/19/2009	Habitat**
Normal	8.21	290	8.49	300	8.269	292	Medium (Q3)	7/27/2010	Habitat
			14.15	500	–	–	Q4	–	–
Wet	14.16	500	28.74	1015	30.59	1080	High (Q5)	2/1/2010	Habitat
			35.40	1250	–	–	Q6 (>Q5)	–	–

*Base levels are defined by observing fish habitat weighted usable area (WUA) (River2D) (TIFP, 2011; pg. 71, http://www.twdb.state.tx.us/surfacewater/flows/instream/lower_san_antonio/doc/LSAR_FINAL_INTERIM_REPORT_20110831.pdf)

Dry: typically based on minimum to get 20% habitat available for each guild.

Average: typically based on flow to get at least 50% habitat available for each guild.

Wet: typically based on analysis of WUA for habitat degradation.

Table 5.3 summarizes the minimum and maximum values of the hydraulic variables obtained from River2D® models for each discharge condition, from Q1 to Q6 (Table 5.2).

Table 5.3. Summary of River2D® model output parameters and min-max values for modeled discharges, Q1–Q6 for the Goliad study reach (Table 5.2).

Model output parameters	Modeled discharge $\begin{pmatrix} \text{min} \\ \text{max} \end{pmatrix}$					
	Q1	Q2	Q3	Q4	Q5	Q6
Water depth (m)	0.020	0.020	0.020	0.020	0.020	-0.75
	2.845	3.056	3.320	3.556	4.115	4.324
Froude number (–)	0.000	0.000	0.000	0.000	0.000	0.000
	2.736	4.832	2.520	5.083	6.891	3.554
Velocity magnitude (m/s)	0.000	0.000	0.000	0.000	0.000	0.000
	1.836	2.324	2.001	3.039	3.495	2.169
Streamwise velocity (m/s)	-0.626	-0.843	-1.260	-0.994	-1.262	-0.957
	1.836	2.241	2.001	2.985	3.418	2.039
Normal velocity (m/s)	-1.074	-0.903	-0.921	-1.246	-3.462	-1.195
	1.096	1.100	0.989	1.604	2.967	1.135
Shear stress (kg / (m × s ²))	0.000	0.000	0.000	0.000	0.000	0.000
	86.821	83.452	92.578	93.684	99.604	96.894
WSE (m)	28.347	28.593	28.904	29.158	29.764	29.958
	29.541	29.730	29.974	30.162	30.582	30.761

The relationship between discharge and inundated area shows that there is a relatively high change between flow stages for Q1 and Q2. Beyond this large discharge change, the change in inundated area decreases as the discharge increases (Figure 5.4). Overall, the relationship appears to be logarithmic (inundated area = $8368.4 \times \ln(Q) + 60907$, with an R^2 of 0.9872).

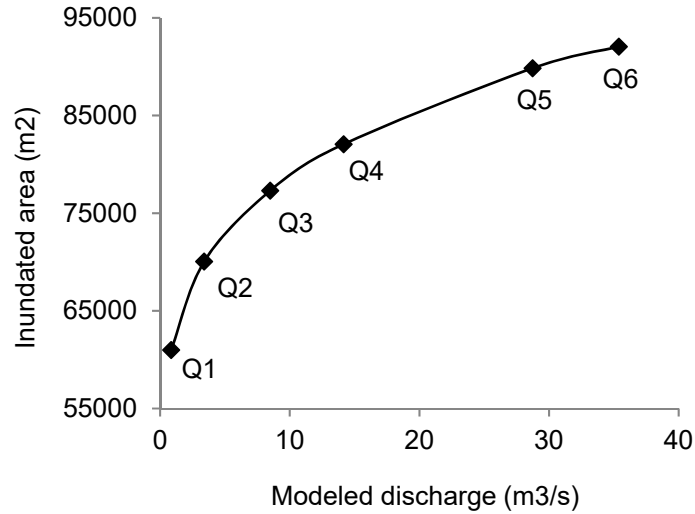


Figure 5.4. Inundated area (m²) vs. modeled discharge (m³/s) for the Goliad study reach.

We examined the distribution of hydraulic variable values (Table 5.3) obtained from River2D® models in relation to geomorphic properties of the study reach and for the modeled discharges, Q1–Q6 (Table 5.2). For this purpose, we analyzed these distributions as discussed in *Section 4.5*.

5.3. WATER DEPTH AND FROUDE NUMBER DISTRIBUTIONS

At the lowest discharge (Q1), water depth for the Goliad study reach starts out as positively skewed on topographic high, low, and combined (stacked) distribution (Table 5.2; Figure 5.5). As the discharge increases, the water depths for topographic lows stays as positively skewed, with mode shifting in a positive direction toward higher water depth values (from around 0.6 meters to 2.2 meters) as expected. This shift occurs faster for discharge levels from Q3 to Q6. For topographic highs, on the other hand, the water depth first appears nearly Gaussian (at Q3) and becomes more negatively skewed as the discharge increases from Q4 to Q6. For combined distribution, the transition to negative skew occurs at Q4 as well. In addition, starting at Q4, water depth becomes widely distributed and slightly bimodal as discharge

approaches high discharge levels Q5 and Q6, characterizing a separation between the depths associated with topographic highs and lows (Table 5.1, Figure 5.5).

At the lowest discharge (Q1), the distribution for Froude number is leptokurtic with a pattern similar to exponential decay for topographic highs, lows, and combined distributions (Figure 5.6). At Q1, the dominant Fr number range is within the lowest range ($Fr = 0-0.04$). This implies that there is flow homogeneity at this condition. Discharge condition Q2 shows a change in the distribution for topographic lows—where it changes from exponential decay to the positive side of a flattened Gaussian-like distribution (Figure 5.6).

The Fr number distribution for the topographic highs is more platykurtic and the positive tail is extended to a minor/secondary mode. The change in the distribution for topographic lows as the discharge increases is reflected in the combined distributions with the presence of the secondary mode. The emergence of the secondary mode is likely because that the flow is becoming more heterogeneous due to the introduction of shallow depths as the wetted extent of the channel widens at higher flow conditions, and velocity magnitude increases in areas associated with the topographic lows. This evolution in the distribution continues until Q6, where distribution of topographic highs are clearly bimodal with the lowest range ($Fr = 0-0.04$) having 20% of all counts and the other mode ($Fr \sim 0.25$) has slightly more than 10% of all values. The distribution for topographic lows represents a Gaussian distribution with negative skew (Figure 5.6).

All locations demonstrate a shape that is bimodal with the first mode corresponding to nearly all topographic highs and the second mode having minor contribution from topographic lows (Figure 5.6). This implies that there are two separate distributions for Froude numbers. There are many low Froude numbers in topographic highs and there are also higher Froude numbers with nearly equal contribution from topographic highs and lows. This could be construed as margin effects being the lesser Froude number mode and a core of higher velocity at the greater Froude number mode. These distributions hint at the fact that there is a relationship between Froude number values and geomorphic unit classes, but this relationship changes as discharge increases.

5.4. VELOCITY MAGNITUDE

5.4.1. *Velocity Magnitude Distribution*

At the lowest discharge, Q1 (Table 5.2), the distribution of velocity magnitudes is very leptokurtic and exponentially decaying for both topographic highs and lows, showing majority of the reach experiences very low velocities (0–0.35 m/s) (Figure 5.7). At Q2, the velocity magnitude features a second mode for topographic highs with a value of around 0.2 m/s. For topographic lows, the distribution of flow velocity magnitudes is still unimodal, but the shape evolves from a very leptokurtic distribution to a more rounded, positively skewed distribution, as the discharge increases from Q1 to Q3, with the mode being around or less than 0.5 m/s. Starting with Q4/Q5, it becomes negatively skewed as stage increases, and with the mode shifting toward higher values from 0.5 to 1 m/s (Figure 5.7).

Overall, the second mode of the velocity magnitude distribution for the topographic highs at low discharge Q2 is less apparent. At intermediate discharge Q3, the alternate mode starts emerging; however, the distribution for the topographic lows is still unimodal (Figure 5.7). As the discharge increases, the bimodality becomes more pronounced and apparent in the velocities for topographic highs, also reflected in combined distributions. This shows the difference in the influence of increasing discharge on topographic highs and lows (Figure 5.7).

5.4.2. *Velocity Magnitude Spatial Distribution*

At low discharge, higher velocity magnitudes are clustered around the areas of constricted flow, for example, in the region A, and the extreme values tend to occur near roughness elements, such as at the region B (Figure 5.8). As the discharge increases, the core of high velocity occurs at locations where the channel is less obstructed by complex margins or edge effects. A particular dynamic is at the region B (Figure 5.8). At Q1, with the region B can be characterized by a small inlet protruding from reach. As discharge increases, this feature evolves into a mid-channel bar as the flow gets connected between the outer tip of the inlet and the main stream (Figure 5.8).

5.4.3. *Velocity Magnitude Relationships*

For the discharge Q1, which is lower than the base level defined as “dry” (Table 5.2), the shape of the envelope around the distribution of the velocity magnitudes in relation to water depth represents an exponential decay pattern (Figure 5.9). Velocities associated with

geomorphic units of topographic highs and lows have a transitional zone at around 0.5-0.75 m. For geomorphic unit classes associated with topographic lows, greatest velocities are observed at the shallower depths. This is also true to a much greater extent for geomorphic units associated with topographic highs (Figure 5.9). In addition, there is a separation of the velocities for topographic lows and topographic highs. Although the velocities range around 0-0.5 m/s for the topographic lows, the range is much larger for topographic highs, being between 0 and ~1.9 m/s. At Q1, the higher velocities are concentrated around shallower areas (Figure 5.9).

As the discharge increases, the envelope around the distribution becomes more linear. The velocity magnitudes associated with topographic lows shift to higher velocity regions for the same depths as the stage increases (i.e., from 0-0.25 m/s to 0.75-0.8 m/s). On the other hand, the highest magnitudes associated with topographic highs shift toward higher depths (from 0.25 m to 1-1.5 m) (Figure 5.9).

For Q1, it may be deduced that there are locations of constricted flow that are prominent, as the topographic highs have a large range of velocity that is much greater than that of the topographic lows. By the discharge Q3, the higher velocity flow is realized as the data points that coincide with the shallow locations of discharges Q1 and Q2. As the discharge increases beyond Q3, this 'high flow' is deepened with a maximum velocity at approximately 1.5-2.0 m/s. Another distinct change in shape is evident between Q4 and Q5; the high velocity decreases slightly, and there is an expansion of the shallow zone and locations (Figure 5.9).

Figure 5.10 shows the distribution of velocity magnitude for topographic high subclasses (+1)–(+4), and topographic low subclasses (-1)–(-4), which, from ± 1 to ± 4 (Figure 4.2). The distribution is only slightly different for the classes -1 and +1 (i.e., 0-25% categories) across all discharges. -2 and +2 classes (25-50% categories) are remarkably disparate in shape. This results from the fact that ± 1 residual classes are physically very similar and ± 4 residual classes have the greatest physical separation (see for example Figure 4.2) and vary in elevation by as much as the entire range of depths shown in Table 5.3. Topographic lows tend to have a variability of velocity magnitude (< 1.5 m/s) whereas for the topographic highs, velocity magnitude varies over a wider range of values (0-3.5 m/s) in relation to water depth. The greatest positive class, +4, is nonexistent for Q1–Q5.

As the discharge increases, the classes ± 1 and ± 2 develop the greatest range and show clear zonation with respect to Froude number groupings (Figure 5.10). It is also evident that as the discharge increases, the areas within the lower Froude number groupings are thinned out and

those with the higher Froude numbers become more prominent (Figure 5.10). In addition, the distribution of the ± 2 classes evolves very similarly with increasing discharge. The ranges of the water depth for both classes are similar at the lowest discharge Q1; however, with increasing discharge, the range for the class +2 increases. For the ± 3 classes, separation in distribution becomes the greatest. The difference in distribution for the class ± 3 is most marked at Q1—with distinct difference in distribution and a wide gap between points associated with topographic highs and lows.

The most prominent change in the shape of the distribution occurs from Q1 to Q2 and from Q4 to Q5, with the greatest change occurring from Q4 to Q5. Another trend evident in Figure 5.10 is the dynamic control that water depth enforces on velocity range, and how this control differs for the different geomorphic unit classes. For the classes ± 1 and ± 2 , the water depth tends to have little control on range for both topographic highs and lows. For the most extreme topographic high class (i.e., +4), a marked control of depth on the range of velocity magnitude is apparent. As discharge increases, this control weakens for all classes.

5.4.4. *Summary on Velocity Magnitude Distribution*

In summary, velocity magnitude is controlled by channel geomorphology influencing water depth and boundary complexity. The distribution of velocity magnitude for topographic high/low subclasses in relation to water depth and Froude number demonstrate the effects of margin complexity where more extreme + classes (i.e., +3/4) are increase in range as discharge increases (Figure 5.10). Areas of concentrated flow, which are common at low discharges, tend to generate high velocities. An example for this is in region B at Q2/Q3 (Figure 5.8), where mid-channel bars obstruct flow and lead to increased magnitudes of flow velocity at this region. In terms of water depth control, a specific example is the decrease in velocity magnitude at the second topographic low region, downstream of region A at Q1. Increase in discharge tends to reduce the effect of channel complexity (Figure 5.8).

5.5. **STREAMWISE VELOCITY DISTRIBUTION**

5.5.1. *Streamwise Velocity Distribution*

Streamwise velocity distribution takes on a pattern (Figure 5.11) analogous to that of velocity magnitude (Figure 5.7). However, it is very important to note that there is a very thin tail at all discharge conditions that have values that are below 0 (Figure 5.11). These negative

velocities correspond to backwater regions along the channel. Another notable difference is the decrease in value for the bin that would be closest to zero velocities. This change is more evident in higher discharge conditions (Q4–Q6). Just as in velocity magnitude distributions (Figure 5.7), the distributions of streamwise velocity become more platykurtic and bimodal as discharge increases (Figure 5.11).

5.5.2. *Streamwise Velocity Spatial Distribution*

Overall, the spatial distribution of streamwise velocity is quite similar to that of velocity magnitude, with the exception of backwaters (Figure 5.12). The backwaters for the Goliad study reach are located at channel margins that are complex or that change dramatically with respect to flow centerline. Overall, there is little increase in locations of backwaters as discharge increases. The only major exception to this observation is the dynamic location at region B (Figure 5.1). At this location, there are multiple ‘bands’ of backwaters present at higher discharges (Figure 5.12); this implies the presence of eddies, which are vortices that form at locations of increased turbulence and flow separation.

5.5.3. *Streamwise Velocity Relationships*

For all discharge conditions, the distribution of streamwise velocity in relation to water depth exhibits trends very close to those of velocity magnitude with one notable exception: the presence of negative values, corresponding to the velocities in the backwaters regions. These values appear to have a relatively constant trend after Q2. They do not appear to have the moving upward trend with a region of low point density as their positive-valued counterparts. Of course, this comparison is quite relative since the point density is far less on the negative-valued end of the distribution as opposed to the positive-valued end (Figure 5.13).

Envelope for the positive streamwise velocity values starts out at Q1 as an exponential decay patterns but it changes its nature as the discharge reaches to Q4 and beyond. As the discharge increases from Q1 to Q6, the highest streamwise velocities also start shifting toward higher water depths (Figure 5.13). This shift becomes significant especially after Q4. A clear pattern associated with the Fr number distribution for different velocities is also observable. The lowest Froude number category (0–0.0295) corresponds to very low velocities (around zero m/s). The distribution of the Froude number values is significantly related to the velocity values (Figures 5.13–5.14) as expected. As the discharge increases, the contribution to different Froude number classes from different geomorphic units changes (Figure 5.13).

The distribution of streamwise velocity in relation to water depth and Froude number (Figure 5.13) also indicates the close coupling between velocity magnitude and stream velocity. One exception to this coupling is the presence of a ‘mirror’ image on the negative end—because of the presence of backwaters. There appear to be symmetry in groupings for Froude number respect to value 0 (Figure 5.13).

Figure 5.14 shows the distribution of streamwise velocity for topographic high subclasses (+1)–(+4), and topographic low subclasses (-1)–(-4), which, from ± 1 to ± 4 . The positive end of the distribution is very similar to velocity magnitude. However, there is unique information on the negative-valued end of the distribution, backwaters. Overall, locations that correspond to backwaters tend to increase in magnitude and number for the less extreme geomorphic unit classes, and tend to decrease in number and magnitude for the more extreme classes. For all discharge conditions, backwaters have very low magnitude for all but the class ± 1 . The range of backwater does tend to increase with increasing discharge, but this increase migrates from class ± 1 to class ± 2 at flow stages Q4–Q6. A complimentary observation is that the highest amount of non-minimal groupings occur at Q3, but then begin to get smaller in succeeding discharges—migrating to class +2 (Figure 5.14). Overall, backwaters do tend to form more often for positive rather than negative geomorphic unit classes. It is likely because backwaters typically form at channel margins, and channel margins are a notably dynamic feature with increasing discharge for a given channel—heavily dependent on channel and floodplain geometry. However, this relationship is held across several positive topographic residuals, especially at region B—since flow divergence occurs at Q5/Q6.

5.5.4. *Summary on Streamwise Velocity Distribution*

Just as in velocity magnitude, stream velocity is controlled by local channel features. In fact, the results suggest that velocity magnitude is dominantly composed of stream velocity. Backwaters are present at several areas of complex wetted channel margins where flow separation would occur. A good example of this occurs at region B from Q1 to Q4 and region A from Q5 to Q6 (Figure 5.12). At region B, there is much complexity in flow environment, and distinct zones of flow separation would form at these complex shapes that diverge away from the flow path. For most of the reach, the locations of backwaters tend to decrease as channel margins become less complex. However, this effect is not gradual and most markedly occurs from Q4 to Q5.

5.6. NORMAL VELOCITY DISTRIBUTION

5.6.1. *Normal Velocity Distribution*

At Q1, the distribution of normal velocity is leptokurtic, nearly symmetric, and centered on zero for topographic highs, lows, and combined distributions (Figure 5.15). Positive values correspond to the flow toward left bank; negative values correspond to the flow toward right bank. As discharge increases to Q3, distributions are noticeably more platykurtic. Topographic highs feature expanded tails in the distribution. Cumulatively, topographic highs and lows still feature a more platykurtic distribution than those of Q1. Normal velocity features a trend of even more platykurtosis for Q4–Q6. At Q5, the distribution of topographic lows begins to be more negatively skewed, although the same cumulative shape is preserved (Figure 5.15).

5.6.2. *Normal Velocity Spatial Distribution*

The spatial distribution of normal velocity values does not change much with increasing discharge. However, dynamic regions such as the region B (Figure 5.1) tend to have varying locations and amounts of positive versus negative velocities. The distribution also appears to become more organized and evenly spaced as flow stage increases—particularly in straight reaches of study reach. In the regions A, B, and C (Figure 5.16), the maximum normal velocity is visually observed at Q4. This may be attributed to the complexity of the wetted surface or margins of the channel.

5.6.3. *Normal Velocity Relationships*

Normal velocity distribution has a bulge or expansive region of higher Froude numbers on the shallow, low end of the water depth axis for low discharges Q1/Q2 (Figure 5.17). At Q3, this region does move up to around 0.25 m, but still exclusively within the topographic high class. Above Q3, this relationship continues with an expanded region moving to 0.5 for Q4, 0.75 for Q5, and roughly 1.5 for Q5 and Q6. With respect to the topographic low classes, higher Froude numbers are not realized in any appreciable amount until Q3. In fact, Q4 also features a patch of rogue high velocity points at an associated water depth of around 2.0 to 2.5 m. This ‘burst’ of higher values at that or deeper depths does not occur in the other discharges. At Q3–Q6, the distribution of normal velocity values becomes progressively longer and thinner. The distribution can be characterized as a set of complimentary bulges that occur where clusters of lower Froude numbers are present on the deeper end of topographic high classes, and this same feature for topographic lows is the same just adjacent of topographic highs.

Distribution of the normal velocity classified for geomorphic subclasses contrast with those of velocity magnitude and stream velocity (Figure 5.18). At all discharge conditions, the less extreme positive geomorphic unit classes, +1/2, feature large ranges of velocity values on the positive and negative ends of the distribution. The less extreme negative geomorphic classes, -1/2, increase in range as discharge increases. For streamwise velocity, there appears to be a distinct zonation with deviation in Froude number classes present only at margins between classes. This is not the case for normal velocity—where low Froude number groupings spread throughout the ranges of magnitudes for normal velocity. At higher flow stages of Q5/Q6, there appears to be a preferential clustering of lower Froude number groupings at the class +1. This does not hold up for topographic low classes, indicating that water depth is a limiting factor for Froude numbers, but this depth is confined within the depths associated with topographic high classes +1/4, and thus, possibly a controlling factor for channel margin environments.

5.6.4. *Summary on Normal Velocity Distribution*

Overall, trends in normal velocity are controlled by channel planform and are not as sensitive to water depth compared to stream velocity and velocity magnitude. Spatially, the areas of high density of normal flow reversals tend to be centered at locations on the reach that feature high curvature and where topographic lows are present. It is also observed that some of the highest normal velocities occur in the very complex geomorphic region in the northeast of the study reach, where a channel bar tends to restrict flow up until flow stage Q5. The area featuring the strong negative normal velocities appears to be in this region, as suggested by region B in flow stage Q4 (Figure 5.16).

5.7. SHEAR STRESS DISTRIBUTION

5.7.1. *Shear Stress Distribution*

Distribution of shear stress is leptokurtic at low discharges, and gradually become more platykurtic as discharge increases (Figure 5.19). However, this distribution evolves differently for topographic lows and highs. As for topographic highs, the distribution takes on a flat and slightly bimodal distribution as discharge approaches Q6. Throughout all discharges, topographic highs have more low values on the distribution than those associated with topographic lows. Additionally, the occurrence of the highest shear stresses (the right most bin) is greater for topographic highs, indicating the presence of the more extreme values in areas of topographic highs. Locations associated with topographic lows demonstrate a more gradual transition from

highest bins to lowest bins and feature a single mode that moves more positively as discharge increases. Cumulatively, the distribution represents exponential decay in bin counts as bin sizes increase for all but the highest discharges (Q5/Q6). At the highest discharges, the central portion of the distribution appears to flatten out. This shape seems to be driven by locations of topographic lows. This would imply that some locations of topographic lows have higher shear stresses that are naturally grouped around a positively migrating mode—which is most likely the effect of stream velocity as the discharge increases.

5.7.2. *Shear Stress Spatial Distribution*

At the lowest discharge, Q1, the high values of shear stress are clustered around the locations of the reach that constricts the flow (Figure 5.20). These locations appear to be only in related to topographic highs; however, there are isolated locations coincident with roughness elements. As the discharge increases, locations of roughness elements are more involved and constricted flows become more prevalent. At higher discharges, there is a significant concentration of higher shear stresses along the centerline of the channel, with roughness elements enhancing the shear stress. Overall, the locations of higher shear stress values roughly coincide to those of velocity magnitude (Figure 5.20).

5.7.3. *Shear Stress Relationships*

The distribution of shear stress in relation to water depth has a very similar pattern to that of the velocity magnitude (Figure 5.21). However, there is a greater spread in terms of velocity magnitudes versus shear stress, and the groupings by Froude number are not as clear-cut; there are low Froude numbered locations across the depths for both topographic highs and lows. High values are clustered around the widest part of the distribution, which increases in depth as discharge increases—just as in velocity magnitude. These high values most likely correspond to the areas affected by roughness elements. When the distributions of velocity magnitude and shear stress compared, the high values are less prevalent in locations of topographic high classes +3/4 at all but highest discharges (Figure 5.22). For topographic low classes -1/2, shear stress values are extreme in range as well; however, these ranges decrease as for the higher subclasses. For topographic highs, it is clear that depth does not have as much control of shear stress as does velocity, and this control decreases more rapidly as the discharge increases. At the highest modeled discharge, Q6, extreme values are present in all topographic high subclasses except +4 and span the entire range of values for shear stress (Figure 5.22).

5.7.4. *Summary on Shear Stress Distribution*

Distribution of shear stress values in relation to the water depth is similar to that of velocity magnitude, implying the fact that higher velocities do contribute to higher shear stresses (Dingman, 2009). However, the results also reveal that roughness elements in the study reach also account for some significant differences in the distributions of shear stress and velocity magnitude. The effect of roughness elements can also lead to localized changes in water surface elevation. The areas of high concentrations of roughness elements, thus, can result in altered water depth and shear stress.

5.8. **SUMMARY ON THE GOLIAD STUDY REACH**

The Goliad study reach consists of a reach of the San Antonio River (Figure 3.3) that is marked by several pools or deeper features near the channel sections with high curvature (Figure 5.1). The planform of the Goliad study reach suggests a gradual decrease in elevation and only slight topographic variation at the influent portion of the reach characterized by a very low curvature. Further downstream, the topography varies significantly through pool-riffle sequences, which spatially seem to correspond to the locations of high curvature (Figure 5.1). Based on these observations, it can be deduced the planform shape of the Goliad reach influences the local morphology along the channel.

The results obtained from River2D models (IIFP and SARA, 2011) demonstrate that the river channel morphology has a large role in influencing the flow velocity magnitude. The topographic high (i.e., positive geomorphic) classes present different velocity magnitude distributions in relation to water depth than those of topographic low (i.e., negative geomorphic) classes. With increasing discharge, the velocity magnitude for topographic high subclasses +3/4 becomes more platykurtic and bimodal; it increases in mode and ‘migrates’ to higher values for the subclasses +1/2 (Figure 5.7). Most of these characteristics can be explained by the following observations. As the discharge increases, a large number of low water depth features typically have lower velocity magnitudes. These lower-velocity features explain the first mode in the distribution for topographic highs—margins. The second higher mode can be explained by a core of higher velocity that is observed at higher discharges for both topographic high and low classes. The greatest range in velocity in relation to water depth is demonstrated by this core of higher velocity as well. At low discharge, the distribution is dominated by low values at all water depths with high values occurring at only constricted and low depth zones, such as regions A,B,

and C (Figure 5.9). As discharge increases, this highest range of velocities moves into locations associated with larger water depths and eventually evolves from an exponentially decaying shape at Q1/Q2 to an exponentially increasing shape at Q6 (Figure 5.10).

This also implies that at lower discharges, high velocities are present at locations of constricted flow and low depth. However, as the discharge increases, higher velocity core develops and mostly migrates to the center of the channel covering larger areas than just localized constricted flow regions. This dynamic also has an impact on backwaters. Backwaters are typically present in locations of low flow and shallow depth. In region A, at Q1, there are two backwater areas that appear to form where a core of higher velocity would develop (Figure 5.12). As discharge increases, the backwater areas tend to shrink, although new backwater areas form at other channel margins. This phenomenon appears to be completely controlled by topography at the local channel level, and not directly by the planform. In contrast, normal velocity seems to have a much stronger planform control, as locations of positive/negative normal velocity do not tend to move dramatically in the streamwise direction with changes in stage level. An exception to this is near meter location 900 where normal velocity spatial distribution is not exclusively controlled by channel planform (Figure 5.1). As discharge increases, a flow-reconnection occurs as the side channel at region B feature forms a mid-channel bar. As a result, new normal velocity zones are created as well as dynamic behavior on the already-existing channel (Figure 5.16).

Distribution of shear stress is low for much of the reach, but elevated shear stress levels are coincident with roughness elements even at low stage (Figure 5.20). With increasing discharge, these locations coincident with roughness elements get higher in shear stress and the effect spreads to nearby locations. This dynamic behavior is primarily driven by velocity magnitude and the locations of roughness elements.

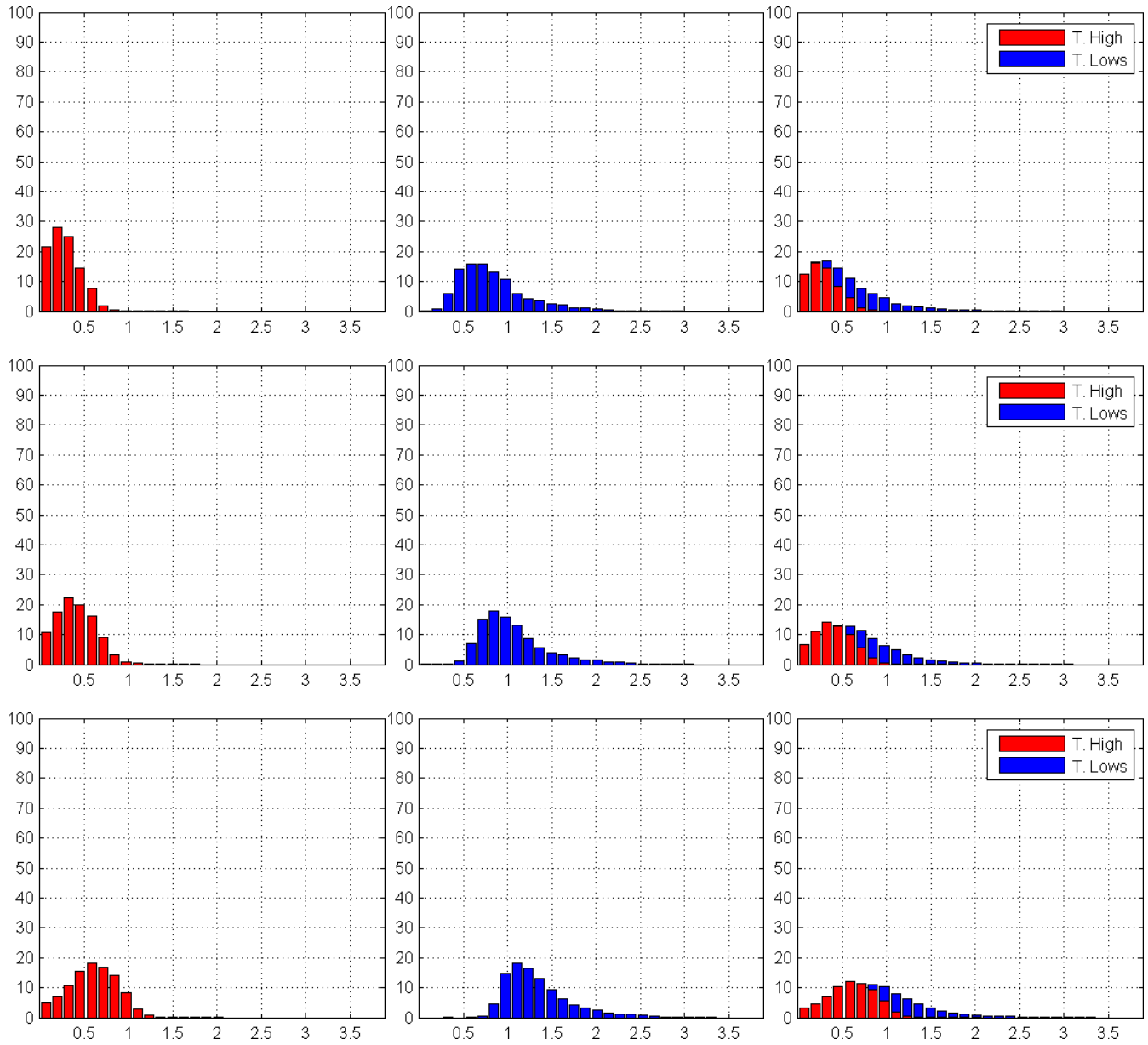


Figure 5.5. Water depth distribution for Q1–Q6 (rows, top to bottom) for topographic highs (marked as T. High) corresponding to the classes (+1)–(+4), topographic lows (marked as T. Lows) corresponding to the classes (-1)–(-4), and combined (columns, left to right). Horizontal and vertical axes correspond to water depth (m) and the percent values of topographic classes, respectively.

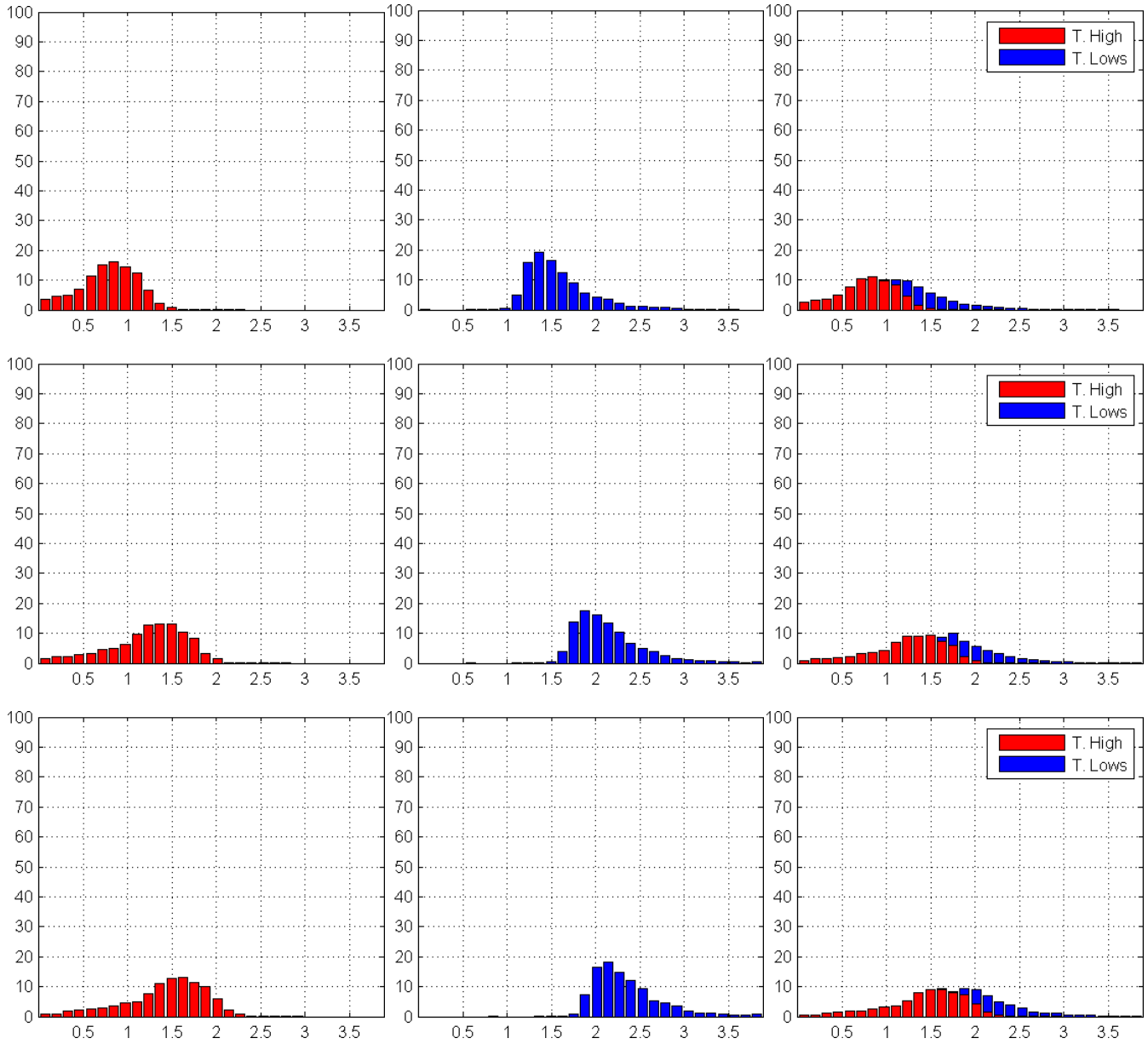


Figure 5.5 (cont'd). Water depth distribution for Q1–Q6 (rows, top to bottom) for topographic highs (marked as T. High) corresponding to the classes (+1)–(+4), topographic lows (marked as T. Low) corresponding to the classes (-1)–(-4), and combined (columns, left to right). Horizontal and vertical axes correspond to water depth (m) and the percent values of topographic classes, respectively.

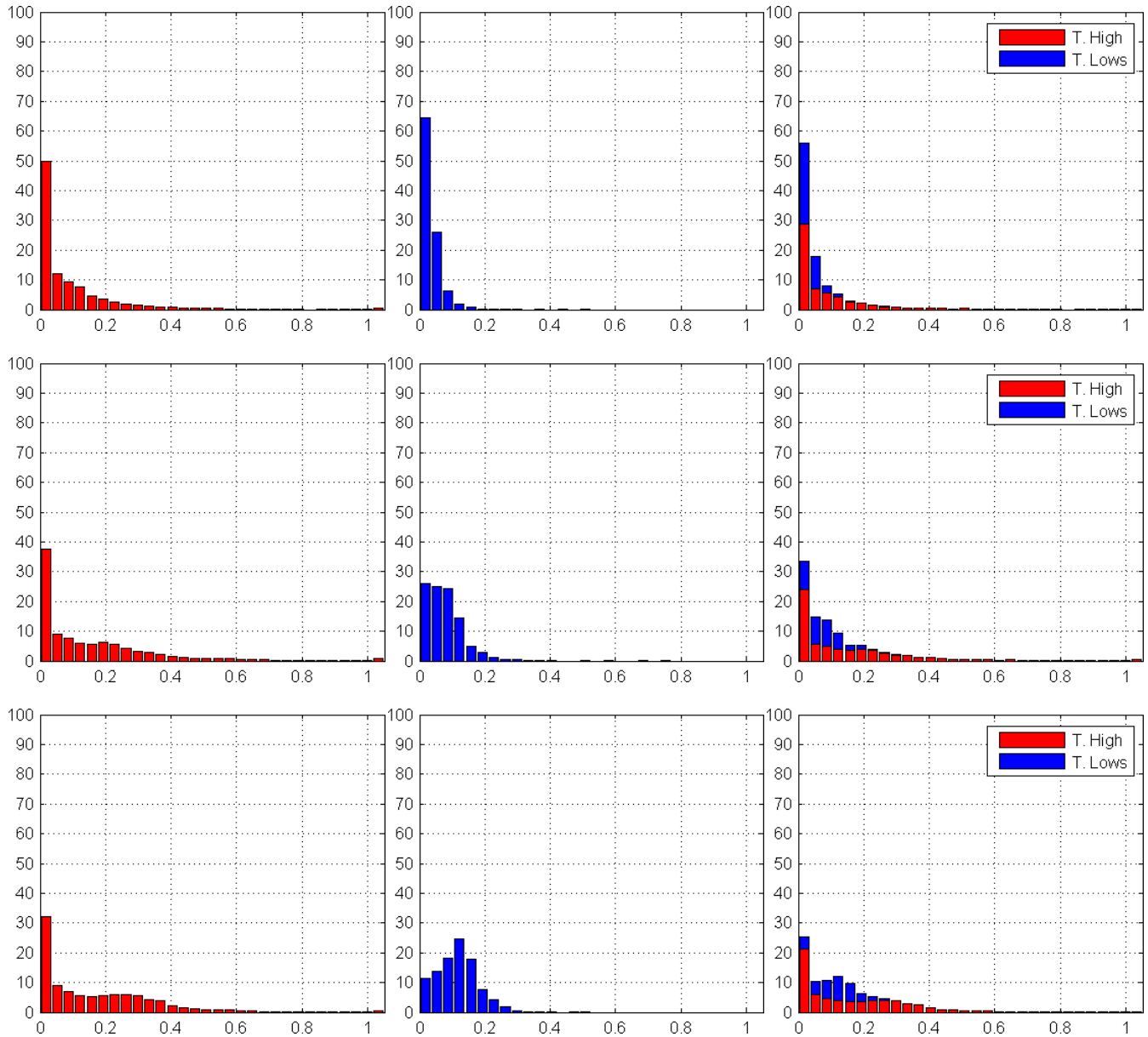


Figure 5.6. Froude number (Fr) distribution for Q1–Q6 (rows, top to bottom) for topographic highs (marked as T. High) corresponding to the classes (+1)–(+4), topographic lows (marked as T. Lows) corresponding to the classes (-1)–(-4), and combined (columns, left to right). Horizontal and vertical axes correspond to Fr and the percent values of topographic classes, respectively.

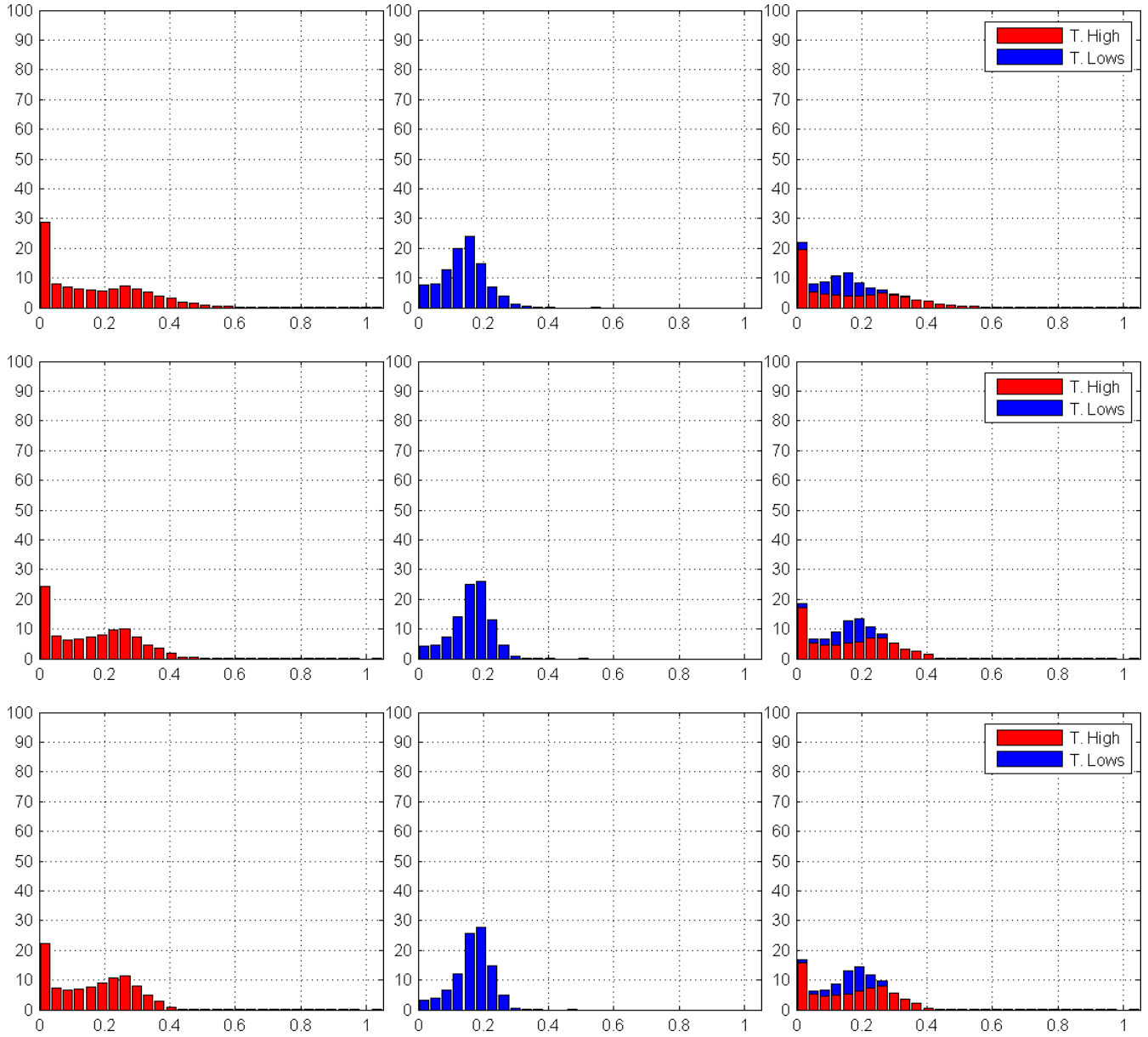


Figure 5.6 (cont'd). Froude number (Fr) distribution for Q1–Q6 (marked as T. High) corresponding to the classes (+1)–(+4), topographic lows (marked as T. Lows) corresponding to the classes (-1)–(-4), and combined (columns, left to right). Horizontal and vertical axes correspond to Fr and the percent values of topographic classes, respectively.

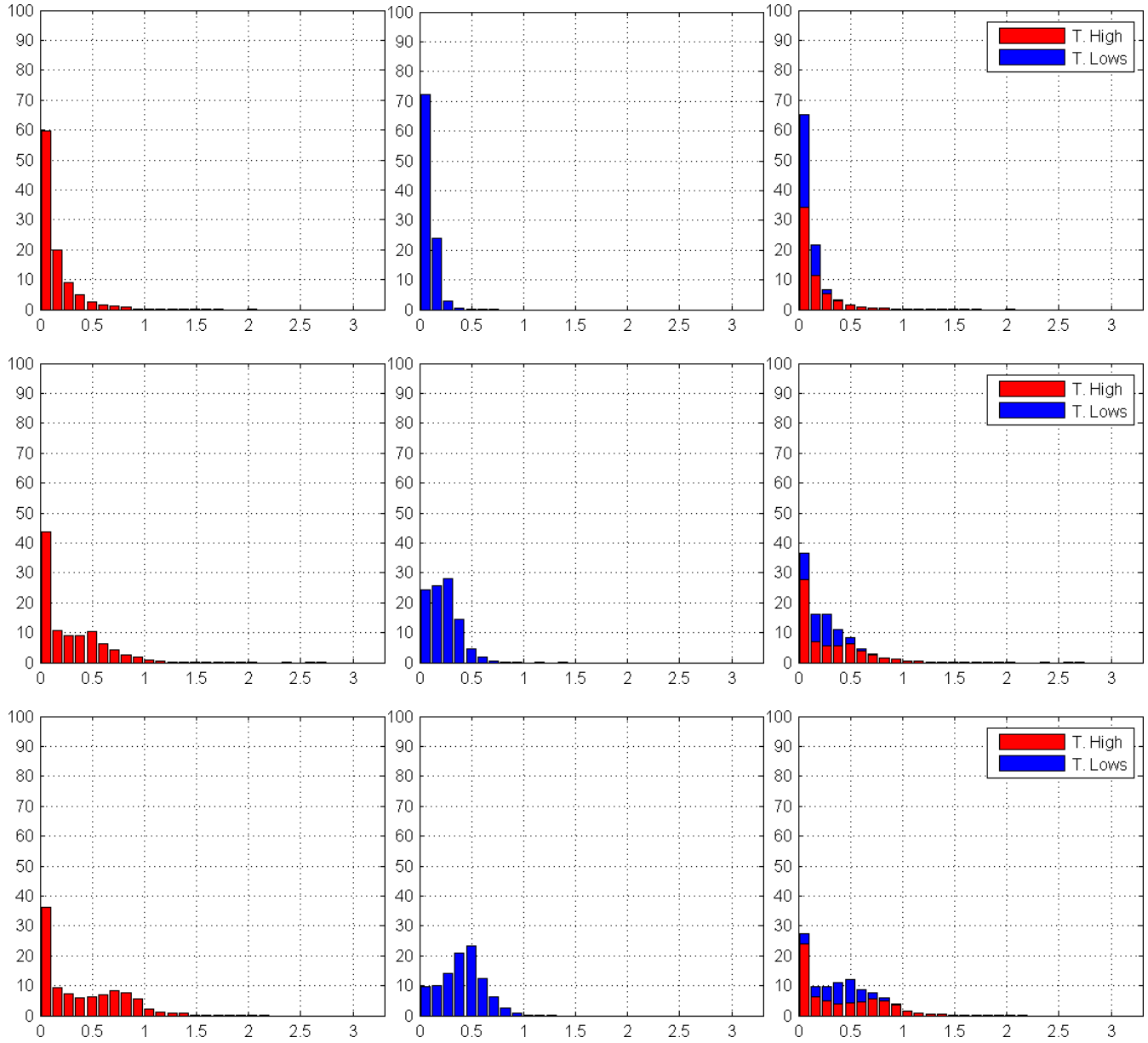


Figure 5.7. Distribution of velocity magnitude for Q1–Q6 (rows, top to bottom) for topographic highs (marked as T. High) corresponding to the classes (+1)–(+4), topographic lows (marked as T. Lows) corresponding to the classes (-1)–(-4), and combined (columns, left to right). Horizontal and vertical axes correspond to velocity magnitude (m/s) and the percent values of topographic classes, respectively.

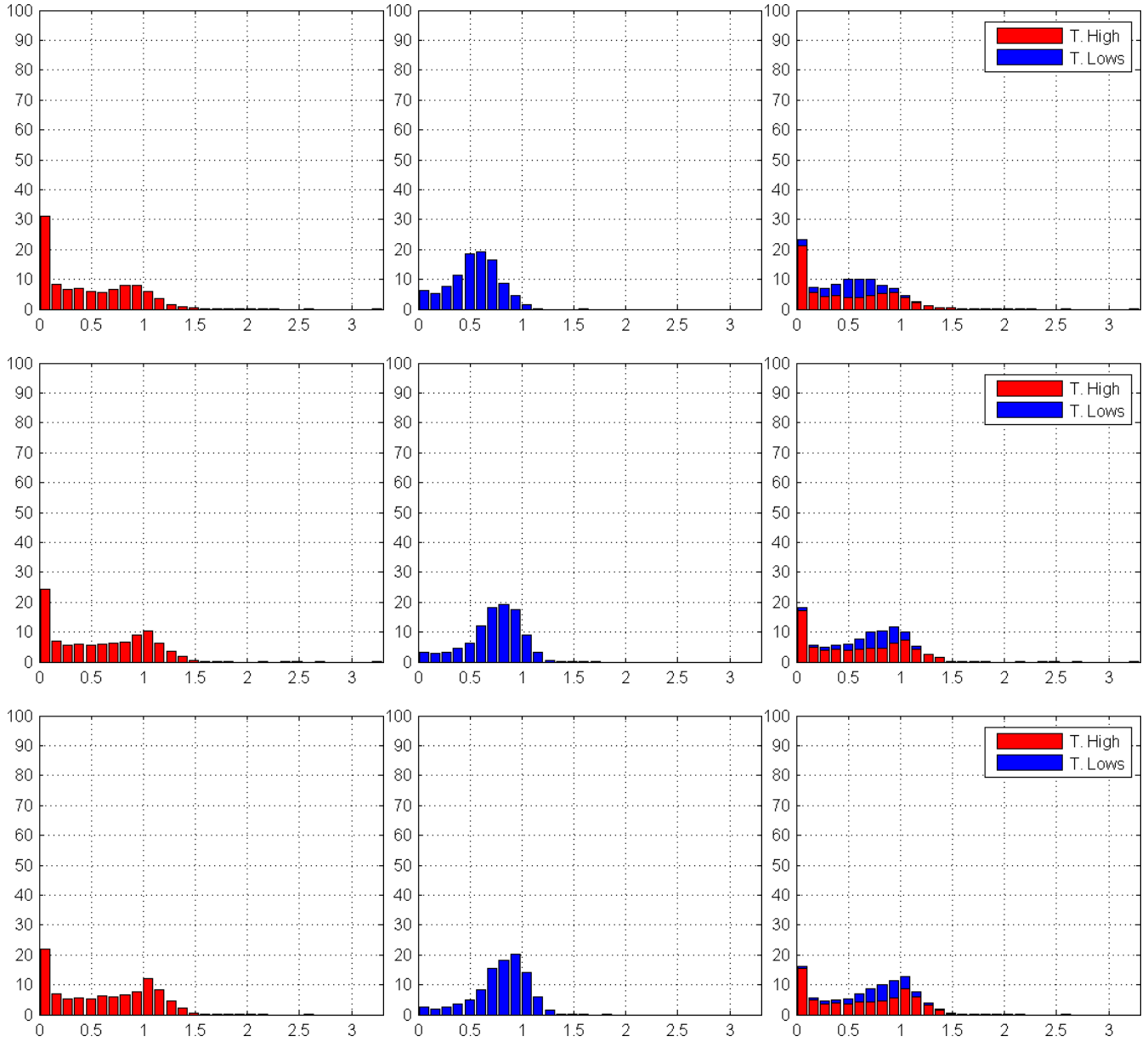


Figure 5.7 (cont'd). Distribution of velocity magnitude for Q1–Q6 (rows, top to bottom) for topographic highs (marked as T. High) corresponding to the classes (+1)–(+4), topographic lows (marked as T. Low) corresponding to the classes (-1)–(-4), and combined (columns, left to right). Horizontal and vertical axes correspond to velocity magnitude (m/s) and the percent values of topographic classes, respectively.

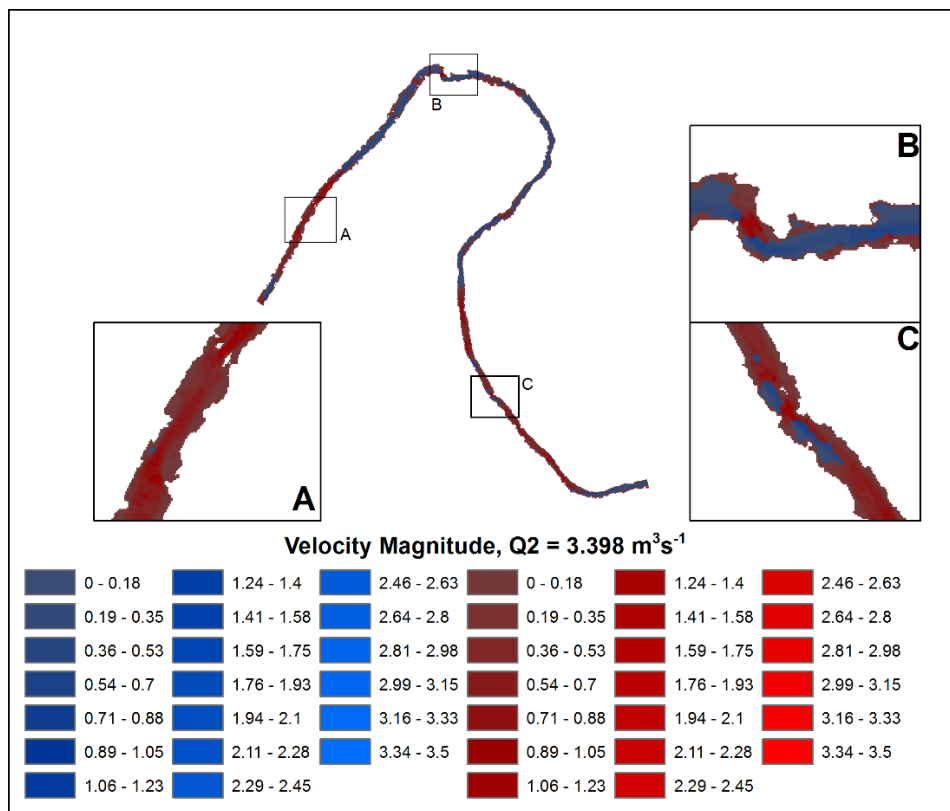
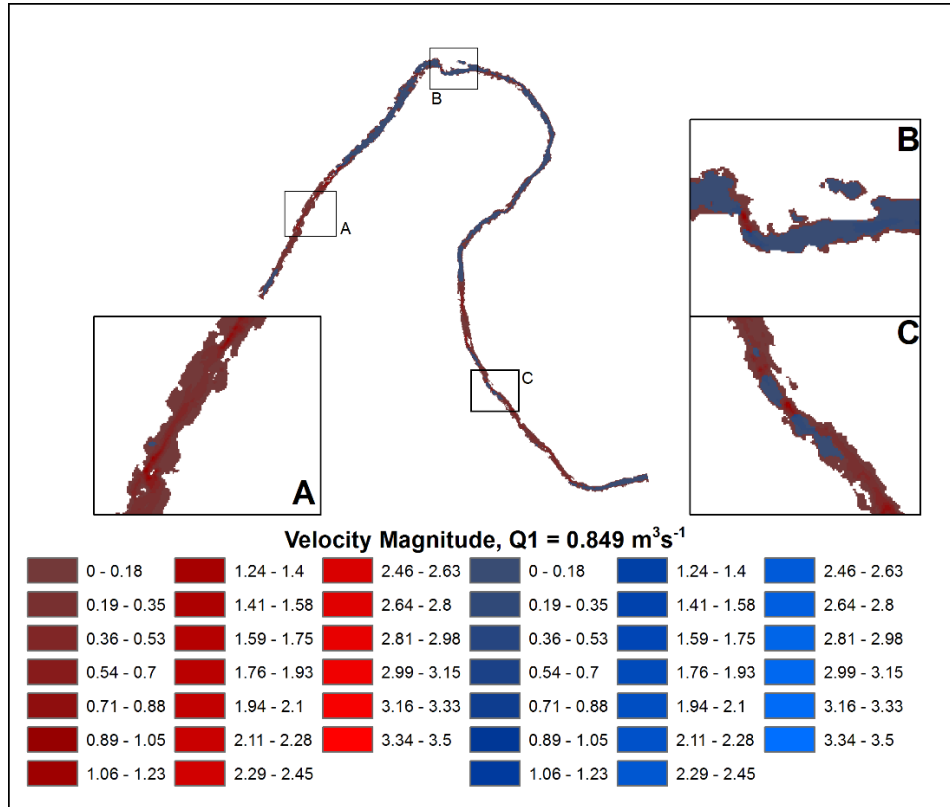


Figure 5.8. Spatial distribution of velocity magnitude (m/s) for Q1–Q6 for topographic highs (red colors) and lows (blue colors).

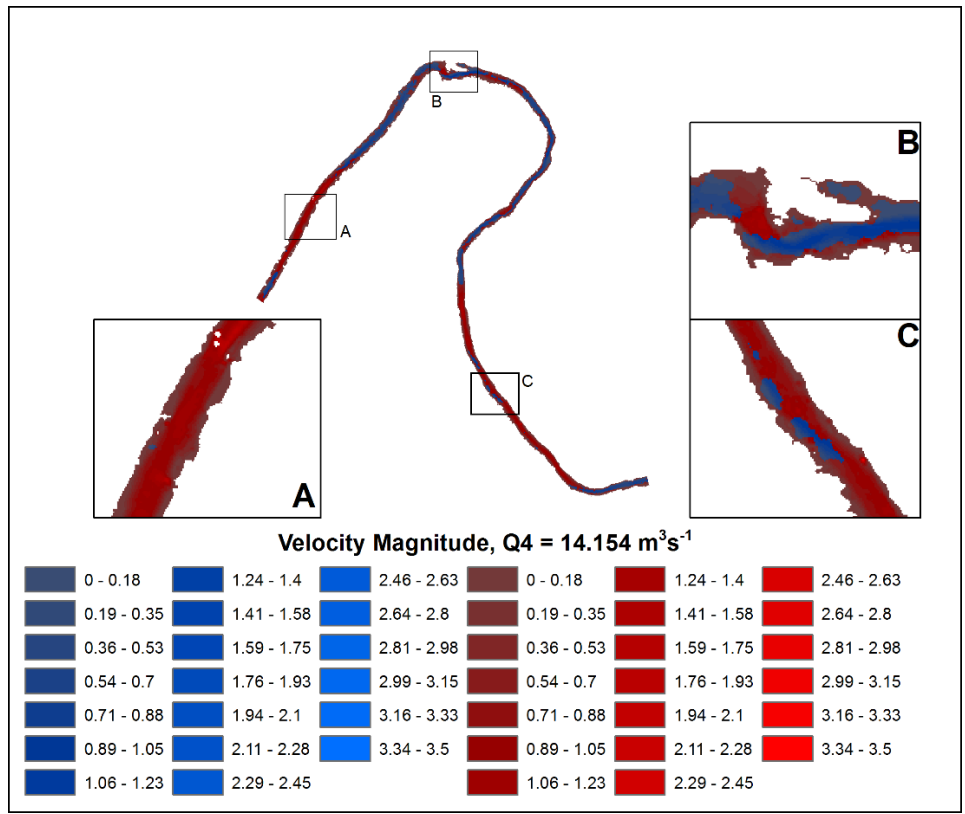
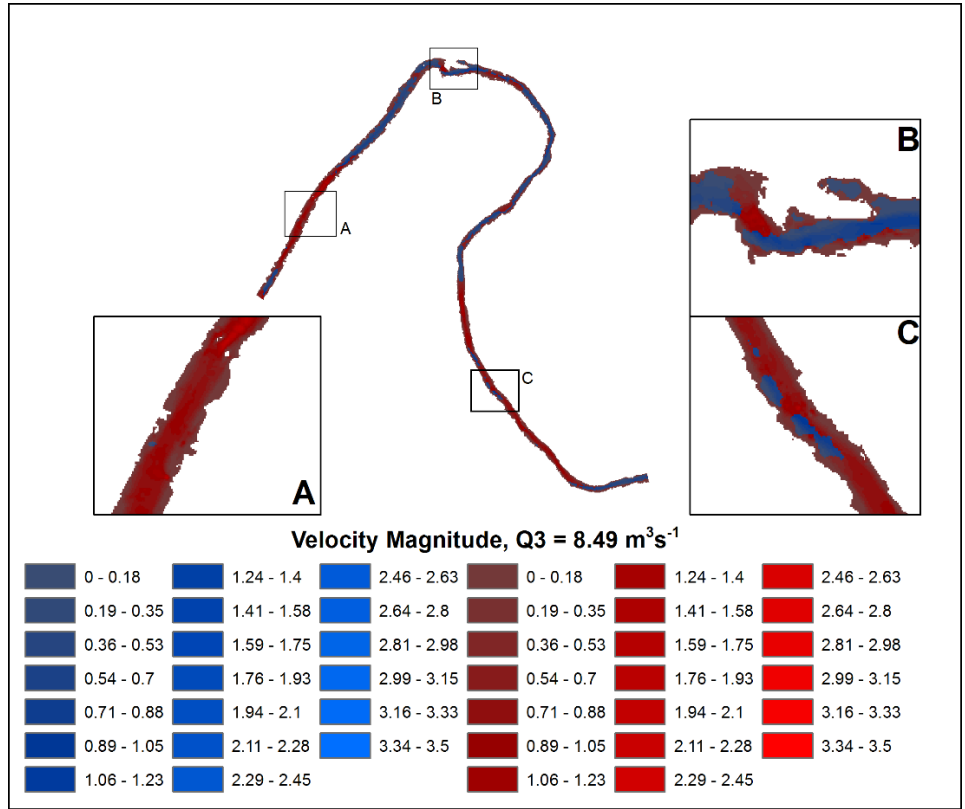


Figure 5.8 (cont'd). Spatial distribution of velocity magnitude (m/s) for Q1–Q6 for topographic highs (red colors) and lows (blue colors).

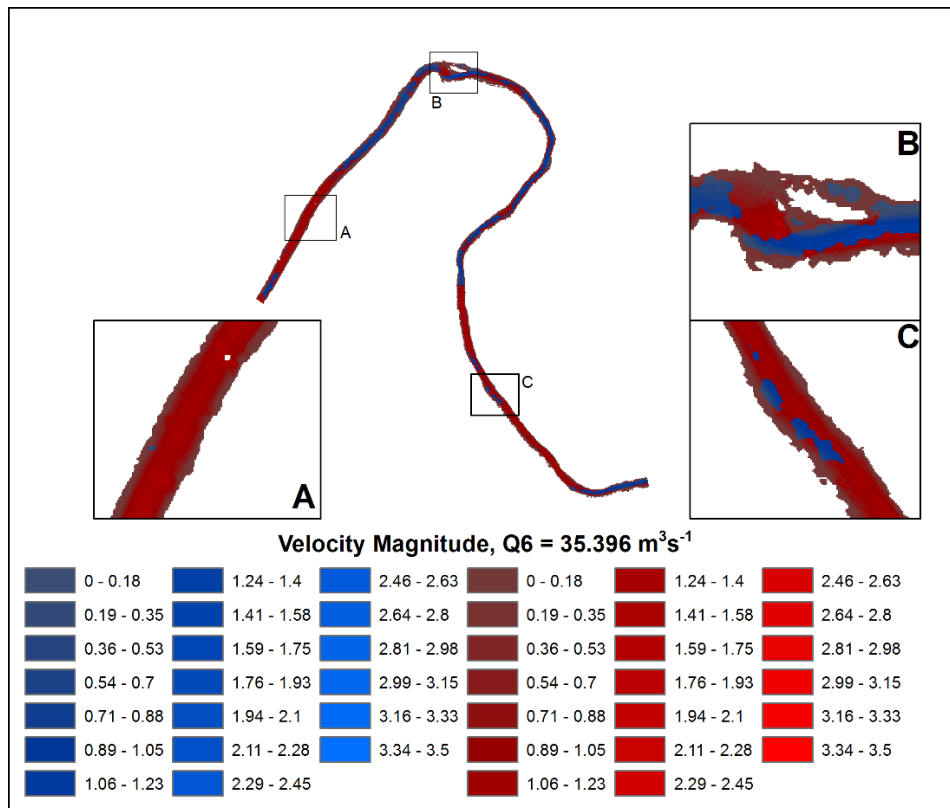
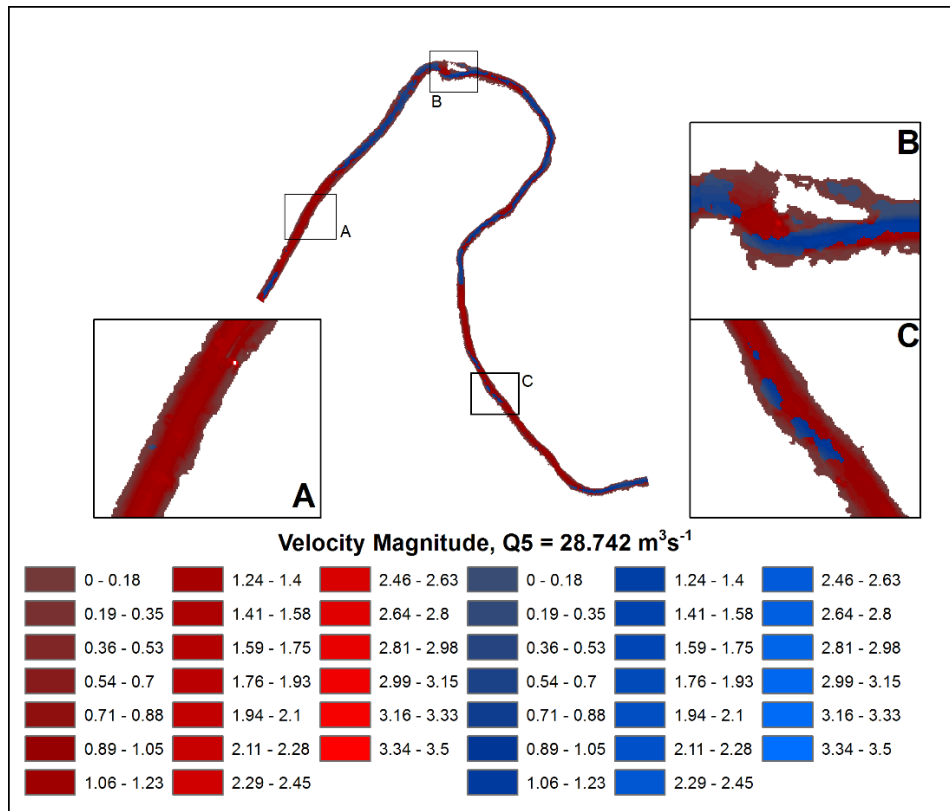


Figure 5.8 (cont'd). Spatial distribution of velocity magnitude (m/s) for Q1–Q6 for topographic highs (red colors) and lows (blue colors).

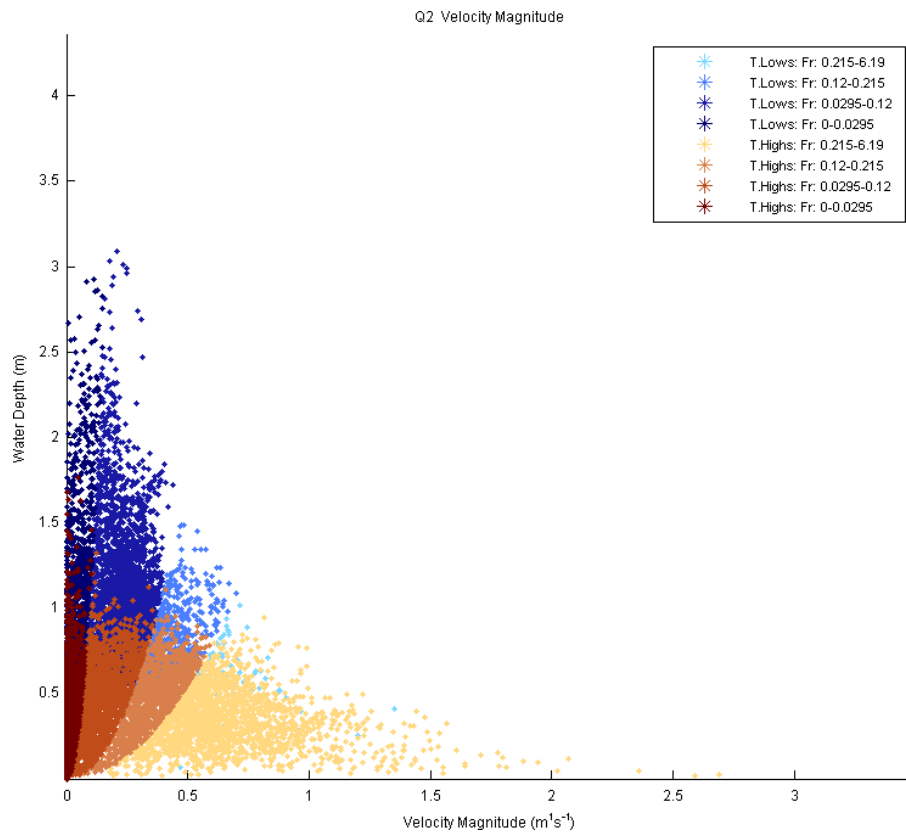
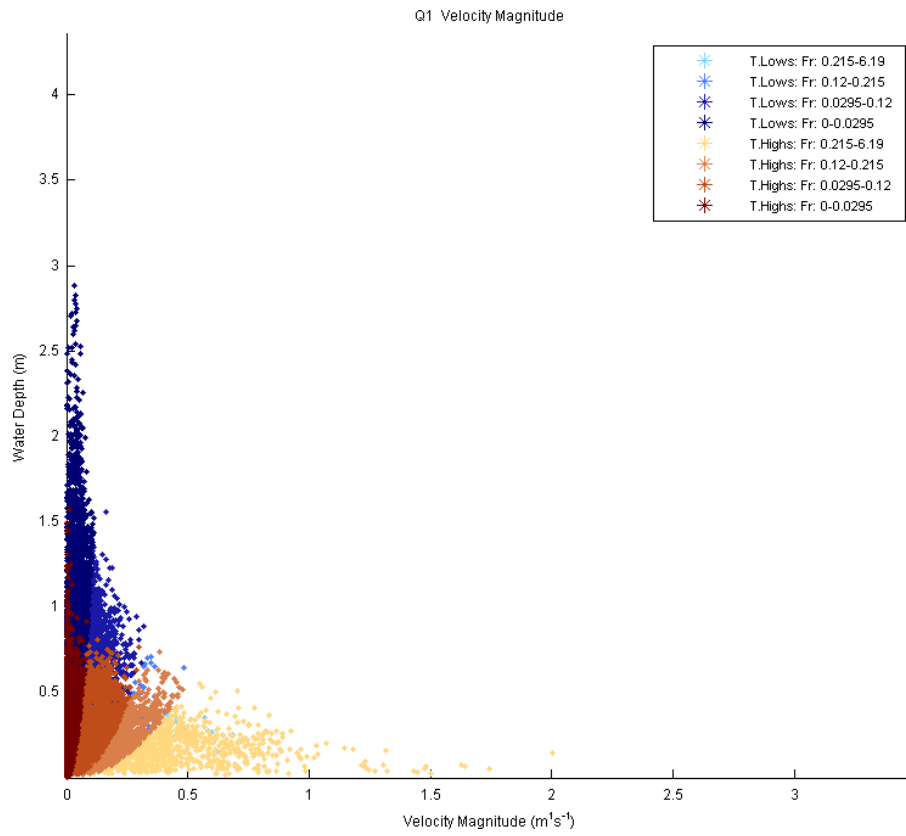


Figure 5.9. Distribution of velocity magnitude in relation to water depth for Q1–Q6 classified by topographic highs marked as 'T'. Highs (brown colors), topographic lows marked as 'T'. Lows (blue colors), and Froude number (Fr).

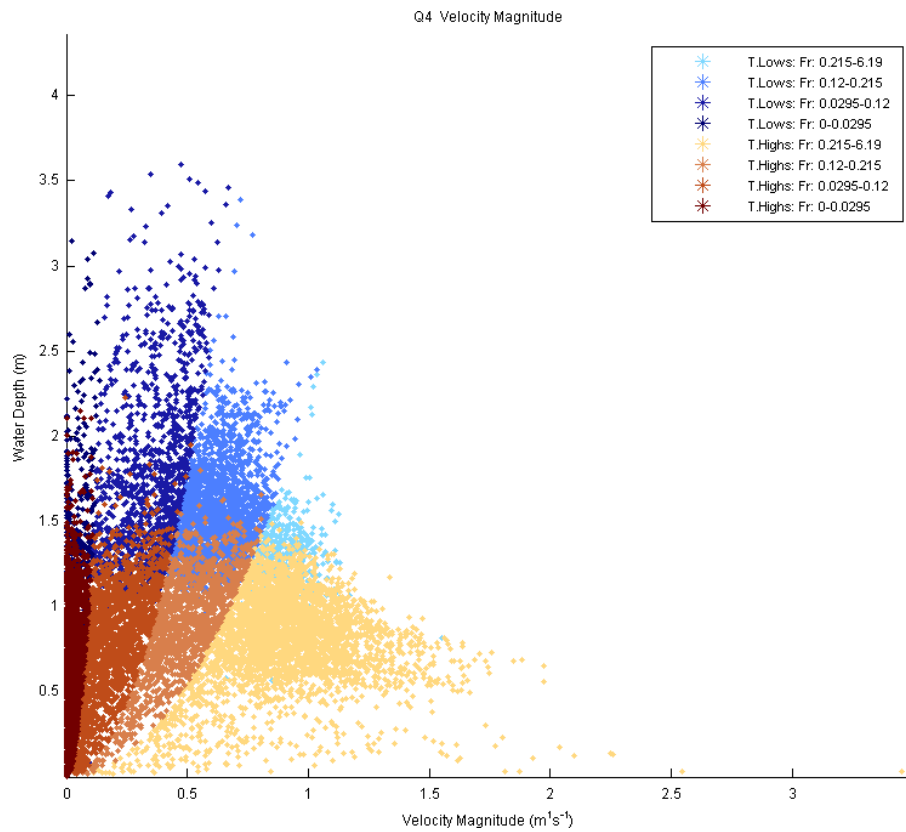
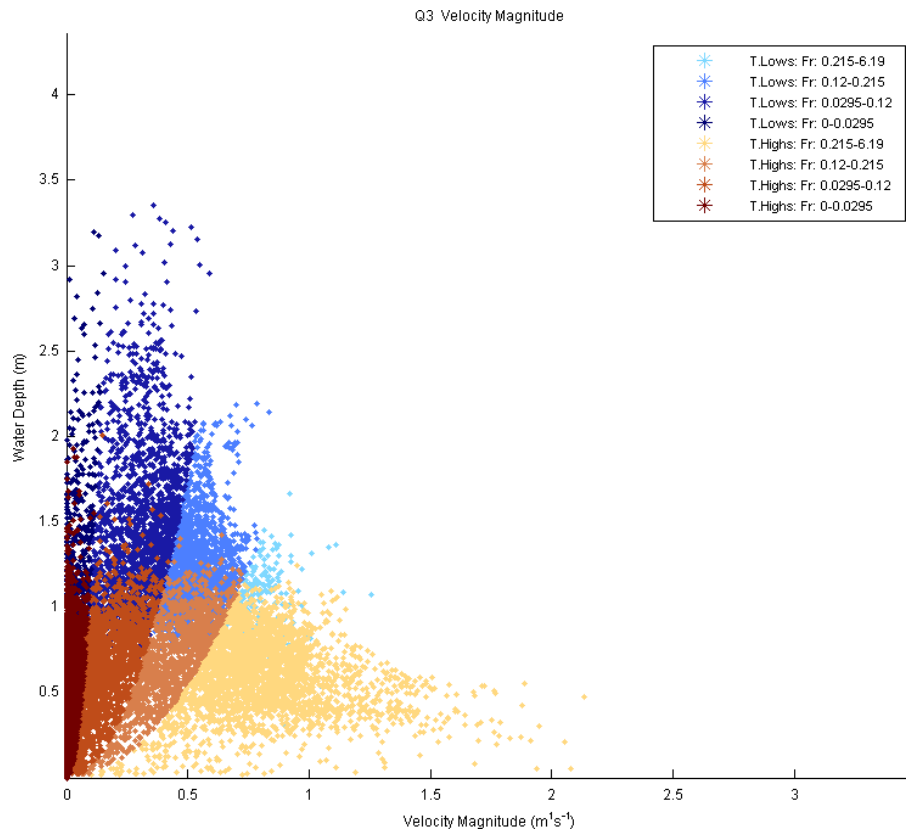


Figure 5.9 (cont'd). Distribution of velocity magnitude in relation to water depth for Q1–Q6 classified by topographic highs marked as T. Highs (brown colors), topographic lows marked as T. Lows (blue colors), and Froude number (Fr).

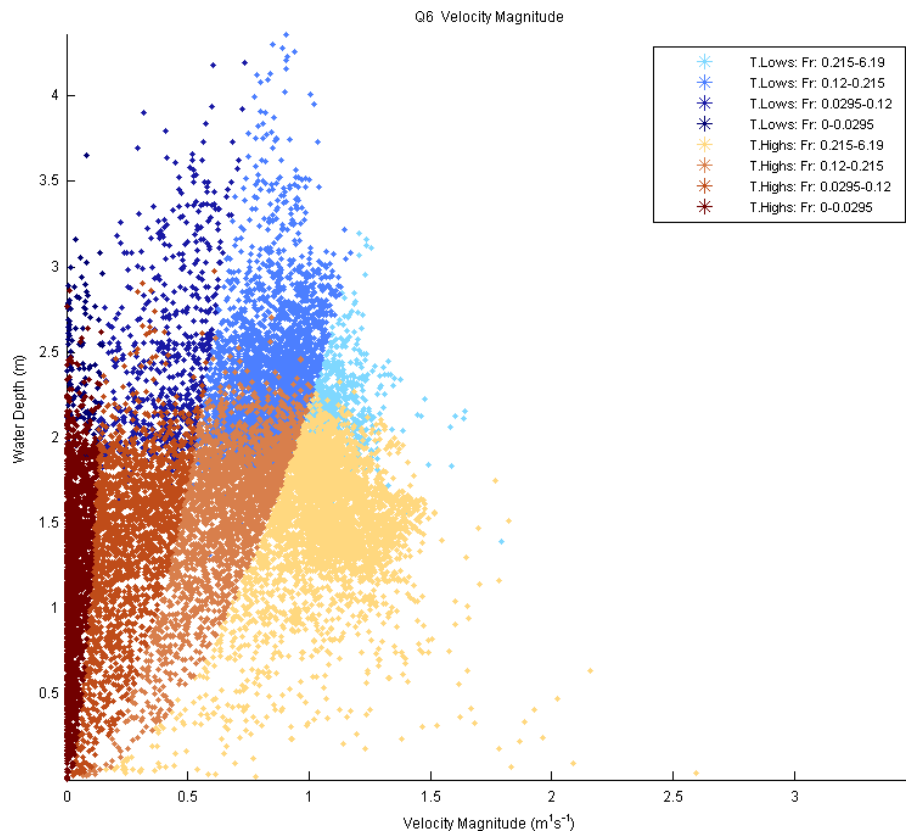
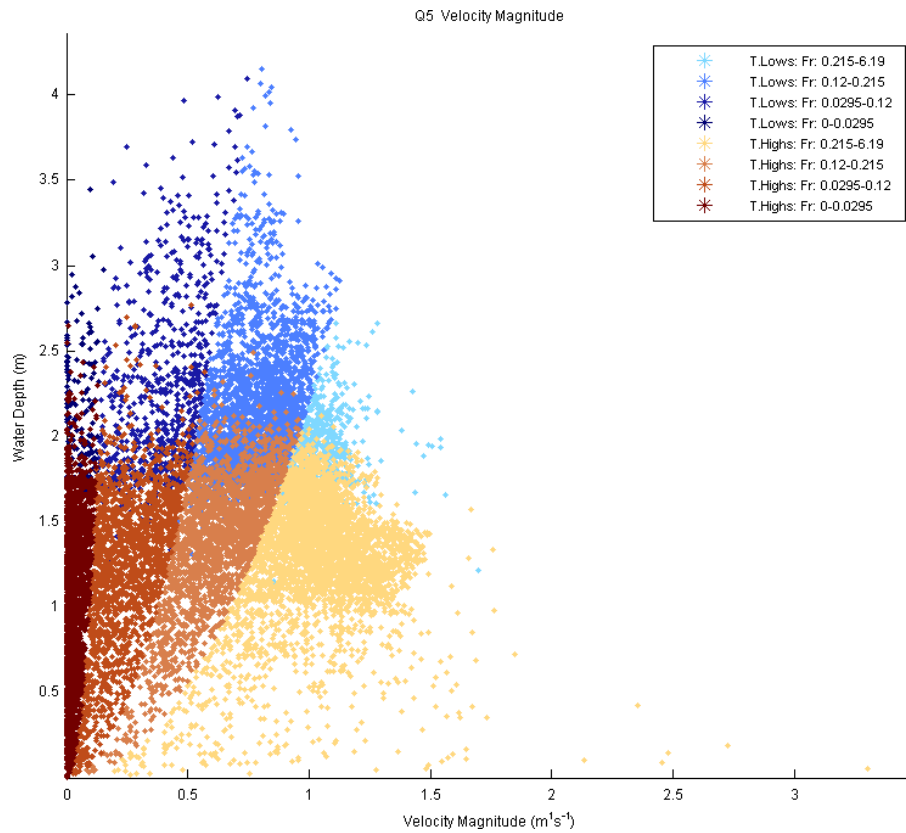


Figure 5.9 (cont'd). Distribution of velocity magnitude in relation to water depth for Q1–Q6 classified by topographic highs marked as T. Highs (brown colors), topographic lows marked as T. Lows (blue colors), and Froude number (Fr).

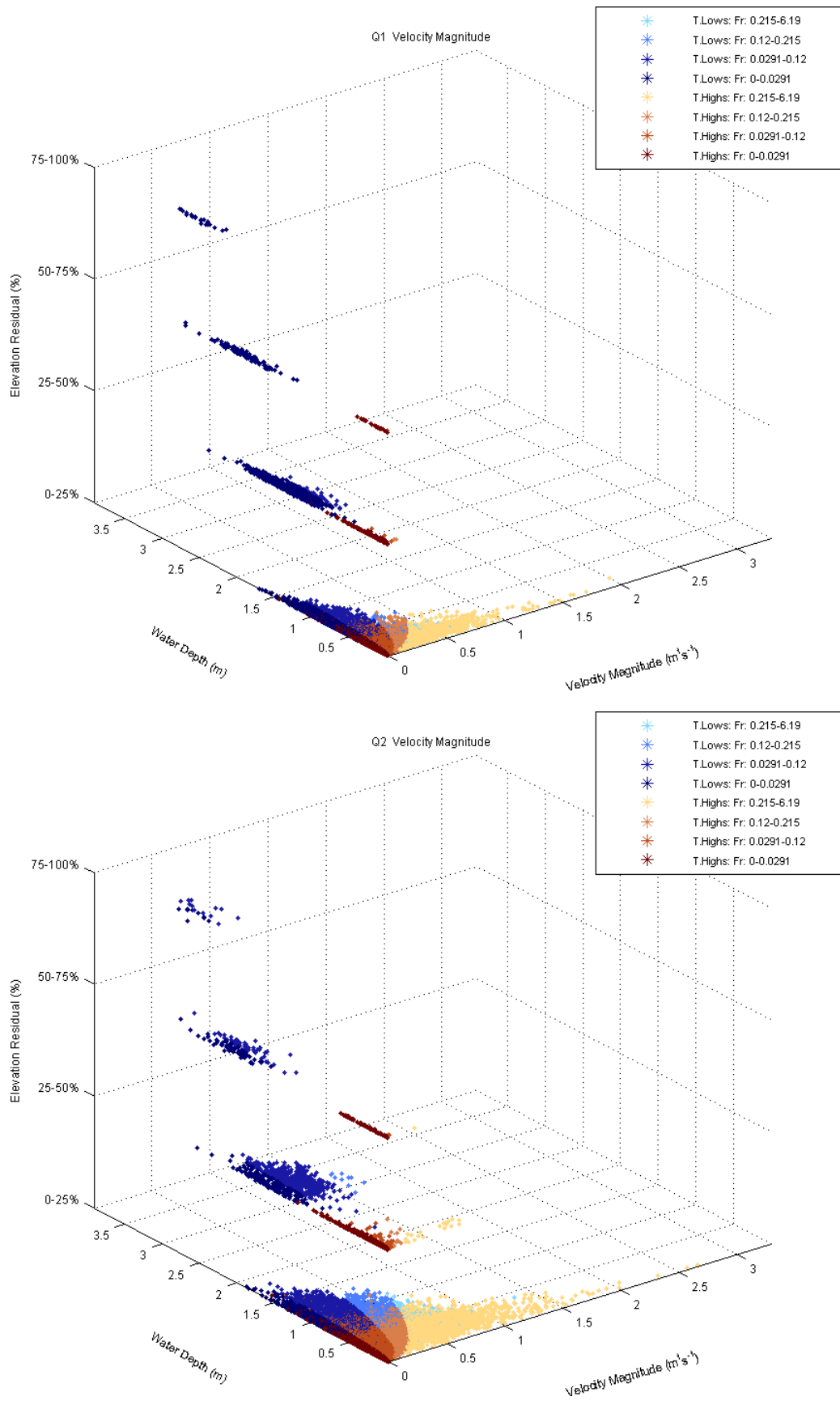


Figure 5.10. Distribution of velocity magnitude for topographic high (T. High)/low (T. Low) subclasses (Figure 4.2) and Q1–Q6, classified by Froude number (Fr).

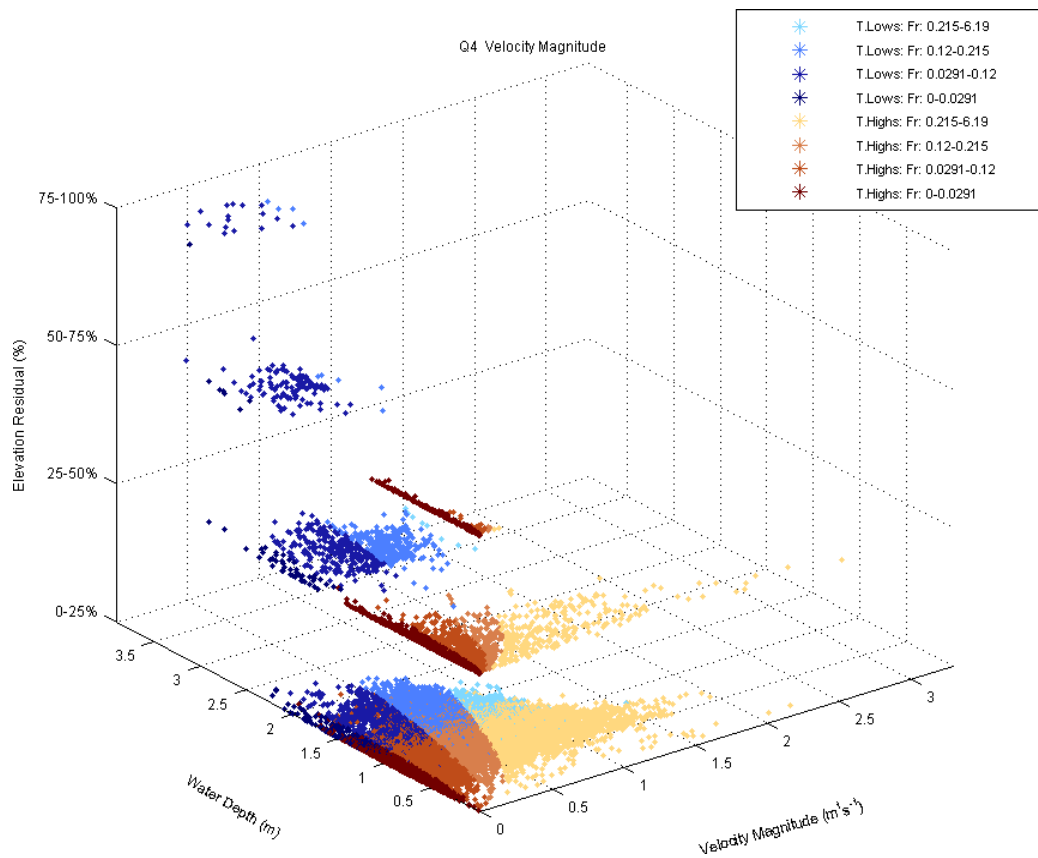
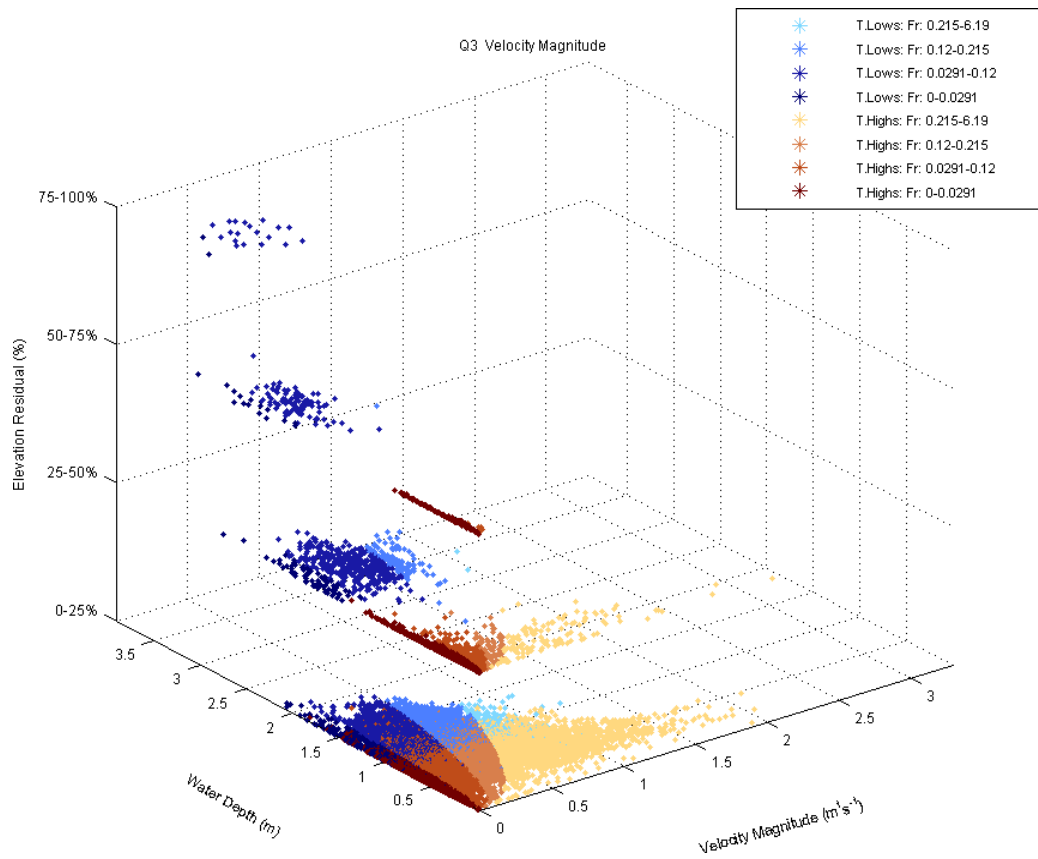


Figure 5.10 (cont'd). Distribution of velocity magnitude for topographic high (T. Highs)/low (T. Lows) subclasses (Figure 4.2) and Q1–Q6, classified by Froude number (Fr).

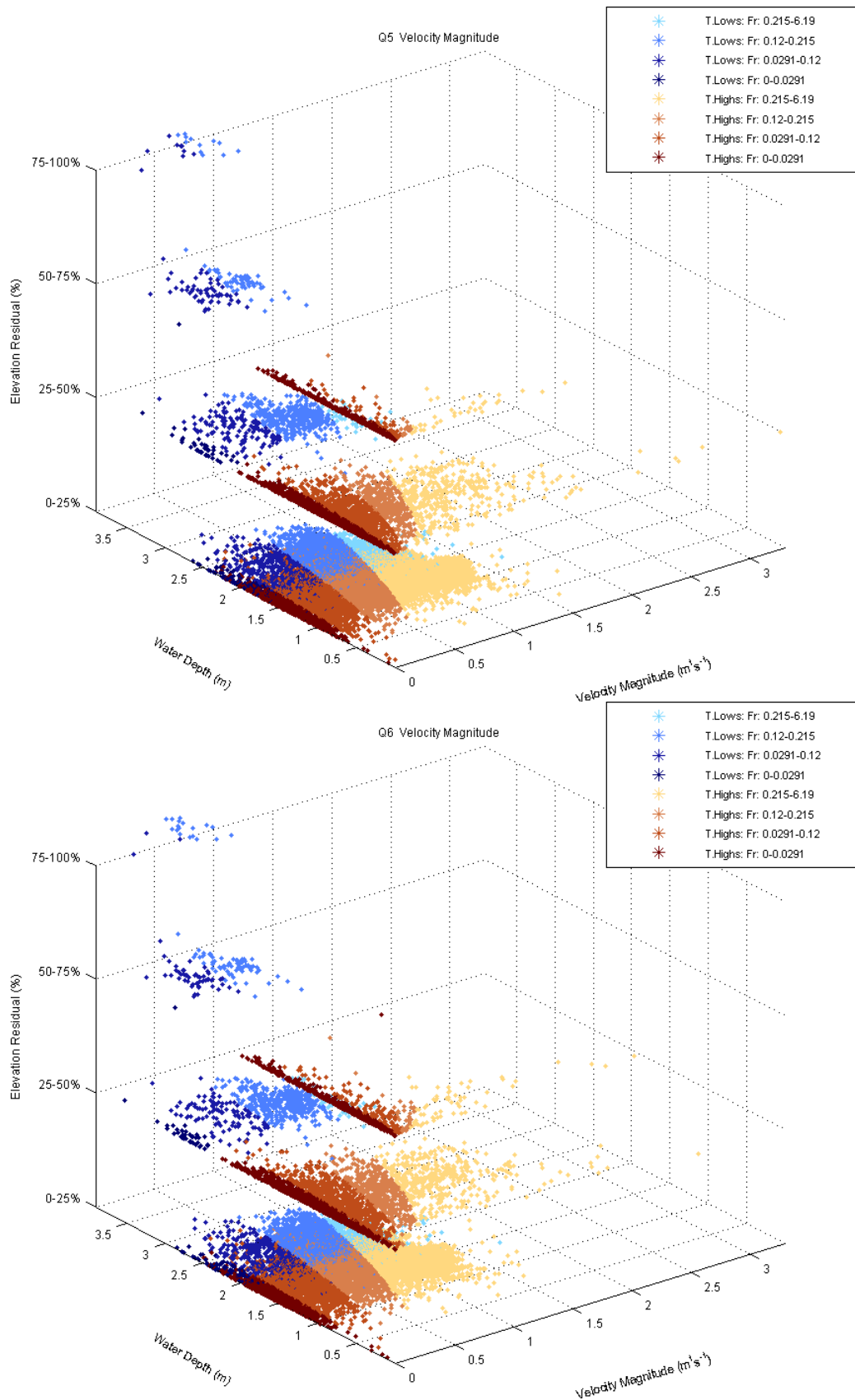


Figure 5.10 (cont'd). Distribution of velocity magnitude for topographic high (T. Highs)/low (T. Lows) subclasses (Figure 4.2) and Q1–Q6, classified by Froude number (Fr).

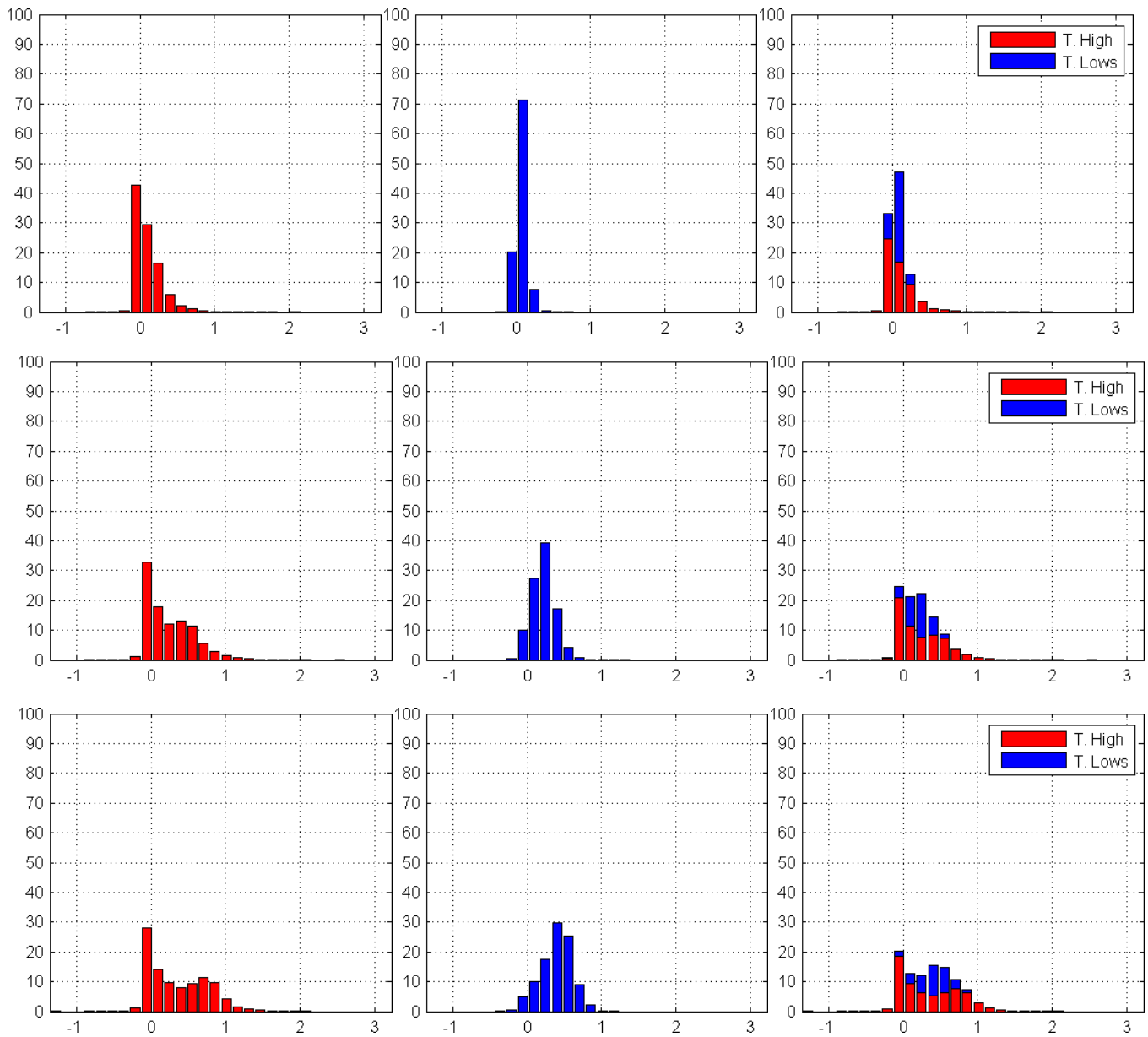


Figure 5.11. Distribution of streamwise velocity component for Q1–Q6 (rows, top to bottom) for topographic highs (marked as T. High) corresponding to the classes (+1)–(+4), topographic lows (marked as T. Lows) corresponding to the classes (-1)–(-4), and combined (columns, left to right). Horizontal and vertical axes correspond to streamwise velocity (m/s) and the percent values of topographic classes, respectively.

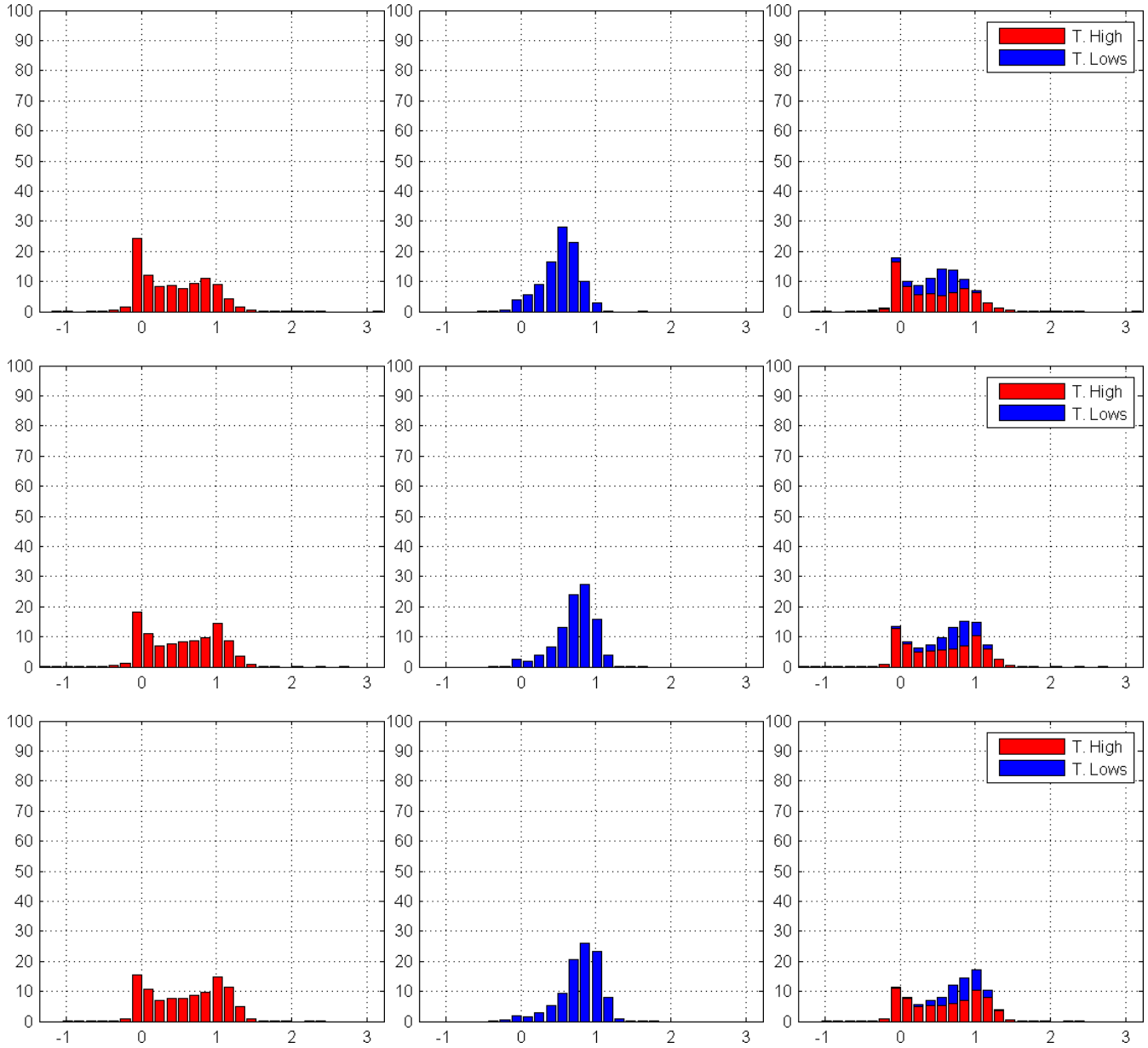


Figure 5.11 (cont'd). Distribution of streamwise velocity component for Q1–Q6 (rows, top to bottom) for topographic highs (marked as T. High) corresponding to the classes (+1)–(+4), topographic lows (marked as T. Lows) corresponding to the classes (-1)–(-4), and combined (columns, left to right). Horizontal and vertical axes correspond to streamwise velocity (m/s) and the percent values of topographic classes, respectively.

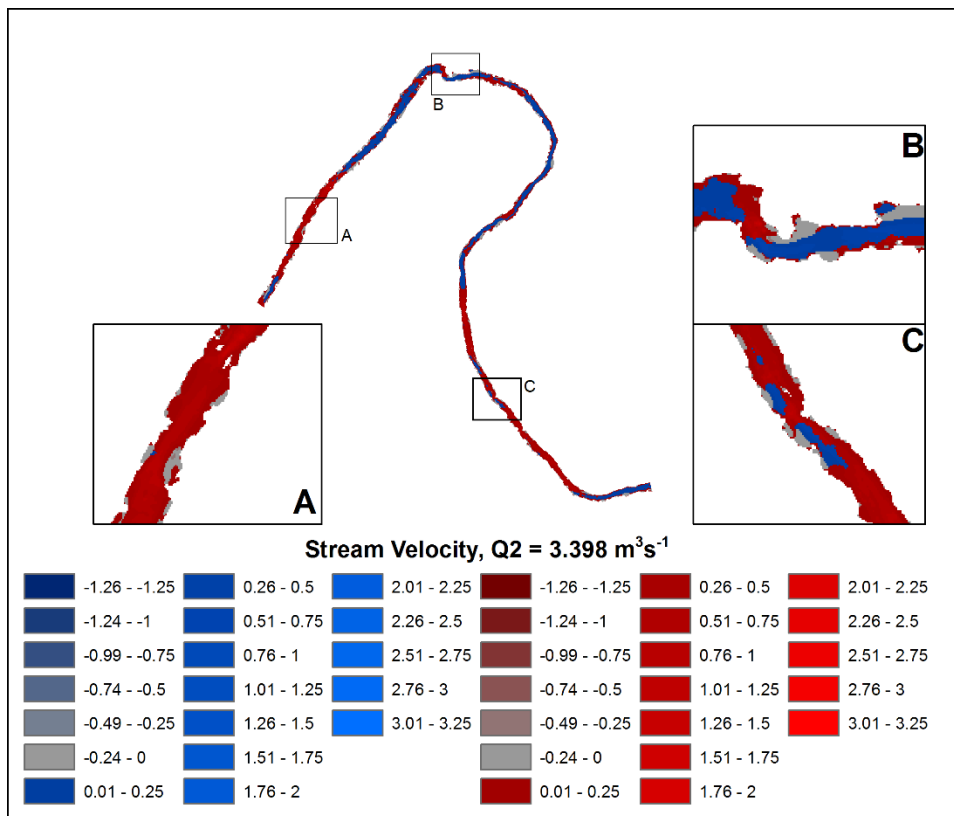
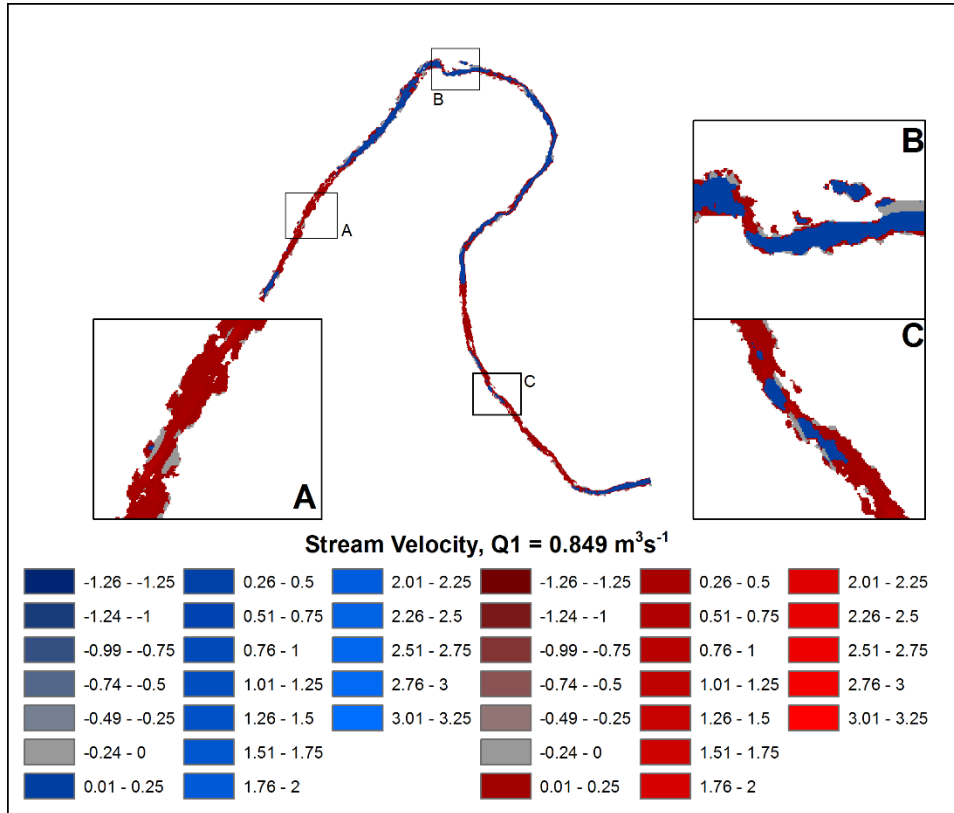


Figure 5.12. Spatial distribution of streamwise velocity (m/s) for Q1–Q6 for topographic highs (red colors) and lows (blue colors).

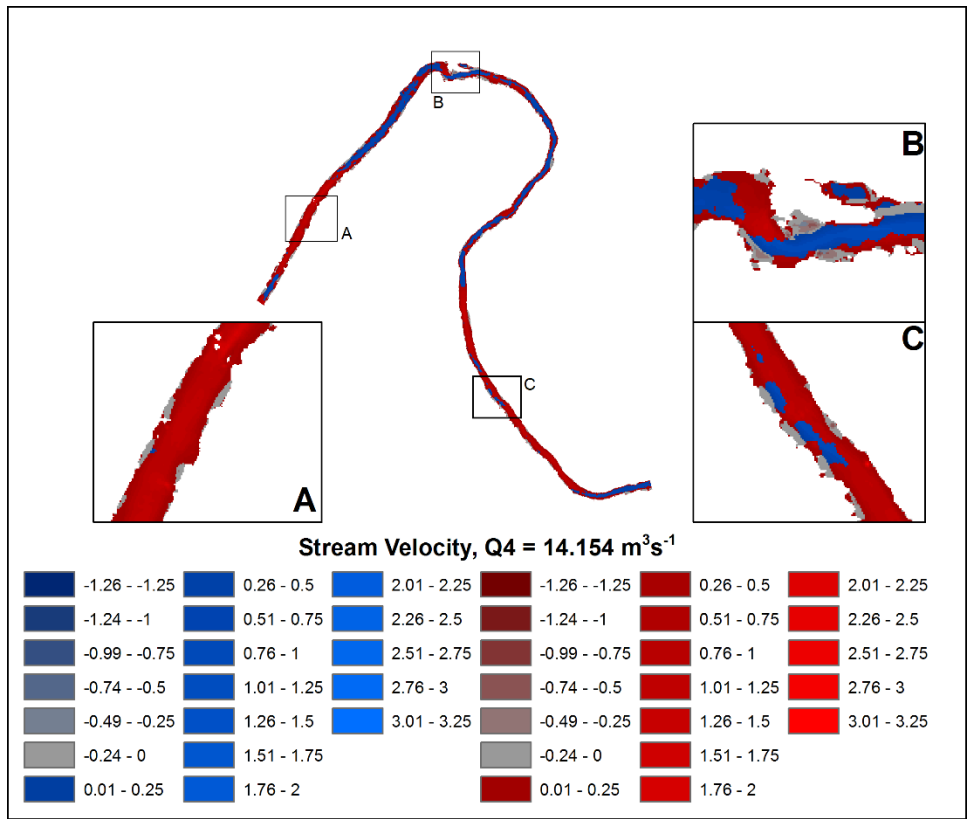
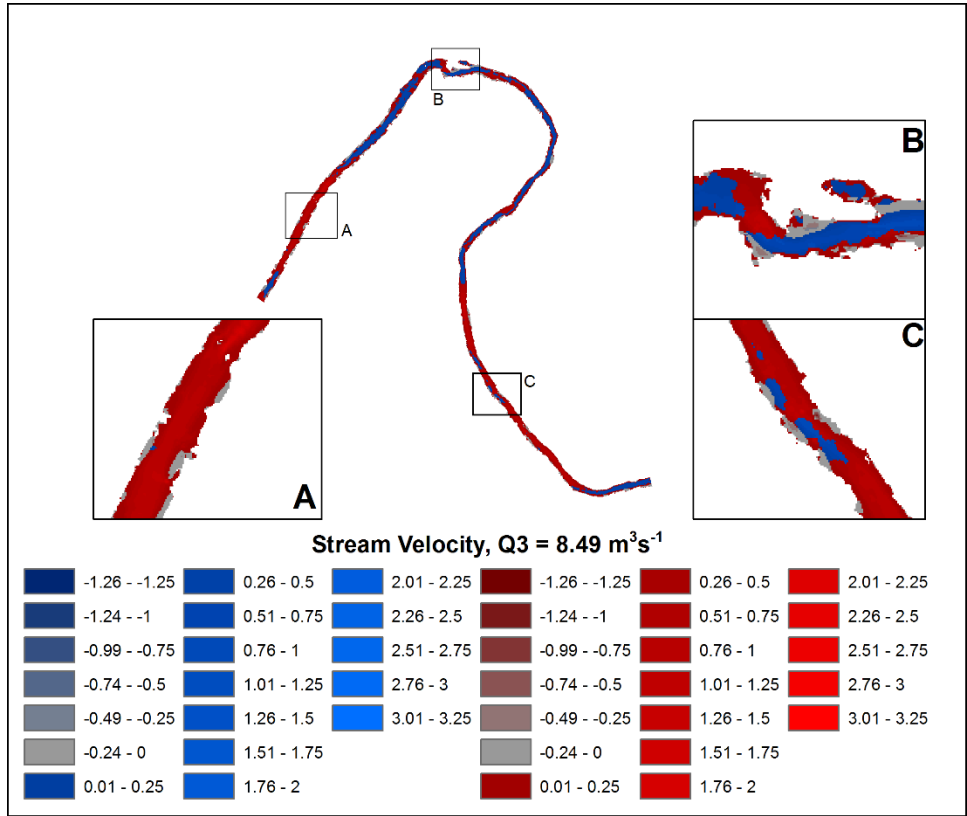


Figure 5.12 (cont'd). Spatial distribution of streamwise velocity (m/s) for Q1–Q6 topographic highs (red colors) and lows (blue colors).

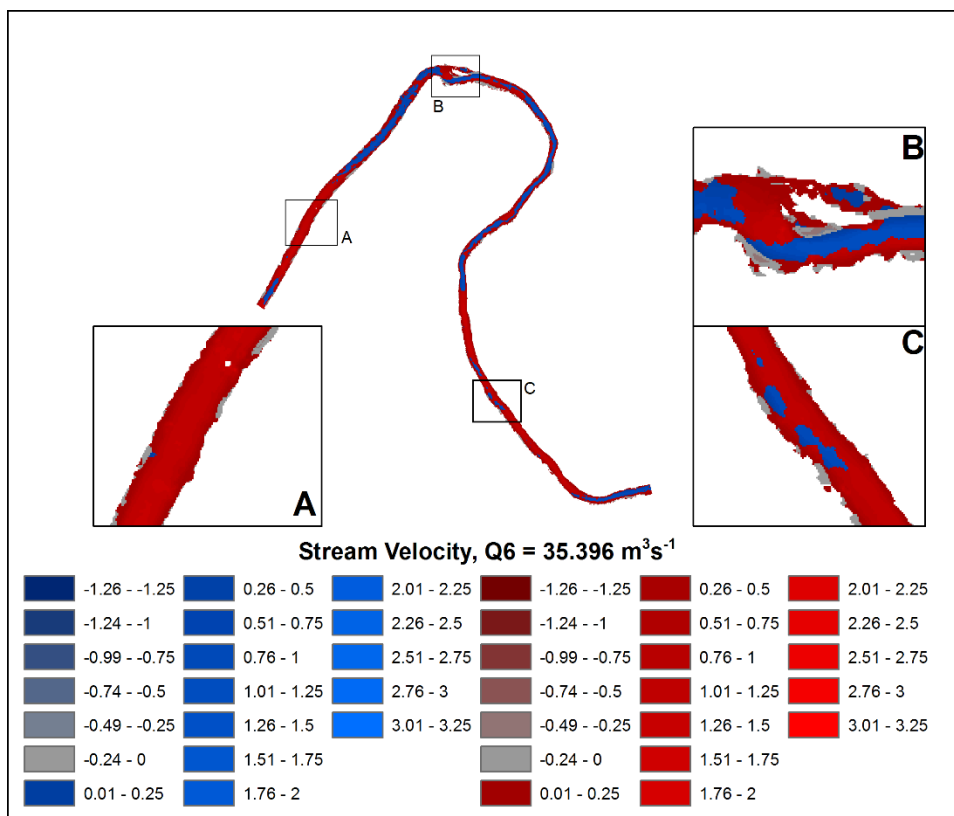
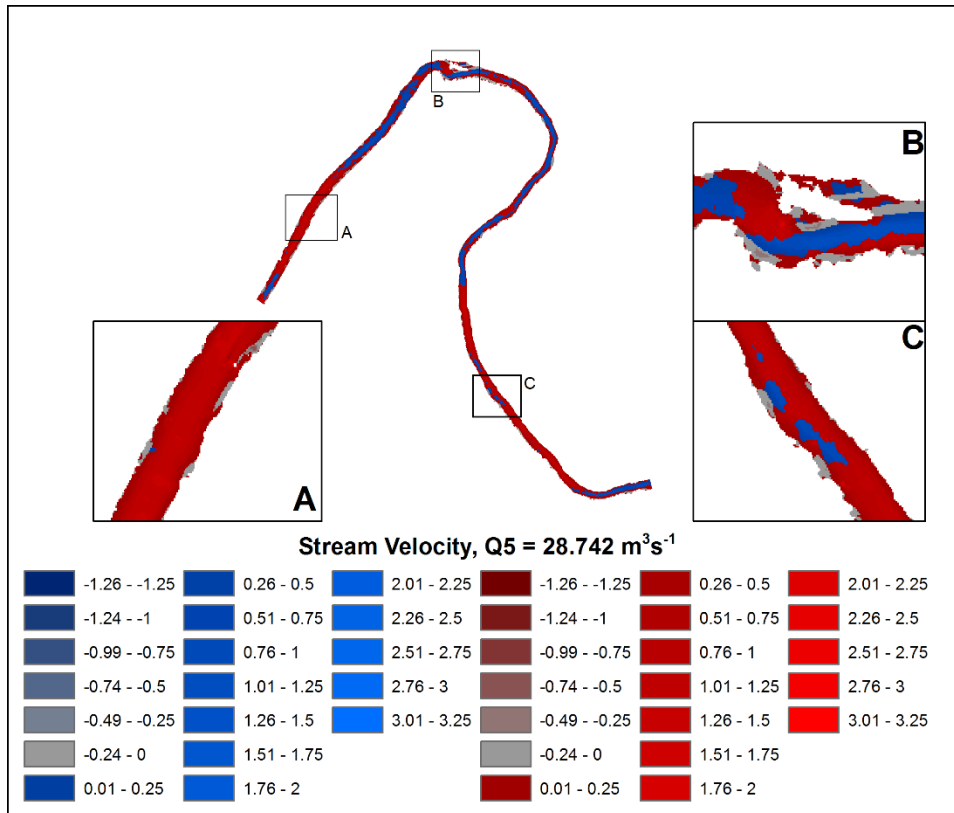


Figure 5.12 (cont'd). Spatial distribution of streamwise velocity (m/s) for Q1–Q6 for topographic highs (red colors) and lows (blue colors).

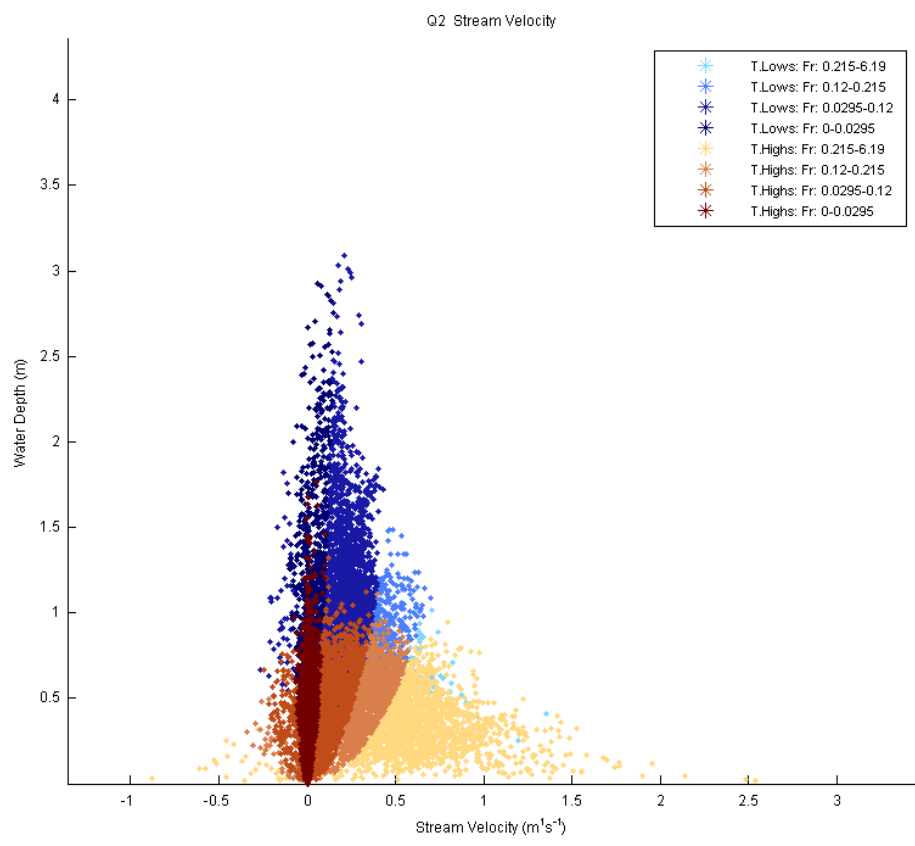
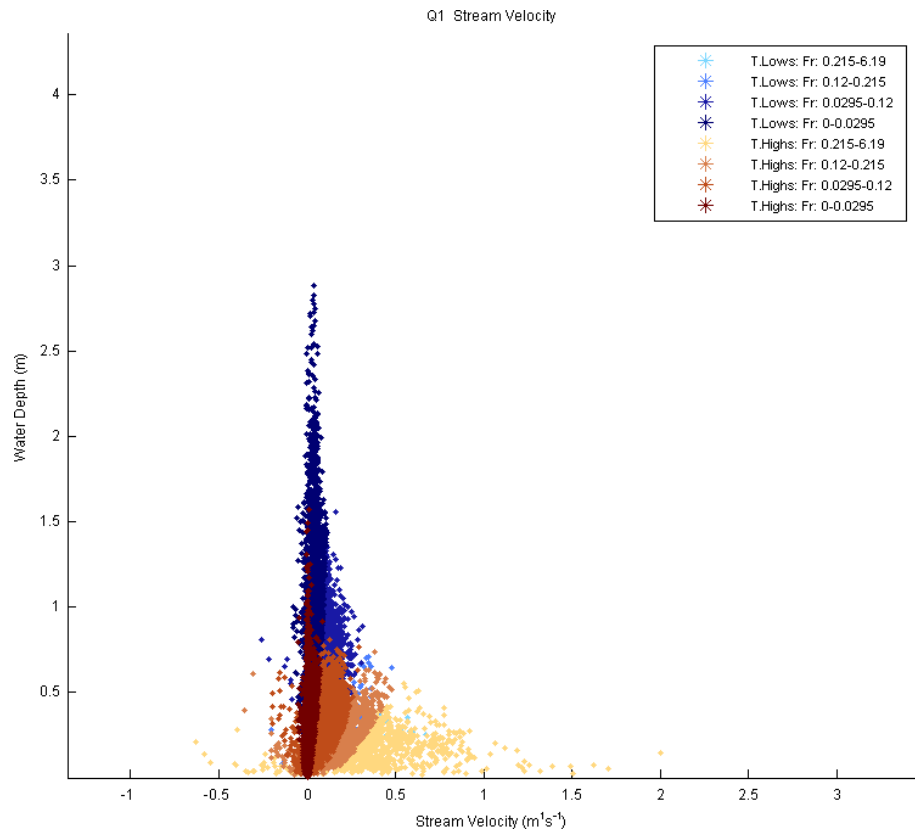


Figure 5.13. Distribution of streamwise velocity in relation to water depth for Q1–Q6 classified by topographic highs marked as 'T. Highs' (brown colors), topographic lows marked as 'T. Lows' (blue colors), and Froude number (Fr).

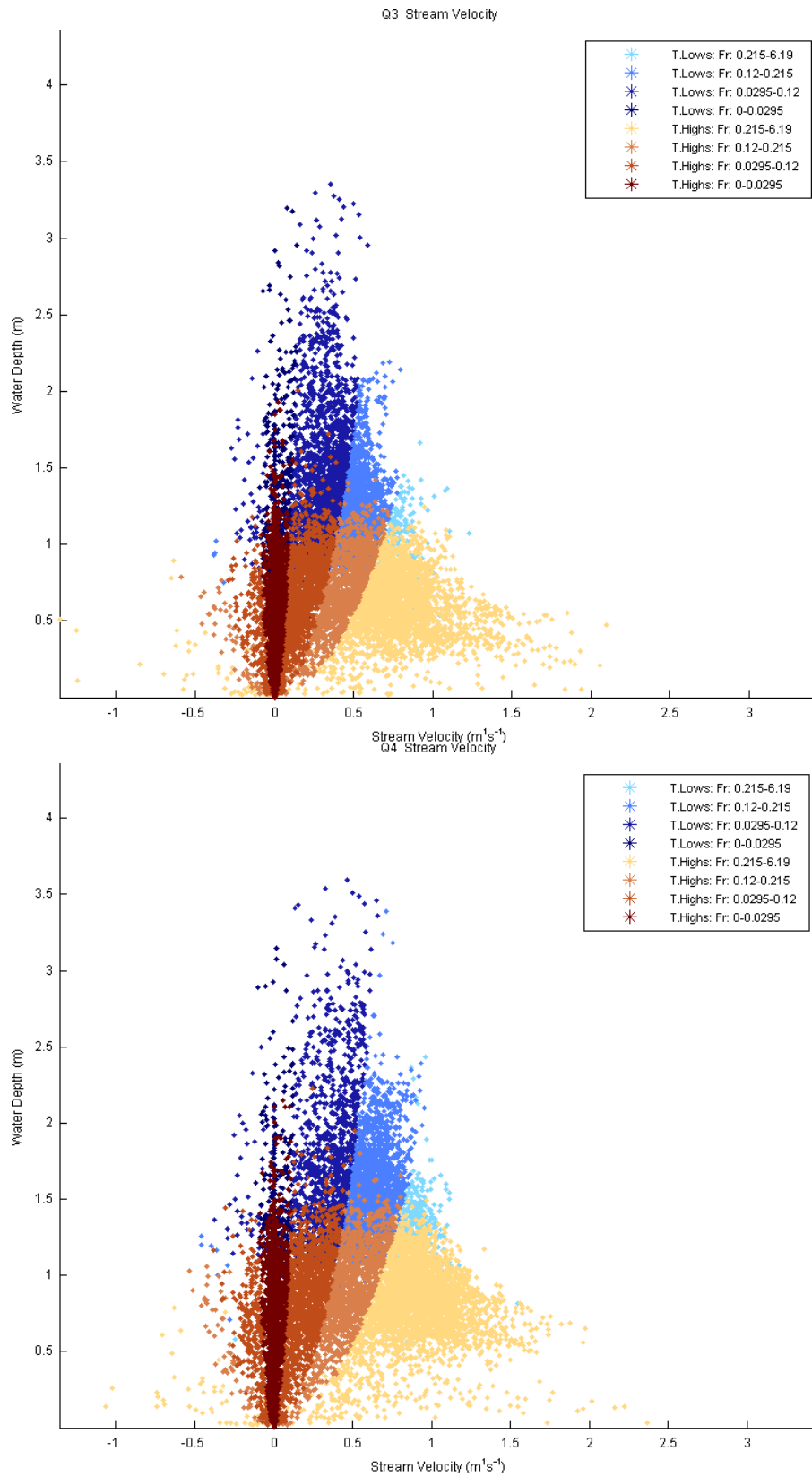


Figure 5.13 (cont'd). Distribution of streamwise velocity in relation to water depth for Q1–Q6 classified by topographic highs marked as T. Highs (brown colors), topographic lows marked as T. Lows (blue colors), and Froude number (Fr).

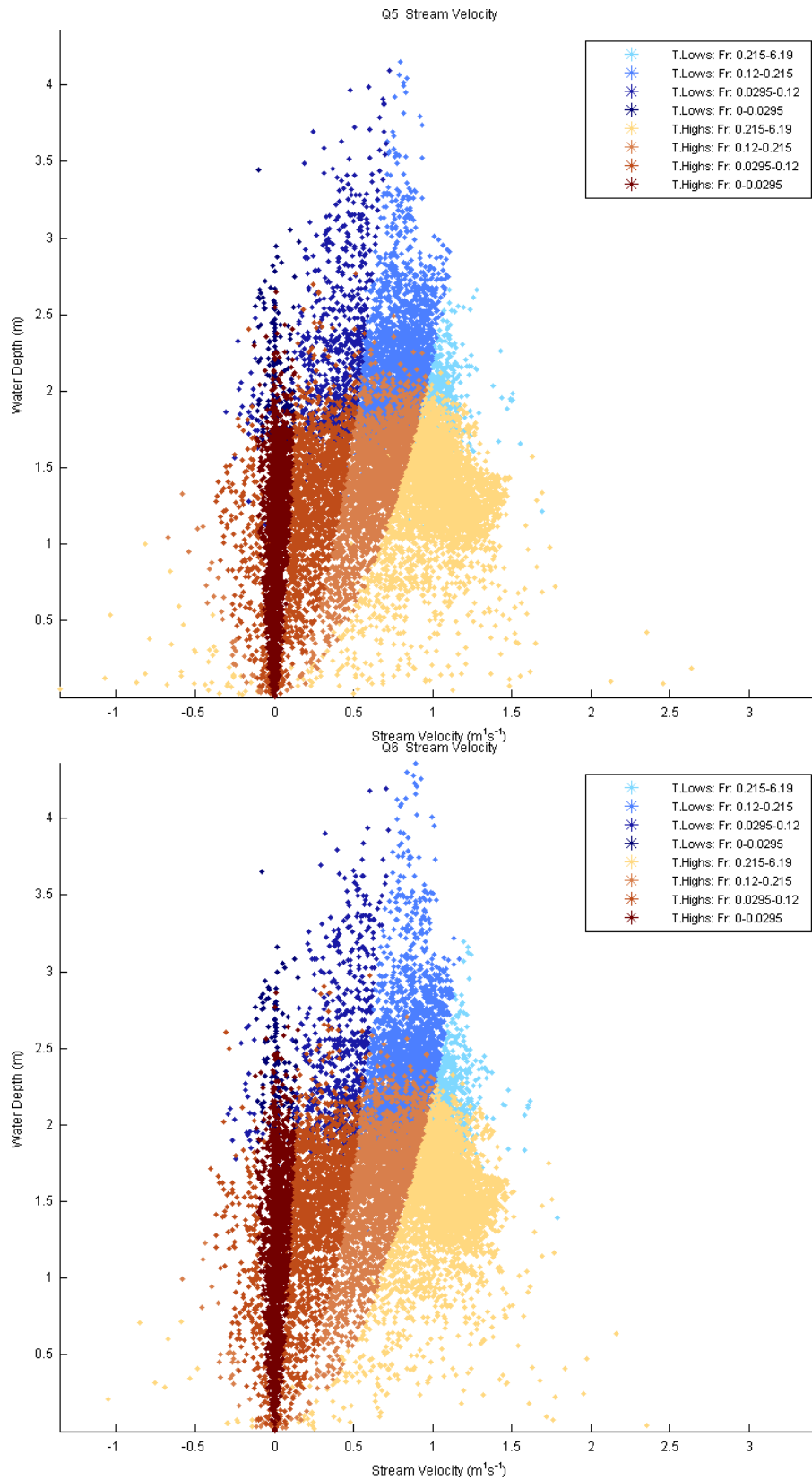


Figure 5.13 (cont'd). Distribution of streamwise velocity in relation to water depth for Q1–Q6 classified by topographic highs marked as T. Highs (brown colors), topographic lows marked as T. Lows (blue colors), and Froude number (Fr).

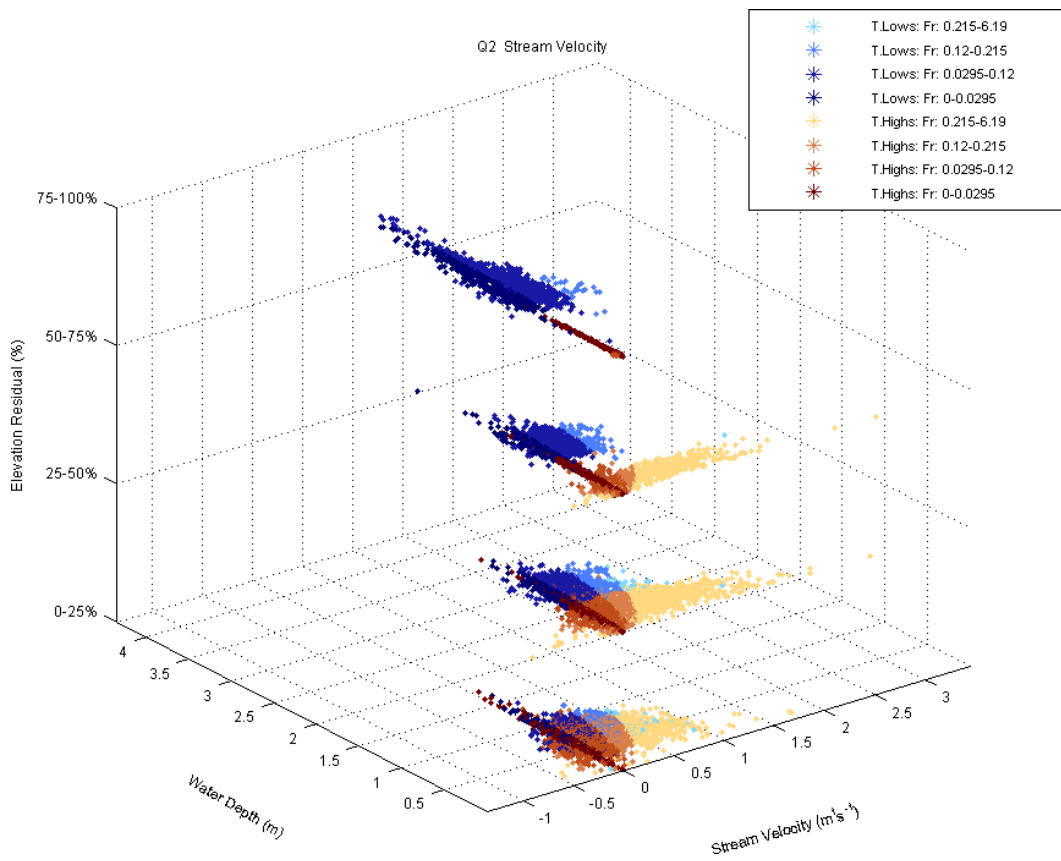
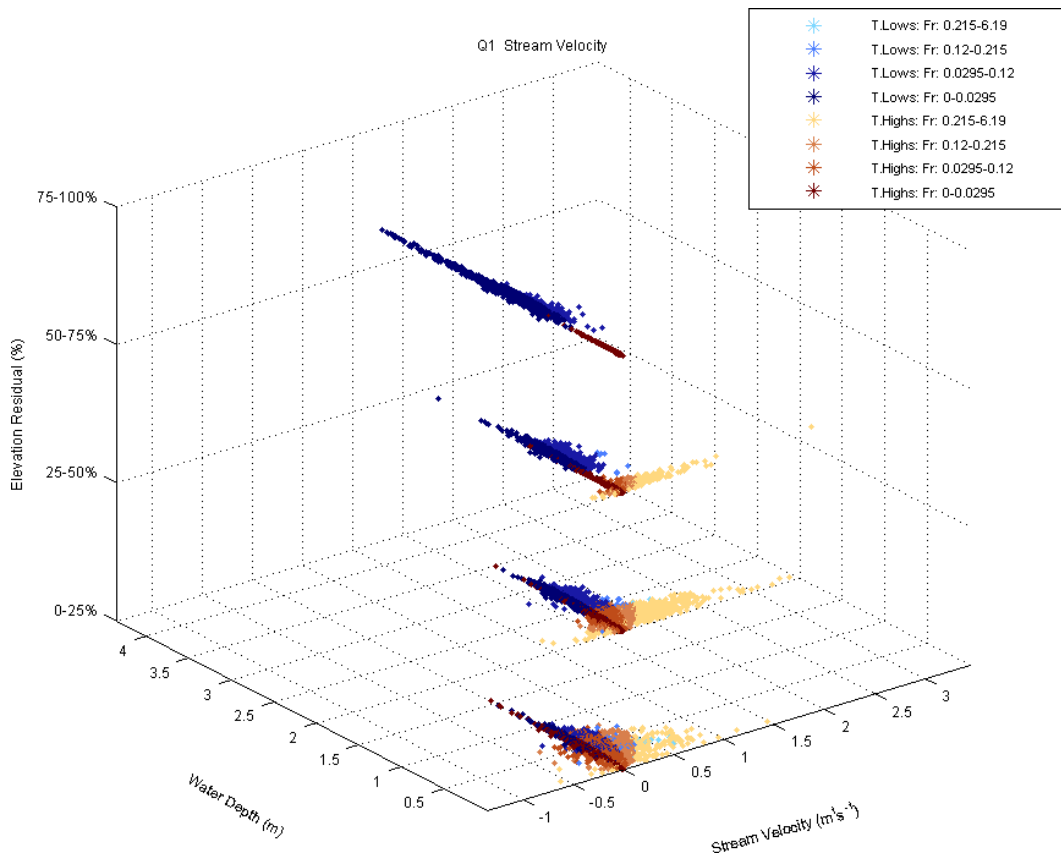


Figure 5.14. Distribution of streamwise velocity for topographic high (T. Highs)/low (T. Lows) subclasses (Figure 4.2) and Q1–Q6, classified by Froude number (Fr).

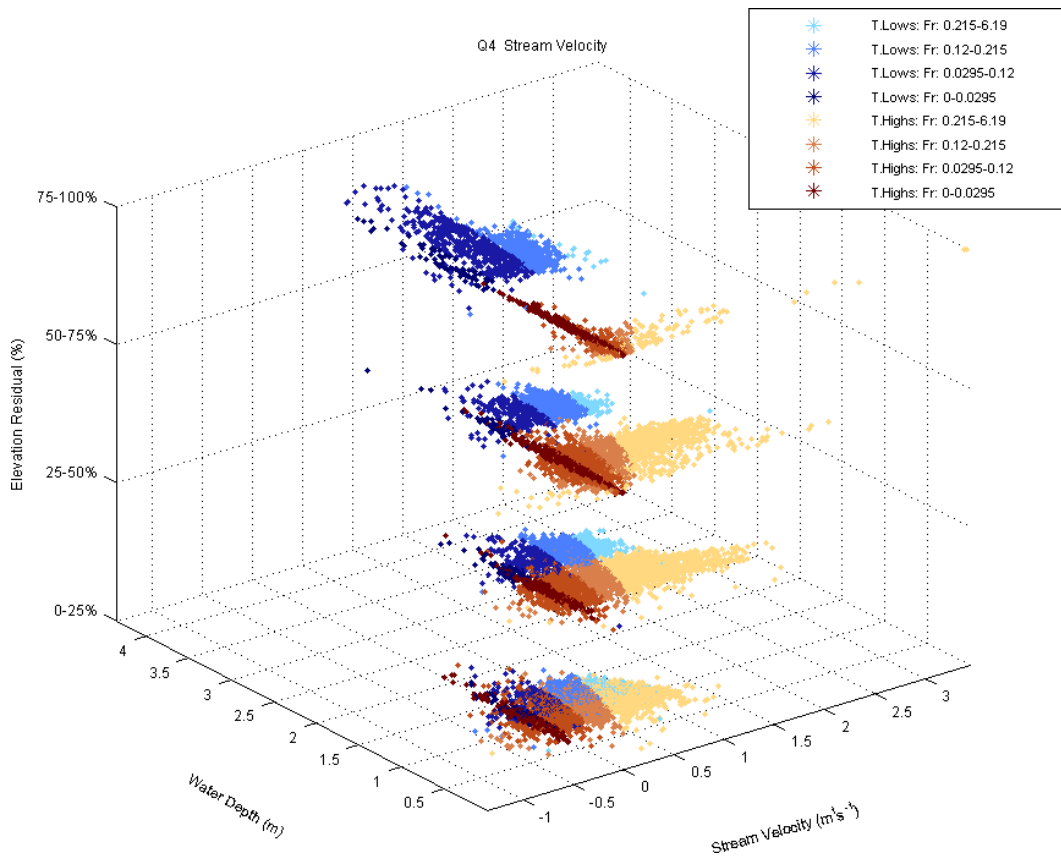
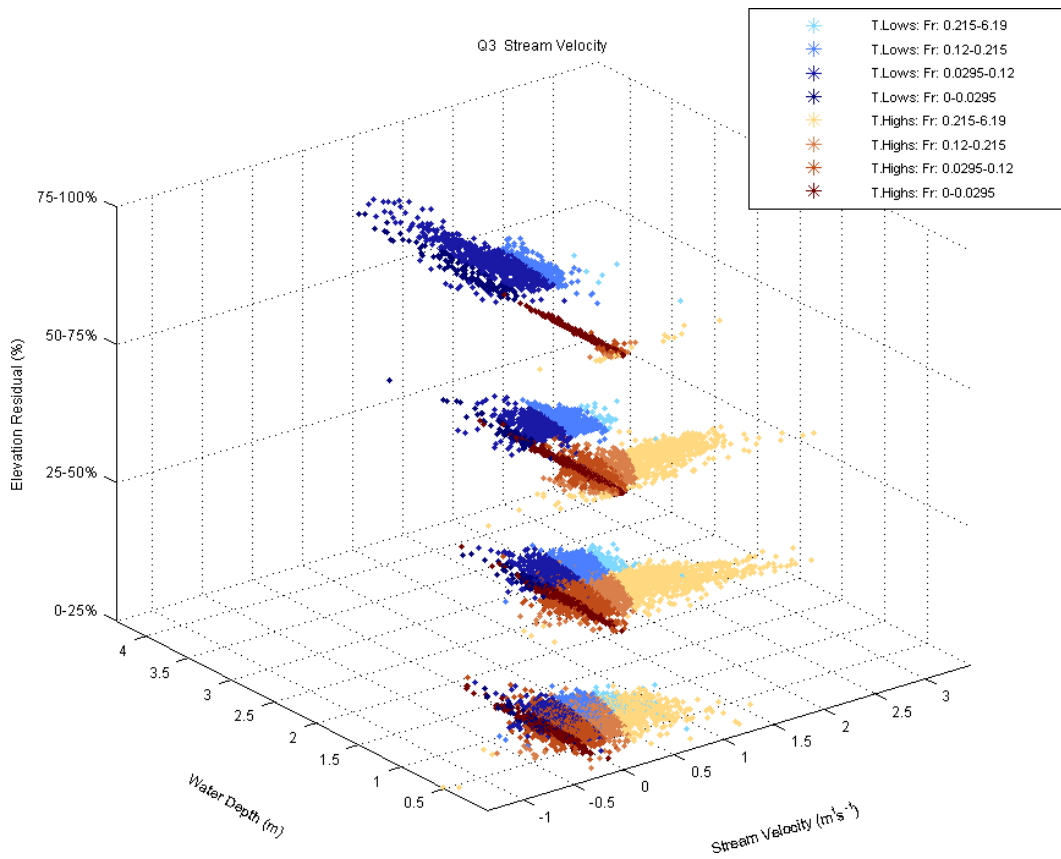


Figure 5.14 (cont'd). Distribution of streamwise velocity for topographic high (T. Highs)/low (T. Lows) subclasses (Figure 4.2) and Q1–Q6, classified by Froude number (Fr).

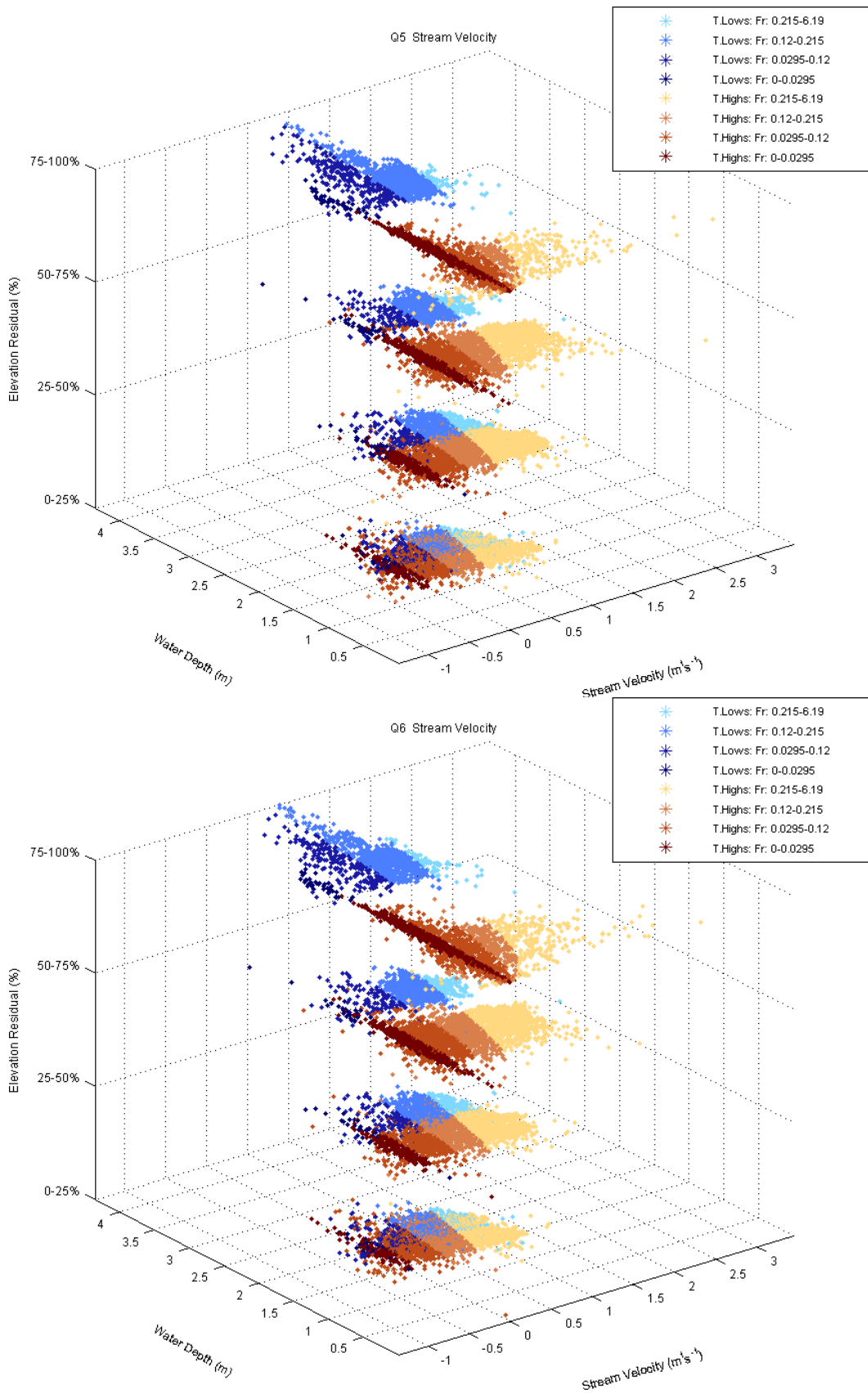


Figure 5.14 (cont'd). Distribution of streamwise velocity for topographic high (T. Highs)/low (T. Lows) subclasses (Figure 4.2) and Q1–Q6, classified by Froude number (Fr).

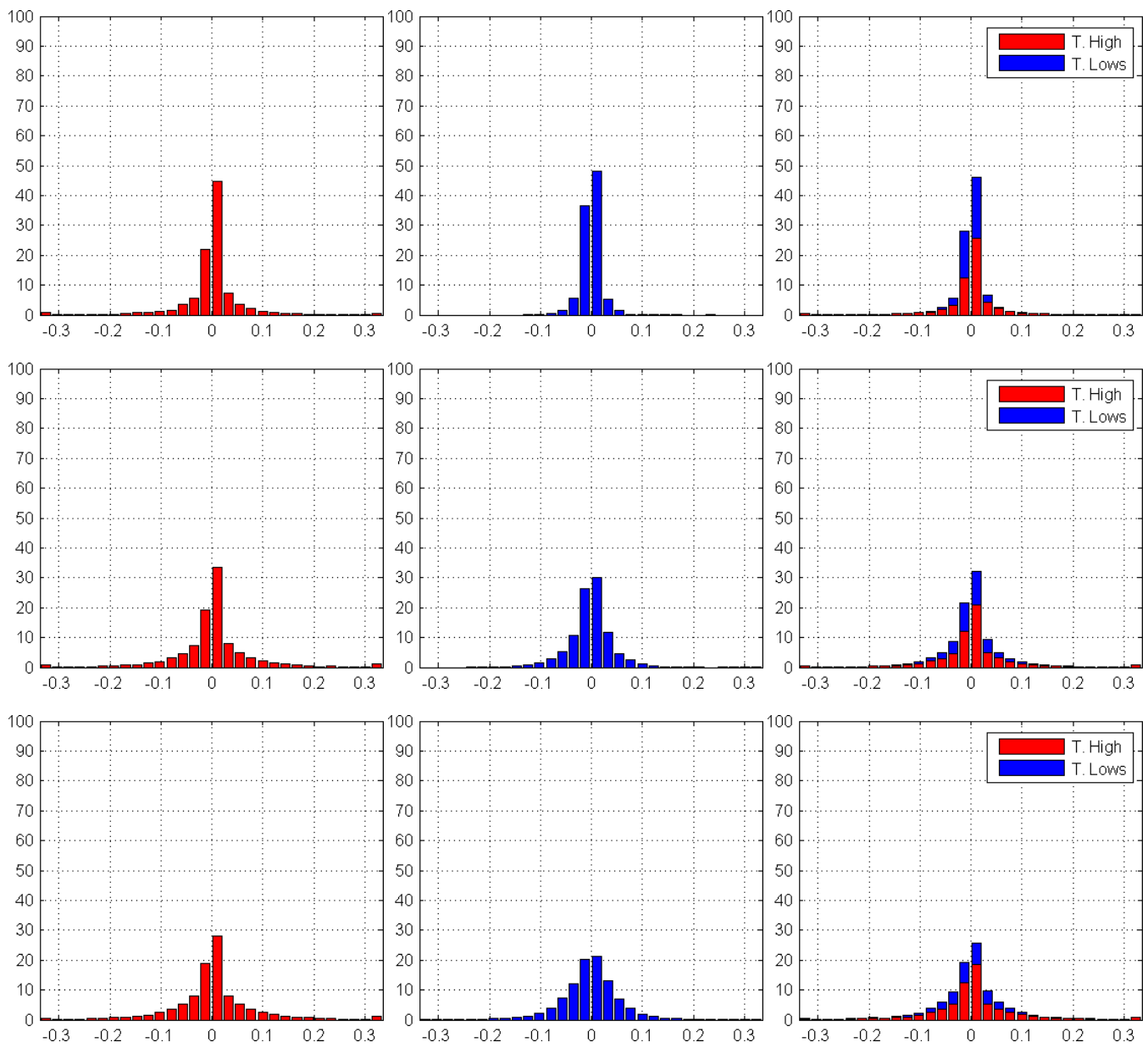


Figure 5.15. Distribution of normal velocity component for Q1–Q6 (rows, top to bottom) for topographic highs (marked as T. High) corresponding to the classes (+1)–(+4), topographic lows (marked as T. Lows) corresponding to the classes (-1)–(-4), and combined (columns, left to right). Horizontal and vertical axes correspond to normal velocity (m/s) and the percent values of topographic classes, respectively.

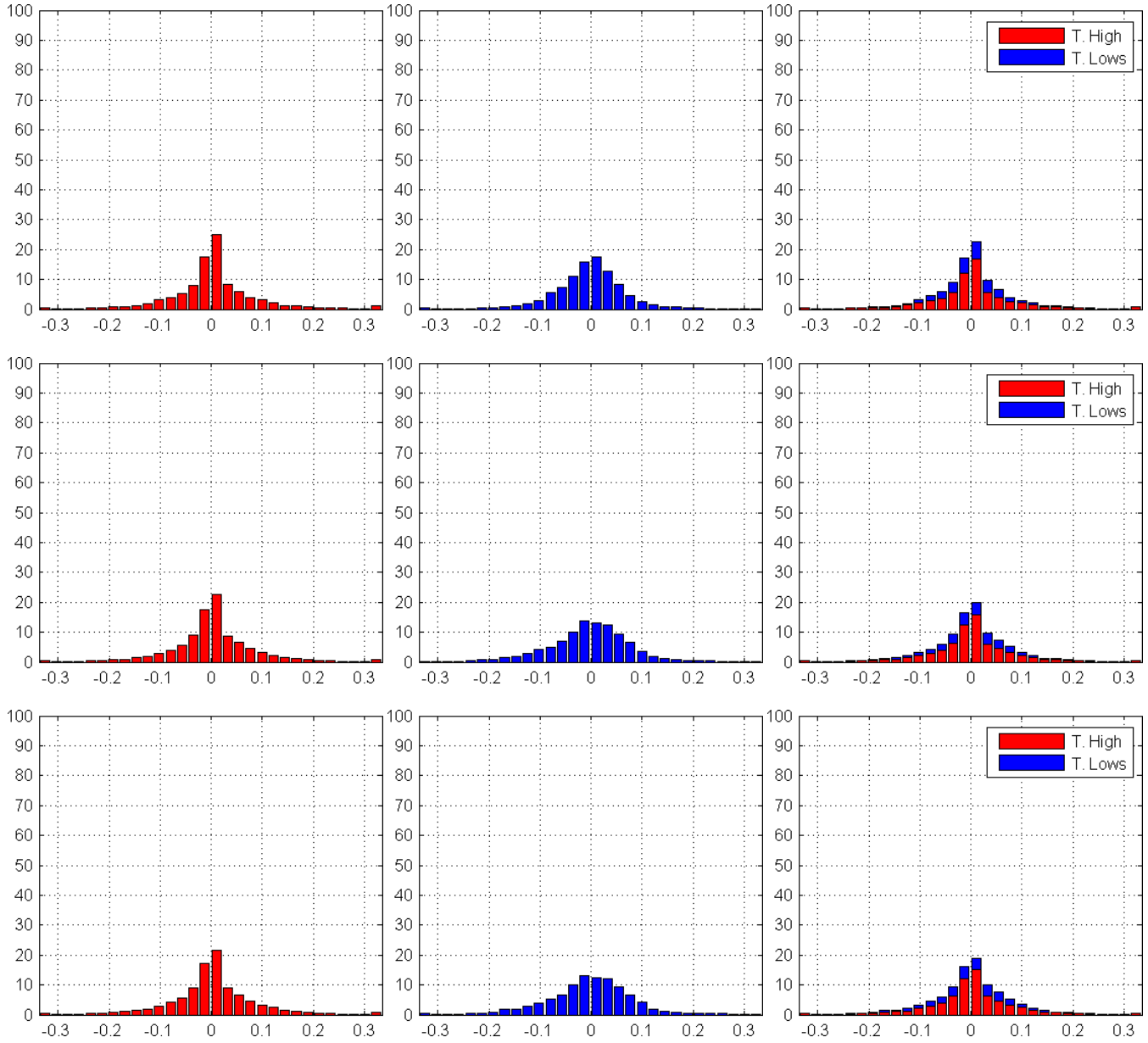


Figure 5.15 (cont'd). Distribution of normal velocity component for Q1–Q6 (rows, top to bottom) for topographic highs (marked as T. High) corresponding to the classes (+1)–(+4), topographic lows (marked as T. Lows) corresponding to the classes (-1)–(-4), and combined (columns, left to right). Horizontal and vertical axes correspond to normal velocity (m/s) and the percent values of topographic classes, respectively.

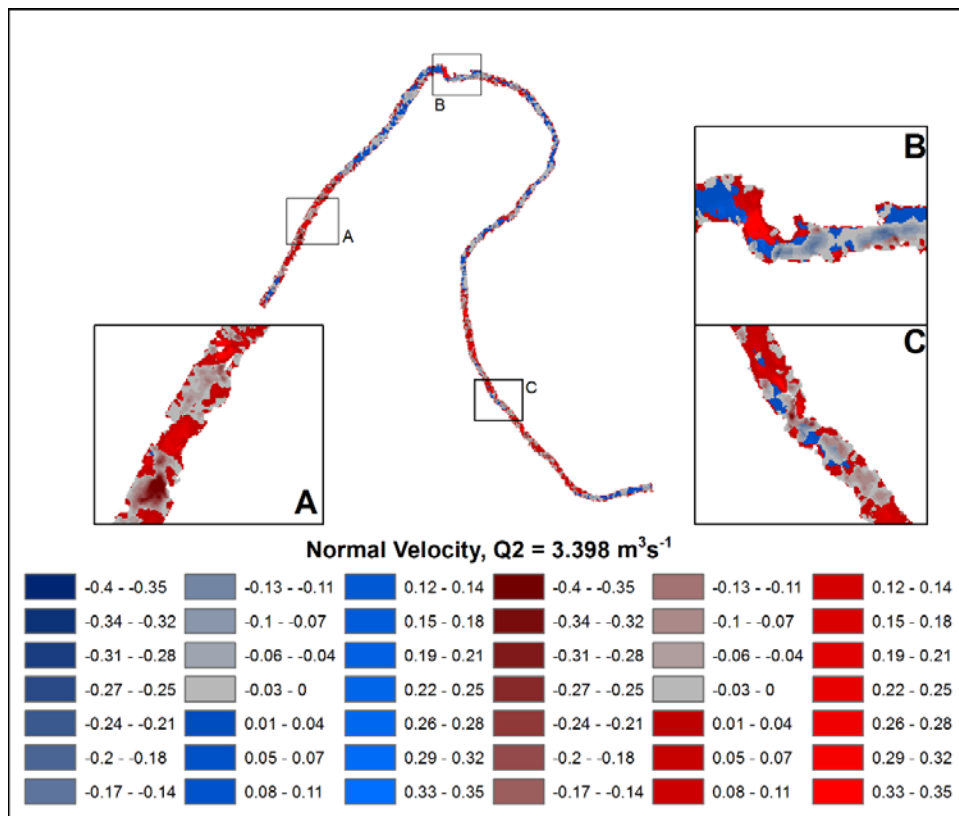
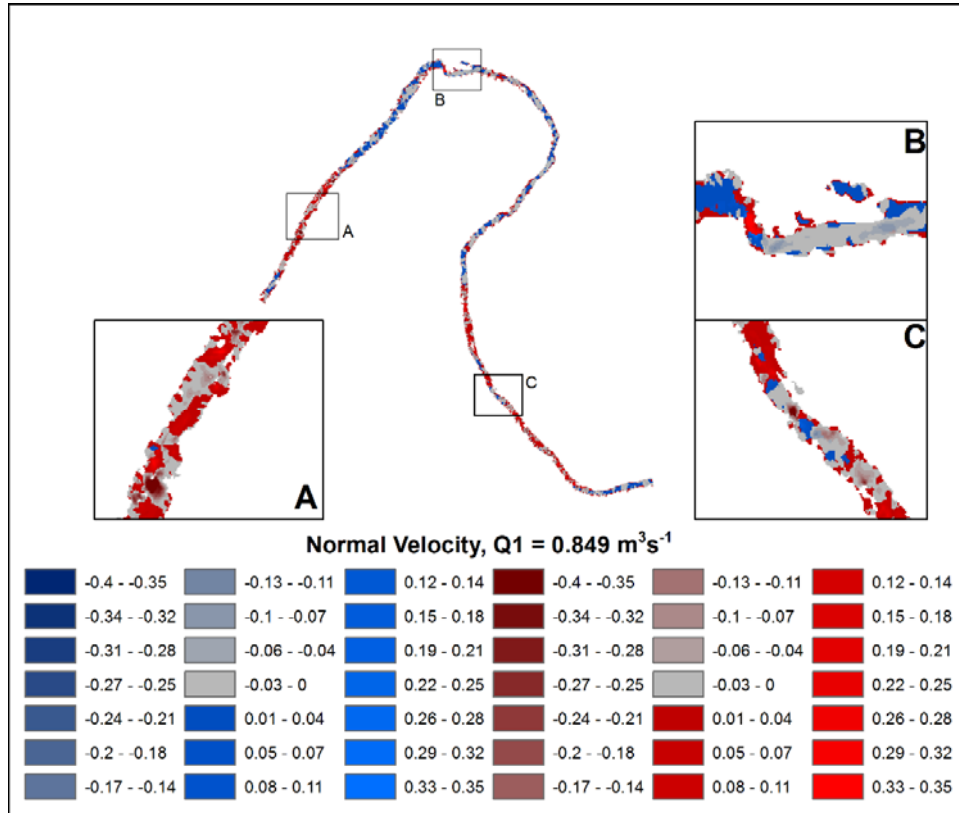


Figure 5.16. Spatial distribution of normal velocity (m/s) for Q1–Q6 for topographic highs (red colors) and lows (blue colors).

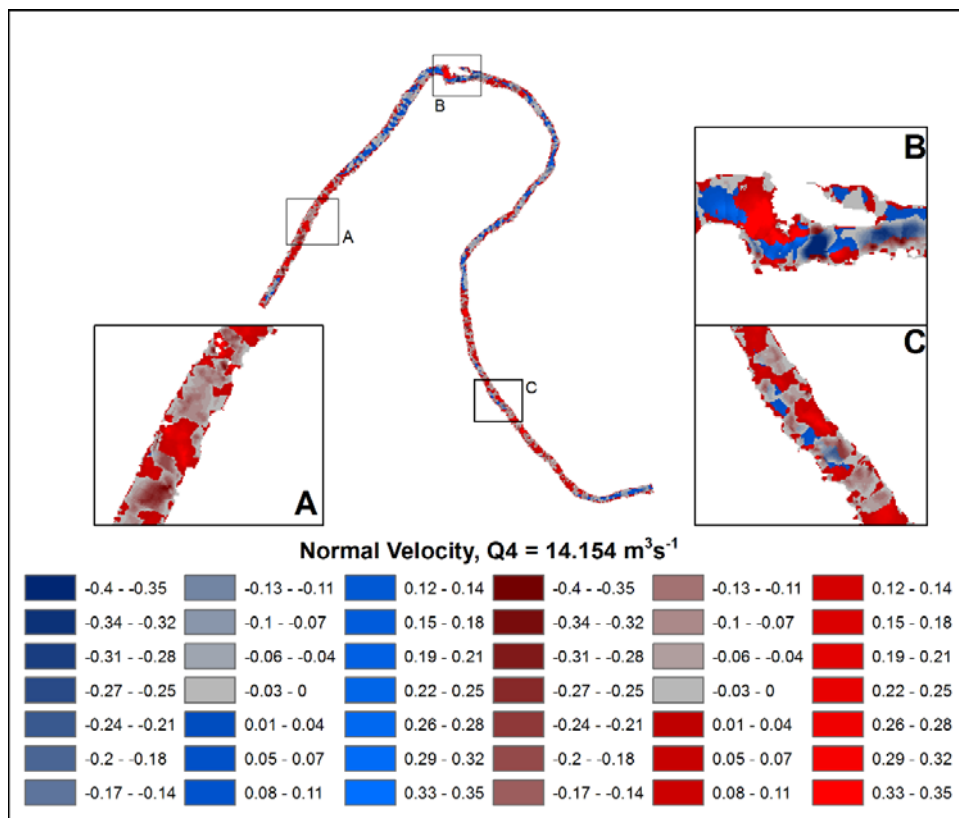
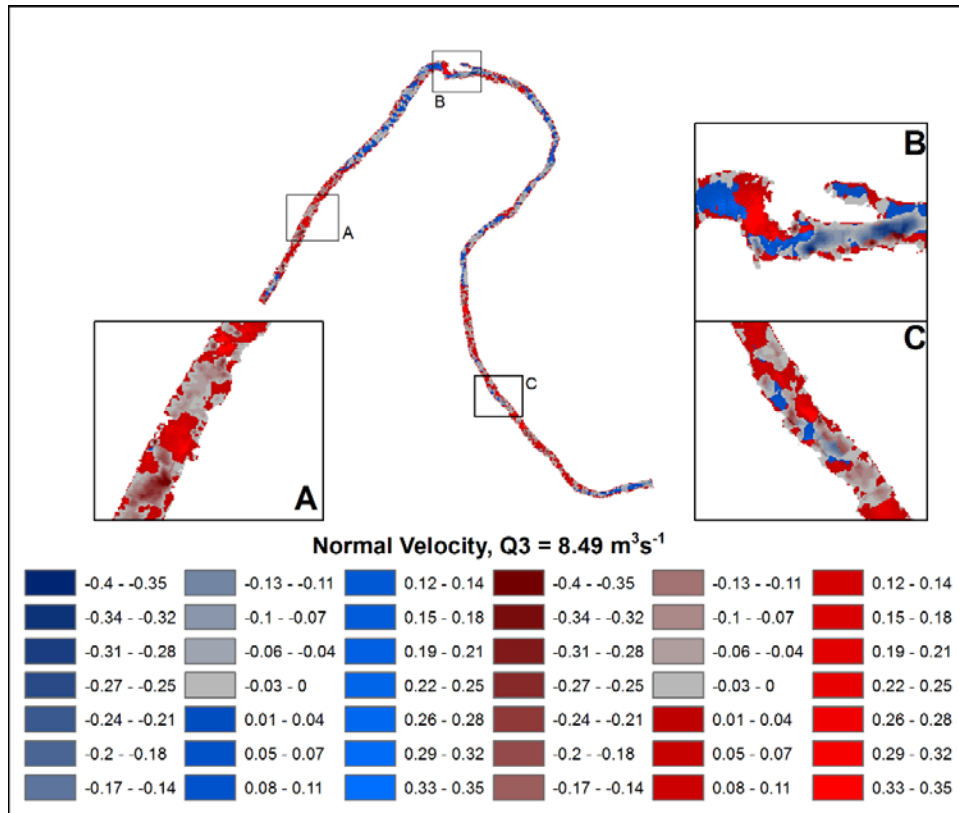


Figure 5.16 (cont'd). Spatial distribution of normal velocity (m/s) for Q1–Q6 for topographic highs (red colors) and lows (blue colors).

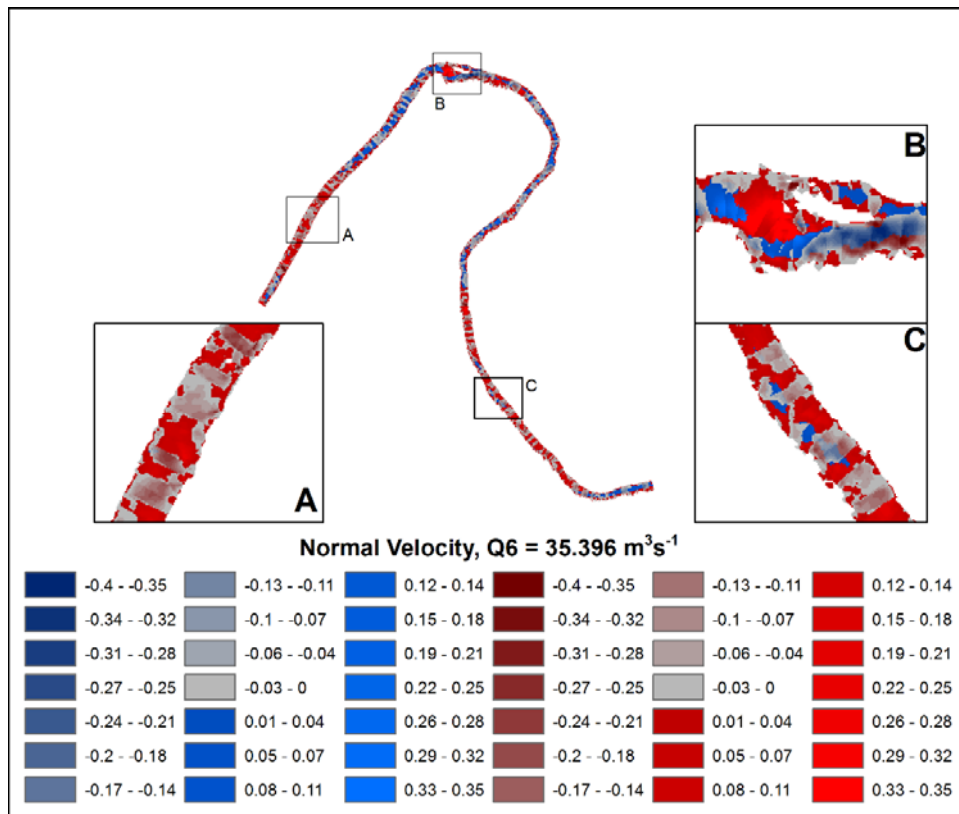
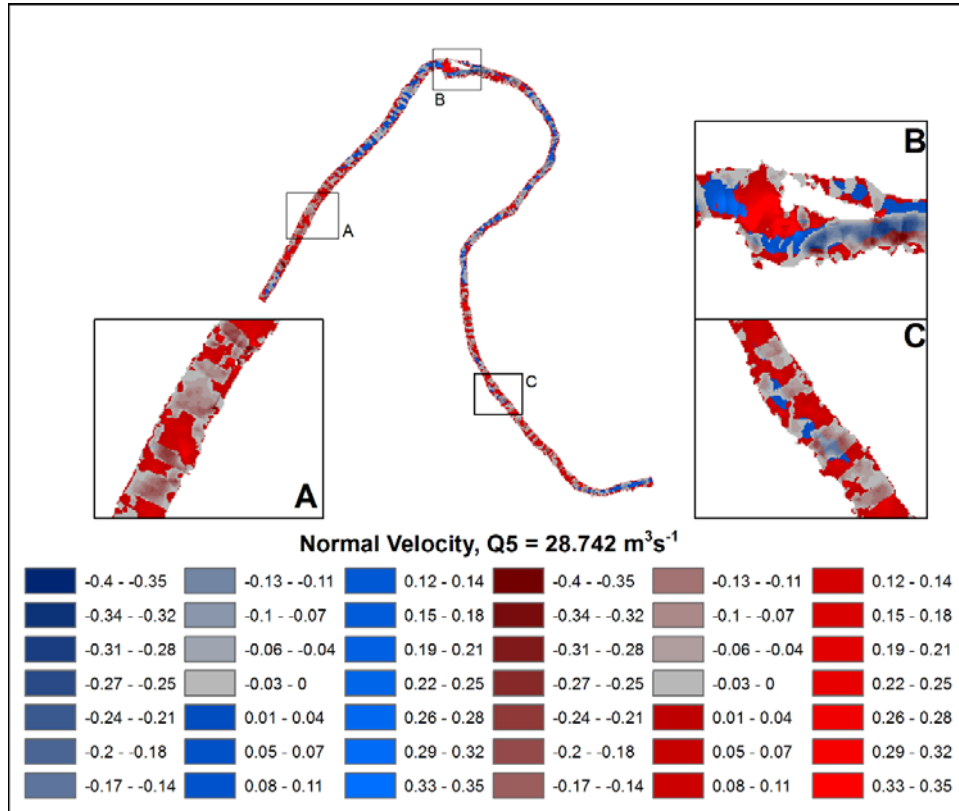


Figure 5.16 (cont'd). Spatial distribution of normal velocity (m/s) for Q1–Q6 for topographic highs (red colors) and lows (blue colors).

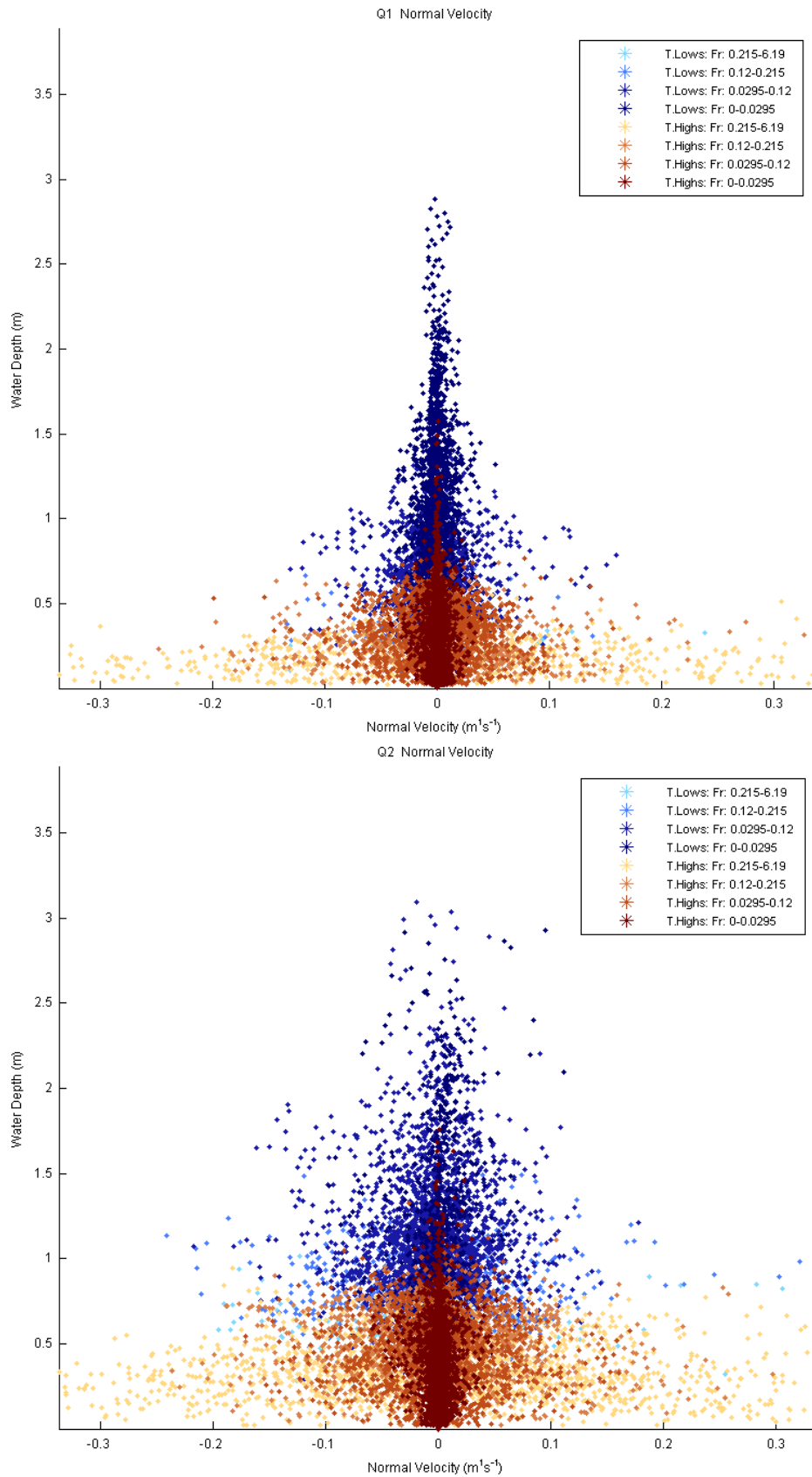


Figure 5.17. Distribution of normal velocity in relation to water depth for Q1–Q6 classified by topographic highs marked as T. Highs (brown colors), topographic lows marked as T. Lows (blue colors), and Froude number (Fr).

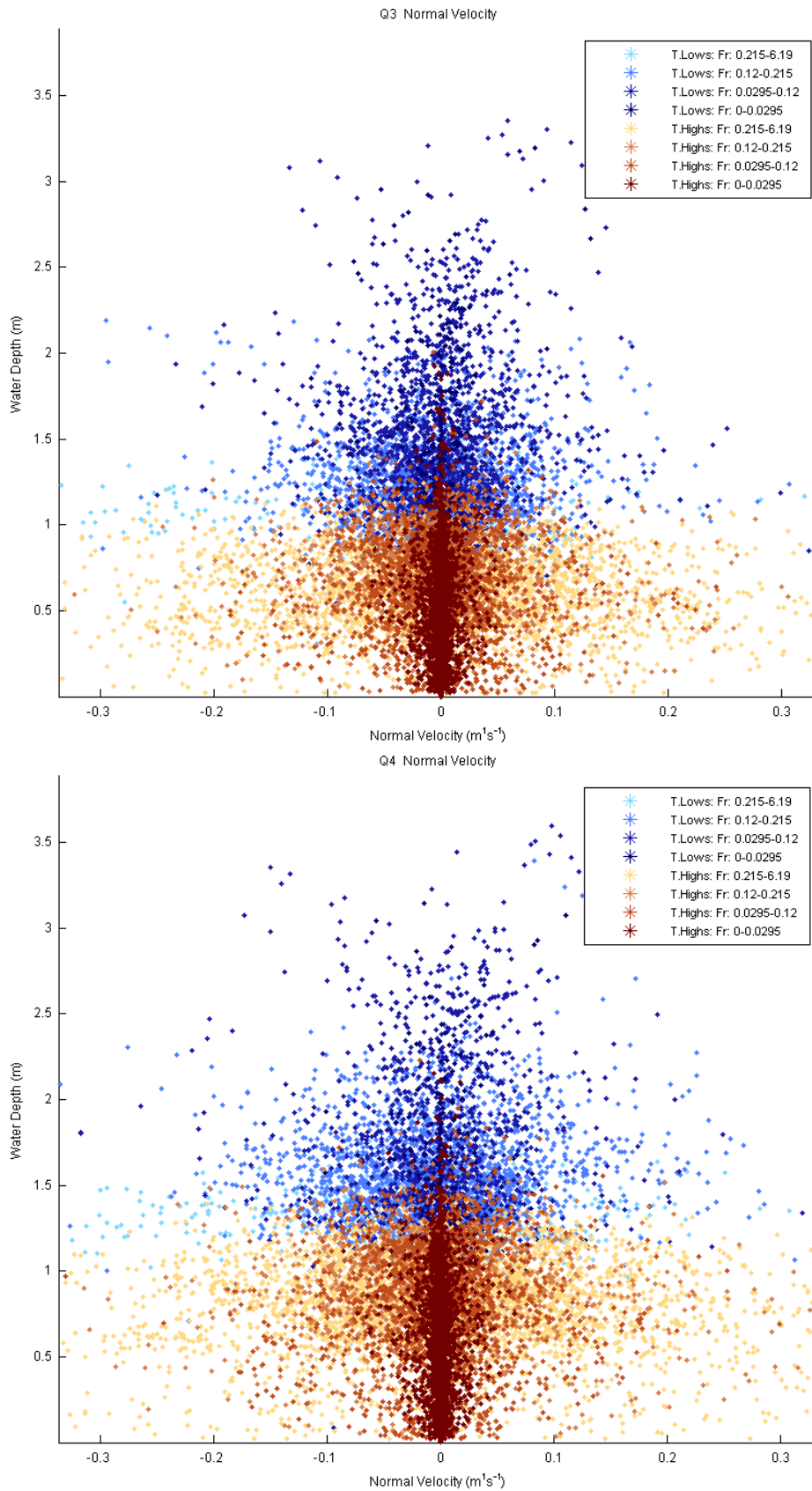


Figure 5.17 (con'td). Distribution of normal velocity in relation to water depth for Q1–Q6 classified by topographic highs marked as T. Highs (brown colors), topographic lows marked as T. Lows (blue colors), and Froude number (Fr).

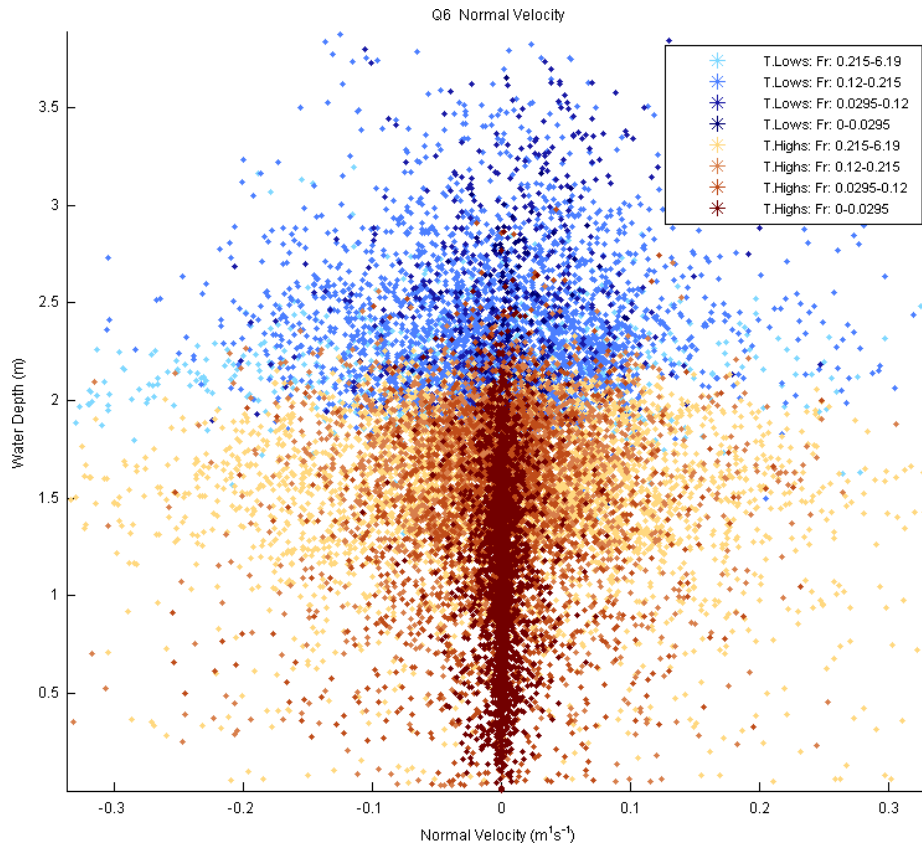
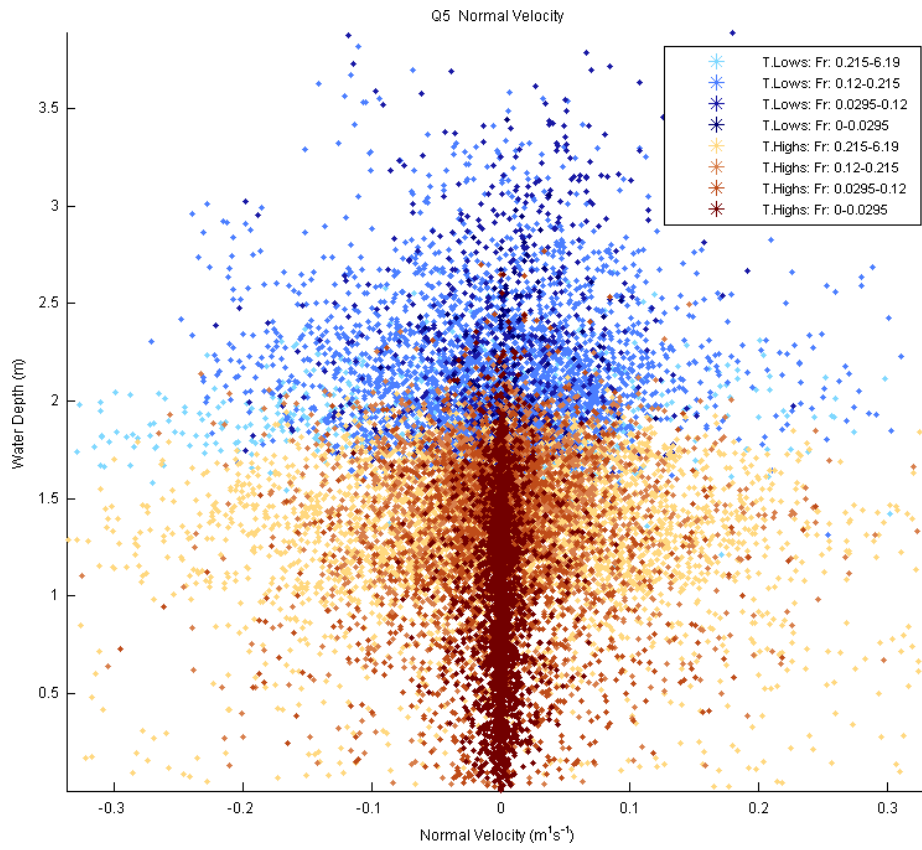


Figure 5.17 (cont'd). Distribution of normal velocity in relation to water depth for Q1–Q6 classified by topographic highs marked as T. Highs (brown colors), topographic lows marked as T. Lows (blue colors), and Froude number (Fr).

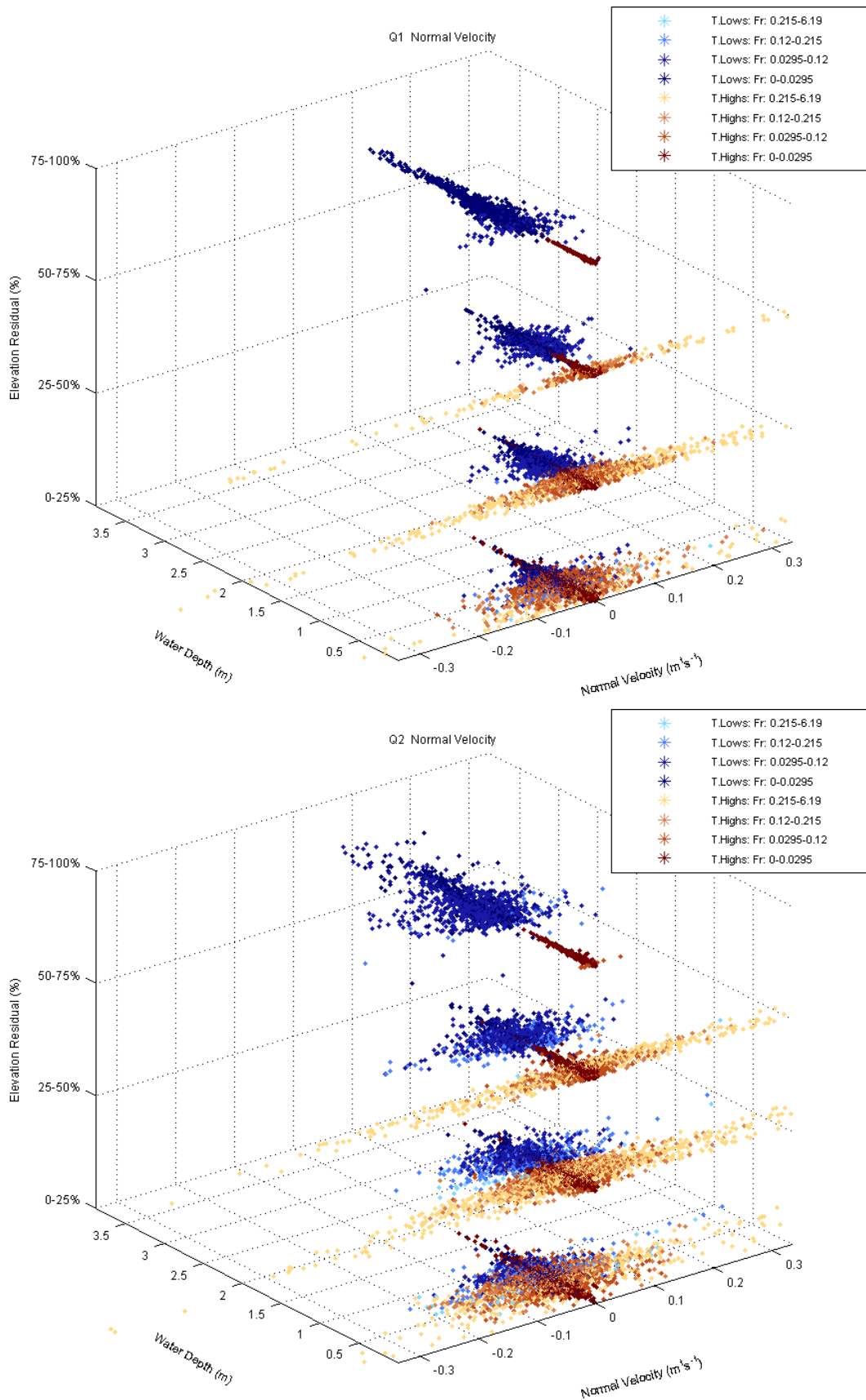


Figure 5.18. Distribution of normal velocity for topographic high (T. Highs)/low (T. Lows) subclasses (Figure 4.2) and Q1–Q6, classified by Froude number (Fr).

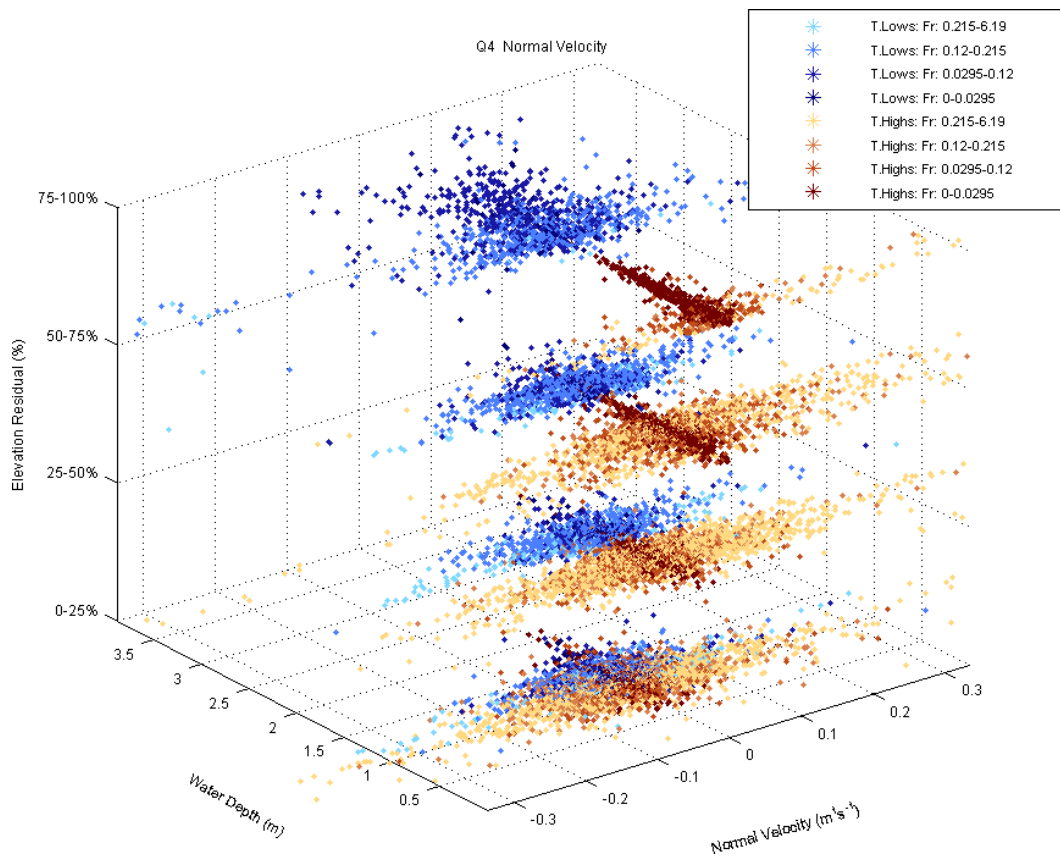
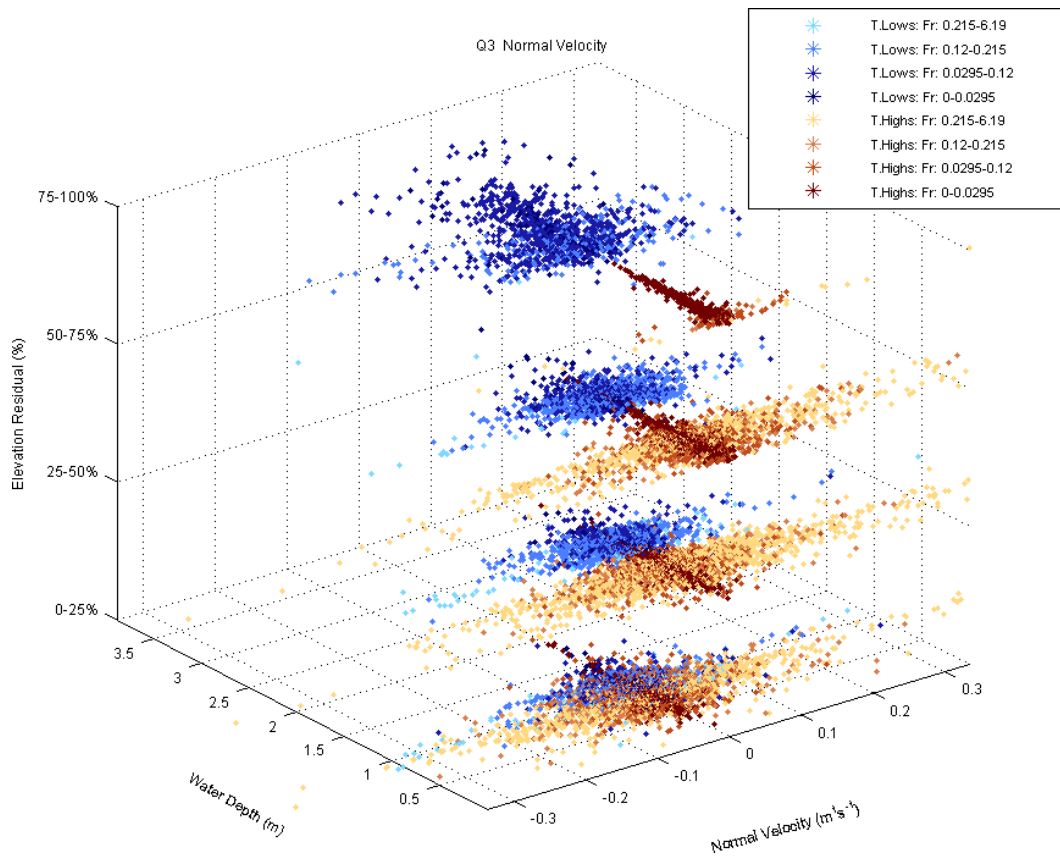


Figure 5.18 (cont'd). Distribution of normal velocity for topographic high (T. Highs)/low (T. Lows) subclasses (Figure 4.2) and Q1–Q6, classified by Froude number (Fr).

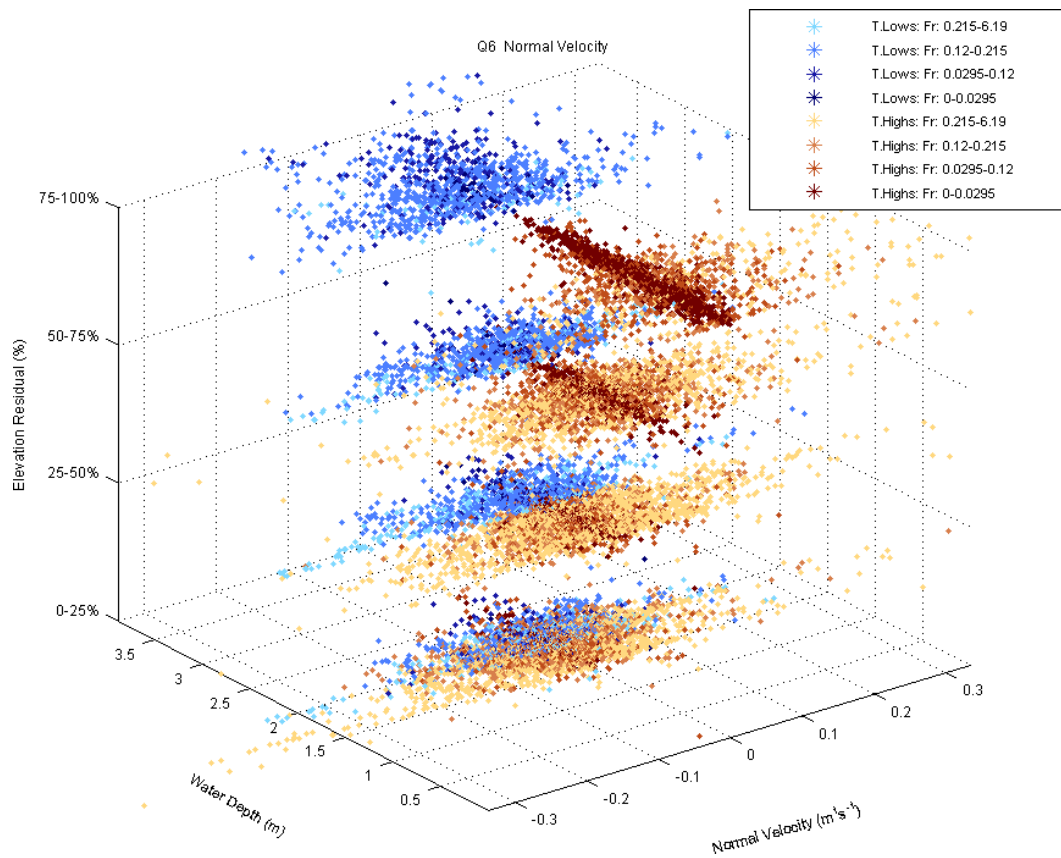
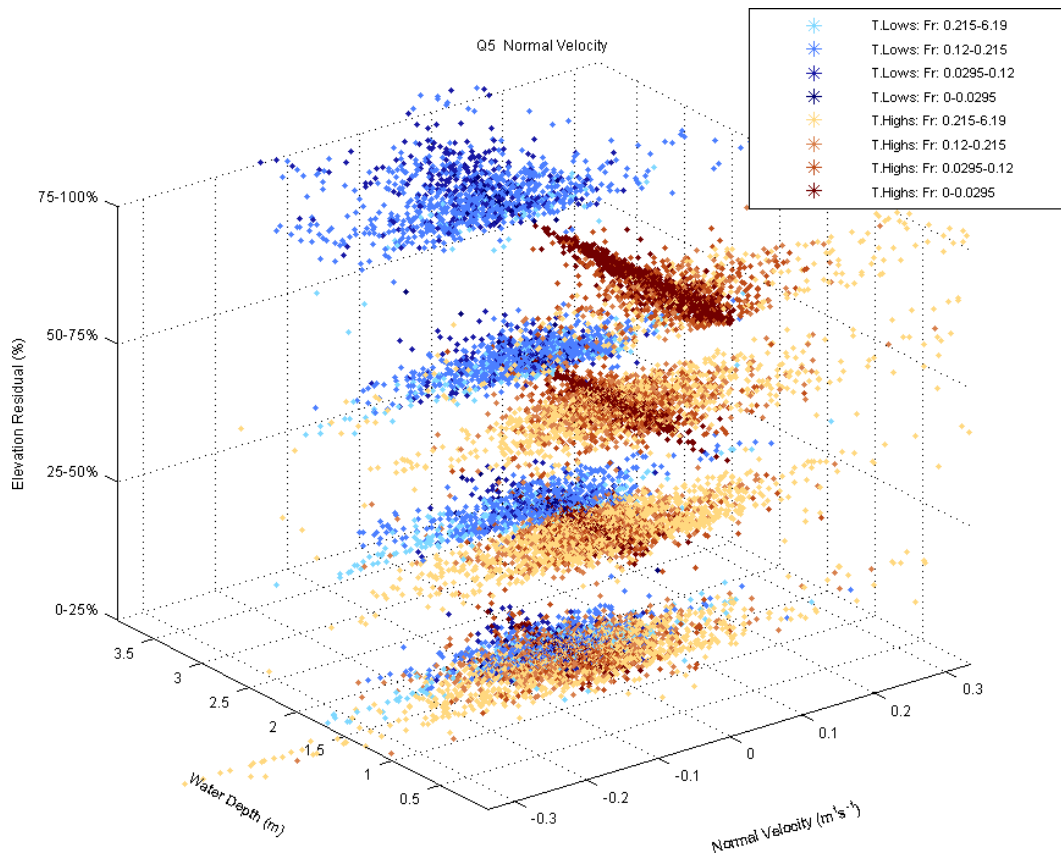


Figure 5.18 (cont'd). Distribution of normal velocity for topographic high (T. Highs)/low (T. Lows) subclasses (Figure 4.2) and Q1–Q6, classified by Froude number (Fr).

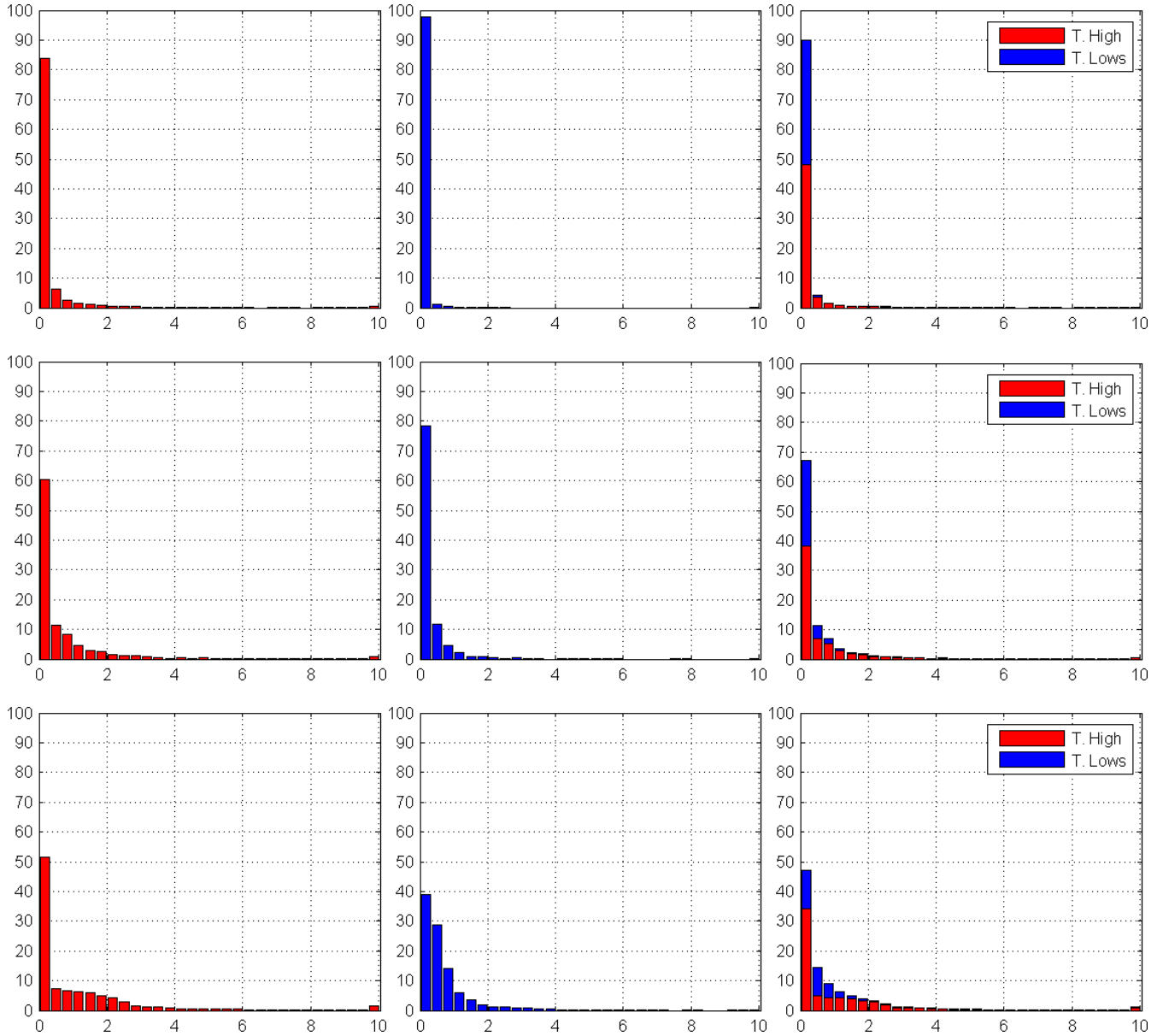


Figure 5.19. Distribution of shear stress for Q1–Q6 (rows, top to bottom) for topographic highs (marked as T. High) corresponding to the classes (+1)–(+4), topographic lows (marked as T. Lows) corresponding to the classes (-1)–(-4), and combined (columns, left to right). Horizontal and vertical axes correspond to shear stress ($\text{kg} \times \text{m/s}^2$) and the percent values of topographic classes, respectively.

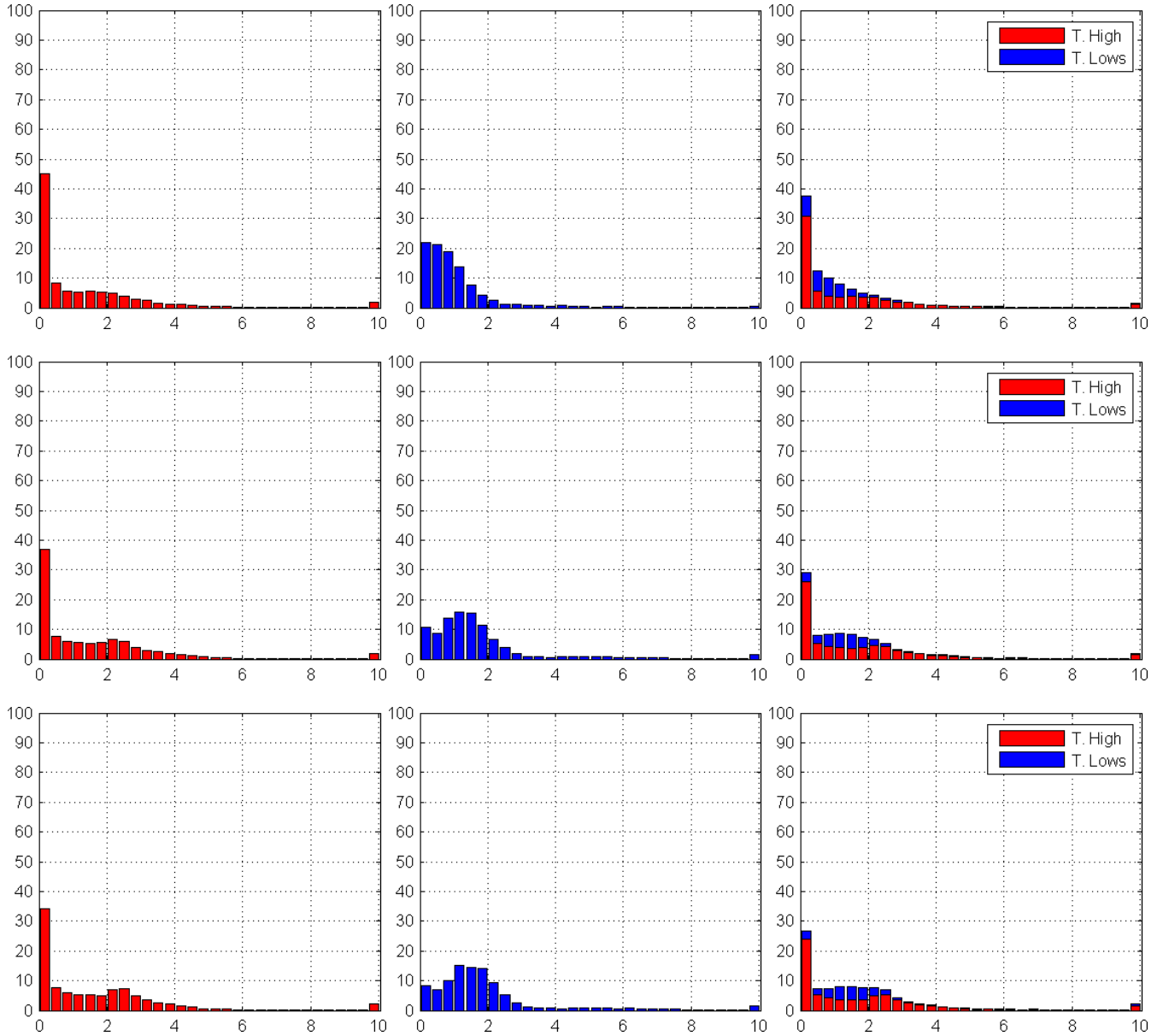


Figure 5.19 (cont'd). Distribution of shear stress for Q1–Q6 (rows, top to bottom) for topographic highs (marked as T. High) corresponding to the classes (+1)–(+4), topographic lows (marked as T. Lows) corresponding to the classes (-1)–(-4), and combined (columns, left to right). Horizontal and vertical axes correspond to shear stress ($\text{kg} \times \text{m/s}^2$) and the percent values of topographic classes, respectively.

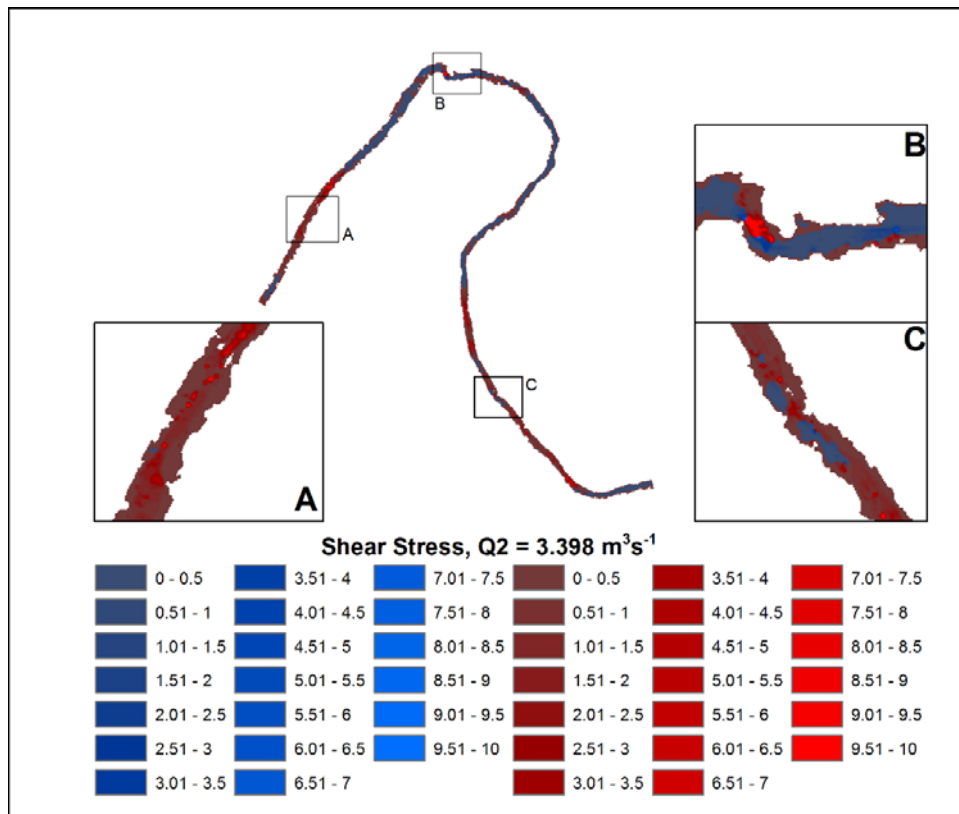
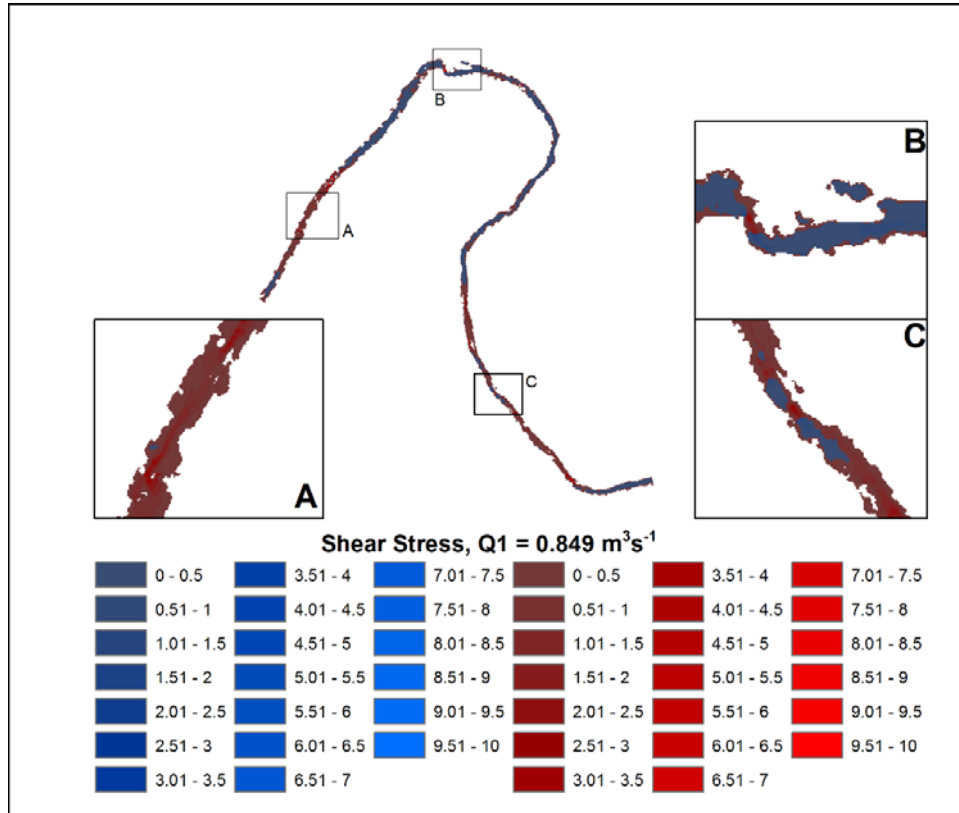


Figure 5.20. Spatial distribution of shear stress ($\text{kg} \times \text{m/s}^2$) for Q1–Q6 for topographic highs (red colors) and lows (blue colors).

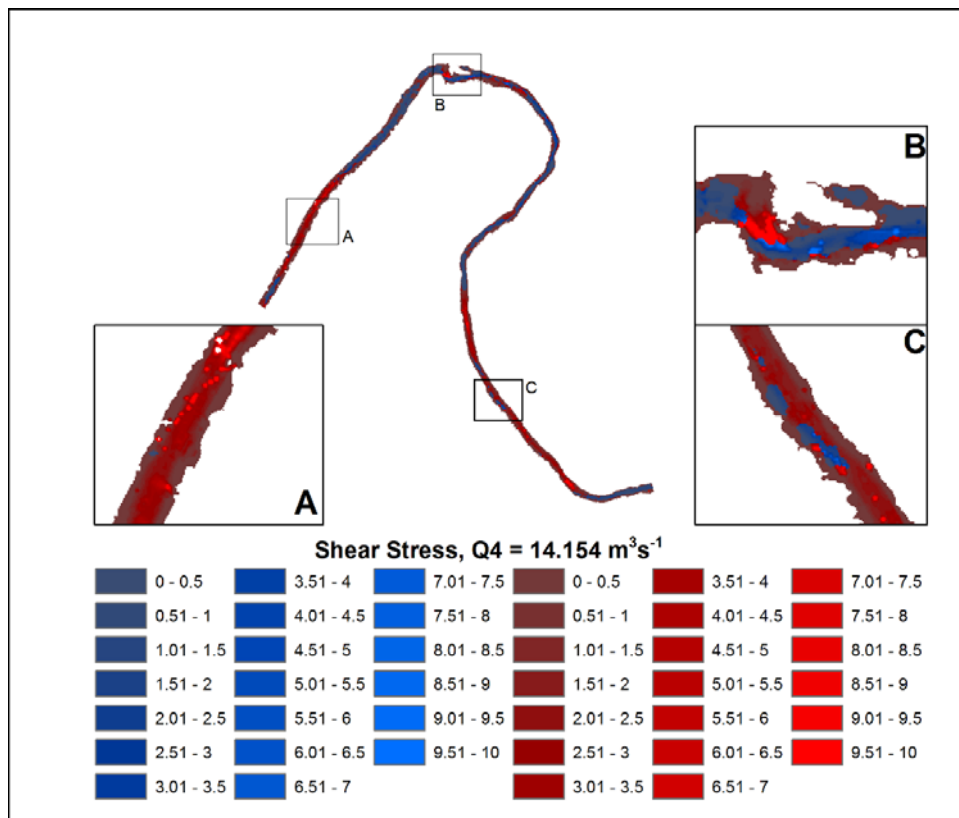
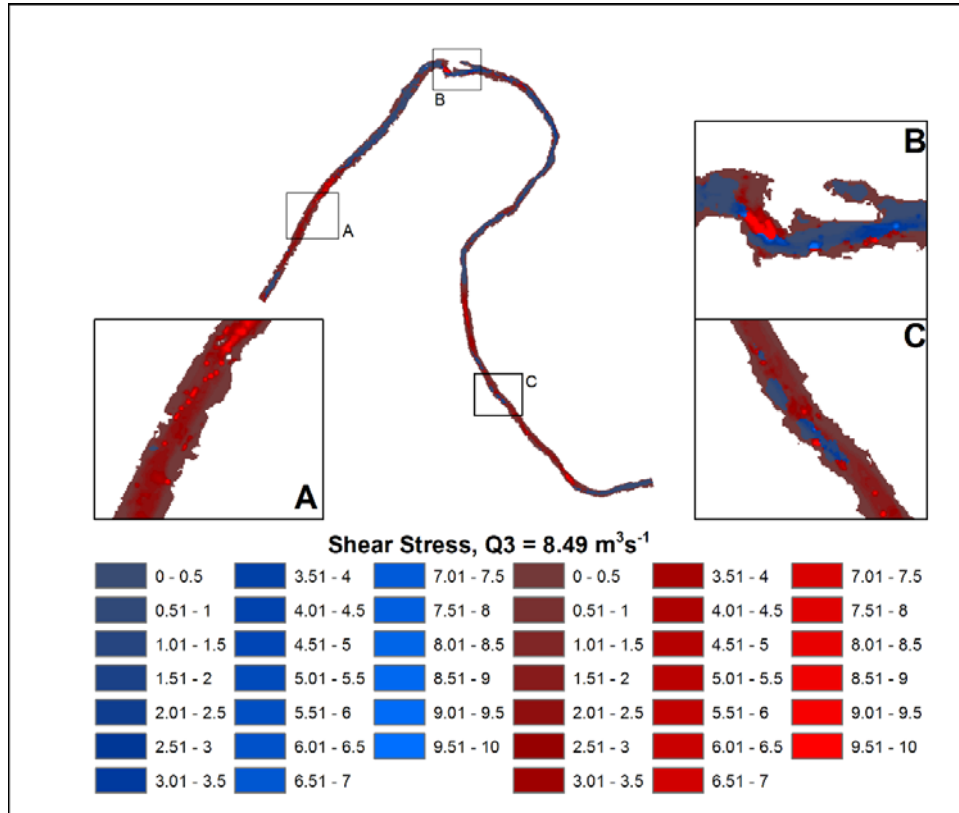


Figure 5.20 (cont'd). Spatial distribution of shear stress ($\text{kg} \times \text{m/s}^2$) for Q1–Q6 for topographic highs (red colors) and lows (blue colors).

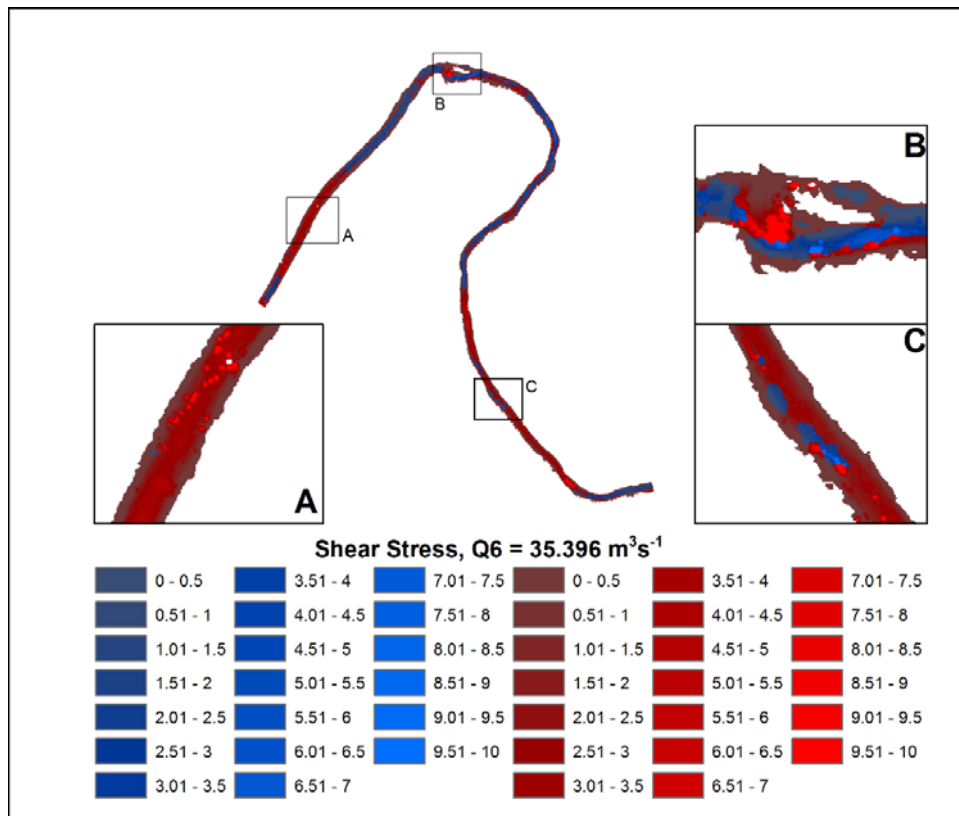
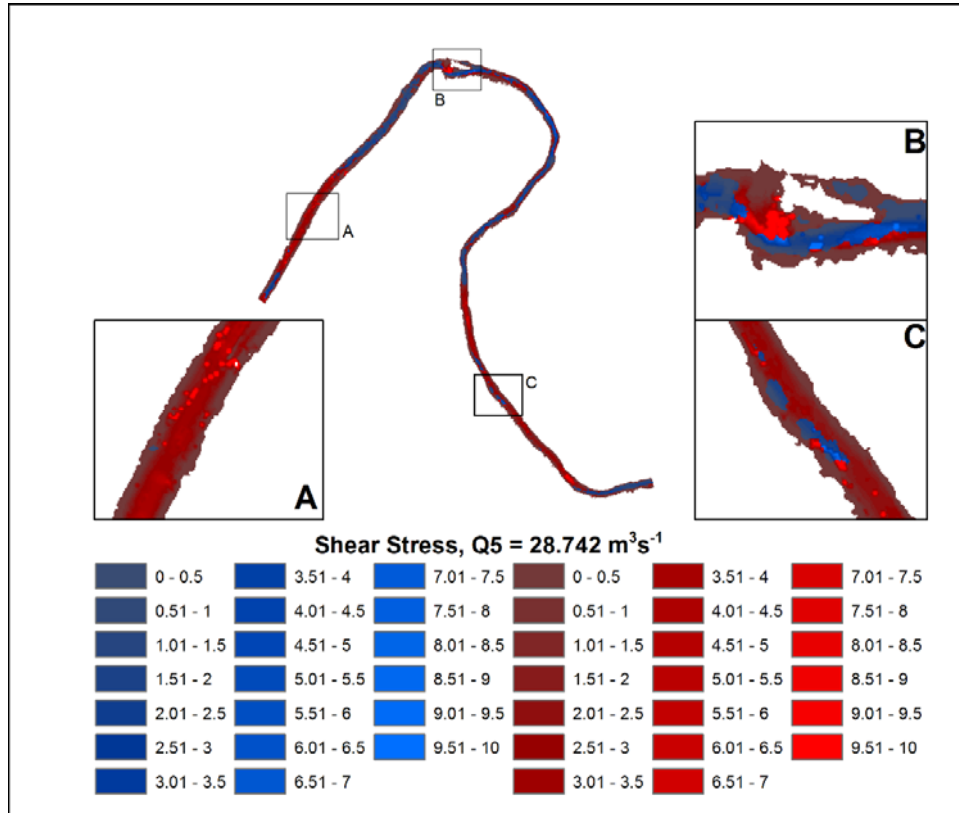


Figure 5.20 (cont'd). Spatial distribution of shear stress ($\text{kg} \times \text{m/s}^2$) for Q1–Q6 for topographic highs (red colors) and lows (blue colors).

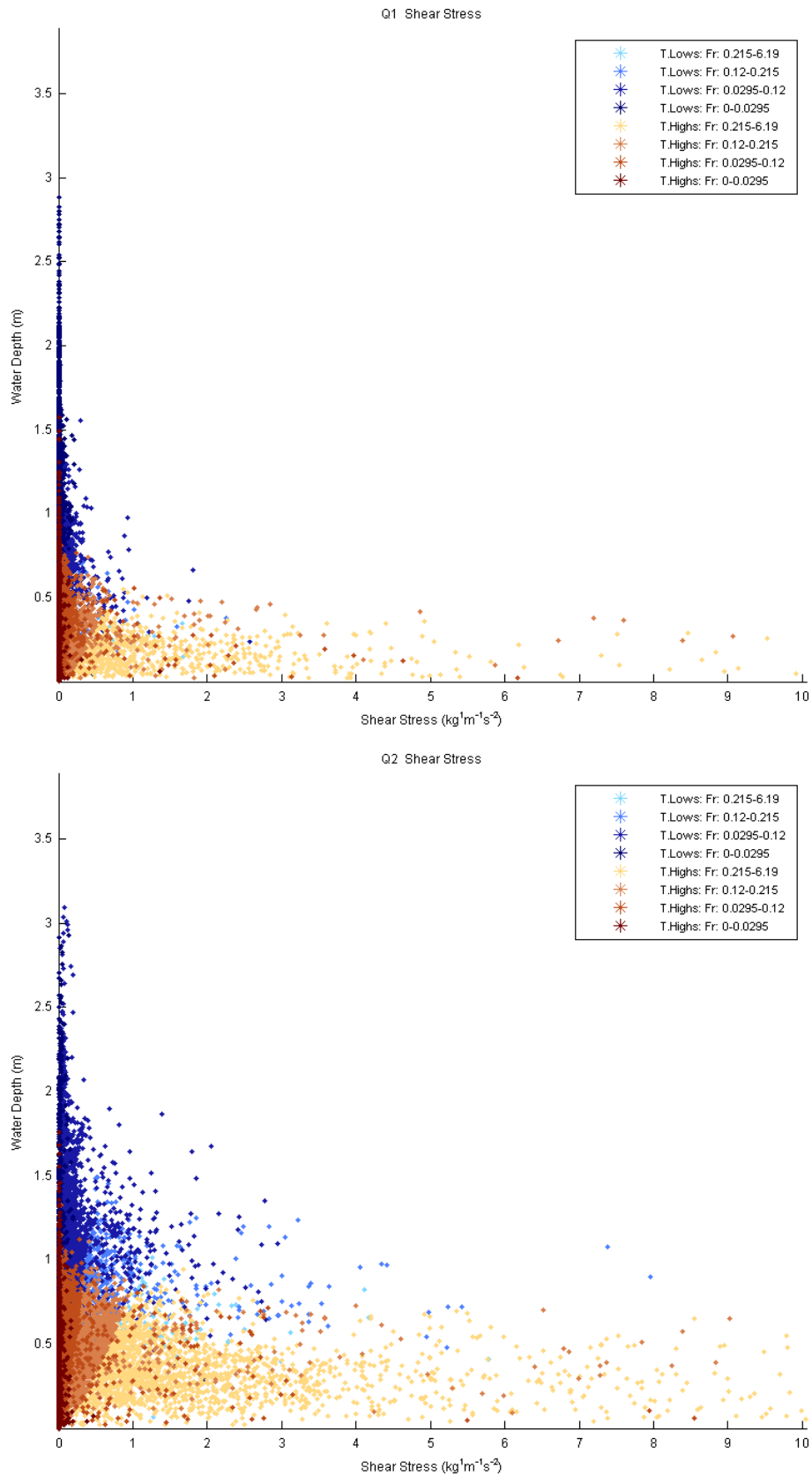


Figure 5.21. Distribution of shear stress in relation to water depth for Q1–Q6 classified by topographic highs marked as T. Highs (brown colors) and topographic lows marked as T. Lows (blue colors) and Froude number (Fr).

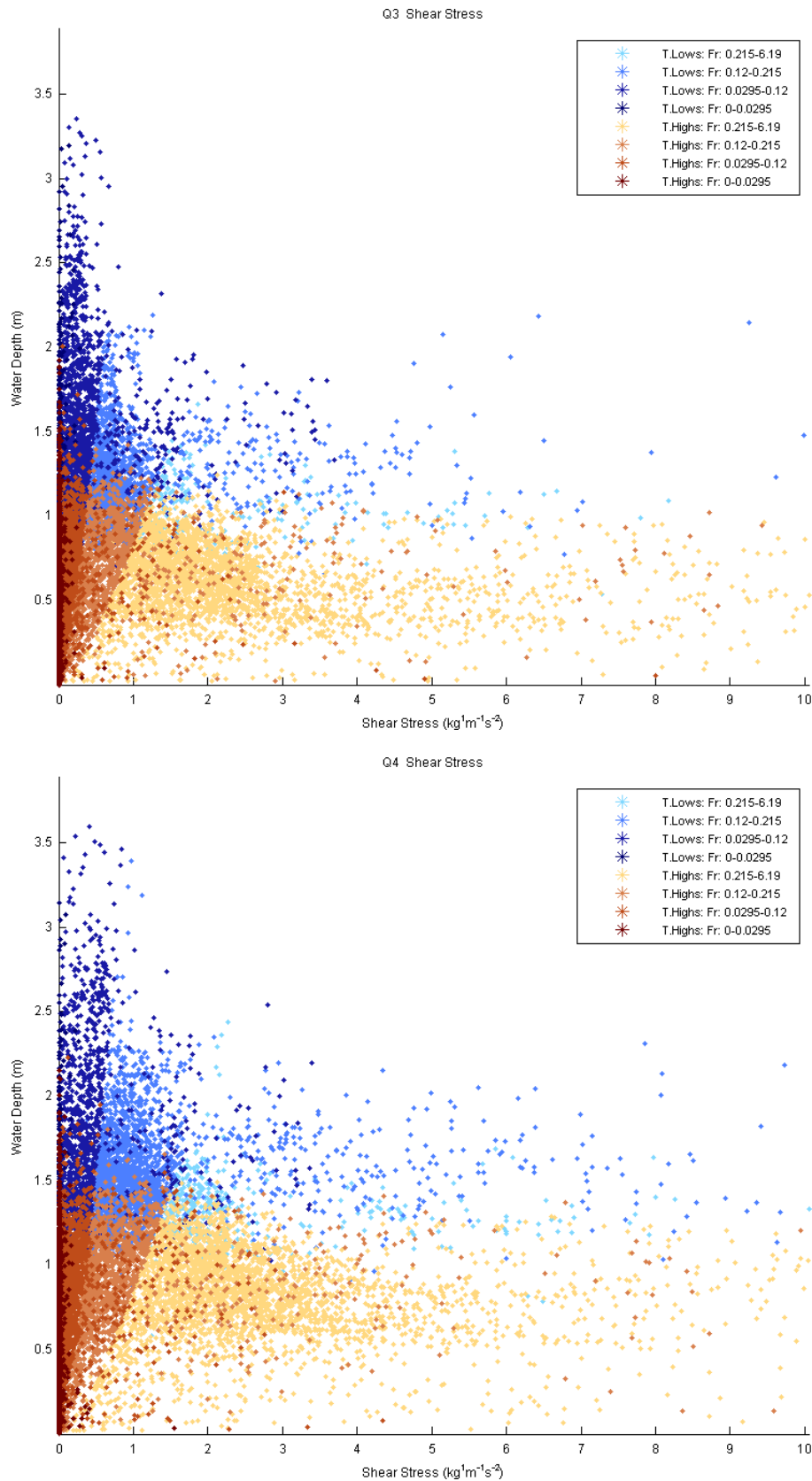


Figure 5.21 (cont'd). Distribution of shear stress in relation to water depth for Q1–Q6 classified by topographic highs marked as T. Highs (brown colors) and topographic lows marked as T. Lows (blue colors) and Froude number (Fr).

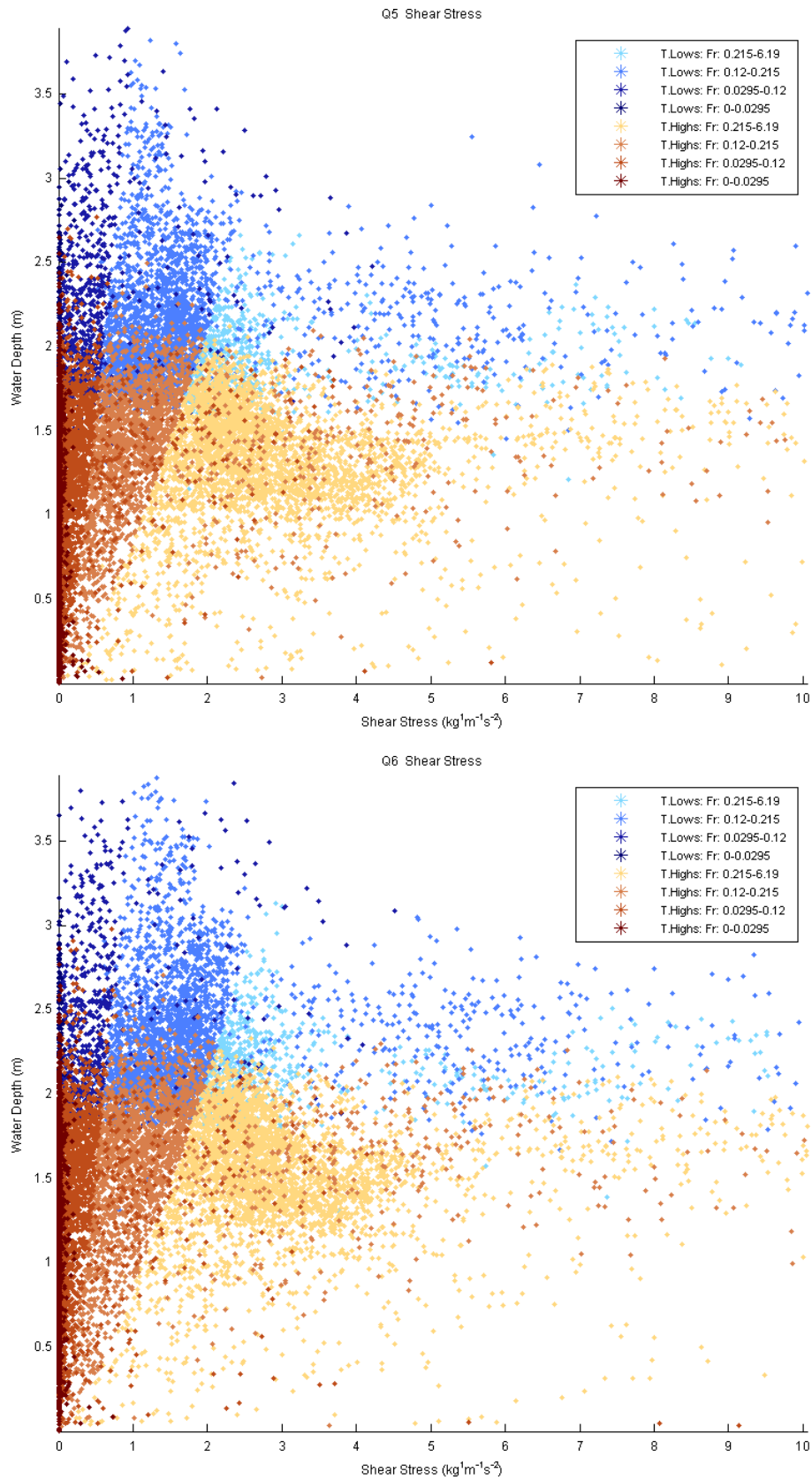


Figure 5.21 (cont'd). Distribution of shear stress in relation to water depth for Q1–Q6 classified by topographic highs marked as T. Highs (brown colors) and topographic lows marked as T. Lows (blue colors) and Froude number (Fr).

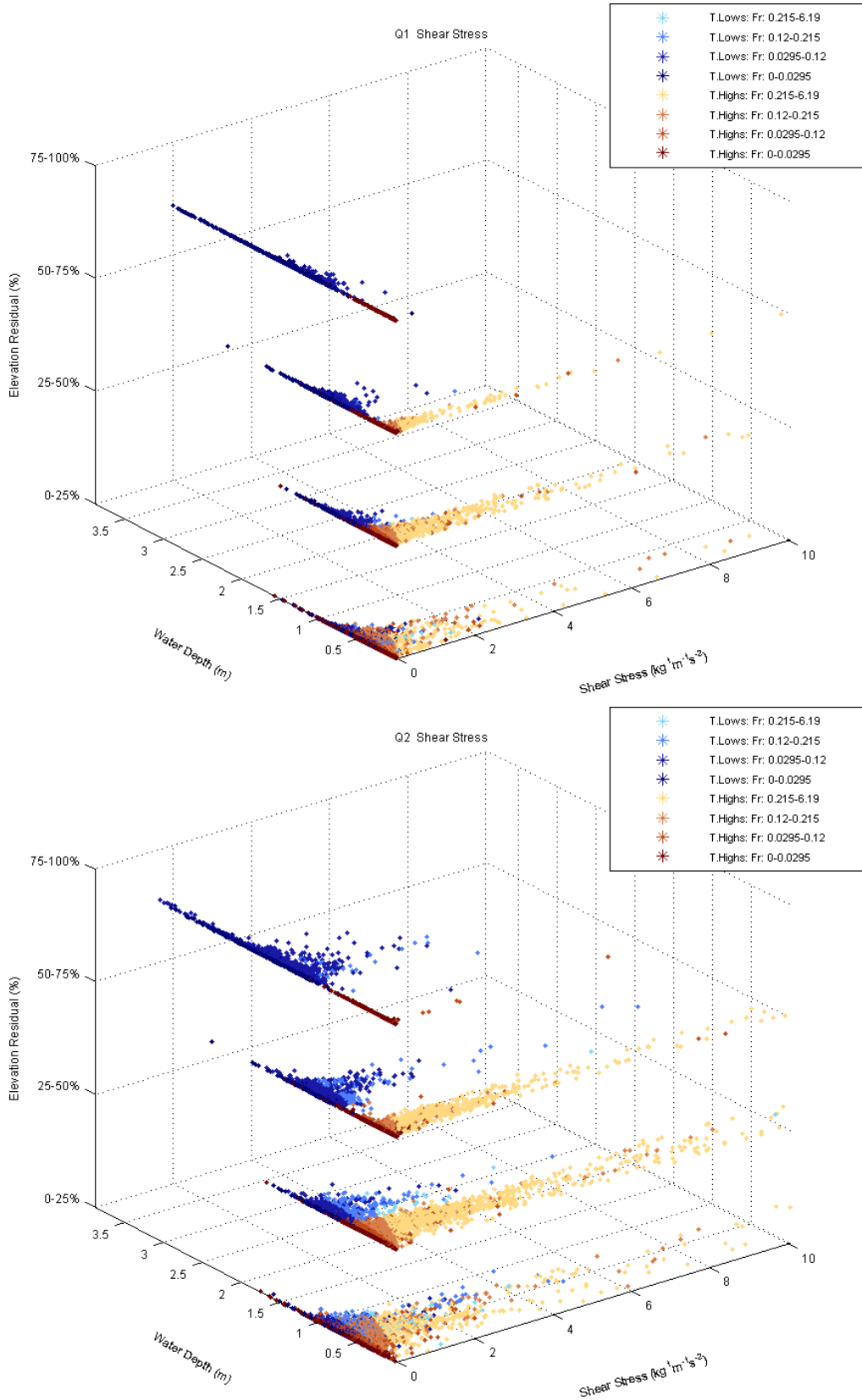


Figure 5.22. Distribution of shear stress for topographic high (T. Highs)/low (T. Lows) subclasses (Figure 4.2) and Q1–Q6, classified by Froude number (Fr).

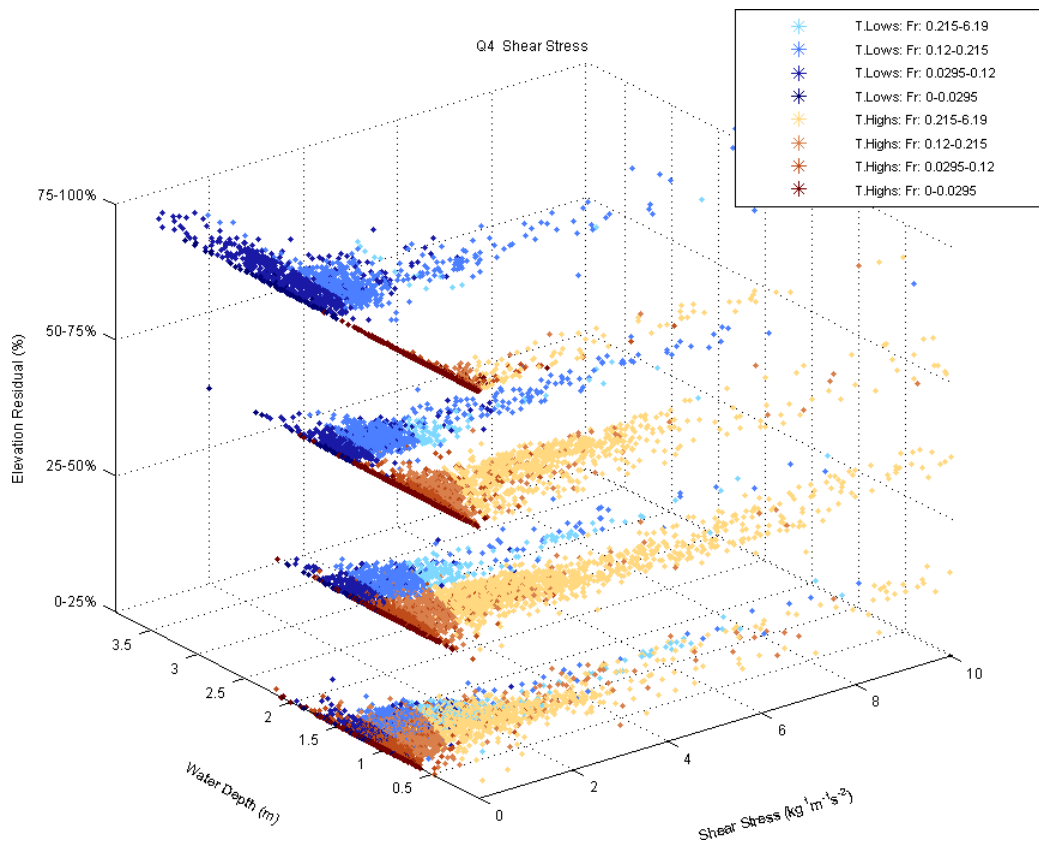
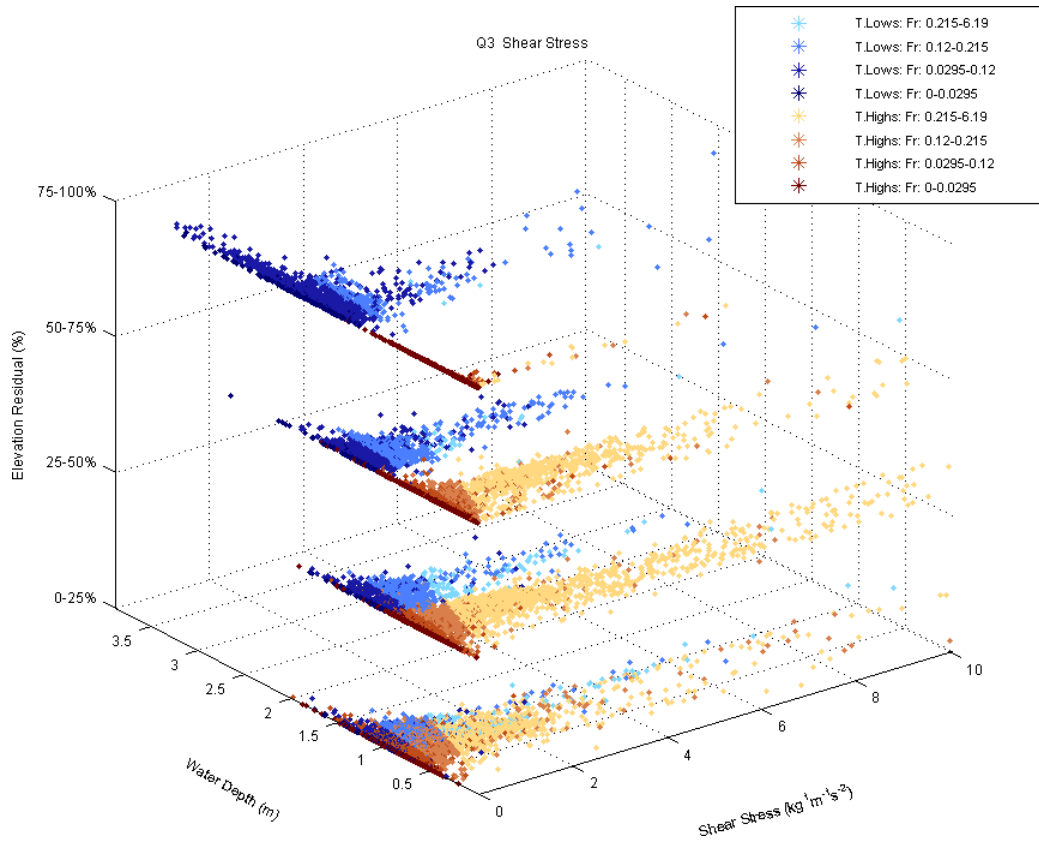


Figure 5.22 (cont'd). Distribution of shear stress for topographic high (T. Highs)/low (T. Lows) subclasses (Figure 4.2) and Q1–Q6, classified by Froude number (Fr).

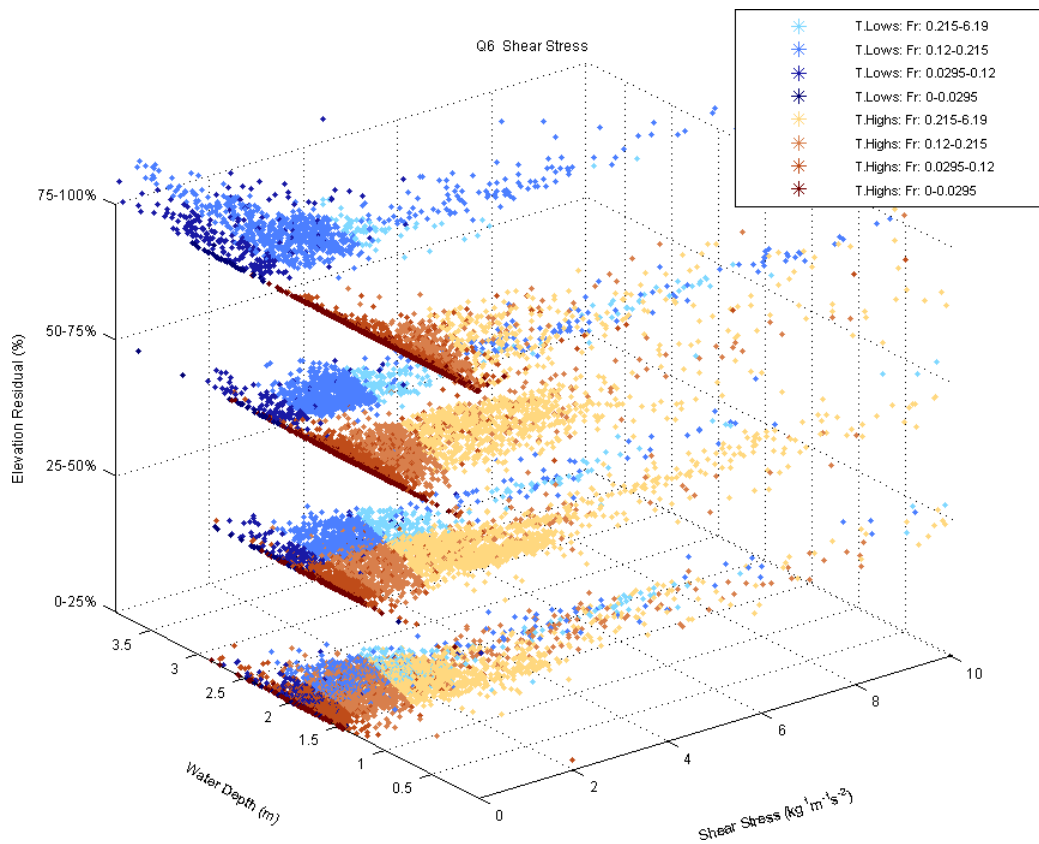
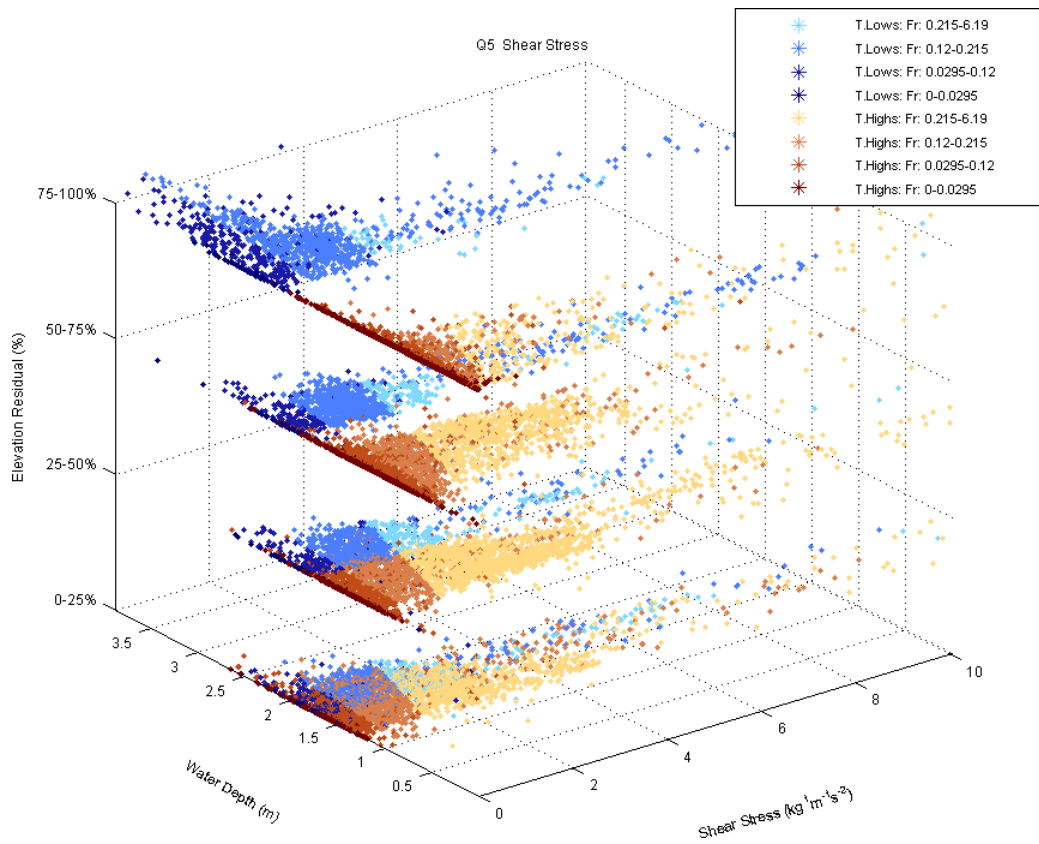


Figure 5.22 (cont'd). Distribution of shear stress for topographic high (T. Highs)/low (T. Lows) subclasses (Figure 4.2) and Q1–Q6, classified by Froude number (Fr).

6. THE FALLS CITY STUDY REACH

The Falls City study reach (Figure 6.1) is one of the study sites on the LSAR (Figure 3.3). This reach is located on LSAR Segment 3 and Reach 5 (Figures 3.1–3.2; TIFP and SARA (2011)).

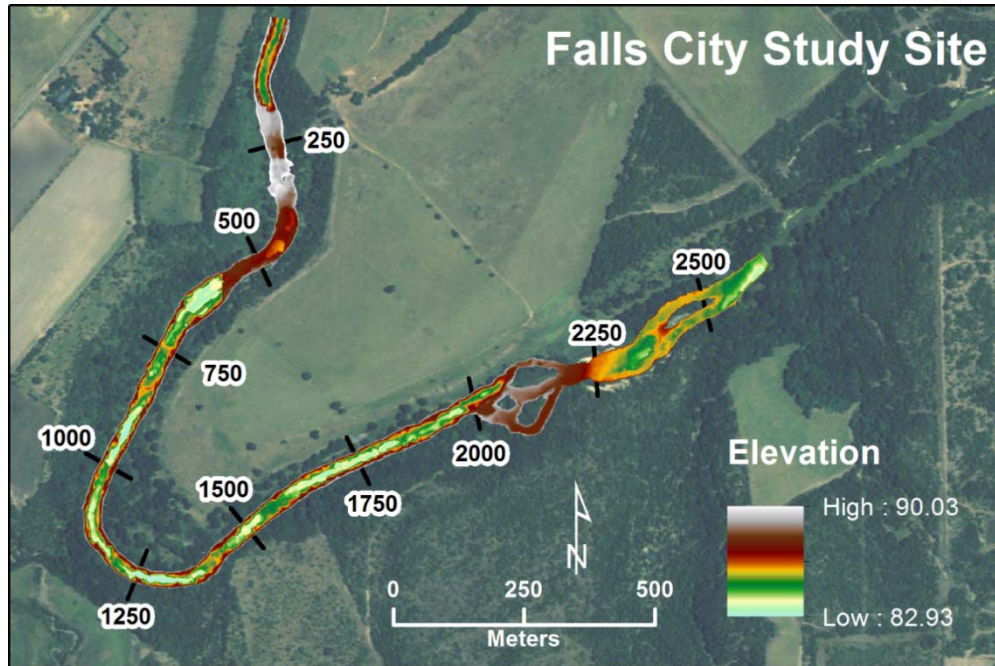


Figure 6.1. The Falls City study reach and its bathymetric distribution.

6.1. GEOMORPHIC CHARACTERISTICS

To determine the geomorphic characteristics of the river channel at the Fall City study reach, first we detrended channel topography using the approach discussed in *Section 4.1* (Figure 4.2). Then, we determined the geomorphic unit classes as topographic highs (sediment bars/riffles/edges) and topographic lows (pools) from the topographic residuals. We subclassified the geomorphic unit classes according to the quartiles of the detrended topographic elevations (i.e., classes (+1)–(+4) for topographic highs and (-1)–(-4) for topographic lows, respectively; Figures 4.2 and 6.2).

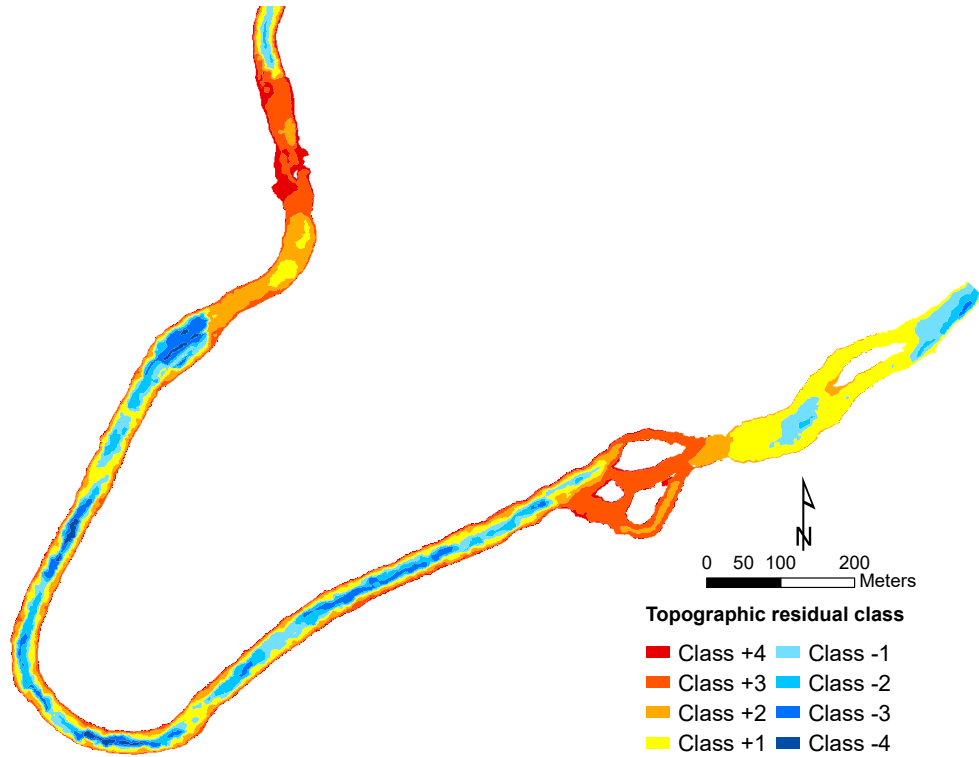


Figure 6.2. Geomorphic unit classes for the Falls City study reach based on the topographic residuals. The (+) classes represent the topographic highs and (-) classes represent topographic lows. Detailed class descriptions are given in Figure 4.2. Flow direction is from left to right.

The distribution of geomorphic unit classes indicates that topographic highs (sediment bars/riffles/edges, corresponding to the classes (+1)–(+4)), Figure 6.2) account for roughly 70% of the total channel area, and the remaining (30%) of the study area is composed of topographic lows (pools, corresponding to the classes (-1)–(-4); Table 6.1, Figures 6.2 and 6.3).

Spatially, the distributions of topographic highs and lows are patchy (Figure 6.2). Locations of topographic lows are grouped at the mid-portion of channel between meter marker 500 and 1750 meters (Figure 6.1) and at the influent and effluent portions. Locations of topographic highs, like in the case of Goliad study reach, are at channel margins and take the entire channel profile at locations that are in between locations of topographic lows. In particular, there are regions featuring multiple mid-channel bars, and exclusively featuring topographic highs without the presence of topographic low classes.

Table 6.1. Areal distribution of geomorphic unit classes in the Falls City study reach.

Geomorphic Unit Class (Topographic residual percentile)	Total Area (m ²)	Percent Coverage (%)	Patch Statistics					
			Mean area (m ²)	Min area (m ²)	Max area (m ²)	StDev (m ²)	Patches (Number)	
Topo Highs (bars/riffles/ edges)	+4 (75-100th)	5529	5.02	7.74	1	1942	88.53	714
	+3 (50-75th)	23880	21.67	426.43	1	12082	1873.76	56
	+2 (25-50th)	19403	17.61	103.76	1	7298	579.22	187
	+1 (0-25th)	28801	26.14	505.28	1	13337	1832.06	57
Topo Lows (pools)	-1 (0-25th)	15286	13.87	65.89	1	2269	257.03	232
	-2 (25-50th)	10624	9.64	104.16	1	1411	242.82	102
	-3 (50-75th)	5668	5.14	157.44	1	1635	336.50	36
	-4 (75-100th)	993	0.90	124.13	13	294	99.13	8

Total area: Total area of a specific class (m²).

Percent (%) coverage: Percentage of the area of a specific class within the total area (%).

Geomorphic Unit Class Patch statistics:

Mean area: Average patch area of individual patches within a class (m²).

Minimum area: Minimum patch area within a specific class (m²).

Maximum area: Maximum patch area within a specific class (m²).

STDev: Standard deviation of patch areas around the mean within a specific class (m²).

Patches: Number of separate patches for each class (Number).

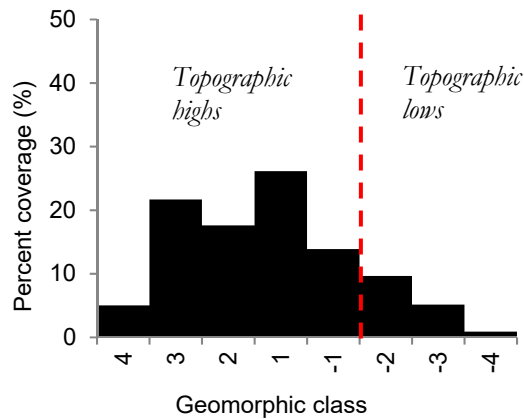


Figure 6.3. Percent coverage of geomorphic classes for the Falls City study reach. The (+) classes represent the topographic highs and (-) classes represent topographic lows. Detailed class descriptions are given in Figure 4.2.

Topographic low subclasses +3/4 in the Falls City reach are grouped as a series of pools in the stream, and topographic high subclasses +3/4 are generally at channel margins. However, the regionally, the channel is dominated by topographic high classes (Table 6.1; Figure 6.3).

Basic patch statistics show that topographic high subclasses +1 and +3 have the highest range of patch areas (1-13337 and 1–12082 m², respectively), with the means of 505.28 and 426.43 m² and STDev of 1832.06 and 1873.76 m², respectively. The highest portion of topographic lows (subclass -1) has the greatest range of patch size (1-2269 m²), with a mean of 65.89 m² and a STDev of 257.06 m² (Table 6.1).

6.2. RELATIONSHIPS BETWEEN GEOMORPHIC UNITS AND HYDRAULIC PROPERTIES

We examined the relationships between geomorphic units (Figure 4.2) and the hydraulic properties of the reach. We obtained these hydraulic properties from the simulations performed using River2D® model developed for the study reach (TIFP and SARA, 2011) at five different discharge conditions, Q1–Q5. Three of these modeled discharges, low, medium, and high discharges (Q2, Q3, and Q4, respectively) correspond to the base level discharges defined as dry, normal, and wet conditions (Table 6.2).

Table 6.2. Information on the Falls City study reach and model input parameters for River2D® model.

Class	Discharge for base levels		Modeled discharge		Field reported discharge		Assessment of field Q	Field data Collection date	Type of field data
	(m3/s)	(cfs)	(m3/s)	(cfs)	(m3/s)	(cfs)			
Dry	3.68	130	0.43	15	–	–	Q1 (<Q2)	–	–
Normal	7.08	250	3.05	108	2.55	90	Low (Q2)	7/30/2009	Habitat
Wet			5.92	209	6.82	241	Medium (Q3)	7/26/2010	Habitat
			12.71	449	–	–	High (Q4)	3/9/2010	Habitat
			35.40	1250	–	–	Q5 (>Q4)	–	–

*Base levels are defined by observing fish habitat weighted usable area (WUA) (River2D) (TIFP, 2011; pg. 71, http://www.twdb.state.tx.us/surfacewater/flows/instream/lower_san_antonio/doc/LSAR_FINAL_INTERIM_REPORT_20110831.pdf)

Dry: typically based on minimum to get 20% habitat available for each guild.

Average: typically based on flow to get at least 50% habitat available for each guild.

Wet: typically based on analysis of WUA for habitat degradation.

The relationship between flow level and inundated area is described in Figure 6.4. There is a relatively high change between flow stages for Q1 and Q2. Especially after Q3, the changes in inundated area between flow levels decrease as flow stage increases. Overall, the relationship appears to be logarithmic (i.e, inundated area = $4493.8 \times \ln(Q) + 92767$, with an R^2 of 0.9752).

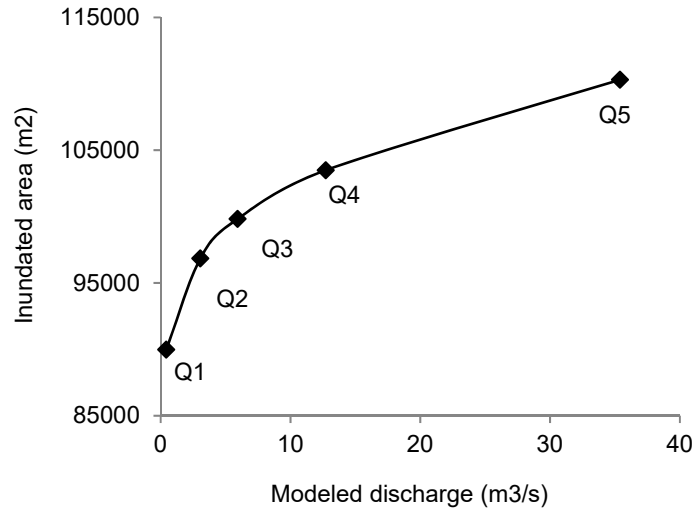


Figure 6.4. Inundated area (m²) vs. modeled discharge (m³/s) for the Falls City study reach.

Table 6.3 summarizes the minimum and maximum values of the hydraulic variables obtained from River2D® models for each discharge condition from Q1 to Q5 (Table 6.2).

Table 6.3. Summary of River2D® model output parameters and min-max values for modeled discharges, Q1–Q5 (Table 6.2).

Model output parameters	Modeled discharge $\begin{pmatrix} \text{min} \\ \text{max} \end{pmatrix}$				
	Q1	Q2	Q3	Q4	Q5
Water depth (m)	0.020	0.020	0.020	0.020	0.020
	5.462	5.581	5.654	5.771	6.020
Froude number (–)	0.000	0.000	0.000	0.000	0.000
	4.151	7.310	5.746	15.431	8.131
Velocity magnitude (m/s)	0.000	0.000	0.000	0.000	0.000
	2.224	4.086	5.406	8.024	7.560
Streamwise velocity (m/s)	-0.092	-0.386	-0.475	-0.852	-2.192
	2.185	3.572	3.931	7.997	6.076
Normal velocity (m/s)	-1.452	-3.638	-4.564	-3.617	-4.499
	0.660	2.113	1.515	2.110	1.989
Shear stress (kg / (m × s ²))	0.000	0.000	0.000	0.000	0.000
	95.830	99.722	99.743	99.947	99.932
WSE (m)	85.103	85.191	85.334	85.531	85.922
	89.098	89.325	89.457	89.657	90.047

We examined the distribution of hydraulic variable values obtained from River2D® models in relation to geomorphic properties of the study reach and also the modeled discharges, Q1–Q5 (Table 6.2). For this purpose, we analyzed these distributions as discussed in *Section 4.5*.

6.3. WATER DEPTH AND FROUDE NUMBER DISTRIBUTIONS

At the lowest discharge (Q1), the water depth associated with topographic highs is most leptokurtic of all discharge levels, Q1–Q5 (Figure 6.5). As the discharge increases, the distribution slightly shifts to a positively skewed platykurtic form. However, at all discharge levels, depths associated with topographic lows are bimodal, with the most contribution being to the second mode. Increasing discharge leads to only minor positive shifting of the two modes present (Figure 6.5). Cumulatively, the water depth distribution changes only slightly with increasing discharge, except for the introduction of low depth features under topographic highs and a small amount for topographic lows (Figure 6.5). This indicates that the local banks of the channel for the Falls City study reach do not change that much with increasing discharge. Depths associated with topographic lows hint that there are two distinct regimes of low features for the reach (Figure 6.5).

Froude number distribution for the Falls City study reach is very leptokurtic with a long positive tail increases in range with increasing discharge (Figure 6.6). In addition to the leptokurtic character of the distribution, the pattern can be characterized as exponential decay. For both topographic high and combined (stacked) distributions, this pattern is evident on all but the highest discharge (Q5). At Q5, the mode of topographic lows increase—as is the case for topographic lows for other reaches at lower discharges. Bimodality is not evident in topographic lows and highs—along with the combined distribution (Figure 6.6).

6.4. VELOCITY MAGNITUDE DISTRIBUTION

6.4.1. *Velocity Magnitude Distribution*

Velocity distribution for the Falls City study reach at Q1 is extremely leptokurtic with nearly all values (above 90%) being in the first (lowest) bin that is centered close to value 0.08 m/s (Figure 6.7). A positive tail begins to develop at discharge Q2. This trend gradually takes place from Q1 to Q3. At Q4, the distributions for topographic lows and combined high and lows are noticeably different than those of Q1–Q3, and mode shifts positively to the values around 0.16 m/s. Both the development of positive tail and the shift in the mode in topographic lows are not readily explained by Figure 6.5; however, they would be attributed to a large scale change from a change that is dominated by inundated area to one that is dominated by discharge.

As the discharge increases to Q5, the distribution for topographic lows becomes negatively skewed platykurtic; with the mode being shifted further to around 0.35 m/s (Figure 6.7). The effect of this change is also reflected in the combined distribution. Overall, the velocity magnitude distribution of the combined topographic highs and lows follows a trend similar to its components up until Q5, where this is marked bimodal distribution, with one mode around 0.08m¹s⁻¹ and the second mode at around 0.42 m¹s⁻¹. This implies that locations associated with topographic lows are being influenced by a higher stage condition unique to discharge Q5 (Figure 6.7).

6.4.2. *Velocity Magnitude Spatial Distribution*

Regions A, B, and C in Figure 6.8 are examples representing the dynamics of velocity magnitude with increase in stage. In these regions, velocity magnitude distribution changes with increasing discharge from Q1 to Q5. In region A, which is the closest to the influent part of the reach, the spatial structure of the velocity magnitude is driven by a high channel bar feature that forms small multi-tread channels as it is inundated (Figure 6.8). There is only one thin flow/channel path available at Q1, which becomes wider with the addition of new treads in Q2. As of Q3, the mid channel bar changes to two small islands with strong velocity magnitude indicated along all paths. For high discharges Q4/Q5, the location of the single island feature changes its position. However, high velocity magnitude is still present on this area as a result of the channel bar extending throughout the width of the channel (Figure 6.8).

The most noticeable dynamic feature of the Falls City study reach is the multi-channel/island portion of the reach between meter markers 2000 and 2250 (Figure 6.1) at region B (Figure 6.8). At the lowest stage (Q1), only two channels of the multi-channel system are connected (Figure 6.8). Flow is concentrated along the northern outer channel, but it becomes more evenly distributed between the central channel and northern outer channel as the stage increases at Q2/Q3. At the higher stages, Q4/Q5, flow is evenly distributed between all effluent channels (Figure 6.8). A major reason for the disconnected southern outer channel at Q1 is the presence of a channel bar in this location.

The region C (Figure 6.8) is at the effluent end of the reach, where high velocities associated with topographic lows (i.e., pools) are caused by flow from topographic highs (i.e., riffles/sediment bars/edges). These high velocities persist and are strong over the pools. This effect is noticeable to a small degree for Q1, but it features a more concentrated flow with increasing stage (Figure 6.8).

6.4.3. *Velocity Magnitude Relationships*

The distribution of velocity magnitude in relation to the water depth is different for topographic lows and highs (Figure 6.9). For both geomorphic classes, however, the distribution varies more as a function of depth—with lower depths experiencing a greater range in velocity magnitudes (Figure 6.9). At high discharges, Q4/Q5, the tails of the range are most likely spatially coincident with the areas of increased core velocity—as the ranges for both velocity magnitudes and corresponding water depths increase with increasing discharge. An example for this is the range of 0–2.5 m/s around a water depth close to a value of 0 m at Q1 in contrast to the range of 0–2.6 m/s around a water depth of 1 m at Q5.

The velocity magnitudes for topographic highs are centrally grouped with a smaller range as depth increases (Figure 6.9). The distribution for topographic lows has two distinct zonations that have a smaller range in magnitudes at the deep zone and a larger range at the shallow zone; and this is visible in all discharge conditions. For example, at Q3, the deeper zone of topographic lows has a velocity magnitude range of 0.25 m/s and the shallow zone has a range of 0.5 m/s. As discharge increases, the ranges for all locations increase. The maximum velocity magnitudes for shallow topographic highs can only be speculated, but the maximum values for both zonations of topographic lows are observed to have maximum increase in highest value between Q4 and Q5. In fact, the trends for topographic lows can be paired into three groups of Q1, Q2–Q4, and Q5.

The distributions of velocity magnitude *versus* depth *versus* geomorphic subclasses have different patterns for topographic lows (pools) and highs (riffles/sediment bars/edges) (Figure 6.10). Furthermore, there are two clusters of locations for each geomorphic class. For topographic highs, the division of two apparent groupings appears to be nonexistent toward the classes +3 and +4 (Figure 6.10). For locations corresponding to topographic lows, on the other hand, the groupings become more disparate as the subclass number increase, and are nonexistent for class -4 (Figure 6.10).

The characteristics of topographic subclasses have some broad similarities, as the low subclasses, $\pm 1/2$, has a much greater range. However, the range generally increases for the high topographic high subclasses (+3/4), but the opposite is generally true for topographic lows (Figure 6.10). This ranged behavior is explained by the fact that class -1 have the least depth with greater range controlled by depth, and topographic high subclasses have the shallowest

values at class +4. In short, depth is a good indicator for the range of velocity magnitudes (Figure 6.10). As discharge increases, the range of velocity magnitudes increases for all topographic lows and high subclasses (Figure 6.10).

6.4.4. *Summary on Velocity Magnitude Distribution*

In summary, velocity magnitude seems to be affected largely by the water depth in the Falls City study reach. The results demonstrate that there are two distinct groupings of topographic highs and topographic lows (Figure 6.10). This further implies that Falls City reach has two regimes of flow present, which is most likely coincident with streamwise variability in topography.

6.5. **STREAMWISE VELOCITY DISTRIBUTION**

6.5.1. *Streamwise Velocity Distribution*

The streamwise velocity distribution is highly leptokurtic at low discharges, as in the case of velocity magnitude distribution (Figure 6.11) with the velocities being in the range of -2.0 m/s and 2.5 m/s. In fact, the histograms of velocity distribution bear much similarity to velocity magnitude. The largest difference is the fact that the streamwise velocity histograms point out the backwaters (i.e., negative velocity values). The areas characterizing backwaters tend to increase as flow stage increases and the distribution becomes more platykurtic (Figure 6.11). Backwaters appear to be more prevalent in topographic high classes relative to topographic low classes in lower discharges of Q1–Q3. However, Q4 onward, backwaters are also present in the topographic lows. Overall, backwaters begin to form a tail in the distribution that is comparable to the positive tail for the discharge Q4 and Q5 (Figure 6.11). This may be because that areas associated with backwaters tend to become more heterogeneous in flow conditions at large areas and that they have higher velocities at margins as flow stage increases.

6.5.2. *Streamwise Velocity Spatial Distribution*

Spatially, the most notable feature of streamwise velocities is backwaters (Figure 6.11), which characterize the locations of flow eddies and are often at margins of complex water boundaries. For all discharge conditions, the large areas of backwaters are found at the complex zone, region B, immediately downstream of the influent side of the stream and at the multichannel region, region A, and the effluent portion of the river (Figures 6.1 and 6.12). For the low discharges, the backwater areas have a small coverage and are located in the zones of low

water depth and complex flows as well as the areas where large pools are first encountered (Figure 6.12).

6.5.3. *Streamwise Velocity Relationships*

The distribution of streamwise velocity in relation to the water depth is very similar to that of velocity magnitude except for: 1) the amount of range and 2) the presence of backwaters (Figure 6.13). For the discharges Q1/Q2, backwaters contribute to only a small part of the distribution (Figures 6.13–6.14). At high discharges, Q4/Q5, there is a distinct grouping of backwaters. Just as in velocity magnitude, the streamwise velocity distribution shows two major groupings for pools and sediments/riffles/edges, although these groupings are affected by the geomorphic subclass category (i.e., 1–4) (Figures 6.13–6.14). For example, for the class +4, the data points in the distribution associated with sediment bars/riffles/edges are grouped together. On the other hand, for +1 class, the distribution is divided into two major groups – a tendency that is also observed in the distribution of velocity magnitude (Figures 6.9–6.10). This is expected, as a major component of velocity magnitude is streamwise velocity. For topographic highs, backwaters have greatest contribution in the subclass +1 for the discharge Q1–Q4. As the discharge increases to Q5, the greatest contribution by the backwaters shifts to subclass +2. This contribution decreases for the topographic high subclasses +3/+4. For the topographic lows, the highest clustering of backwaters in the distribution occurs at the subclass –3. Spatially, this is most likely accounted by the pool unit between meter marker 500 and 750 (Figure 6.1).

6.5.4. *Summary on Streamwise Velocity Distribution*

Streamwise velocity distributions across the reach for different discharge conditions have patterns and relationships very similar to those of velocity magnitude. However, the presence of backwaters is a distinction. The area of the regions defined as backwaters tend to increase as flow stage increases. Furthermore, the backwater regions tend to delineate or bound locations of concentrated flow (Figure 6.12). Concentrated flow regions are likely to be influenced by upstream effects and overall reach geometry. Backwaters are also influenced by local characteristics of the channel such as water depth and the presence of an adjacent pool as is suggested by the locations of many of the large backwater areas (Figure 6.12).

6.6. NORMAL VELOCITY DISTRIBUTION

6.6.1. Normal Velocity Distribution

Normal velocity distribution starts out quite leptokurtic at low discharges (Q_1/Q_2) (Figure 6.15). As the discharge increases, the distribution becomes more platykurtic. Distribution of normal velocity is different from those of velocity magnitude (Figure 6.7) and streamwise velocity (Figure 6.11). This distribution is symmetric around a mode with value 0 m/s. Furthermore, the distribution for the sediment bars/riffles/edges (topographic highs) and pools (topographic lows) are similar at all discharge conditions (Figure 6.15).

6.6.2. Normal Velocity Spatial Distribution

Spatial distribution of normal velocity seems independent from the geomorphic unit classes (Figure 6.16). In particular, it is important to note the alternating nature between positive and negative velocity values throughout the channel. As discharge increases, flows tend to become stronger at the sections with complex geometry, such as the island at region B, the multichannel location at region A, and the region C (Figure 6.1). Furthermore, flow patterns tend to become less complex with increasing discharge (Figure 6.16).

6.6.3. Normal Velocity Relationships

The distribution of normal velocity in relation to water depth depicts topographic highs (sediment bars/riffles/edges) and lows (pools) in one cluster and topographic lows in two clusters—just as in velocity magnitude and streamwise velocity distributions (Figure 6.17). This pattern can be explained by the conditions of regions A and B (Figure 6.16), which are much higher in local relief than other parts of the channel as well as the topographic lows that bound them. Also, at the discharges Q_1 – Q_3 , normal flow velocities at shallower water depths tend to have greater range in magnitude than those at deeper water depths. As the discharge increases to Q_5 , velocities tend to have a large range at all depths. In addition, the Froude number groupings do not hold the regular pattern as they do for velocity magnitude and streamwise velocity, supporting that velocity magnitude is dominated by streamwise flow.

The distributions of normal velocity *versus* depth *versus* geomorphic subclasses (Figure 6.17) show that there is depth-wise less overlap between topographic highs and lows at lower discharges (Q_1 – Q_3). This relationship is the same for velocity magnitude and stream velocity. Just as in the Goliad study reach, higher Froude numbers tend to be more numerous and prevalent in the distribution as discharge increases. Similar to the velocity magnitude

distributions (Figure 6.10), normal velocity distribution has the greatest range at shallower depths (Figure 6.18). However, this situation changes as the discharge increases to Q4/Q5, where the water depth seems to have less of an effect on the range of normal velocity (Figure 6.18). This can be attributed to the increasing strength of streamwise flow (Figure 6.12) with increasing discharge. At the most extreme topographic residuals, -/+4, the range is lower for Q2–Q5.

6.6.4. *Summary on Normal Velocity Distribution*

The distribution of normal velocity in the Fall City study reach is largely invariant with increase in discharge (Figure 6.16). However, the magnitudes of the normal velocities do change as the discharge increases (Figures 6.17–6.18). This suggests that normal velocity is influenced by channel morphology on its distribution and by the discharge on its magnitude. Shallow depths tend to be associated with greater range in normal velocity magnitudes—just as in the other velocity parameters.

6.7. SHEAR STRESS DISTRIBUTION

6.7.1. *Shear Stress Distribution*

Shear stress distribution is highly leptokurtic throughout all flow stages. The majority of areas in the channel are characterized by shear stress values less than $1 \text{ kg}^1\text{m}^{-1}\text{s}^{-2}$ (Figure 6.19). A positive tail forms and becomes more prominent with increasing discharge. Furthermore, the extreme values are around $11 \text{ kg}^1\text{m}^{-1}\text{s}^{-2}$ and mainly associated with some areas within topographic high geomorphic unit classes. The range of these extreme values increases in shallower locations with increasing discharge (Figure 6.19).

6.7.2. *Shear Stress Spatial Distribution*

Spatial distribution of the shear stress values supports the findings from the shear stress frequency distributions (Figure 6.19). The shear stress values less than $2 \text{ kg}^1\text{m}^{-1}\text{s}^{-2}$ are widely distributed along the channel (Figure 6.20). The areas subject to higher shear stresses coincide with the regions dominated by higher velocity magnitudes. These areas are concentrated at geomorphically complex regions and/or at the regions of confined/concentrated flow—such as region B (Figure 6.20).

6.7.3. *Shear Stress Relationships*

Overall, the distribution of shear stress in relation to the water depth shows a pattern similar to that of velocity magnitude (Figures 6.21, 6.9). However, this distribution has greater range in values. Water depth seems to have a strong effect on shear stresses in all but the highest discharge condition (Figure 6.21). The relation among shear stress, water depth, and Froude number indicates that geomorphic unit class does not play a dominant role in controlling the range of shear stress values; the high shear stress values with similar ranges are equally present at all but the most extreme geomorphic classes (Figure 6.22). However, the topographic lows tend to have lower ranges (i.e., from ~ 0 to $6 \text{ kg}^1\text{m}^{-1}\text{s}^{-2}$) at Q1–Q3 (Figure 6.22). At higher discharges (i.e. at Q4–Q5), the ranges for topographic lows are similar to those of topographic highs. This is especially evident for the classes ± 1 at the highest discharge Q5.

6.7.4. *Summary on Shear Stress Distribution*

Spatially, shear stress seems to be strongly controlled by geomorphic complexities and/or whether the flow is confined by the channel morphology (Figure 6.20). Distribution of high shear stress is largely controlled by the amount of discharge/flow stage, with a substantial increase in the channel area subject to high shear stresses especially in the highest discharge, Q5. These areas closely mimic the core of high flow velocity observed in spatial distributions of velocity magnitude and stream velocity within the channel (Figures 6.8 and 6.12) implying that shear stress is strongly coincident with areas of high velocity.

6.8. SUMMARY ON THE FALLS CITY STUDY REACH

The Falls City study reach (Figure 3.3) is characterized by a planform that bents like a ‘v’ just southwest of the Falls City (Figure 6.1). The reach is characterized by alternating pools and riffles/sediments bars (Figure 6.2). However, this alternation in height is a bit higher in amplitude than other study reaches. The influent portion of the study reach features a low area until meter marker 250 meters (Figure 6.1). There is also a very dramatic decrease in elevation between meter marker 250 meters and about one hundred meters past meter marker 500 (Figure 6.1). The decrease in elevation from this point downstream is not monotonic (Figure 6.1). Between meter marker 2000 and 2250 meters, there is a steep increase in elevation of more than 5 meters. After this region, there is a sharp decrease of less magnitude, but a gradual lowering downstream to the effluent portion of the reach (Figure 6.1). This strong variability in topography is controlled by the geology. The northern leg of this ‘v’ in planform is composed of

Quaternary alluvium, and the southern or lower leg of the 'v' is composed of the upper portion of the Jackson Group. The upper portion, the Whitsett formation, is characterized as clay mixed with volcanic tuffs near the top and sandstones near the base (Eargle and Snider 1956). All considered, these materials have differing levels of erodibility, and this difference could perhaps explain the intense change in topography throughout the Falls City study reach.

Although distributions of geomorphic unit classes (i.e., pools and sediments/riffles/edges) are not unusual when compared to other reaches (Table 6.2), their spatial distribution is quite unique to the study reach (Figure 6.16). The most extreme class of topographic highs +4 is generally at channel margins throughout most of the study reaches, but in the Falls City reach, they are along the two topographic high regions at regions A and B (Figure 6.20) and the regions dominated by topographic lows have the other classes present, but very few of the most extreme class -4 (Figure 6.2). This bodes an interesting scenario in the interpretation of results of Falls City where the most extreme topographic highs actually represent regions of flow and the other classes represent the normal arrangement of channel center to margin elevation.

Similar to the other study sites, topographic highs and lows both demonstrate very leptokurtic distribution at low discharge conditions (Figure 6.7). However, unlike other reaches, the Falls City reach has a unique topography resulting in different hydraulic conditions. The results from the analysis of the distribution of hydraulic variables in relation to water depth and geomorphic unit subclasses demonstrate two different groupings of topographic lows and highs with a water depth that seems to lack as many values as the other areas (**Figure 6.8**). The spatial distribution of velocity magnitudes suggest that constrained channels do not seem to play as large a role as that of the depth, and the core of high velocity is constrained to the two high regions at regions A and B (Figure 6.20) and adjacent topographic highs (Figure 6.8). Some regions of topographic lows do exhibit high velocities, as in region C (Figure 6.8). As such, velocity magnitude is even influenced by local channel topography more than in the other study sites such as the Goliad reach.

The distribution of backwater regions has a very dynamic character at low discharges with the development of high velocities just downstream of the constricted zone at region B (Figure 6.12). At all discharges, most of the backwater regions are present at and immediately downstream of the two 'high' areas. The section downstream of meter marker 500 (Figure 6.1) present flow eddies alternating between Q4 and Q5. In fact, the backwater regions at the

northern leg of the 'v' planform present large changes in area and location as a response to a very dynamic high velocity core (Figure 6.12). The high velocity core changes its position as the discharge increases/decreases suggesting that channel planform has a noticeable influence on streamwise flow velocities. Backwaters also occur at shallow locations of flow reattachment, such as region C (Figure 6.12) at Q2. In addition, overall, the direction patterns of normal velocity along the channel do not appear to change much (Figure 6.16). One exception to this is the large pool just downstream of meter marker 500 (Figure 6.1). At this location, the direction of normal velocity appear to switch as the discharge progresses from low water stage at Q1 to Q2, and then again from high stage at Q4 to Q5 (Figure 6.16).

Shear stress distribution in the Fall City reach demonstrates an exceptionally high range of values. Although the values are displayed using an extreme outlier criterion (Ott and Longnecker, 2010), there are still many elevated values coincident with the two locations with higher elevations at regions A and B (Figure 6.20). The local and overall channel morphology—when taken in a more extreme case—can have a profound influence on shear stress. All considered, the Falls City study reach gives us insight into the controls that geology can play on local channel morphology and resultant hydraulics.

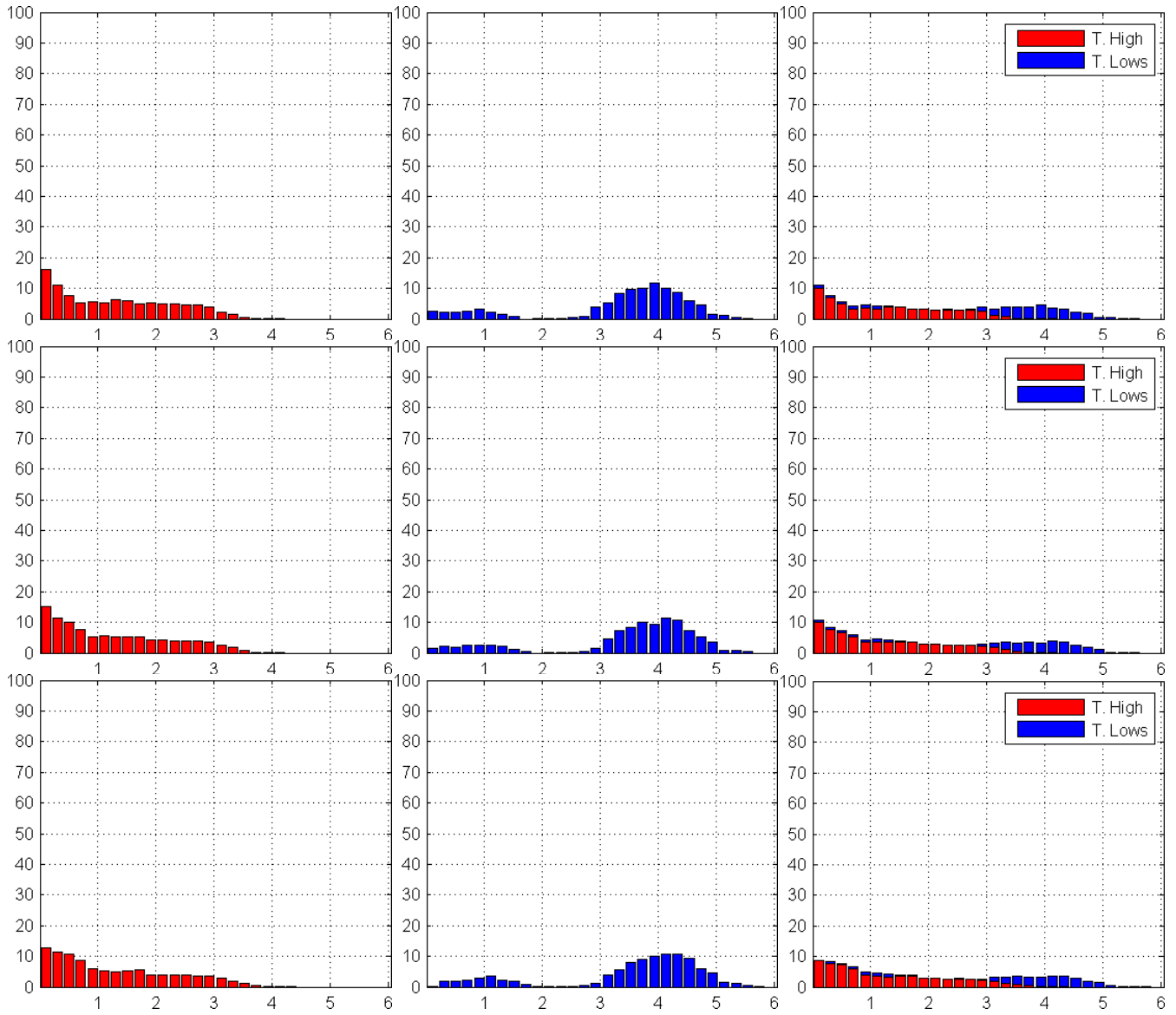


Figure 6.5. Water depth distribution for Q1–Q5 (rows, top to bottom) for topographic highs (marked as T. High) corresponding to the classes (+1)–(+4), topographic lows (marked as T. Lows) corresponding to the classes (-1)–(-4), and combined (columns, left to right). Horizontal and vertical axes correspond to water depth (m) and the percent values of topographic classes, respectively.

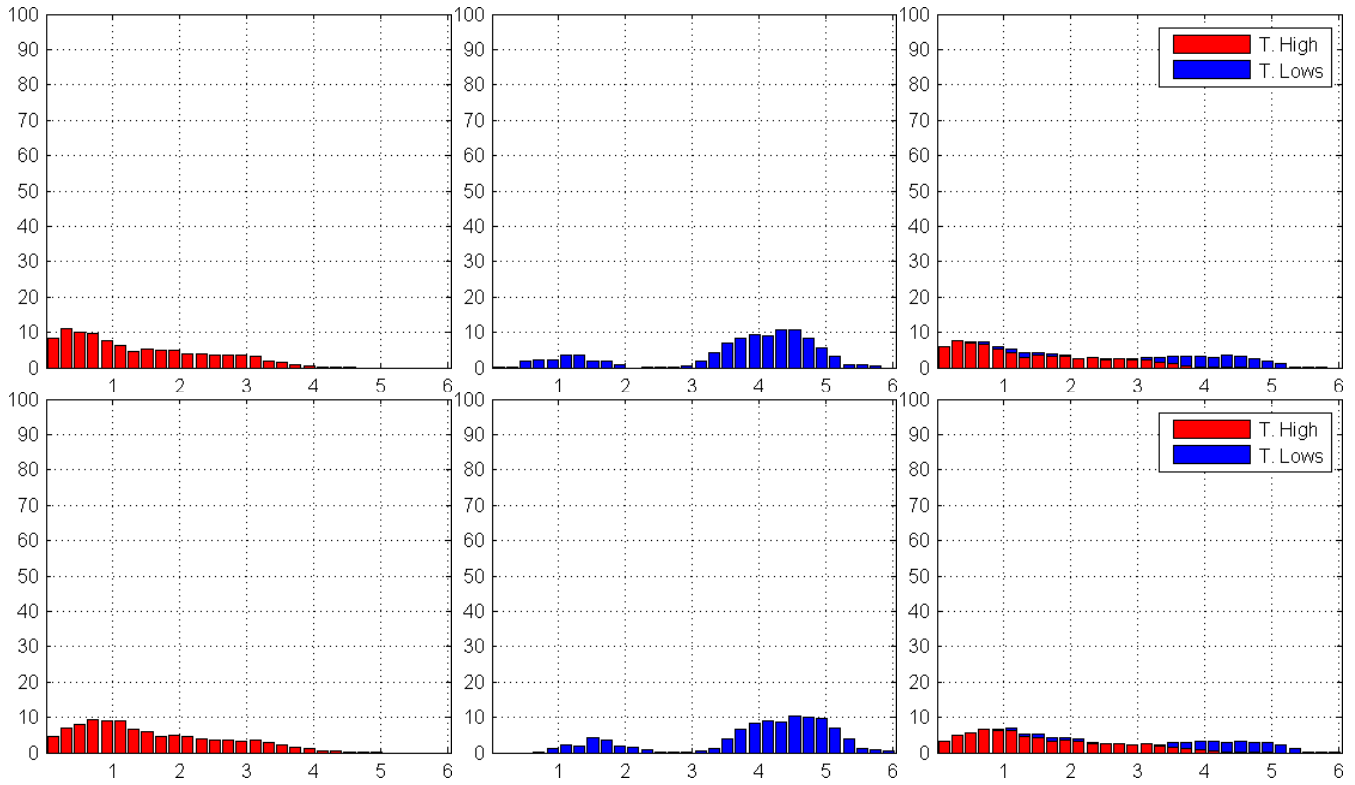


Figure 6.5 (cont'd). Water depth distribution for Q1–Q5 (rows, top to bottom) for topographic highs (marked as T. High) corresponding to the classes (+1)–(+4), topographic lows (marked as T. Low) corresponding to the classes (-1)–(-4), and combined (columns, left to right). Horizontal and vertical axes correspond to water depth (m) and the percent values of topographic classes, respectively.

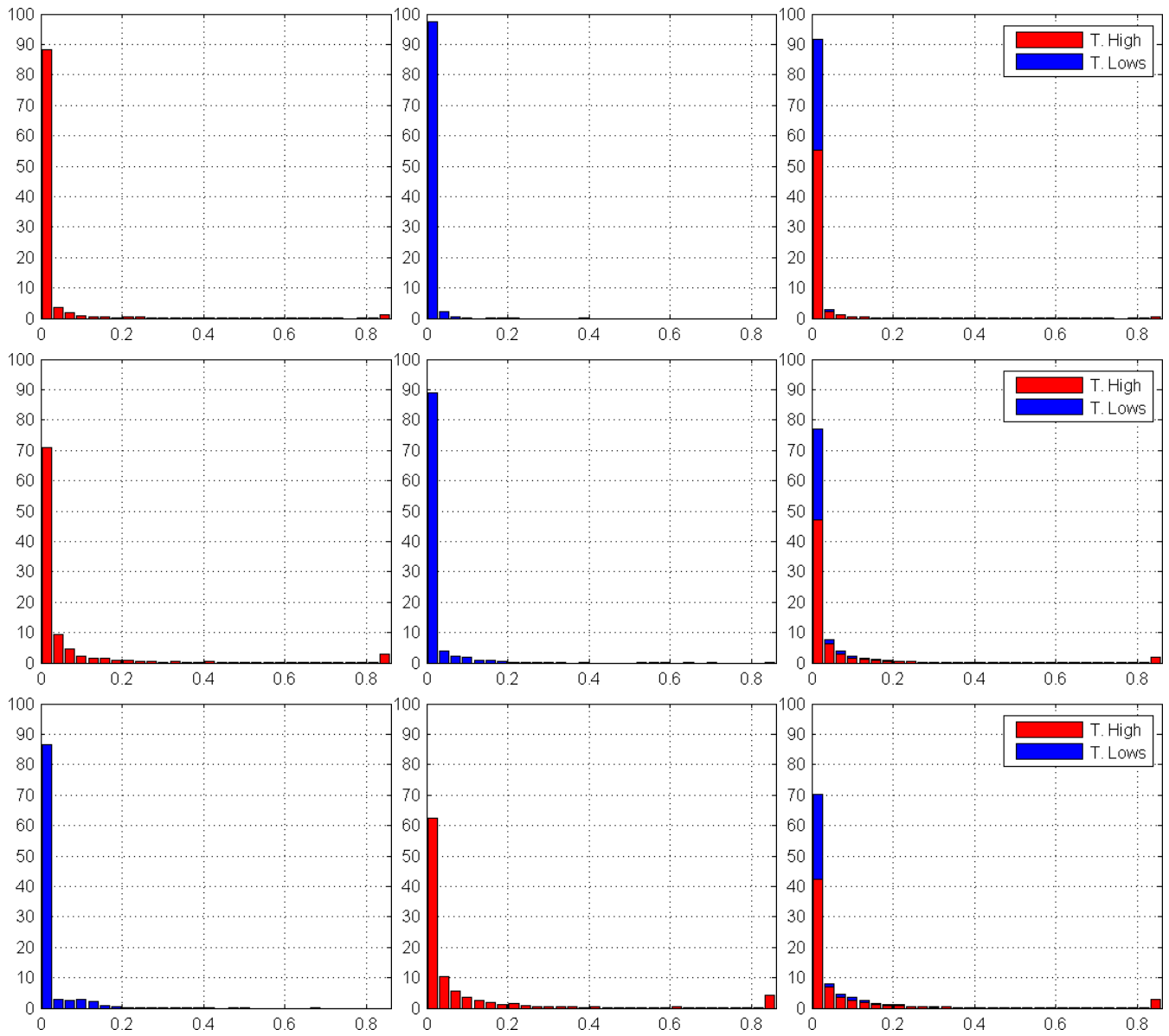


Figure 6.6. Froude number (Fr) distribution for Q1–Q5 (rows, top to bottom) for topographic highs (marked as T. High) corresponding to the classes (+1)–(+4), topographic lows (marked as T. Lows) corresponding to the classes (-1)–(-4), and combined (columns, left to right). Horizontal and vertical axes correspond to Fr and the percent values of topographic classes, respectively.

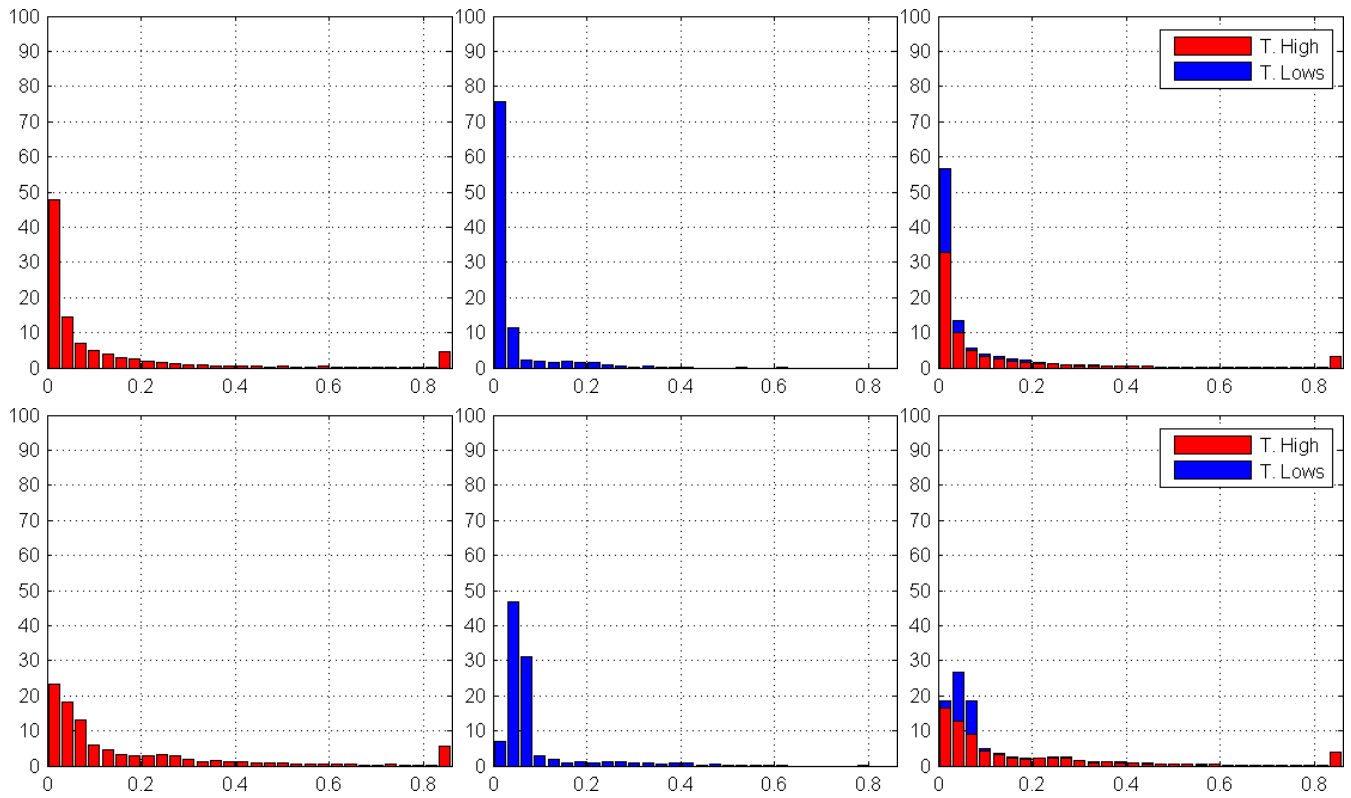


Figure 6.6 (cont'd). Froude number (Fr) distribution for Q1–Q5 (rows, top to bottom) for topographic highs (marked as T. High) corresponding to the classes (+1)–(+4), topographic lows (marked as T. Lows) corresponding to the classes (-1)–(-4), and combined (columns, left to right). Horizontal and vertical axes correspond to Fr and the percent values of topographic classes, respectively.

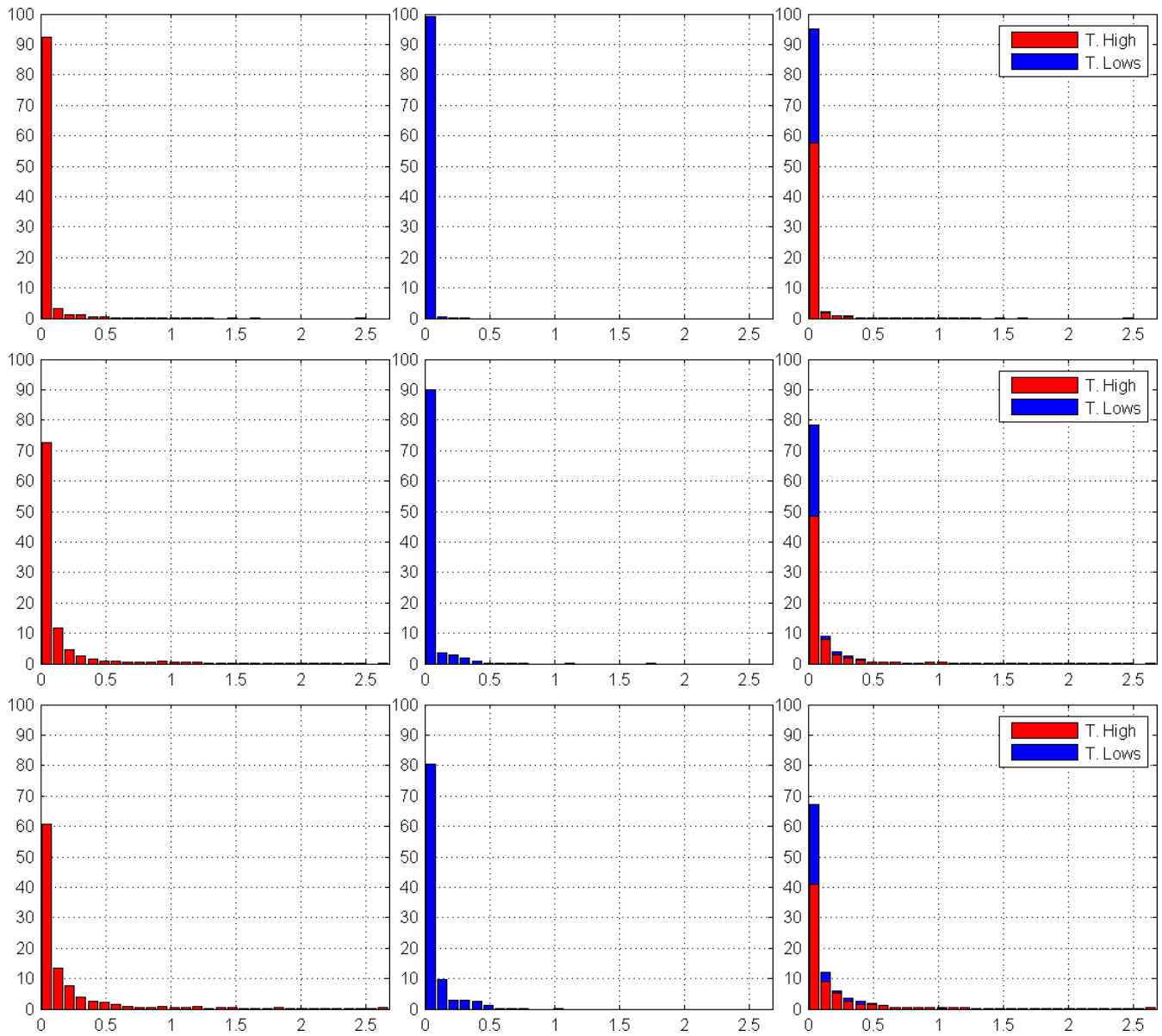


Figure 6.7. Distribution of velocity magnitude for Q1–Q5 (rows, top to bottom) for topographic highs (marked as T. High) corresponding to the classes (+1)–(+4), topographic lows (marked as T. Lows) corresponding to the classes (-1)–(-4), and combined (columns, left to right). Horizontal and vertical axes correspond to velocity magnitude (m/s) and the percent values of topographic classes, respectively.

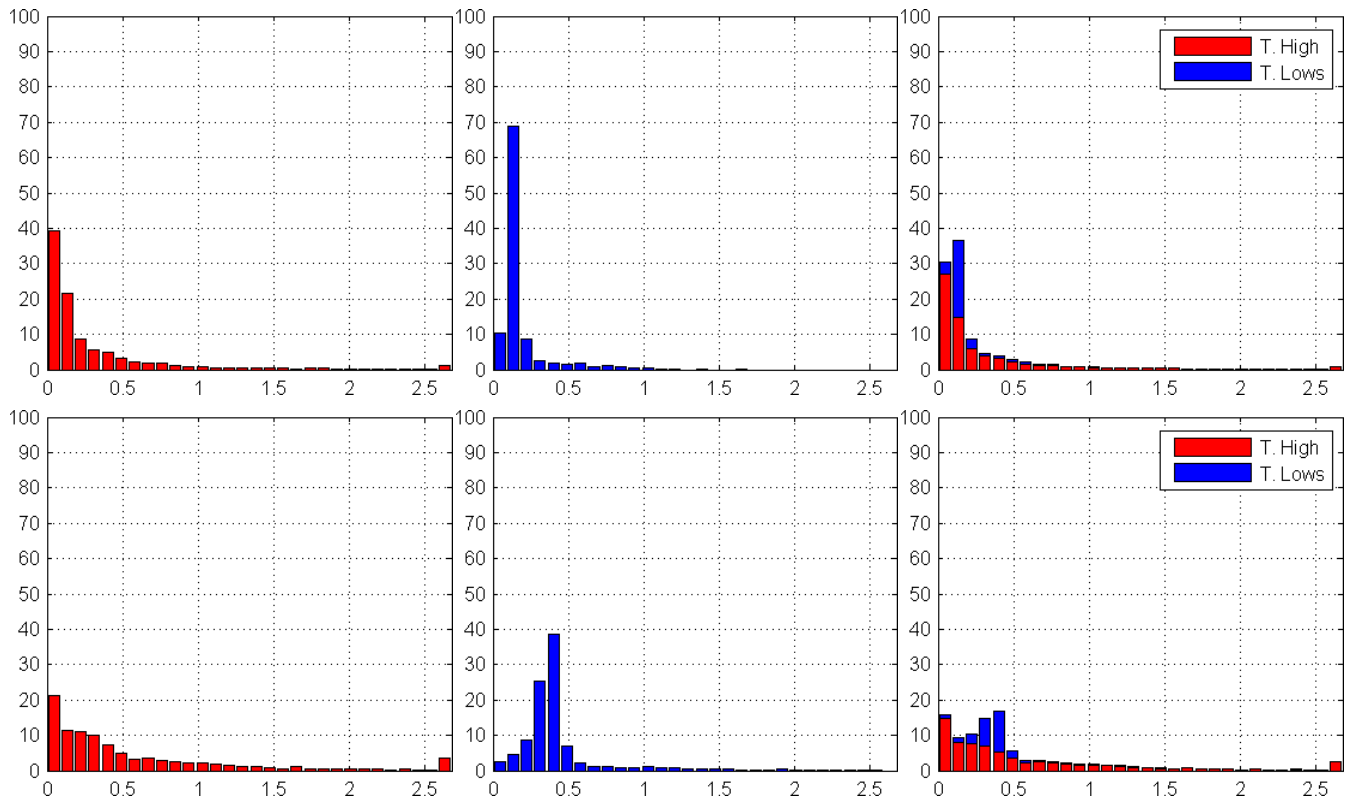


Figure 6.7 (cont'd). Distribution of velocity magnitude for Q1–Q5 (rows, top to bottom) for topographic highs (marked as T. High) corresponding to the classes (+1)–(+4), topographic lows (marked as T. Lows) corresponding to the classes (-1)–(-4), and combined (columns, left to right). Horizontal and vertical axes correspond to velocity magnitude (m/s) and the percent values of topographic classes, respectively.

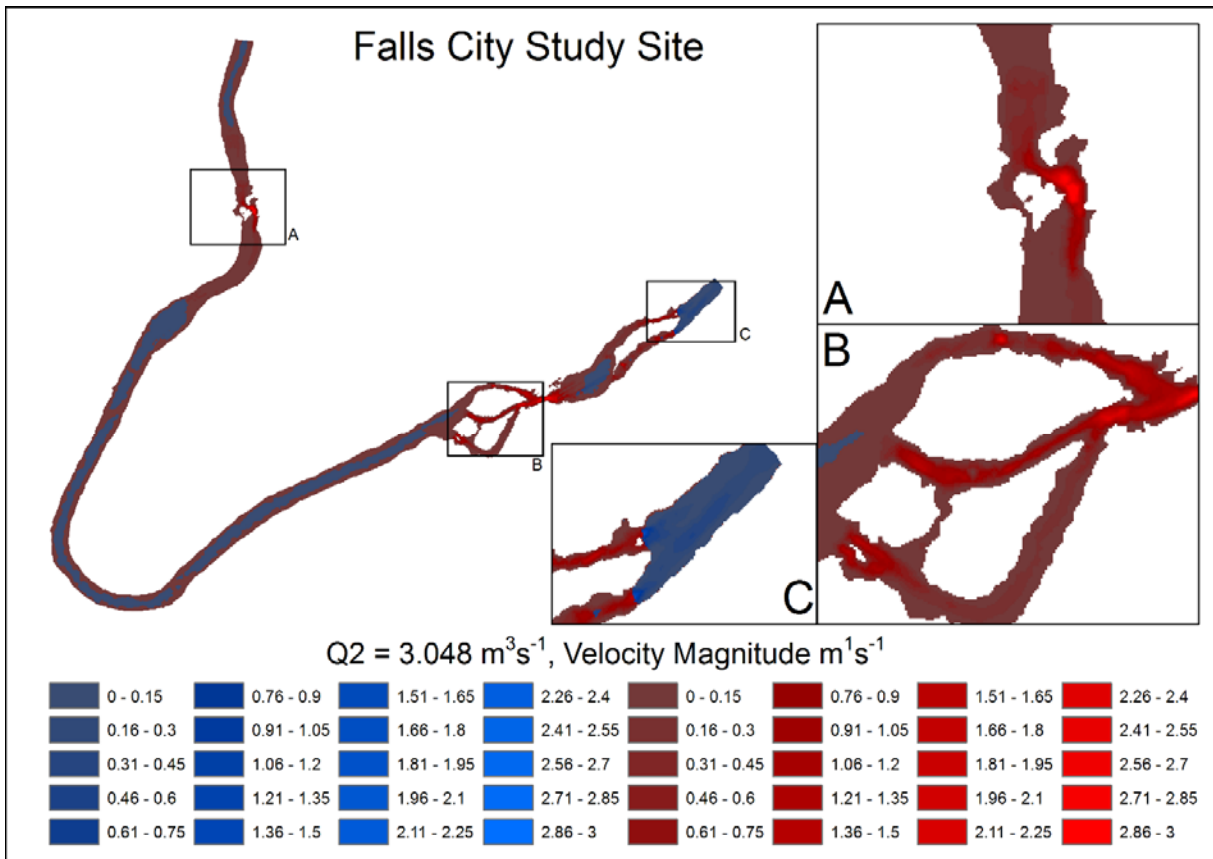
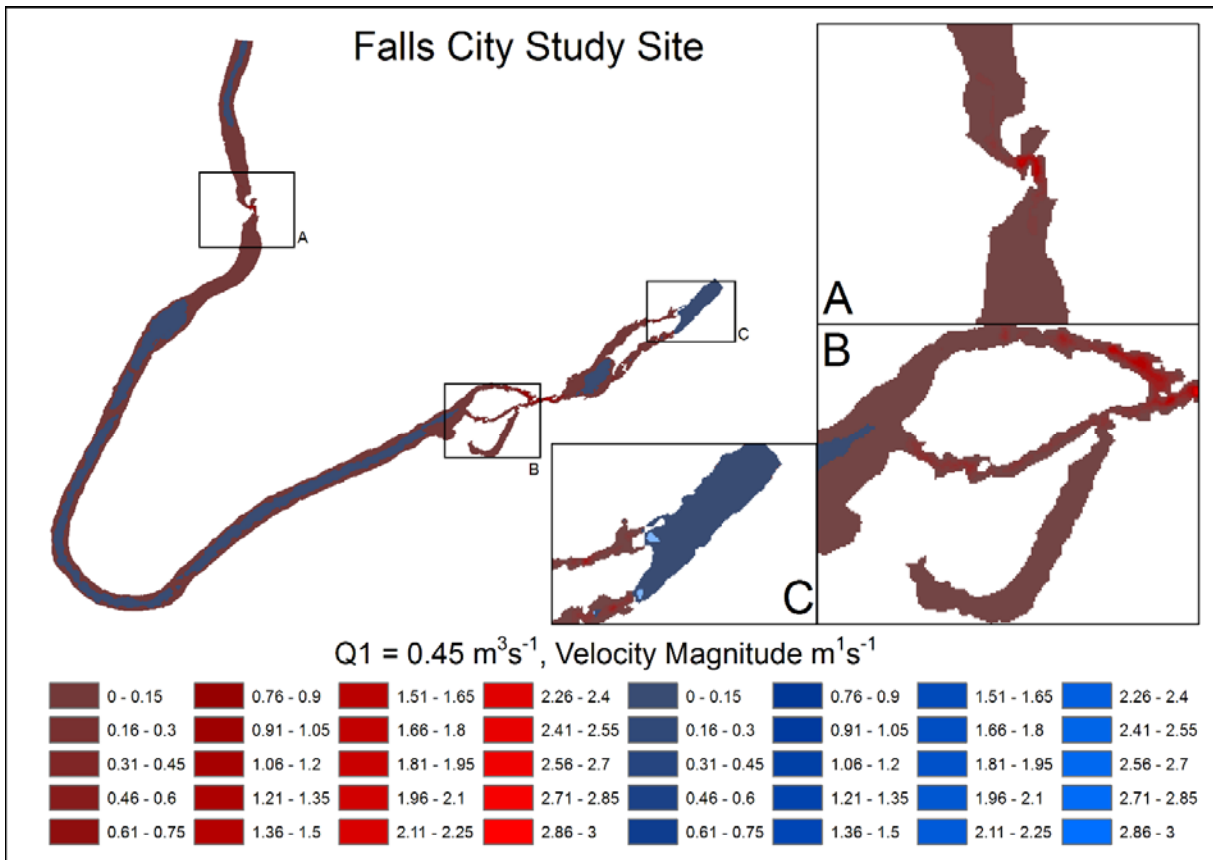


Figure 6.8. Spatial distribution of velocity magnitude (m/s) for Q1–Q5 for topographic highs (red colors) and lows (blue colors).

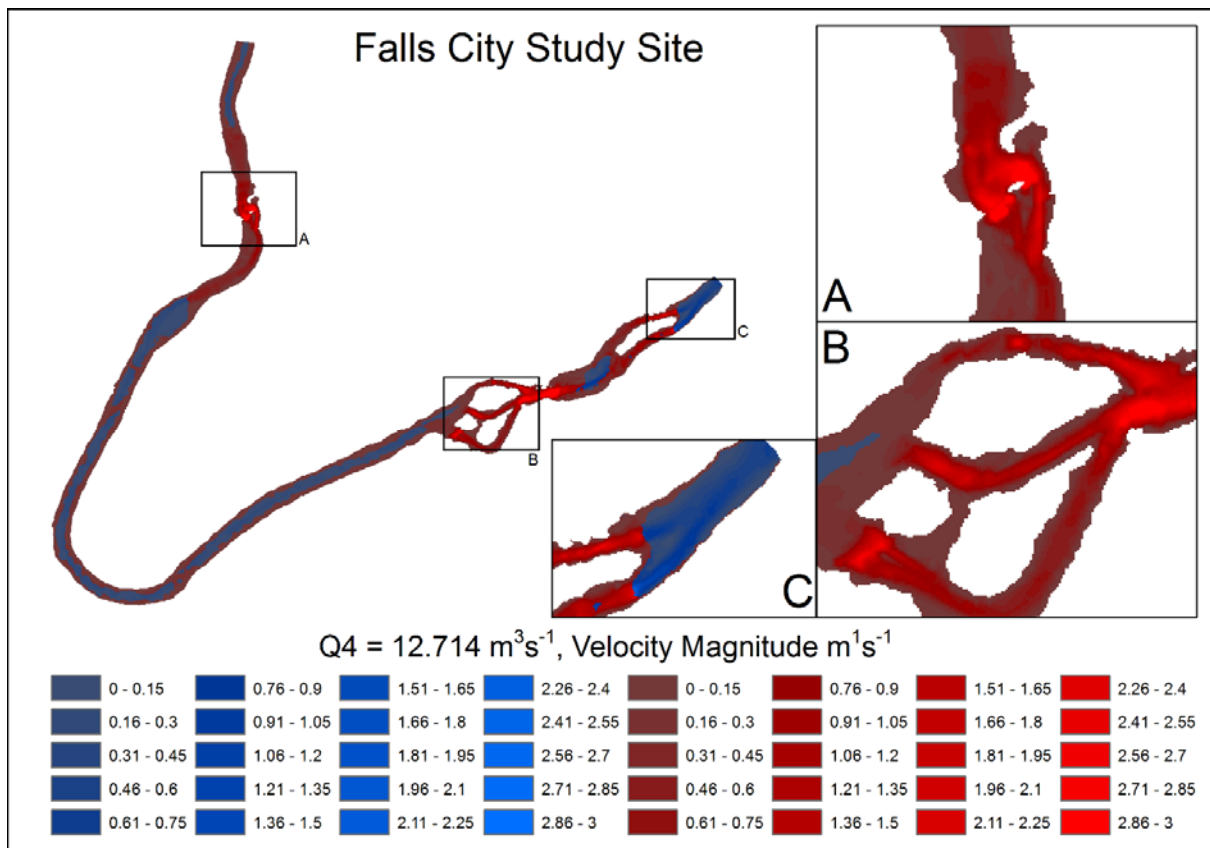
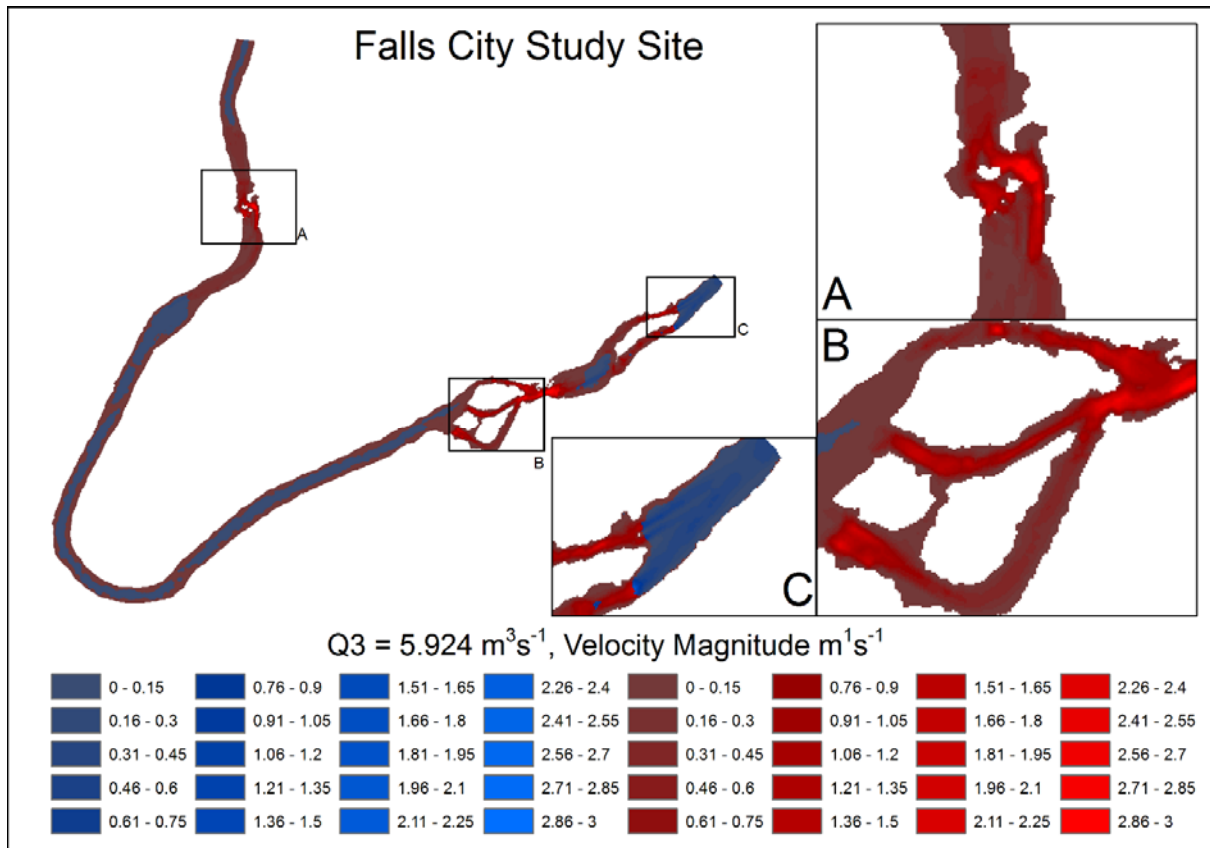


Figure 6.8 (cont'd). Spatial distribution of velocity magnitude (m/s) for Q1–Q5 for topographic highs (reds) and lows (blues).

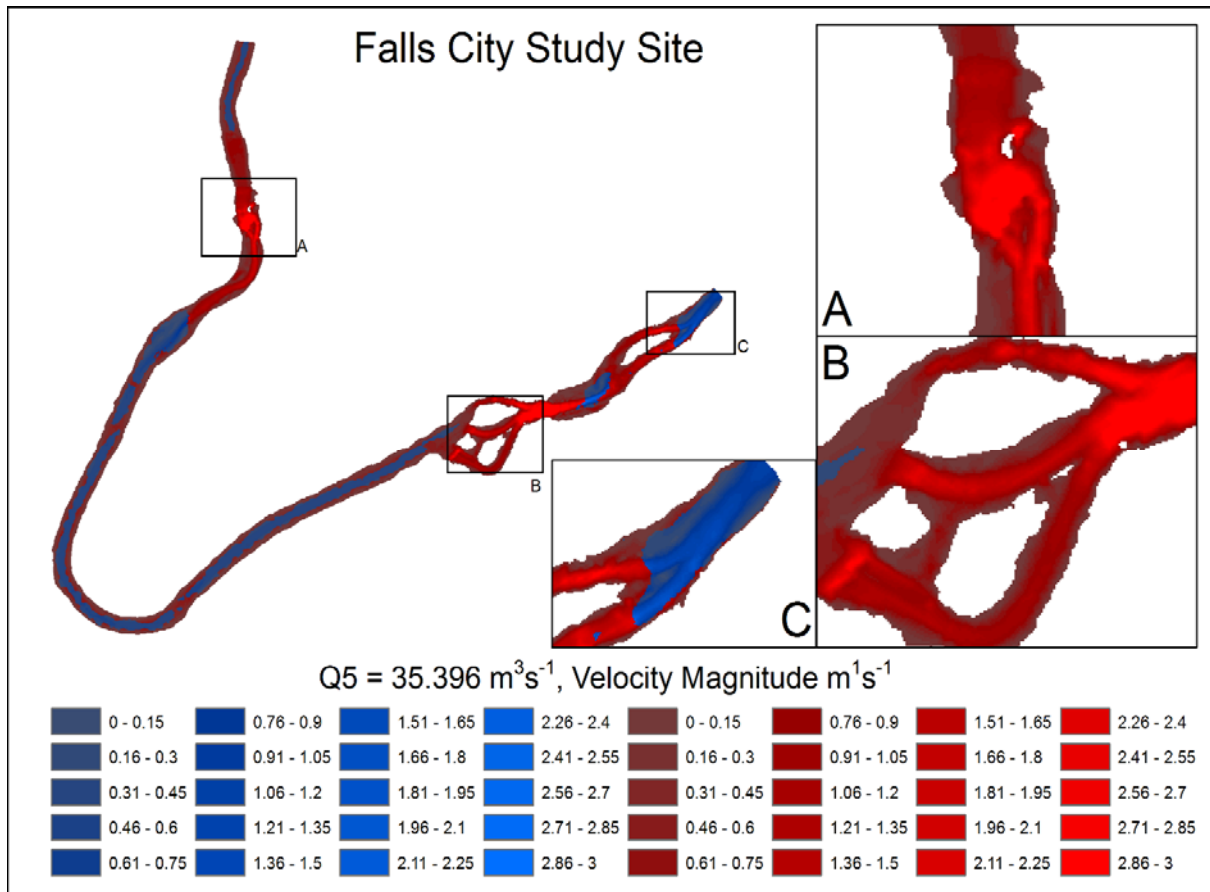


Figure 6.8 (cont'd). Spatial distribution of velocity magnitude (m/s) for Q1–Q5 for topographic highs (reds) and lows (blues).

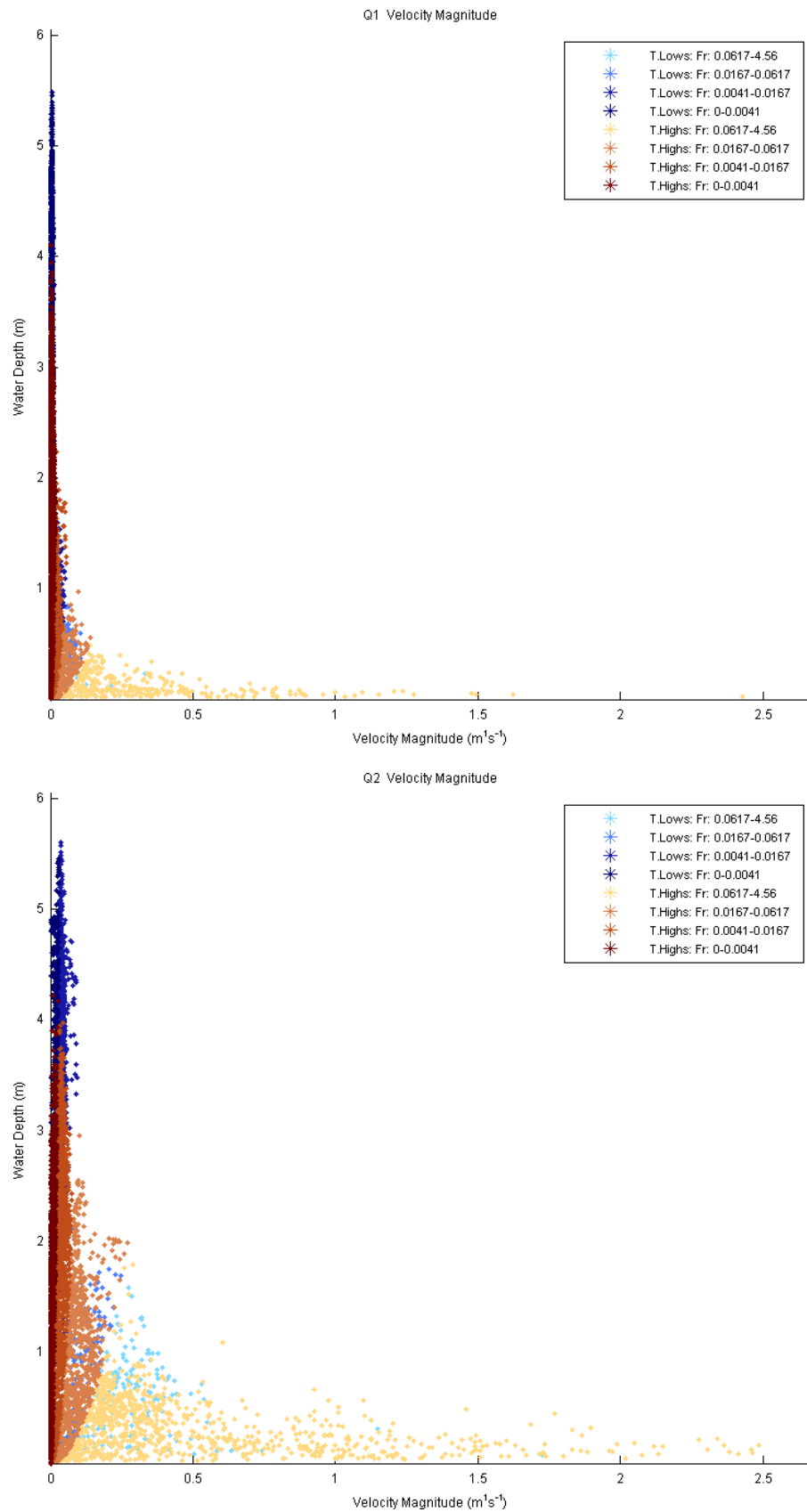


Figure 6.9. Distribution of velocity magnitude in relation to water depth for Q1–Q5 classified by topographic highs marked as T. Highs (brown colors), topographic lows marked as T. Lows (blue colors), and Froude number (Fr).

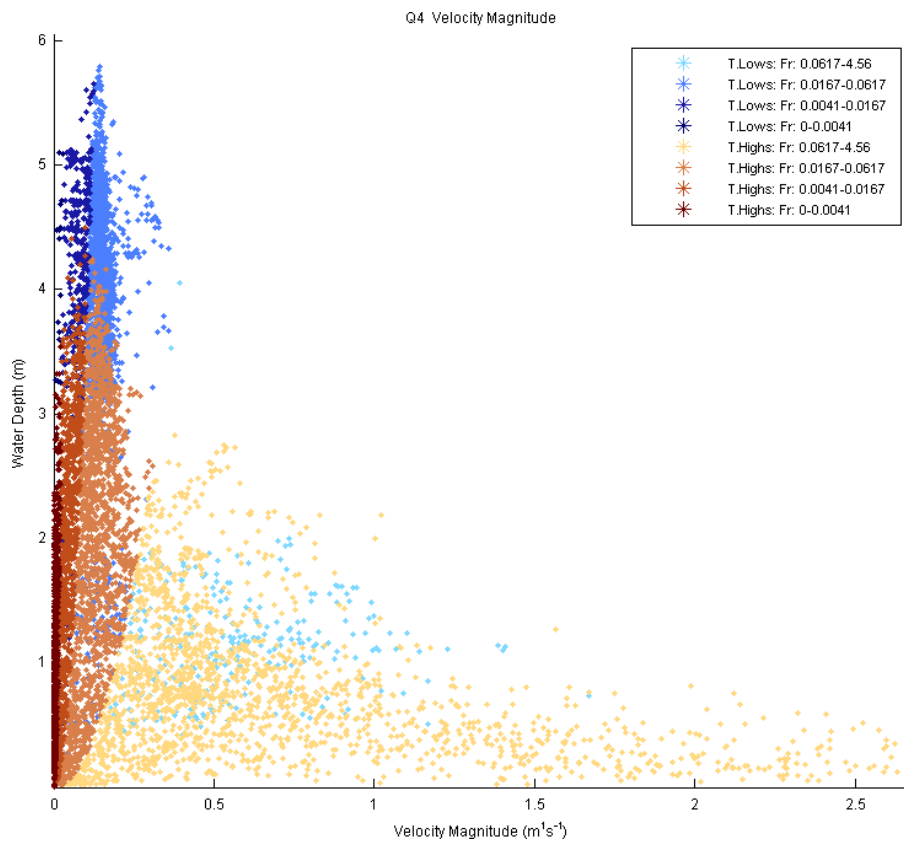
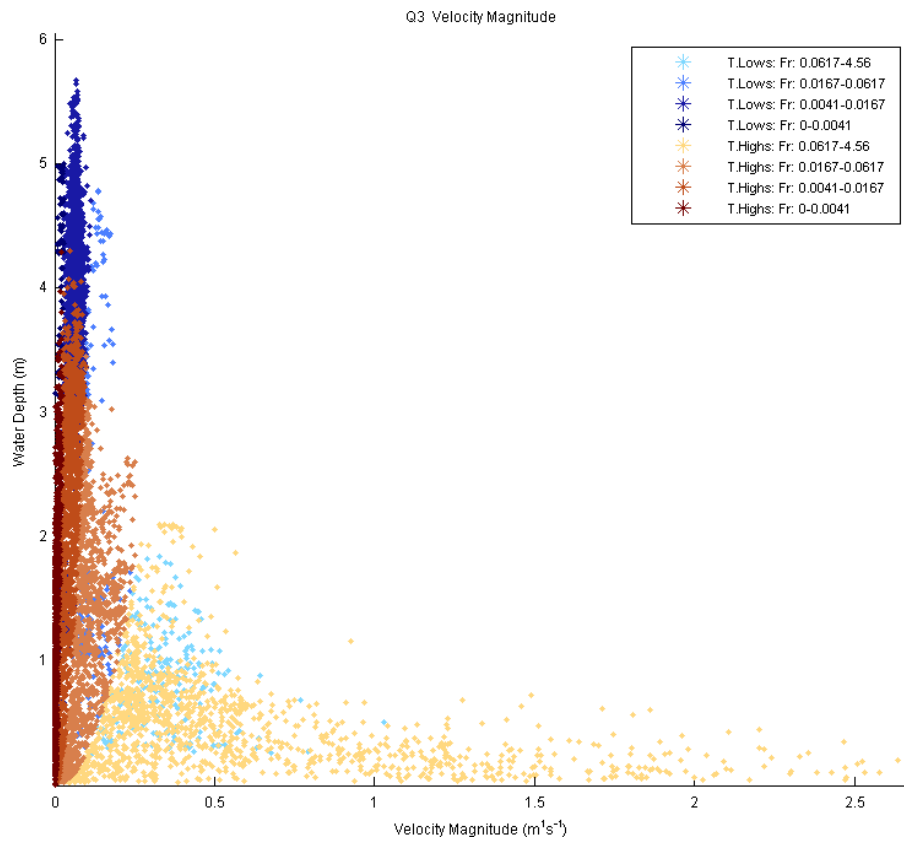


Figure 6.9 (cont'd). Distribution of velocity magnitude in relation to water depth for Q1–Q5 classified by topographic highs marked as T. Highs (brown colors), topographic lows marked as T. Lows (blue colors), and Froude number (Fr).

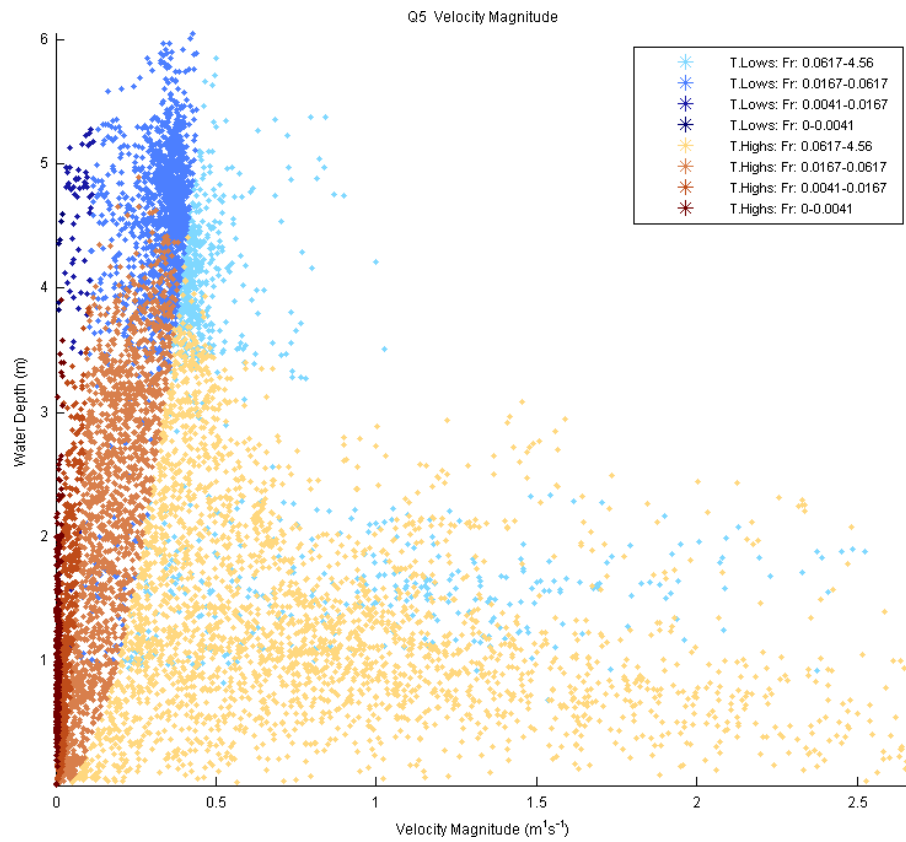


Figure 6.9 (cont'd). Distribution of velocity magnitude in relation to water depth for Q1–Q5 classified by topographic highs marked as T. Highs (brown colors), topographic lows marked as T. Lows (blue colors), and Froude number (Fr).

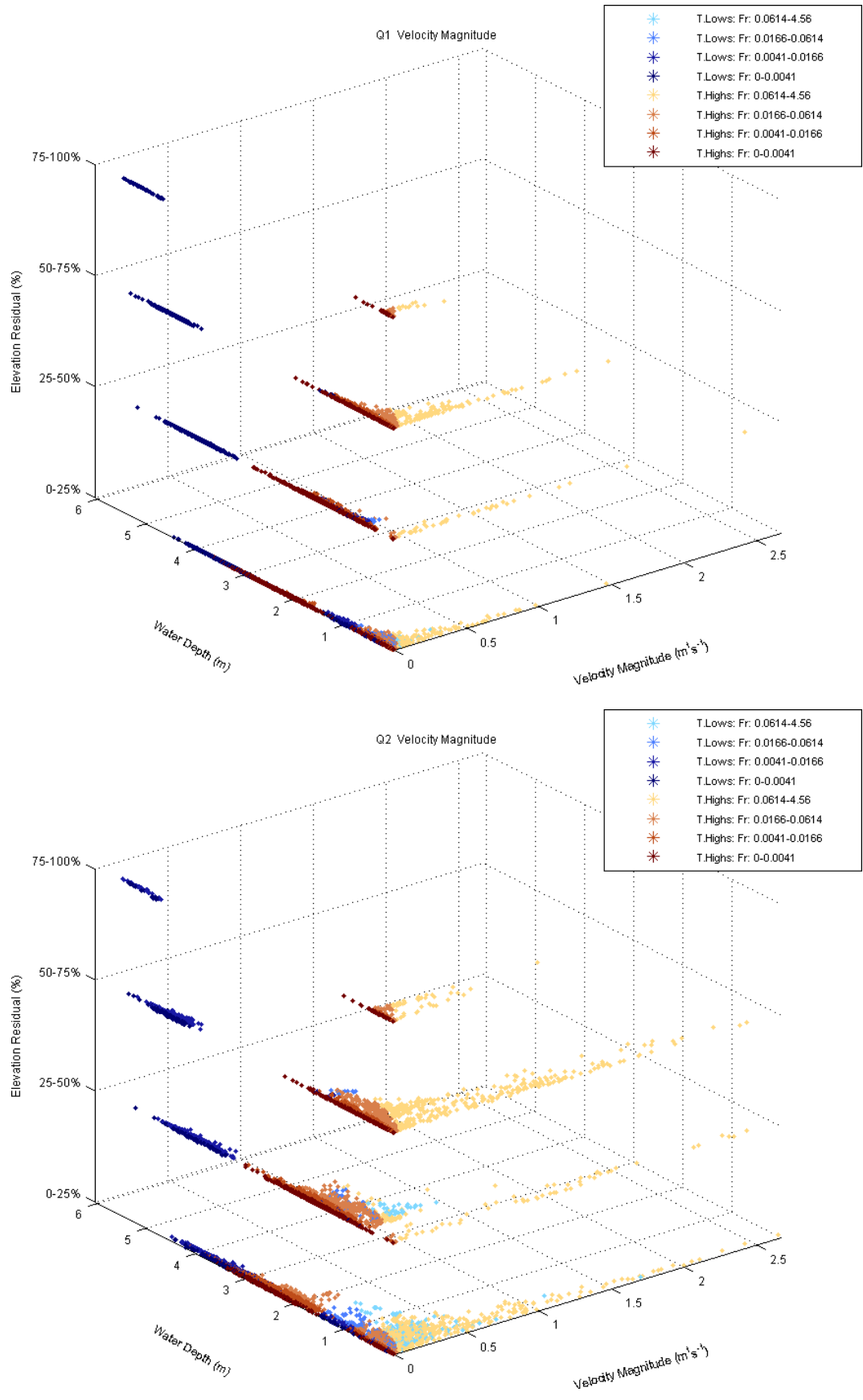


Figure 6.10. Distribution of velocity magnitude for topographic high (T. Highs)/low (T. Lows) subclasses (Figure 4.2) and Q1–Q5, classified by Froude number (Fr).

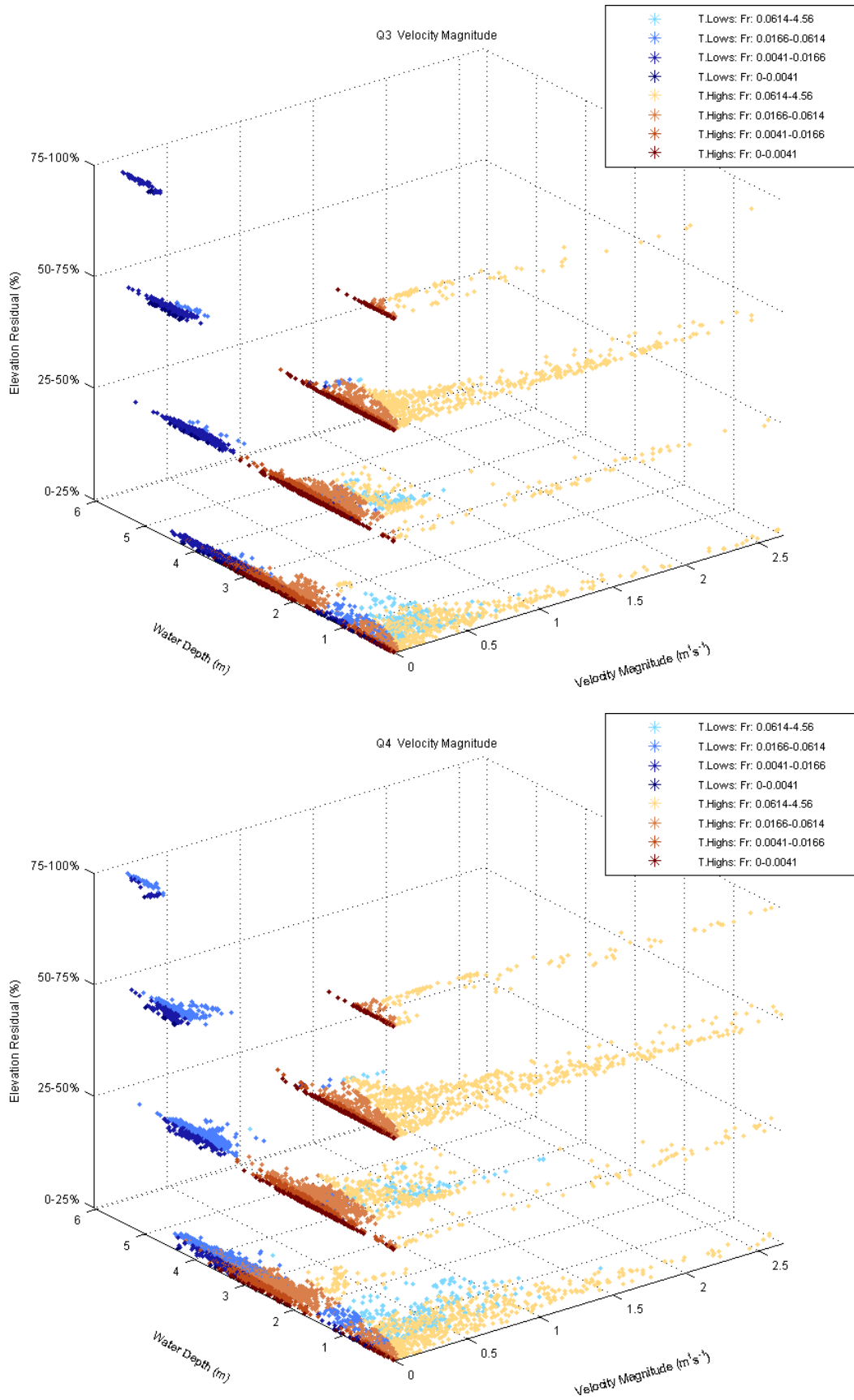


Figure 6.10 (cont'd). Distribution of velocity magnitude for topographic high (T. Highs)/low (T. Lows) subclasses (Figure 4.2) and Q1–Q5, classified by Froude number (Fr).

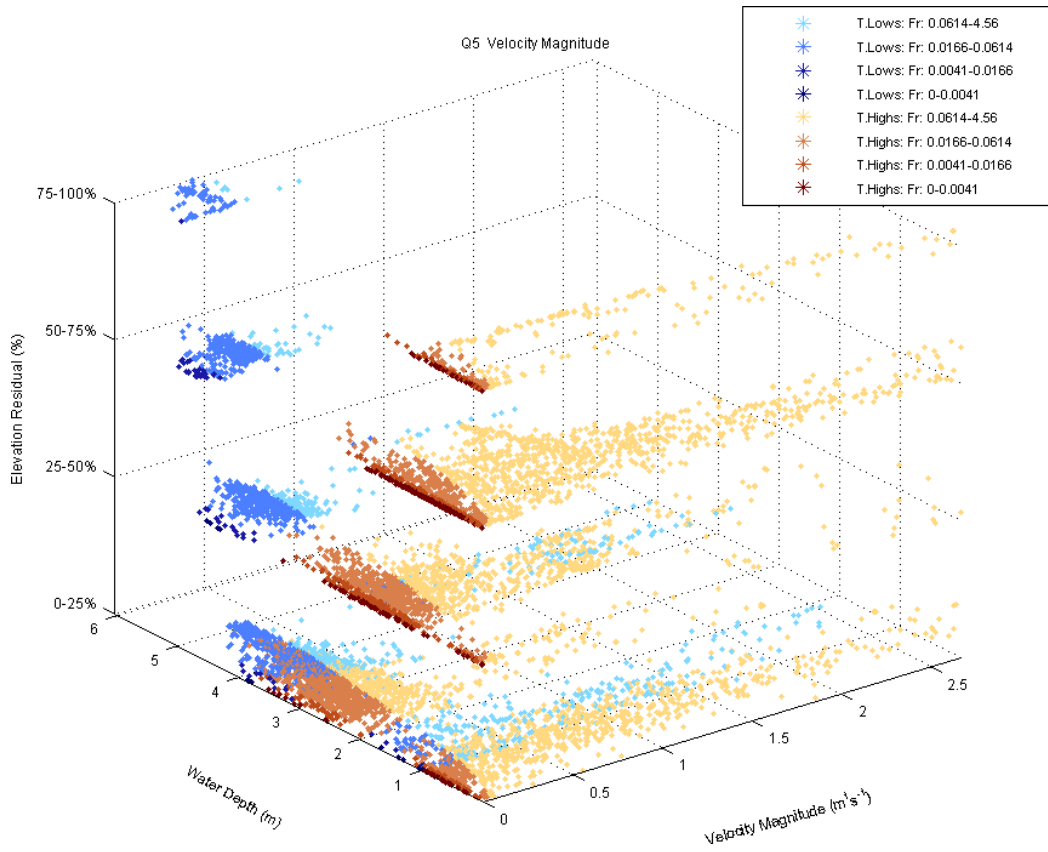


Figure 6.10 (cont'd). Distribution of velocity magnitude for topographic high (T. Highs)/low (T. Lows) subclasses (Figure 4.2) and Q1–Q5, classified by Froude number (Fr).

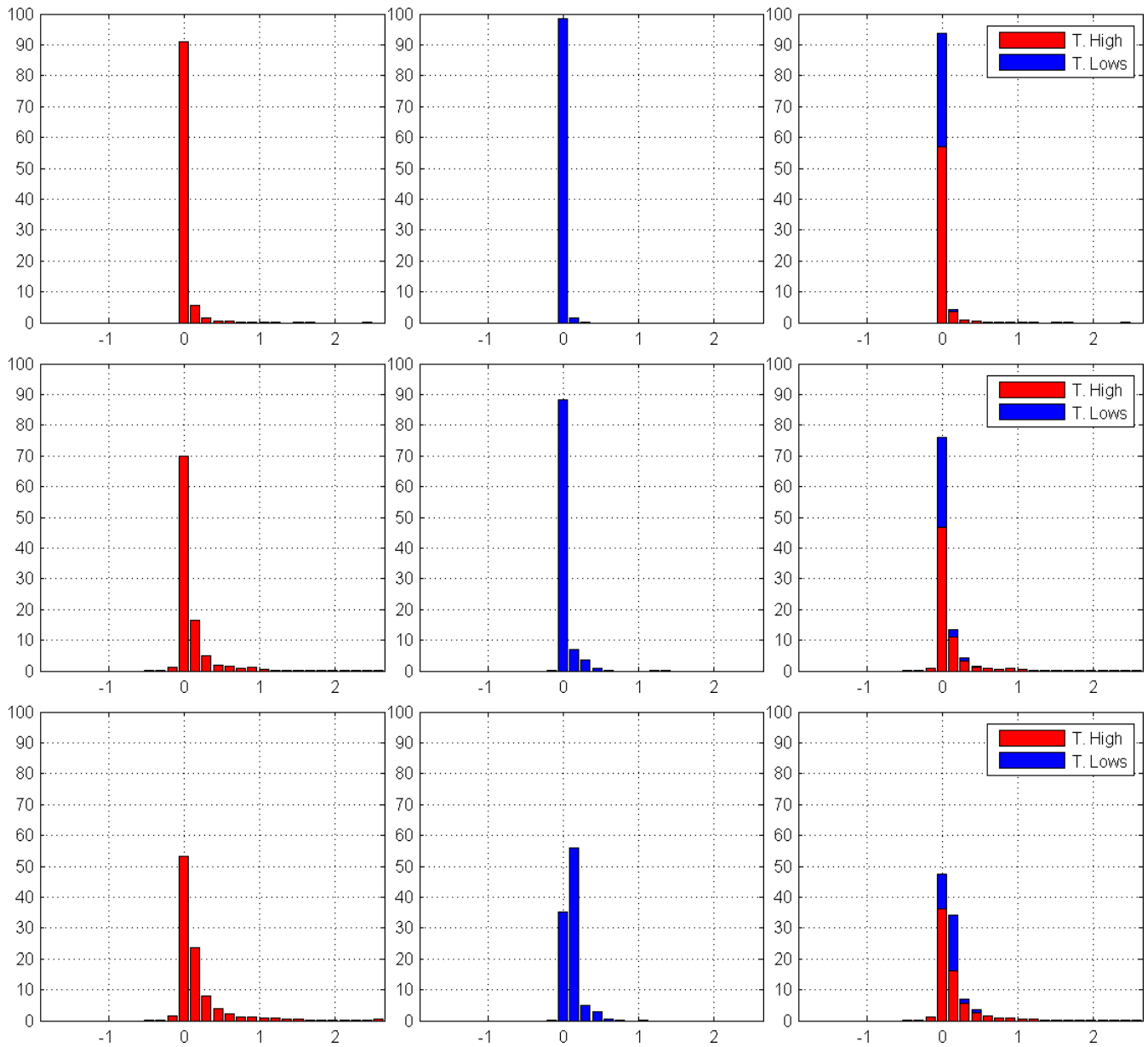


Figure 6.11. Distribution of streamwise velocity component for Q1–Q5 (rows, top to bottom) for topographic highs (marked as T. High) corresponding to the classes (+1)–(+4), topographic lows (marked as T. Lows) corresponding to the classes (-1)–(-4), and combined (columns, left to right). Horizontal and vertical axes correspond to streamwise velocity (m/s) and the percent values of topographic classes, respectively.

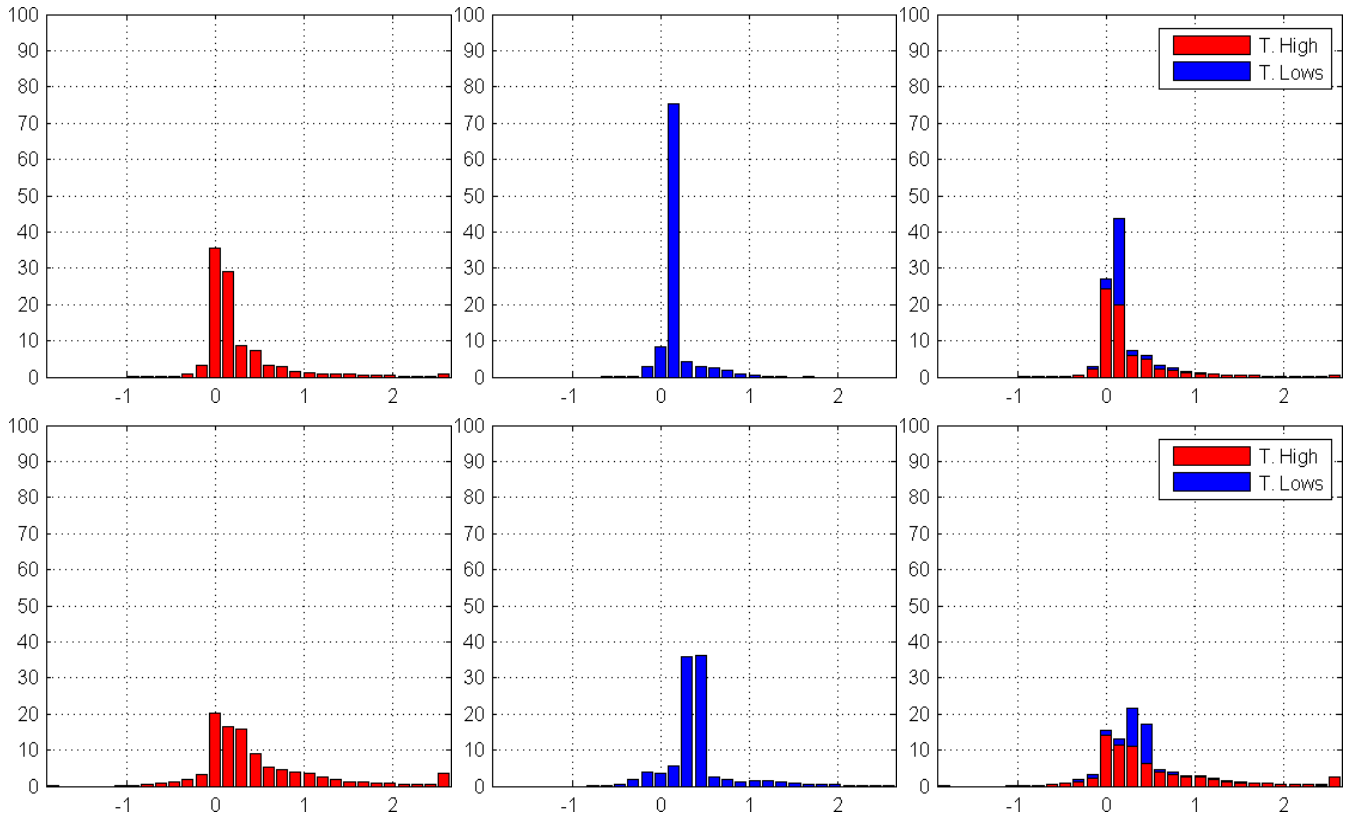


Figure 6.11 (cont'd). Distribution of streamwise velocity component for Q1–Q5 (rows, top to bottom) for topographic highs (marked as T. High) corresponding to the classes (+1)–(+4), topographic lows (marked as T. Lows) corresponding to the classes (-1)–(-4), and combined (columns, left to right). Horizontal and vertical axes correspond to streamwise velocity (m/s) and the percent values of topographic classes, respectively.

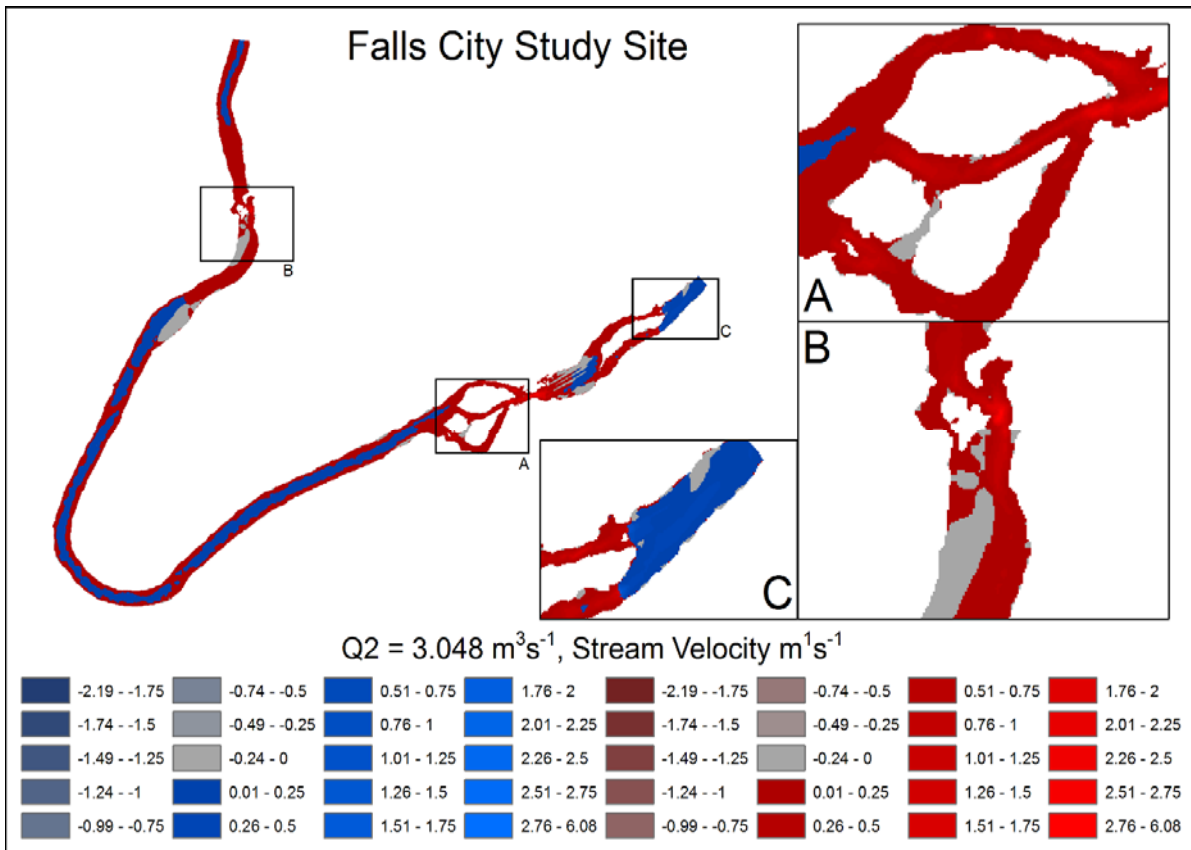
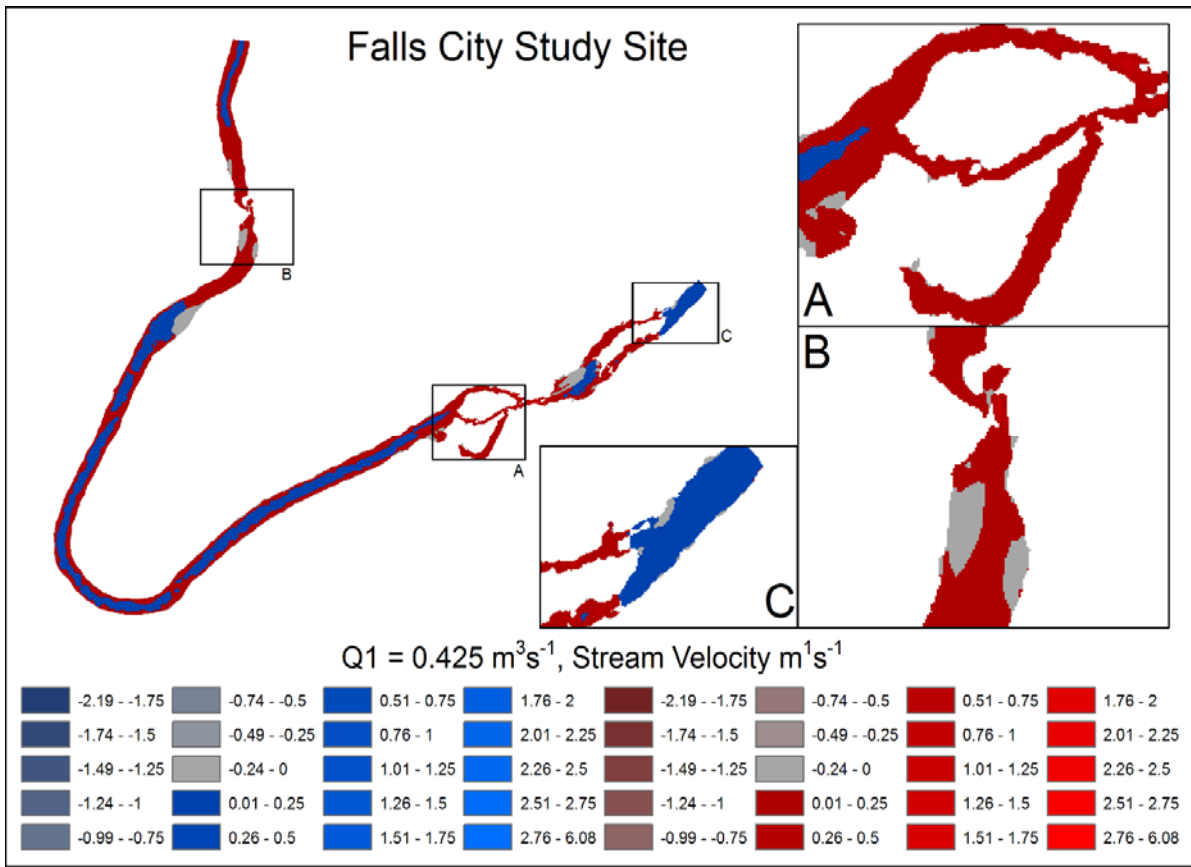


Figure 6.12. Spatial distribution of streamwise velocity (m/s) for Q1–Q5 for topographic highs (red colors) and lows (blue colors).

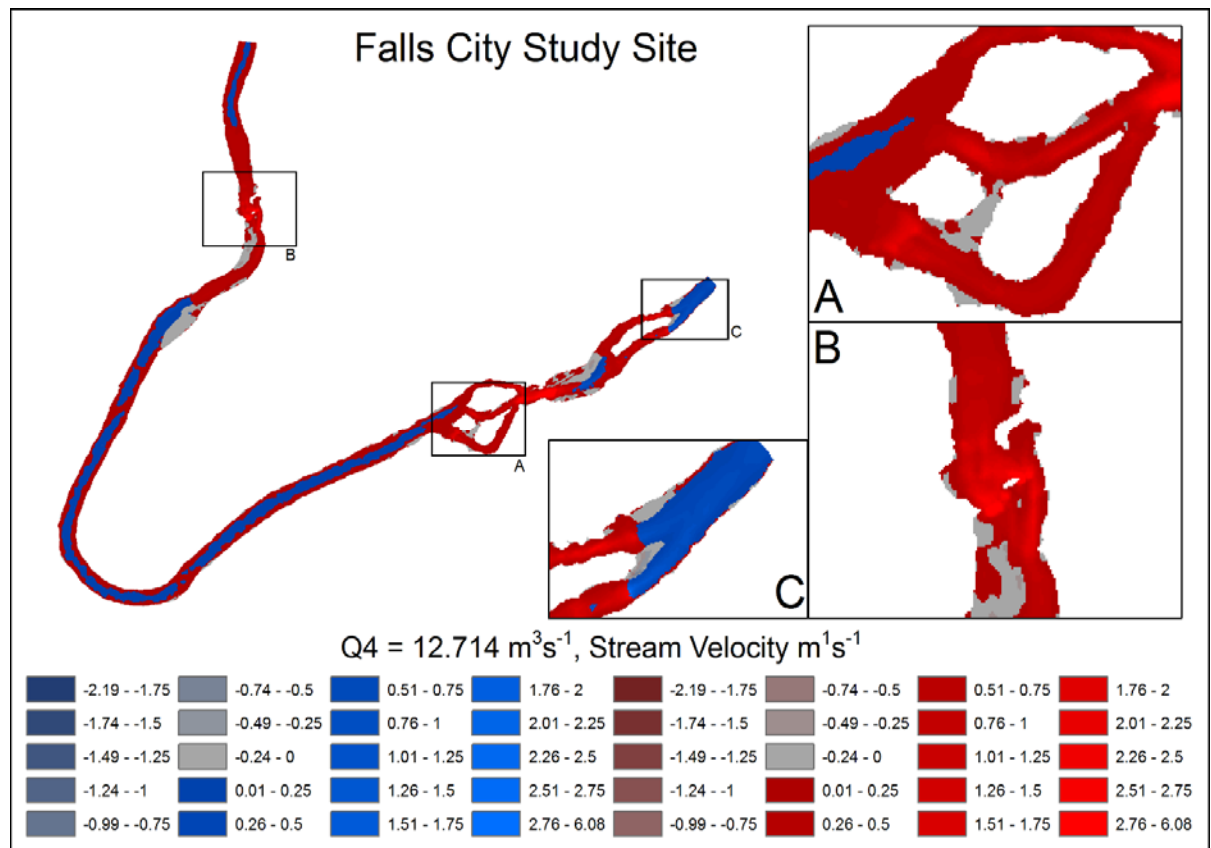
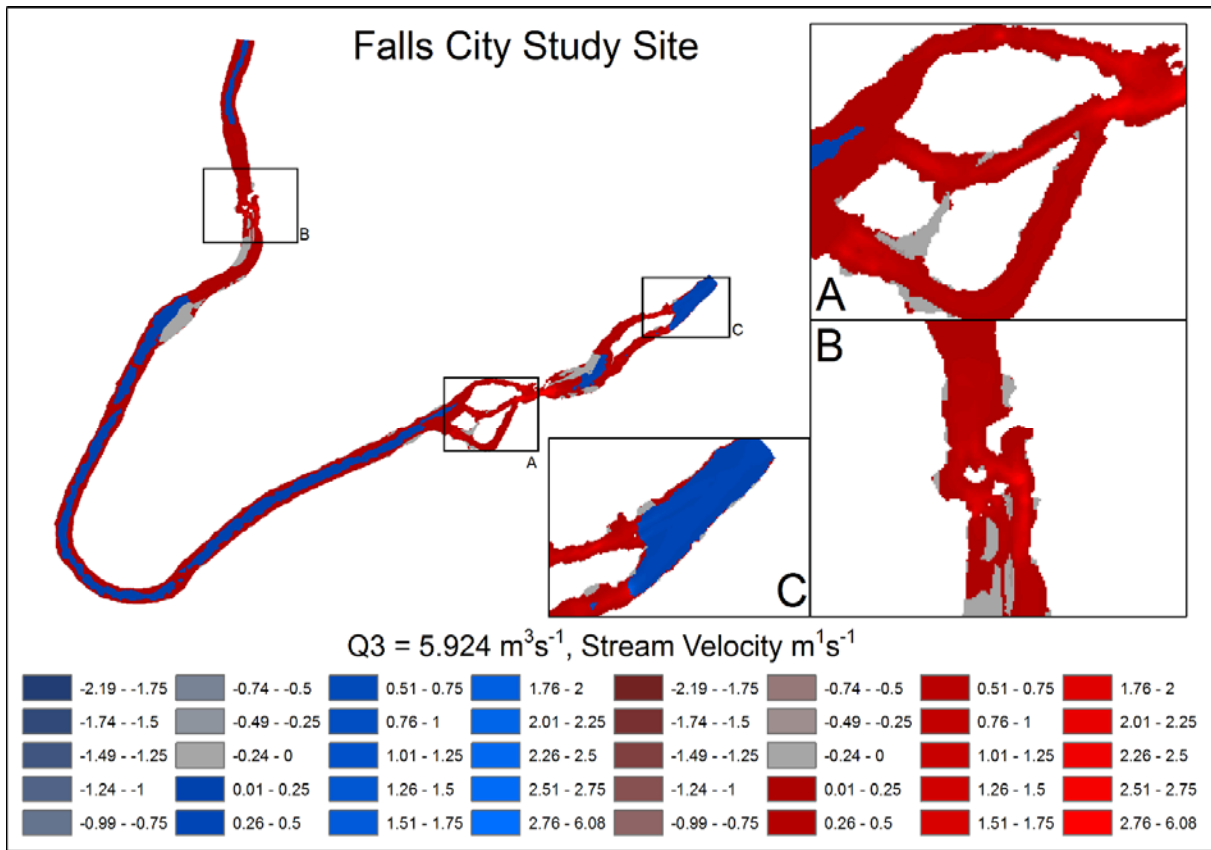


Figure 6.12 (cont'd). Spatial distribution of streamwise velocity (m/s) for Q1–Q5 for topographic highs (red colors) and lows (blue colors).

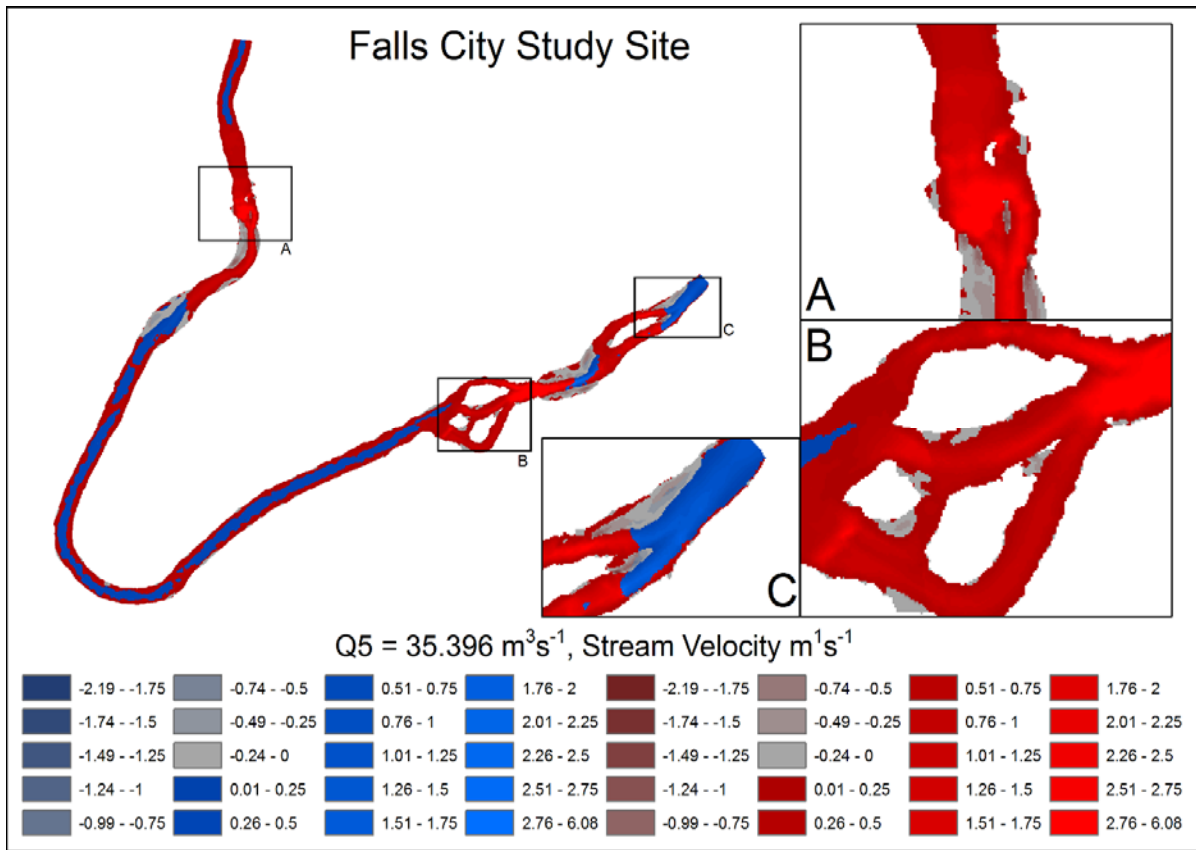


Figure 6.12 (cont'd). Spatial distribution of streamwise velocity (m/s) for Q1–Q5 for topographic highs (red colors) and lows (blue colors).

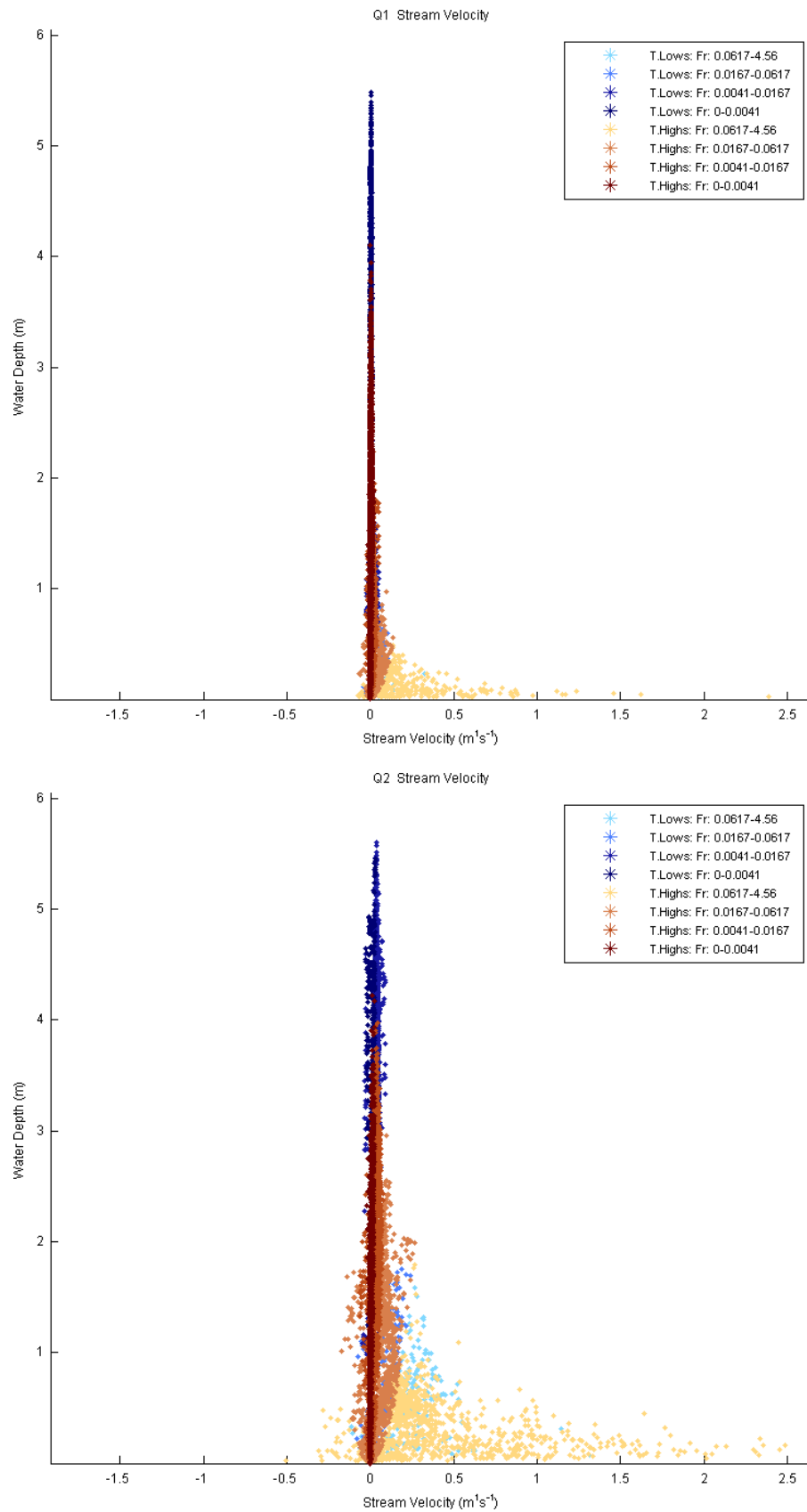


Figure 6.13. Distribution of streamwise velocity in relation to water depth for Q1–Q5 classified by topographic highs marked as T. Highs (brown colors), topographic lows marked as T. Lows (blue colors), and Froude number (Fr).

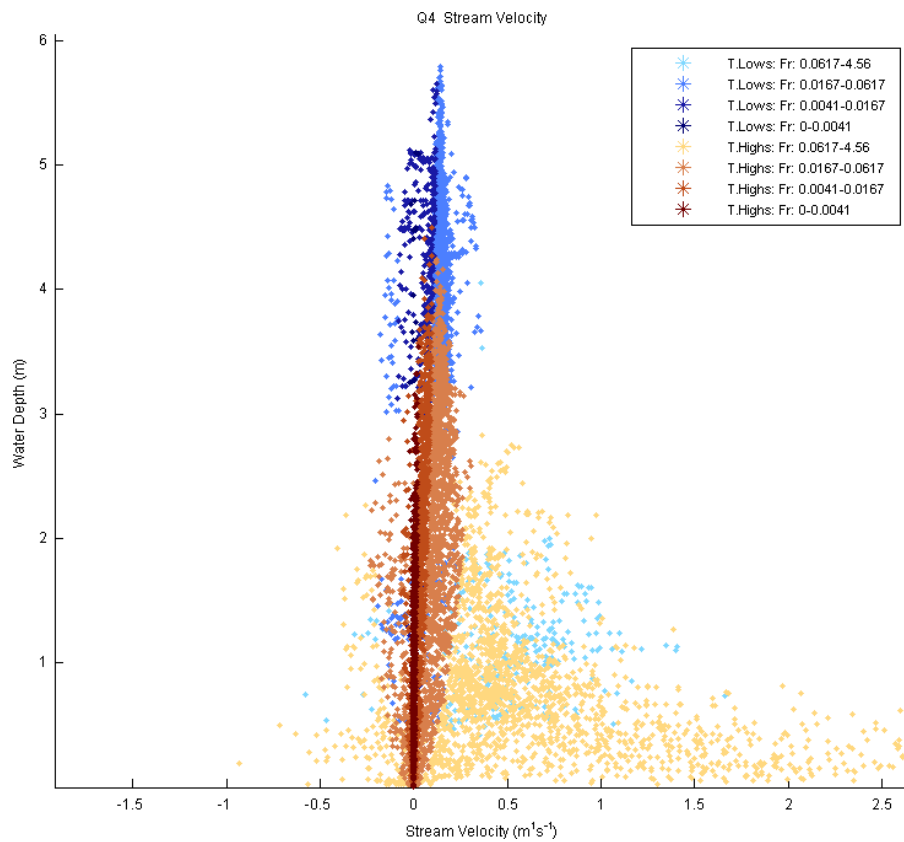
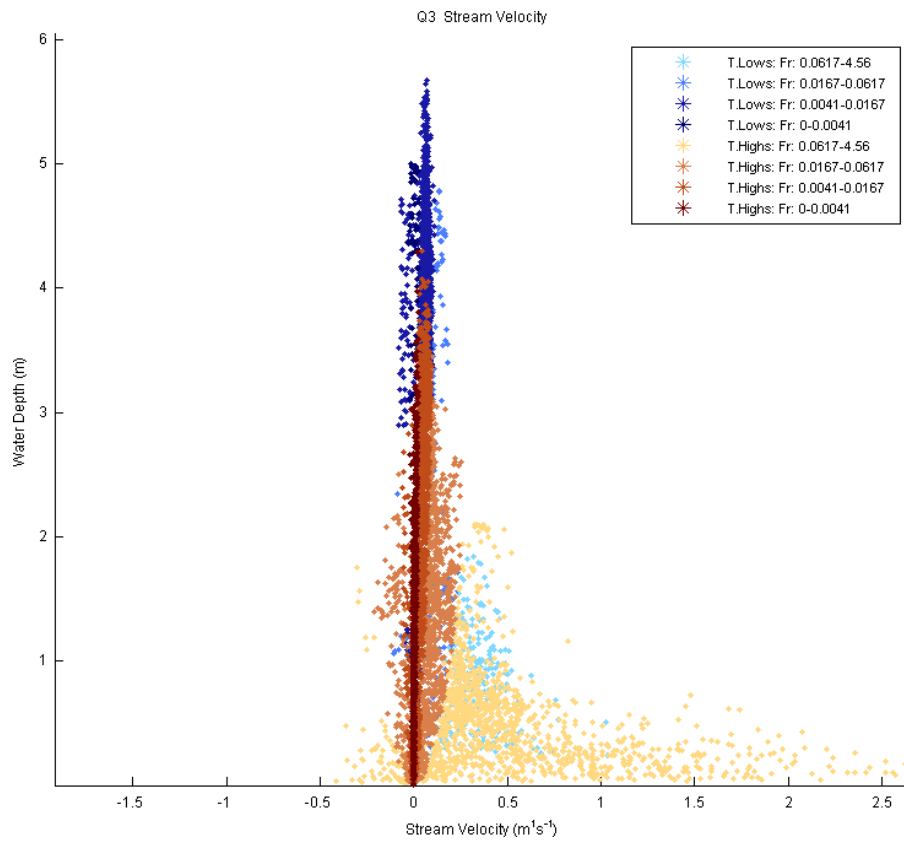


Figure 6.13 (cont'd). Distribution of streamwise velocity in relation to water depth for Q1–Q5 classified by topographic highs marked as T. Highs (brown colors), topographic lows marked as T. Lows (blue colors), and Froude number (Fr).

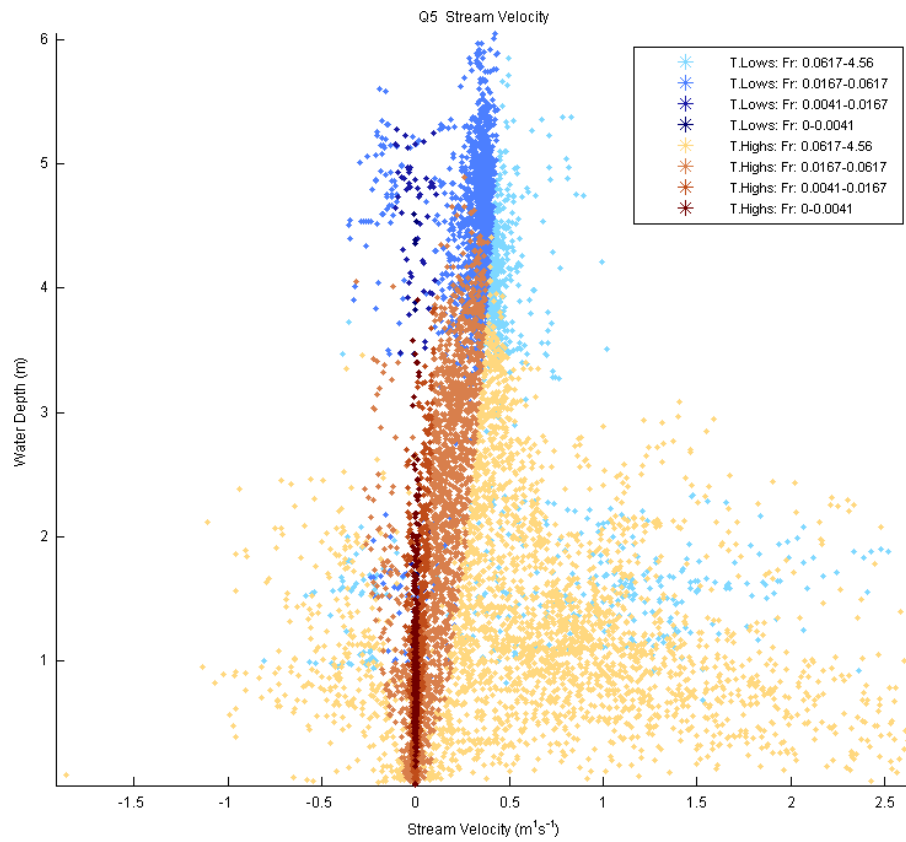


Figure 6.13 (cont'd). Distribution of streamwise velocity in relation to water depth for Q1–Q5 classified by topographic highs marked as T. Highs (brown colors), topographic lows marked as T. Lows (blue colors), and Froude number (Fr).

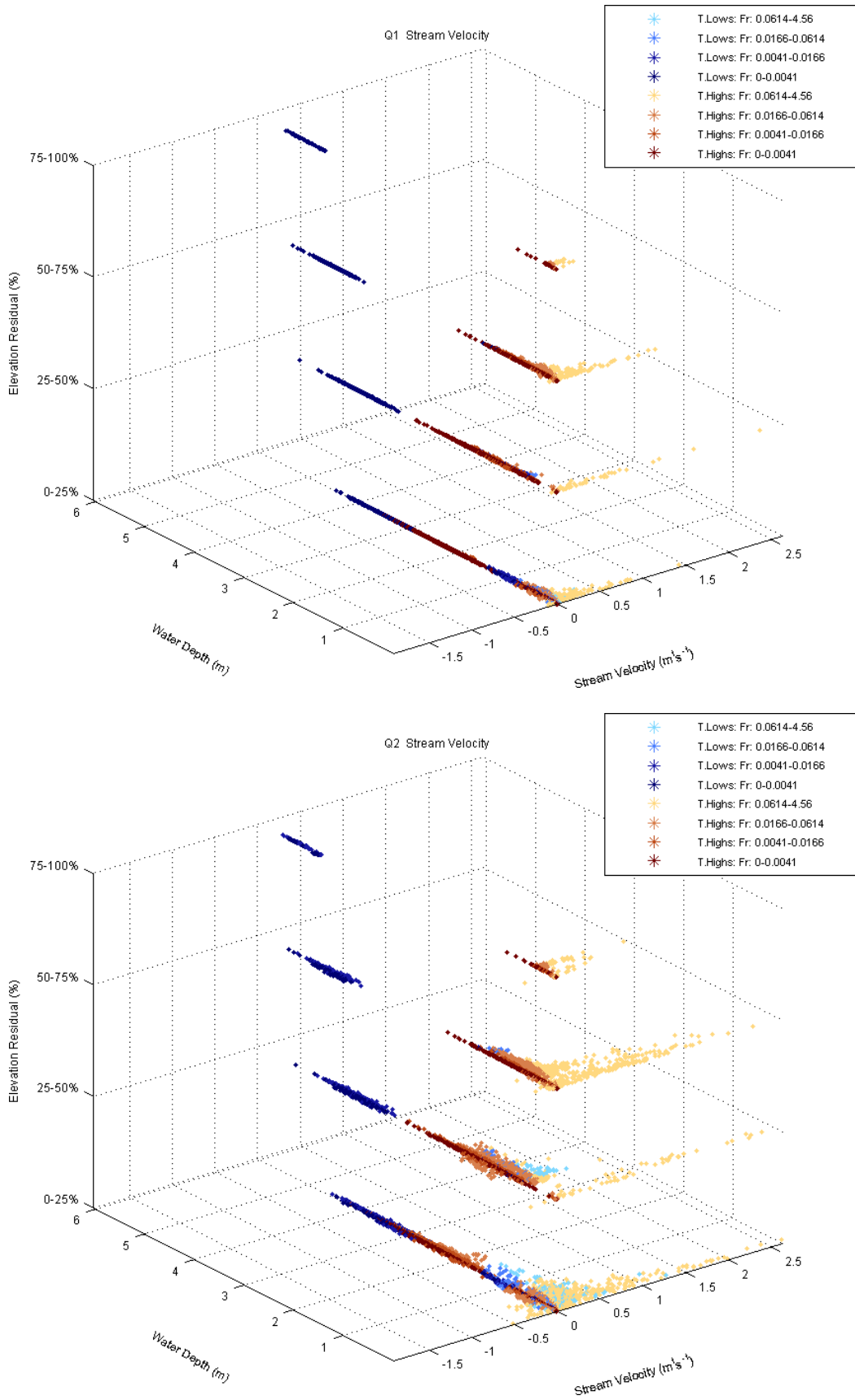


Figure 6.14. Distribution of streamwise velocity for topographic high (T. Highs)/low (T. Lows) subclasses (Figure 4.2) and Q1–Q5, classified by Froude number (Fr).

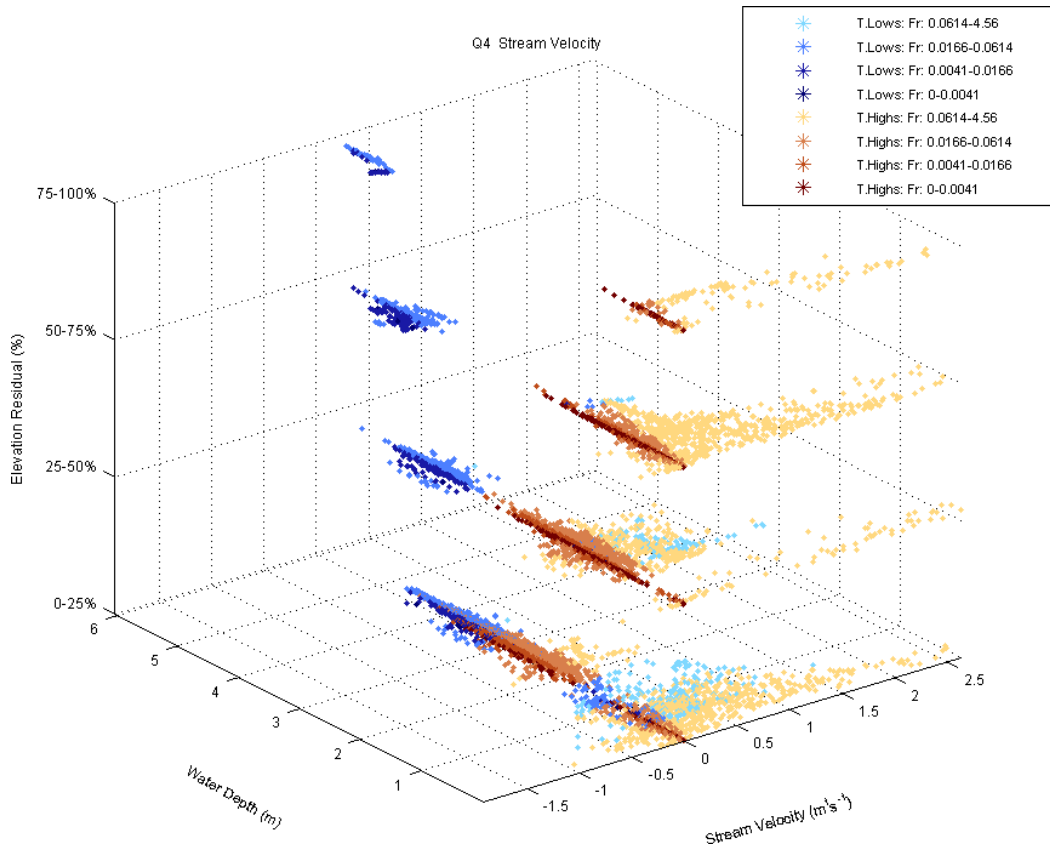
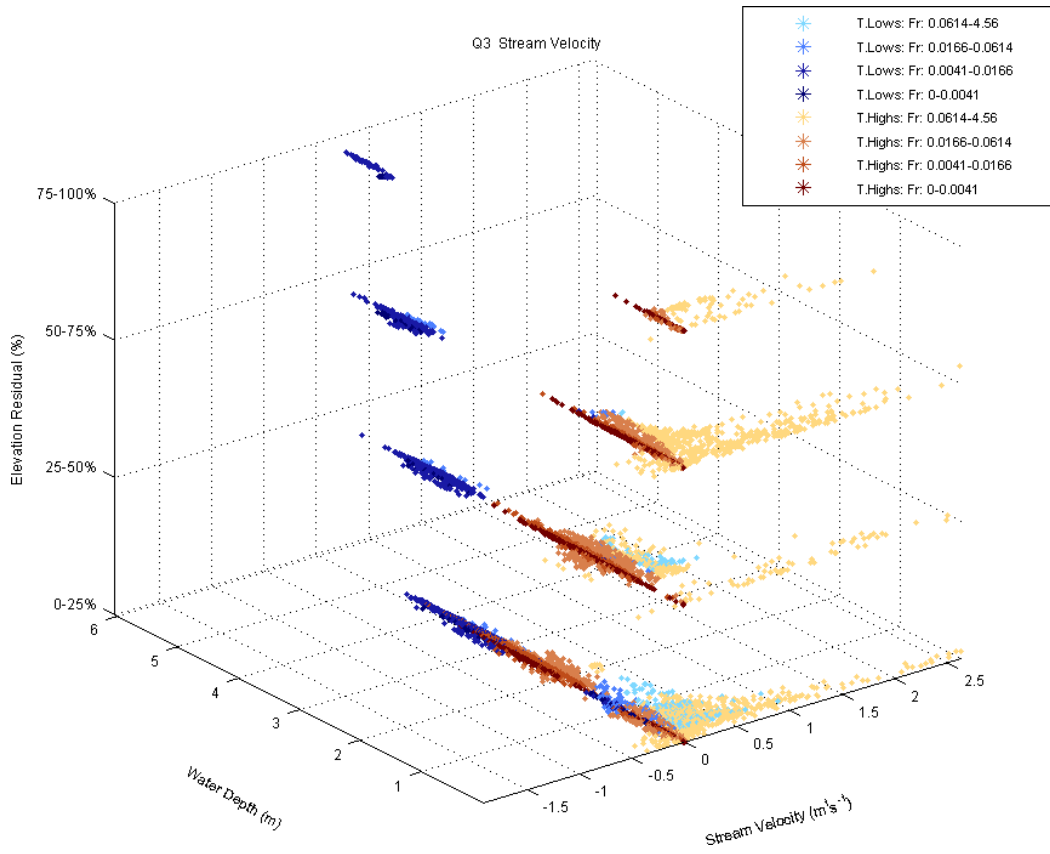


Figure 6.14 (cont'd). Distribution of streamwise velocity for topographic high (T. Highs)/low (T. Lows) subclasses (Figure 4.2) and Q1–Q5, classified by Froude number (Fr).

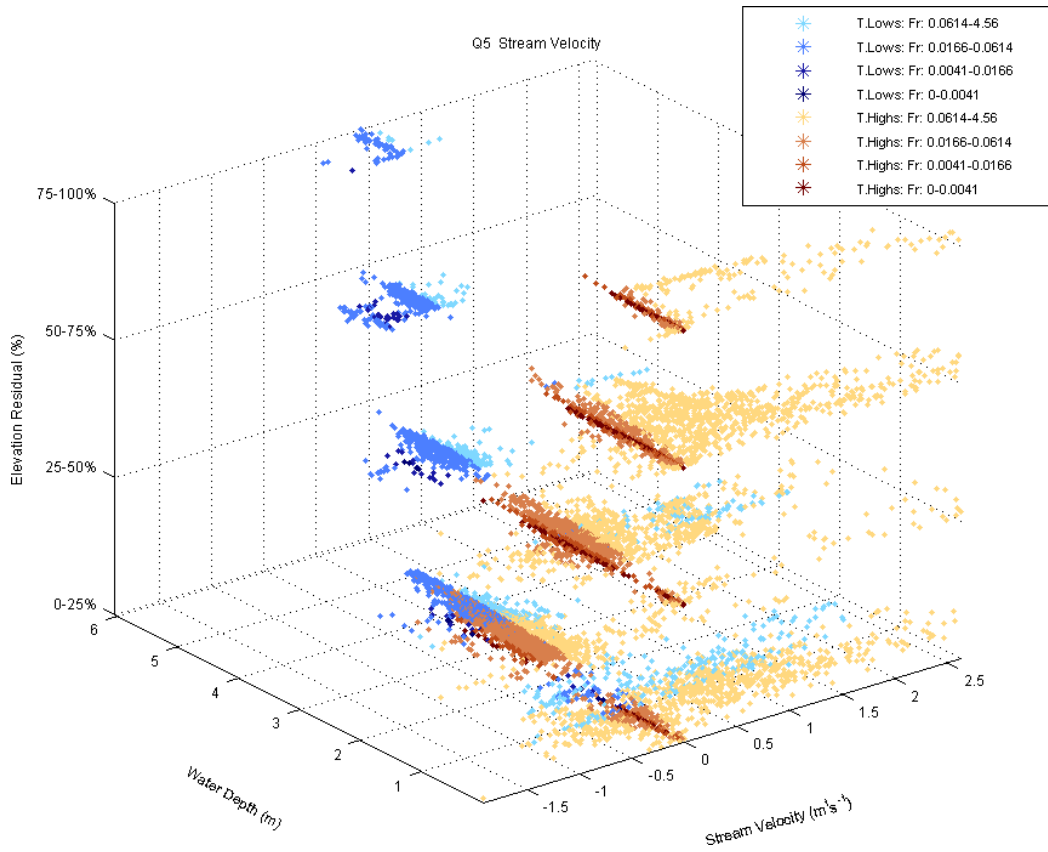


Figure 6.14 (cont'd). Distribution of streamwise velocity for topographic high (T. Highs)/low (T. Lows) subclasses (Figure 4.2) and Q1–Q5, classified by Froude number (Fr).

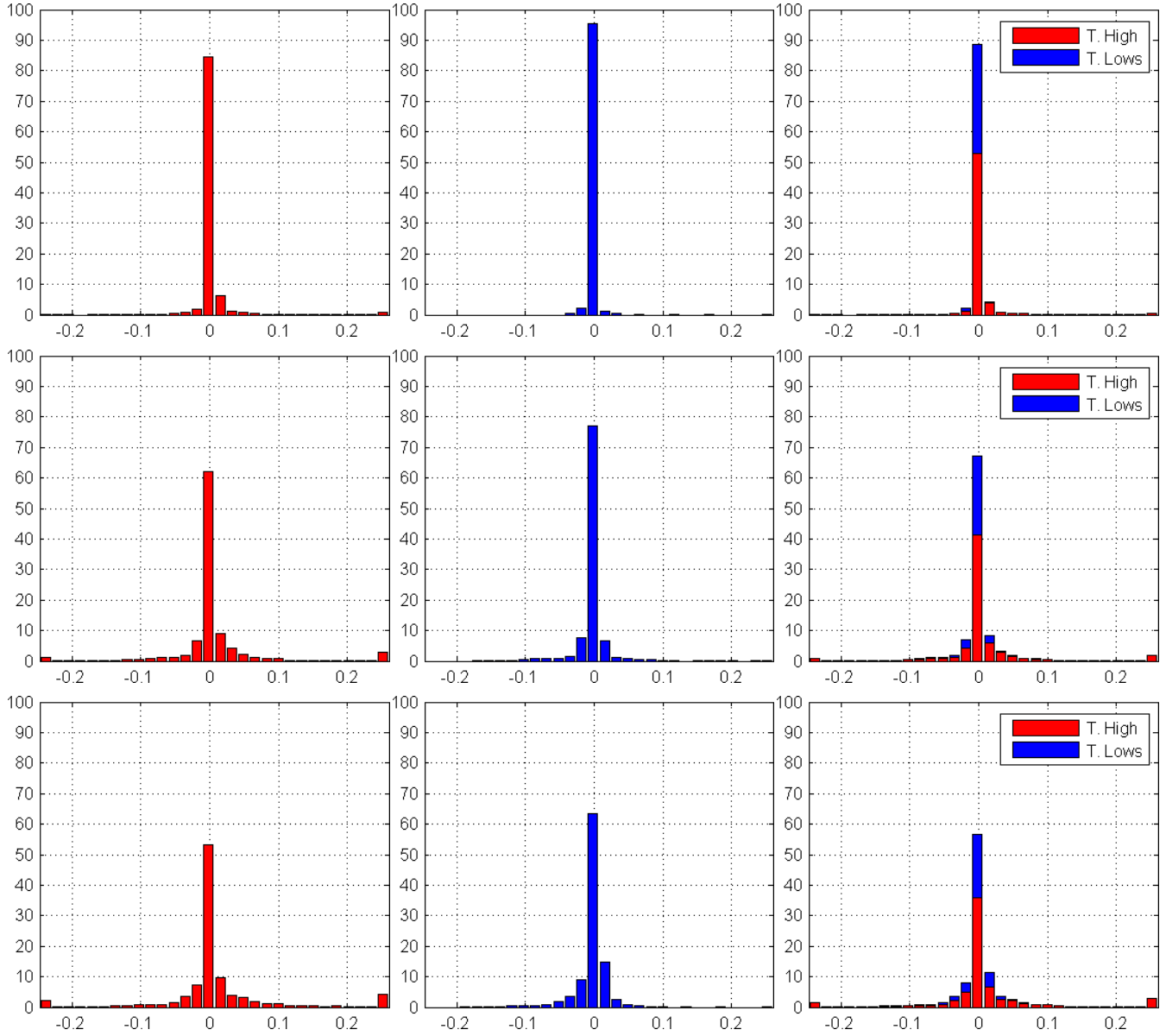


Figure 6.15. Distribution of normal velocity component for Q1–Q5 (rows, top to bottom) for topographic highs (marked as T. High) corresponding to the classes (+1)–(+4), topographic lows (marked as T. Lows) corresponding to the classes (-1)–(-4), and combined (columns, left to right). Horizontal and vertical axes correspond to normal velocity (m/s) and the percent values of topographic classes, respectively.

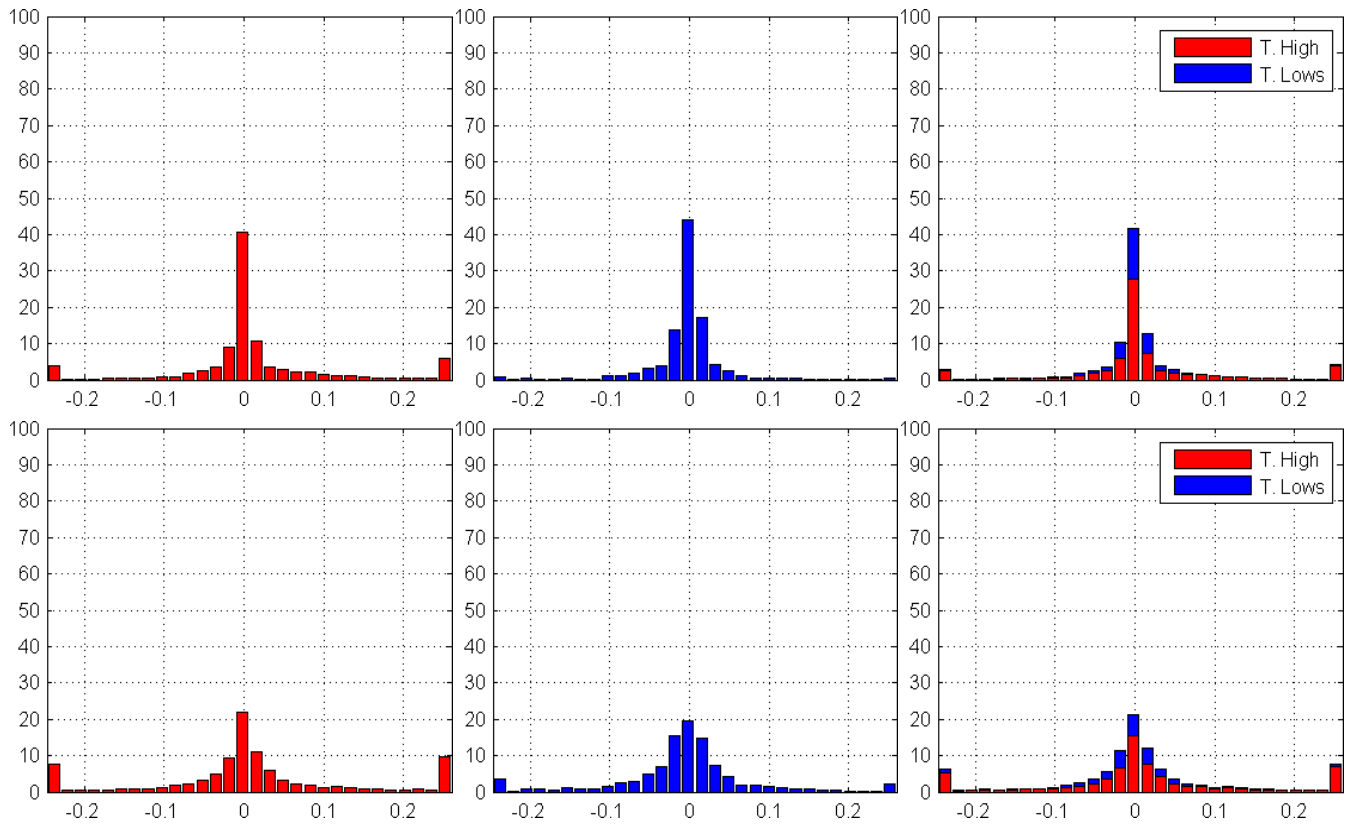


Figure 6.15 (cont'd). Distribution of normal velocity component for Q1–Q5 (rows, top to bottom) for topographic highs (marked as T. High) corresponding to the classes (+1)–(+4), topographic lows (marked as T. Lows) corresponding to the classes (-1)–(-4), and combined (columns, left to right). Horizontal and vertical axes correspond to normal velocity (m/s) and the percent values of topographic classes, respectively.

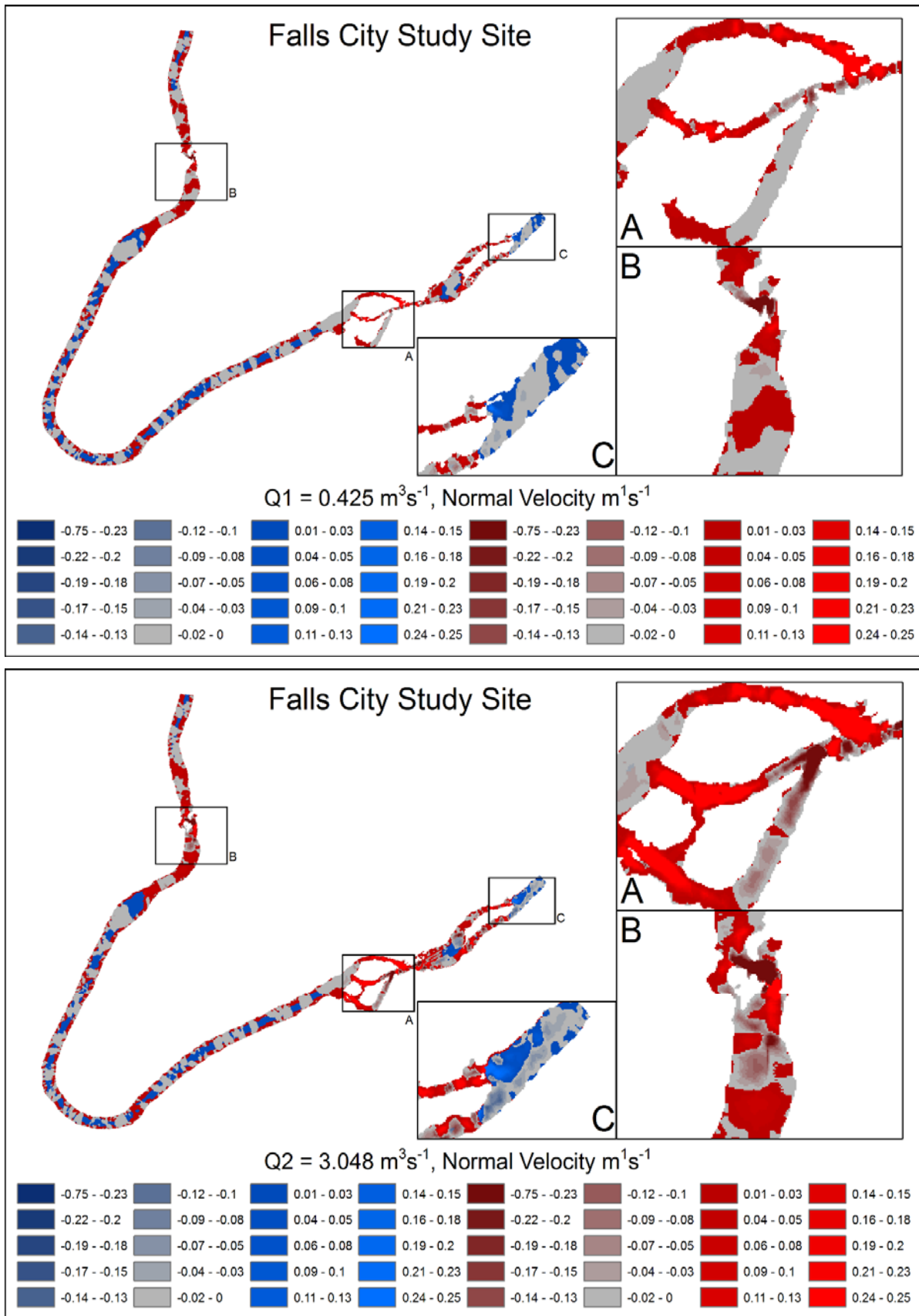


Figure 6.16. Spatial distribution of normal velocity (m/s) for Q1–Q5 for topographic highs (red colors) and lows (blue colors).

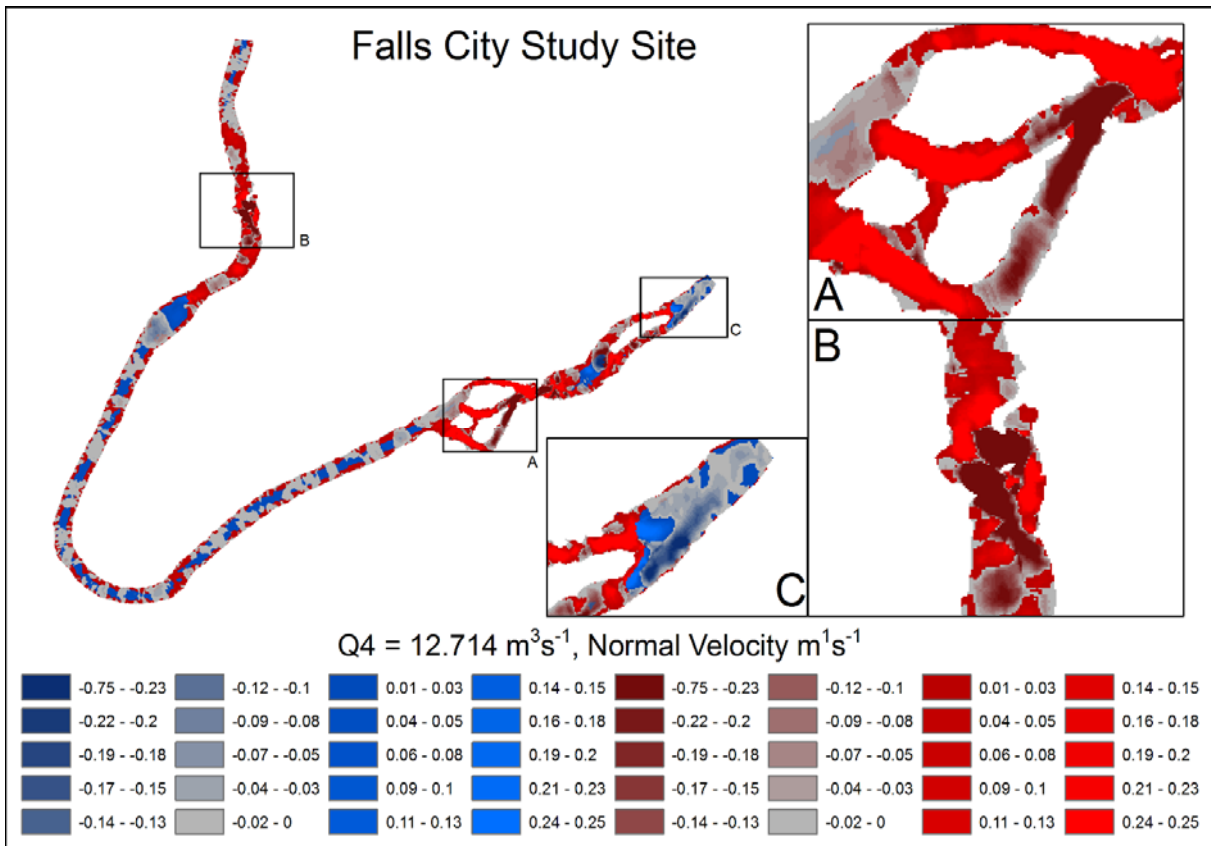
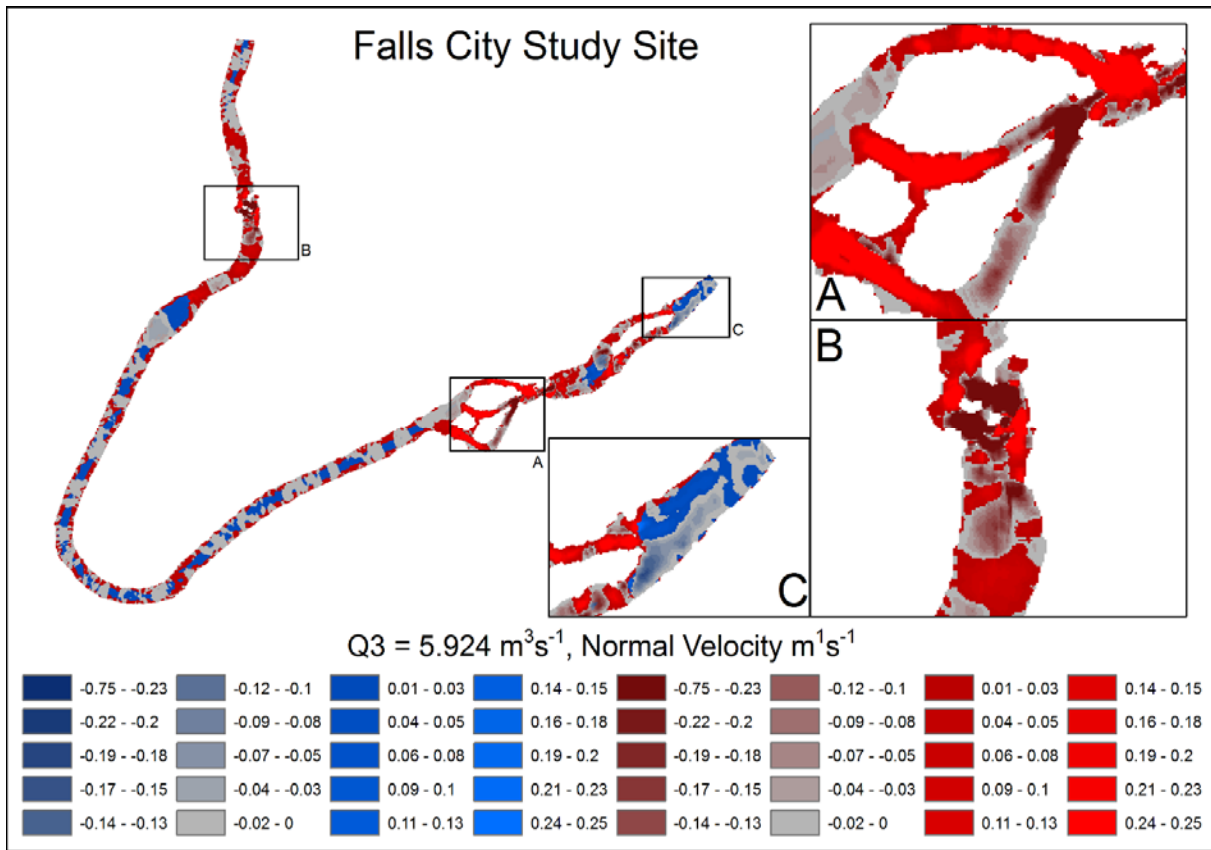


Figure 6.16 (cont'd). Spatial distribution of normal velocity (m/s) for Q1–Q5 for topographic highs (red colors) and lows (blue colors).

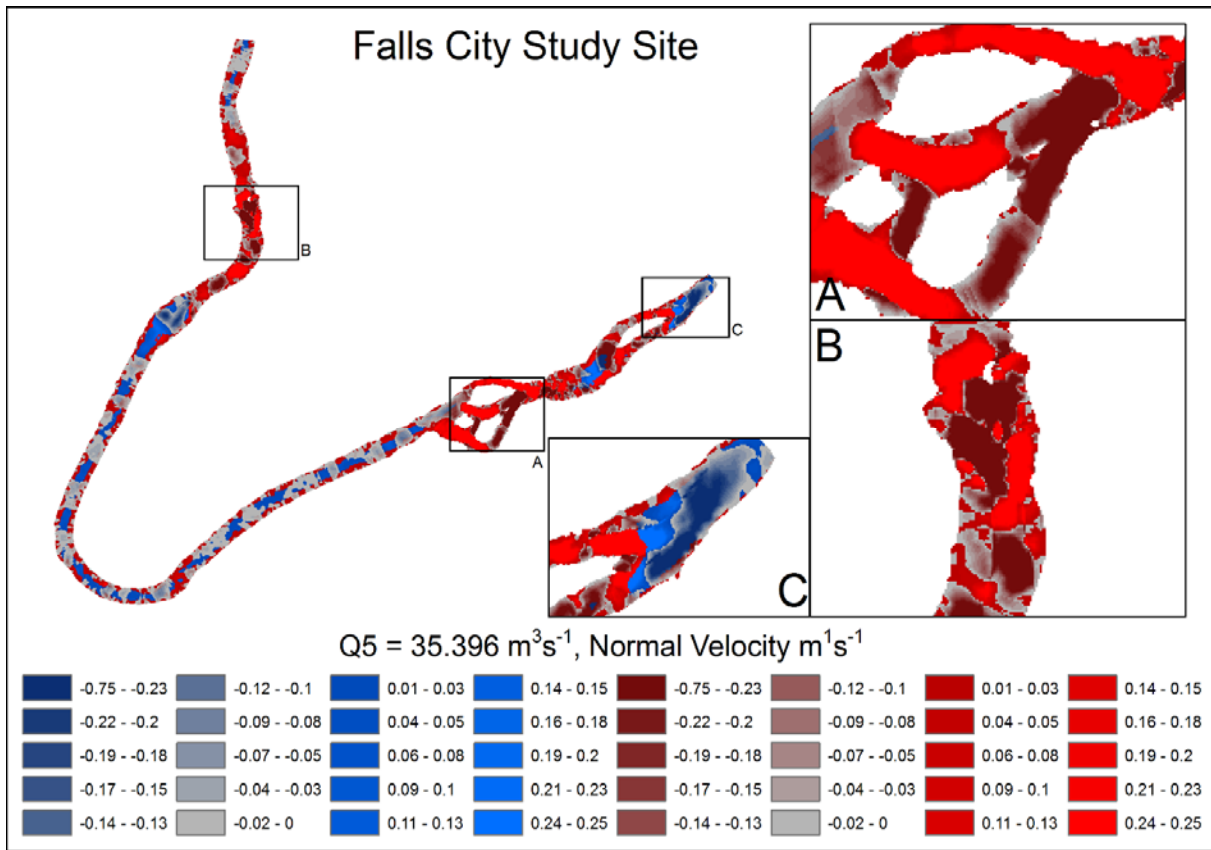


Figure 6.16 (cont'd). Spatial distribution of normal velocity (m/s) for Q1–Q5 for topographic highs (red colors) and lows (blue colors).

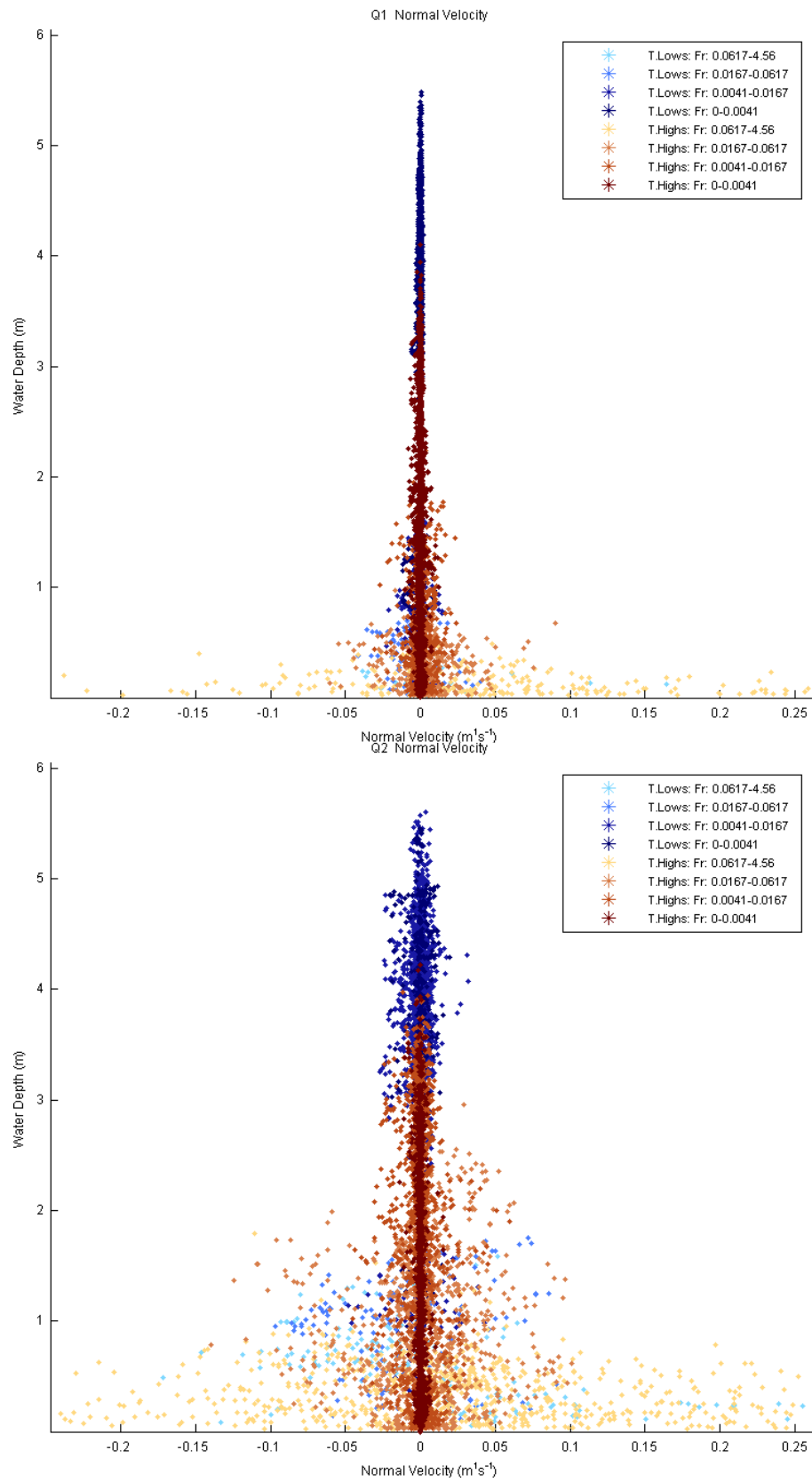


Figure 6.17. Distribution of normal velocity in relation to water depth for Q1–Q5 classified by topographic highs marked as T. Highs (brown colors), topographic lows marked as T. Lows (blue colors), and Froude number (Fr).

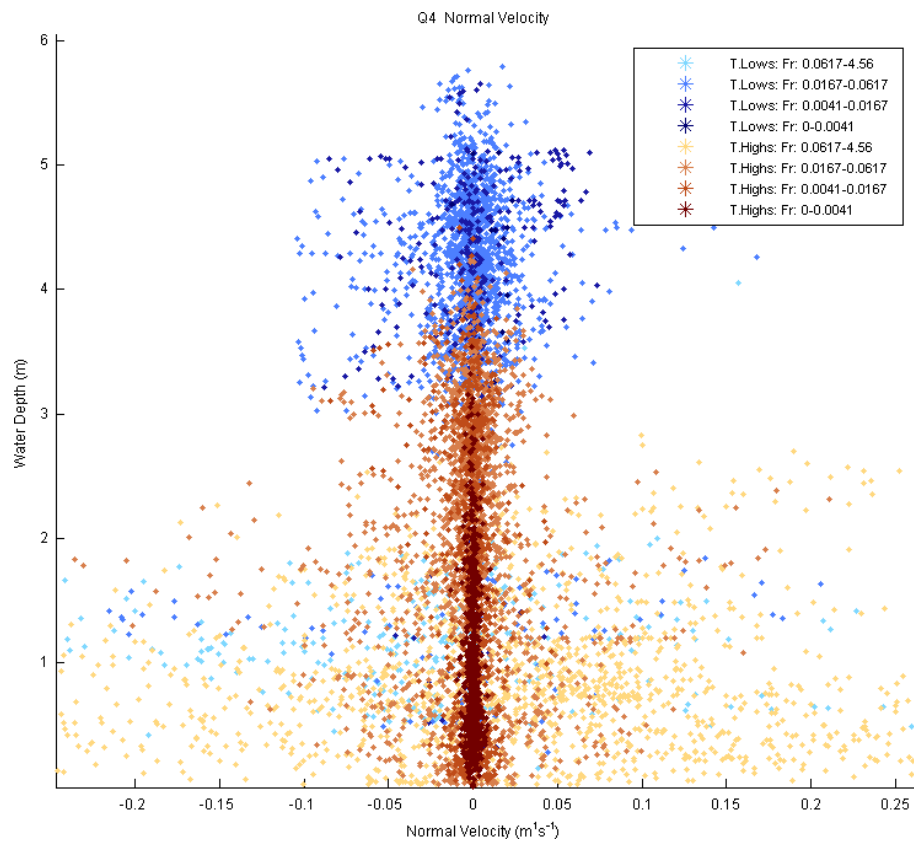
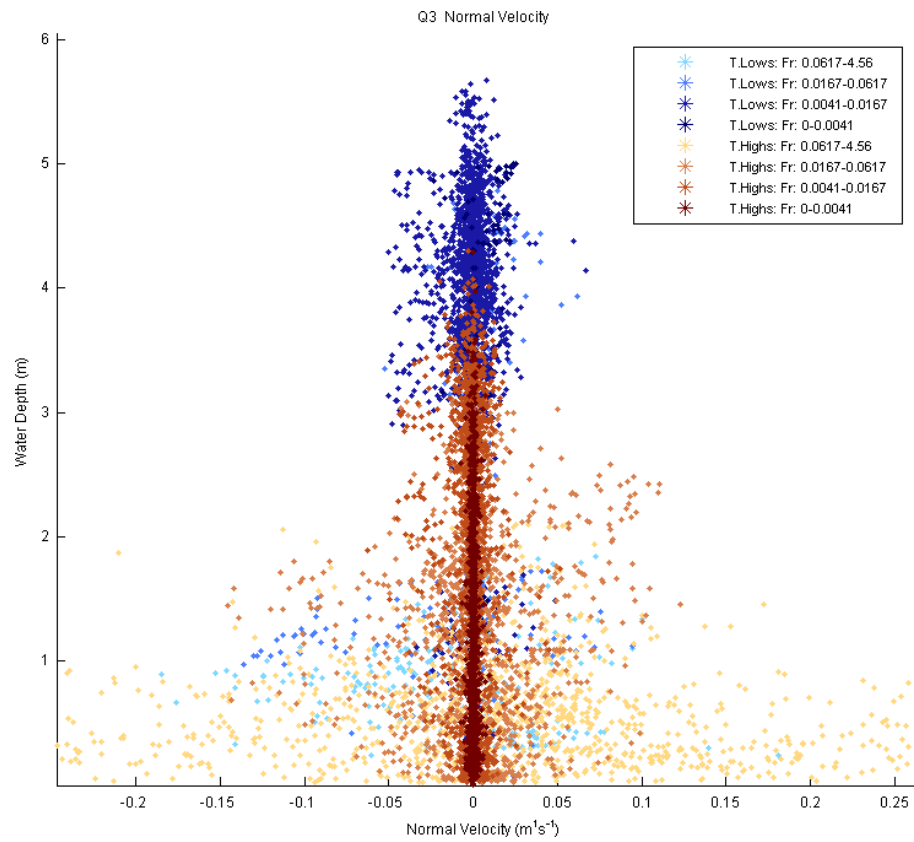


Figure 6.17 (con'td). Distribution of normal velocity in relation to water depth for Q1–Q5 classified by topographic highs marked as T. Highs (brown colors), topographic lows marked as T. Lows (blue colors), and Froude number (Fr).

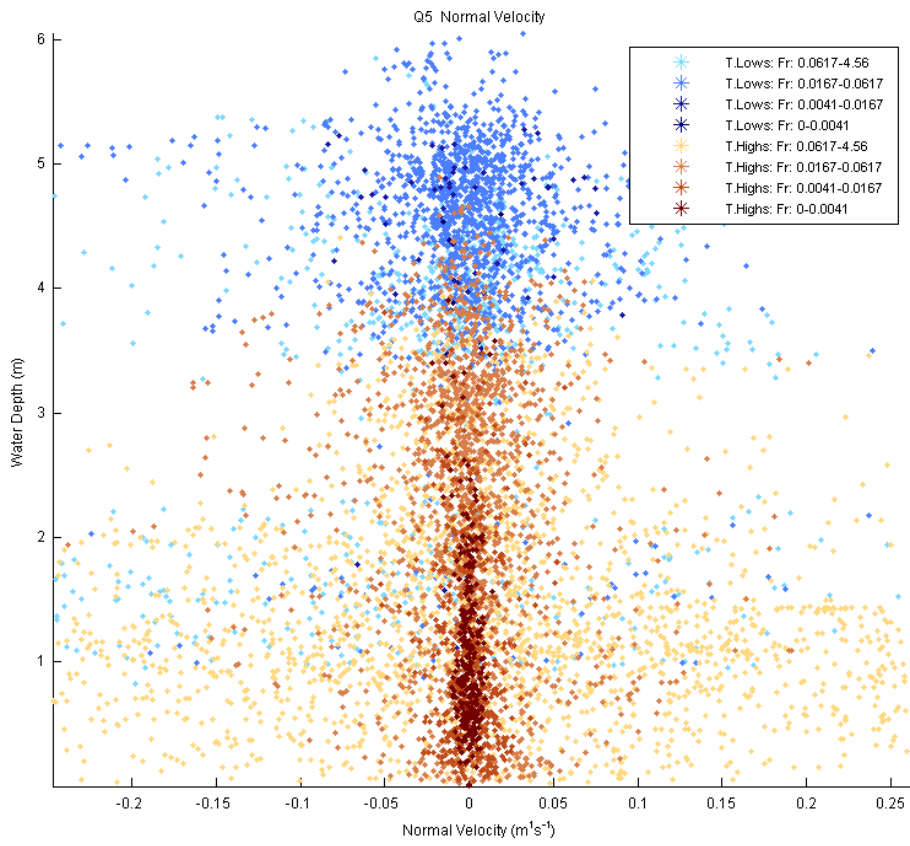


Figure 6.17 (cont'd). Distribution of normal velocity in relation to water depth for Q1–Q5 classified by topographic highs marked as T. Highs (brown colors), topographic lows marked as T. Lows (blue colors), and Froude number (Fr).

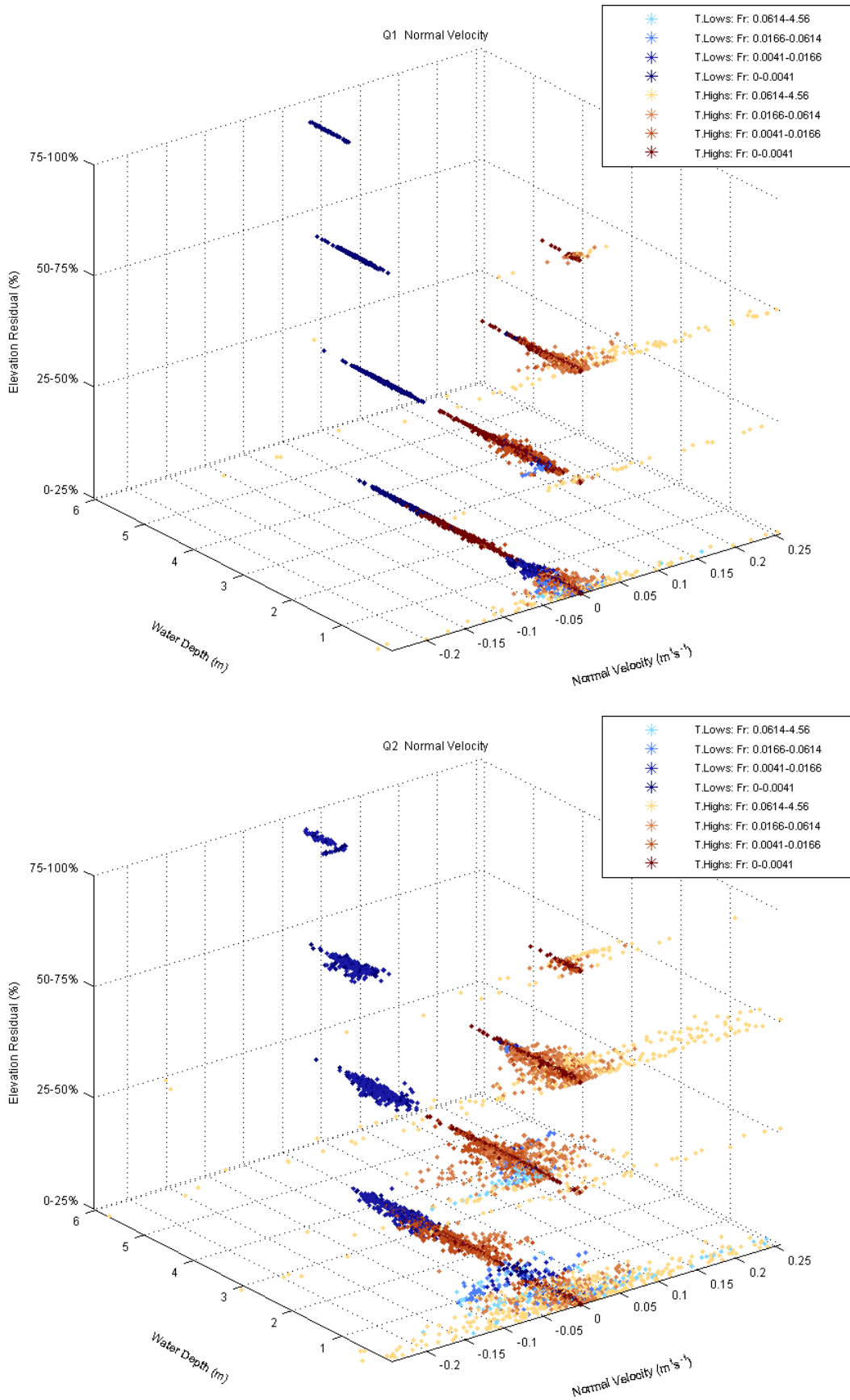


Figure 6.18. Distribution of normal velocity for topographic high (T. Highs)/low (T. Lows) subclasses (Figure 4.2) and Q1–Q5, classified by Froude number (Fr).

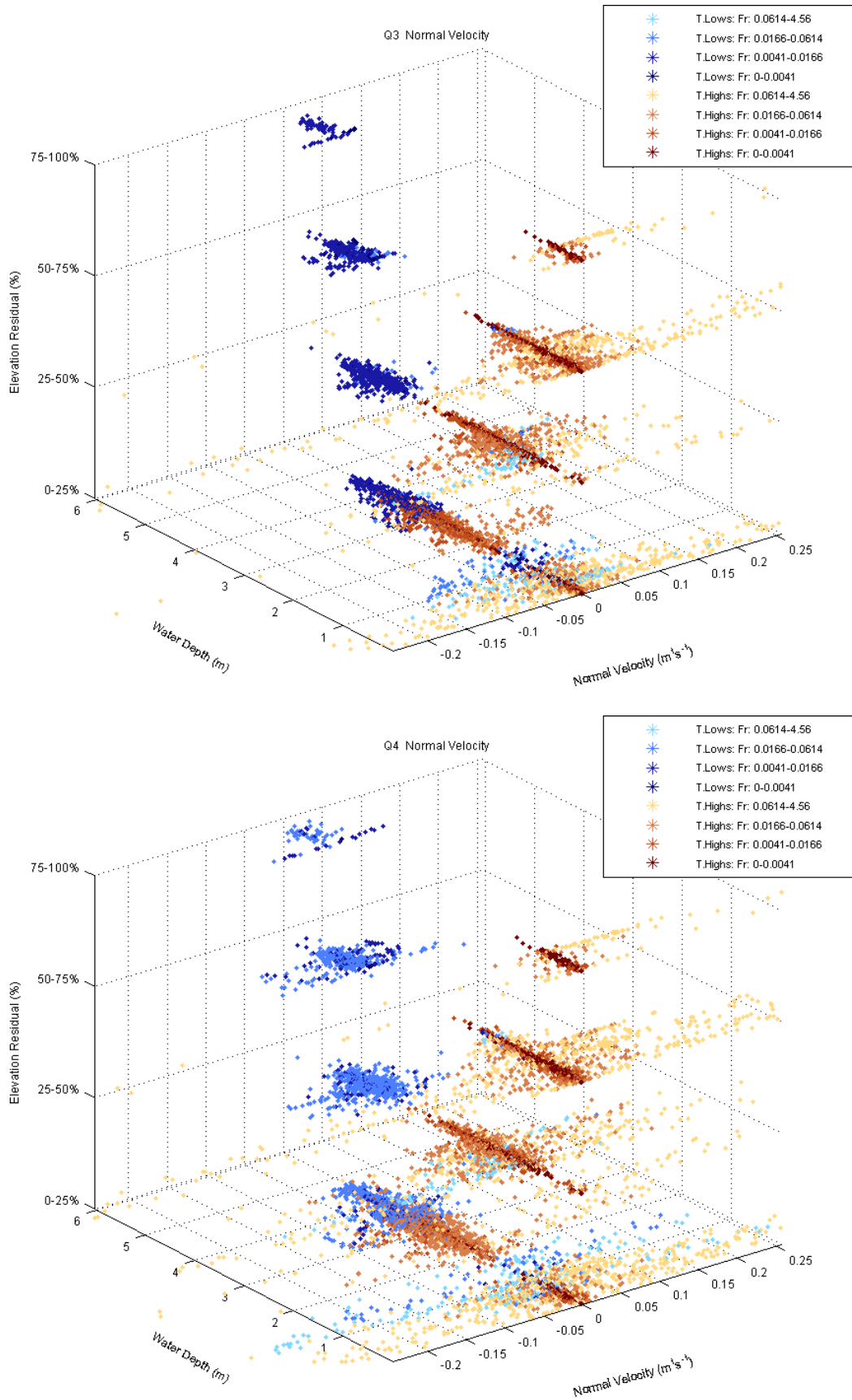


Figure 6.18 (cont'd). Distribution of normal velocity for topographic high (T. Highs)/low (T. Lows) subclasses (Figure 4.2) and Q1–Q5, classified by Froude number (Fr).

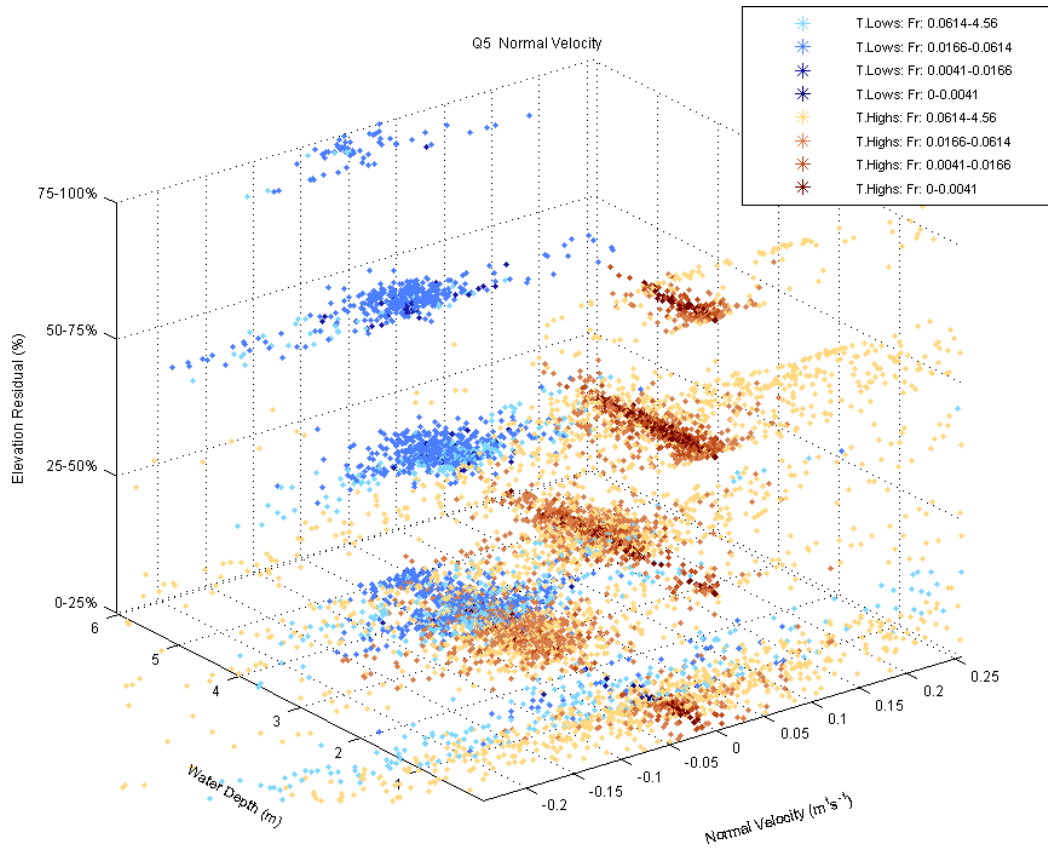


Figure 6.18 (cont'd). Distribution of normal velocity for topographic high (T. Highs)/low (T. Lows) subclasses (Figure 4.2) and Q1–Q5, classified by Froude number (Fr).

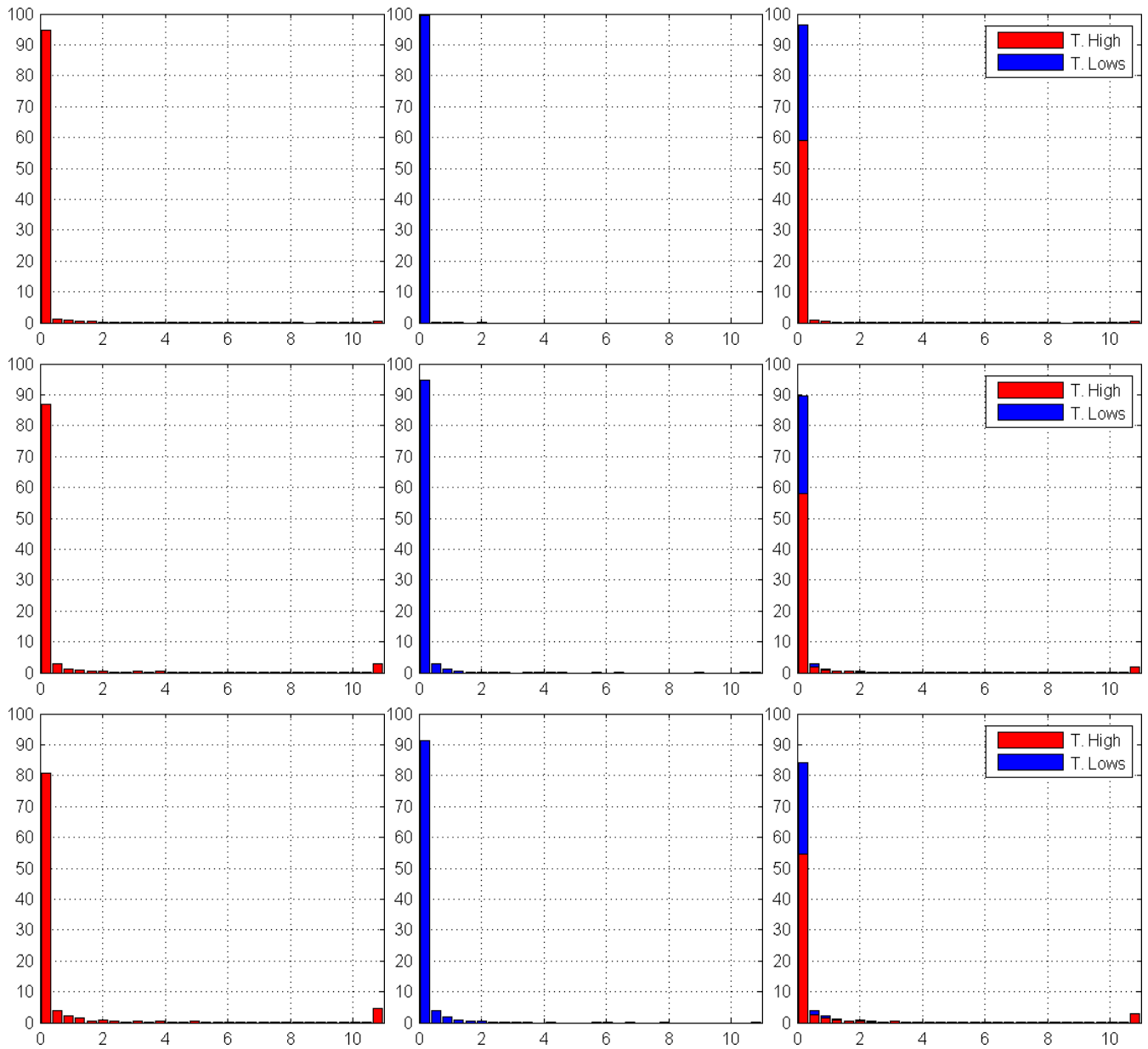


Figure 6.19. Distribution of shear stress for Q1–Q5 (rows, top to bottom) for topographic highs (marked as T. High) corresponding to the classes (+1)–(+4), topographic lows (marked as T. Lows) corresponding to the classes (-1)–(-4), and combined (columns, left to right). Horizontal and vertical axes correspond to shear stress ($\text{kg} \times \text{m/s}^2$) and the percent values of topographic classes, respectively.

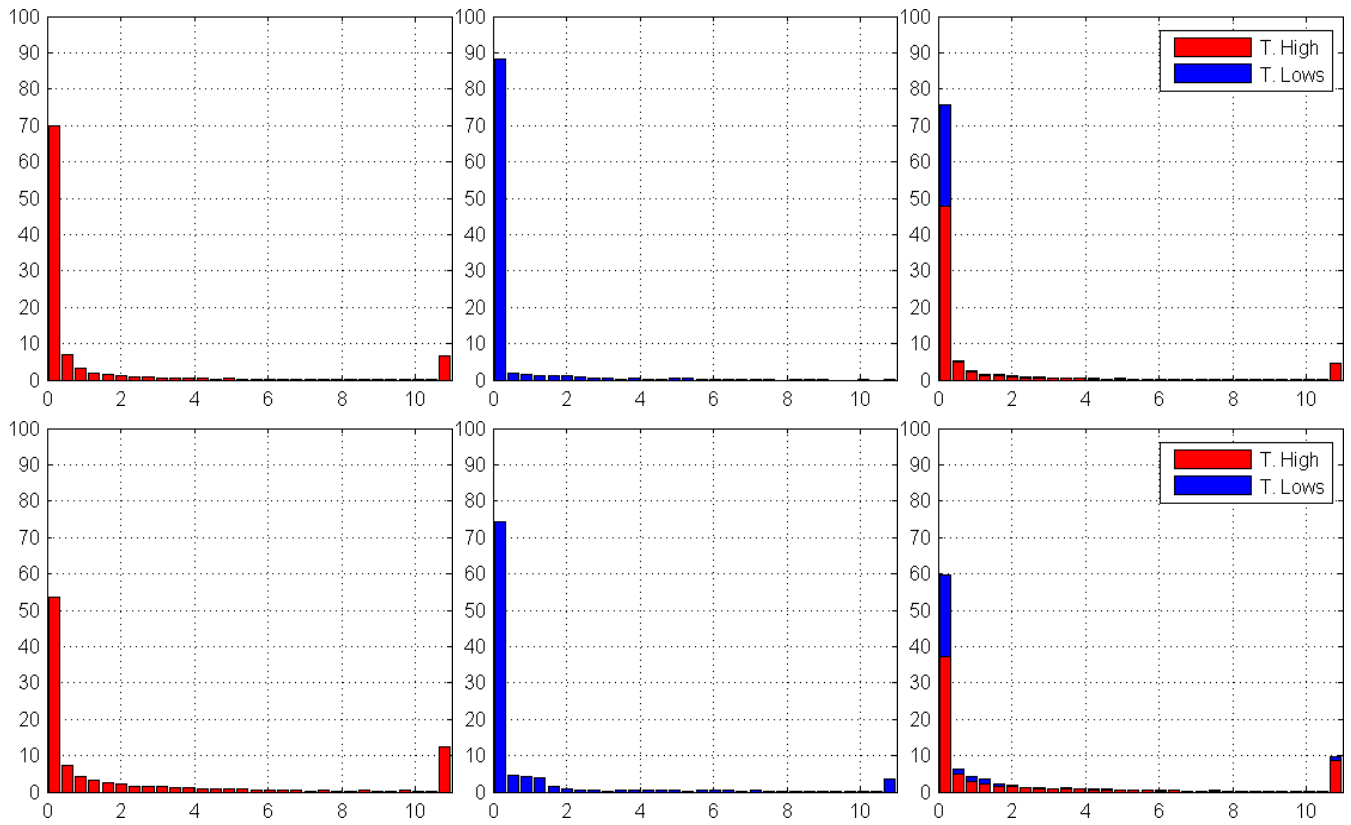


Figure 6.19 (cont'd). Distribution of shear stress for Q1–Q5 (rows, top to bottom) for topographic highs (marked as T. High) corresponding to the classes (+1)–(+4), topographic lows (marked as T. Lows) corresponding to the classes (-1)–(-4), and combined (columns, left to right). Horizontal and vertical axes correspond to shear stress ($\text{kg} \times \text{m/s}^2$) and the percent values of topographic classes, respectively.

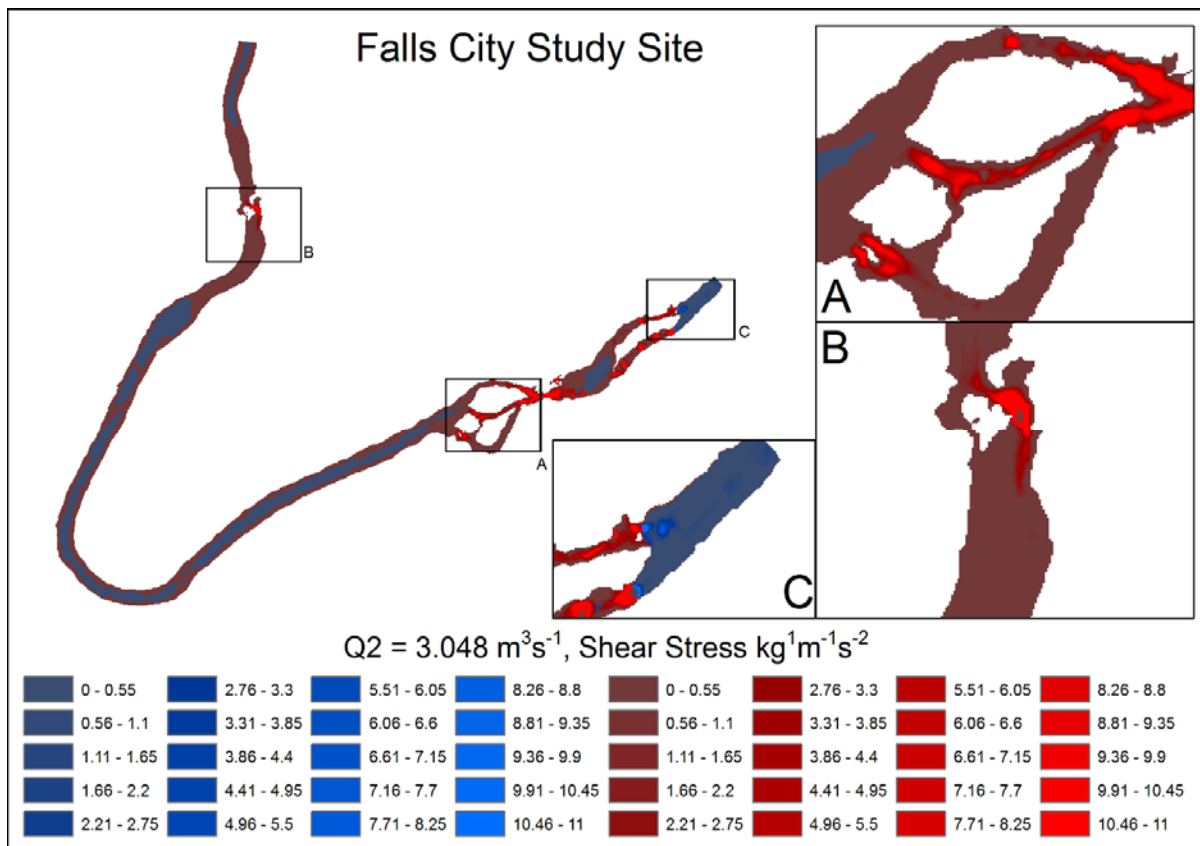
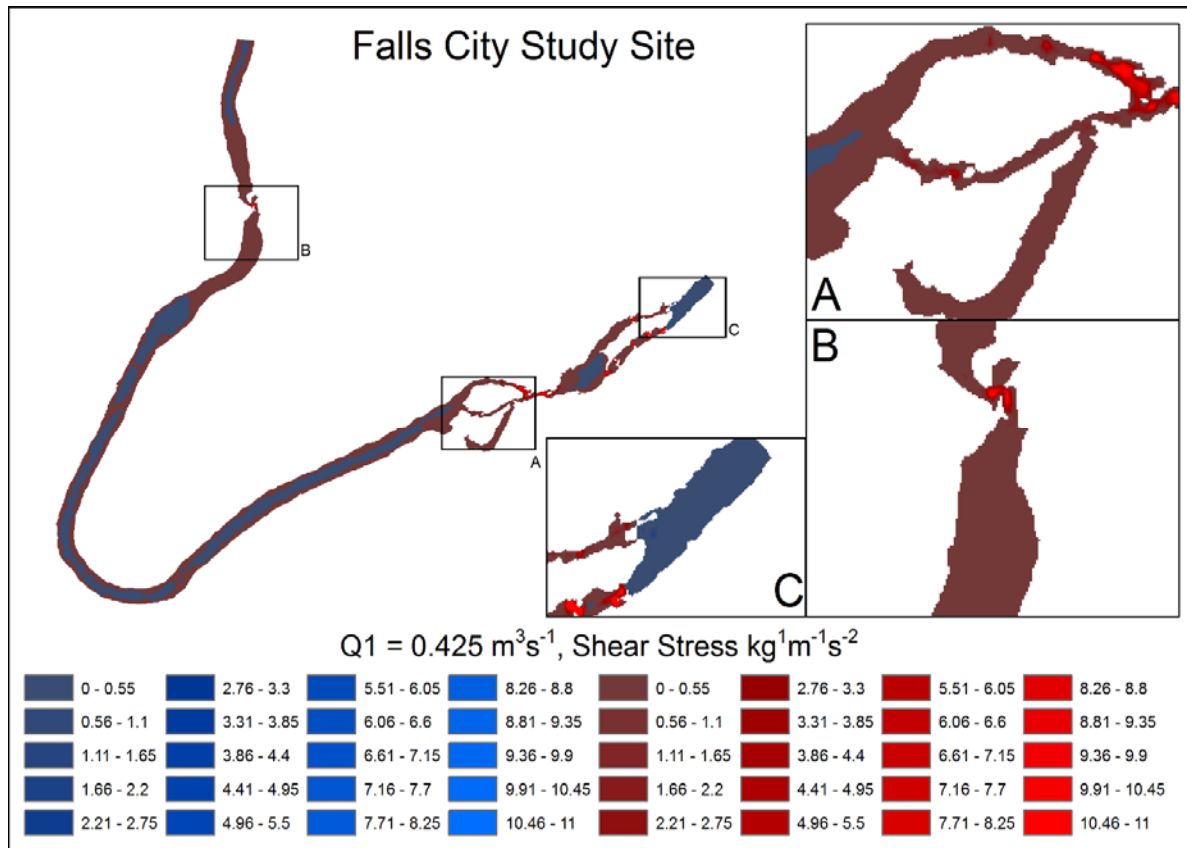


Figure 6.20. Spatial distribution of shear stress ($\text{kg} \times \text{m/s}^2$) for Q1–Q5 for topographic highs (red colors) and lows (blue colors).

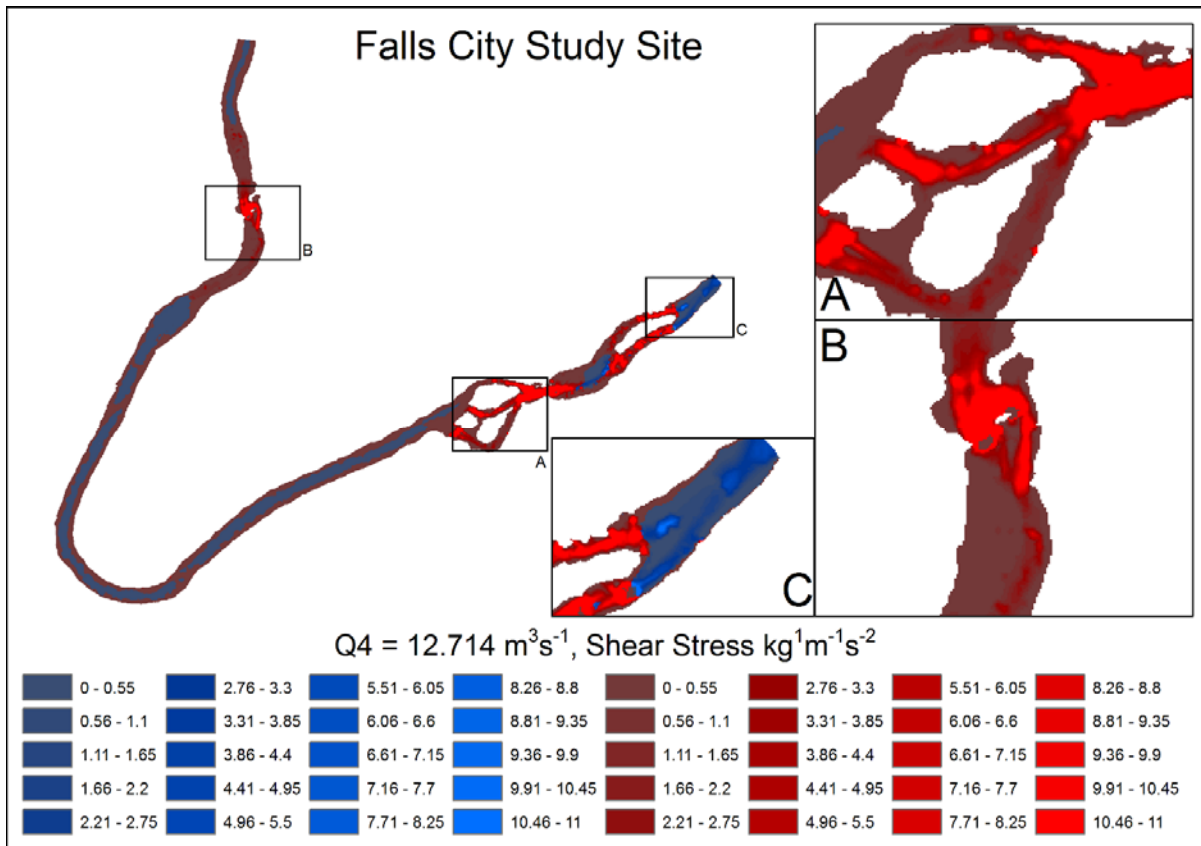
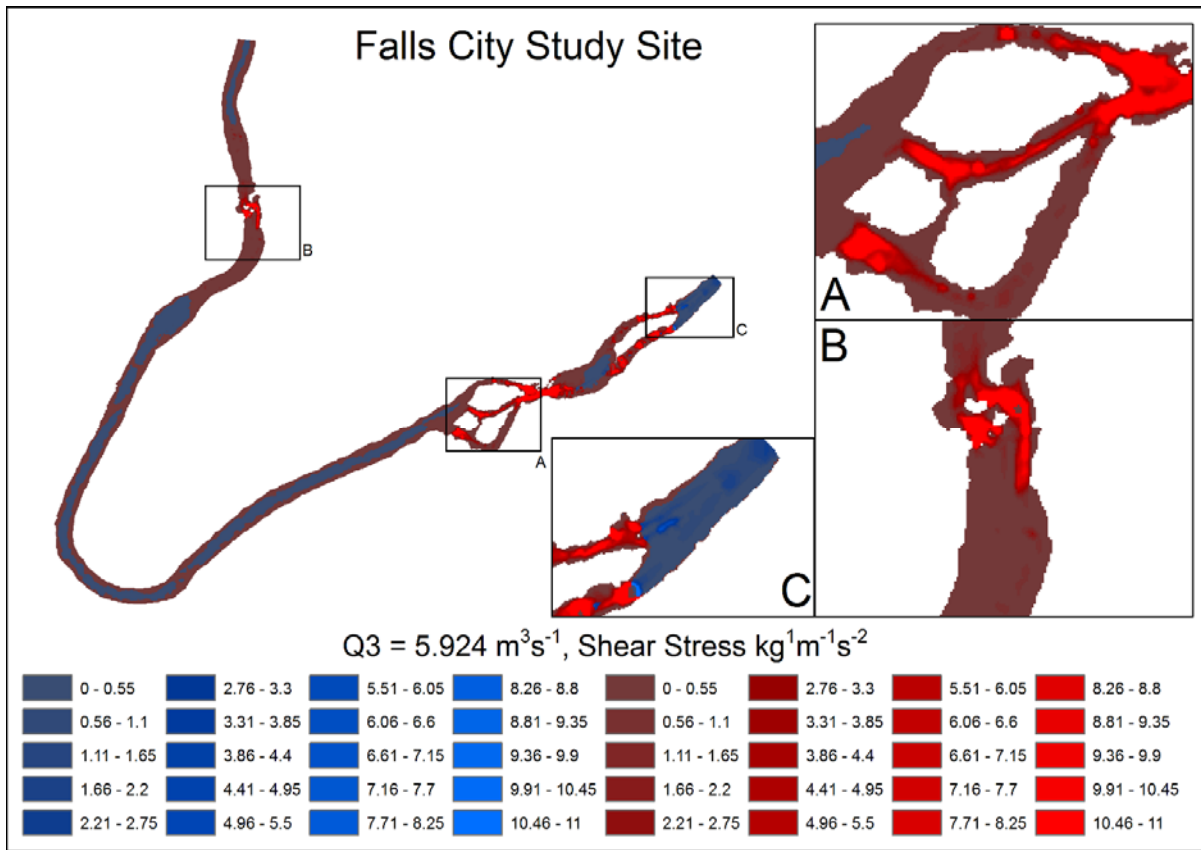


Figure 6.20 (cont'd). Spatial distribution of shear stress ($\text{kg} \times \text{m}/\text{s}^2$) for Q1–Q5 for topographic highs (red colors) and lows (blue colors).

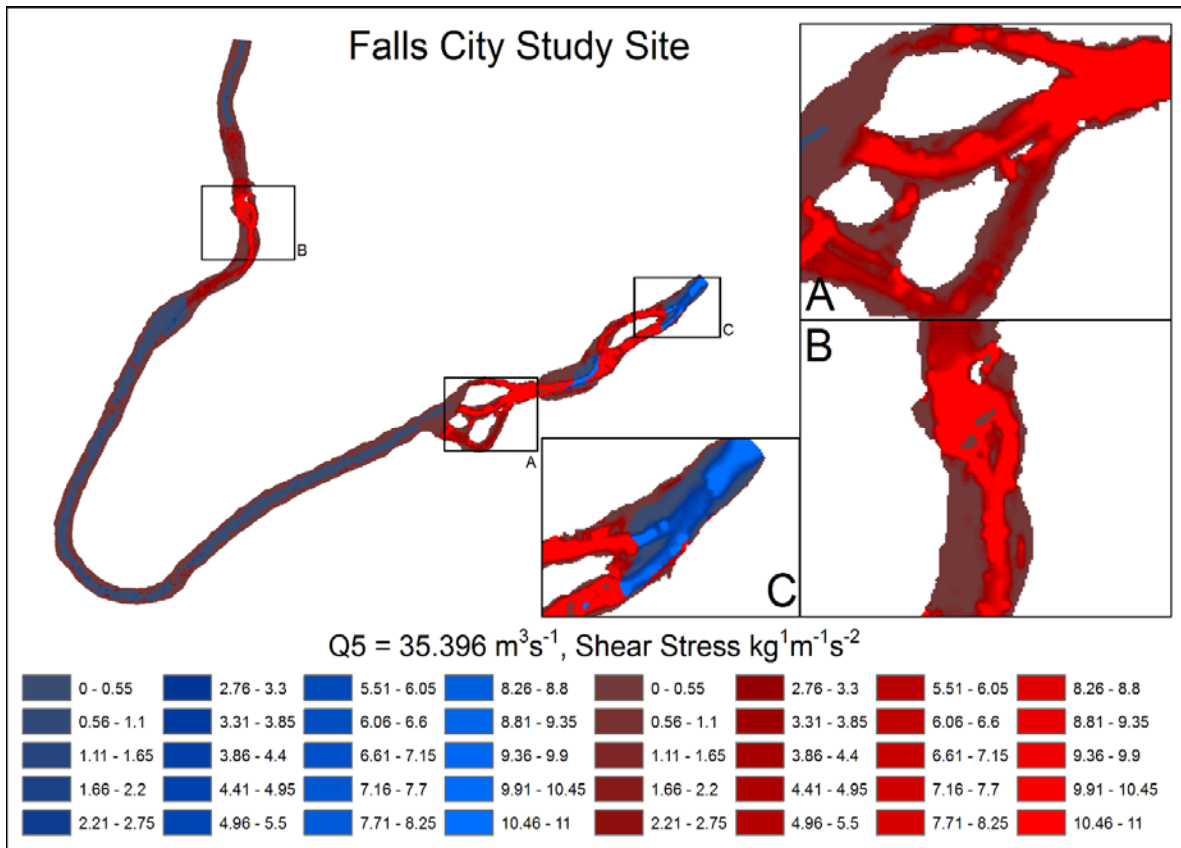


Figure 6.20 (cont'd). Spatial distribution of shear stress ($\text{kg} \times \text{m}/\text{s}^2$) for Q1–Q5 for topographic highs (red colors) and lows (blue colors).

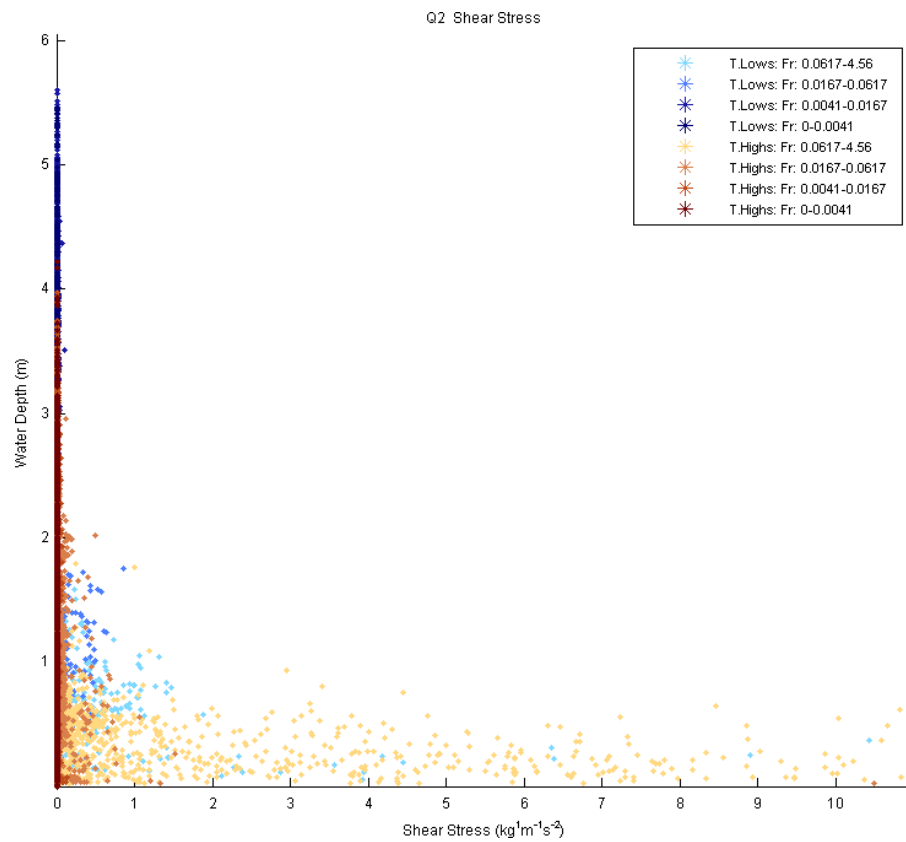
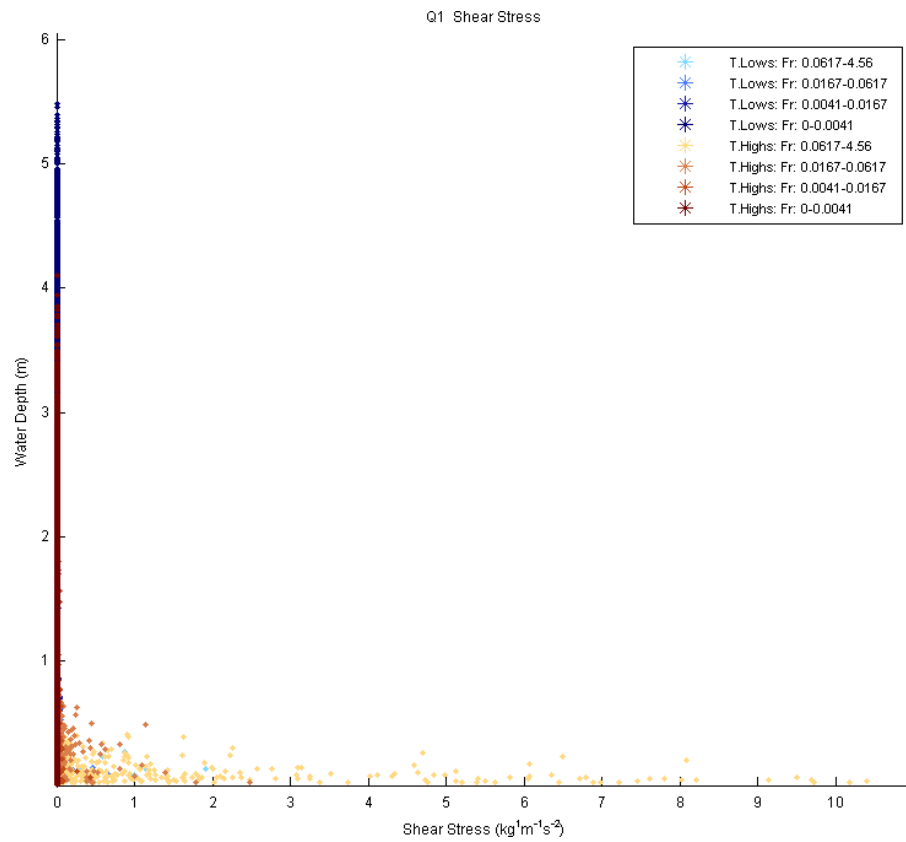


Figure 6.21. Distribution of shear stress in relation to water depth for Q1–Q5 classified by topographic highs marked as T. Highs (brown colors) and topographic lows marked as T. Lows (blue colors) and Froude number (Fr).

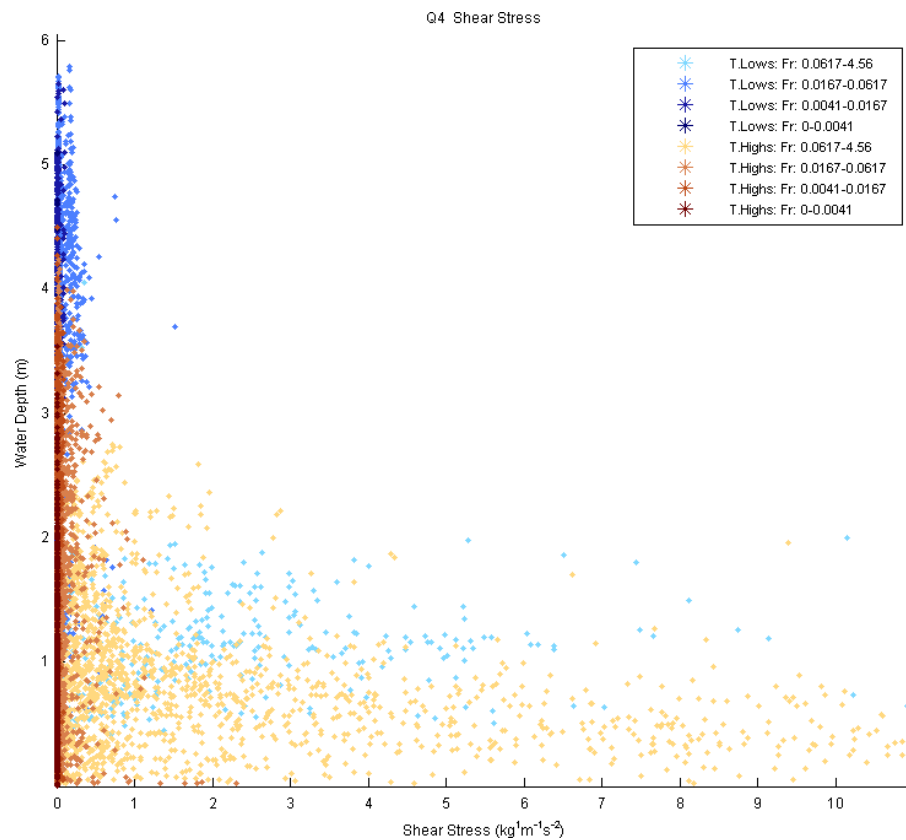
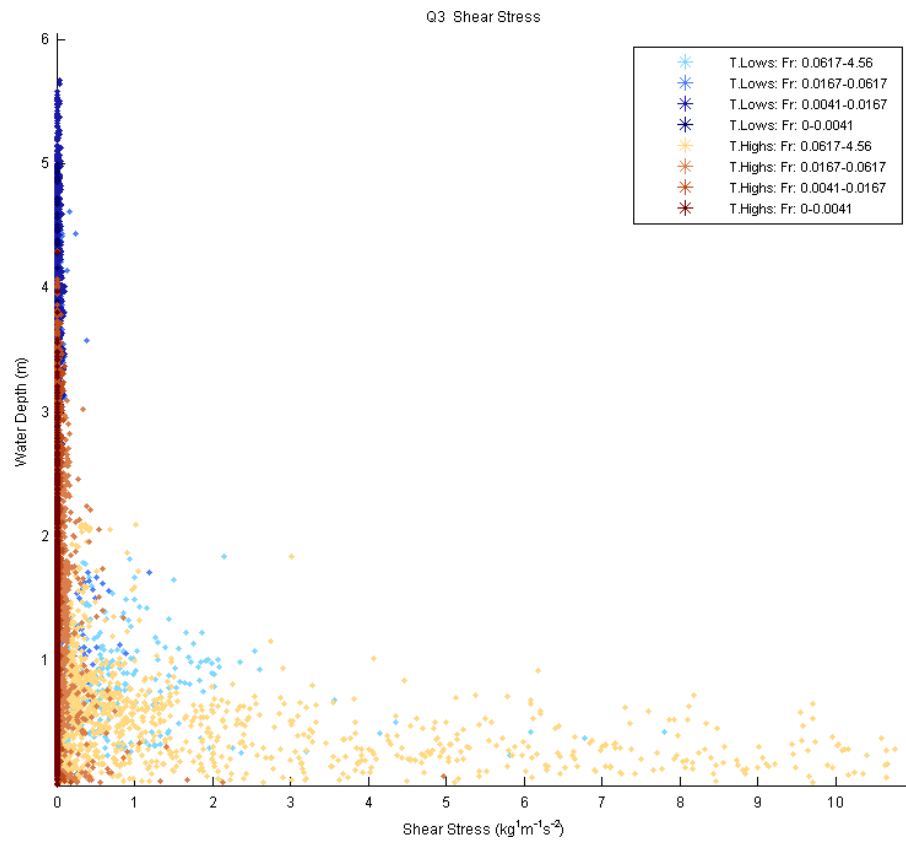


Figure 6.21 (cont'd). Distribution of shear stress in relation to water depth for Q1–Q5 classified by topographic highs marked as T. Highs (brown colors) and topographic lows marked as T. Lows (blue colors) and Froude number (Fr).

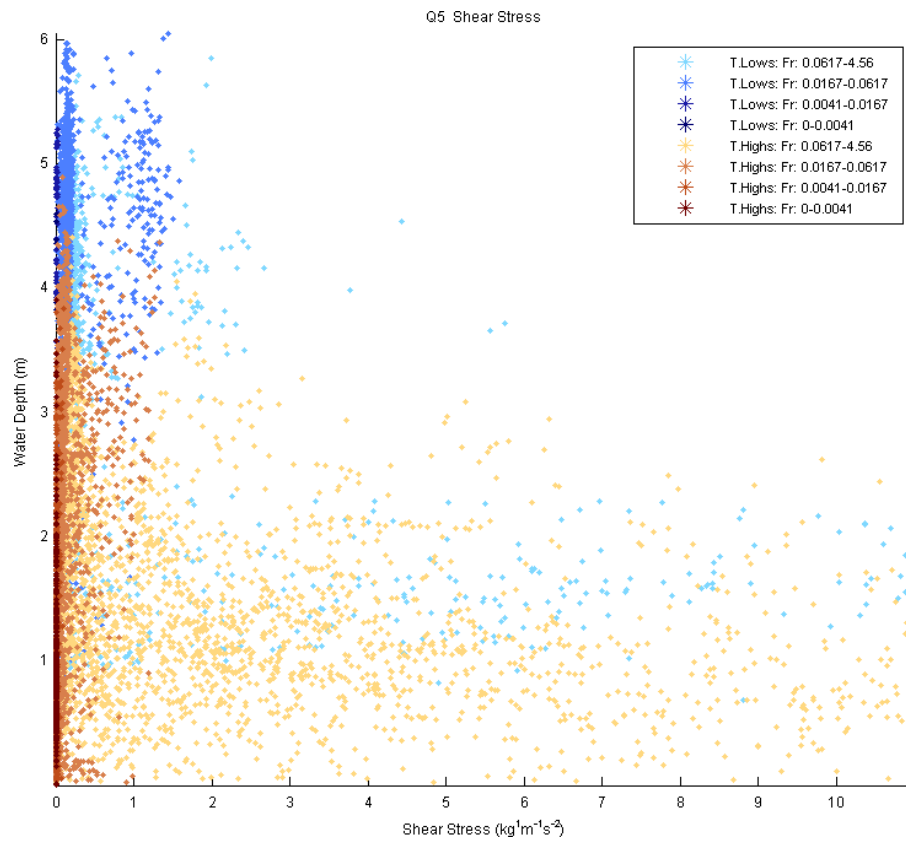


Figure 6.21 (cont'd). Distribution of shear stress in relation to water depth for Q1–Q5 classified by topographic highs marked as T. Highs (brown colors) and topographic lows marked as T. Lows (blue colors) and Froude number (Fr).

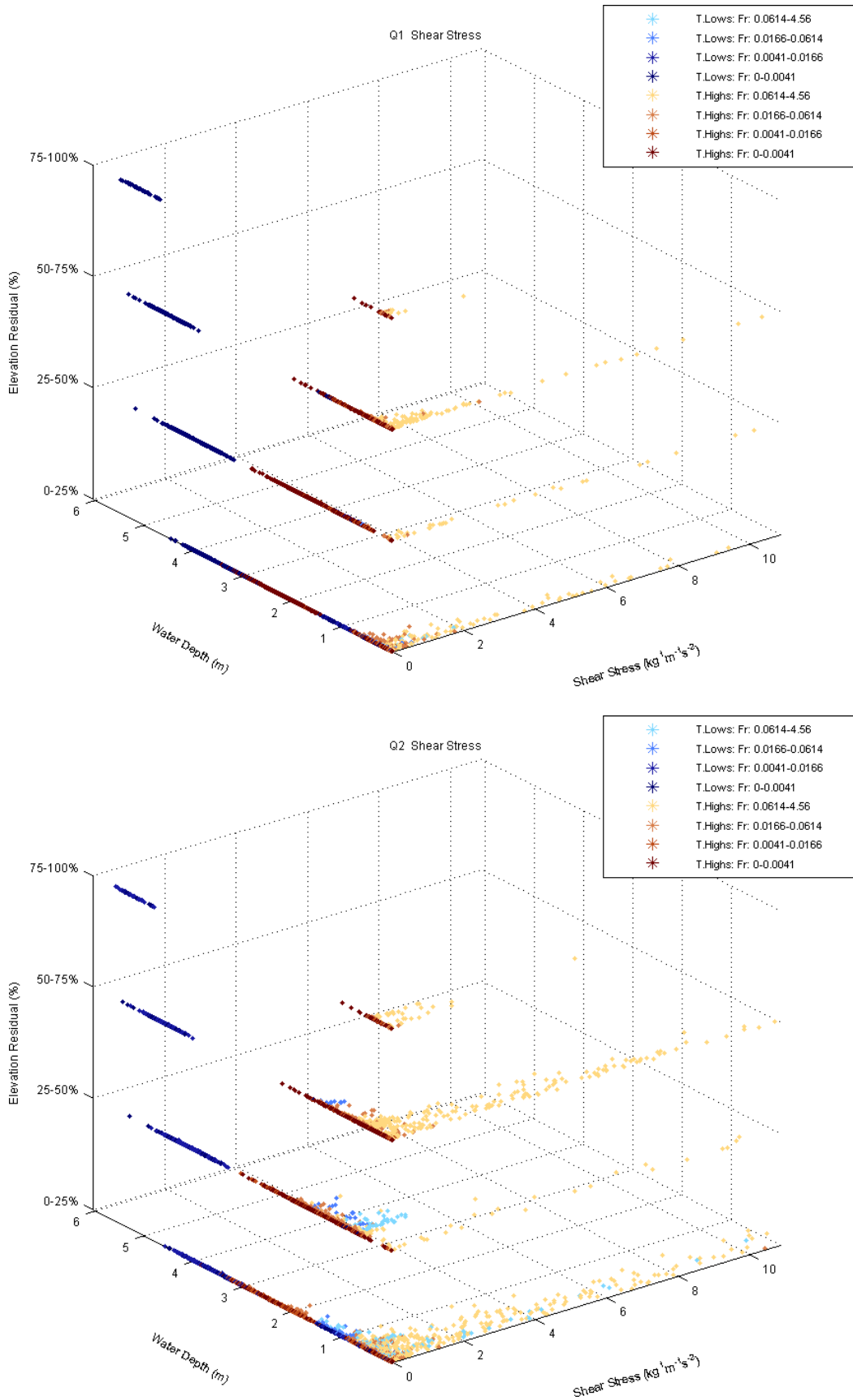


Figure 6.22. Distribution of shear stress for topographic high (T. Highs)/low (T. Lows) subclasses (Figure 4.2) and Q1–Q5, classified by Froude number (Fr).

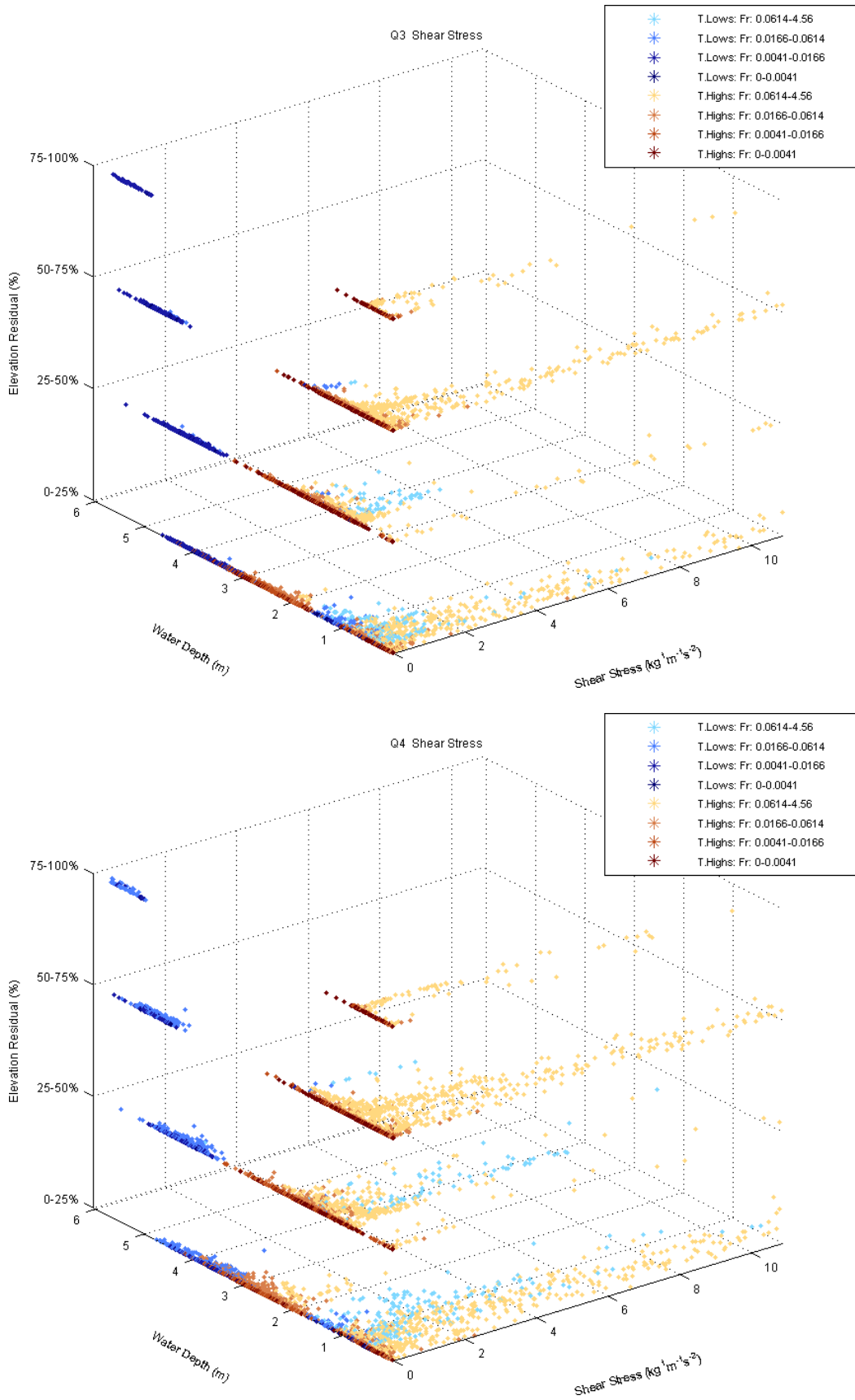


Figure 6.22 (cont'd). Distribution of shear stress for topographic high (T. Highs)/low (T. Lows) subclasses (Figure 4.2) and Q1–Q5, classified by Froude number (Fr).

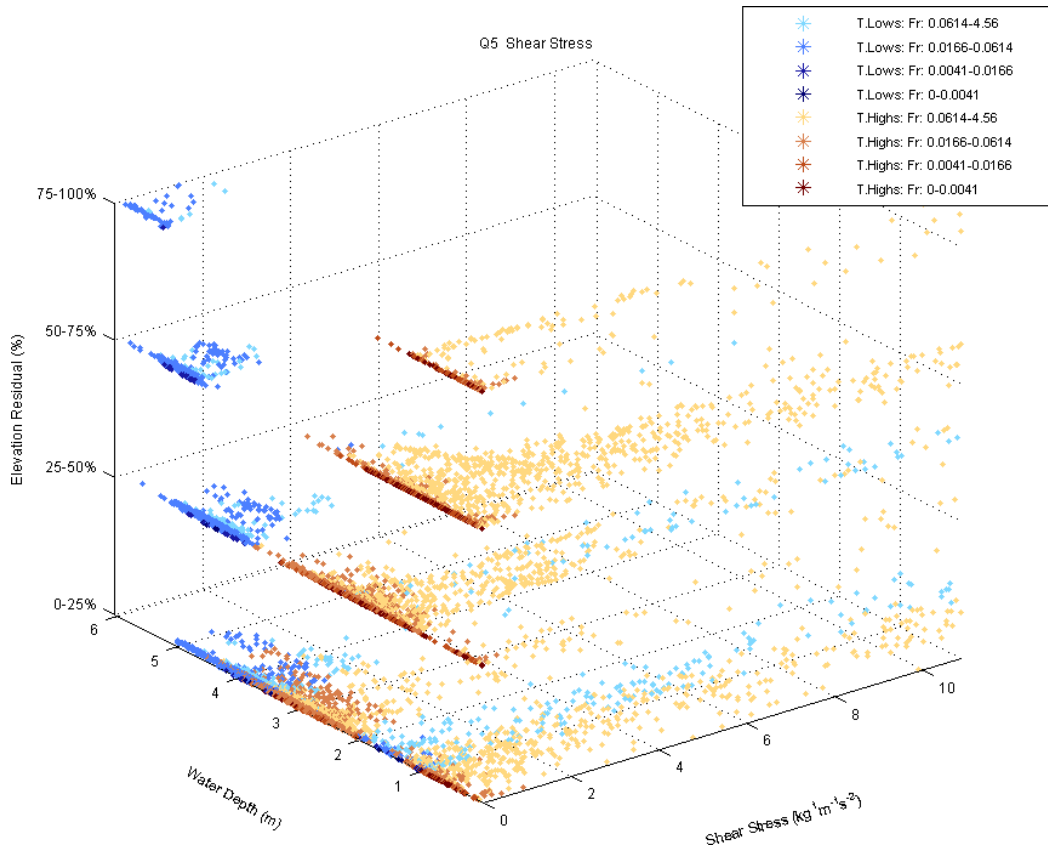


Figure 6.22 (cont'd). Distribution of shear stress for topographic high (T. Highs)/low (T. Lows) subclasses (Figure 4.2) and Q1–Q5, classified by Froude number (Fr).

7. THE CALAVERAS STUDY REACH

The Calaveras reach (Figure 7.1) is one of the study sites on the LSAR (Figure 3.3). This reach is located on LSAR Segment 3 and Reach 8 (Figures 3.1–3.2; TIFP and SARA (2011)).

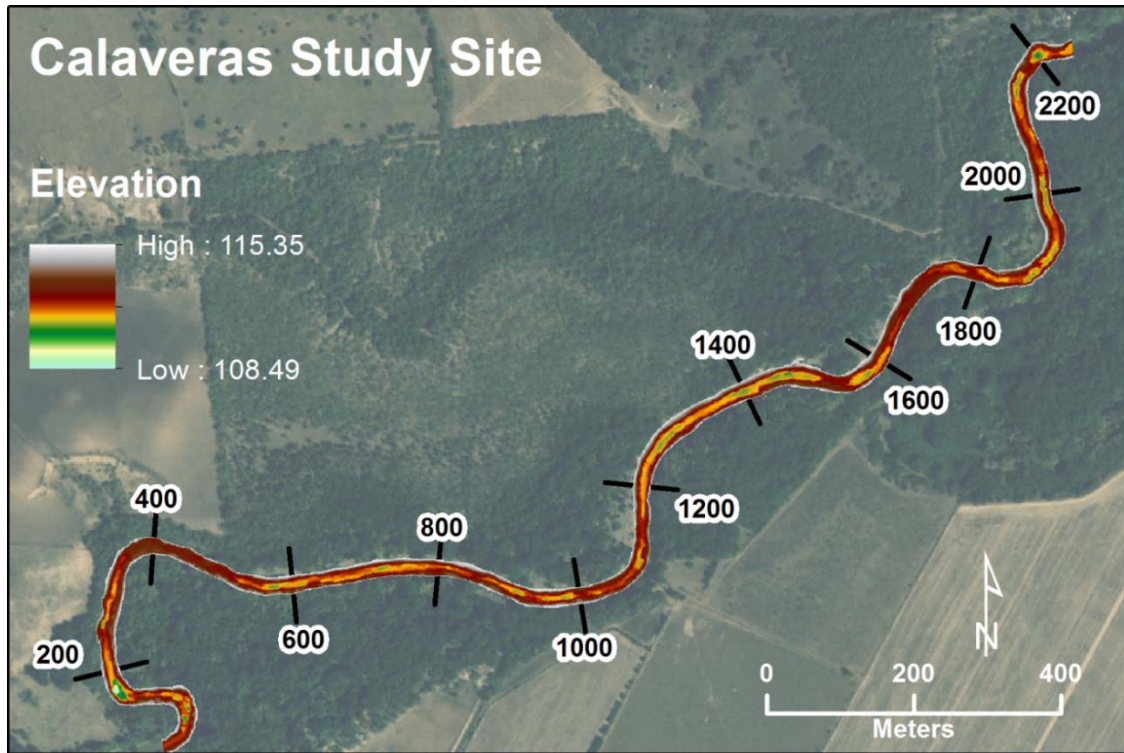


Figure 7.1. The Calaveras study reach and its bathymetric distribution.

7.1. GEOMORPHIC CHARACTERISTICS

To determine the geomorphic characteristics of the river channel at the Calaveras study reach, first we detrended channel topography using the approach discussed in *Section 4.1* (Figure 4.2). Then, we determined the geomorphic unit classes as topographic highs (sediment bars/riffles/edges) and topographic lows (pools) from the topographic residuals. We subclassified the geomorphic unit classes according to the quartiles of the detrended topographic elevations (i.e., classes (+1)–(+4) for topographic highs and (-1)–(-4) for topographic lows, respectively; Figures 4.2 and 7.2).

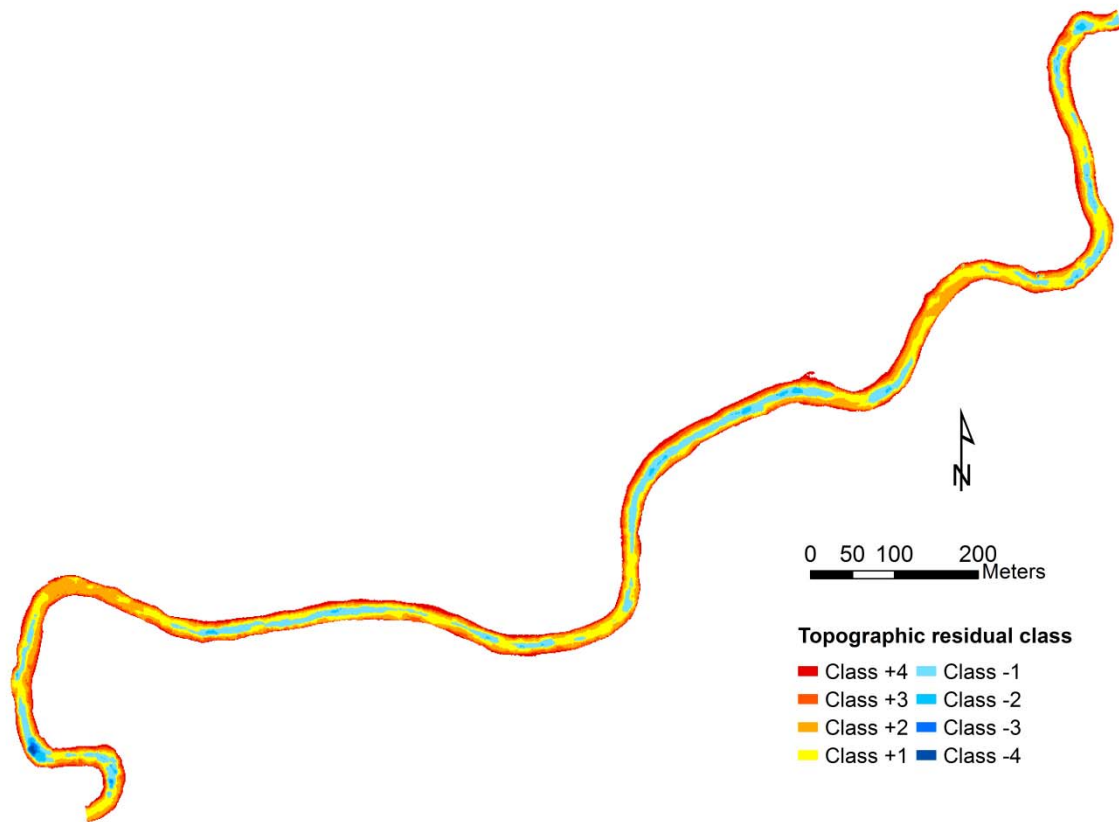


Figure 7.2. Geomorphic unit classes for the Calaveras study reach based on the topographic residuals. The (+) classes represent the topographic highs and (-) classes represent topographic lows. Detailed class descriptions are given in Figure 4.2. Flow direction is from left to right.

The Calaveras study site features a study reach that is approximately 2.25 kilometers long (Figure 7.1). The reach has topographic highs at the margins and is marked by long, thin, and continuous regions of topographic lows. The pools within the geomorphic unit subclass -4 are the largest in size at the influent edge (Figure 7.2).

The distribution of geomorphic unit classes indicate that topographic highs (sediment bars/riffles/edges, corresponding to the classes (+1)–(+4)) dominate the channel morphology and account for roughly 81% of the total channel area. The remaining (19%) of the study area is composed of topographic lows (pools, corresponding to the classes (-1)–(-4); Table 7.1, Figures 7.2 and 7.3).

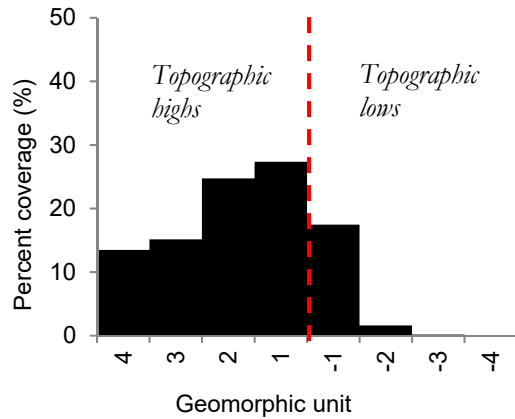


Figure 7.3. Percent coverage of geomorphic unit classes for the Calaveras study reach. The (+) classes represent the topographic highs and (-) classes represent topographic lows. Detailed class descriptions are given in Figure 4.2.

Table 7.1. Areal distribution of geomorphic unit classes in the Calaveras study reach.

Geomorphic Unit Class (Topographic residual percentile)	Total Area (m ²)	Percent Coverage (%)	Patch Statistics					
			Mean area (m ²)	Min area (m ²)	Max area (m ²)	StDev (m ²)	Patches (Number)	
Topo Highs								
+4 (75-100th)	7459	13.47	16.65	1	1147	80.58	448	
(bars/riffles/edges)								
+3 (50-75th)	8376	15.13	23.73	1	1063	78.31	353	
+2 (25-50th)	13686	24.72	91.24	1	3311	331.76	150	
+1 (0-25th)	15142	27.35	199.24	1	5436	817.05	76	
Topo Lows								
(pools)								
-1 (0-25th)	9664	17.46	172.57	1	2715	429.83	56	
-2 (25-50th)	892	1.61	14.16	1	203	29.90	63	
-3 (50-75th)	90	0.16	12.86	1	65	21.53	7	
-4 (75-100th)	55	0.10	55.00	55	55	0.00	1	

Total area: Total area of a specific class (m²).

Percent (%) coverage: Percentage of the area of a specific class within the total area (%).

Geomorphic Unit Class Patch statistics:

Mean area: Average patch area of individual patches within a class (m²).

Minimum area: Minimum patch area within a specific class (m²).

Maximum area: Maximum patch area within a specific class (m²).

STDev: Standard deviation of patch areas around the mean within a specific class (m²).

Patches: Number of separate patches for each class (Number).

Spatially, the distributions of the topographic highs and lows are patchy (Figure 7.2, Table 7.1). Basic patch statistics show that topographic high subclass class +1 has the highest range (1-5436 m²) of patch sizes (in terms of area), with a mean of 199.24 m² and a STDev of 817.05 m². This is followed by the topographic highs subclass +2 (Table 7.1). In addition, the shallowest pool class (i.e., topographic low subclass -1) has the greatest range of patch sizes (1-2715 m²), with a mean of 172.57 m² and STDev of 429.83 m² (Table 7.1). This class (-1) is patchy than other topographic low subclasses.

7.2. RELATIONSHIPS BETWEEN GEOMORPHIC UNITS AND HYDRAULIC PROPERTIES

We examined the relationships between geomorphic units (Figure 4.2), and the hydraulic properties of the reach. We obtained these hydraulic properties from the simulations performed using River2D® model developed for the study reach (TIFP and SARA, 2011) at five different discharge conditions, Q1–Q5. Three of these modeled discharges, low, medium, and high Qs (Q2, Q3, and Q4, respectively) correspond to the base level discharges defined as dry, normal, and wet conditions (Table 7.2).

Table 7.2. Information on the Calaveras study reach and model input parameters for River2D® model.

Class	Discharge for base levels		Modeled discharge		Field reported discharge		Assessment of field Q	Field data Collection date	Type of field data
	(m ³ /s)	(cfs)	(m ³ /s)	(cfs)	(m ³ /s)	(cfs)			
			0.43	15	–	–	Q1 (<Q2)	–	–
Dry	2.83	100	1.87	66	1.81	64	Low (Q2)	6/17/2009	Substr. Pts, Vel Points, Habitat
Normal	6.37	225	7.45	263	7.45	269	Medium (Q3)	11/18/2009	Habitat
Wet	9.91	350	9.79	346	9.77	345	High (Q4)	3/30/2010	FISH_HMU, Habitat
			28.32	1000	–	–	Q5 (>Q4)	–	–

*Base levels are defined by observing fish habitat weighted usable area (WUA) (River2D) (TIFP, 2011; pg. 71, http://www.twdb.state.tx.us/surfacewater/flows/instream/lower_san_antonio/doc/LSAR_FINAL_INTERIM_REPORT_20110831.pdf)

Dry: typically based on minimum to get 20% habitat available for each guild.

Average: typically based on flow to get at least 50% habitat available for each guild.

Wet: typically based on analysis of WUA for habitat degradation.

The relationship between flow level and inundated area is described in Figure 7.4. There is a relatively high change between flow stages for Q2 and Q3 and for Q4 to Q5. Overall, the changes in inundated area slightly decrease as discharge increases (Figure 7.4). Overall, the relationship appears to be logarithmic (inundated area = $-29.01 \times \ln(Q)^2 + 1757.1 \times \ln(Q) + 29003$, with an R² of 0.9979).

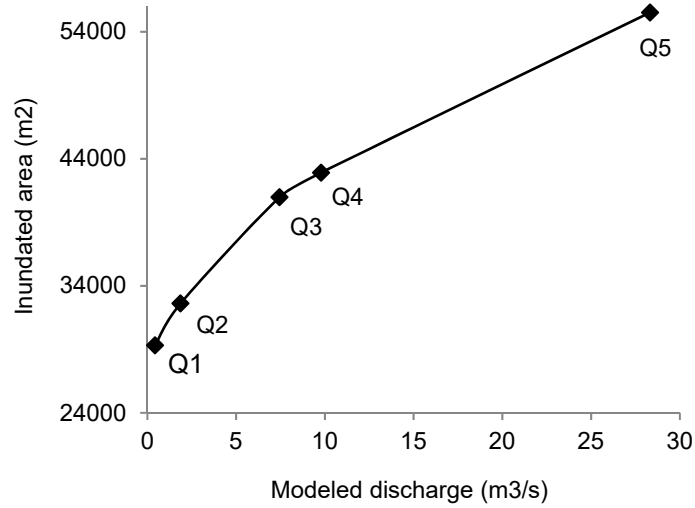


Figure 7.4. Inundated area (m²) vs. modeled discharge (m³/s) for the Calaveras study reach.

Table 7.3 summarizes the minimum and maximum values of these variables obtained from River2D® models for each discharge condition from Q1 to Q5 (Table 7.2).

Table 7.3. Summary of River2D® model output parameters for Calaveras and min-max values for modeled discharges, Q1–Q5 (Table 7.2).

Model output parameters	Modeled discharge $\begin{pmatrix} \text{min} \\ \text{max} \end{pmatrix}$				
	Q1	Q2	Q3	Q4	Q5
Water depth (m)	0.020	0.020	0.020	0.020	0.012
	4.536	4.762	5.184	5.337	6.674
Froude number (-)	0.000	0.000	0.000	0.000	0.000
	1.556	1.612	3.632	3.038	0.659
Velocity magnitude (m/s)	0.000	0.000	0.000	0.000	0.000
	1.521	2.061	2.480	2.302	1.088
Streamwise velocity (m/s)	-0.194	-0.468	-0.860	-1.039	-0.366
	1.511	2.032	2.317	2.289	1.067
Normal velocity (m/s)	-0.527	-0.560	-1.125	-0.741	-0.377
	0.470	0.767	1.451	1.525	0.276
Shear stress (kg / (m × s ²))	0.000	0.000	0.000	0.000	0.000
	75.629	67.669	98.964	98.229	94.349
WSE (m)	112.467	112.498	113.460	113.658	115.115
	113.254	113.489	113.949	114.102	115.391

We examined the distribution of hydraulic variable values obtained from River2D® models in relation to geomorphic properties of the study reach and also the modeled discharges, Q1–Q5 (Table 7.2). For this purpose, we analyzed these distributions as discussed in *Section 4.5*.

7.3. WATER DEPTH AND FROUDE NUMBER DISTRIBUTIONS

The distributions of the water depth start out as a one-sided Gaussian-like distribution for topographic highs (sediment bars/riffles/edges) and a roughly Gaussian distribution associated with topographic lows (pools) (Figure 7.5). Cumulatively, the water depth distribution associated with the lowest discharge Q1 (Table 7.1) has two weak modes. As the discharge increases, the regions associated with sediment bars/riffles/edges tend to become less positively skewed and more round (Figure 7.5). With increasing discharge, the distribution of the depths associated with pools do not change shape that much, but do progress to higher values and adopt a slightly positive skewness. Combined water depth distribution has a weakly bimodal character at all flow stages, but becomes increasingly platykurtic (Figure 7.5). As the discharge increases, the increasingly platykurtic shape of the depth distribution combined for pools and sediment bars/riffles/edges imply no contribution to areas associated with topographic highs, and contribution of topographic lows to the distribution the overall distribution (Figure 7.5).

At very low flow (Q1), the distribution for Froude number is leptokurtic with a negatively exponential shape for topographic highs, lows and combined distributions (Figure 7.6). Discharge condition Q2 shows a significant change in shape for topographic lows—where the shape has changed from exponential decay to a Gaussian-like distribution with positive skewness. Topographic highs are more platykurtic since the mode has about 25% less counts and the positive tail is extended such that the last (largest) bin adjacent to value 0.4 has slightly higher counts. As discharge condition increases, regions associated with topographic highs (riffles/sediment bar/edges) tend to become more platykurtic, and regions associated with the topographic lows (pools) tend to their modes shift to higher values. At discharge condition Q5, the shape of distribution associated with topographic highs has shifted mode from the lowest bin adjacent to value 0 to a value of 0.1. The distribution for topographic lows changes slightly from a symmetric Gaussian-like distribution to a Gaussian distribution with negative skew. At discharge Q5, all locations demonstrate a cumulative shape that is unimodal with the mode position being adjacent to value 0.1. At the mode, there appears to be approximately two-thirds contribution from topographic highs with about one third contribution from topographic lows (Figure 7.6).

There are many low Froude numbers that are associated sediment bars/riffles/edges and there are also higher Froude numbers with contributions from topographic highs and lows. This could be construed as margin effects being the lesser Froude mode and a core of higher velocity at the greater Froude mode. These distributions hint at the fact that there is a relationship between Froude number and topographic residual, but these dynamic changes as flow stage increases (Figure 7.6). For the Calaveras study reach, distributions of Froude number suggest that the core of higher flow occupies more of the channel at Q5 than other, lesser, discharge conditions.

7.4. VELOCITY MAGNITUDE

7.4.1. *Velocity Magnitude Distribution*

At the lowest modeled discharge (Q1, Table 7.1), all locations in the Calaveras study reach have velocity magnitude distribution that is very leptokurtic with an exponentially decaying shape (Figure 7.7). This represents very limited flow variability with very low flow velocities—of which the bin is centered on $0.05 \text{ m}^1\text{s}^{-1}$ —being common, and higher ones, above $0.5 \text{ m}^1\text{s}^{-1}$ uncommon (Figure 7.7). At the discharge Q2, the distribution of the velocity magnitudes for the regions associated with topographic highs and lows have different shapes. The topographic highs preserve their exponentially decaying shape with the mode centered at a value of zero m/s (Figure 7.7). On the other hand, topographic lows have a Gaussian-like shape with positive skew. A change in the shape of the distribution is evident between the discharge levels Q2 to Q3, suggesting the influence of the break point in inundated area-discharge relationship (Figure 7.4).

At the discharge Q3, where the inundated area-discharge relationship starts flattening out, the shape of the velocity magnitude distributions for topographic highs is platykurtic with a difference of 10% between the mode and the rest of the distribution (Figure 7.7). This represents great variability in flow velocity conditions with the only clear majority grouping being the mode associated with a velocity magnitude of zero m/s . The distribution of topographic lows is symmetric Gaussian with a mode that moves in a positive direction from $0.05 \text{ m}^1\text{s}^{-1}$ to $0.15 \text{ m}^1\text{s}^{-1}$ m/s , as the discharge increases. The combined distribution for the topographic highs and lows at the Q3 has two modes, associated with value zero and 0.3 m/s , respectively (Figure 7.7).

As the discharge increases to Q5, which is the highest modeled discharge (Table 7.1), the regions associated with topographic highs have a platykurtic distribution with two modes: one

with $0.05 \text{ m}^1\text{s}^{-1}$ while the other one is ambiguous, but within the range of 0.045 to $0.055\text{m}^1\text{s}^{-1}$ (Figure 7.7). This is most likely associated with the added values in extreme topographic high classes as flow stage increases or locations that have low velocity evolving to regions that have high velocity. These locations associated with pools have a normal-like distribution that develops a slight negative skew. This represents no new areas being added or major changes in distribution (Figure 7.7).

7.4.2. *Velocity Magnitude Spatial Distribution*

At the lowest discharge (Q1, which is less than the ‘dry’ base level, Table 7.1) the Calaveras study reach has a velocity magnitude distribution that has elevated values at flow-constricted areas, such as location C in (Figure 7.8). There are enhanced flow velocities at some locations of high curvature and high topographic residual between meter marker 200 to 600 meters and 1600 to 1800 meters (Figure 7.1). At the discharge Q2, which corresponds to dry base level, the regions associated with topographic lows begin to have elevated values of velocity magnitudes as at location C (Figure 7.8). Noticeable higher velocities are evident in locations associated with topographic highs at discharge level Q3, at locations A and B. Anomalous locations of high velocity are present at location A during the discharge levels of Q3 and Q4 (Figure 7.8).

7.4.3. *Velocity Magnitude Relationships*

2D plots describe the dynamics of depth versus velocity magnitude. (Figure 7.9) When compared to depth (ordinate), velocity magnitude (abscissa) has an exponentially decaying distribution at lowest discharge level (Q1 < “dry” baseline level). There is also overlap in velocity magnitude values between the locations associated with topographic lows and highs, centered on depths of 1.0 m and have a range of 0 to $0.2 \text{ m}^1\text{s}^{-1}$ (Figure 7.9). As an exponentially decaying shape, the areas with lowest depth have the most range, and are associated exclusively with topographic highs at low flow stage (Q1). As discharge increases, the velocity magnitudes increases in range at shallow areas, and these locations are less exclusive to those associated with topographic highs (Figure 7.9). As flow stage increases, the limbs of this exponentially decaying distribution move away from the depth and velocity magnitude axes, and begin to evolve to a shape of exponential growth. As of flow stage Q3, the largest range of velocity magnitudes, which is across the entire plot from 0 to $1.5 \text{ m}^1\text{s}^{-1}$, for topographic highs move from depths at 0.25m to just below 1.0m. The number of locations along the reach with extreme velocity

magnitudes decrease at discharge level Q4, as the shape becomes exponentially increasing (Figure 7.9). This suggests the influence of the inundation area-discharge relationship, which significantly flattens out discharges following Q3 (Figure 7.9).

A detailed information on the velocity–water depth–geomorphic unit relationship by a finer partitioning of the geomorphic classes are given in Figure 7.10. There is a large amount of overlap that is present at topographic residuals near the channel bed, for the topographic high and low subclasses +/- 1-2 for flow stages at Q1-Q2. At the lowest discharge, Q1, few large velocity magnitude values that are greater than $1 \text{ m}^1\text{s}^{-1}$ are observed at the subclasses of +1 and +2. At higher discharge levels (Q4-Q5), large flow velocity magnitudes above $1 \text{ m}^1\text{s}^{-1}$ are clustered at the topographic high subclasses + 1-3. High values above $0.5 \text{ m}^1\text{s}^{-1}$ velocity magnitude for topographic lows are present throughout all geomorphic units, but topographic highs feature higher values (Figure 7.10). There is also a distinct change in shape or clustering at the highest stage or the discharge Q5. Although maxima for topographic highs are greater, the clustering appears to be localized around 0 and $0.75 \text{ m}^1\text{s}^{-1}$.

7.4.4. *Summary on Velocity Magnitude Distribution*

In summary, increasing discharge level tends to bring about increased range in velocity magnitude values, and this exerts a platykurtic character that is apparent in component velocity (streamwise, normal) and shear stress at high discharge levels. As the discharge increases, the velocity magnitude distribution tends to originate and behave differently depending on whether the location is characterized by a topographic high (sediment bar/riffle/edge) or topographic low (pool) geomorphic unit (Figure 7.7). This implies that the local channel topography plays a role in overall character of a specific reach with respect to velocity magnitude.

As discharge increases, the distributions for the two major geomorphic unit classes, topographic highs and lows, tend to have Gaussian-like distributions that are negatively skewed for topographic highs and positively skewed for topographic lows (Figure 7.7). These skewed distributions tend to evolve into a single Gaussian-like distribution with reduced skewness.

The combined distribution of the velocity magnitude for topographic highs and lows is quite platykurtic with a negative elongated tail (Figure 7.7). This distribution is manifested in the spatial arrangement as a core of higher velocity, where highest values are near the center of this core, and lower values are increasingly at the margins (Figure 7.8). The elongated negative tail represents the regions that are most likely not within this core of higher velocity. This core of

higher velocity represents a region of greater depth where the local channel topography has a decreased influence and overall channel planform is the major factor at play (Figure 7.8). The spatial patterns of this core of higher velocity also affect other parameters including stream velocity and shear stress.

7.5. STREAMWISE VELOCITY DISTRIBUTION

7.5.1. *Streamwise Velocity Distribution*

Overall, streamwise velocity distribution has similar shape to velocity magnitude, as similar to the other study reaches, although less platykurtic (Figure 7.11). This is mostly due to the presence of a thin tail at the negative end, given that the positive side has a reduced range in favor of the negative side—as velocity magnitude has no negative values. This thin, negative tail on the negative side represents backwaters (Figure 7.11).

For topographic highs, the velocities of backwaters increase in range, as evidenced by darker colors appearing in the grey patches (Figure 7.11) as flow stage or discharge increases. This increase in range occurs until Q4, the discharge condition where maximum backwater flow range is observed. Again, this trend reflects the relationship between inundated area and discharge, the increasing trend of which starts flattening out at Q3 (Figure 7.4).

At the low discharge levels (i.e., Q1, Q2), the distribution of streamwise velocity component is unimodal with a very thin tail on the negative side (Figure 7.11). With the exception of the lowest discharges Q1 and Q2, and the highest one, Q5 (> Q4), the combined distribution of stream velocity values takes on two modes, with one mode centered on zero m^1s^{-1} , and the other at $0.58 \text{ m}^1\text{s}^{-1}$. At Q5, the mode centered at zero m/s is very weak and the distribution has negative skewness. At the lower flow stages associated with Q1-Q3, the skewness is positive in for topographic highs and cumulative distribution (Figure 7.11).

7.5.2. *Streamwise Velocity Spatial Distribution*

The regions that correspond to backwaters represent eddy flow and are often at complex channel margins where the water depth is minimal (Figure 7.12). As discharge increases, these channel margins become less complex—compare margins at Q1 to Q5 in Figure 7.12. Many of these backwater regions demonstrate a spatiotemporally dynamic behavior as a result of changing flow characteristics as represented at the region B at all flow stages (Figure 7.12). Given that backwaters appear more often at locations of minimal depth, they should be expected at locations such as those that seem to bound point bars (e.g., the region A) (Figure 7.12).

At the regions of high curvature with high discharge and flow level (e.g., the region A), the backwaters begin to outline a core of higher velocity, as in the case of discharges Q4 and Q5. This is evident for Q5 at the region A, where backwaters are present on both sides of the channel. This is also evident at the region C for all flow levels as the area of backwater shrinks with higher flow stage (Figure 7.12).

7.5.3. *Streamwise Velocity Relationships*

The distribution of streamwise velocity in relation to water depth exhibits trends very similar to that of velocity magnitude when positive streamwise velocity values are considered (Figure 7.13). Overall, the greatest change in shape occurs for the negative values for the discharge levels ranging from Q1 to Q3, where locations initially have very small range in streamwise velocity except for the smallest water depth regions. At the smallest water depths, negative streamwise velocity values demonstrate greatest ranges, at $-0.8 \text{ m}^1\text{s}^{-1}$ to $0 \text{ m}^1\text{s}^{-1}$ at the discharge level Q3 (Figure 7.13). Preferential depth does not change except for the highest discharge level, Q5. At Q5, the ranges decrease for negative velocities, just as in positive velocities for Q5 (Figure 7.13). This shows that backwater velocities are most strongly associated with the water depth as stream velocity is also related to channel shape and location along the channel.

For positive values, the distribution of streamwise velocity for topographic high subclasses (+1)–(+4), and topographic low subclasses (-1)–(-4) have very similar shape to their corresponding distributions for the velocity magnitude (Figure 7.14). Streamwise velocity response seems to have a different dynamic for the negative values. On the negative end of the streamwise velocity axis, the velocities do not get as large with respect to the streamwise velocity axis as positive velocities do (Figure 7.14). Just as is the case for the positive velocities, the backwaters have greatest range at very shallow water depths for topographic highs, but at the flow stages associated with the discharges Q3 and Q4, the values seem to not be as related to the water depth as they are for Q1 and Q2. At Q5, the backwaters seem to decrease in number, but do not appear to decrease in magnitude. At Q5, the +4 residual appears to increase in range—which is in keeping with the evolution in shape associated with Q5 on velocity magnitude. For all other flows, the residual class +4 has a very restricted range of stream velocities.

7.5.4. *Summary on Streamwise Velocity Distribution*

The similarity of distributions of the velocity magnitude (Figure 7.7) and the streamwise velocity (Figure 7.11) indicates that the velocity magnitude is dominated by the streamwise velocity. The major difference between the velocity magnitude and the streamwise velocity is the presence of backwaters. Although backwaters are often thinly distributed at complex channel margins at the low discharges, their positions tend to change as flow stage increases as in the region B of Figure 7.12. In some locations, where there are divergent channel margin features, such as the region C in Figure 7.12, the region of backwaters actually shrink while the regions of high curvature (that outline the low depth/high topographic features such as sediment bars/riffles/edges) tend to get larger except at the discharge Q5 (e.g., the region A, Figure 7.12). This is explained by the positioning of the high velocity core as discussed in the case of velocity magnitude.

7.6. **NORMAL VELOCITY DISTRIBUTION**

7.6.1. *Normal Velocity Distribution*

At the lowest discharge, Q1, the distributions of normal velocity component is leptokurtic and symmetric for both topographic highs and lows (Figure 7.15). The most noticeable change in the distribution happens between the discharge level Q2 and Q3. Between these two levels, the large modes centered at zero m/s become much less dominant and form a smooth bell-like distribution at Q3. As such, the distributions become more platykurtic (Figure 7.15). This change would represent a more evenly distributed values rather than a clear dominance of low positive and negative velocity values. Thus, there is greater heterogeneity of flow as flow stage increases.

7.6.2. *Normal Velocity Spatial Distribution*

Regions of alternating positive and negative values of the normal velocity remain at roughly the same locations throughout all flow stages examined (Figure 7.16). At low discharge conditions, the positions of negative and positive normal velocity tend to have less separation between them as the discharge increases. This might be attributable to the more complex wetted boundaries at low flows (Figure 7.16).

One notable change between different discharge levels is that the regions of positive and negative normal flow tend to develop higher velocity ‘cores’ as flow stage increases (Figure 7.16). The reason for these high normal velocities occur in the cores is that the outer region of these

areas are probably transitional from negative to positive normal velocities. At the region C (Figure 7.16), it is obvious that there is deflection—since the areas of positive and negative velocities at this region is cleanly divided and stays in the same position for all flow stages.

7.6.3. *Normal Velocity Relationships*

The distribution of normal velocity with respect to the water depth is symmetric around a value of zero m/s (Figure 7.17). At low discharges, the distribution has the greatest range at the low water depths with high Froude numbers. There is a large amount of overlap between topographic lows and highs at the low flow (Figure 7.17). As discharge increases, high range exists at the smallest depth for both topographic highs and lows. Initially, this depth of greatest normal velocity range is close to 0 meters and extends down to 0.5 meters. This relationship involves deeper and deeper depths as water stage increases, until Q5 (Figure 7.17) with a depth range that is ubiquitous throughout the study reach, which is 0 to nearly 7 meters. At the water stage associated with the Q5, there is a decreased range of -0.15 to 0.1 m^1s^{-1} at the smallest depths, and the greatest ranges that span the plot at -0.15 to 0.15 m^1s^{-1} are between 2 and 4 meters.

In addition, the overlap of the distributions for the topographic lows and highs tend to decrease with increased water stage (Figure 7.17). One possible explanation for these patterns is that locations in the core of the channel have a systematic increase in depth as water stage increases, but additional values at the low depth values. This would imply that as water stage increases, locations at margins (the new added locations) tend to have lower ranges. This behavior appears to be related to the loss of shape complexity at local areas as water stage increases, as shown at the region C, Figure 7.16.

Water stage has greatest change between the discharges Q2 and Q3 (Figure 7.4). At low water stages associated with Q1-Q2, the distribution of velocity vs water depth by a finer partitioning of the geomorphic classes suggest that +1-2 positive residual classes have the greatest range for all water stages, the span beyond the chart minima and maxima at approximately -0.25 to 0.15 m^1s^{-1} (Figure 7.18). Negative residual classes have large ranges comparable and greater than positive residual classes for greater water stages, Q3-Q5 at the least extreme topographic level, $-/+1$. These tendencies could be explained by two round pools in the study reach around just upstream of meter marker 200 and at meter marker 2200 (Figures 7.1, 7.2, and 7.16) For discharge levels higher than Q3, all residual classes kept a roughly similar

shape with the most extreme example being for Q5 (Figure 7.18). In the case of Q5, the range of topographic residuals has decreased in range for classes -4 and -3.

7.6.4. *Summary on Normal Velocity Distribution*

With the normal velocity, there is greater heterogeneity in the distributions as the discharge increases (Figure 7.15) as evidenced by the cores of higher velocity at each region of positive or negative velocities (Figure 7.16). As the discharge increases, the regions become more consolidated and stay roughly at the same position, which seems to be controlled by flow margins and inundated topography. The locations of these regions do not change that much and this may be related to characteristics of the channel planform instead of strictly local channel features. The relationship to Froude number is weakened for normal velocity, and this is most likely a measure of the reduced degree of coupling that normal velocity has to velocity magnitude (Figure 7.17).

As with other flow parameters such as velocity and component velocity, normal velocity has the greatest range at the lower residuals—such as the topographic high subclasses +1 and +2. For topographic lows, the regions with the deepest pools (class -4) are the greatest in range (Figure 7.17). All of these suggest that the normal velocity for Calaveras study reach is sensitive to the heterogeneity in the local channel topography. In terms of locations of the regions with positive/negative normal velocities, the channel planform seems to have a larger influence. Increasing flow stage/discharge level tends to bode greater flow heterogeneity as the subclass +1 tend to bode the greatest range at locations of topographic highs (Figures 7.17–7.18).

7.7. **SHEAR STRESS DISTRIBUTION**

7.7.1. *Shear Stress Distribution*

The shear stress distribution is quite leptokurtic with one bin between 0 and 0.2 $\text{kg}^1\text{m}^{-1}\text{s}^{-2}$ representing nearly all values for topographic lows (pools), and a similar situation with a tiny positive tail for topographic highs (sediment bars/riffles/edges) (Figure 7.19). The greatest change in the distribution is observed between the discharges Q2 and Q3. At the discharge level Q3, the distribution evolves from one primary bin between 0 and 0.2 $\text{kg}^1\text{m}^{-1}\text{s}^{-2}$ to a continuum that represents an exponentially decaying pattern for the topographic highs and a partially obstructed Gaussian-like distribution for the topographic lows (Figure 7.19). As the discharge increases and, thus, does the flow stage, the distribution of the shear stress values for topographic highs change very little, and those for topographic lows migrate slightly in the

positive direction (Figure 7.19). At the highest modeled discharge, Q5, the distribution for topographic highs develop a secondary mode.

At the Q5, the ombined distribution represents a bimodal distribution with one of the modes being at value zero, and the second mode being slightly less than $1 \text{ kg}^1\text{m}^{-1}\text{s}^{-2}$ (Figure 7.19). In the distributions of many other parameters, this represents a transition from local effects to channel-wide effects. However, it is not readily apparent in the case of shear stress.

7.7.2. *Shear Stress Spatial Distribution*

At all discharge levels, the regions of high shear stress seem to be coincident with roughness elements (Figure 7.20). However, at low discharges, other factors must be present—such as constrained channel width—as in the region C at the discharges Q1-Q2. As flow stage increases with increasing discharge, other roughness elements get involved as high shear stress locations. These locations are shown to coalesce at regions at 200-600 meters and 1600-1800 meters (Figure 7.1). Other notable patches of roughness elements also exist, such as those in the regions A and C (Figure 7.20).

7.7.3. *Shear Stress Relationships*

At low discharge conditions Q1 and Q2, the distribution of shear stress in relation to water depth has an exponentially decreasing shape (Figure 7.21). However, this pattern changes at the onset of the discharge Q3 (Figure 7.21). At the new distribution pattern, the maximum range of values that span between 0 and $6.5 \text{ kg}^1\text{m}^{-1}\text{s}^{-2}$ are still in associated with the topographic highs. However, the range of depth for topographic highs increases with increased flow stage, and this range in shear stress ($\text{kg}^1\text{m}^{-1}\text{s}^{-2}$) does not appear to decrease that much with depth (Figure 7.21). In fact, a preferential zone appears to exist with a maximum range that is from 0 to $0.5 \text{ kg}^1\text{m}^{-1}\text{s}^{-2}$ at Q1. This extent increases as flow stage increases, such as from 0 to $3.5 \text{ kg}^1\text{m}^{-1}\text{s}^{-2}$ at the discharge level Q5. At the Q5, this grouping appears to be around 2 meters in depth (Figure 7.21).

The distribution of shear stress in relation to water depth indicates that the relationship to Froude number is not as strong in shear stress as it is for streamwise velocity and velocity magnitude; however, there seems to be some kind of grouping based on the Froude number (Figure 7.21). This grouping suggests that the shear stress is related to the velocity—as depth appears to have different classes present at any given depth. Such distribution seems reasonable

as higher flow stages and higher core velocities allow for a greater spread of high shear stresses around roughness elements (Figure 7.20).

The distributions of velocity magnitude *versus* depth *versus* geomorphic subclasses also support this relationship, but with residual class grouping (based on quartiles) also considered (Figure 7.22). This consideration suggests that there is preference in topographic high (sediment bar/riffle/edge) and low (pool) classes of 0-50th percentiles (+/- 1-2) at low flows, Q1 and Q2, for high shear stress ranges. The more extreme +/- classes at 75-100th percentiles (+/-4) have lower values of shear stress associated with them for all but the most extreme flow stage, Q5 (Figure 7.22). At the discharge level Q5, the positive topographic residuals classes cover the minima and maxima of the plots at 0-6 kg¹m⁻¹s⁻². The regions associated with pools do tend to have higher ranges as flow stage increase, but these ranges are less than the range of sediment bars/riffles/edges. As is the case for other study reaches, there is an overlap of the shear stress distributions for topographic highs and lows for the classes of +/- 1-2 (Figure 7.22).

7.7.4. *Summary on Shear Stress Distribution*

Overall, shear stress development is quite dependent on the location of roughness elements with conditions conducive to elevated velocity (Figure 7.20). At low flow stages, this is often at constricted channel margins where continuity bodes higher velocity. They are not as likely to happen at complex channel margins where velocity is not as high (Figure 7.20). The distribution of shear stress in relation to water depth demonstrates that there is a grouping of shear stress values based on Froude number, but this grouping is not as clean as that of component velocity (Figure 7.21). Unlike other parameters, such as normal velocity and velocity magnitude at higher discharge levels, where channel planform seems to make a larger influence than local channel features at higher flow stages, shear stress seems to be governed by local channel velocity and the location of roughness elements.

7.8. SUMMARY ON THE CALAVERAS STUDY REACH

The Calaveras study reach features a reach of the San Antonio River (Figure 7.1) and is the most upstream of all study sites (Figure 3.3). The planform shape of this reach can be characterized as undulations of several amplitudes and frequencies, hence varying degrees of sinuosity. Several extreme topographic lows (i.e., deep pools) are present throughout the reach, with smaller and more frequent lows (i.e., pools) that are clustered around high curvature zones and fewer locations that are sparse throughout areas with low sinuosity (Figure 7.2). Many of the

pools and topographic highs (sediment bars/riffles/edges) suggest point bar accretion and cutbank erosion—such as the region between meter markers 1600 and 1800 meters (Figure 7.1).

At the lowest modeled discharge Q1, the distribution of velocity magnitude for the topographic highs is negatively exponential and has one large mode at the smallest bin, between 0 and 0.05 m¹s⁻¹ (Figure 7.7). The same is true for topographic lows. However, the evolution of these distributions differ with increasing flow stage, as is the case with other study sites. At the discharge level Q3, the cumulative distribution of velocity magnitude takes on a distinctly bimodal character with the primary mode being at velocity bin 0 m¹s⁻¹, and the secondary mode corresponding to a greater bin being around velocity bin 0.3 m¹s⁻¹ (Figure 7.7). As flow stage increases even more to Q4, the topographic high and cumulative distribution becomes more platykurtic. The final distribution at Q5 is bimodal, but the first bin near velocity zero (i.e., 0 – 0.05m¹s⁻¹) has much less percentage contribution than that in lower discharges (Figure 7.7).

These findings indicate that the magnitude of flow velocity tends to become more evenly distributed as the flow stage increases (Figure 7.8). As also observed in the other study sites, this shows the presence of a core of higher velocity representing the higher mode, and the channel margins representing the lower mode. One interesting characteristic of the velocity magnitude is the core of higher velocity (Figure 7.8), observed at meter marker 400 (Figure 7.1). At this location, the core of higher velocity seems to be the strongest at the discharge Q4 and diffuse to a lower magnitude at Q5 (Figure 7.8). This implies that the core of higher velocity is closely related to the channel margins and can be stunted once inundation of a certain depth occurs above constricting topographic features. Also, the distribution of the velocity magnitude becoming increasingly platykurtic could indicate more control attributed to upstream planform geometry than local channel topography, and that there are unique circumstances where the topography can also keep the effect of upstream planform geometry in check.

Backwaters are generally found at margins and low depth areas with lower velocities at other sites. This is also true for the Calaveras study reach (Figure 7.12). As flow stage increases, the locations of backwaters do not change much, but they exhibit a change in size, as many get smaller (Figure 7.12). This decrease in areal size demonstrates that they often bound the cores of high velocity once those developed. This behavior is quite noticeable when comparing discharges at or above Q3. As for the other study sites, this strongly supports the control on the velocity magnitude by the local channel topography and channel planform with weights assigned to whether the flow stage is low or high.

Normal velocity component, as is the case for other study sites, does not change that much in stream position with increasing discharge (Figure 7.16). The alternations between positive/negative normal velocity values are higher in frequency for portions of the reach with high sinuosity than those with the low sinuosity (Figure 7.16). This is also observed in the case of the Cibolo Creek and the Calaveras study sites. Findings suggest that control of normal velocity is heavily influenced by channel planform and less by topography.

Shear stress distribution, similar other study reaches, has spatial arrangement contingent with the locations of roughness elements (Figure 7.20). Unlike the Falls City study site, for example, there does not appear to be a pattern that can be attributed to the topography or channel planform. As flow stage increases, the locations of elevated shear stress are allowed to go slightly beyond the spatially-coincident roughness elements and coalesce with other roughness elements (Figure 7.20). However, the location near meter marker 400 (Figure 7.1) features a very high shear stress in the constricted location (Figure 7.20). This region has few individual roughness elements within the channel at this portion of the reach, but it seems to have large roughness elements that could only be described as a terrace or extra-channel feature. This explanation should be examined in more detail for the validity of these features. Over the majority of the reach, a pattern similar to other study sites, with the exception of the Falls City, is observed (Figure 7.20).

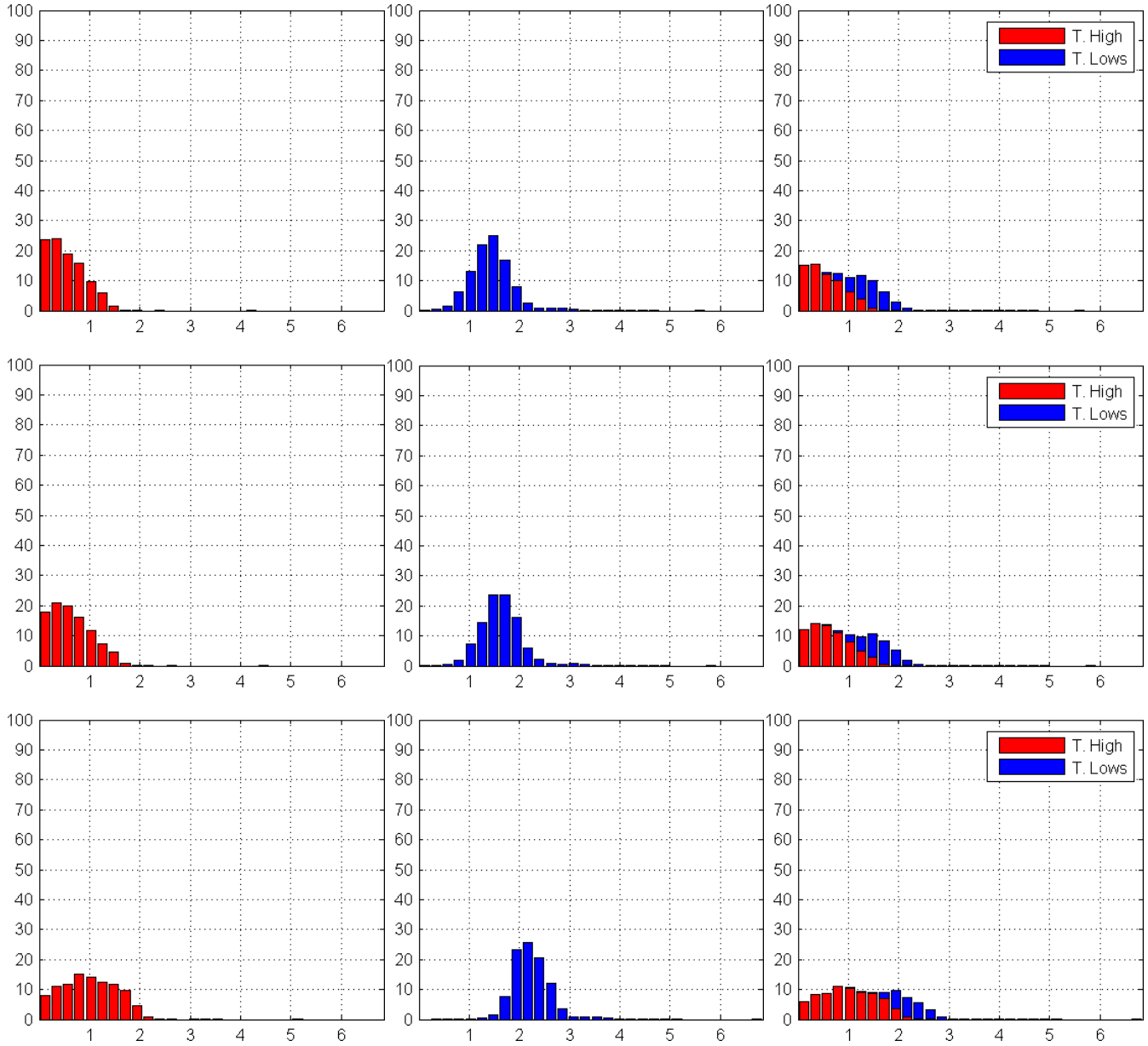


Figure 7.5. Water depth distribution for Q1–Q5 (rows, top to bottom) for topographic highs (marked as T. High) corresponding to the classes (+1)–(+4), topographic lows (marked as T. Lows) corresponding to the classes (-1)–(-4), and combined (columns, left to right). Horizontal and vertical axes correspond to water depth (m) and the percent values of topographic classes, respectively.

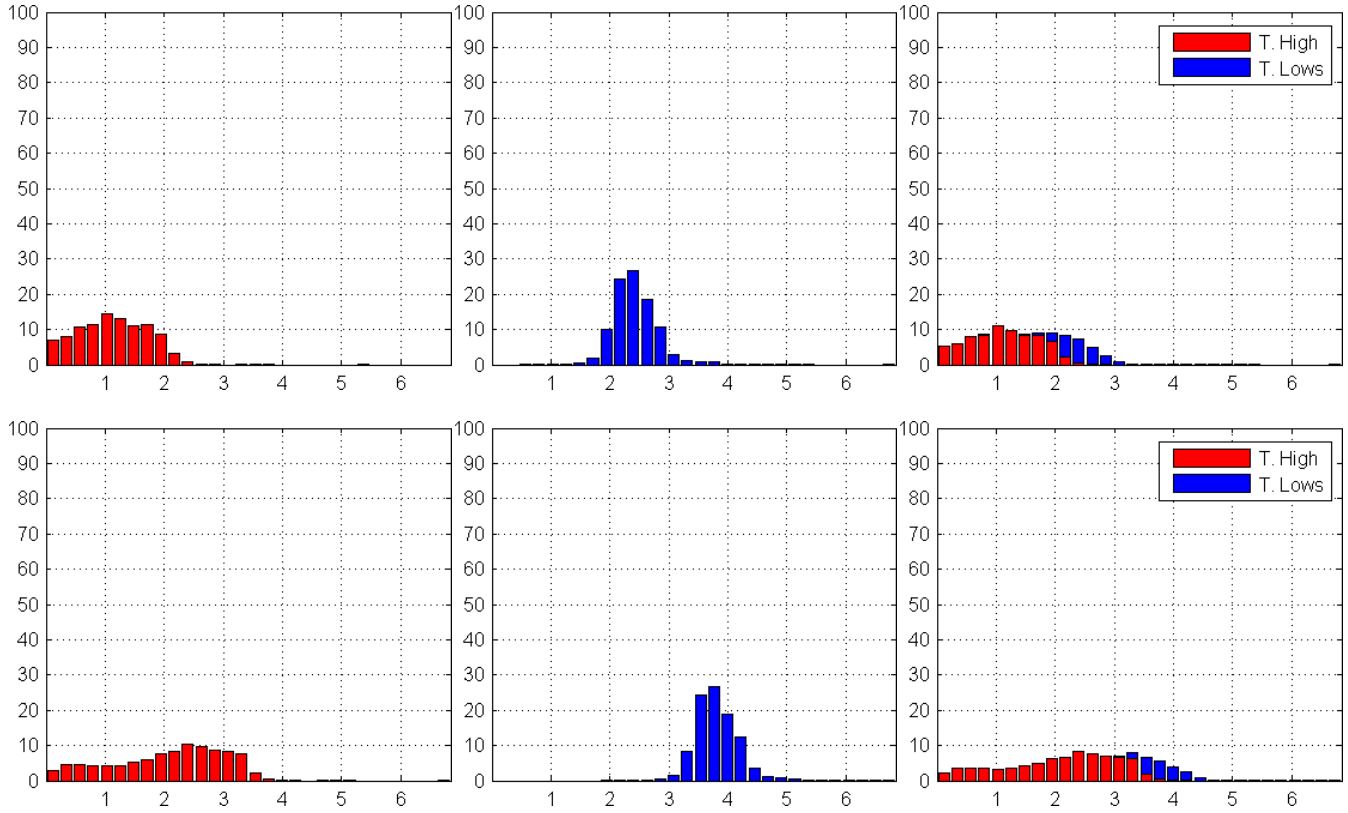


Figure 7.5 (cont'd). Water depth distribution for Q1–Q5 (rows, top to bottom) for topographic highs (marked as T. High) corresponding to the classes (+1)–(+4), topographic lows (marked as T. Lows) corresponding to the classes (-1)–(-4), and combined (columns, left to right). Horizontal and vertical axes correspond to water depth (m) and the percent values of topographic classes, respectively.

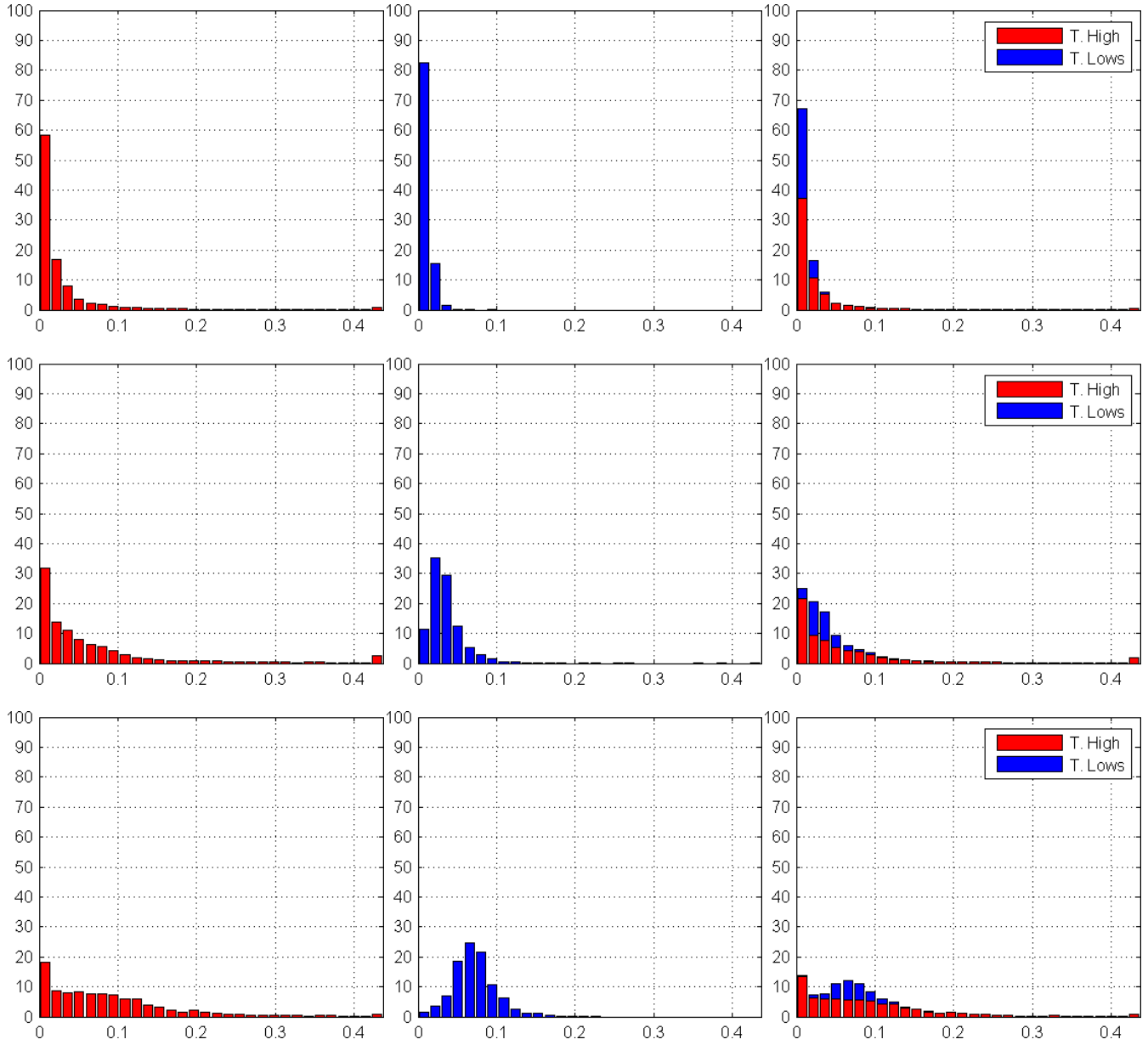


Figure 7.6. Froude number (Fr) distribution for Q1–Q5 (rows, top to bottom) for topographic highs (marked as T. High) corresponding to the classes (+1)–(+4), topographic lows (marked as T. Lows) corresponding to the classes (-1)–(-4), and combined (columns, left to right). Horizontal and vertical axes correspond to Fr and the percent values of topographic classes, respectively.

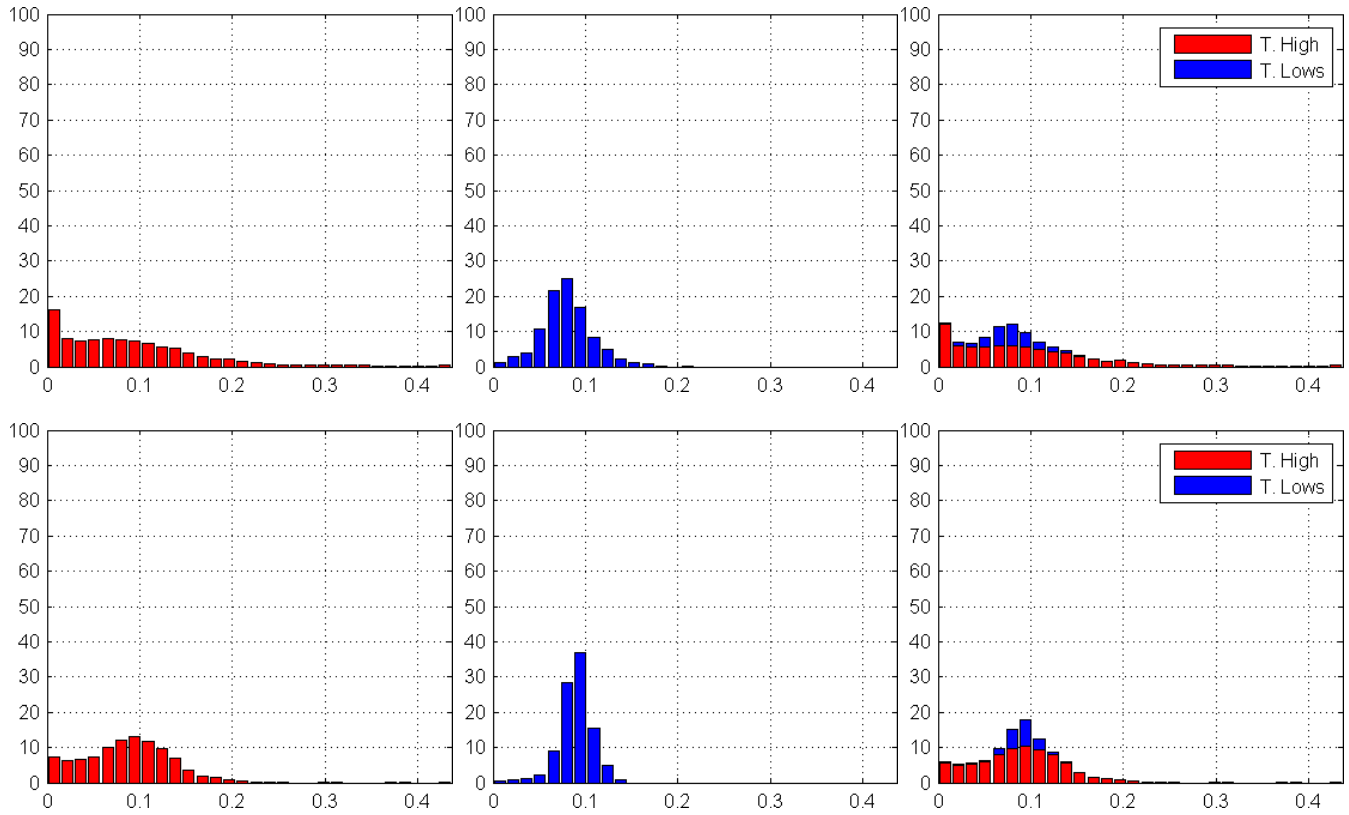


Figure 7.6 (cont'd). Froude number (Fr) distribution for Q1–Q5 (rows, top to bottom) for topographic highs (marked as T. High) corresponding to the classes (+1)–(+4), topographic lows (marked as T. Lows) corresponding to the classes (-1)–(-4), and combined (columns, left to right). Horizontal and vertical axes correspond to Fr and the percent values of topographic classes, respectively.

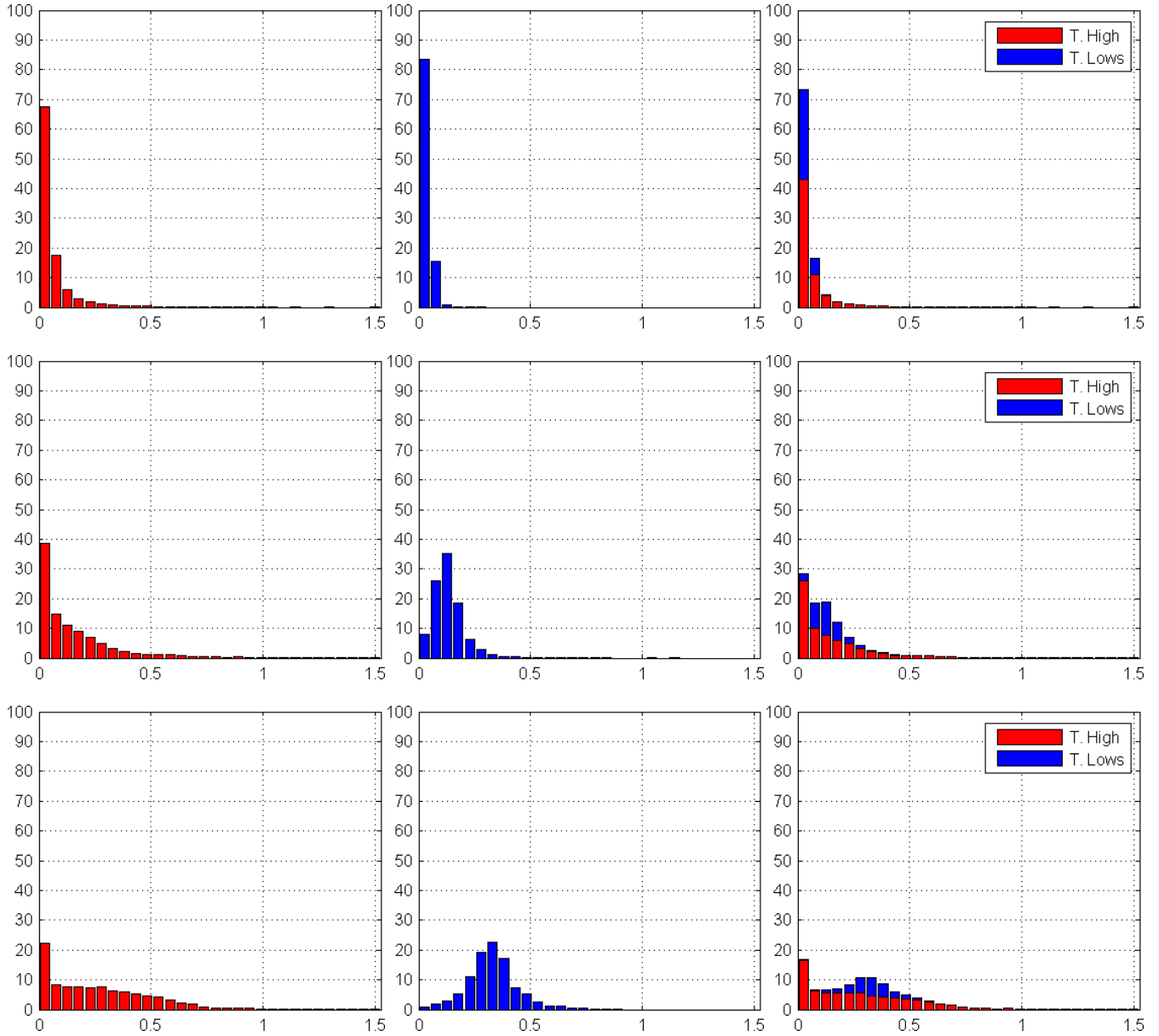


Figure 7.7. Distribution of velocity magnitude for Q1–Q5 (rows, top to bottom) for topographic highs (marked as T. High) corresponding to the classes (+1)–(+4), topographic lows (marked as T. Lows) corresponding to the classes (-1)–(-4), and combined (columns, left to right). Horizontal and vertical axes correspond to velocity magnitude (m/s) and the percent values of topographic classes, respectively.

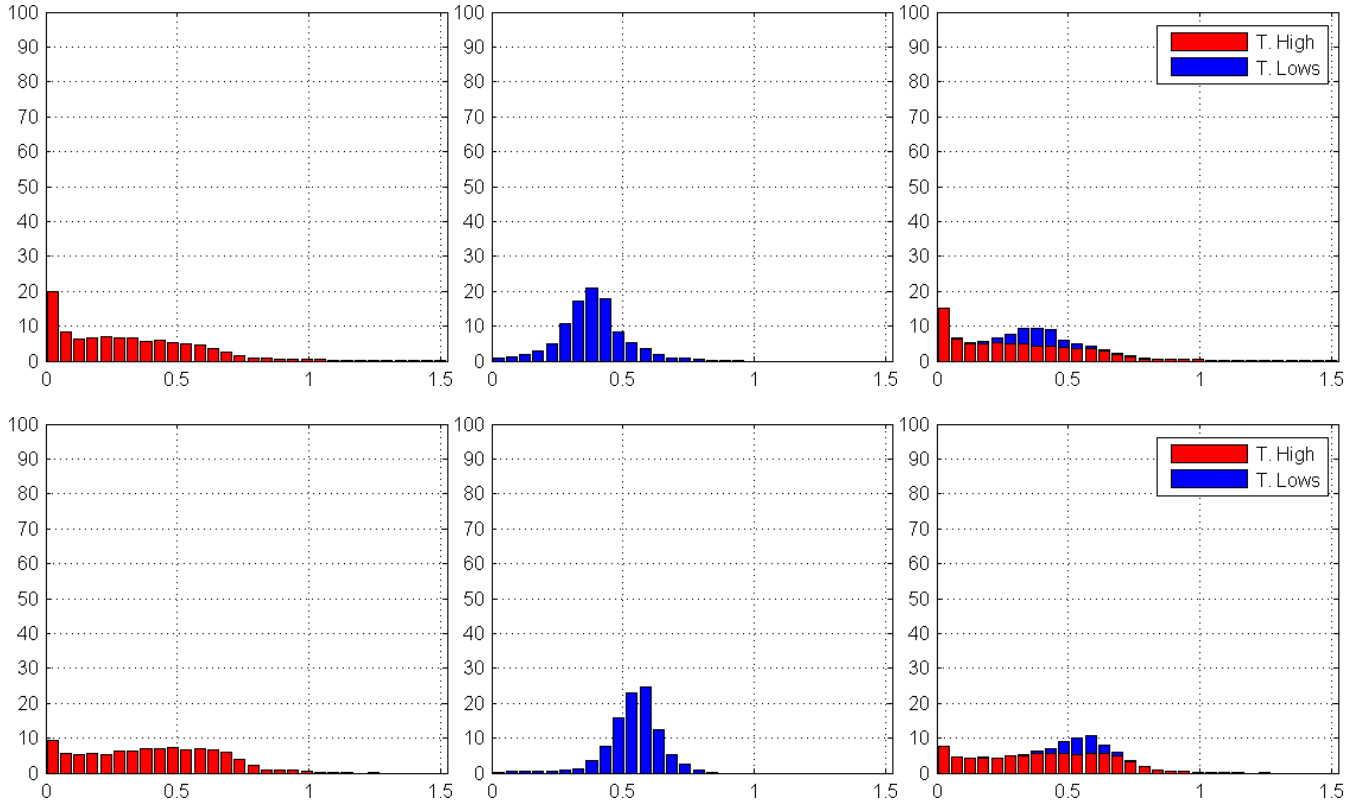


Figure 7.7 (cont'd). Distribution of velocity magnitude for Q1–Q5 (rows, top to bottom) for topographic highs (marked as T. High) corresponding to the classes (+1)–(+4), topographic lows (marked as T. Lows) corresponding to the classes (-1)–(-4), and combined (columns, left to right). Horizontal and vertical axes correspond to velocity magnitude (m/s) and the percent values of topographic classes, respectively.

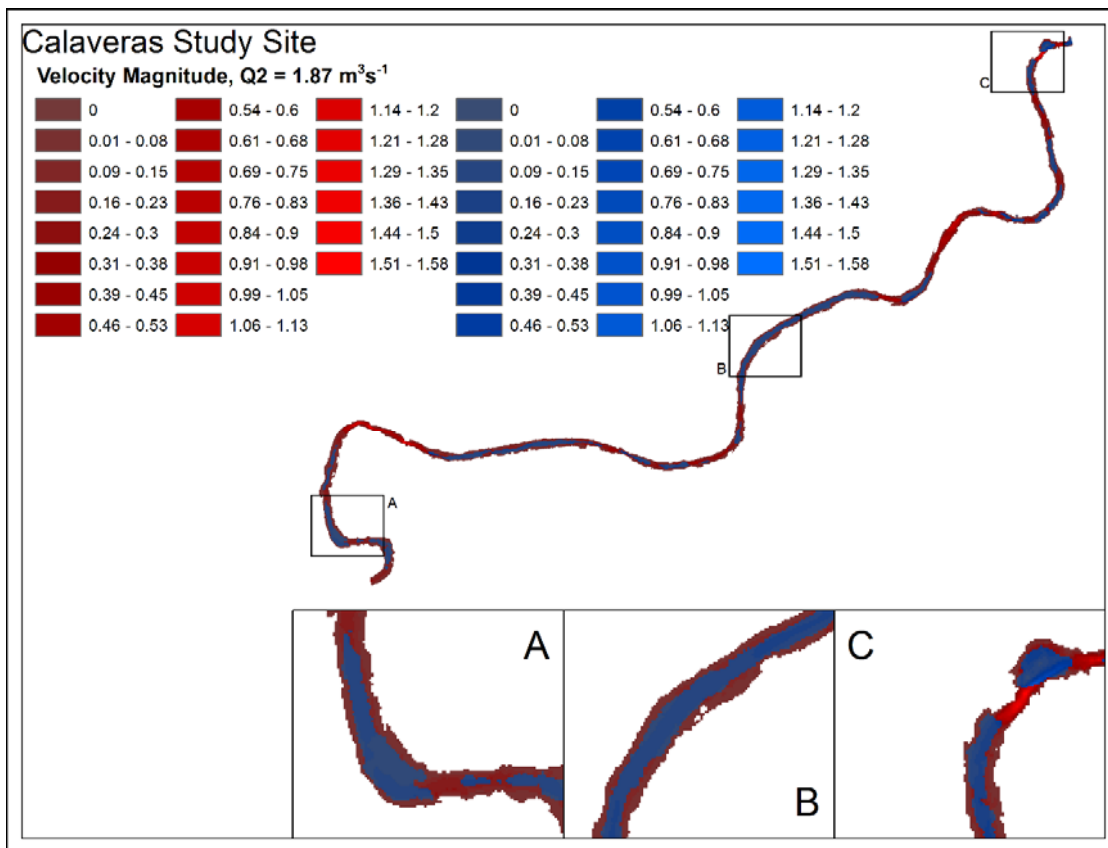
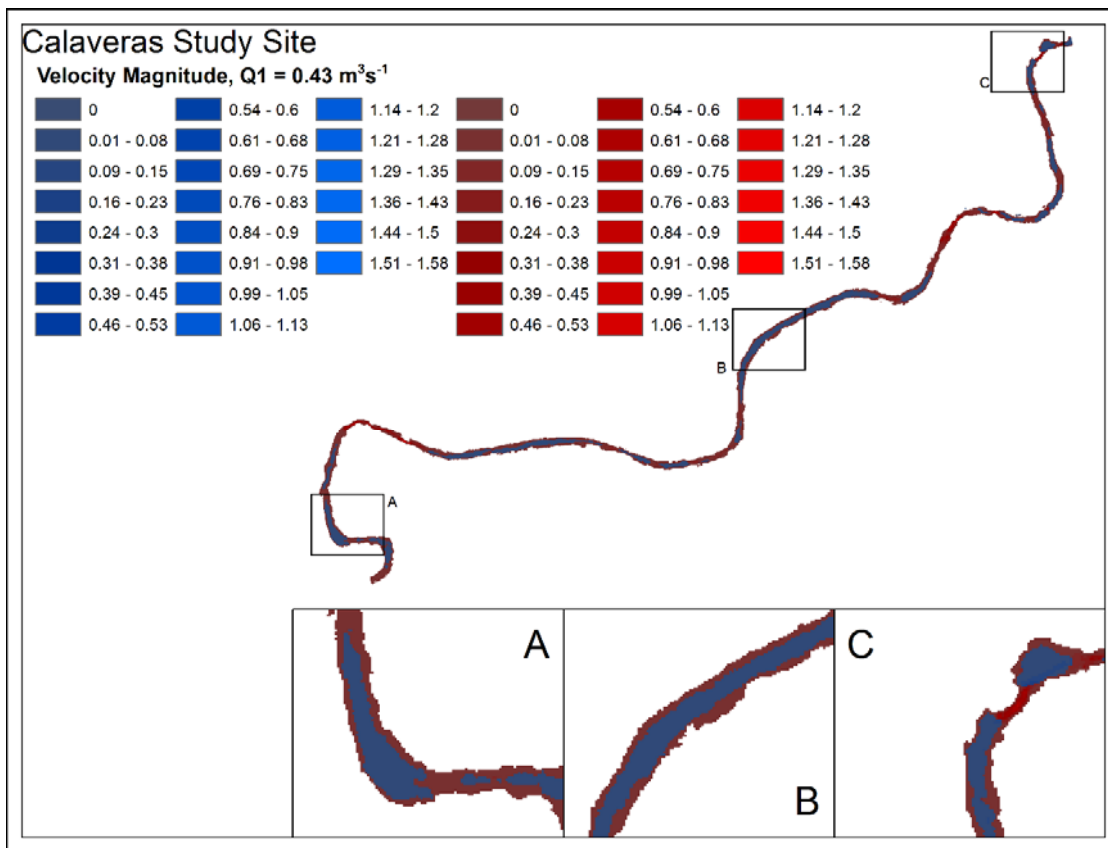


Figure 7.8. Spatial distribution of velocity magnitude (m/s) for Q1–Q5 for topographic highs (red colors) and lows (blue colors).

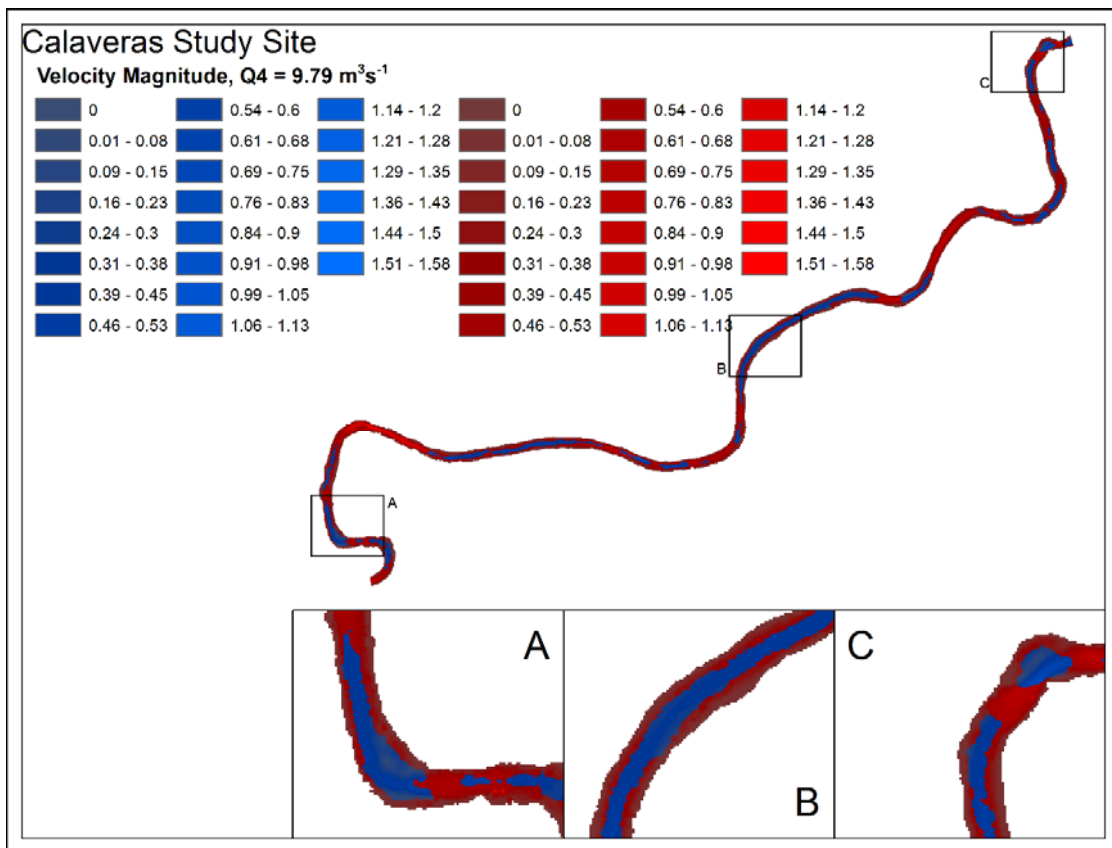
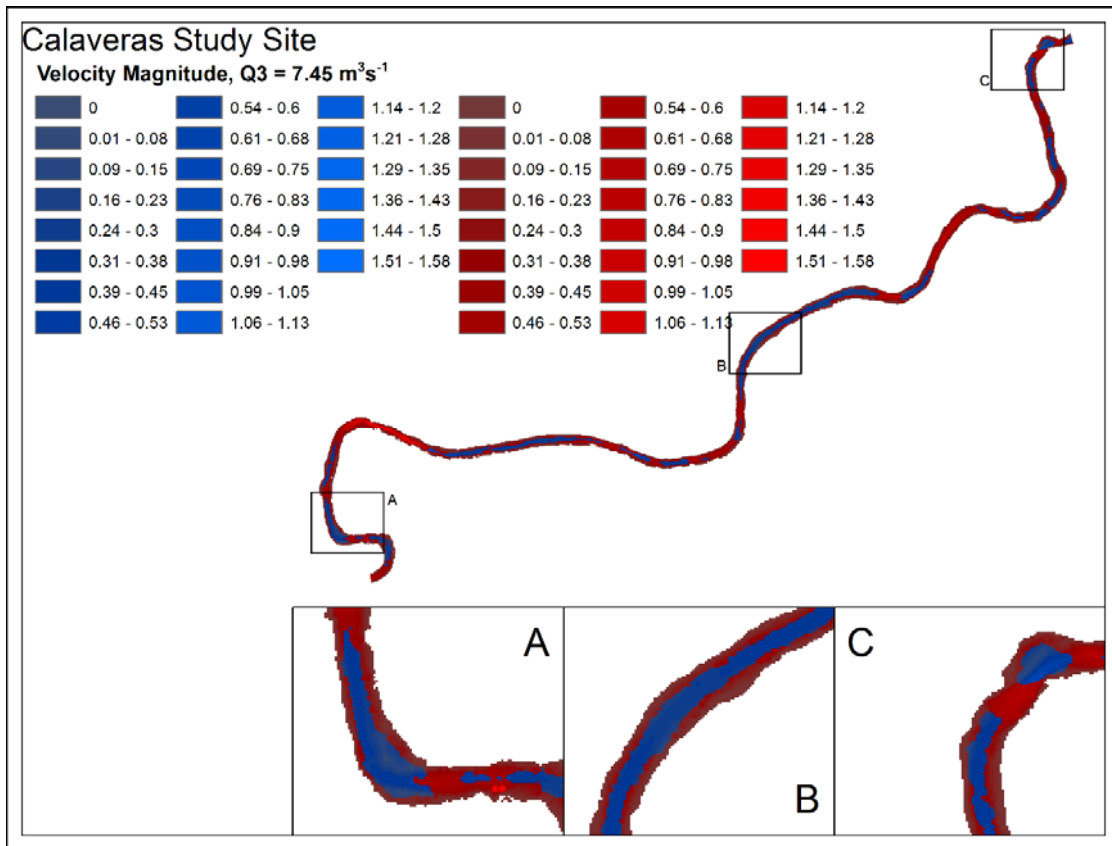


Figure 7.8 (cont'd). Spatial distribution of velocity magnitude (m/s) for Q1–Q5 for topographic highs (red colors) and lows (blue colors).

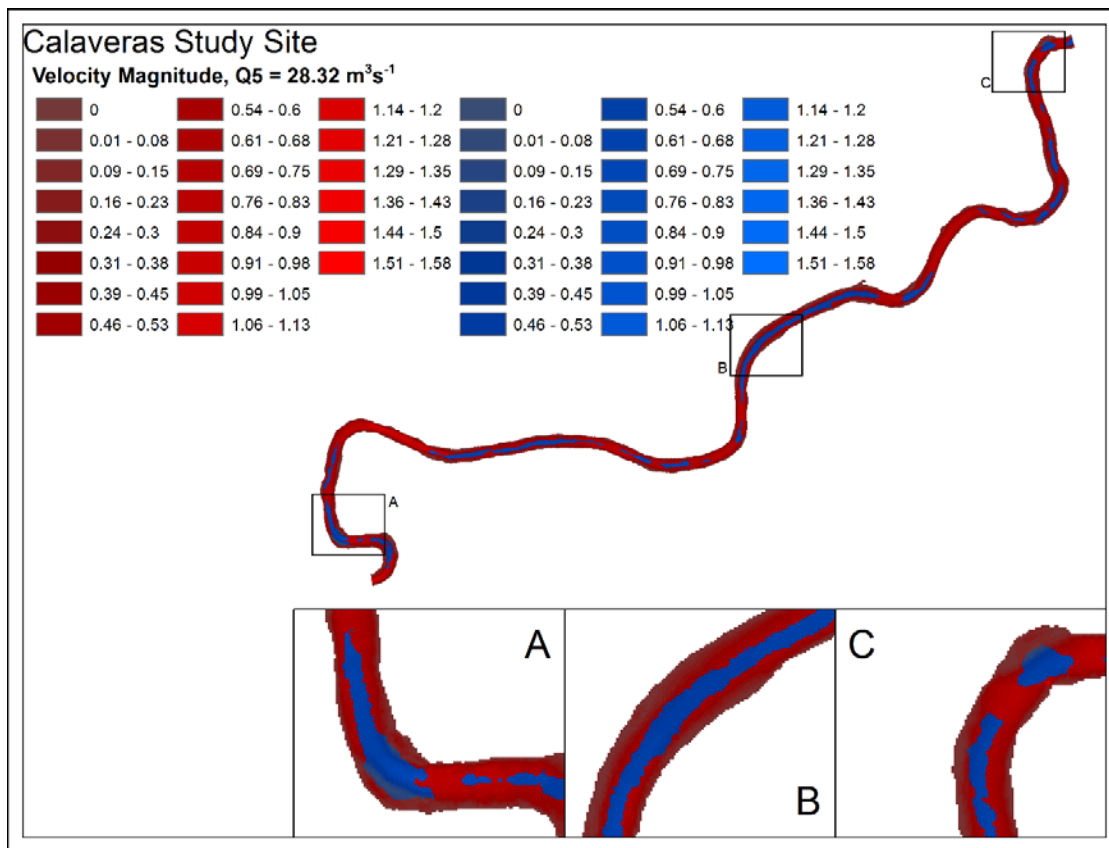


Figure 7.8 (cont'd). Spatial distribution of velocity magnitude (m/s) for Q1–Q5 for topographic highs (red colors) and lows (blue colors).

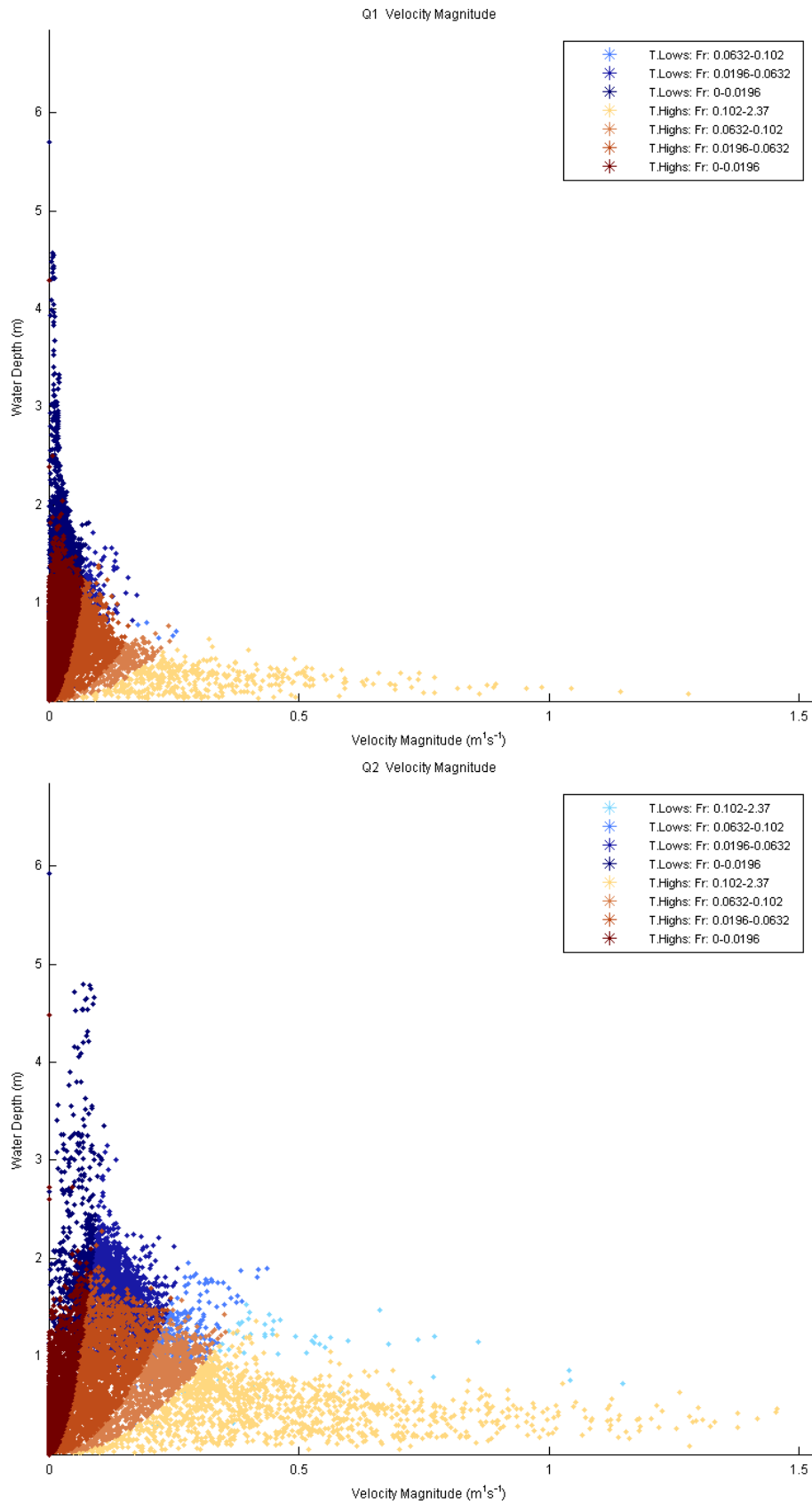


Figure 7.9. Distribution of velocity magnitude in relation to water depth for Q1–Q5 classified by topographic highs marked as T. Highs (brown colors), topographic lows marked as T. Lows (blue colors), and Froude number (Fr).

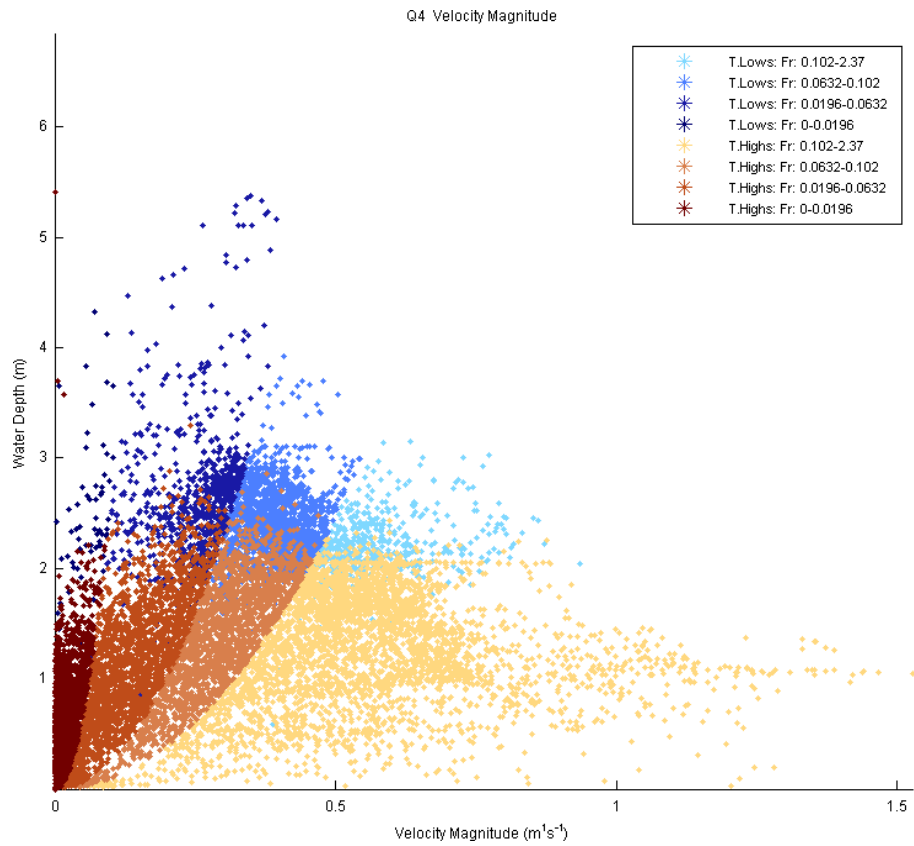
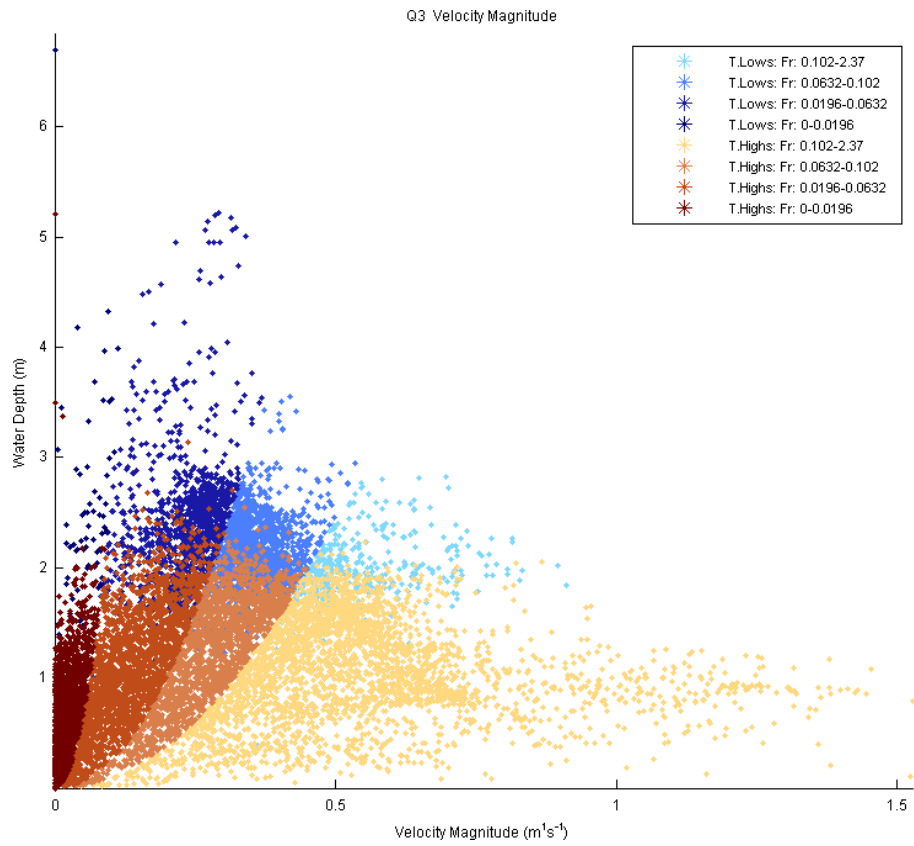


Figure 7.9 (cont'd). Distribution of velocity magnitude in relation to water depth for Q1–Q5 classified by topographic highs marked as T. Highs (brown colors), topographic lows marked as T. Lows (blue colors), and Froude number (Fr).

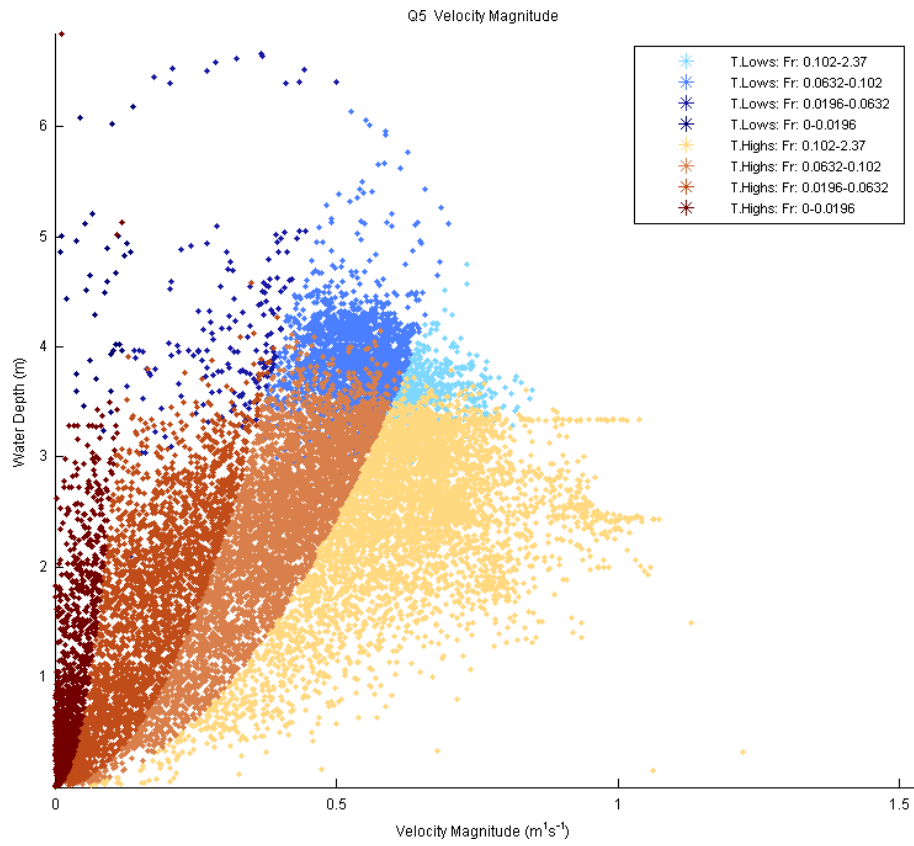


Figure 7.9 (cont'd). Distribution of velocity magnitude in relation to water depth for Q1–Q5 classified by topographic highs marked as T. Highs (brown colors), topographic lows marked as T. Lows (blue colors), and Froude number (Fr).

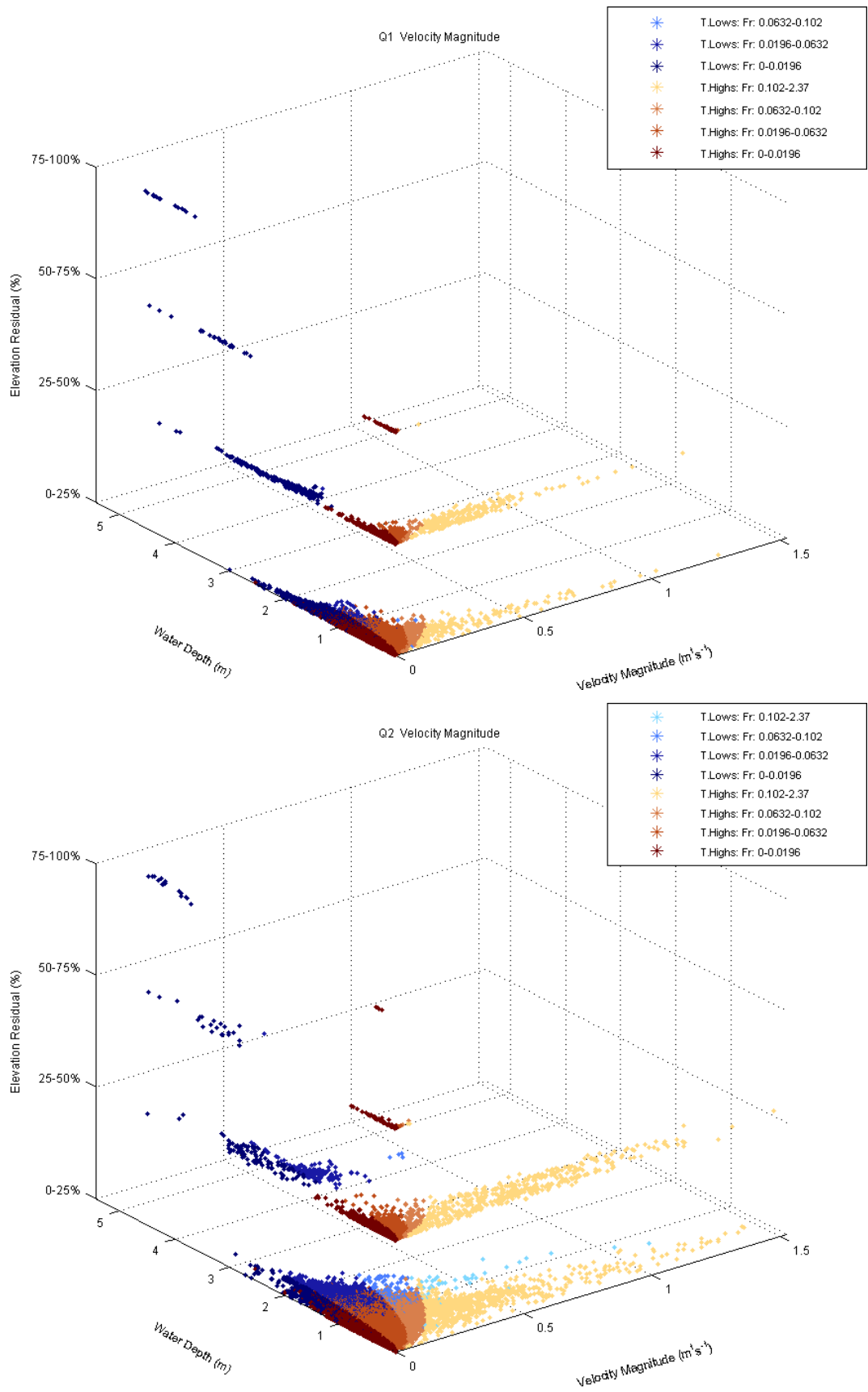


Figure 7.10. Distribution of velocity magnitude for topographic high (T. Highs)/low (T. Lows) subclasses (Figure 4.2) and Q1–Q5, classified by Froude number (Fr).

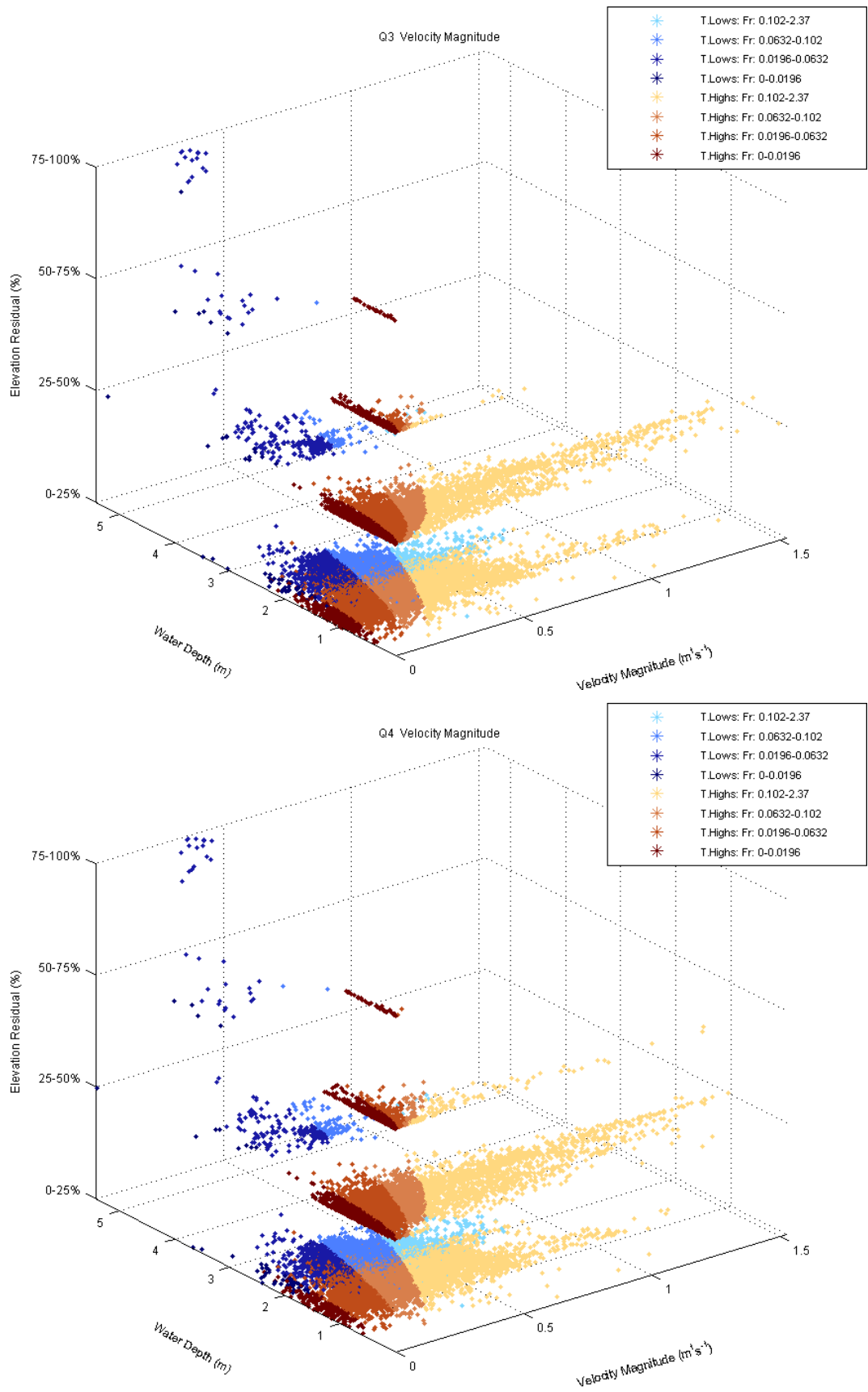


Figure 7.10 (cont'd). Distribution of velocity magnitude for topographic high (T. Highs)/low (T. Lows) subclasses (Figure 4.2) and Q1–Q5, classified by Froude number (Fr).

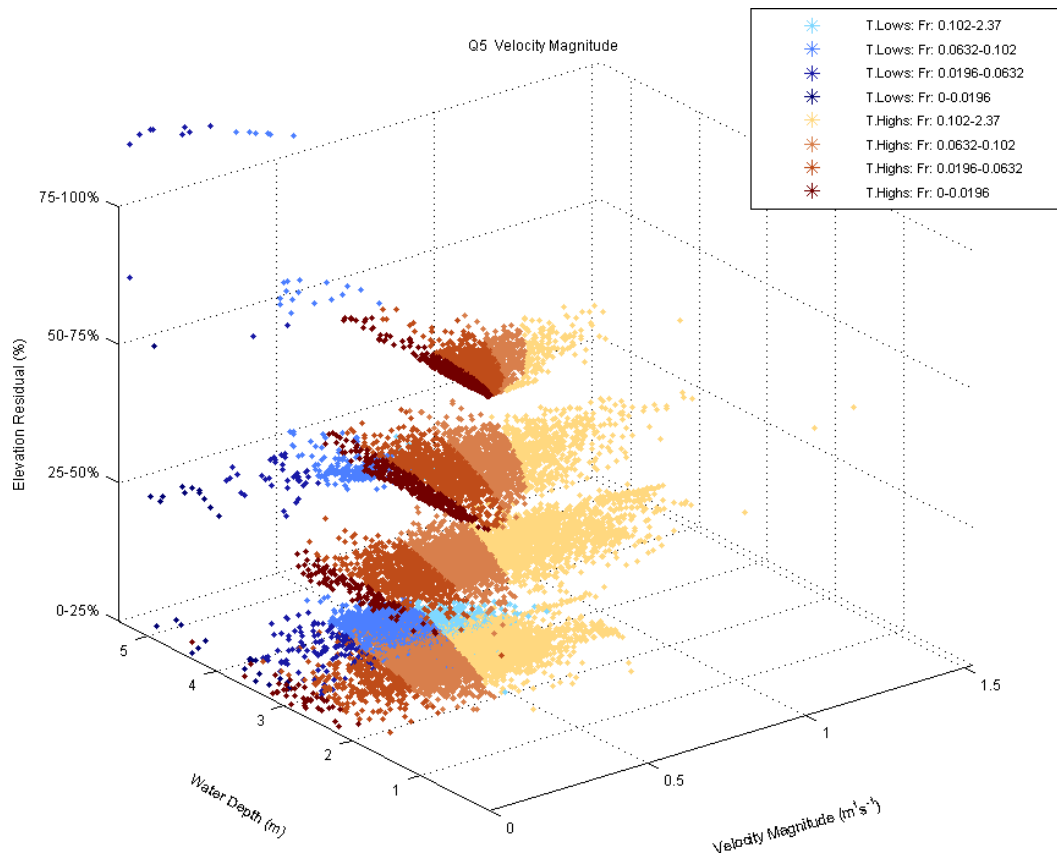


Figure 7.10 (cont'd). Distribution of velocity magnitude for topographic high (T. Highs)/low (T. Lows) subclasses (Figure 4.2) and Q1–Q5, classified by Froude number (Fr).

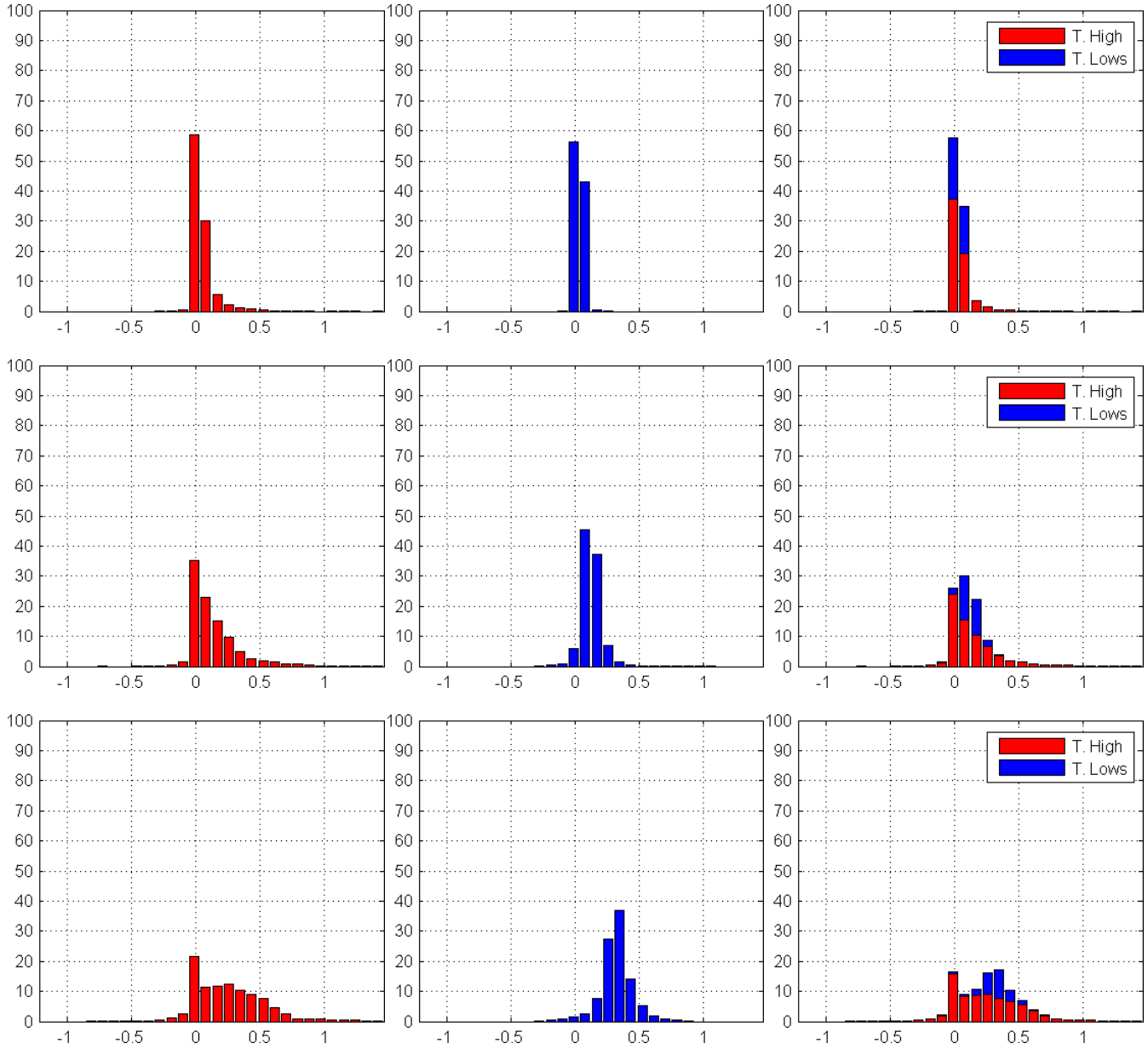


Figure 7.11. Distribution of streamwise velocity component for Q1–Q5 (rows, top to bottom) for topographic highs (marked as T. High) corresponding to the classes (+1)–(+4), topographic lows (marked as T. Lows) corresponding to the classes (-1)–(-4), and combined (columns, left to right). Horizontal and vertical axes correspond to streamwise velocity (m/s) and the percent values of topographic classes, respectively.

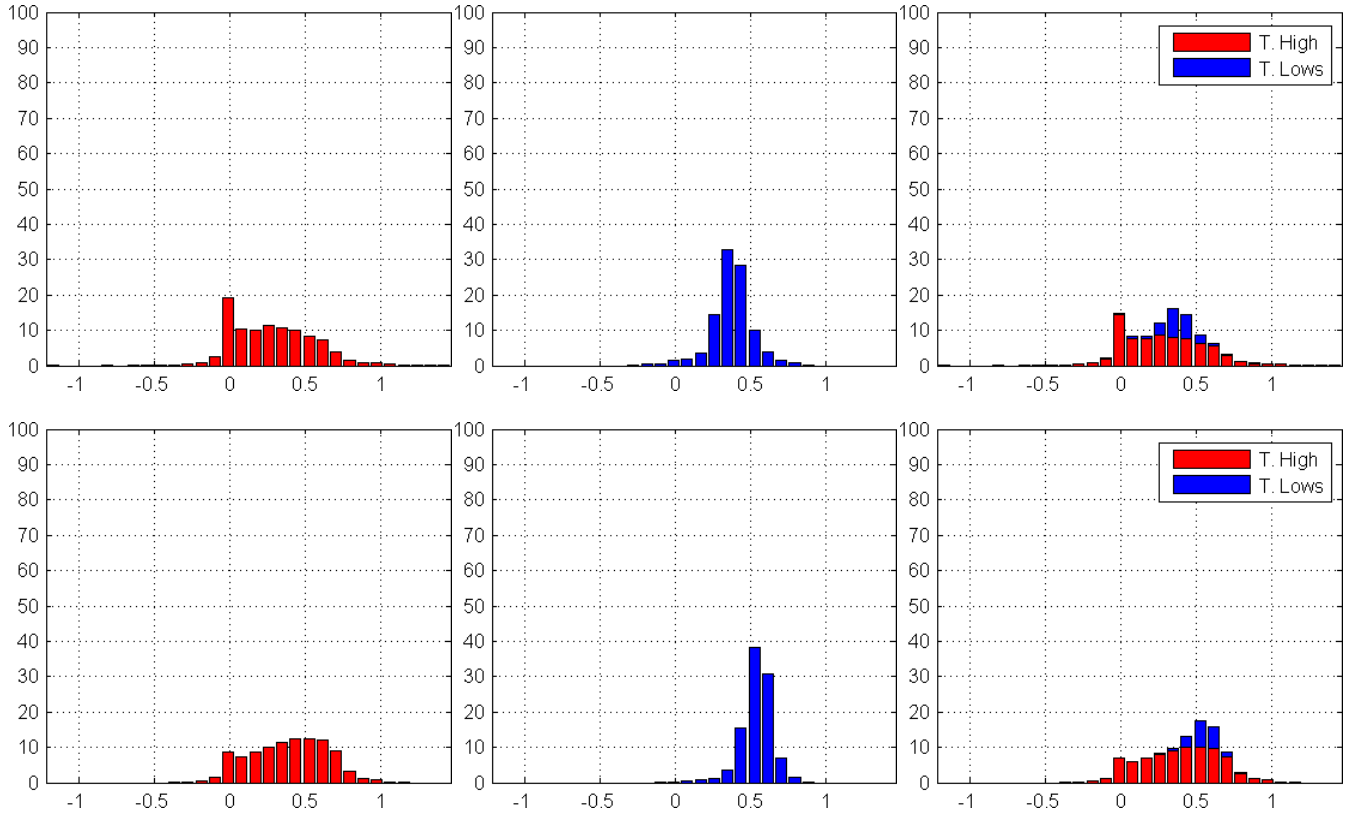


Figure 7.11 (cont'd). Distribution of streamwise velocity component for Q1–Q5 (rows, top to bottom) for topographic highs (marked as T. High) corresponding to the classes (+1)–(+4), topographic lows (marked as T. Lows) corresponding to the classes (-1)–(-4), and combined (columns, left to right). Horizontal and vertical axes correspond to streamwise velocity (m/s) and the percent values of topographic classes, respectively.

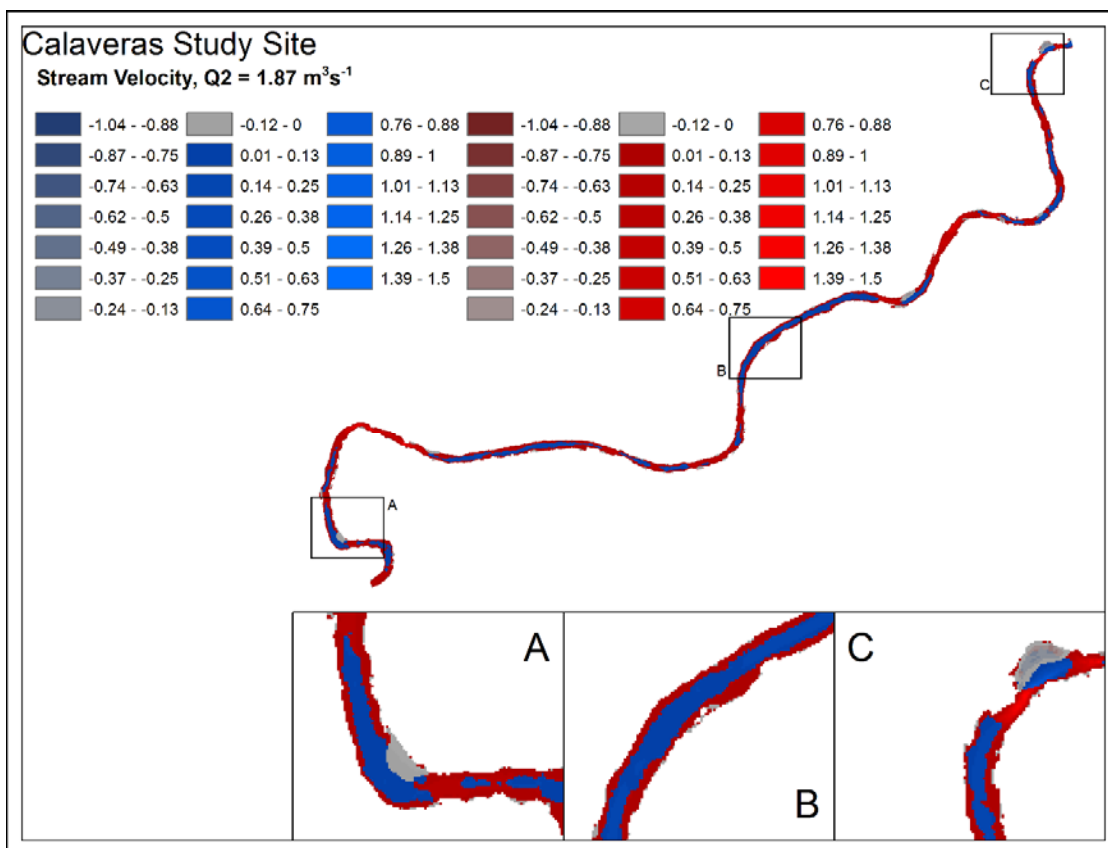
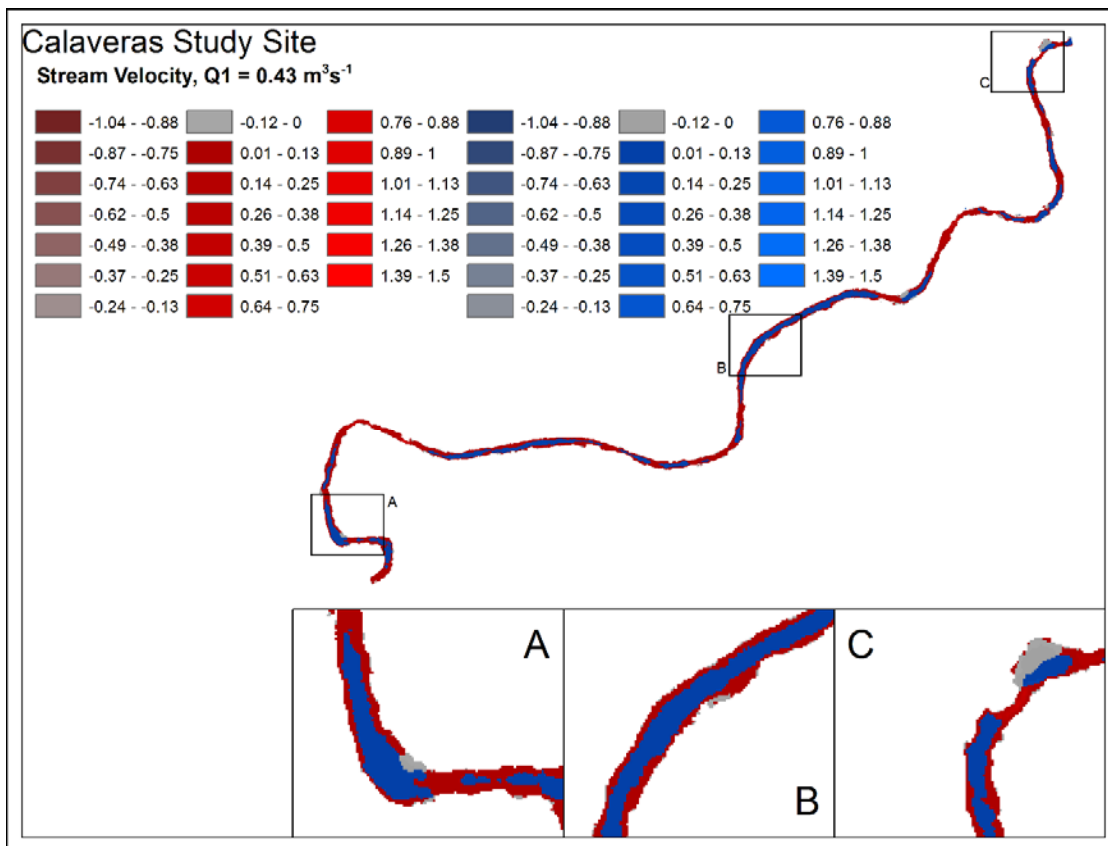


Figure 7.12. Spatial distribution of streamwise velocity (m/s) for Q1–Q5 for topographic highs (red colors) and lows (blue colors).

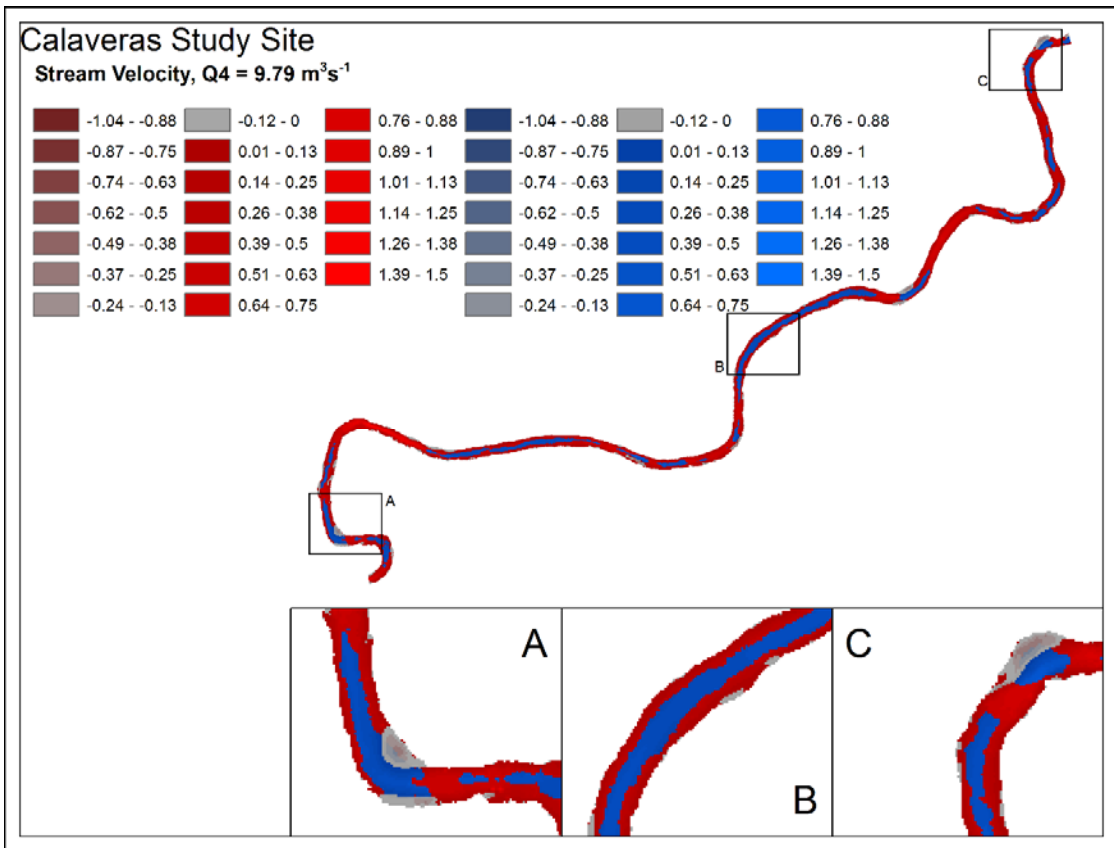
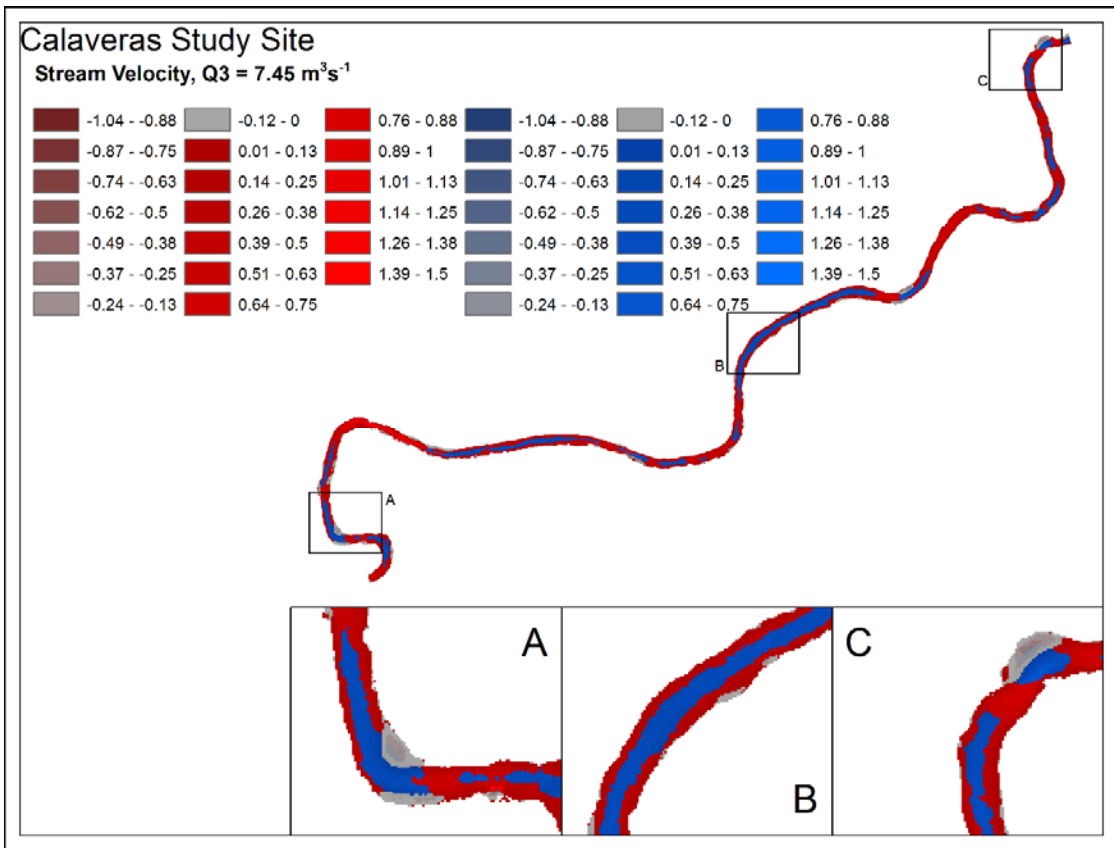


Figure 7.12 (cont'd). Spatial distribution of streamwise velocity (m/s) for Q1–Q5 for topographic highs (red colors) and lows (blue colors).

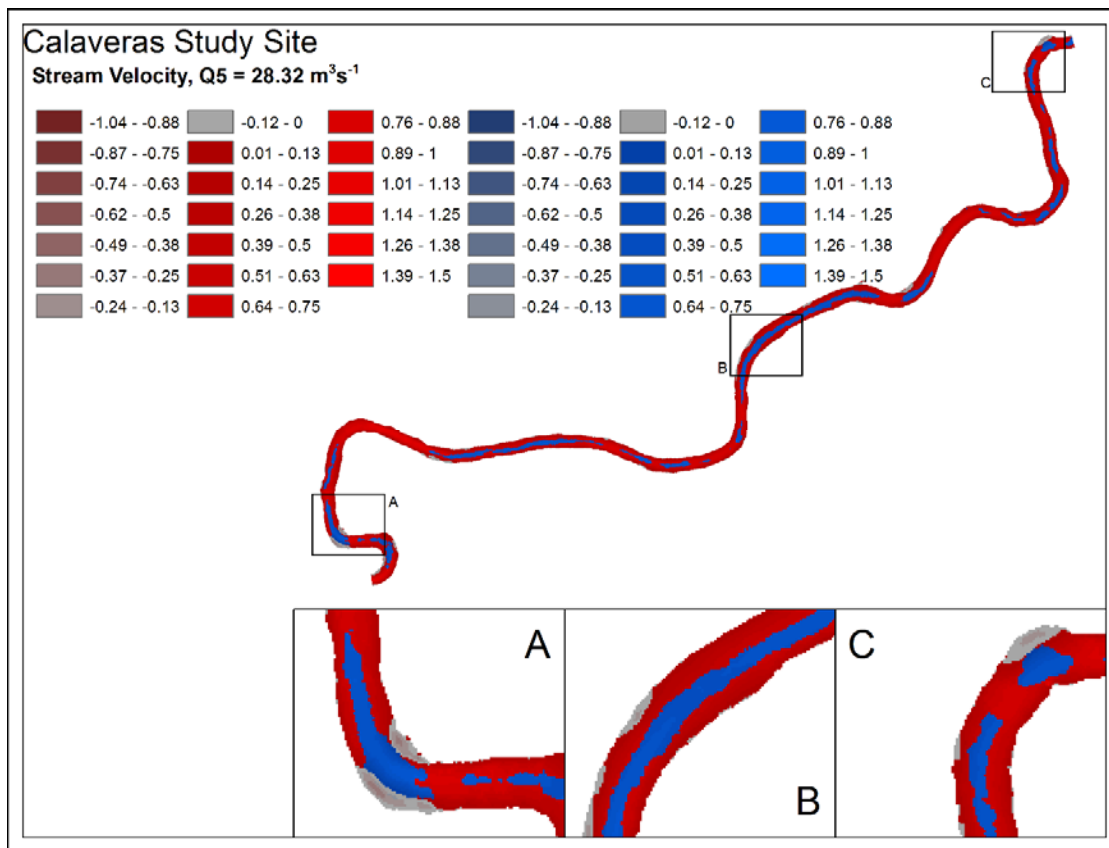


Figure 7.12 (cont'd). Spatial distribution of streamwise velocity (m/s) for Q1–Q5 for topographic highs (red colors) and lows (blue colors).

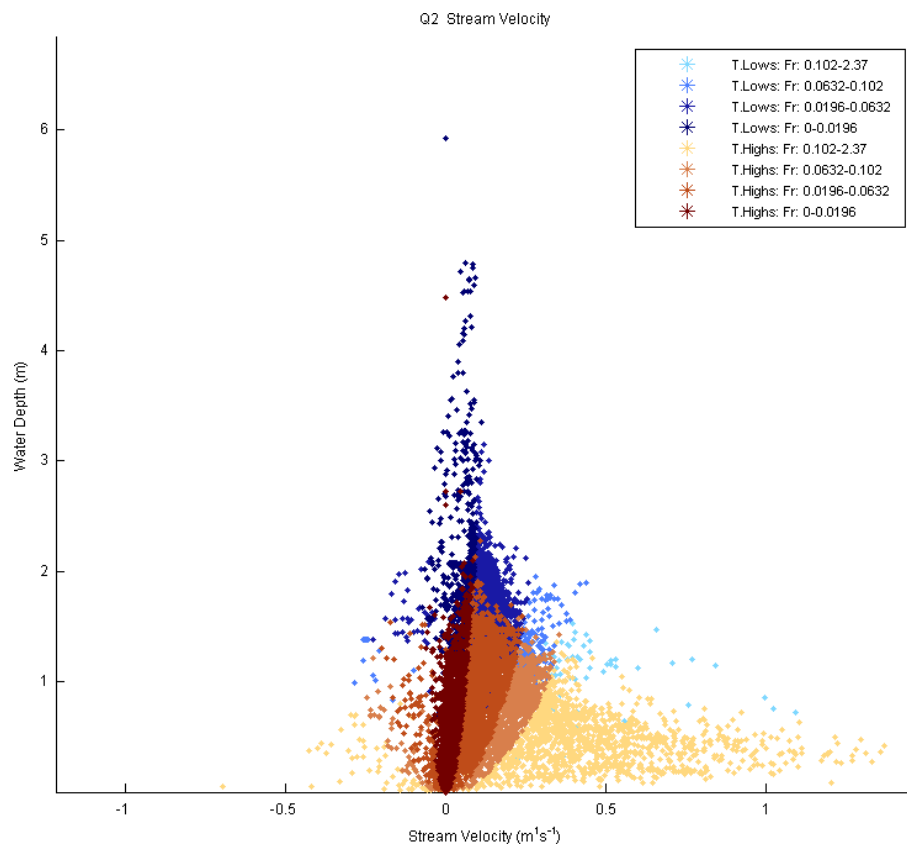
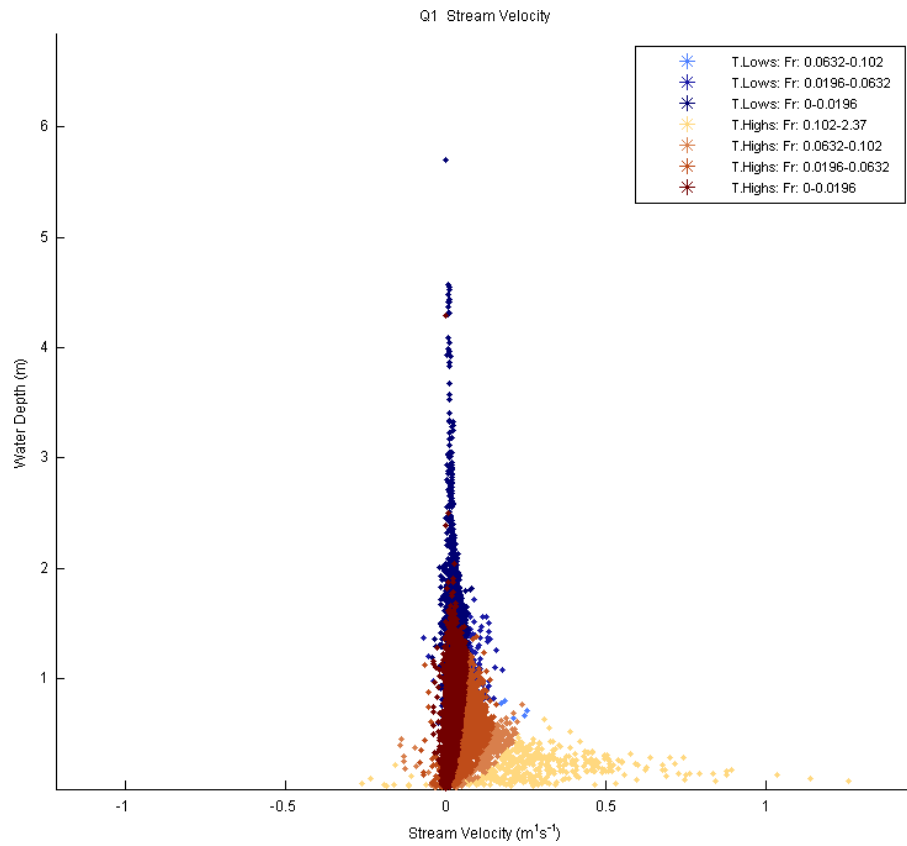


Figure 7.13. Distribution of streamwise velocity in relation to water depth for Q1–Q5 classified by topographic highs marked as T. Highs (brown colors), topographic lows marked as T. Lows (blue colors), and Froude number (Fr).

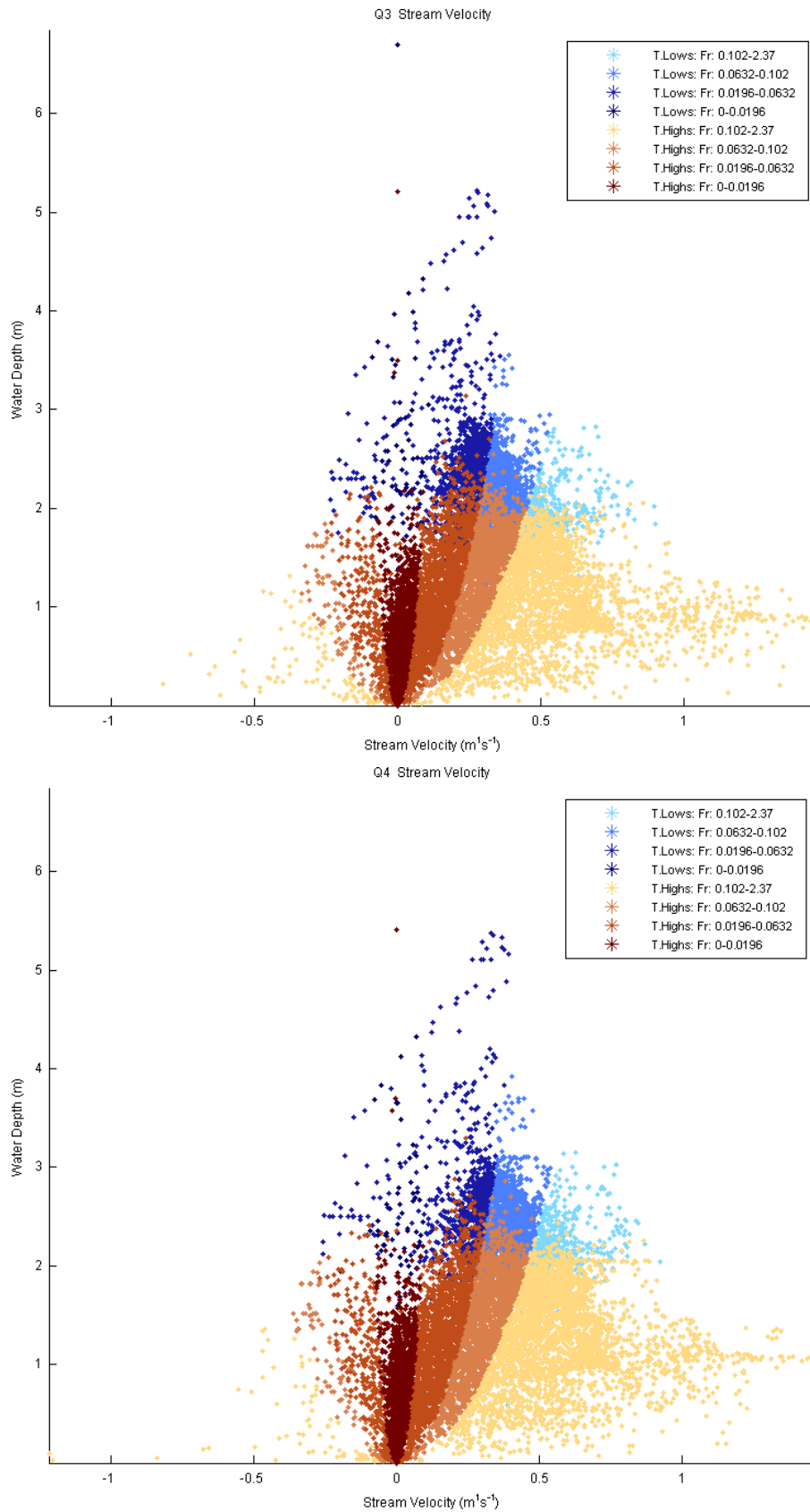


Figure 7.13 (cont'd). Distribution of streamwise velocity in relation to water depth for Q1–Q5 classified by topographic highs marked as T. Highs (brown colors), topographic lows marked as T. Lows (blue colors), and Froude number (Fr).

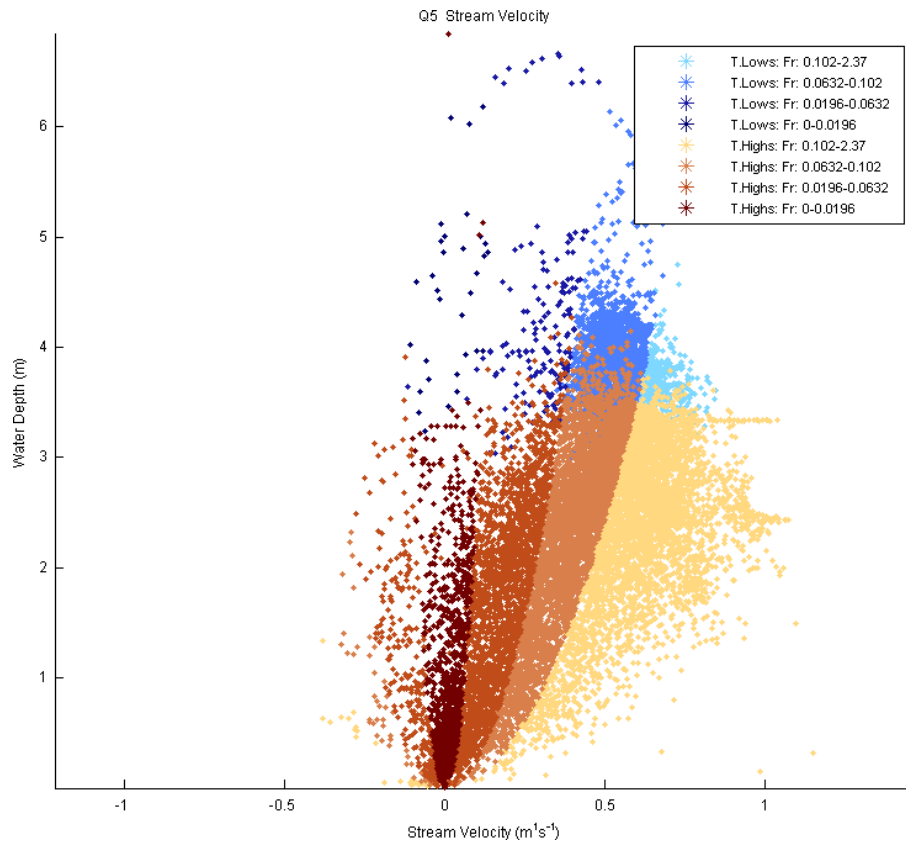


Figure 7.13 (cont'd). Distribution of streamwise velocity in relation to water depth for Q1–Q5 classified by topographic highs marked as T. Highs (brown colors), topographic lows marked as T. Lows (blue colors), and Froude number (Fr).

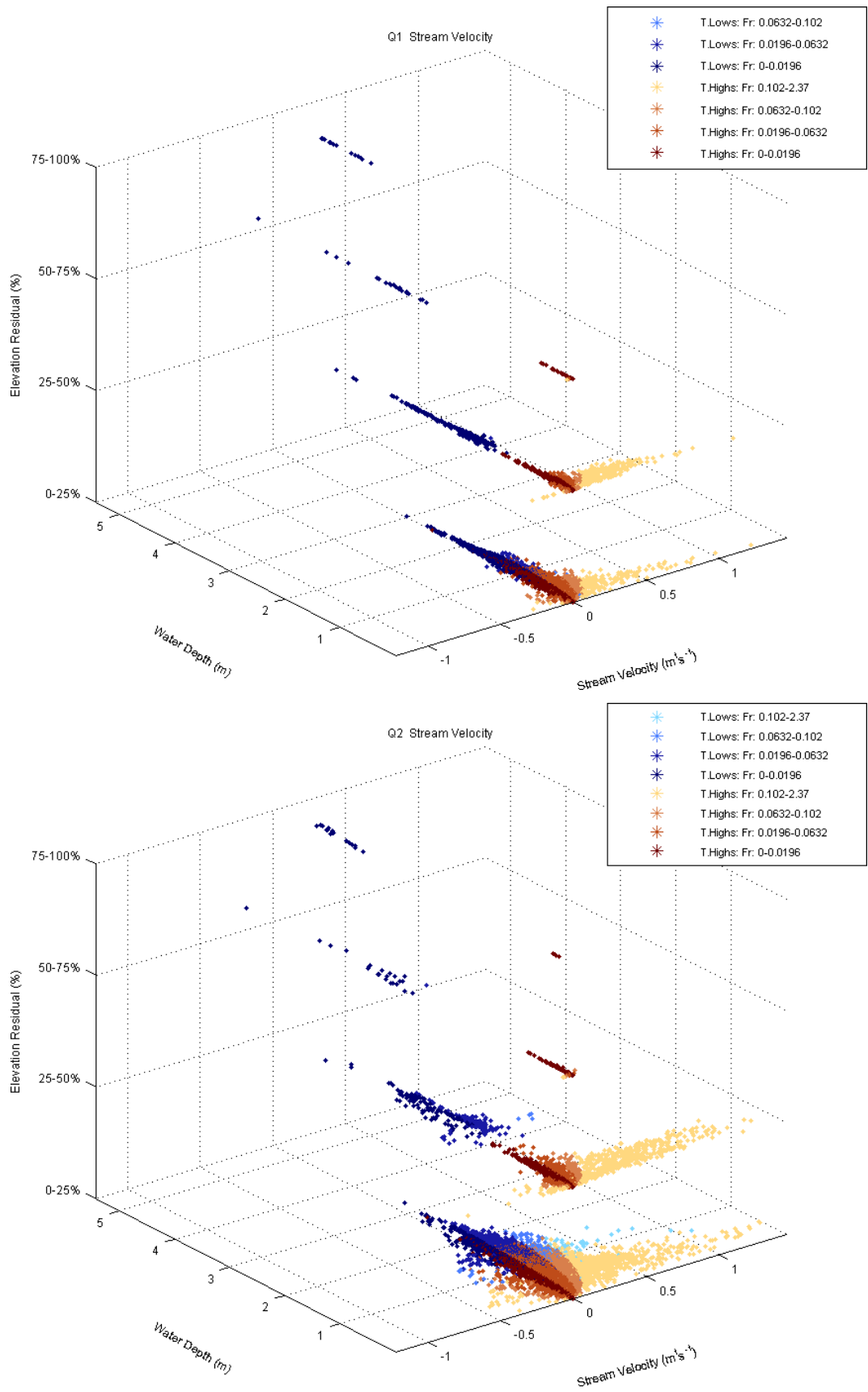


Figure 7.14. Distribution of streamwise velocity for topographic high (T. Highs)/low (T. Lows) subclasses (Figure 4.2) and Q1–Q5, classified by Froude number (Fr).

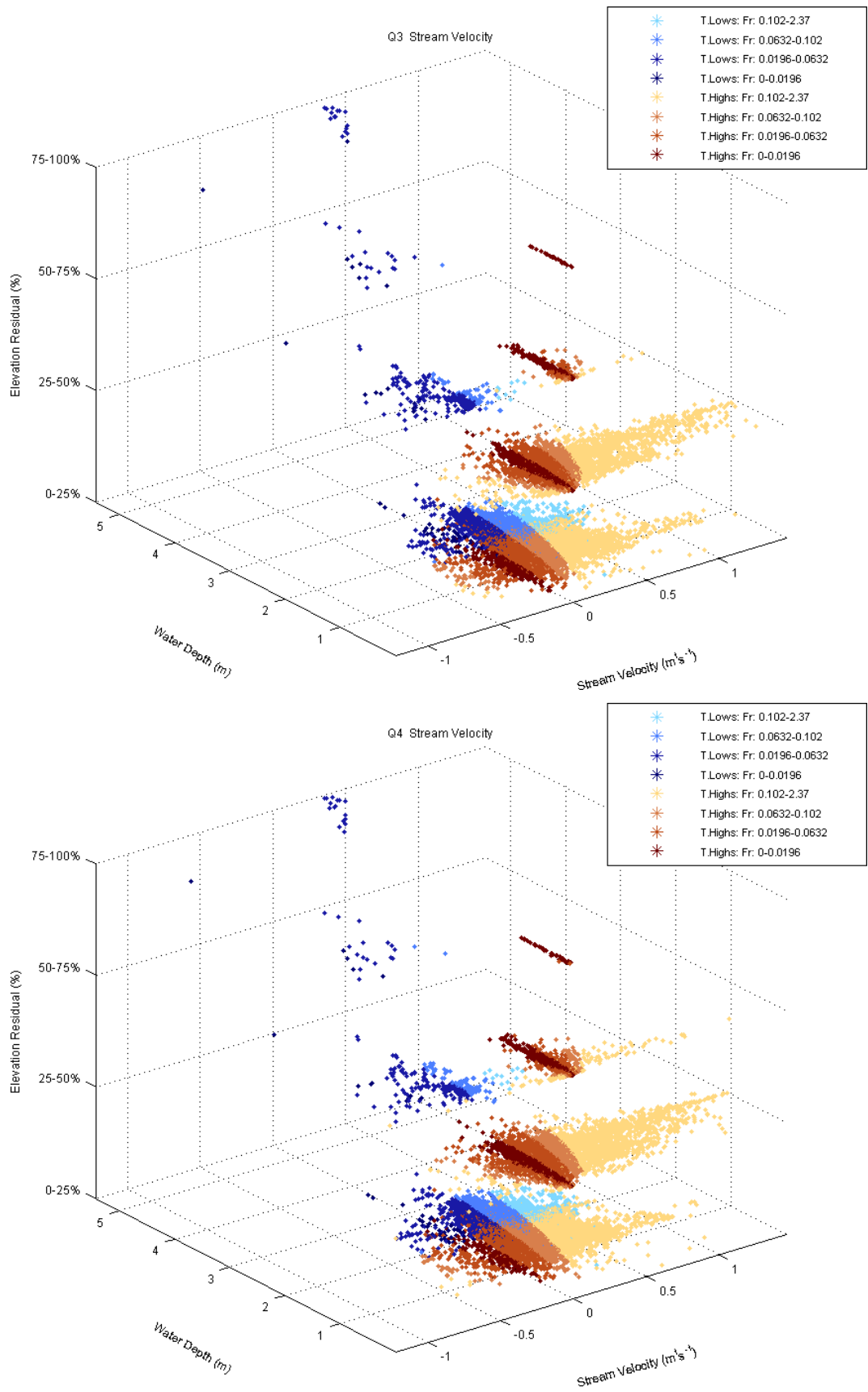


Figure 7.14 (cont'd). Distribution of streamwise velocity for topographic high (T. Highs)/low (T. Lows) subclasses (Figure 4.2) and Q1–Q5, classified by Froude number (Fr).

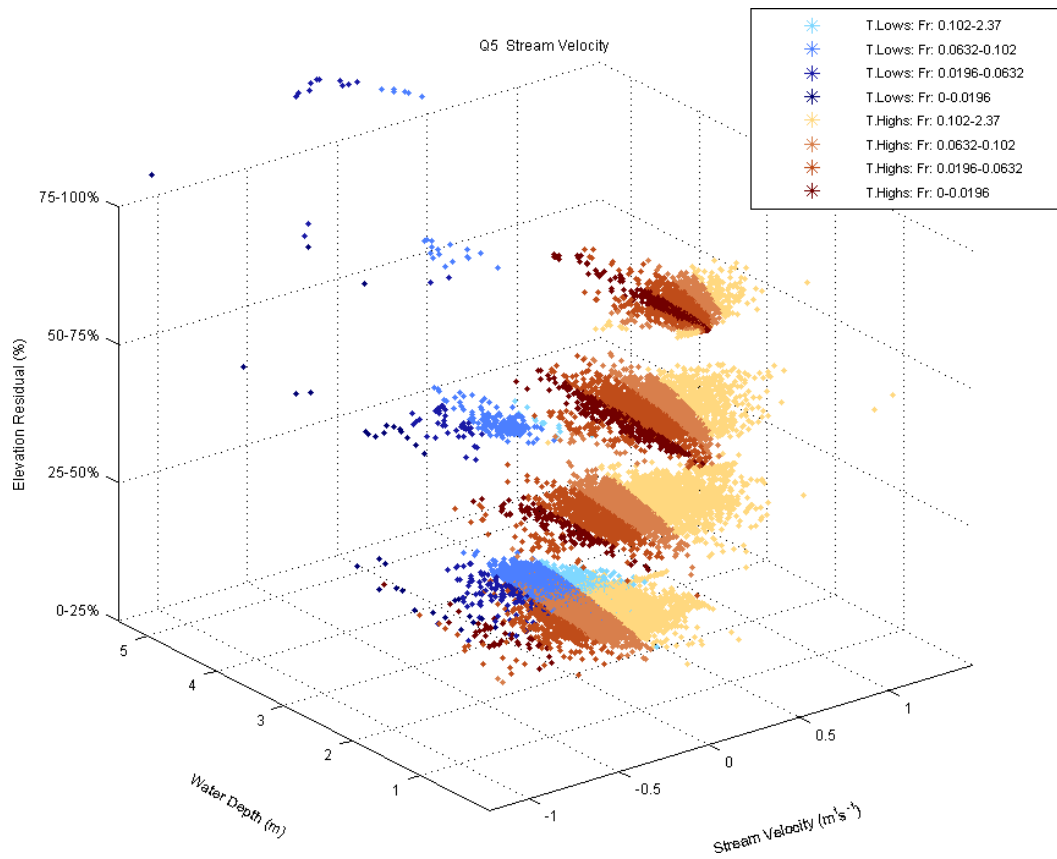


Figure 7.14 (cont'd). Distribution of streamwise velocity for topographic high (T. Highs)/low (T. Lows) subclasses (Figure 4.2) and Q1–Q5, classified by Froude number (Fr).

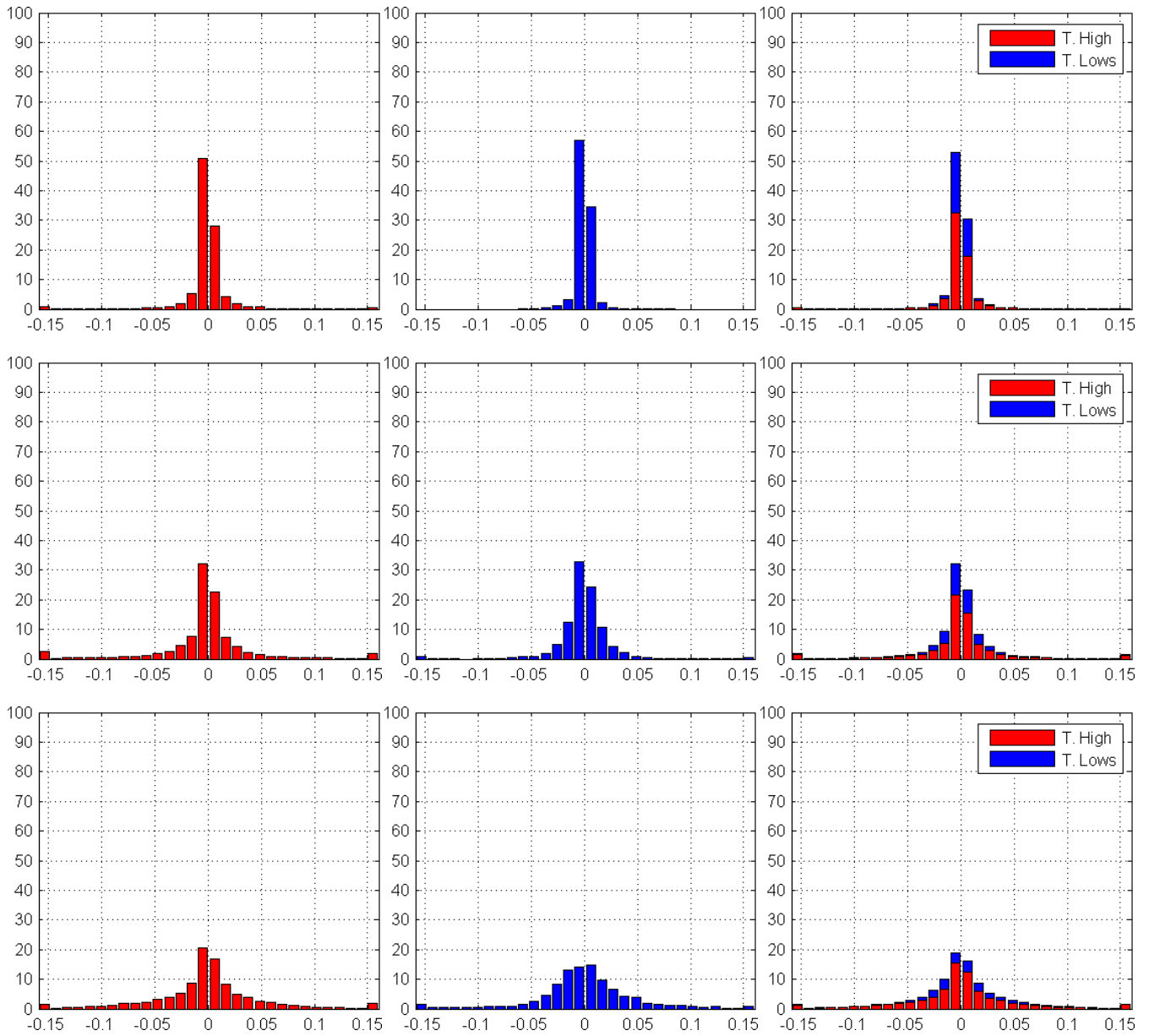


Figure 7.15. Distribution of normal velocity component for Q1–Q5 (rows, top to bottom) for topographic highs (marked as T. High) corresponding to the classes (+1)–(+4), topographic lows (marked as T. Lows) corresponding to the classes (-1)–(-4), and combined (columns, left to right). Horizontal and vertical axes correspond to normal velocity (m/s) and the percent values of topographic classes, respectively.

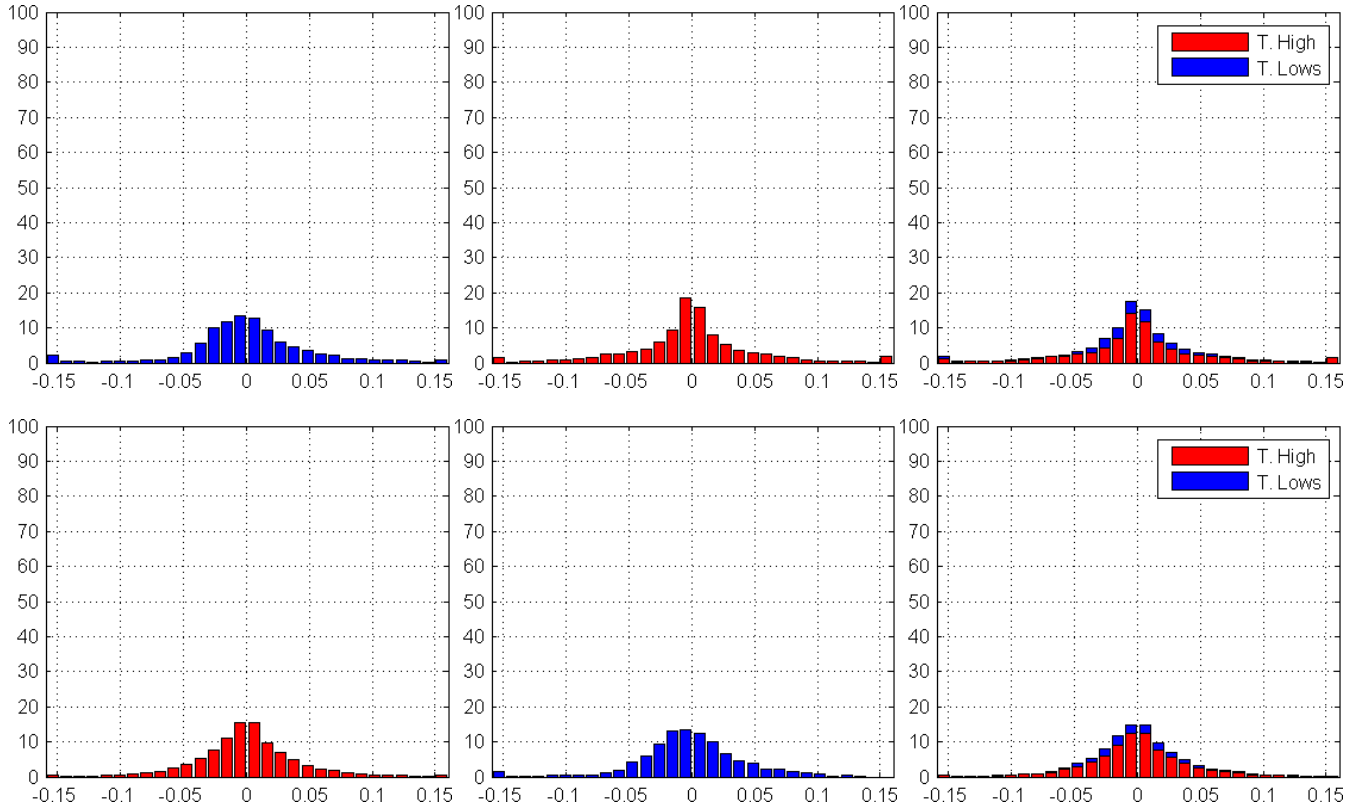


Figure 7.15 (cont'd). Distribution of normal velocity component for Q1–Q5 (rows, top to bottom) for topographic highs (marked as T. High) corresponding to the classes (+1)–(+4), topographic lows (marked as T. Lows) corresponding to the classes (-1)–(-4), and combined (columns, left to right). Horizontal and vertical axes correspond to normal velocity (m/s) and the percent values of topographic classes, respectively.

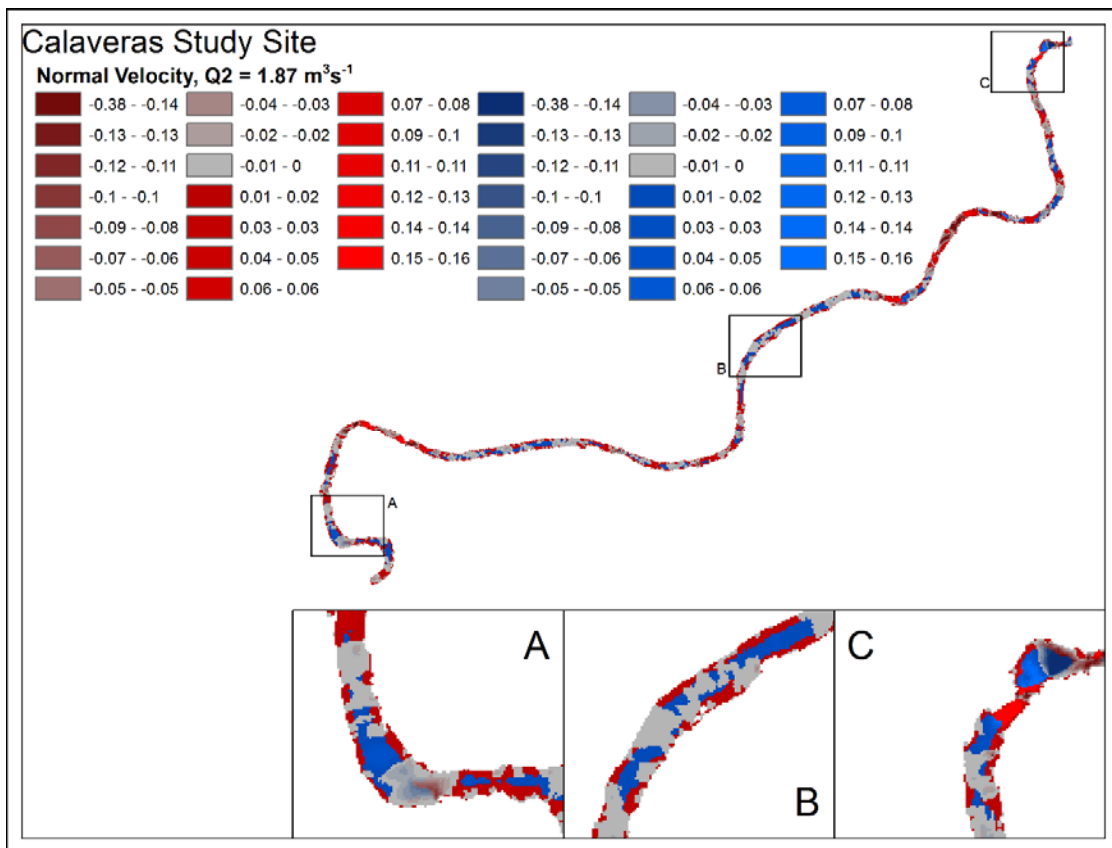
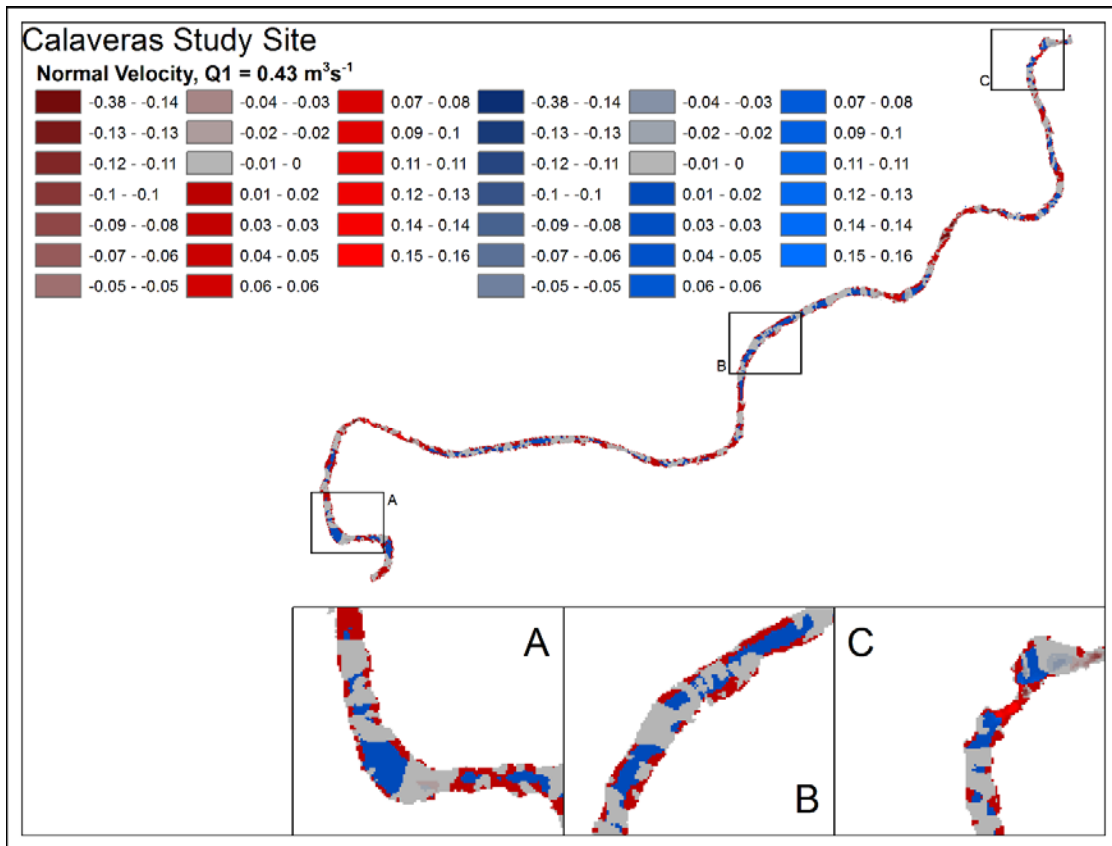


Figure 7.16. Spatial distribution of normal velocity (m/s) for Q1–Q5 for topographic highs (red colors) and lows (blue colors).

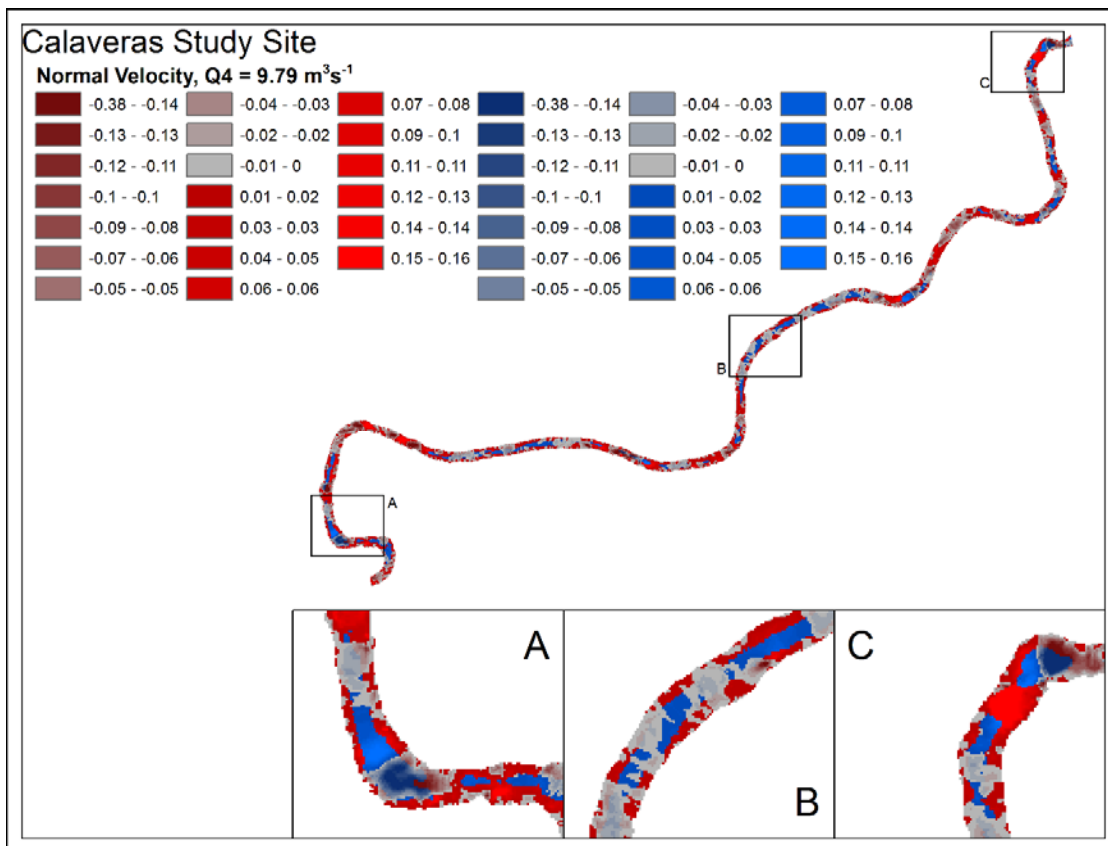
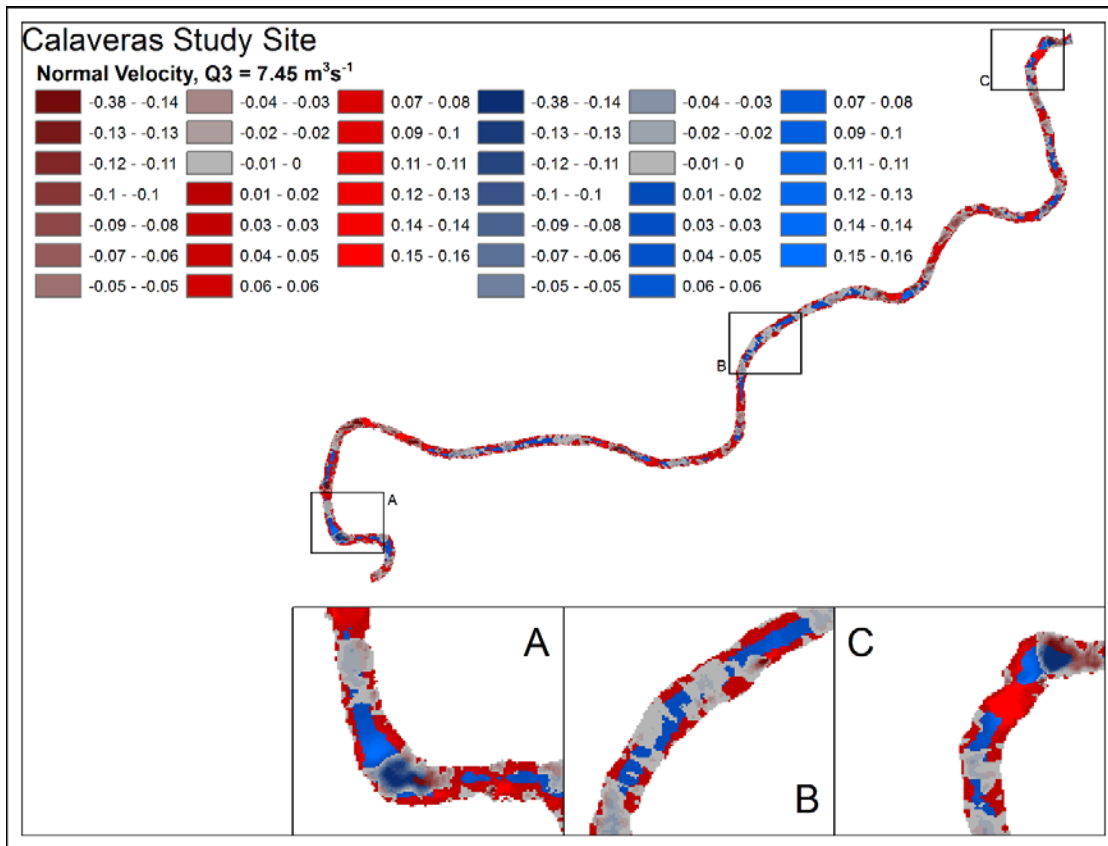


Figure 7.16 (cont'd). Spatial distribution of normal velocity (m/s) for Q1–Q5 for topographic highs (red colors) and lows (blue colors).

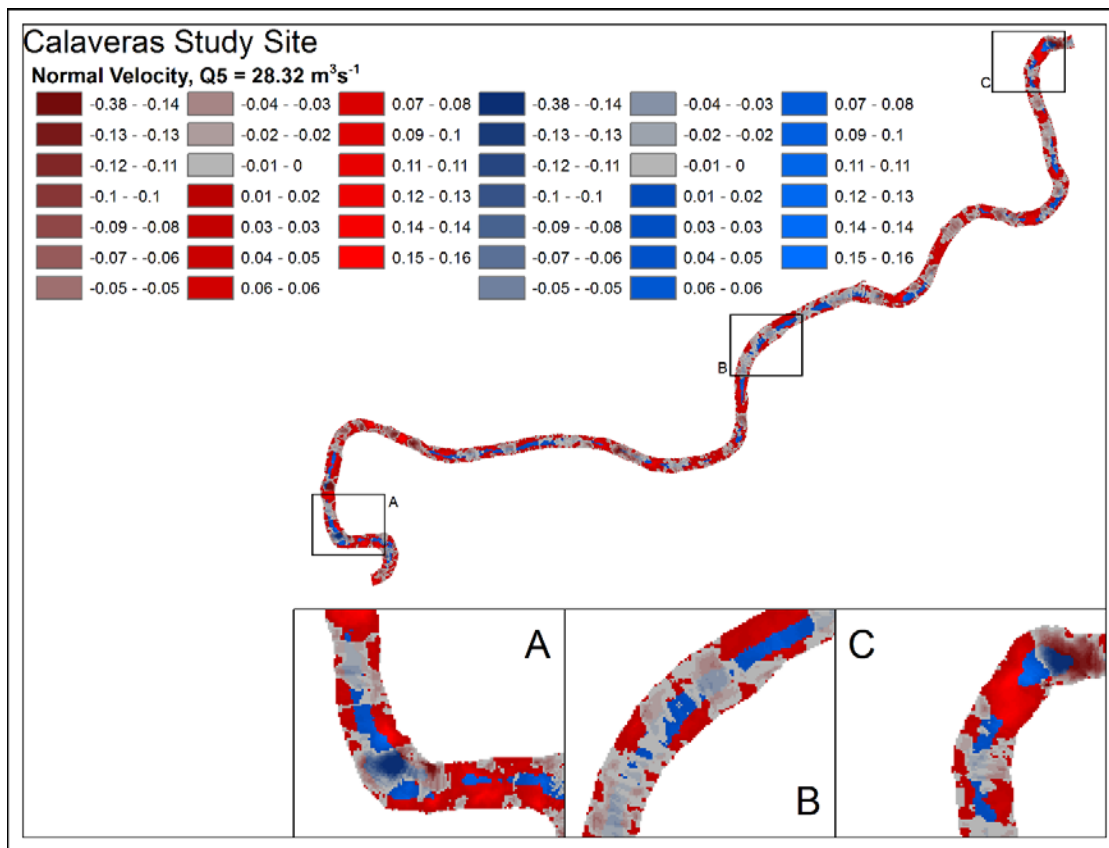


Figure 7.16 (cont'd). Spatial distribution of normal velocity (m/s) for Q1–Q5 for topographic highs (red colors) and lows (blue colors).

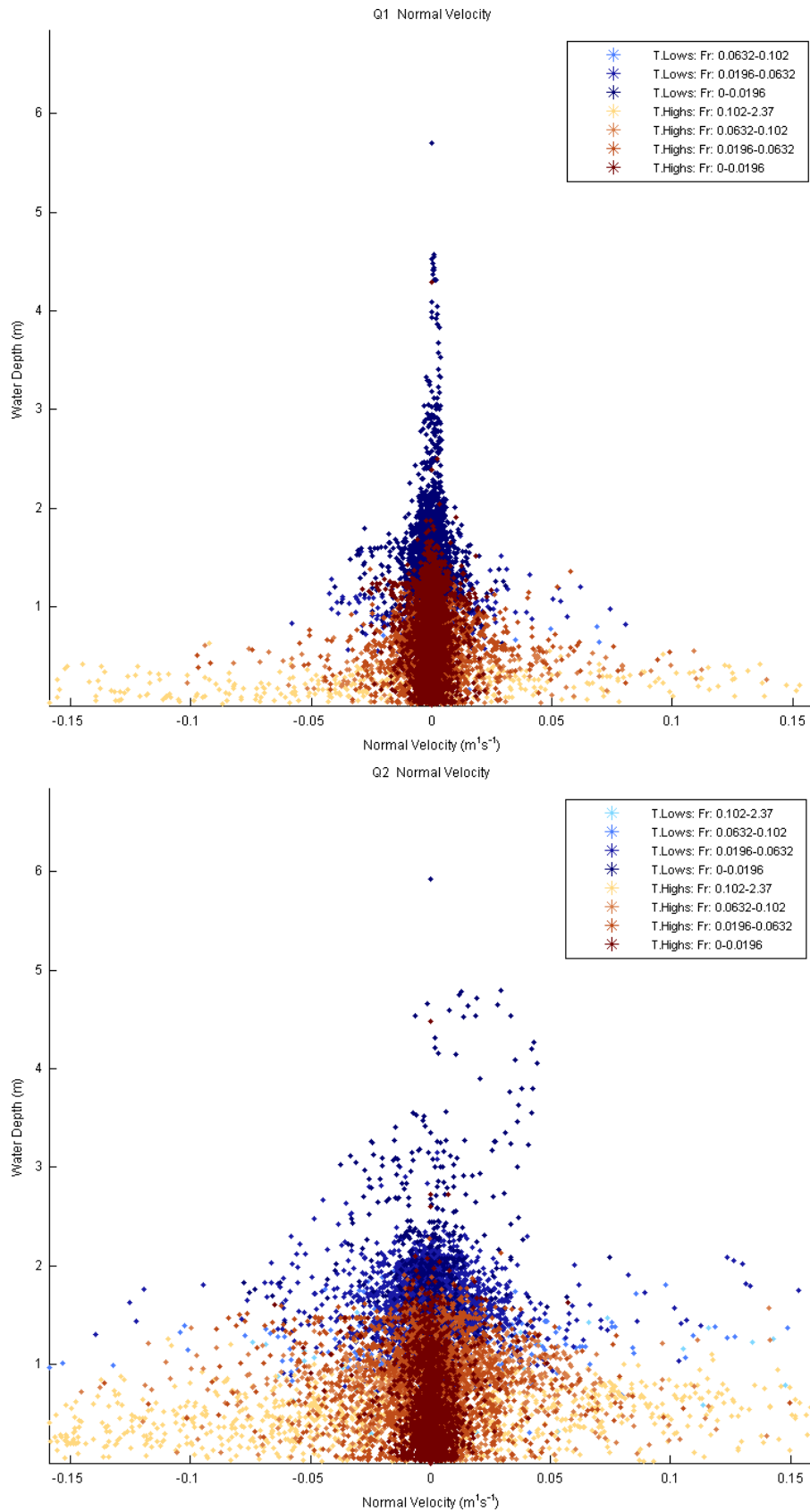


Figure 7.17. Distribution of normal velocity in relation to water depth for Q1–Q5 classified by topographic highs marked as T. Highs (brown colors), topographic lows marked as T. Lows (blue colors), and Froude number (Fr).

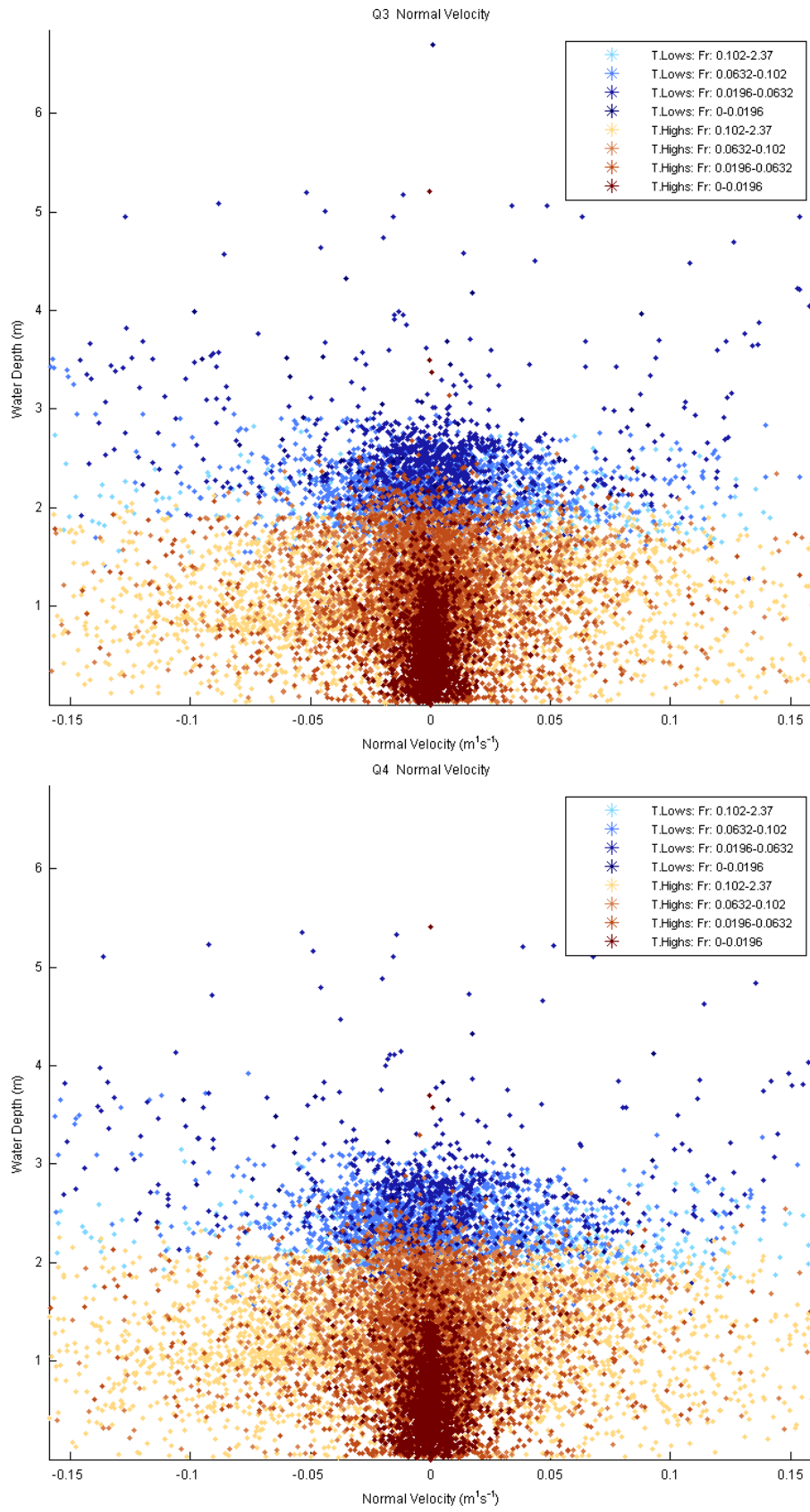


Figure 7.17 (con'td). Distribution of normal velocity in relation to water depth for Q1–Q5 classified by topographic highs marked as T. Highs (brown colors), topographic lows marked as T. Lows (blue colors), and Froude number (Fr).

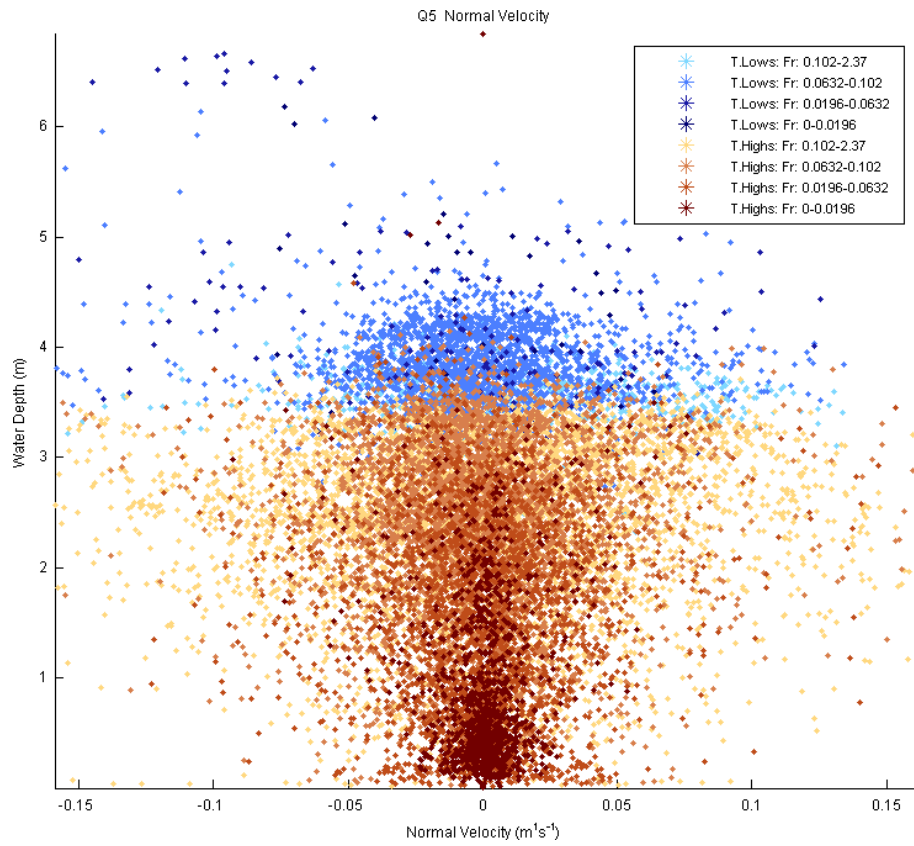


Figure 7.17 (cont'd). Distribution of normal velocity in relation to water depth for Q1–Q5 classified by topographic highs marked as T. Highs (brown colors), topographic lows marked as T. Lows (blue colors), and Froude number (Fr).

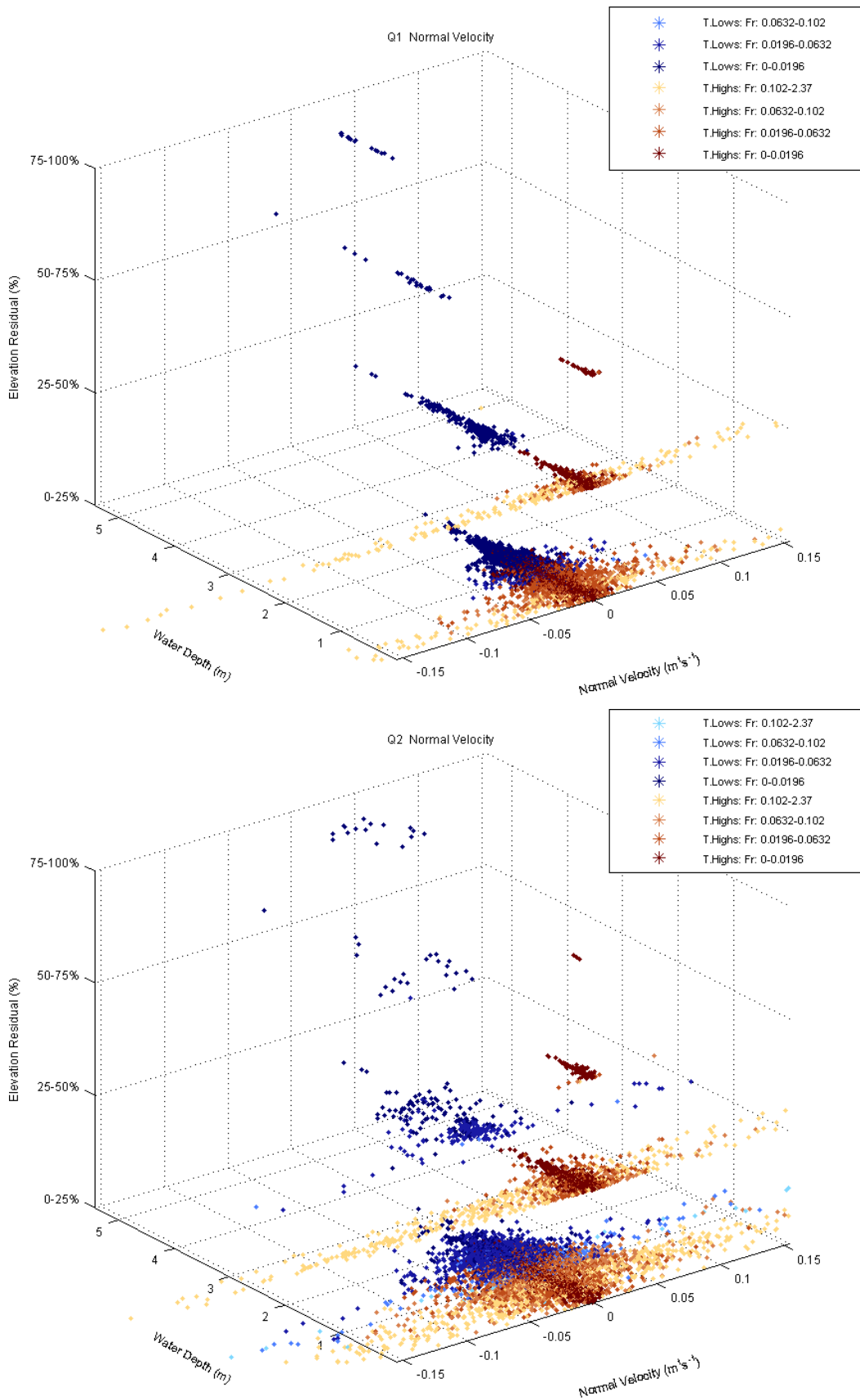


Figure 7.18. Distribution of normal velocity for topographic high (T. Highs)/low (T. Lows) subclasses (Figure 4.2) and Q1–Q5, classified by Froude number (Fr).

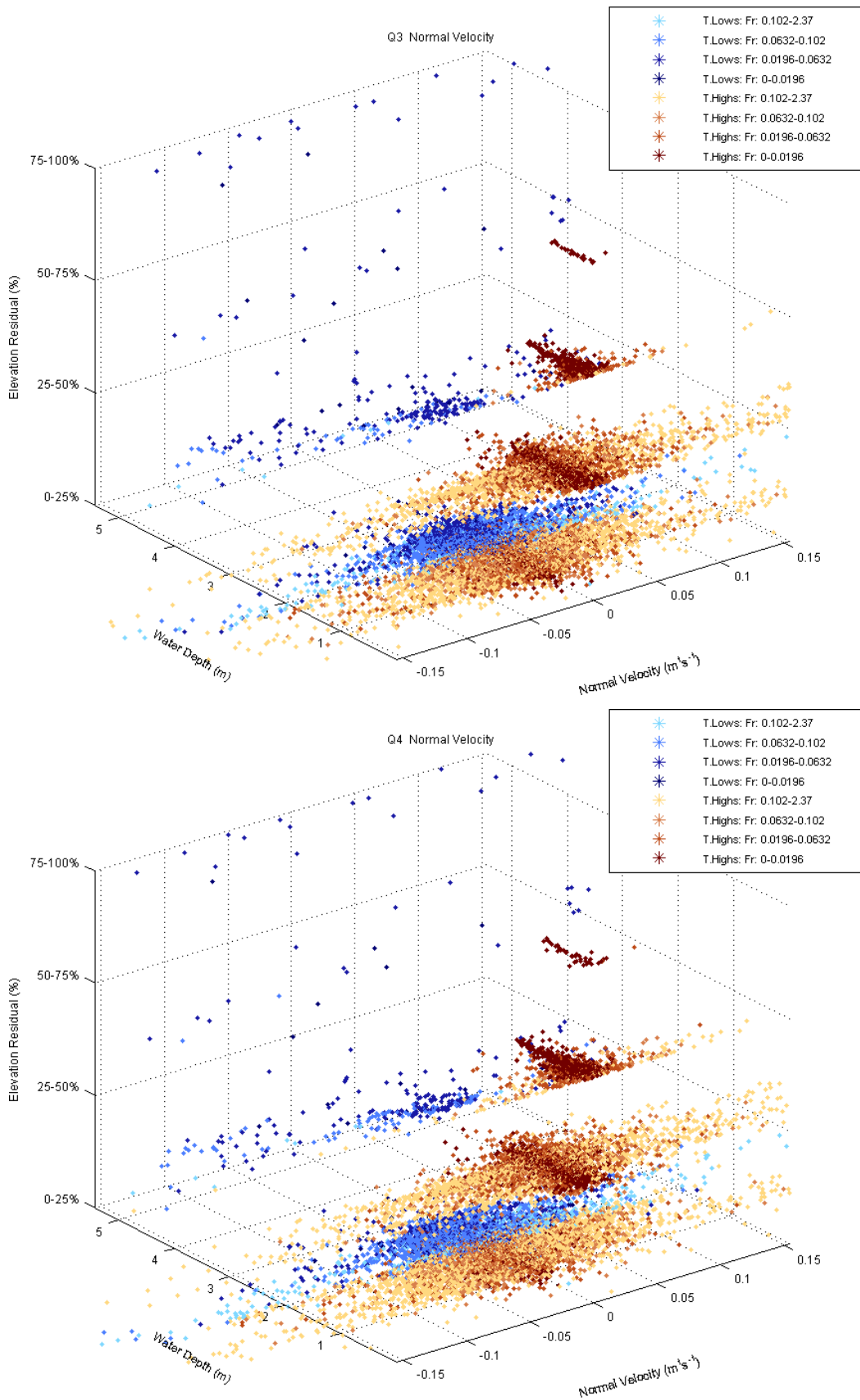


Figure 7.18 (cont'd). Distribution of normal velocity for topographic high (T. Highs)/low (T. Lows) subclasses (Figure 4.2) and Q1–Q5, classified by Froude number (Fr).

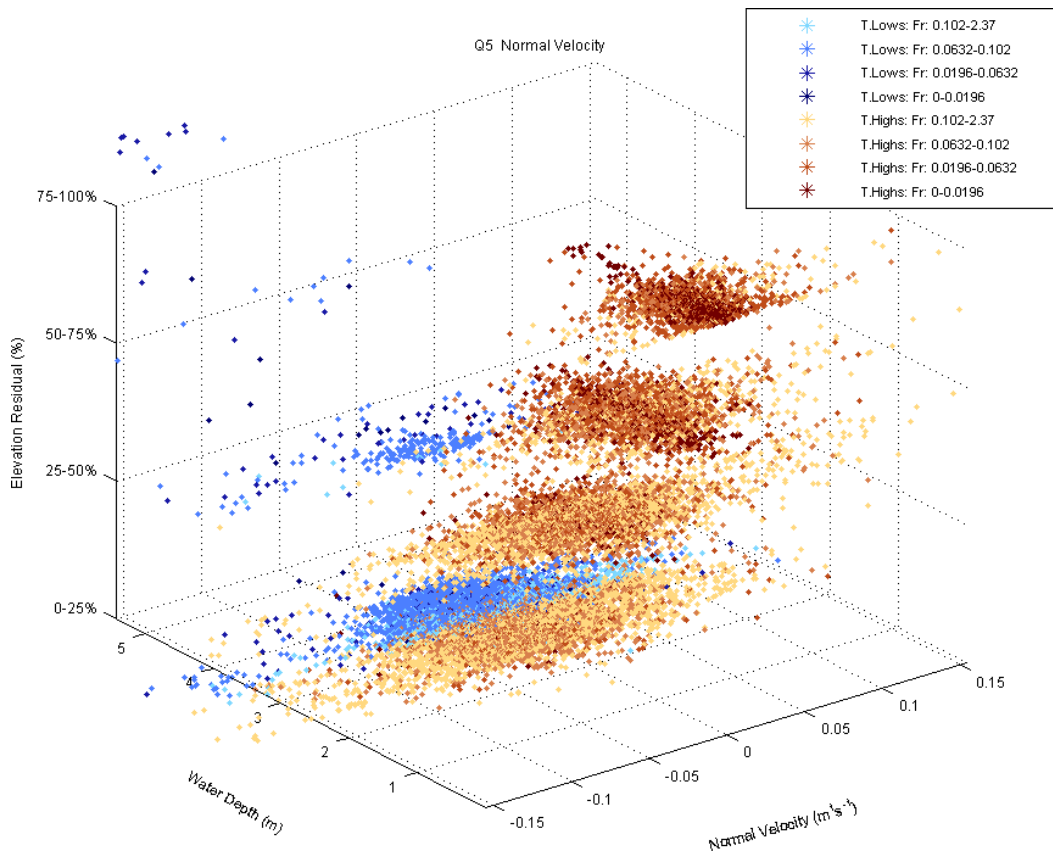


Figure 7.18 (cont'd). Distribution of normal velocity for topographic high (T. Highs)/low (T. Lows) subclasses (Figure 4.2) and Q1–Q5, classified by Froude number (Fr).

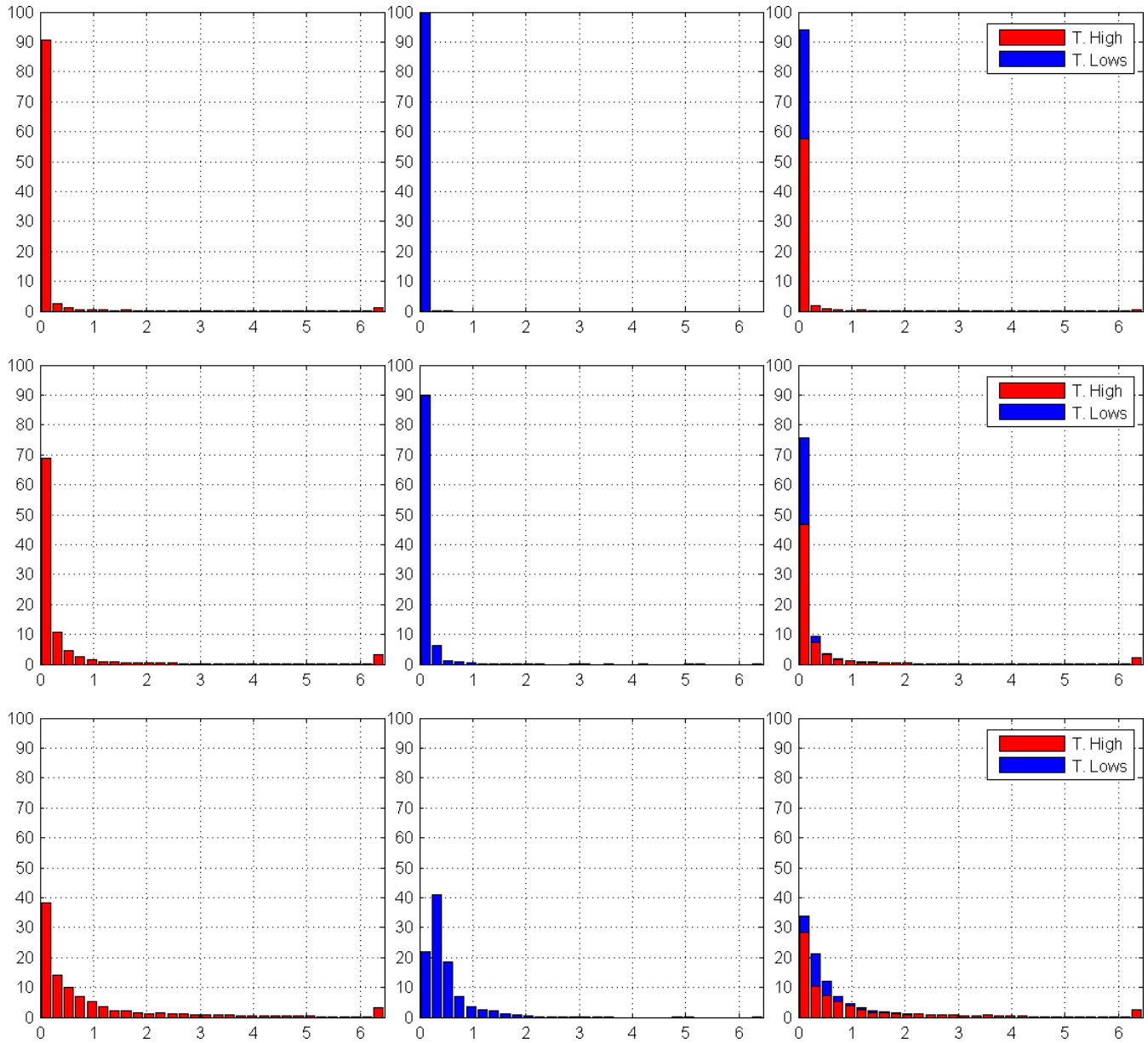


Figure 7.19. Distribution of shear stress for Q1–Q5 (rows, top to bottom) for topographic highs (marked as T. High) corresponding to the classes (+1)–(+4), topographic lows (marked as T. Lows) corresponding to the classes (-1)–(-4), and combined (columns, left to right). Horizontal and vertical axes correspond to shear stress ($\text{kg} \times \text{m/s}^2$) and the percent values of topographic classes, respectively.

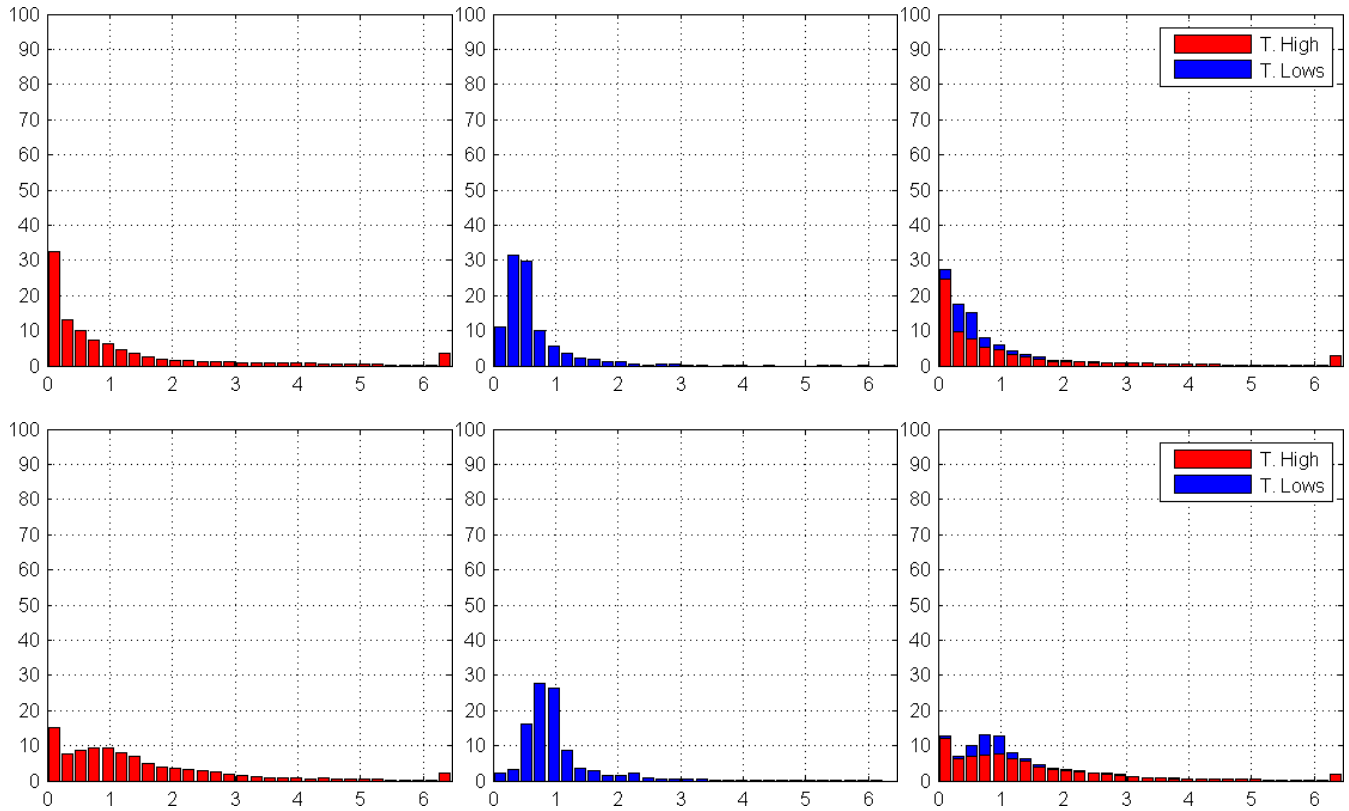


Figure 7.19 (cont'd). Distribution of shear stress for Q1–Q5 (rows, top to bottom) for topographic highs (marked as T. High) corresponding to the classes (+1)–(+4), topographic lows (marked as T. Lows) corresponding to the classes (-1)–(-4), and combined (columns, left to right). Horizontal and vertical axes correspond to shear stress ($\text{kg} \times \text{m/s}^2$) and the percent values of topographic classes, respectively.

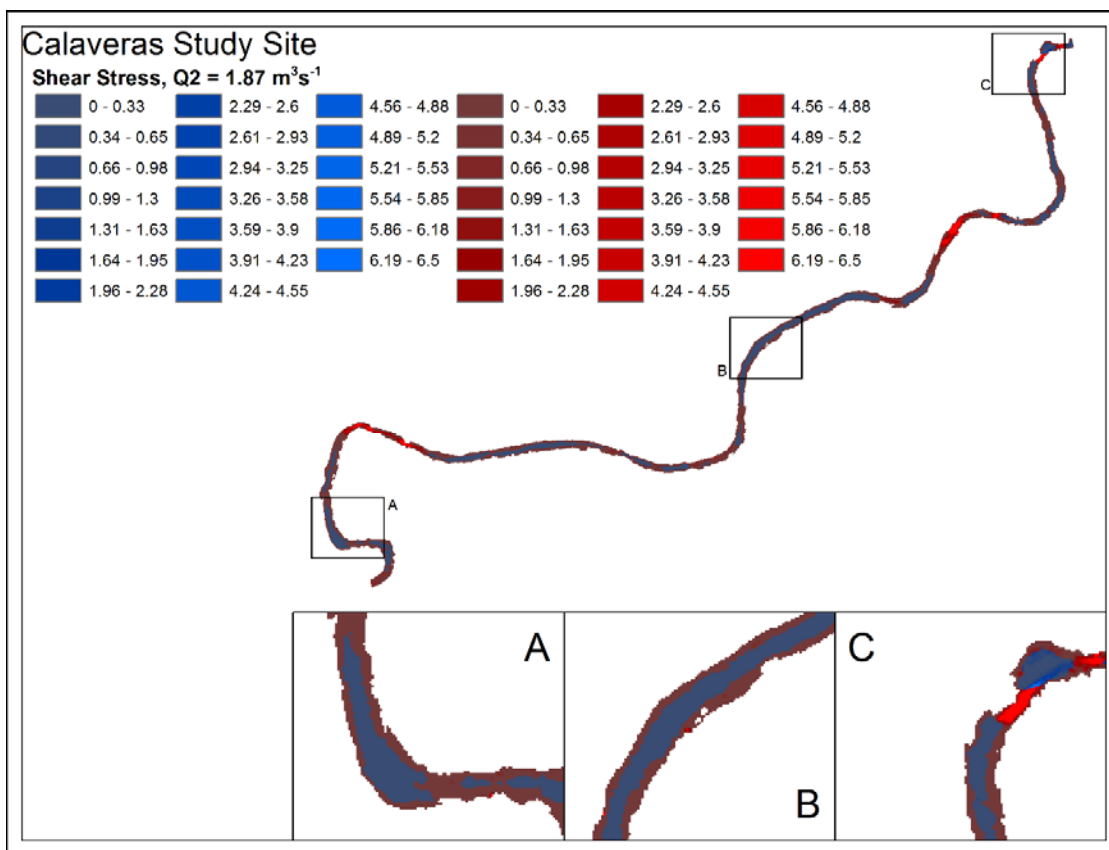
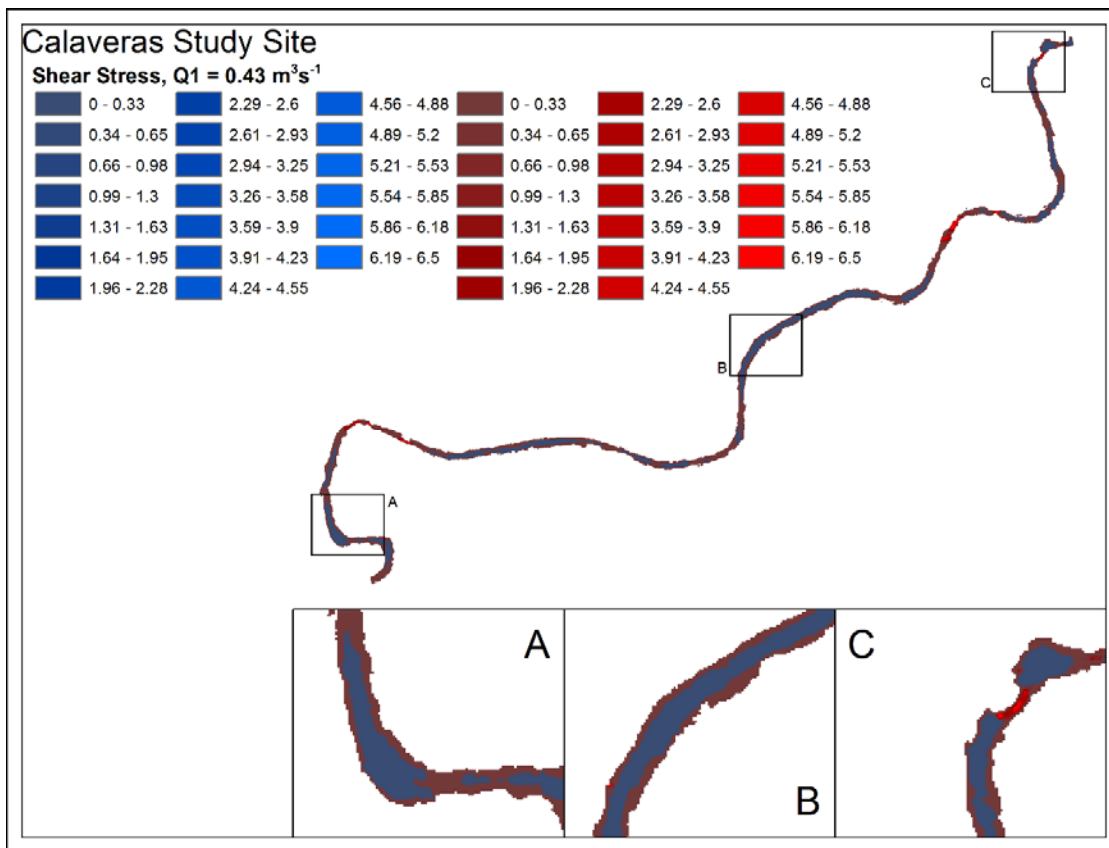


Figure 7.20. Spatial distribution of shear stress ($\text{kg} \times \text{m}^2/\text{s}^2$) for Q_1 – Q_5 for topographic highs (red colors) and lows (blue colors).

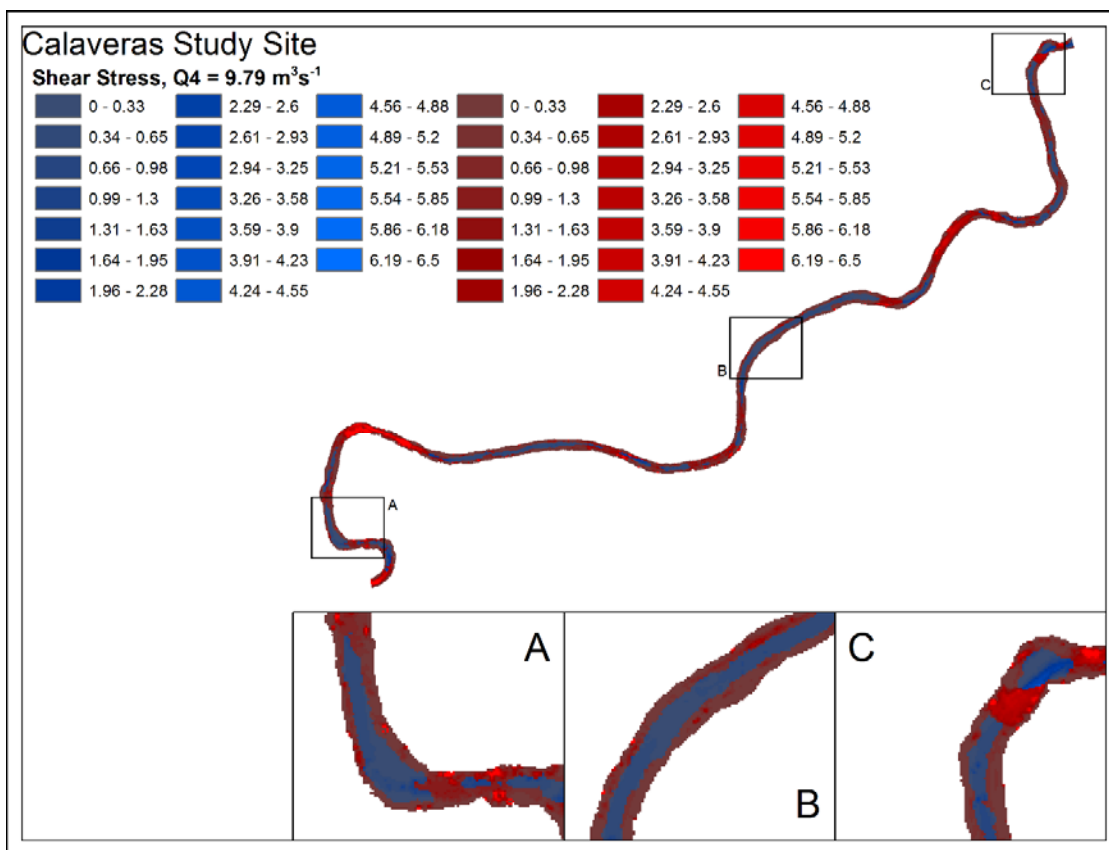
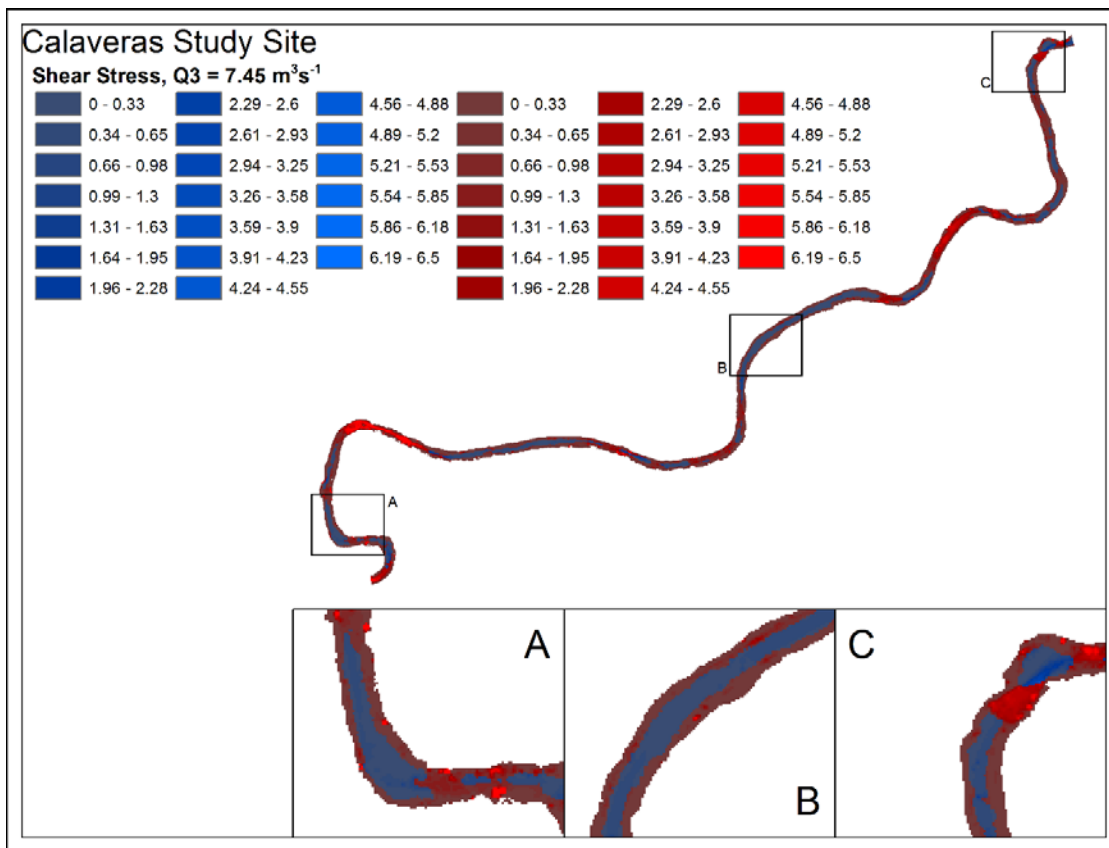


Figure 7.20 (cont'd). Spatial distribution of shear stress ($\text{kg} \times \text{m/s}^2$) for Q1–Q5 for topographic highs (red colors) and lows (blue colors).

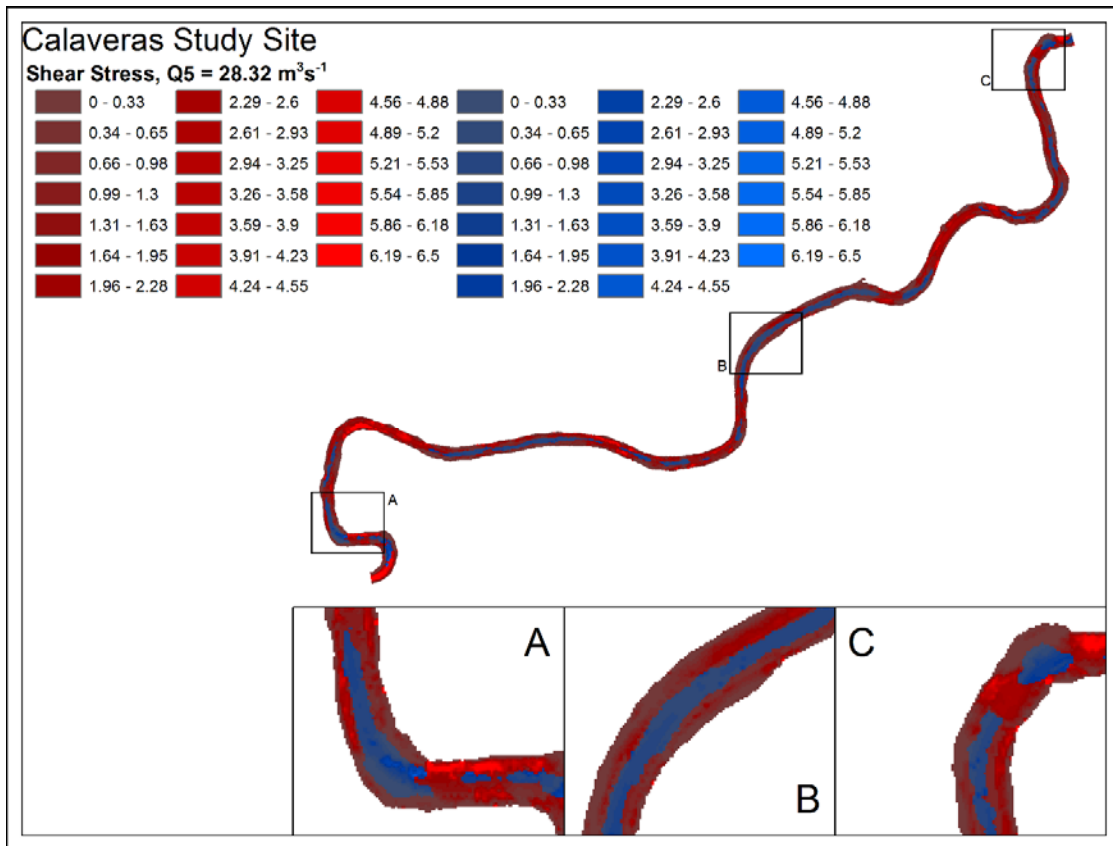


Figure 7.20 (cont'd) Spatial distribution of shear stress ($\text{kg} \times \text{m/s}^2$) for Q1–Q5 for topographic highs (red colors) and lows (blue colors).

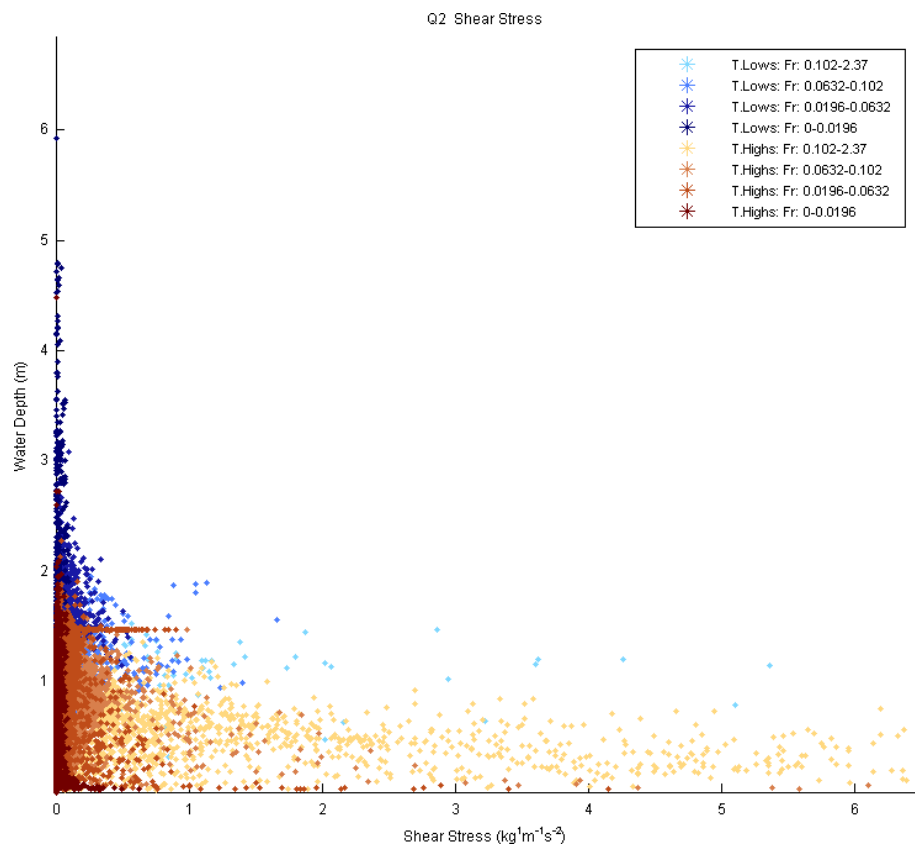
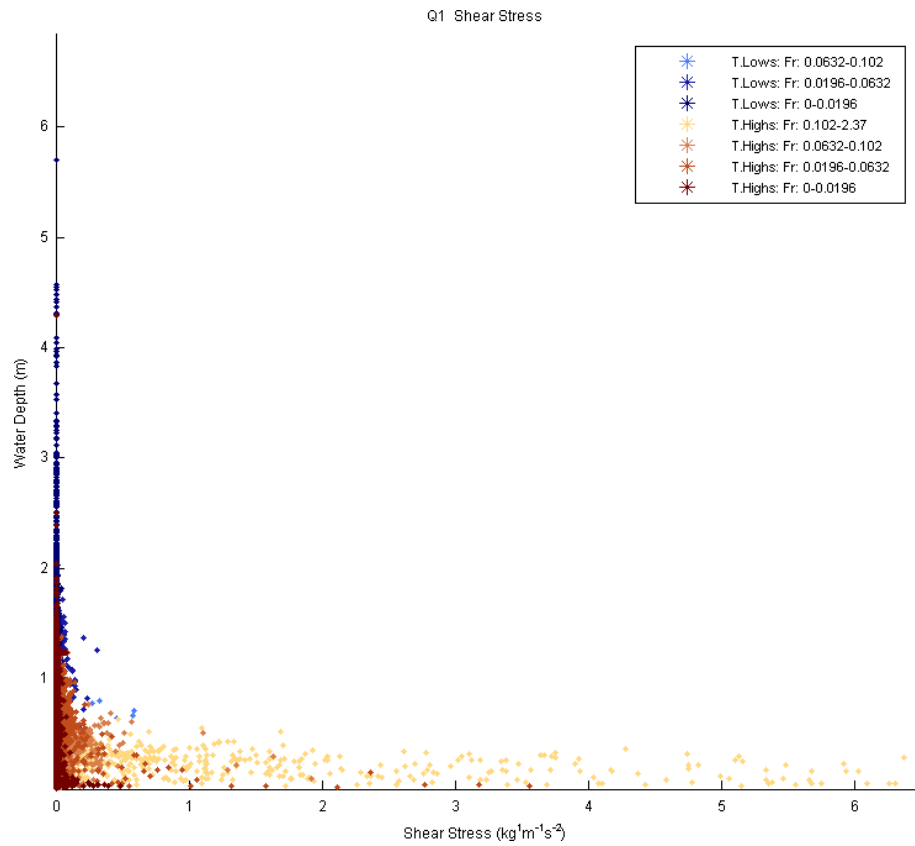


Figure 7.21. Distribution of shear stress in relation to water depth for Q1–Q5 classified by topographic highs marked as T. Highs (brown colors) and topographic lows marked as T. Lows (blue colors) and Froude number (Fr).

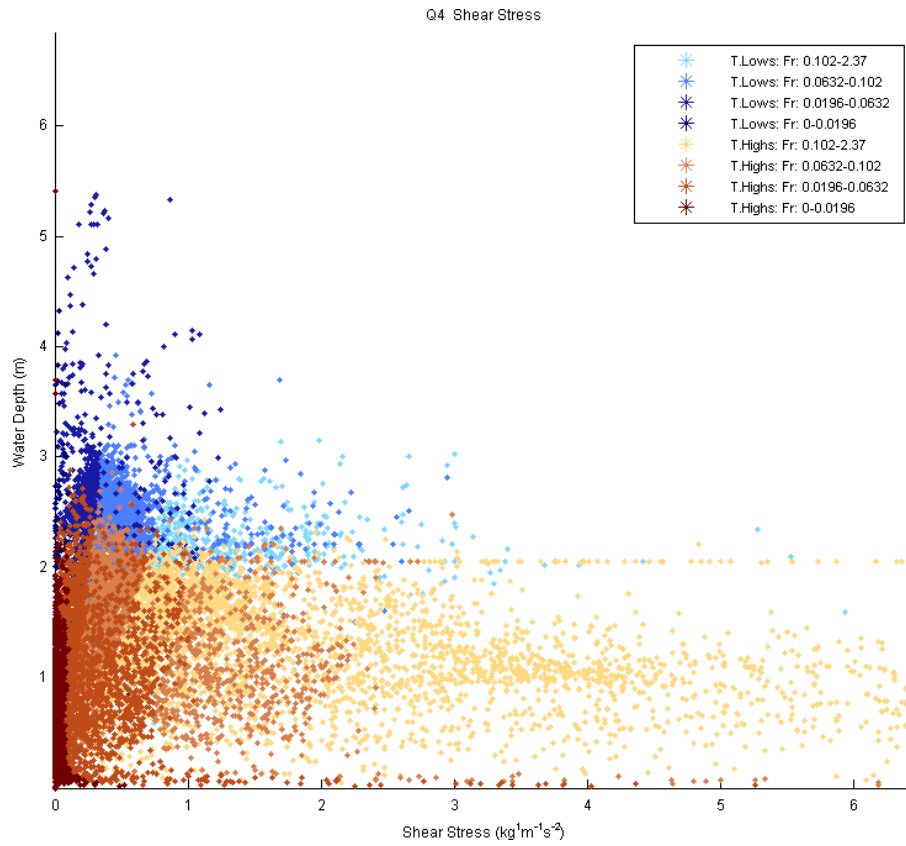
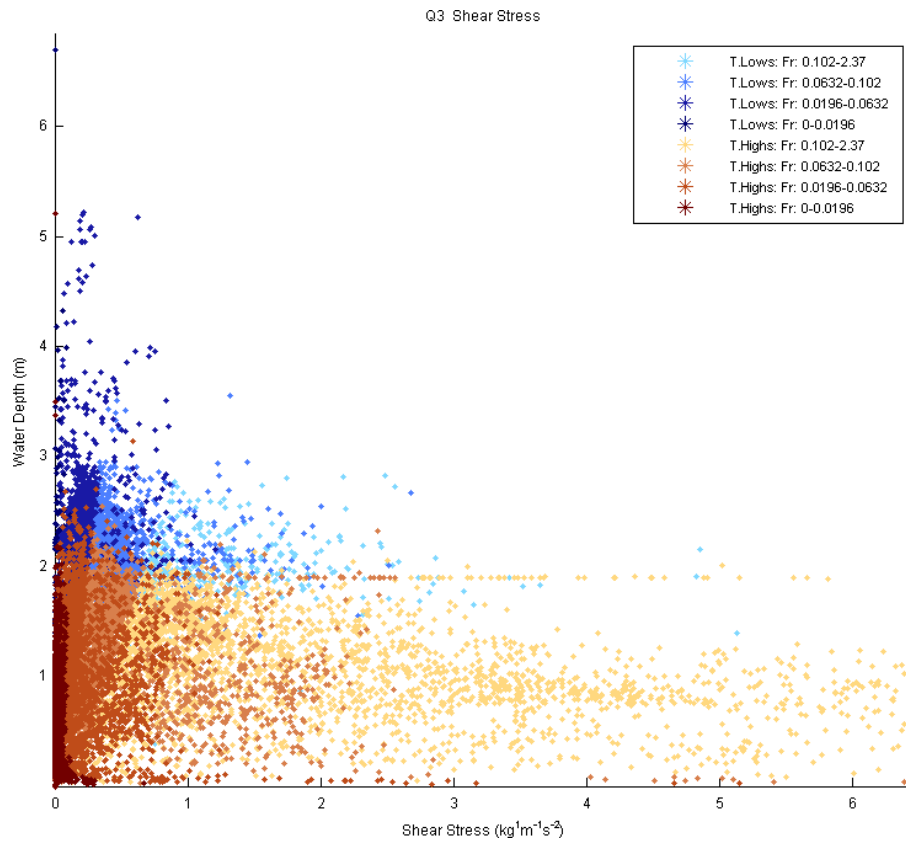


Figure 7.21 (cont'd). Distribution of shear stress in relation to water depth for Q1–Q5 classified by topographic highs marked as T. Highs (brown colors) and topographic lows marked as T. Lows (blue colors) and Froude number (Fr).

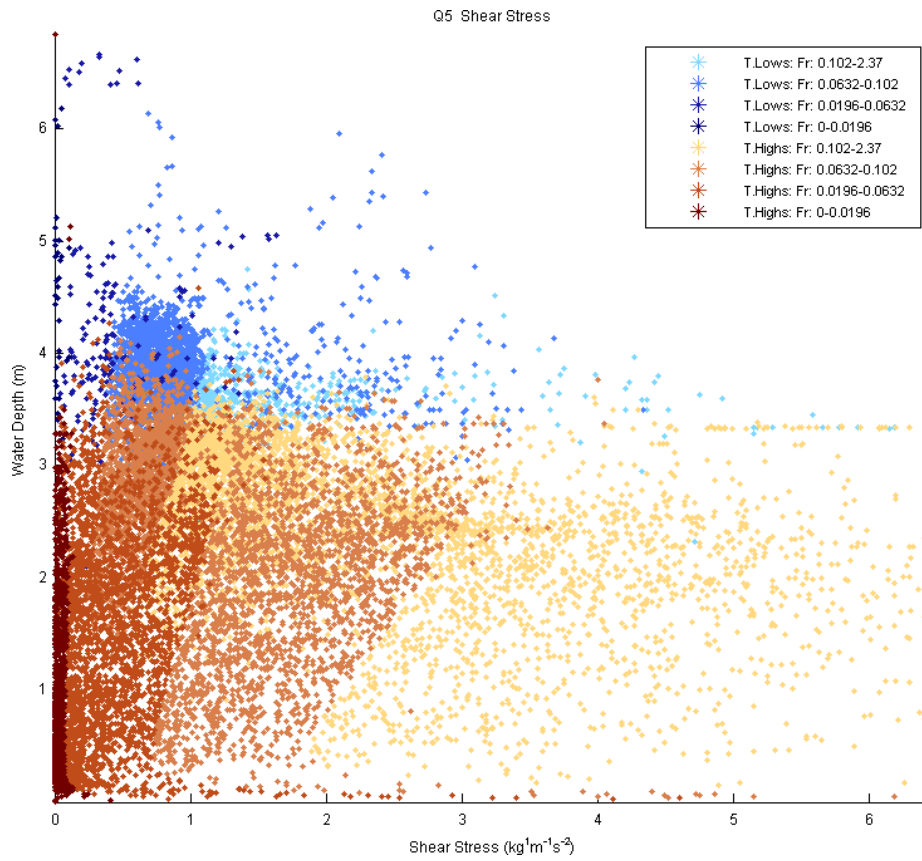


Figure 7.21 (cont'd). Distribution of shear stress in relation to water depth for Q1–Q5 classified by topographic highs marked as T. Highs (brown colors) and topographic lows marked as T. Lows (blue colors) and Froude number (Fr).

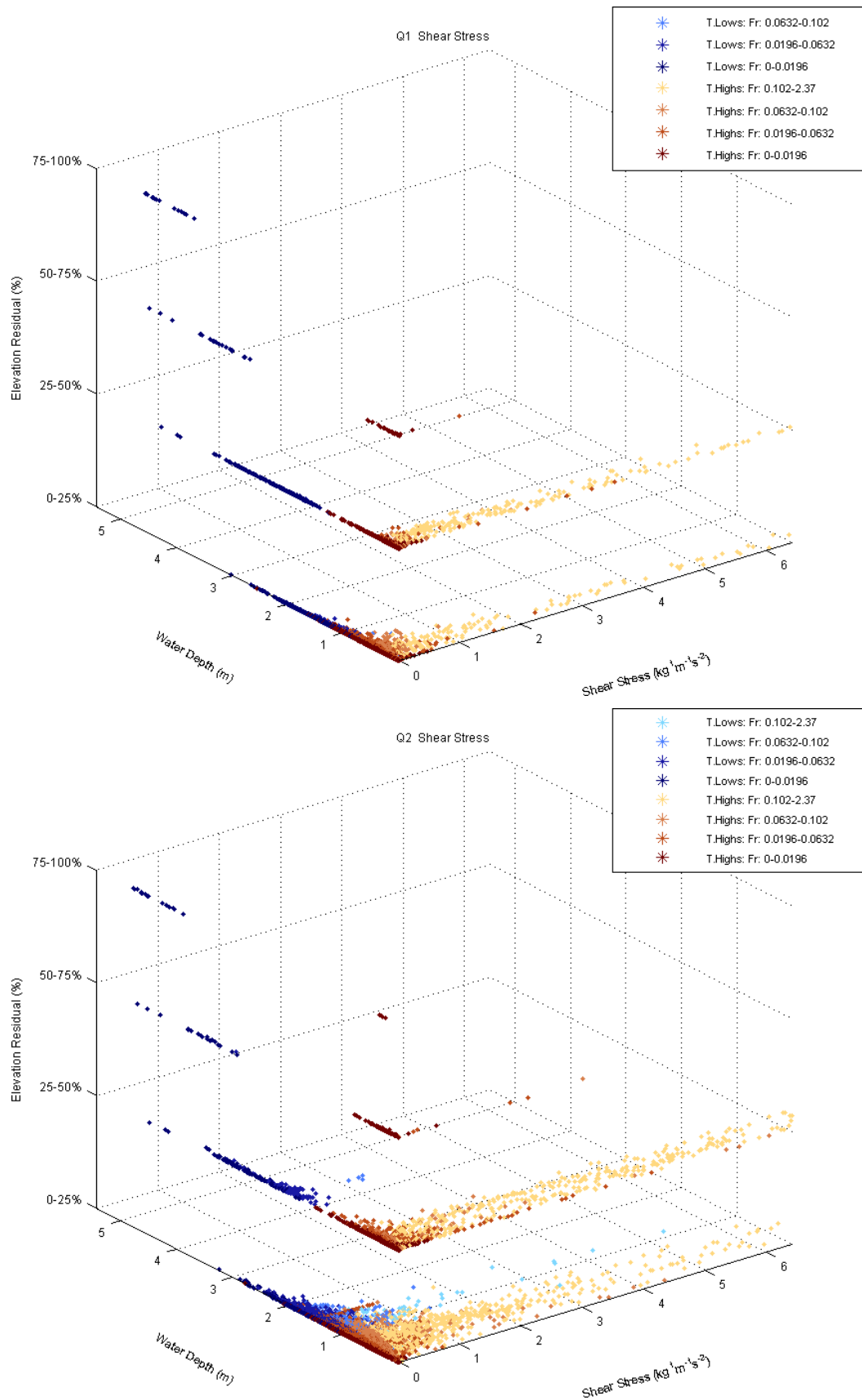


Figure 7.22. Distribution of shear stress for topographic high (T. Highs)/low (T. Lows) subclasses (Figure 4.2) and Q1–Q5, classified by Froude number (Fr).

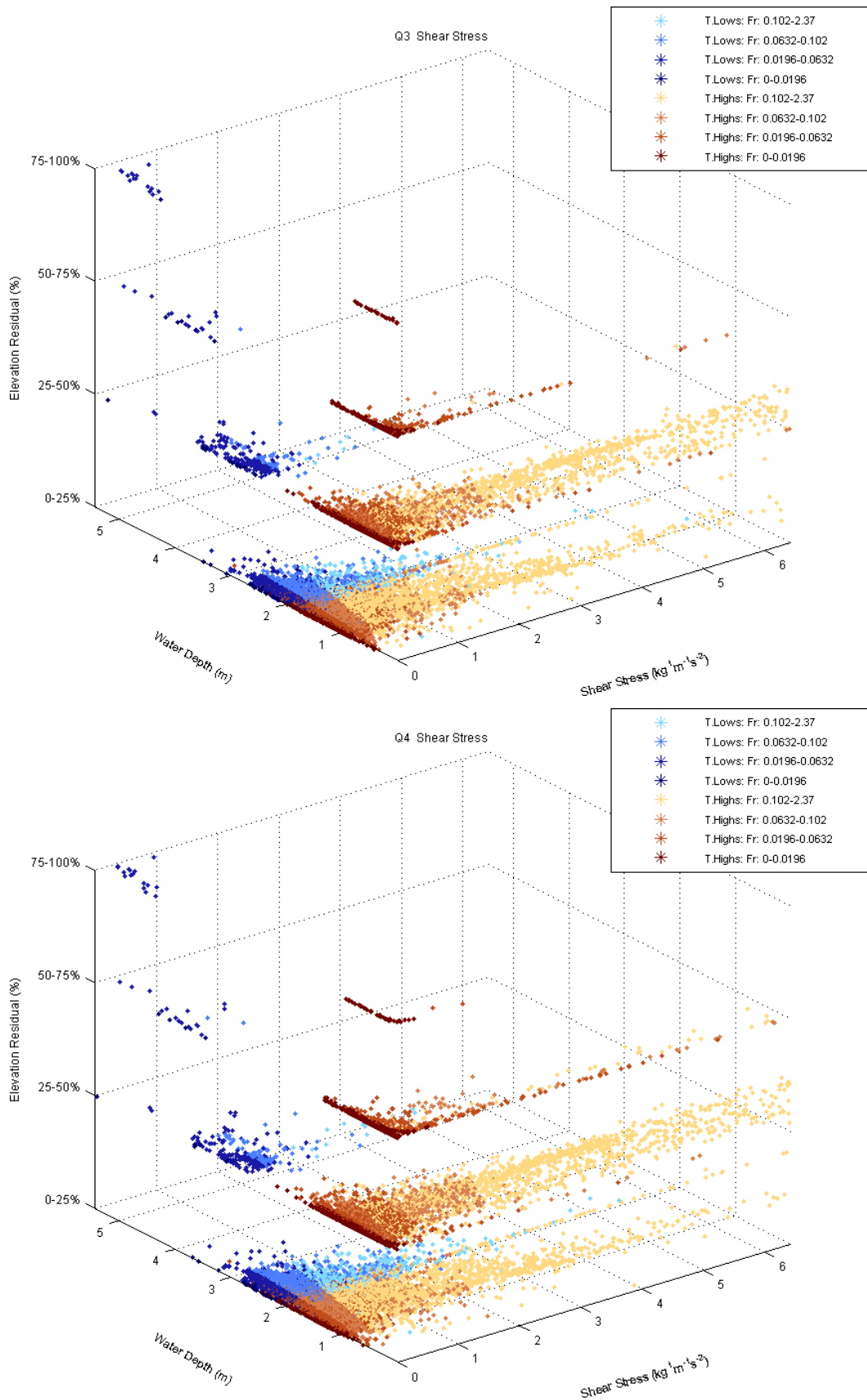


Figure 7.22 (cont'd). Distribution of shear stress for topographic high (T. Highs)/low (T. Lows) subclasses (Figure 4.2) and Q1–Q5, classified by Froude number (Fr).

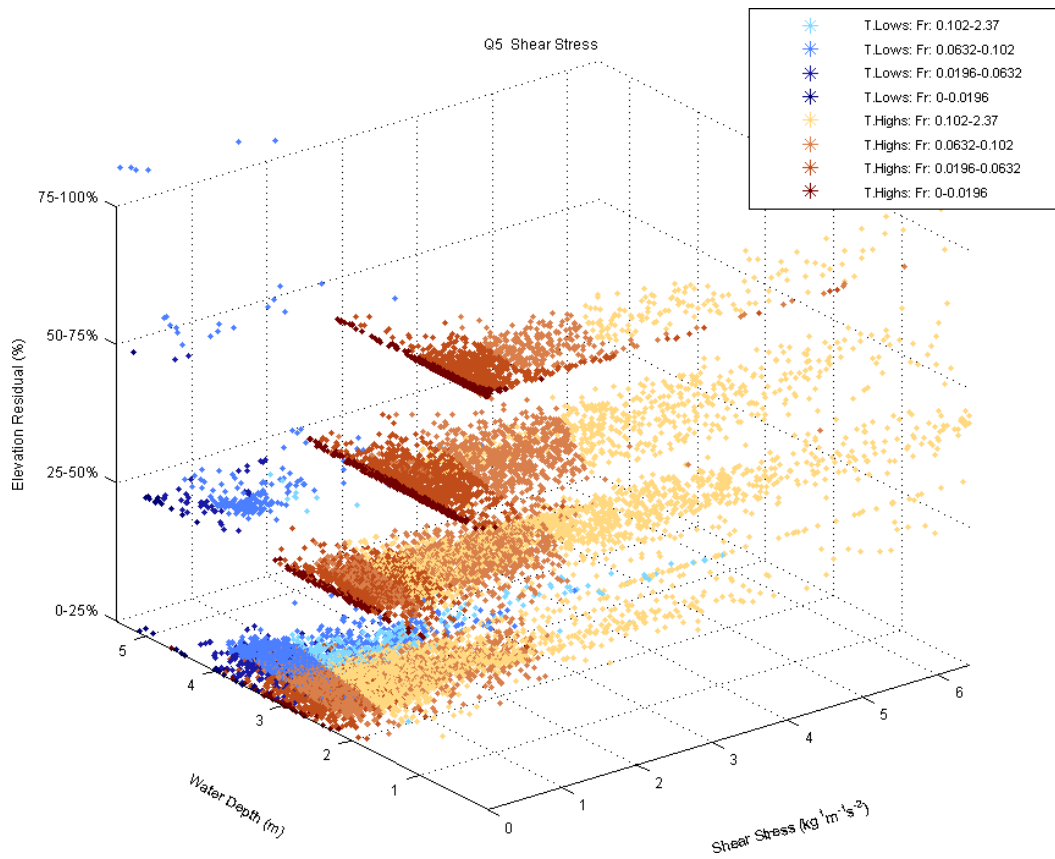


Figure 7.22 (cont'd). Distribution of shear stress for topographic high (T. Highs)/low (T. Lows) subclasses (Figure 4.2) and Q1–Q5, classified by Froude number (Fr).

8. THE CIBOLO STUDY REACH

The Cibolo study reach (Figure 8.1) is one of the study sites on the Lower Cibolo Creek (LCC) (Figure 3.3). This reach is located on the LCC Segment 2 and Reach 10 (Figures 3.1–3.2; TIFP, 2011, 2012).

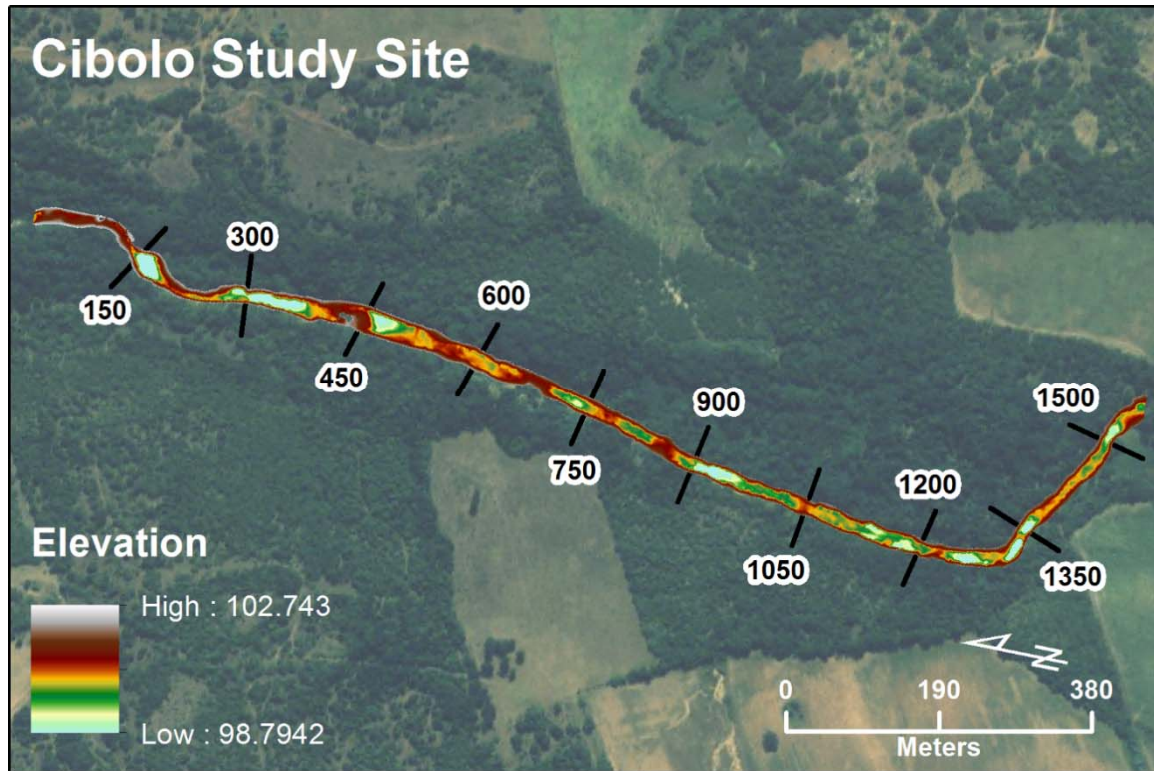


Figure 8.1. The Cibolo study reach on the LCC and its bathymetric distribution.

8.1. GEOMORPHIC CHARACTERISTICS

To determine the geomorphic characteristics of river channel at the Cibolo reach, we utilized detrended channel topography. We detrended the topographic data, including the bathymetry, of the Cibolo reach using the approach discussed in detail in *Section 4.1* (Figure 4.2). Next, we determined the geomorphic unit classes as topographic highs (sediment bars/riffles/edges) and topographic lows (pools) from the topographic residuals. We subclassified the topographic highs and lows according to the quartiles of the detrended topographic elevations (i.e., geomorphic unit classes named as (+1)–(+4) for topographic highs and (-1)–(-4) for topographic lows, respectively; Figures 4.2 and 8.2).

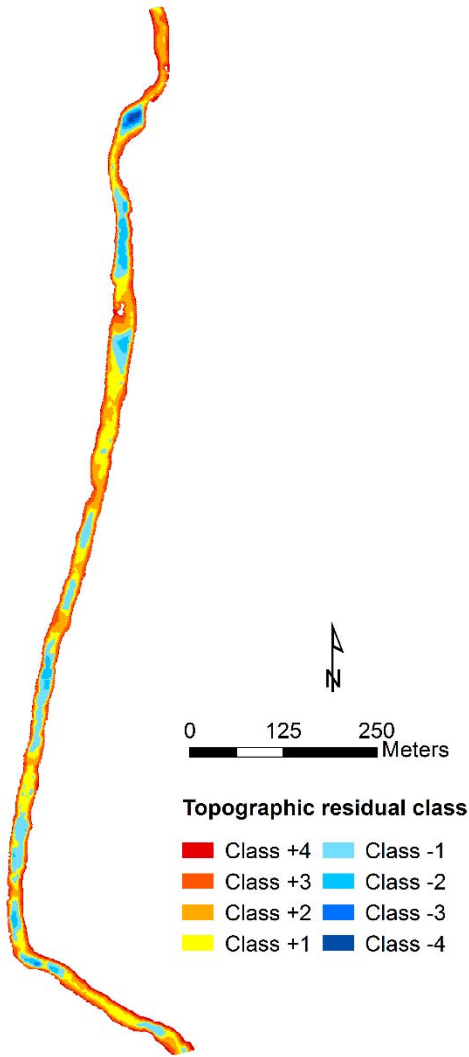


Figure 8.2. Geomorphic unit classes for the Cibolo study reach based on the topographic residuals. The (+) classes represent the topographic highs and (-) classes represent topographic lows. Detailed class descriptions are given in Figure 4.2. Flow direction is from top to bottom.

The Cibolo reach features a study reach that is approximately 1.50 kilometers long (Figure 8.1). For the Cibolo, the regions of topographic lows alternate with bounding regions of topographic highs (Figure 8.2). Local regions of interest include the round and constricted topographically low region located 75 meters upstream and downstream of meter marker 150, the constricted region at meter marker 450, and the constricted region between meter marker 600 and 750 (Figure 8.1).

The distribution of geomorphic unit classes indicates that the reach dominated by topographic highs (sediment bars/riffles/edges), corresponding to the classes (+1)–(+4) and

account for nearly 77% of the reach (Table 8.1). The remaining (23%) of the study area are composed of topographic lows (pools, corresponding to the classes (-1)–(-4); Table 5.2, Figures 5.2 and 5.3). The largest regions of topographic lows are larger and more closely packed around the north influent end of the site (Figure 8.2)..

Table 8.1. Areal distribution of geomorphic unit classes in the Cibolo study reach.

Geomorphic Unit Class (Topographic residual percentile)	Total area (m ²)	Percent coverage (%)	Patch Statistics					
			Mean area (m ²)	Min area (m ²)	Max area (m ²)	StDev (m ²)	Patches (Number)	
Topo Highs (bars/riffles/ edges)	+4 (75-100th)	3448	9.6	6.91	1	502	28.27	499
	+3 (50-75th)	7849	21.86	140.16	1	1554	314.2	56
	+2 (25-50th)	8017	22.32	36.61	1	2520	196.65	219
	+1 (0-25th)	8231	22.92	39	1	1160	143.67	211
Topo Lows (pools)	-1 (0-25th)	6229	17.35	168.35	1	977	278.43	37
	-2 (25-50th)	1805	5.03	164.09	2	622	175.82	11
	-3 (50-75th)	208	0.58	104	26	182	104	78
	-4 (75-100th)	125	0.35	125	125	125	0	1

Total area: Total area of a specific class (m²).

Percent (%) coverage: Percentage of the area of a specific class within the total area (%).

Geomorphic Unit Class Patch statistics:

Mean area: Average patch area of individual patches within a class (m²).

Minimum area: Minimum patch area within a specific class (m²).

Maximum area: Maximum patch area within a specific class (m²).

STDev: Standard deviation of patch areas around the mean within a specific class (m²).

Patches: Number of separate patches for each class (Number).

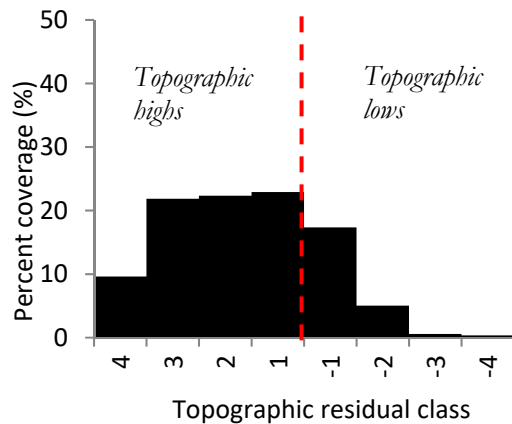


Figure 8.3. . Percent coverage of geomorphic unit classes for the Cibolo study reach. The (+) classes represent the topographic highs and (-) classes represent topographic lows. Detailed class descriptions are given in Figure 4.2.

Spatially, the distributions of topographic highs and lows are patchy (Figure 8.2, Table 8.1). Basic patch statistics show that topographic high classes of +2 has the highest range (1-2520 m²) between its patch sizes (in terms of area, with a mean of 36.61 m² and a STDev of 196.65 m, which is followed by topographic highs class +3 (Table 8.1) In addition,

topographically the shallowest pool class -1 has the greatest range of patch sizes (1-977 m²), with a mean of 168.35 m² and STDev of 278.43 m, which is closely followed by the topographic low class of -2 (Table 8.1).

8.2. RELATIONSHIPS BETWEEN GEOMORPHIC UNITS AND HYDRAULIC PROPERTIES

We examined the relationships between geomorphic units (Figure 4.2) and the hydraulic properties of the reach. We obtained these hydraulic properties from the simulations performed using River2D® model developed for the study reach (TIFP and SARA, 2011) at six different discharge conditions, Q1–Q5. Three of these modeled discharges, low, medium, and high discharges (Q2, Q3, and Q4, respectively) correspond to the base level discharges defined as dry, normal, and wet conditions (Table 8.2). Table 8.2 presents the information on the study reach and model input parameters for River2D® models.

Table 8.2. Information on the Cibolo study reach and model input parameters for River2D® model.

Class	Discharge for base levels		Modeled discharge		Field reported discharge		Assessment of field Q	Field data collection date	Type of field data
	(m ³ /s)	(cfs)	(m ³ /s)	(cfs)	(m ³ /s)	(cfs)			
			0.05	2	–	–	Q1 (<Q2)	–	–
Dry	0.42	15	0.45	16	0.40	14	Low (Q2)	7/21/2009	Habitat**
Normal	0.71	25	1.33	47	1.25	44	Medium (Q3)	8/25/2010	Habitat
Wet	1.13	40	1.79	63	2.01	71	High (Q4)	11/10/2009	Habitat
			4.25	150	–	–	Q5 (>Q4)	–	–

*Base levels are defined by observing fish habitat weighted usable area (WUA) (River2D) (TIFP, 2011; pg. 71,

http://www.twdb.state.tx.us/surfacewater/flows/instream/lower_san_antonio/doc/LSAR_FINAL_INTE RIM_REPORT_20110831.pdf)

Dry: typically based on minimum to get 20% habitat available for each guild.

Average: typically based on flow to get at least 50% habitat available for each guild.

Wet: typically based on analysis of WUA for habitat degradation.

The largest increase in inundated area corresponds to discharge level Q1 (Figure 8.4). The inundated area versus flow stage/Q relationship presents one distinct breakpoint, right at Q2. The slope of the relationship is lower between Q2 and Q5, where the latter corresponds to the wet base level conditions (Figure 8.3).

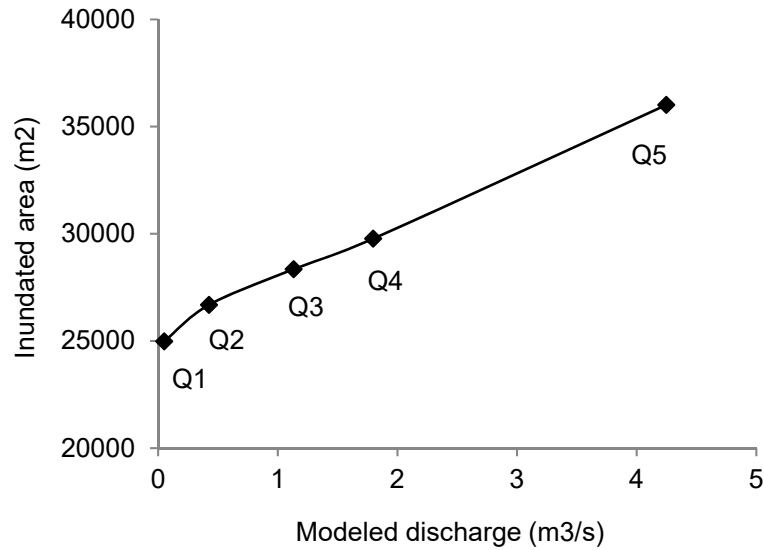


Figure 8.4. Inundated area (m²) vs. modeled discharge (m³/s) for the Cibolo study reach.

Table 8.3 summarizes the minimum and maximum values of these variables obtained from River2D® models for each discharge condition, from Q1 to Q5 (Table 8.2).

Table 8.3. Summary of River2D® model output parameters for Cibolo and min-max values for modeled discharges, Q1–Q5 (Table 8.2).

Model output parameters	Modeled discharge $\begin{pmatrix} \text{min} \\ \text{max} \end{pmatrix}$					
	Q1	Q2	Q3	Q4	Q5	Q6
Water depth (m)	0.020	0.020	0.020	0.020	0.020	0.020
	3.178	3.276	3.385	3.462	3.705	3.178
Froude number (-)	0.000	0.000	0.000	0.000	0.000	0.000
	0.267	0.621	0.748	0.759	12.388	0.267
Velocity magnitude (m/s)	0.000	0.000	0.000	0.000	0.000	0.000
	0.187	0.871	1.295	1.449	5.710	0.187
Streamwise velocity (m/s)	-0.176	-0.057	-0.208	-0.656	-0.655	-0.176
	0.164	0.789	1.177	1.321	5.635	0.164
Normal velocity (m/s)	-0.091	-0.370	-0.539	-0.597	-0.719	-0.091
	0.072	0.164	0.301	0.361	0.919	0.072
Shear stress (kg / (m × s ²))	0.000	0.000	0.000	0.000	0.000	0.000
	29.898	50.290	68.808	72.283	94.603	29.898
WSE (m)	101.958	102.025	102.076	102.110	102.348	101.958
	102.155	102.338	102.483	102.569	102.788	102.155

We examined the distribution of hydraulic variable values (Table 4.1) obtained from River2D® models in relation to geomorphic properties of the study reach and also for five

modeled discharges, Q1–Q5 (Table 8.2). For this purpose, we analyzed these distributions as discussed in *Section 4.5*.

8.3. WATER DEPTH AND FROUDE NUMBER DISTRIBUTIONS

At low discharges, the distribution of water depths associated with topographic highs (sediment bars/riffles/edges) is nearly Gaussian, but truncated at a value of 0 (Figure 8.5). As for topographic lows (pools), the distribution is platykurtic and positively skewed. Cumulatively, the water depth distribution is positively skewed, with that character being majority contributed from locations associated with pools (Figure 8.5).

As the discharge increase, the distribution of water depths associated with the topographic highs tend to take on a more negative skew, with this change in shape starting to appear at discharge level of Q3 (Figure 8.5). At highest discharge Q5, it is noticeable that there is a small mode or spike in between 0.125 and 0.250 meters. There is also a general migration of the major peak/mode from 0.5 to 1.0 meters. As for the topographic lows, the distribution changes only slightly, but the mode migrates from 0.9 meters to 1.2 meters. The largest change in the mode migration in both topographic classes is between Q4 and Q5, at 1.0 to 1.2 meters and 0.5 to 1.0 meters for topographic lows and highs, respectively. This largest change is most likely related to change in inundated area, as this is the largest change in all the flow stages (Figure 8.4). The change in the shape of the distribution associated with topographic highs is most driven by the fact that new locations of topographic highs are introduced as flow stage increases.

At the lowest discharge Q1, the distribution for the Froude number is leptokurtic with a negatively exponential shape for topographic highs, lows and stacked distributions (Figure 8.6). For topographic highs, there is a steep, but smooth exponential decay such that the other bins are much smaller than the mode. In both situations, this implies that there is flow homogeneity at this discharge level. The discharge level Q3 results in change in the distributions for topographic highs and lows. For topographic highs, the distribution is much more platykurtic with the mode taking up less than 20% of counts instead of over 80% with discharge level Q1. For topographic lows, the negatively exponential shape changes into a Gaussian-like distribution with positive skewness (Figure 8.6).

For both topographic highs and lows, the shape of the distribution is bimodal with the first mode being the first bin, centered at value 0.011 (Figure 8.6). One possible explanation for

this evolution in Froude number being more platykurtic is that flows are becoming more heterogeneous, and this is likely because of the introduction of shallow depths as the wetted extent of the channel widens at higher flow conditions, and velocity magnitude must be increasing in areas classified as topographic lows. This is because that the core of higher flow that forms at higher discharge levels Q4-Q5. This evolution in the shape of the distribution continues until the discharge condition Q5, at which that of topographic highs is clearly bimodal with the lowest bin centered at value 0.011 has 10% of all counts and the other mode has a little more than 10% of all values. The distribution for topographic lows represents a Gaussian distribution with a thin positive tail. Five percent separate contribution between the greater mode at the lowest bin, centered at 0.011 and the second mode centered at 0.78. This implies that there are two separate distributions for Froude numbers at the highest discharge level. There are many low Froude numbers that are in topographic highs and there are also higher Froude numbers with nearly equal contribution from topographic highs and lows. This could be construed as margin/edge effects being the lesser Froude mode and a core of higher velocity at the greater Froude mode. These distributions hint at the fact that there is a relationship between Froude number and topographic residual, but this relationship changes as flow stage increases (Figure 8.6).

8.4. VELOCITY MAGNITUDE

8.4.1. Velocity Magnitude Distribution

Starting from the low discharges and moving to high discharges, the distributions of velocity magnitude are leptokurtic and become more platykurtic with a thin tail at the positive end for both topographic highs and lows (Figure 8.7). This evolution from leptokurtic to platykurtic is more profound for topographic highs. Topographic highs feature a high count, a mode, for the lowest bin that is between 0 and 0.029 m¹s⁻¹, but have a second mode that goes from 0.11-0.14 m¹s⁻¹ at discharge level Q3 to 0.23 to 0.26 m¹s⁻¹ as the discharge increases. The velocity magnitudes associated with the pools have a unimodal distribution that migrates from the lowest bin that is bounded by 0 and 0.033 m¹s⁻¹ to a plateau of higher values between 0.17 to 0.2 m¹s⁻¹. At the discharge level Q5, the stacked distribution is more platykurtic, and is very profound. This suggests that velocity magnitude becomes more heterogeneous as flow stage increases. Distribution of velocity magnitude resembles to that of the water depth at the highest flow stage (Figures 8.5–8.7).

8.4.2. *Velocity Magnitude Spatial Distribution*

At low flows, there is homogeneity of velocity magnitude for most of the reach (Figure 8.8). Higher velocity magnitudes are clustered at constricted locations, but they do not extend downstream beyond them. At the discharge Q2, clustered high velocity magnitudes are connected between areas of constricted flow that are close together, an example is at the region A (Figure 8.8). From the discharge level Q3 onward, higher velocity is present throughout the channel that spans locations of topographic highs and lows. At the region A, there are two paths of high velocity magnitudes that bound the deeper pool feature. At constricted flow locations at the regions A, B, and C, velocity magnitude is higher than those for higher discharge conditions of Q3-Q5 (Figure 8.8).

8.4.3. *Velocity Magnitude Relationships*

At the lowest discharge level (Q1), the velocity magnitudes are clustered between 0 and 0.2 m¹s⁻¹ at the water depths between 0 and 0.25 meters and the bounded shape appears to be asymptotic (Figure 8.9). The velocity magnitudes associated with the topographic highs show greater scatter than their counterparts. In fact, there is very little scatter evident for topographic lows at the discharge Q1. This disparity in range between topographic highs and lows becomes less as the flow stage increases with increasing discharge (Figure 8.9). This reduced disparity is most likely attributable to the core of higher velocity that is ubiquitous throughout the channel past discharge condition Q3 (Figure 8.8).

For each discharge, there is a specific depth that has the greatest range, and that depth is greater as flow stage increases, from 0-0.25 meters at the discharge Q1 to 0-1.25 meters (Figure 8.9). The distribution patterns depicted by all the locations tend to be similar but gradually wider—which indicates greater range in velocity magnitude. However, at the highest discharge (Q5), the distribution is more diffuse and greater in range throughout all depths (Figure 8.9). This greater range of values is most likely associated with the higher velocities at the constricted locations, such as those in the regions A, B, and C (Figure 8.8). The addition of new locations is greatest between the discharge levels of Q4 and Q5, but the difference in discharge is also greatest as well (Figure 8.4). The distribution of velocity magnitude in relation to depth also demonstrates clear clustering for Froude number (Fr) values throughout all discharge levels (Figure 8.9).

The distributions of velocity magnitude *versus* depth *versus* geomorphic subclasses show separation of topographic highs and lows that is only evident at most extreme geomorphic subclasses corresponding to the classes of -/+4 (Figure 8.10). For topographic highs, the greatest range—that spans the entire plot from 0 to 0.9 m¹s⁻¹ for the discharges Q2–Q5, and 0 to 0.02 m¹s⁻¹ for the discharge Q1 in velocity magnitude—is at the subclass +3 for all flow stages. The differences in range for all geomorphic classes are greatest at the discharge level of Q2, which has the greatest ratio of discharge to inundated area (Figure 8.4). For topographic lows, the greatest range is at the lowest subclass -1 corresponding to the shallowest of the topographic lows (Figure 8.10). This relationship of locations of topographic low and highs to greatest range in velocity magnitude is most likely attributable to the fact that subclass +4 of topographic highs represent channel margins and the subclasses -3/-4 of topographic lows represent deeper, slower waters.

8.4.4. *Summary on Velocity Magnitude Distribution*

In summary, the velocity magnitude distribution is closely associated with depth at the high discharge levels, but start out as very leptokurtic and homogenous at the low ones (Figure 8.7). At low discharges, the distributions are very similar, but not kurtosis. This would imply that velocity magnitude has the water depth as a large controlling factor, which is of no surprise. However, the level of control by the water depth on velocity magnitude seems to have a different effect depending on flow stage. At low flow stage, there is no core of higher velocity apparent (Figure 8.8). However, at the flow stage associated with Q5, this core of higher velocity is quite noticeable. Where that core of higher velocity appears is controlled by the upstream channel shape. This is evident even for topographic lows such as the two different flow paths present at the region A (Figure 8.8).

8.5. STREAMWISE VELOCITY DISTRIBUTION

8.5.1. *Streamwise Velocity Distribution*

The distribution of the streamwise velocity starts off as very leptokurtic at the lowest discharge Q1—as nearly all locations are in one bin, between 0 and 0.063 m¹s⁻¹ for locations associated with topographic highs and lows (Figure 8.11). At the discharge Q2, the distribution becomes very similar to that of velocity magnitude. For the Q1, the bins associated with negative values, -0.25 to 0 m¹s⁻¹, or backwaters, are thin and not very apparent (Figure 8.11). As the discharge approaches the Q3, these same bins are visible and prominent.

At the higher flow stages associated with the discharges Q4 and Q5, the backwaters have formed their own gradually increasing negative tail on the distribution. Combined flow indicates that nearly all flow stages are unimodal except for the flow stage at Q5. At Q5, there are two modes, one that is bound by 0 and $0.0625 \text{ m}^3\text{s}^{-1}$ and the other higher value mode is bound by 0.25 and $0.31 \text{ m}^3\text{s}^{-1}$. The first mode that is bound by $0 \text{ m}^3\text{s}^{-1}$ is first apparent at discharge level Q4. This low value is associated with areas of topographic highs, and is most likely attributable to the added locations at channel margins (Figure 8.11).

8.5.2. *Streamwise Velocity Spatial Distribution*

Streamwise velocity has spatial patterns similar to that of velocity magnitude with one exception, backwaters. At the low flow stages, backwaters are clustered around the regions A, B, and C, (Figure 8.12). As flow stage increases with increasing discharge, the regions of backwaters cumulatively increase. However, the streamwise velocity patterns at the region A does not really change shape or increase in size, with the exception of the dramatic change between the flow stages at Q2 and Q3 (Figure 8.12). The region B appears to change gradually as flow stage increases, in a pattern reminiscent of a wake (Figure 8.12). The region C starts out with only one region of flow separation, but eventually gets two regions of flow separation at the flow stage of Q4. The dramatic change at the region A between the flow stages of Q2 and Q3 is the shifting of the backwater region from one side of the channel to the other. This marks the presence of a core of high velocity that occupies the location where the backwater was at.

8.5.3. *Streamwise Velocity Relationships*

The distribution of stream velocity in relation to depth takes on a shape very similar to that of velocity magnitude for the two lowest discharge levels Q1 and Q2 (Figure 8.13). Even at these low discharge levels, backwaters are present. After the discharge level Q2, the locations associated with backwaters are more apparent, and make up a sizeable portion of the overall distribution shape. For the higher discharges (Q3-Q4), there is a water depth associated with the greatest backwater velocity (Figure 8.13). At the greatest discharge (Q5), there seems to be no preferable depth at which the backwater velocity is greatest.

The distribution of streamwise velocity in relation to water depth for topographic high subclasses (+1)–(+4), and topographic low subclasses (-1)–(-4), which, from ± 1 to ± 4 . show that backwaters areas show no preference with respect to topographic subclass level for all flow stages (Figure 8.14). The distributions are very similar to that of velocity magnitude (Figure 8.10),

and there is still greatest range for topographic highs at the subclass level of +3. It is noteworthy that the Froude number designation such that most backwaters have low Froude number, between 0-0.0273. The distributions of streamwise velocity in relation to water depths and the subclasses clearly demonstrate the clustering for Fr values (Figure 8.14). Groupings with respect to Fr are very similar to those for velocity magnitude. This indicates a very close relationship between velocity magnitude and streamwise velocity. In short, the two variables are closely coupled. One exception to this coupling is the presence of a ‘mirror’ image on the negative end—all because of the presence of backwaters.

8.5.4. *Summary on Streamwise Velocity Distribution*

The locations of backwaters are closely linked to this core of higher streamwise velocity that becomes apparent as flow stage increases. This is given by the increasing wake evident in the region B (Figure 8.12). Even more indicative is the switching of backwater location in the region A. This indicates that the core of higher velocity was originally going straight through the locations of topographic lows, but eventually followed upstream channel characteristics. At the region A, the dynamics of waters and backwaters are indicative of an eddy. Interestingly, the core of high velocity eventually makes the eddy rotate differently (Figure 8.12).

8.6. **NORMAL VELOCITY DISTRIBUTION**

8.6.1. *Normal Velocity Distribution*

Just as other attributes—such as velocity magnitude and streamwise velocity, normal velocity starts out as a very leptokurtic distribution at the low discharges, which implies very homogenous velocity (Figure 8.15). As flow stage increases with increasing discharge from Q1 to Q5, the distribution evolves to a symmetric distribution with its mode around zero m^1s^{-1} . With increasing discharge, the distributions gets more and more dispersed with larger ranges for greater flow stages (Figure 8.15). The range for the discharge level Q1 is bounded by -0.1 and 0.1 m^1s^{-1} . Starting at the discharge Q4, the range goes beyond the edges of the plot, which is approximately bounded by -0.15 to 0.15 m^1s^{-1} .

8.6.2. *Normal Velocity Spatial Distribution*

Normal velocity component alternates between positive and negative values along the reach in the downstream direction (Figure 8.16). Alternating flow positions do not change that much between flow stages, but they tend to become less complex. Local changes in position of

interest consist of a juxtaposition of negative and positive normal velocity at the round topographic low at the region A, and the dynamic behavior at constricted flow at the region C (Figure 8.16). A similar behavior is also observed at the region A for streamwise velocity (Figure 8.12). This is most likely characteristic of eddy behavior. As for the region C, this could be attributable to the expanding wake that occurs as the flow stage increases. This feature most likely affects the normal velocity component as well. Further downstream, the positions of normal velocity are observed to stay in roughly similar positions (Figure 8.16). One factor that changes with increasing flow stage is that the centroids of the patches of positive and negative normal velocities have higher values than the outer bounds (Figure 8.16).

8.6.3. *Normal Velocity Relationships*

At the low water stages, the the distribution of normal velocity in relation to water depth shows a clustering that decrease in range as the depth increases and centered around a value of 0 m^1s^{-1} . As flow stage increases with increasing discharge, the distribution start to disperse around the centers of the clusters formed in the discharge level Q1 (Figure 8.17). This highly dispersed pattern appears in all flow stages after Q1. However, it gets much more diffuse as the discharge level reaches to the highest modeled discharge, Q5 (Figure 8.17).

The boundary between topographic lows (pools) and highs (sediment bars/riffles/edges) does not change that much for the discharges Q1-Q4, but there is a upward shift in this division at the Q5 (Figure 8.17). It can also be observed that the relationship between the distribution normal velocity component and that of Froude number as orderly as those for velocity magnitude and streamwise velocity component, and looks completely irregular in the discharge Q5 (Figure 8.17). This suggests that normal velocity component is not well correlated to velocity magnitude and streamwise velocity component, and it becomes even less correlated as flow stage increases.

The dispersed distribution of normal velocities in relation to depth and Fr numbers also keeps among all geomorphic subclasses, at it is not wholly detectable at any residual level (Figure 8.18). The greatest normal velocity belongs to negative normal velocity at topographic highs subclass +3 for all discharges Q1–Q5. Just as for streamwise velocity, the disparity between these residual levels becomes less notable as flow stage increases (Figure 8.18). Groupings with respect to Fr are not as clearly delineated as for velocity magnitude and streamwise velocity. There does appear to be some delineation in the case of larger positive or negative values, but this delineation has profound overlap and large scatter.

8.6.4. *Summary on Normal Velocity Distribution*

The distributions of normal velocity in relation to water depth show a pattern that appears to be dispersed around a large range of depths 0–3.5 meters (Figure 8.17). This suggests that the distribution of normal velocity component in relation to water depth do not change that much with increasing flow stage. This suggests that normal velocity is controlled more by channel planform and not as much local channel effects. However, the flow stage has a greater effect on the values (or range of values) of normal velocity components (Figure 8.17). The distributions of normal velocity in relation to water depth also present large negative values, indicating large flows toward the left bank. This is most likely attributable to the channel bar feature evident at the region B (Figure 8.16).

8.7. SHEAR STRESS DISTRIBUTION

8.7.1. *Shear Stress Distribution*

At the discharge Q1, shear stress distribution starts out as very leptokurtic and consists of only one bin that is bounded by 0–0.1 $\text{kg}^1\text{m}^{-1}\text{s}^{-2}$ (Figure 8.19). As the flow stage increases with increasing discharge to Q2, a positive tail begins to develop and gets more diffused toward systematically higher values of shear stress. This is evidenced by the increasing frequency in the shear stress values bounded by 2.6 to 2.7 $\text{kg}^1\text{m}^{-1}\text{s}^{-2}$; the percent coverage of locations within this range is about zero at the discharge level Q1 and increases to 6% at the discharge Q5. This indicates an increasing variability in the spatial distribution (Figure 8.19). Both topographic highs and lows have the same overall distribution shape, which can be characterized as exponential decay. The exponential decay pattern is also evident in the distributions for combined topographic high and lows (Figure 8.19), suggesting similar contributions from topographic highs and low classes.

8.7.2. *Shear Stress Spatial Distribution*

At the lowest modeled discharge Q1, the spatial distribution of the shear stress consists of nearly all low values below 0.3 $\text{kg}^1\text{m}^{-1}\text{s}^{-2}$ with the exception of the most constricted flow and roughness elements—such as at the regions A (Figure 8.20). At the discharge Q2, the areas of high shear stress (such as 2.11 to 3 $\text{kg}^1\text{m}^{-1}\text{s}^{-2}$) are grouped in constricted flow locations and are clustered around roughness elements—such as at the regions A and B (Figure 8.20). At the higher discharges (Q4 and Q5), the higher values of shear stress are at the margins of

topographic lows (pools). At the highest modeled discharge Q5, there is a very thin trail of high shear stress values (at 2.11 to 3 $\text{kg}^1\text{m}^{-1}\text{s}^{-2}$) throughout the channel that is focused on roughness elements, but they are mostly confined to locations of topographic highs (sediment bars/riffles/edges). However, there still appears to be a dearth of high shear stress values at areas along the reach that are relatively straight and not constrained, such as that between the regions B and C. At Q5, the influent end of the stream has high shear stress values (Figure 8.20).

8.7.3. *Shear Stress Relationships*

At the lowest discharge (Q1), the distribution of the shear stress values for both topographic highs and lows are clustered around very low shear stress values (Figure 8.21). For the waters depths less than 1–1.5 meters, there is slight variability in the shear stress values, with most of the values clustered around a range of 0-0.5 $\text{kg}^1\text{m}^{-1}\text{s}^{-2}$. The range of shear stress distribution for topographic lows (i.e., water depth higher than ~1 meter) is limited to zero to very low values (i.e., 0-0.5 $\text{kg}^1\text{m}^{-1}\text{s}^{-2}$). However, the range for topographic highs is quite large—even for low flow stage; and stretching to the values of 2-2.5 $\text{kg}^1\text{m}^{-1}\text{s}^{-2}$ (Figure 8.21).

At increased flow stage with increasing discharge, the distribution of the shear stress values associated with topographic lows demonstrates greater variety, with the greatest change in distribution shape happening between the discharges Q2 to Q3 (Figure 8.21). This change in discharge from Q2 to Q3 is the first that does not involve the steeper portion of the inundation-discharge relationship (Figure 8.4). Just as in the case of the velocity magnitude and streamwise velocity, the regions A, B, and C have greatest range in shear stress. The water depth value that this range is located at increases with flow stage. At highest flow stage corresponding to Q5, the depth value of these highest shear stresses are not apparent. This range of depth that highest shear stresses occupy most of the water column, from 0 to 2 meters depth. Just as the normal velocity component, the delineation based on Froude number is not as distinct (Figure 8.21). There is significant mixing of different Froude number classes, although the lowest class still immediately proximal to the water depth axis. This mixing is most likely attributable to the roughness elements affecting the shear stress and that the Froude number does not account for (Figure 8.21).

The distribution of shear stress in relation to water depth and for geomorphic subclasses also support this relationship (Figure 8.22). At the lowest discharge Q1, this distribution demonstrates very low values of shear stress values at nearly all levels of water depth, with a few possible outlier points apparent in topographic high subclasses of +2 and +3. At the next

discharge (Q2), this relationship still holds with some values associated with topographic lows having higher values. For topographic highs, these locations are not apparent, but they are most likely attributable to locations at edges (margins) that are roughness elements, as is the case of the flow stage corresponding to Q3, such as at the region B (Figure 8.20). At the Q3, shear stress values have considerable high values at locations associated with topographic lows. The depth corresponding to these high shear stress values is the shallowest for topographic lows subclass – 1. Locations with topographic highs still have higher shear stress levels (Figure 8.22). At the highest flow stage corresponding to Q5, there is an abundance of high shear stress values in both topographic lows and highs.

8.7.4. *Summary on Shear Stress Distribution*

Over 50% of shear stress values are concentrated at the lowest values in the distribution that is bounded by 0 and $0.1 \text{ kg}^1\text{m}^{-1}\text{s}^{-2}$ for nearly all flow stages except that for Q5 (Figure 8.19). Spatially, higher shear stress values seem clustered at roughness elements (Figure 8.20). The distributions based on the Froude number ranges indicate that the distribution of the shear stress values (Figures 8.21–8.22) are not as clearly identifiable as those of velocity magnitude (Figure 8.9–8.10) and streamwise velocity (Figure 8.13–8.14). This demonstrates that shear stress is not only dependent on water depth and velocity magnitude, but it also significantly influenced by the roughness. This is also evident on the spatial distribution patterns of the shear stress (Figure 8.20). These findings indicate that high shear stress appears to be as a result of two conditions: presence of low water depth or/and constricted flow (e.g., at region A) and roughness elements present at otherwise high velocity conditions (e.g., at region C) (Figure 8.20). For the Cibolo reach, roughness elements are highly deterministic for locations of high shear stress at all but the highest water stage corresponding to Q5. This would indicate that roughness elements in deep areas do not experience high shear stress except at the highest of flows, due in part to the core of higher velocity magnitude (Figure 8.8).

8.8. SUMMARY ON THE CIBOLO STUDY REACH

The Cibolo reach located on the Lower Cibolo Creek (Figure 3.3), a tributary of the San Antonio River, is a fairly straight reach that has one simple bend around 200 meters from the effluent end (Figure 8.1). The Cibolo reach is marked by the smallest values of discharge for all flow stages (Figure 8.4). Another property of the Cibolo is the nearly linear flow stage vs. inundated area (Figure 8.4). Elevations for this reach have a range that is a little less than 4

meters (Figure 8.1). At the straight portion of the reach, there is an alternation with a near constant frequency of low and high elevations, similar to a classic pool-riffle topography. At the simple bend, there is a greater concentration of pools. Considering topographic residuals, extreme topographic lows (deepest pools), characterized as subclass -4 are spatially clustered in two major locations, at the low curvature influent portion of the reach between 150 and 500 meters downstream of the influent end of the reach and the region that is closest to the bend.

Velocity magnitude is characterized by flows that start out very leptokurtic with low values (Figure 8.7). As flow stage increases with increasing discharge to the level of Q5, the topographic highs (sediment bars/riffles/edges) demonstrate two modes, one bounded by 0 and 0.033 m¹s⁻¹ and the other bounded by 0.23 and 0.27 m¹s⁻¹ (Figure 8.7). In contrast, topographic lows (pools) feature a unimodal Gaussian-like distribution that tends to become more platykurtic. In addition, the mode associated with this distribution migrates to higher values, with the mode at discharge level Q1 bounded by 0 and 0.033 m¹s⁻¹ and an ambiguous mode that is between 0.17 and 0.3 m¹s⁻¹ at the discharge level of Q5. Cumulatively, the larger mode of topographic highs likely represents a distribution associated with a core of higher velocity that is observed at discharge levels Q2–Q5 (Figure 8.8). The core of higher velocity is observed exclusively at the constricted areas of discharge level Q2. The characteristic distribution patterns of velocity magnitude *versus* water depth (Figure 8.9) are similar to those of the Goliad reach, but it is notable that the pattern does not quite evolve into that of a positively exponential shape as in the case of Goliad reach. The division between topographic lows and highs does not seem to move that much except for Q5. This is most likely because of the low discharge values. With the exception of a concentration of pool features at the bend near the effluent side of the reach, there is really nothing remarkable about this high curvature bend (Figure 8.1).

The regions of backwaters tend to be more numerous than those in other reaches (Figure 8.8). Representing flow separation, backwaters are known to bound cores of high velocity at high flow stage and are common at complex channel margins. In terms of backwaters, there are a few notable sites, the regions of A, B, and C (Figure 8.8). These locations reveal certain aspects of the reach as flow stage increases, such as the dynamic behavior of the core of higher velocity. This is readily observable at the region A (Figure 8.8). At the flow stages for Q1–Q2, the backwaters are present on the northern side of the area. However, at the flow stage for Q3, the backwaters occupied the other side of the area (Figure 8.8), demonstrating how upstream planform geometry plays a role in the location of high velocity. Another region on the reach that exhibits dynamic behavior with the same flow regimes (Q1–Q2 and Q3–Q5) is just

downstream of the region A near meter marker 300 (Figure 8.1), where the backwaters the bound the channel tend to outline the core of high velocity. As such, stream velocity is tightly coupled to velocity magnitude, and has similar influences that vary with flow stage, where low flow stages are dominated by channel topography and high flow stages are dominated by upstream planform geometry.

As is the case of other study reaches, the locations of normal velocity component do not change that much with increasing flow stage, which suggests that the channel planform has the largest influence. However, there are exceptions to this observation, such as at the region A (Figure 8.16). At region A, the backwater areas nearly bound a pool feature, then occupy the northern half of the pool, and switch at the flow stage for Q3. As suggested earlier, this is an example of an eddy circulation that has changed direction of flow in response to the core of high velocity exhibiting dynamic behavior and being more dependent on upstream channel planform geometry. Also, the spacing of the alternations between negative and positive normal velocity component appears to get higher as one gets closer to the bend feature—as opposed to further upstream (Figure 8.16).

For the Cibolo reach, shear stress distribution exhibits high range and is very leptokurtic at low discharge levels (Figure 8.19). There are only a few locations of the elevated shear stress values near locations where the channel is constricted (Figure 8.20) For other reaches, the shear stress is generally coincident with the locations of roughness elements, and that increasing flow stage actually allows for more roughness elements to feature elevated shear stress. Some notable exceptions to this exist, such as that for the Falls City reach. At the Cibolo reach, observations regarding shear stress tend to hold similar as those for other reaches.

In summary, the Cibolo gives us suggestions as to how curvature influences hydraulics. Unlike other sites, this particular reach has two high curvature areas with one near the influent and the other near the effluent side of the reach (Figure 8.1). The location at the influent side has less curvature, and the one on the effluent side has higher curvature. These findings suggest that curvature plays a role in the frequency and spacing of normal velocity distributions and the concentrations of extreme topographic lows or deep pools.

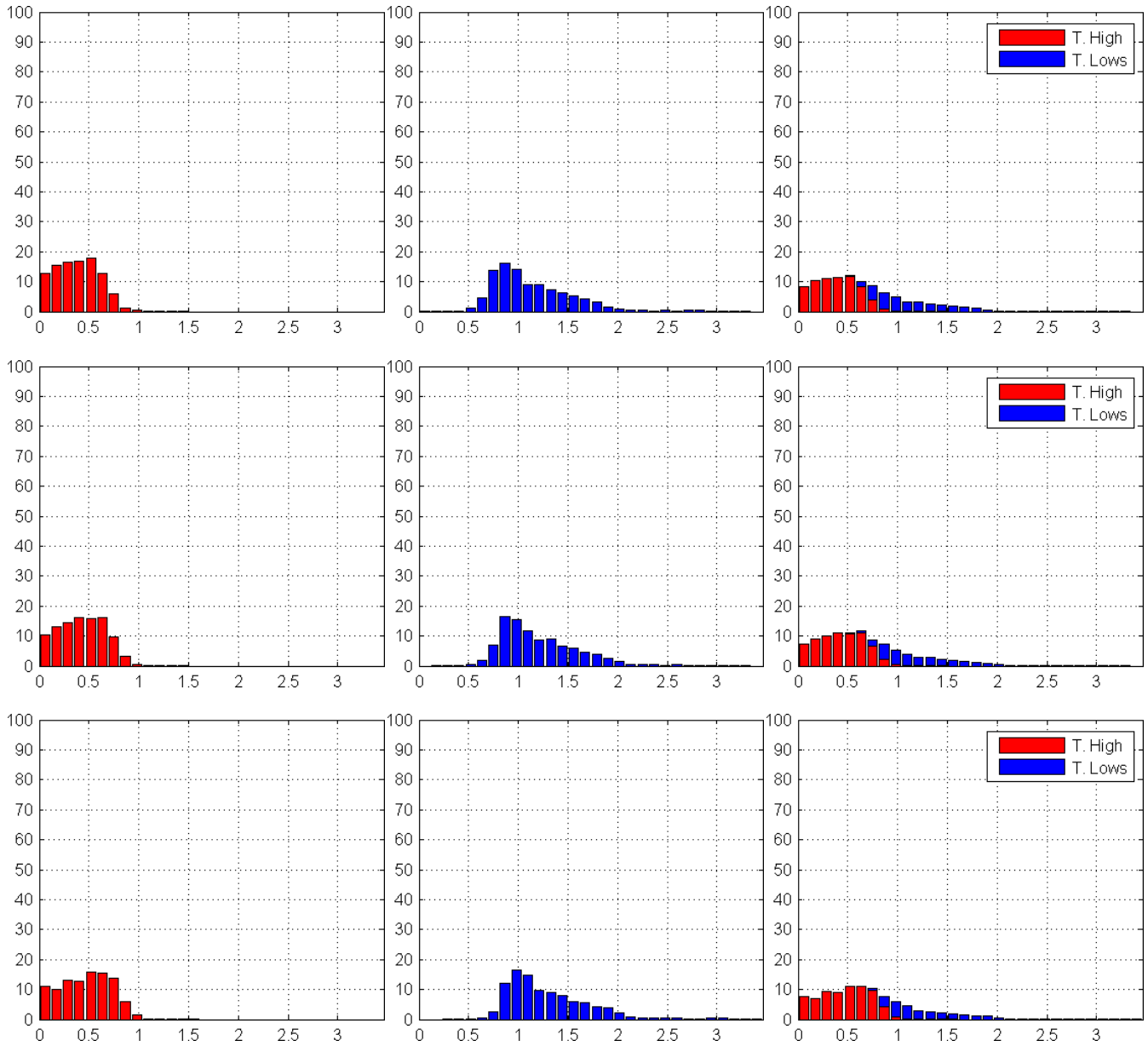


Figure 8.5. Water depth distribution for Q1–Q5 (rows, top to bottom) for topographic highs (marked as T. High) corresponding to the classes (+1)–(+4), topographic lows (marked as T. Lows) corresponding to the classes (-1)–(-4), and combined (columns, left to right). Horizontal and vertical axes correspond to water depth (m) and the percent values of topographic classes, respectively.

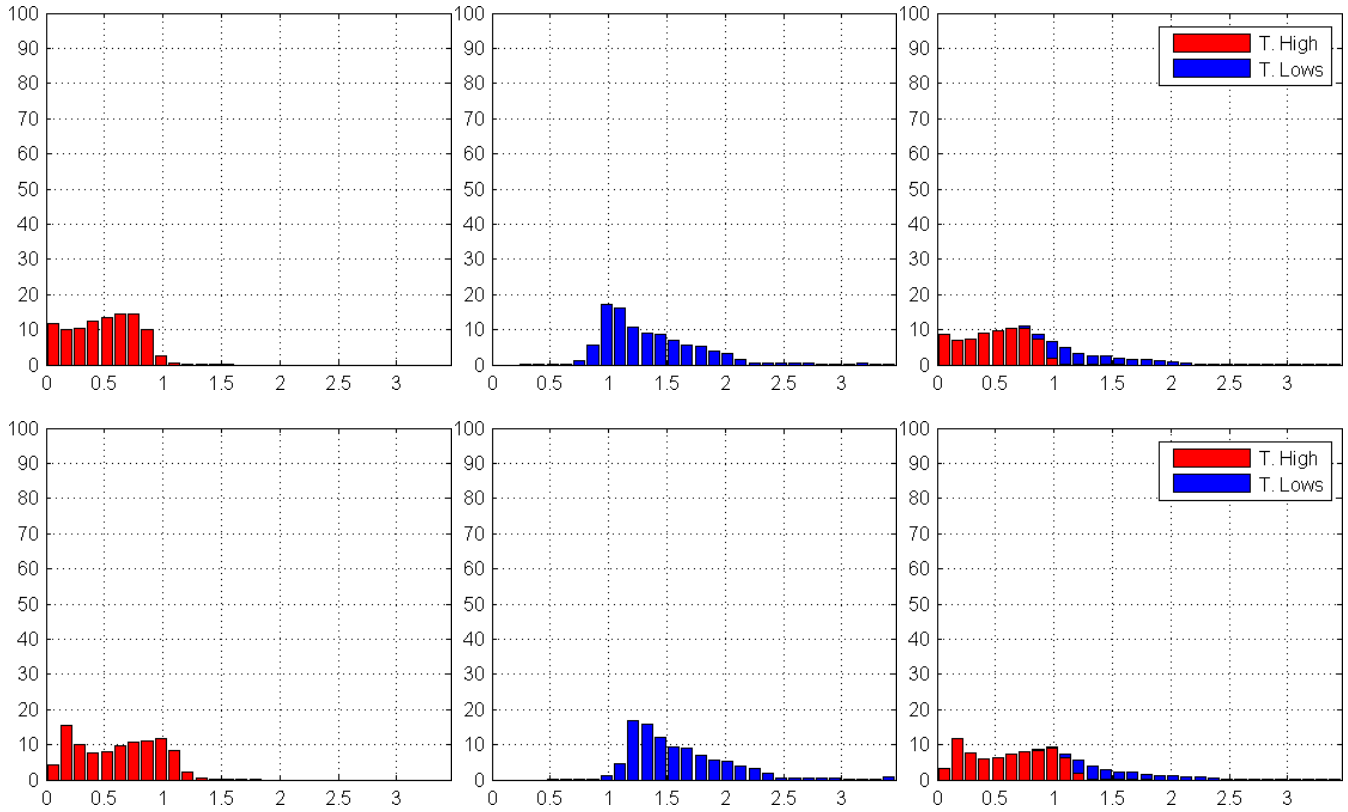


Figure 8.5 (cont'd). Water depth distribution for Q1–Q5 (rows, top to bottom) for topographic highs (marked as T. High) corresponding to the classes (+1)–(+4), topographic lows (marked as T. Lows) corresponding to the classes (-1)–(-4), and combined (columns, left to right). Horizontal and vertical axes correspond to water depth (m) and the percent values of topographic classes, respectively.

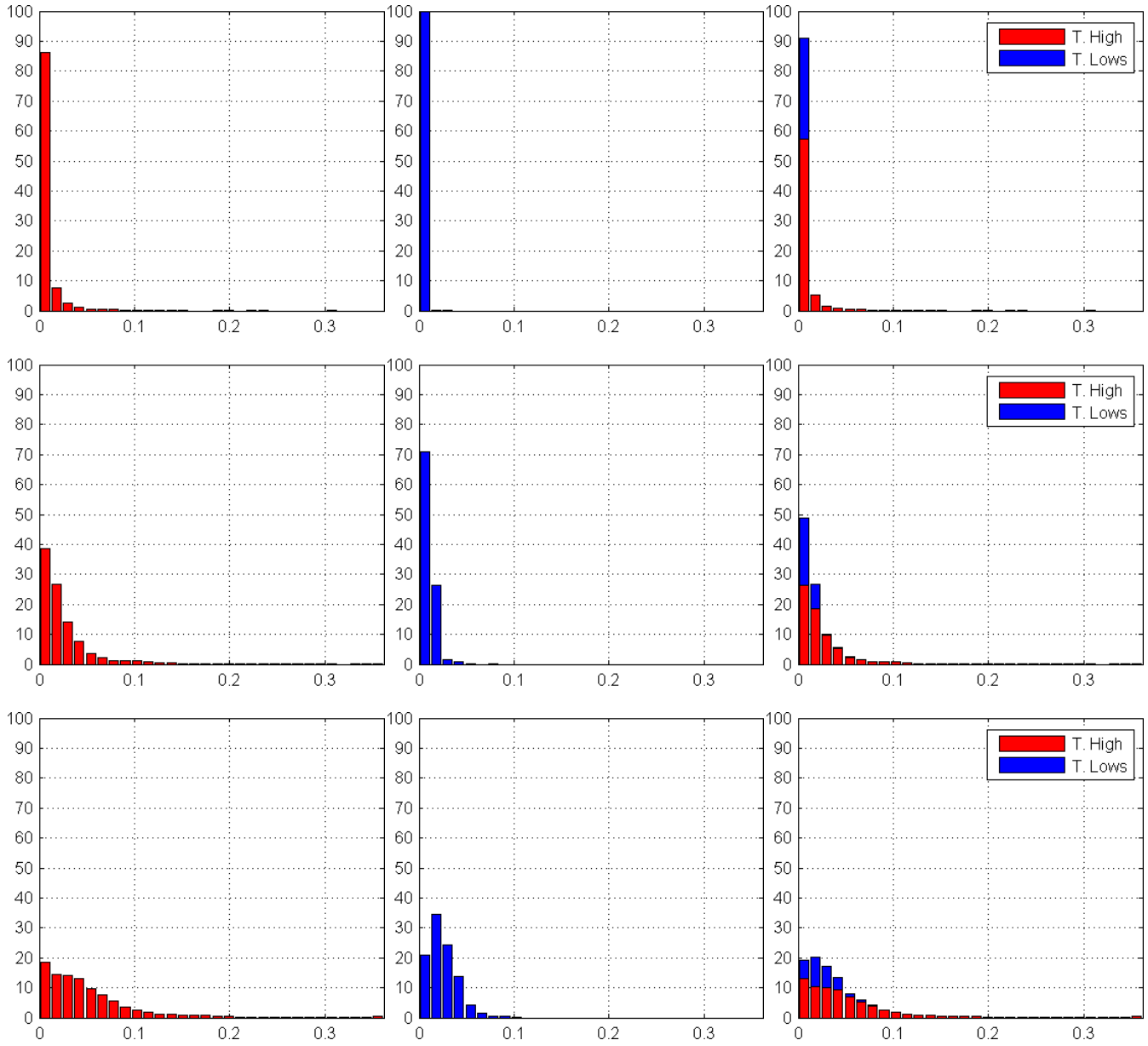


Figure 8.6. Froude number (Fr) distribution for Q1–Q5 (rows, top to bottom) for topographic highs (marked as T. High) corresponding to the classes (+1)–(+4), topographic lows (marked as T. Lows) corresponding to the classes (-1)–(-4), and combined (columns, left to right). Horizontal and vertical axes correspond to Fr and the percent values of topographic classes, respectively.

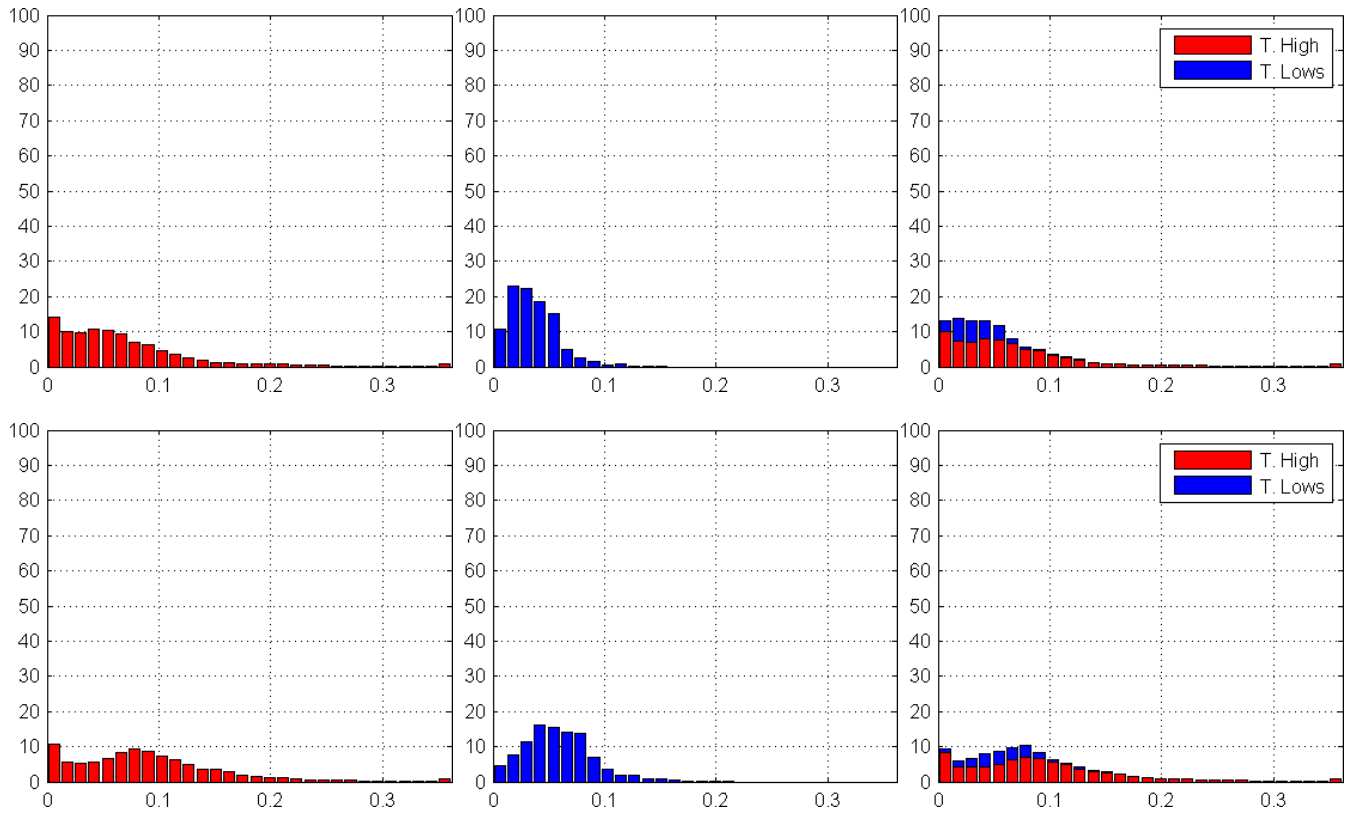


Figure 8.6 (cont'd). Froude number (Fr) distribution for Q1–Q5 (rows, top to bottom) for topographic highs (marked as T. High) corresponding to the classes (+1)–(+4), topographic lows (marked as T. Lows) corresponding to the classes (-1)–(-4), and combined (columns, left to right). Horizontal and vertical axes correspond to Fr and the percent values of topographic classes, respectively.

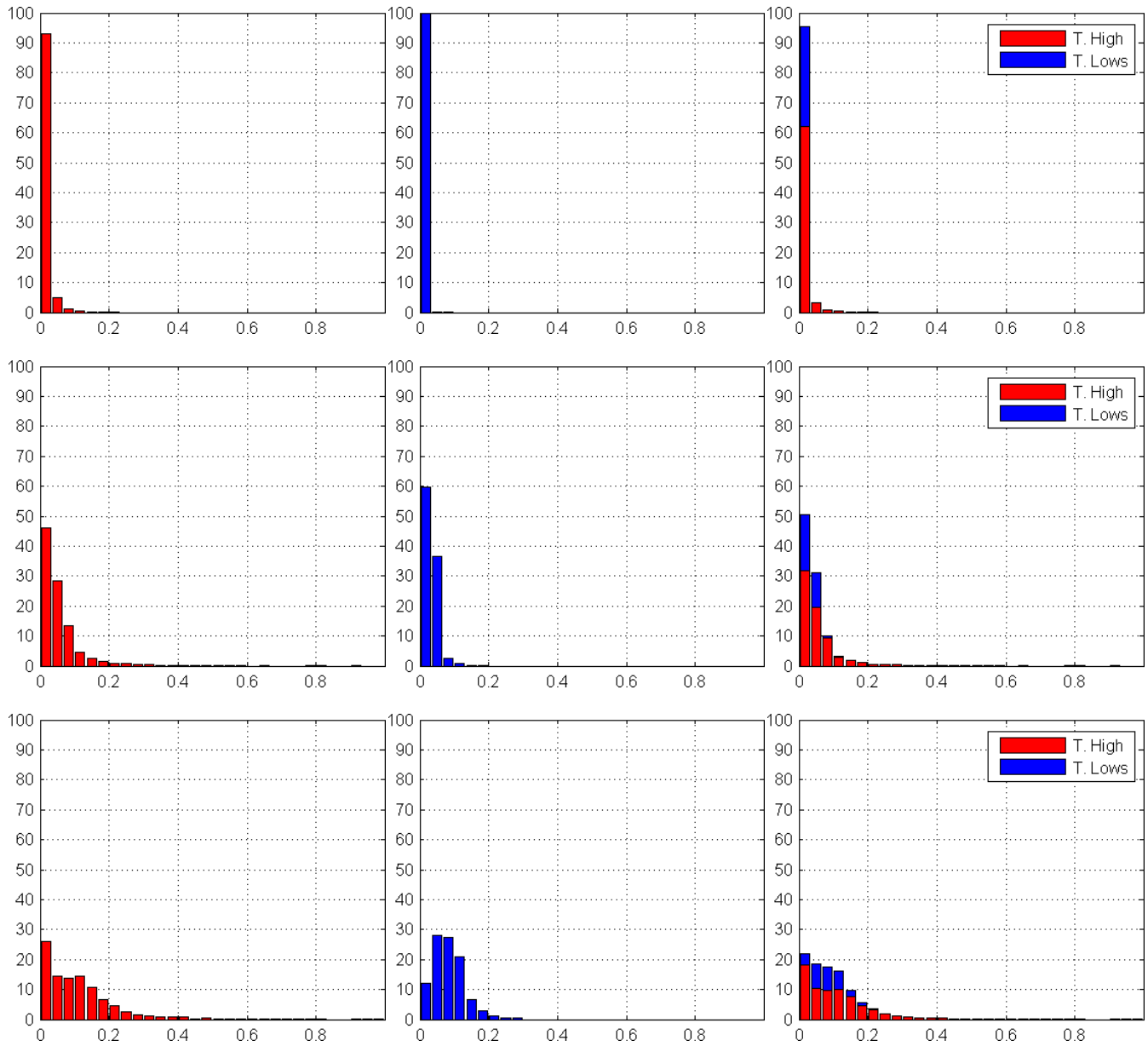


Figure 8.7. Distribution of velocity magnitude for Q1–Q5 (rows, top to bottom) for topographic highs (marked as T. High) corresponding to the classes (+1)–(+4), topographic lows (marked as T. Lows) corresponding to the classes (-1)–(-4), and combined (columns, left to right). Horizontal and vertical axes correspond to velocity magnitude (m/s) and the percent values of topographic classes, respectively.

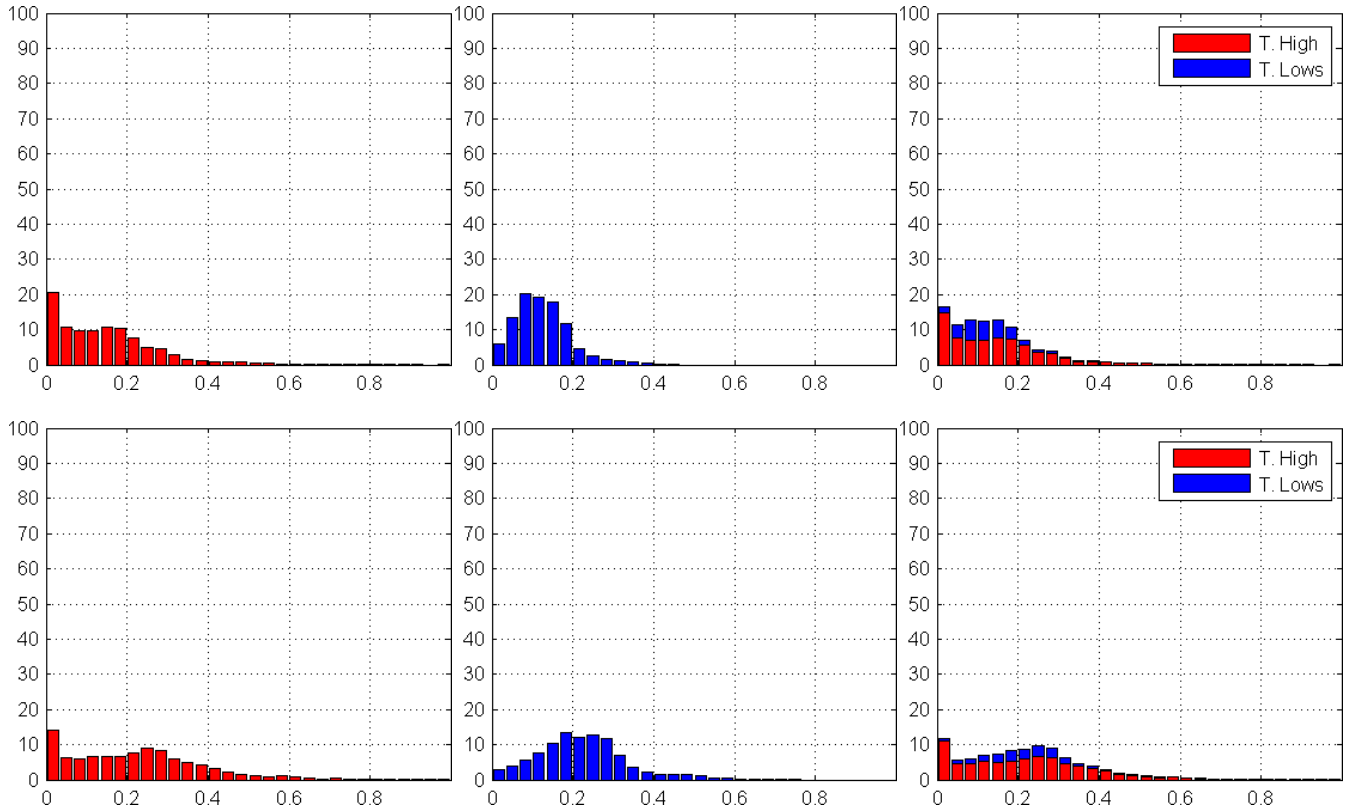


Figure 8.7 (cont'd). Distribution of velocity magnitude for Q1–Q5 (rows, top to bottom) for topographic highs (marked as 'T. High') corresponding to the classes (+1)–(+4), topographic lows (marked as 'T. Lows') corresponding to the classes (-1)–(-4), and combined (columns, left to right). Horizontal and vertical axes correspond to velocity magnitude (m/s) and the percent values of topographic classes, respectively.

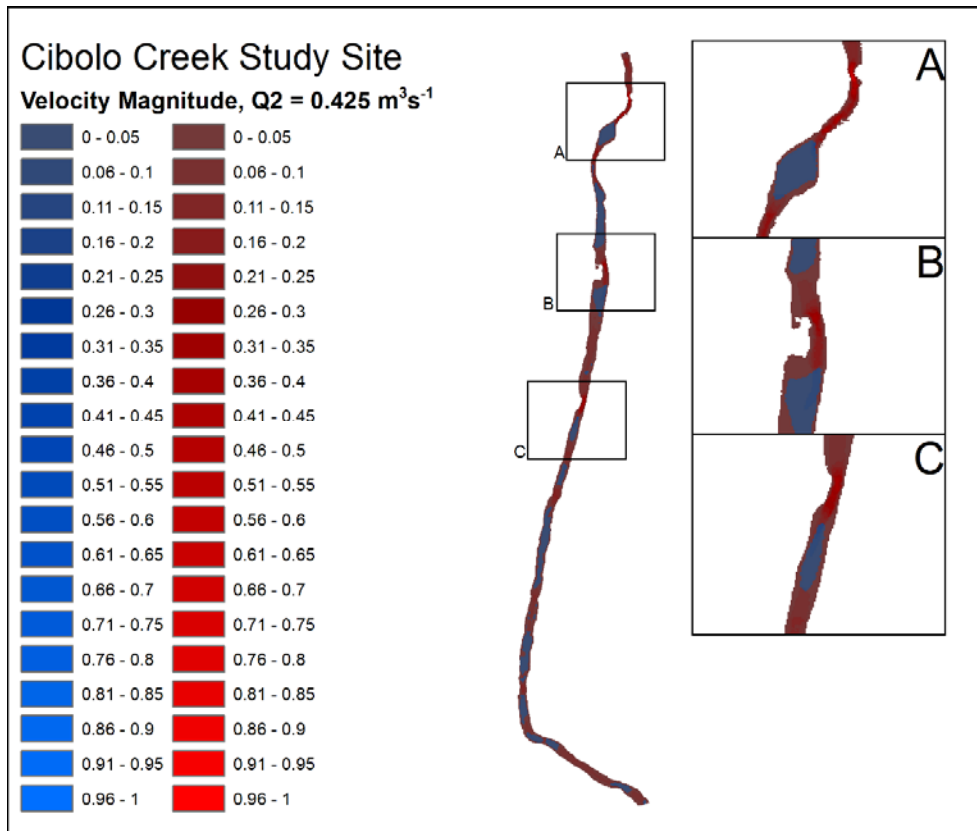
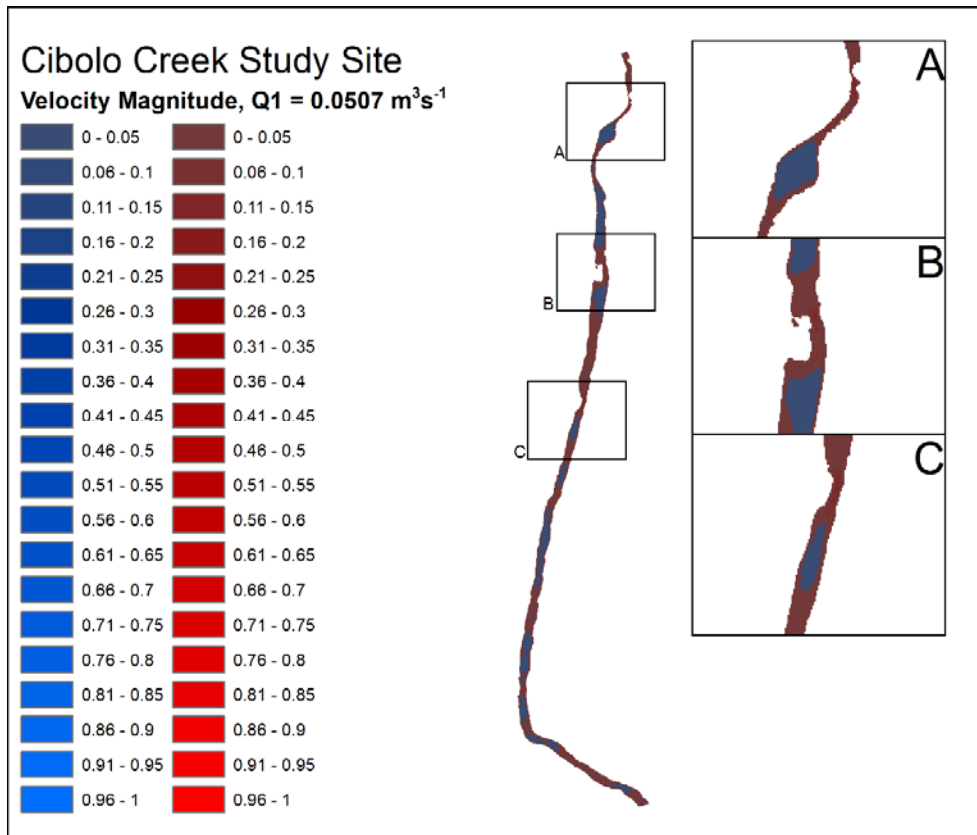


Figure 8.8. Spatial distribution of velocity magnitude (m/s) for Q1–Q5 for topographic highs (red colors) and lows (blue colors).

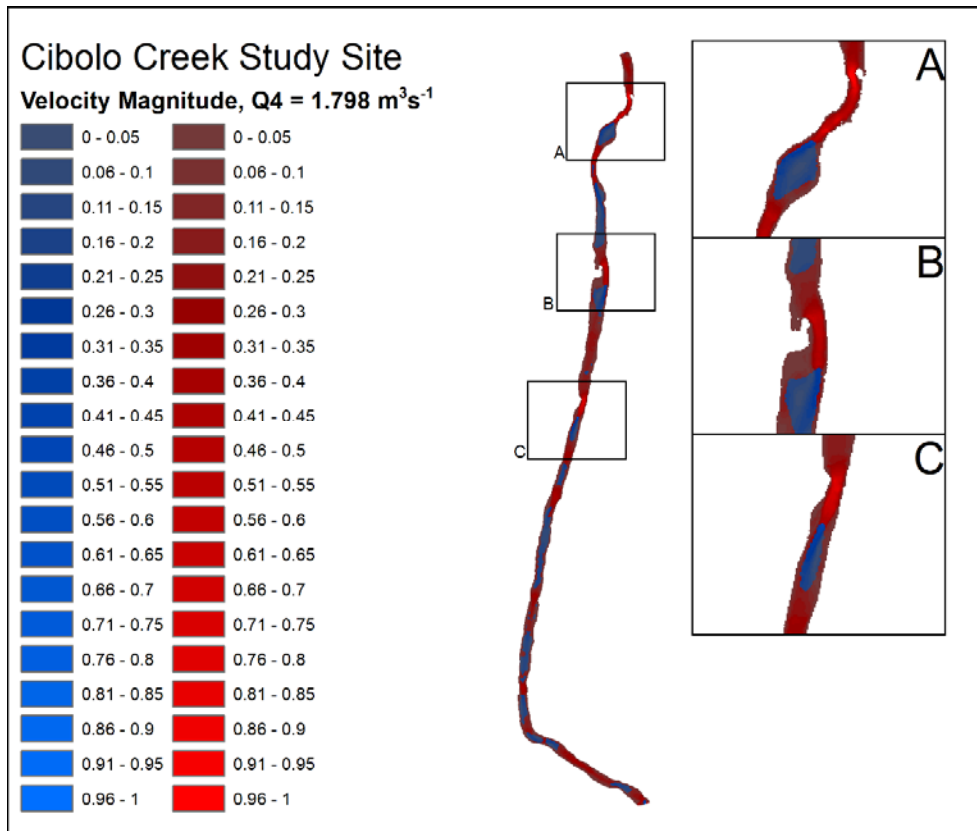
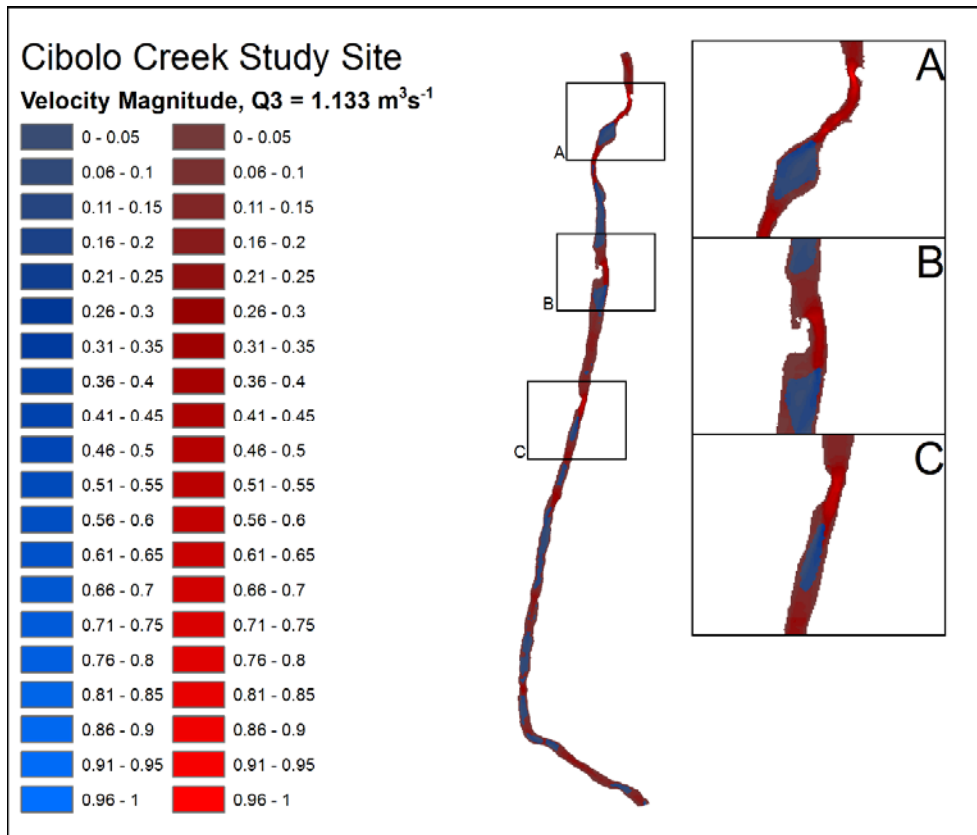


Figure 8.8 (cont'd). Spatial distribution of velocity magnitude (m/s) for Q1–Q5 for topographic highs (red colors) and lows (blue colors).

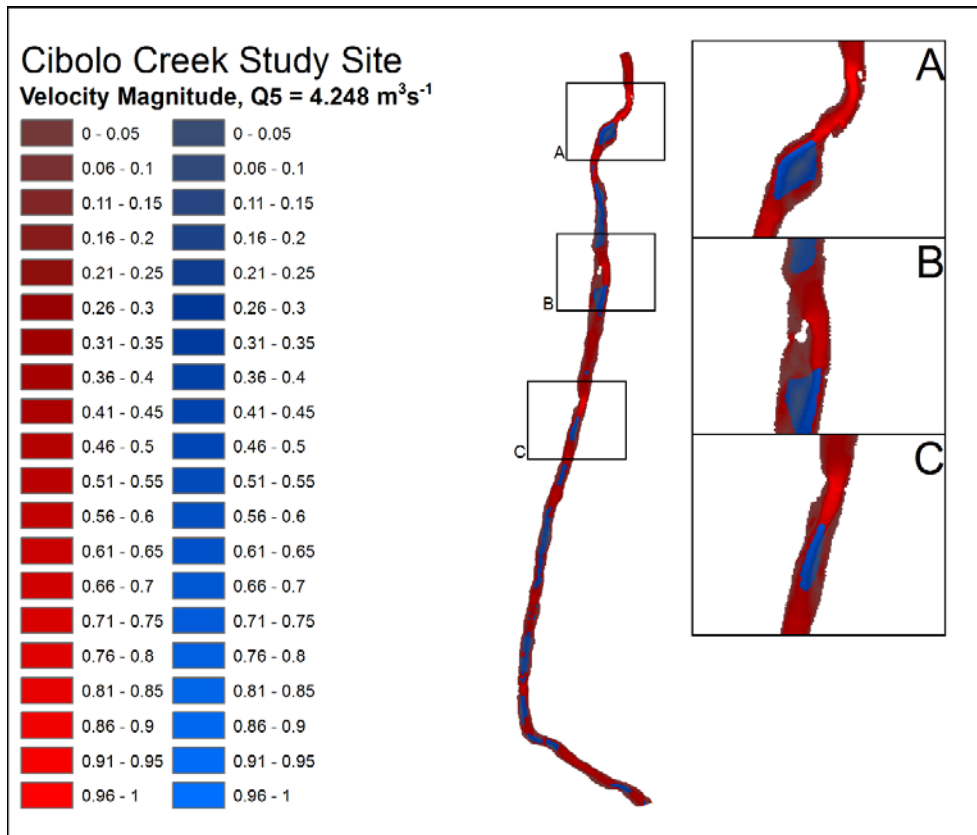


Figure 8.8 (cont'd). Spatial distribution of velocity magnitude (m/s) for Q1–Q5 for topographic highs (red colors) and lows (blue colors).

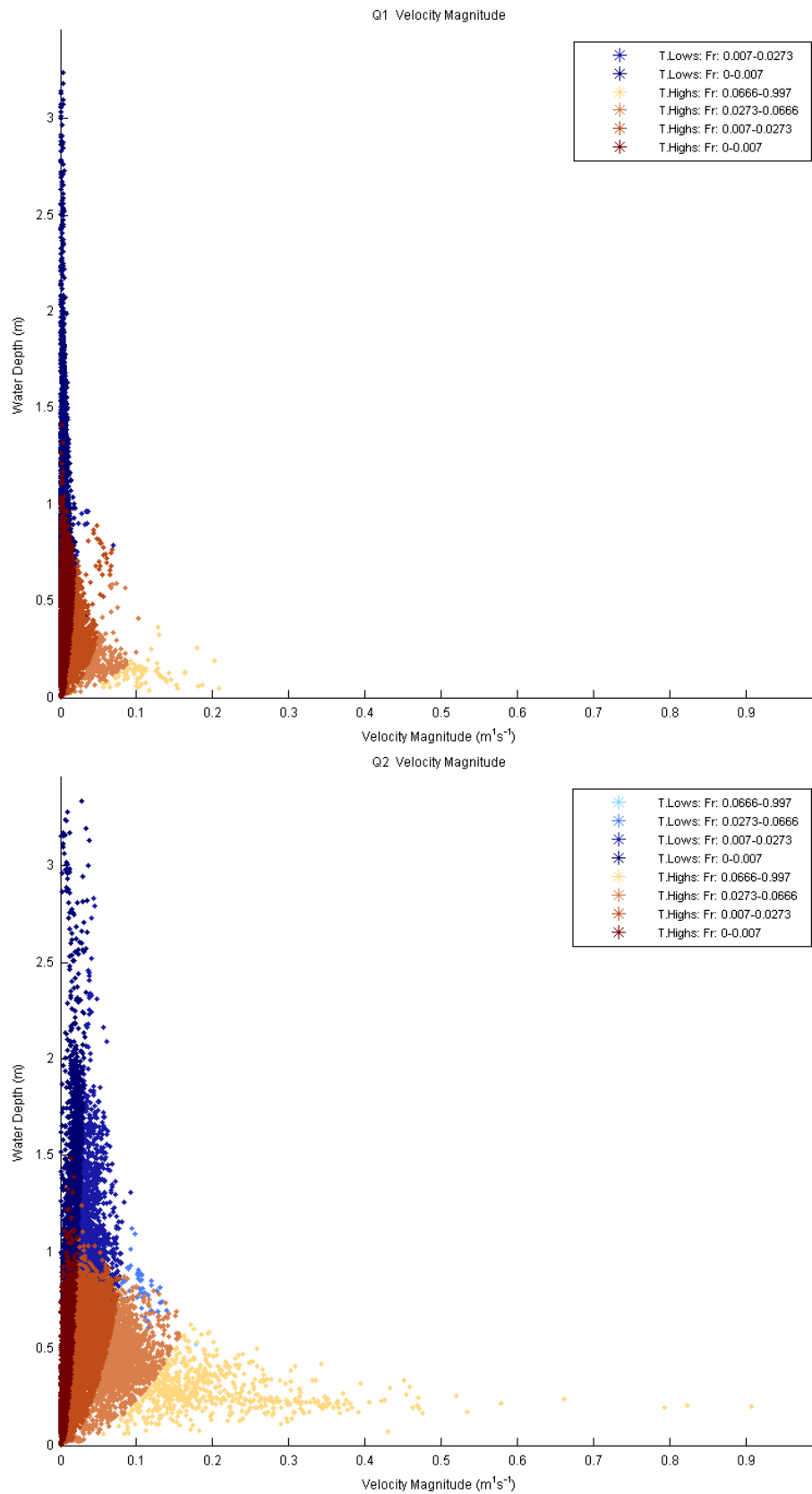


Figure 8.9. Distribution of velocity magnitude in relation to water depth for Q1–Q5 classified by topographic highs marked as T. Highs (brown colors), topographic lows marked as T. Lows (blue colors), and Froude number (Fr).

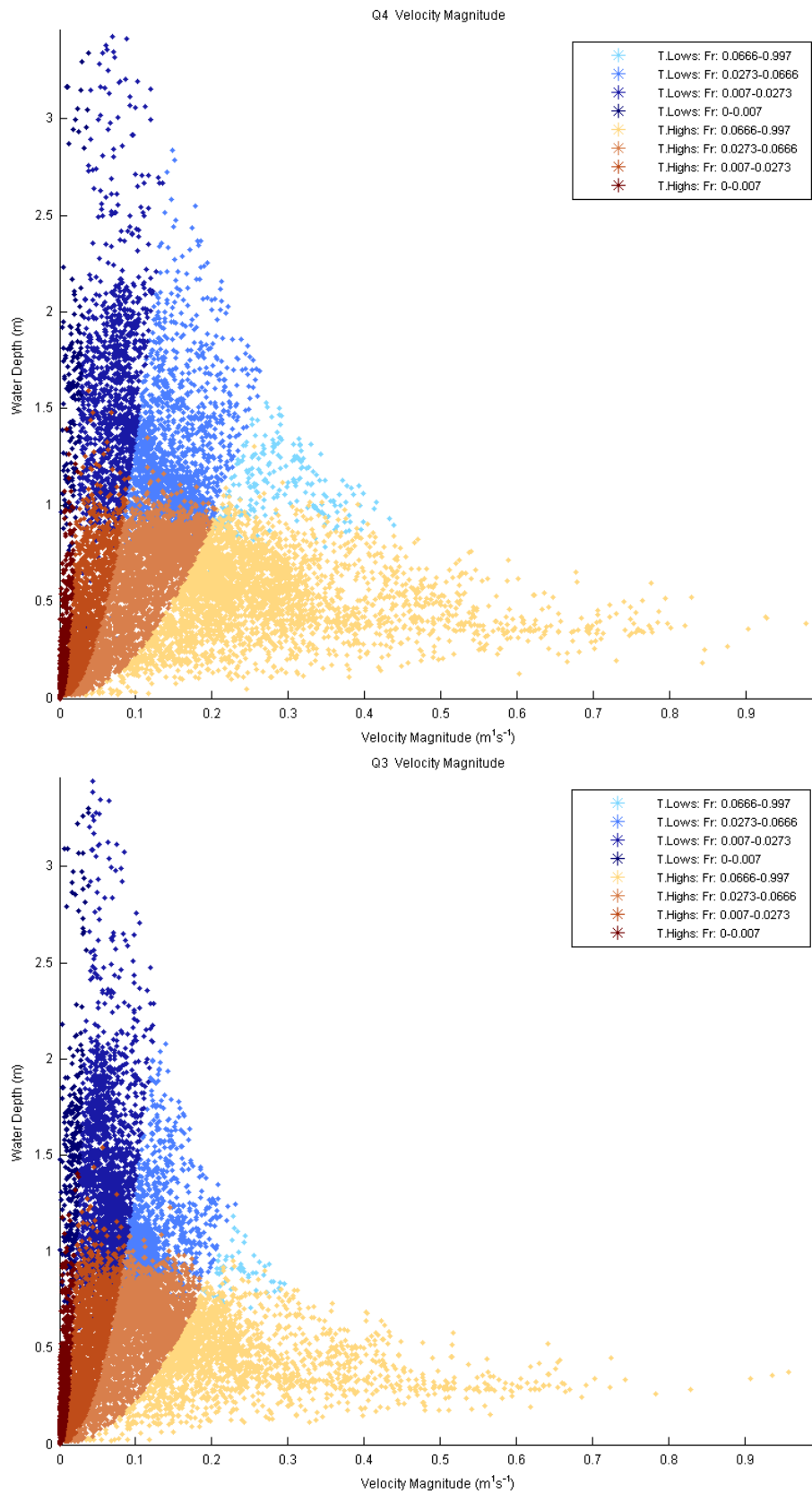


Figure 8.9 (cont'd). Distribution of velocity magnitude in relation to water depth for Q1–Q5 classified by topographic highs marked as T. Highs (brown colors), topographic lows marked as T. Lows (blue colors), and Froude number (Fr).

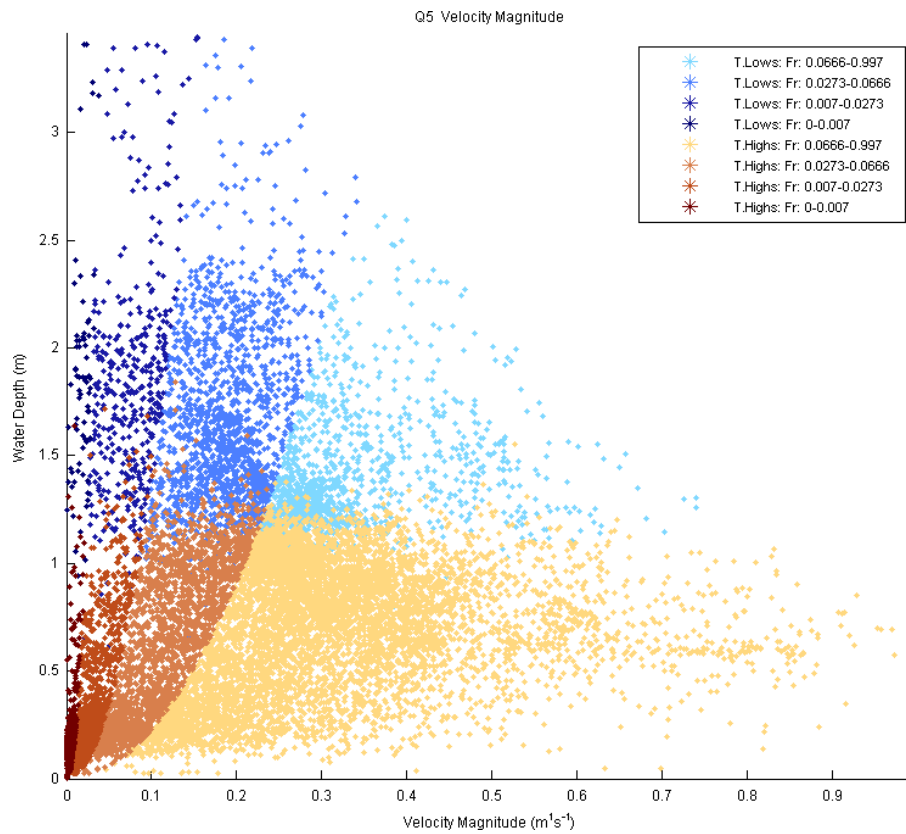


Figure 8.9 (cont'd). Distribution of velocity magnitude in relation to water depth for Q1–Q5 classified by topographic highs marked as T. Highs (brown colors), topographic lows marked as T. Lows (blue colors), and Froude number (Fr).

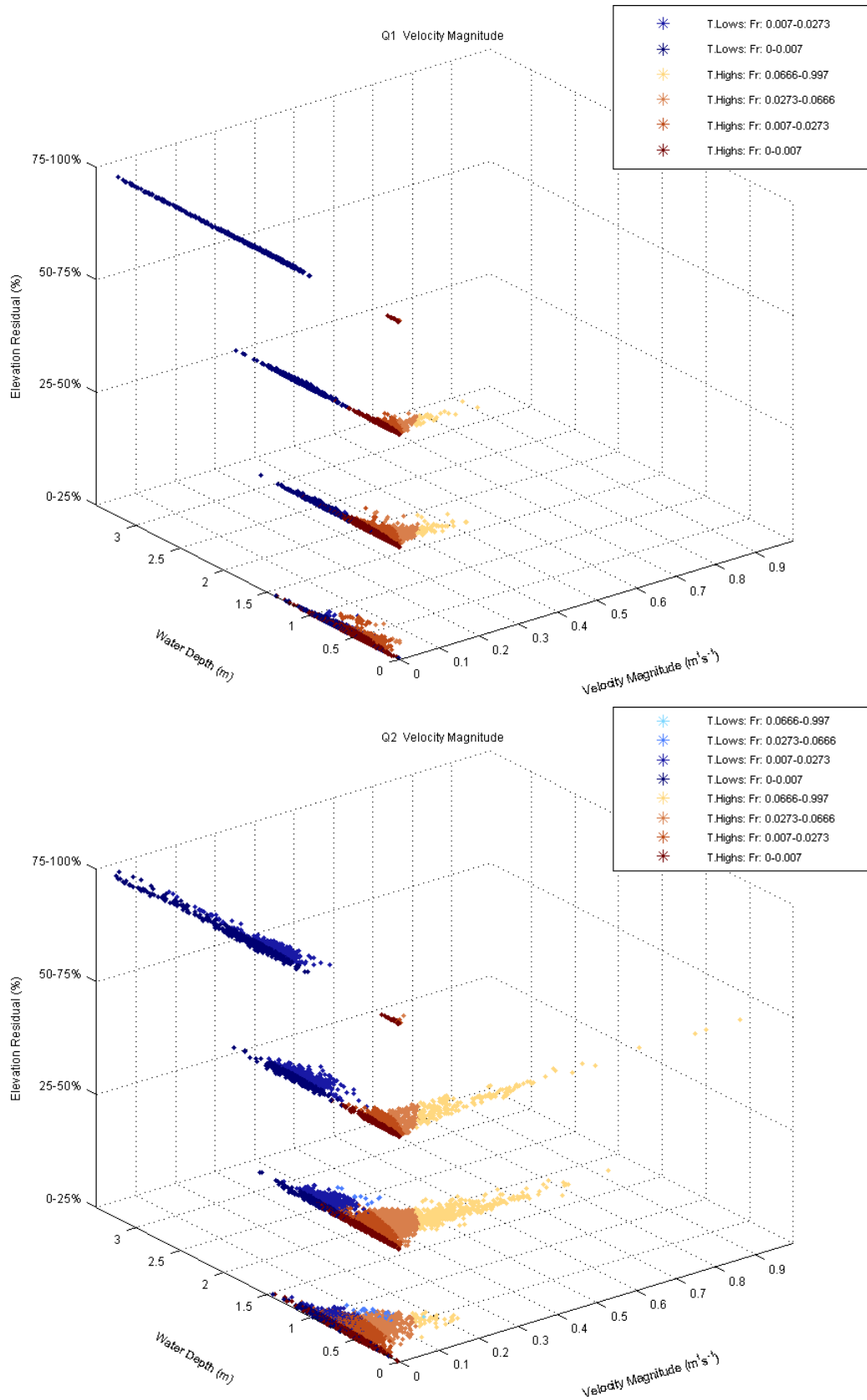


Figure 8.10. Distribution of velocity magnitude for topographic high (T. Highs)/low (T. Lows) subclasses (Figure 4.2) and Q1–Q5, classified by Froude number (Fr).

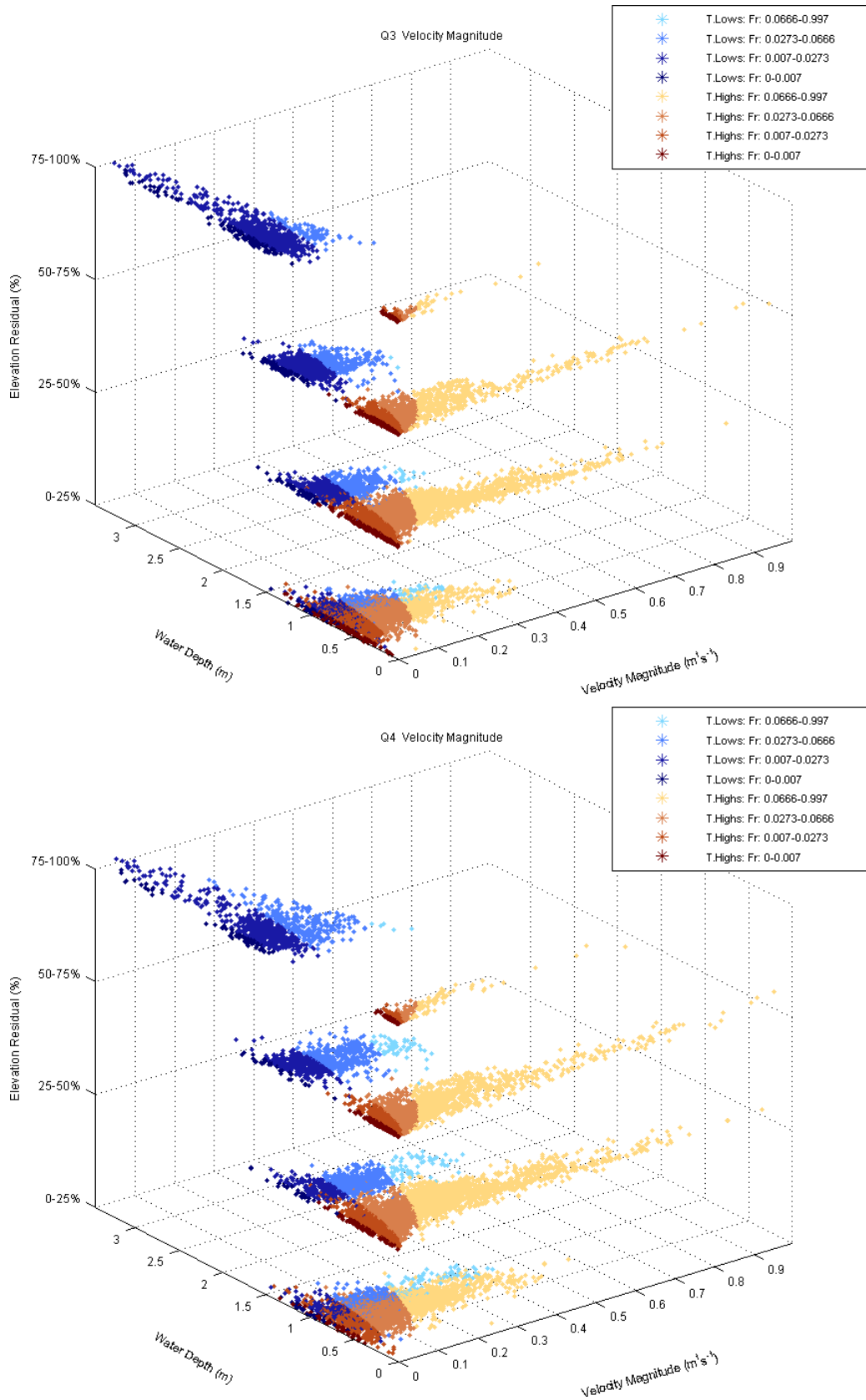


Figure 8.10 (cont'd). Distribution of velocity magnitude for topographic high (T. Highs)/low (T. Lows) subclasses (Figure 4.2) and Q1–Q5, classified by Froude number (Fr).

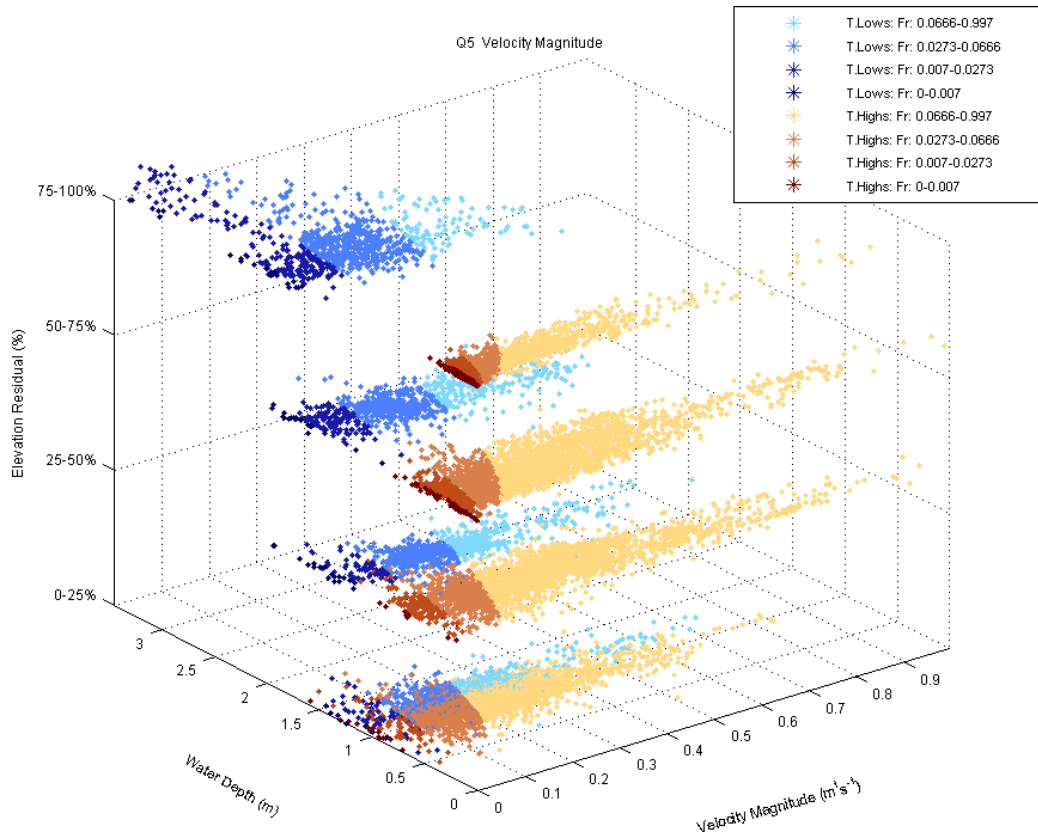


Figure 8.10 (cont'd). Distribution of velocity magnitude for topographic high (T. Highs)/low (T. Lows) subclasses (Figure 4.2) and Q1–Q5, classified by Froude number (Fr).

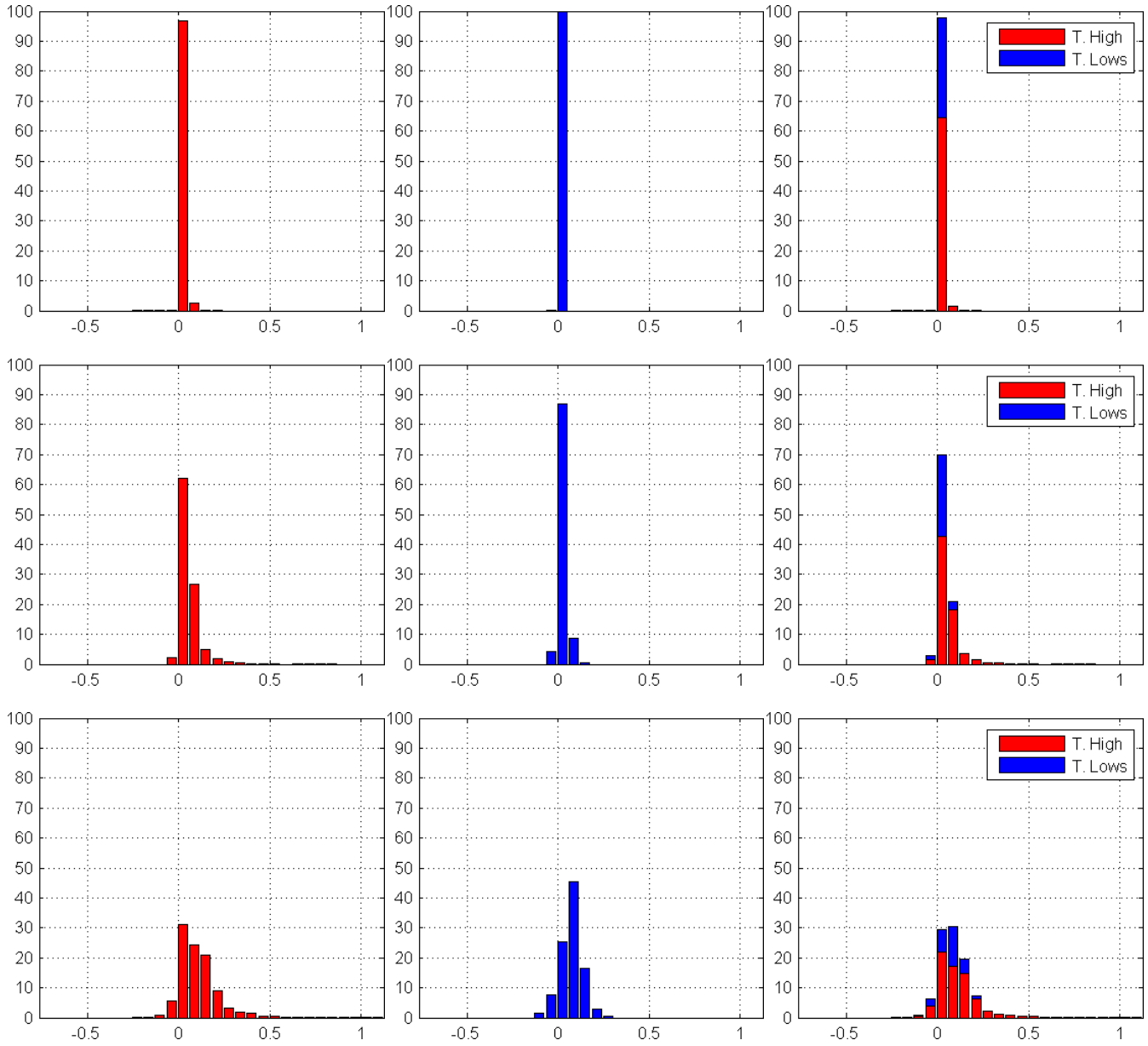


Figure 8.11. Distribution of streamwise velocity component for Q1–Q5 (rows, top to bottom) for topographic highs (marked as T. High) corresponding to the classes (+1)–(+4), topographic lows (marked as T. Lows) corresponding to the classes (-1)–(-4), and combined (columns, left to right). Horizontal and vertical axes correspond to streamwise velocity (m/s) and the percent values of topographic classes, respectively.

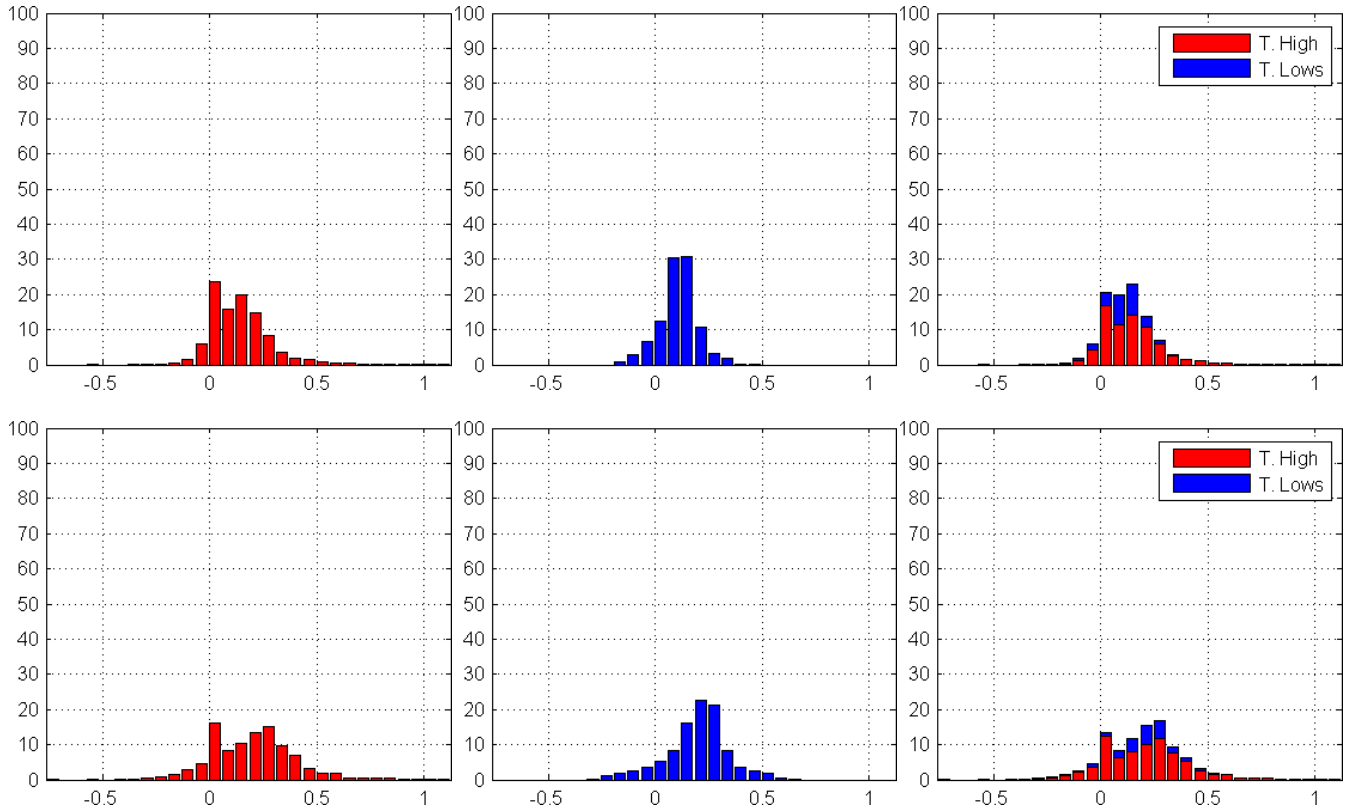


Figure 8.11 (cont'd). Distribution of streamwise velocity component for Q1–Q5 (rows, top to bottom) for topographic highs (marked as T. High) corresponding to the classes (+1)–(+4), topographic lows (marked as T. Lows) corresponding to the classes (-1)–(-4), and combined (columns, left to right). Horizontal and vertical axes correspond to streamwise velocity (m/s) and the percent values of topographic classes, respectively.

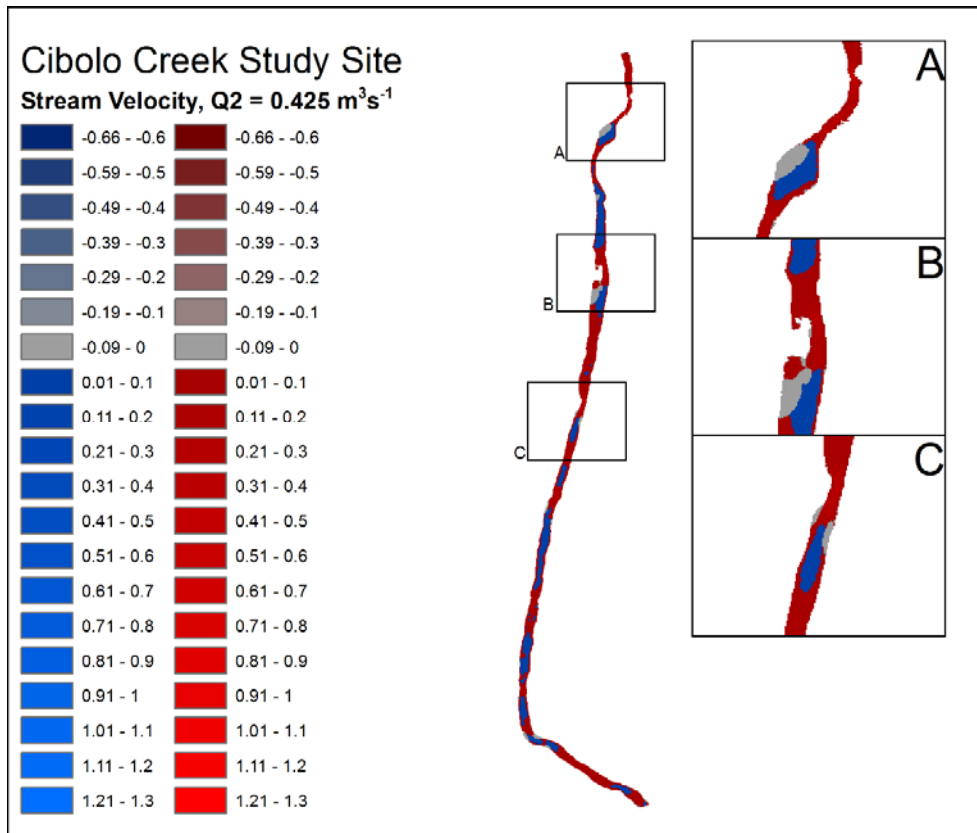
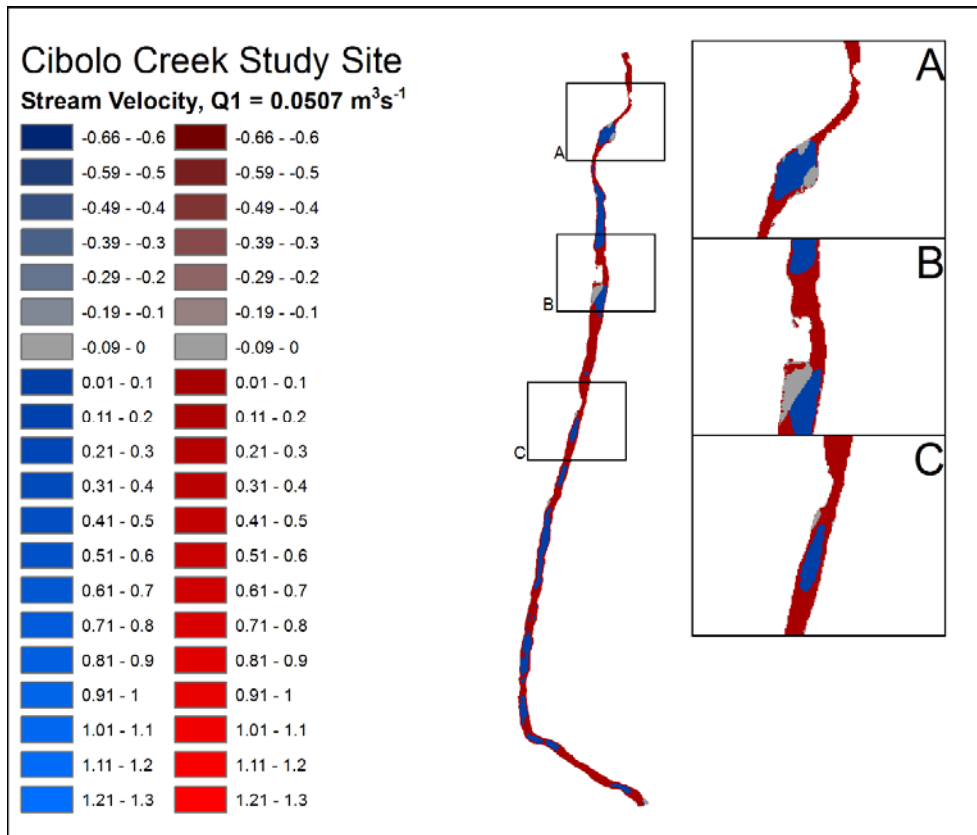


Figure 8.12. Spatial distribution of streamwise velocity (m/s) for Q1–Q5 for topographic highs (red colors) and lows (blue colors).

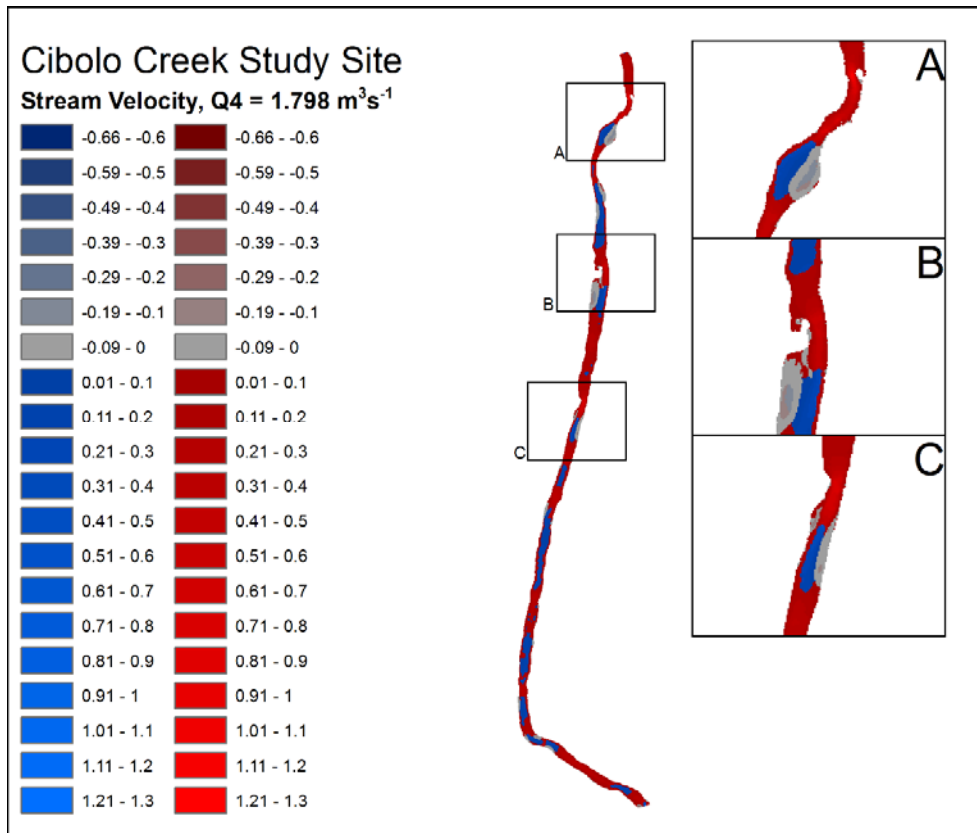
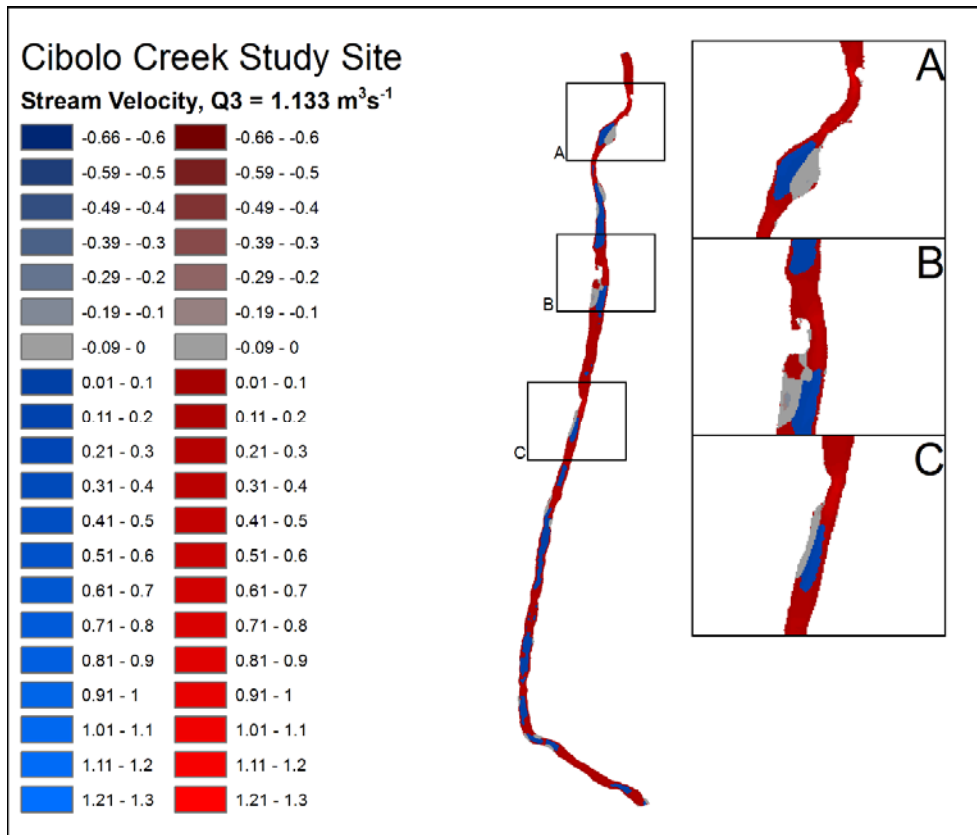


Figure 8.12 (cont'd). Spatial distribution of streamwise velocity (m/s) for Q1–Q5 for topographic highs (red colors) and lows (blue colors).

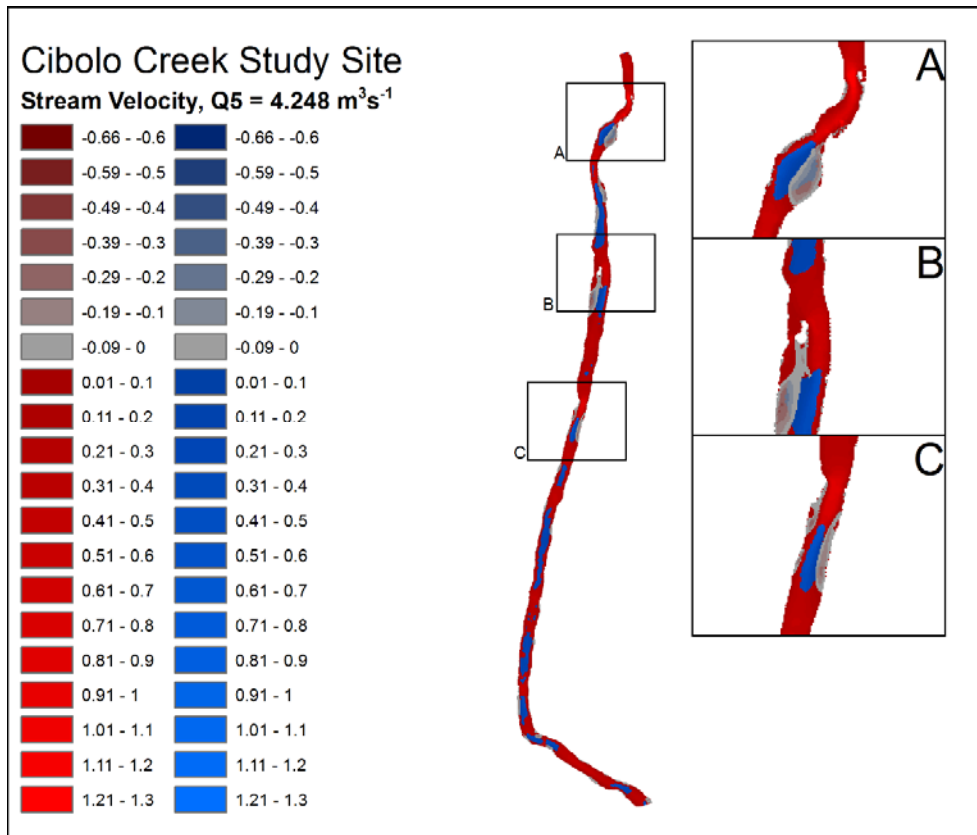


Figure 8.12 (cont'd). Spatial distribution of streamwise velocity (m/s) for Q1–Q5 for topographic highs (red colors) and lows (blue colors).

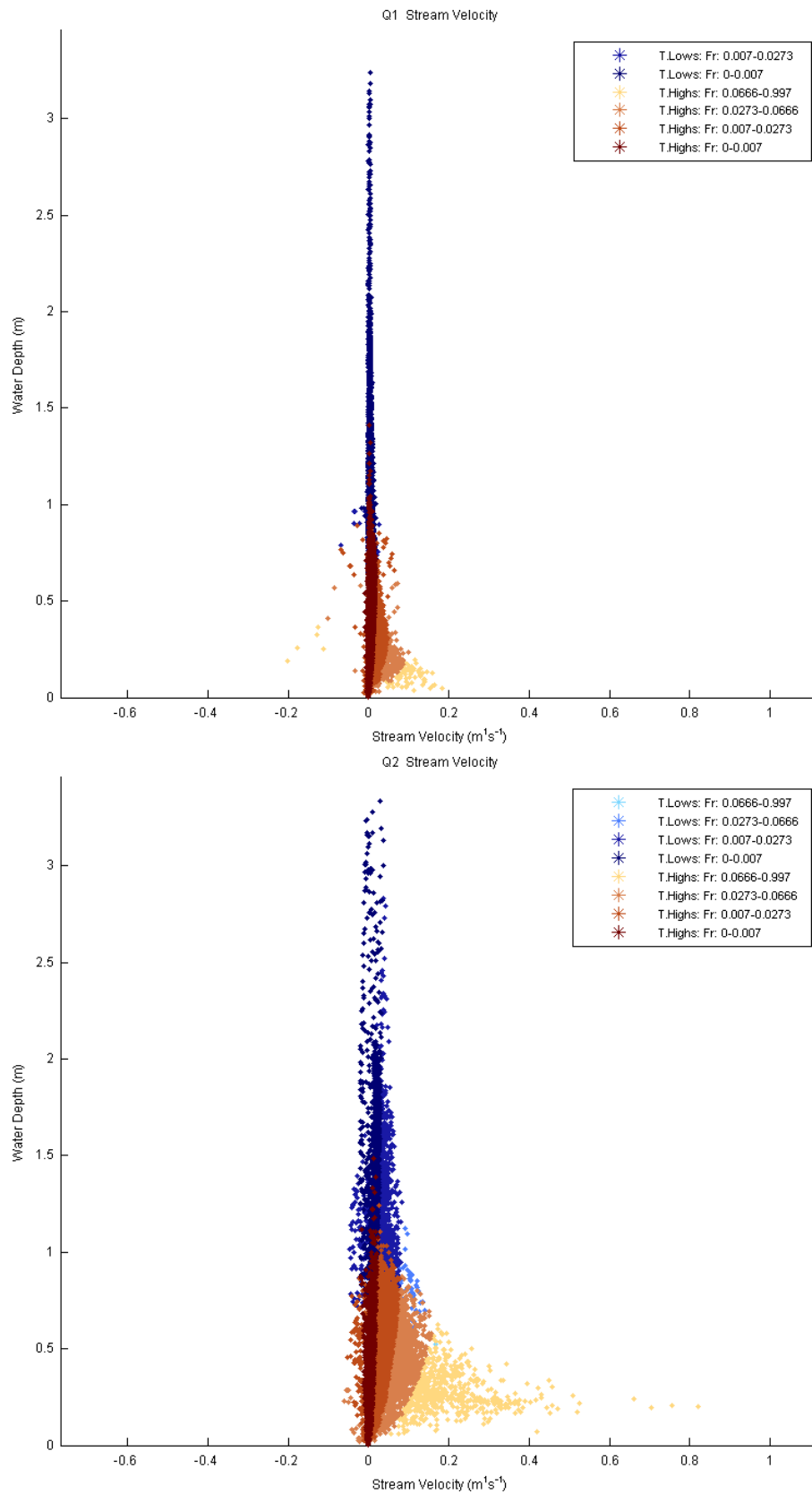


Figure 8.13. Distribution of streamwise velocity in relation to water depth for Q1–Q5 classified by topographic highs marked as T. Highs (brown colors), topographic lows marked as T. Lows (blue colors), and Froude number (Fr).

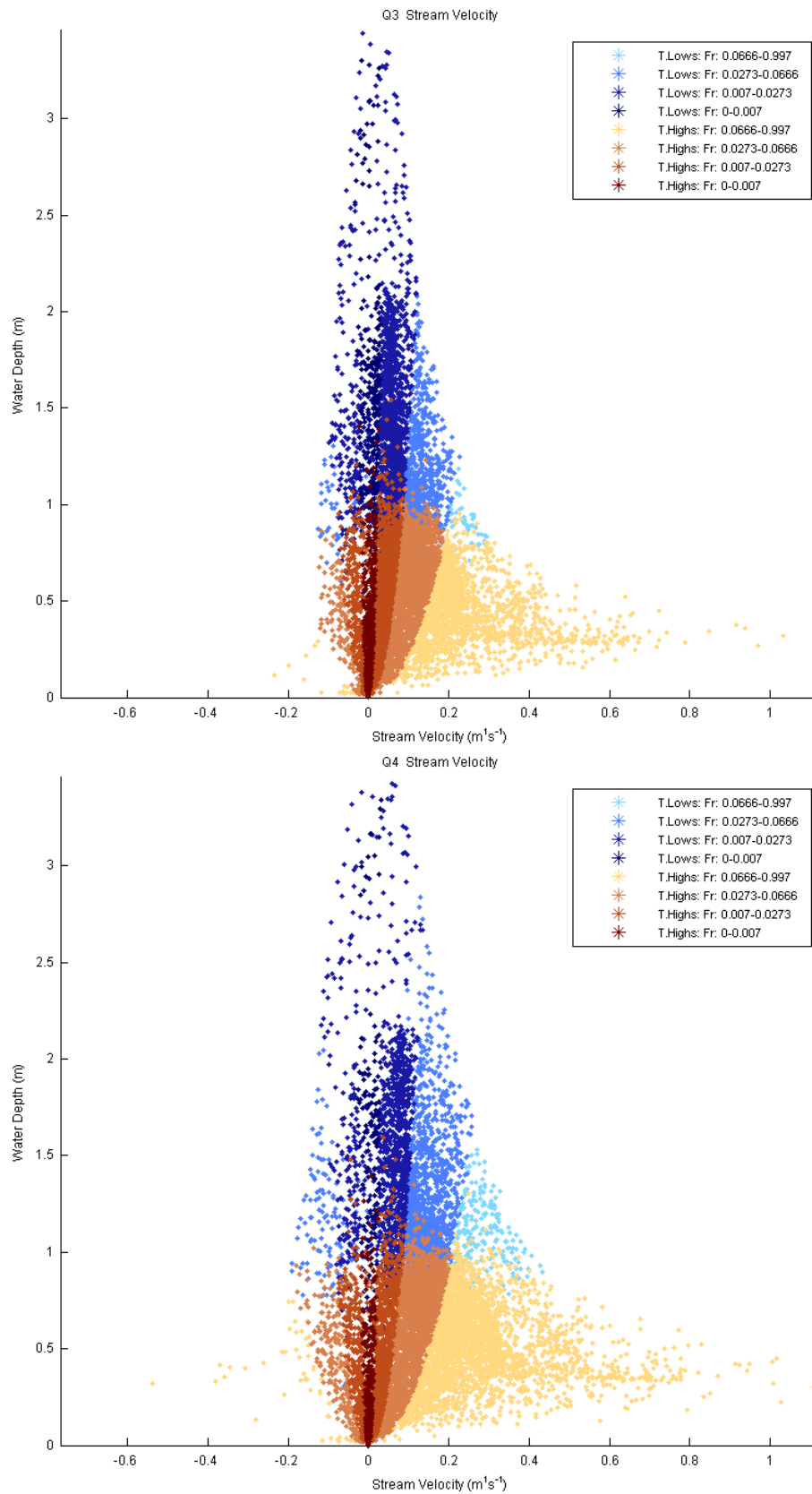


Figure 8.13 (cont'd). Distribution of streamwise velocity in relation to water depth for Q1–Q5 classified by topographic highs marked as T. Highs (brown colors), topographic lows marked as T. Lows (blue colors), and Froude number (Fr).

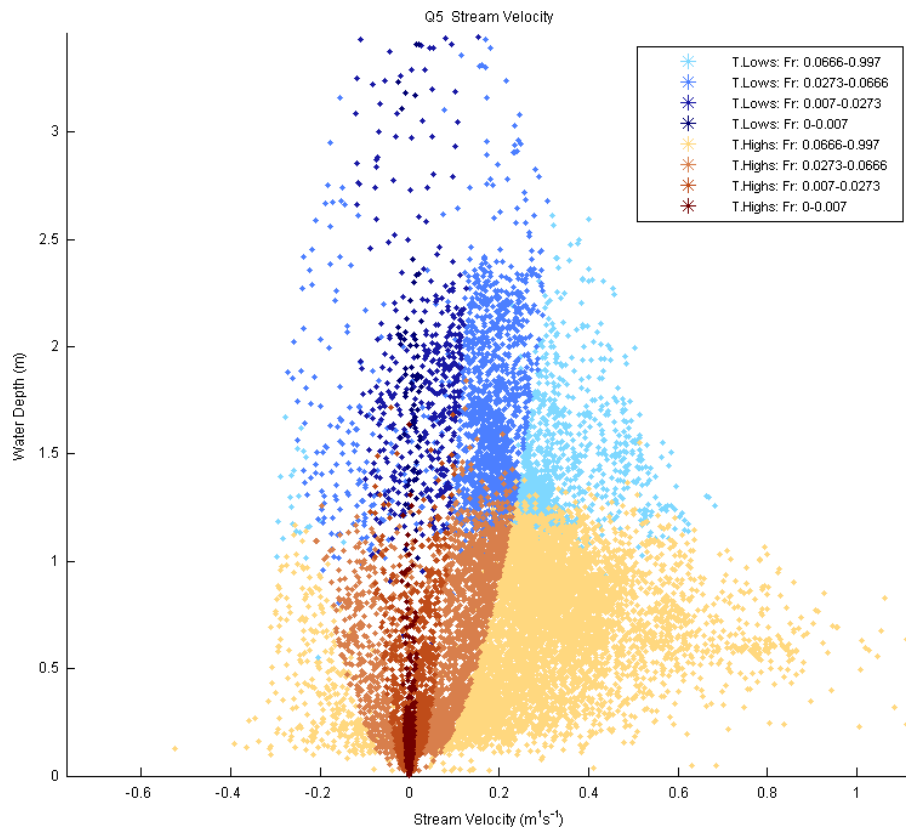


Figure 8.13 (cont'd). 3. Distribution of streamwise velocity in relation to water depth for Q1–Q5 classified by topographic highs marked as T. Highs (brown colors), topographic lows marked as T. Lows (blue colors), and Froude number (Fr).

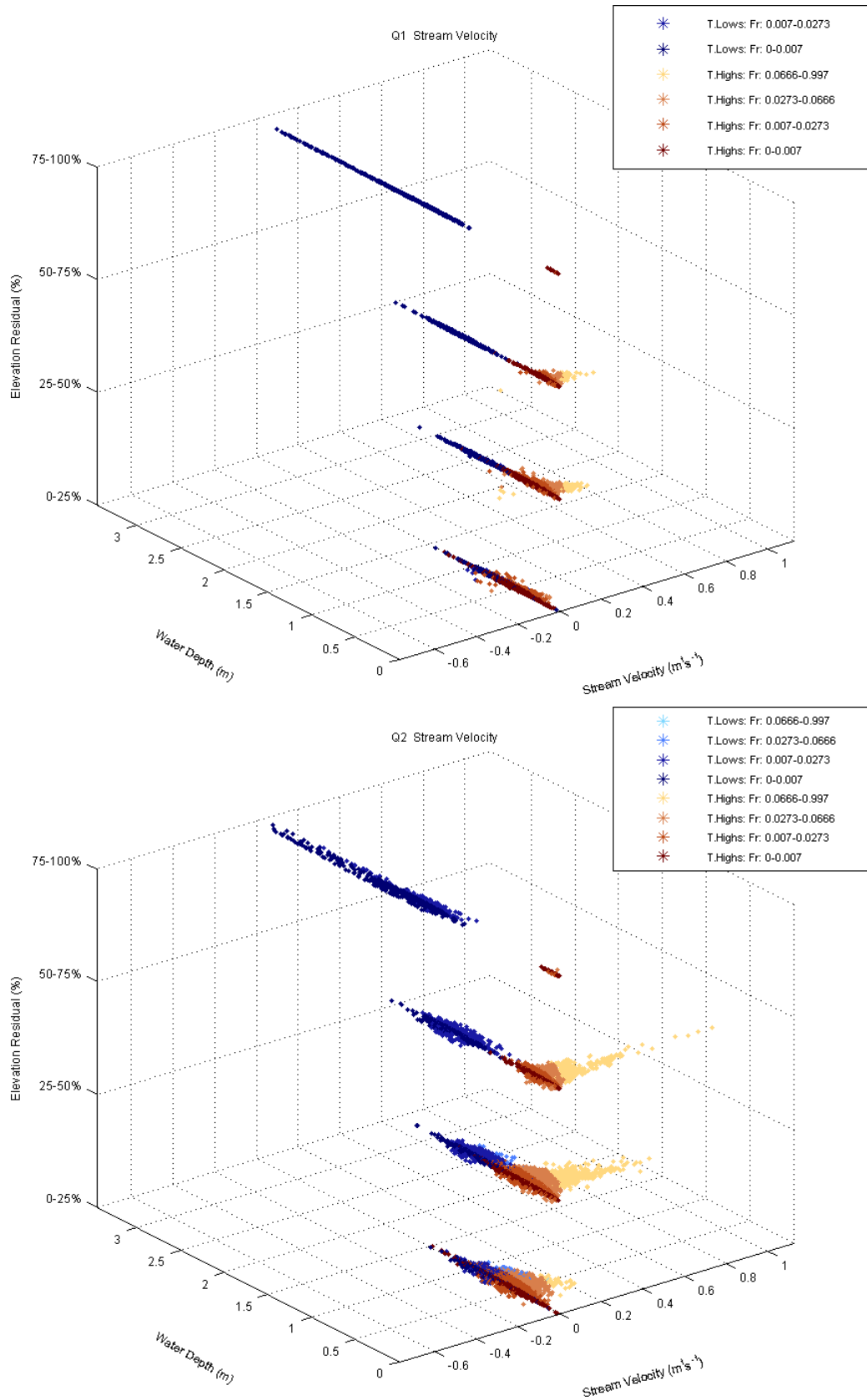


Figure 8.14. Distribution of streamwise velocity for topographic high (T. Highs)/low (T. Lows) subclasses (Figure 4.2) and Q1–Q5, classified by Froude number (Fr).

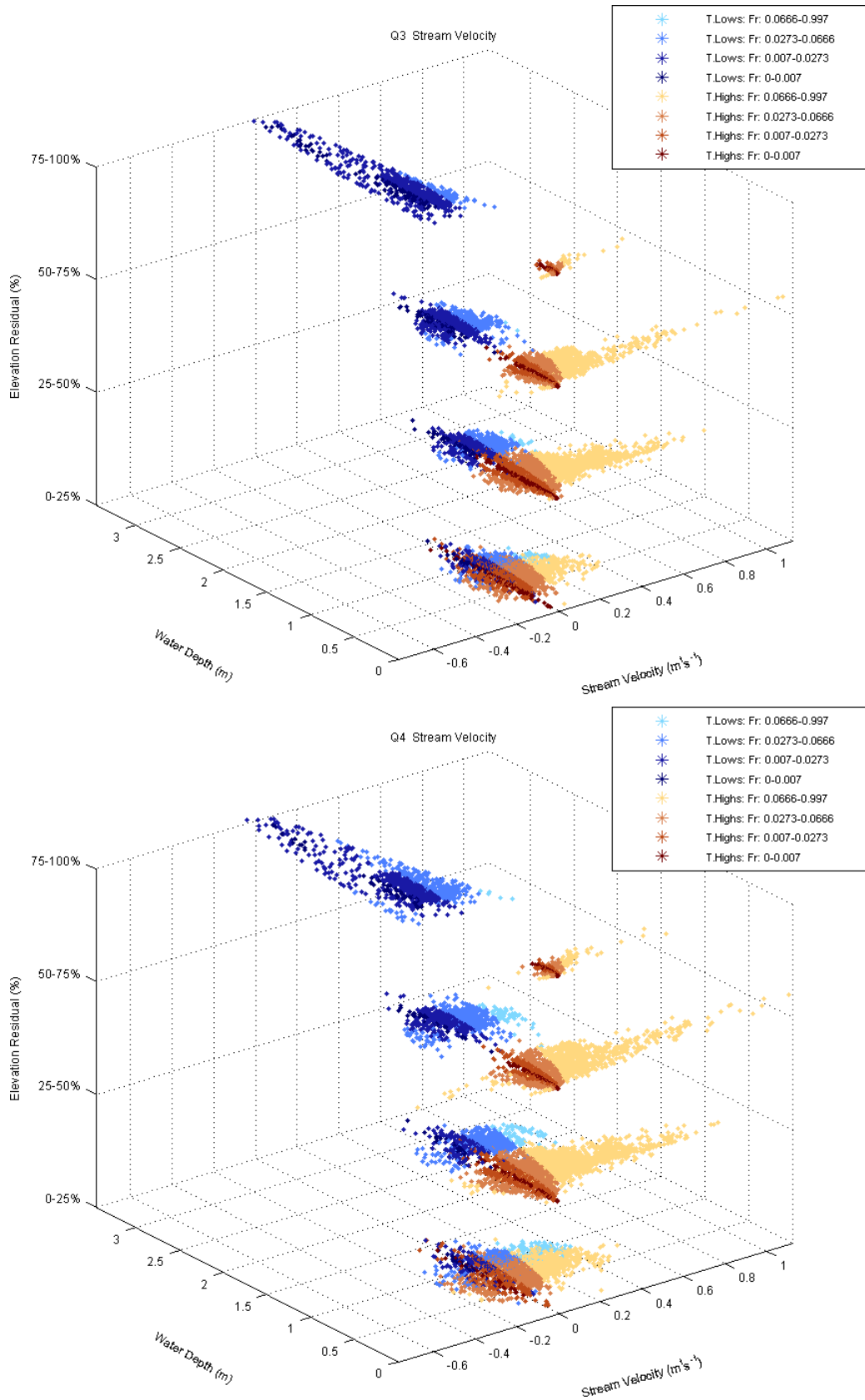


Figure 8.14 (cont'd). Distribution of streamwise velocity for topographic high (T. Highs)/low (T. Lows) subclasses (Figure 4.2) and Q1–Q5, classified by Froude number (Fr).

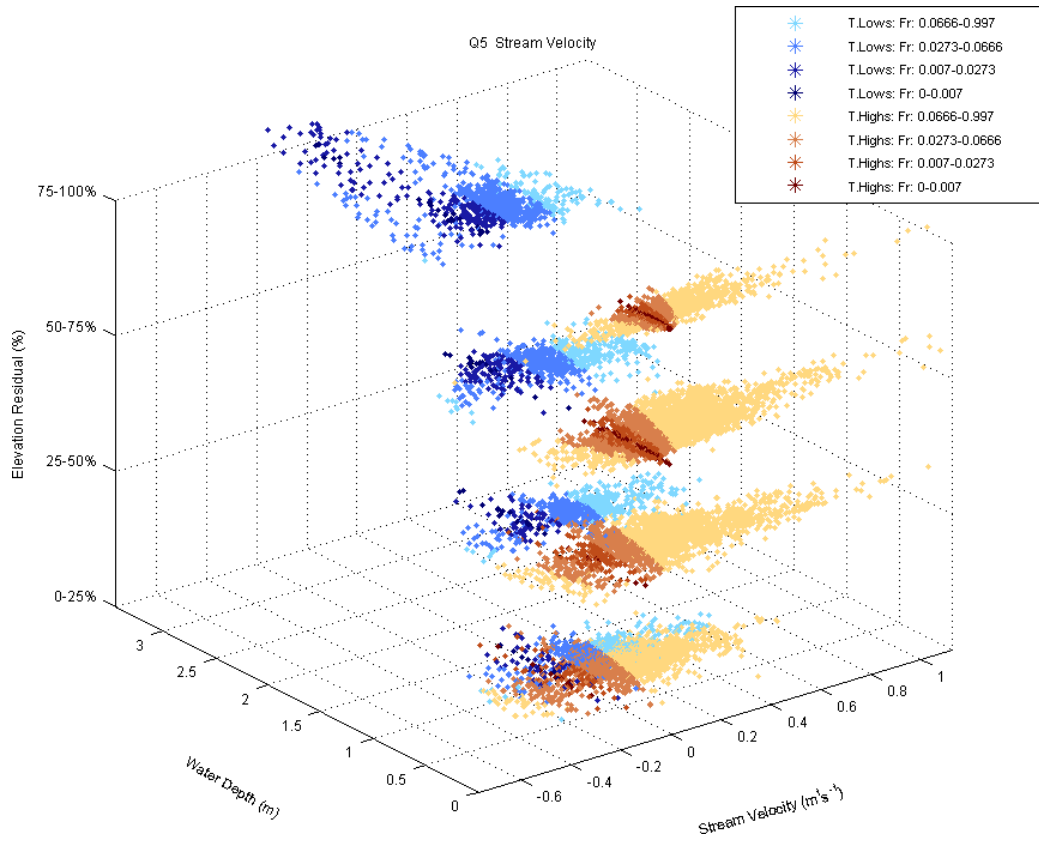


Figure 8.14 (cont'd). Distribution of streamwise velocity for topographic high (T. Highs)/low (T. Lows) subclasses (Figure 4.2) and Q1–Q5, classified by Froude number (Fr).

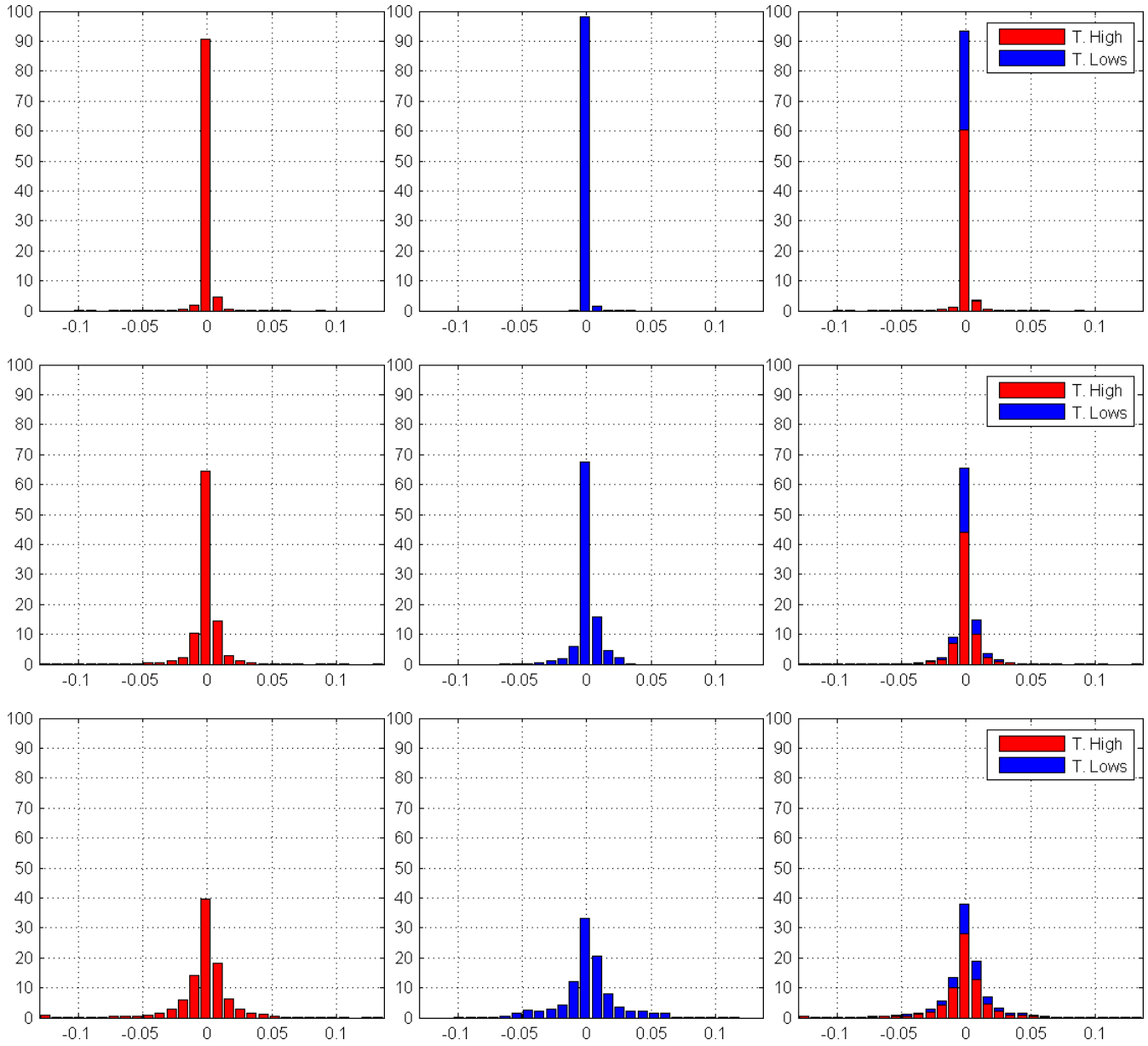


Figure 8.15. Distribution of normal velocity component for Q1–Q5 (rows, top to bottom) for topographic highs (marked as 'T. High') corresponding to the classes (+1)–(+4), topographic lows (marked as 'T. Lows') corresponding to the classes (-1)–(-4), and combined (columns, left to right). Horizontal and vertical axes correspond to normal velocity (m/s) and the percent values of topographic classes, respectively.

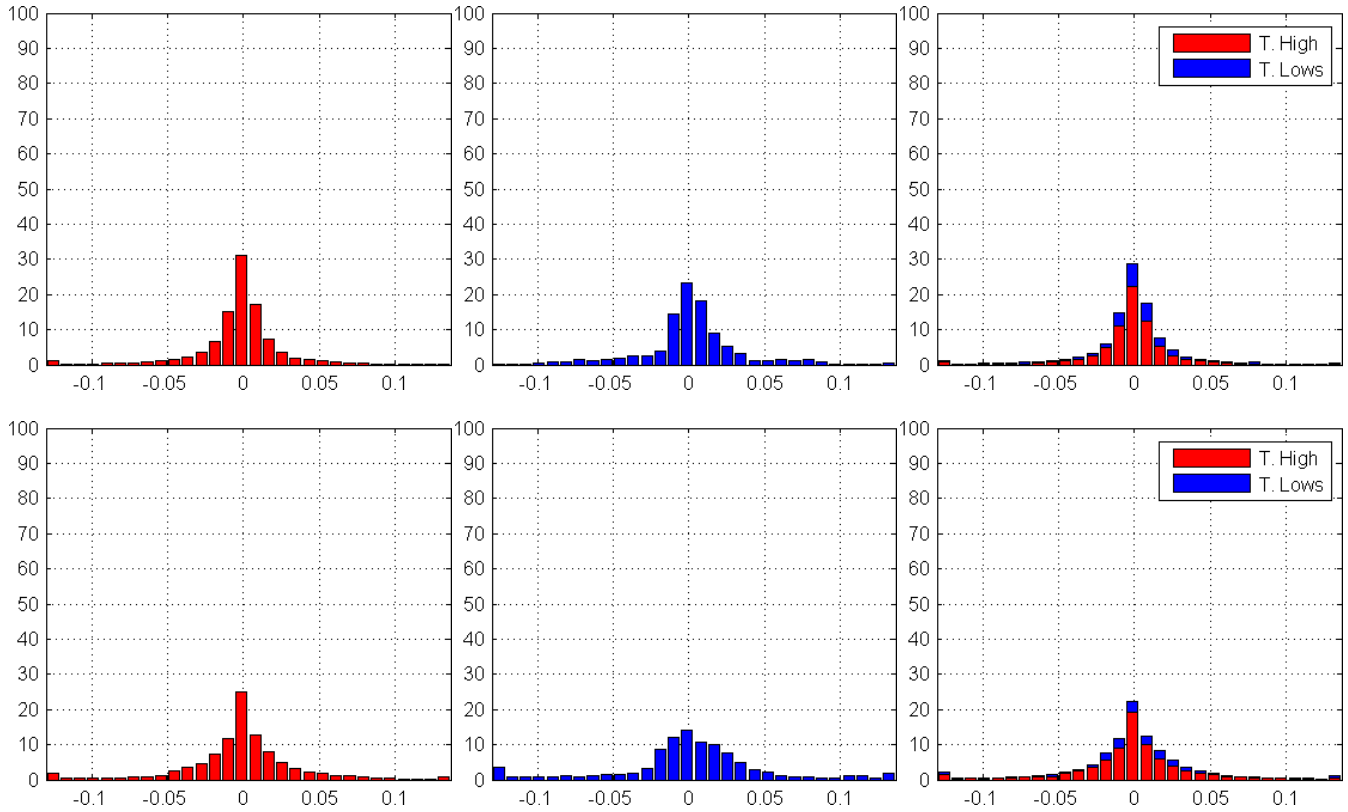


Figure 8.15 (cont'd). Distribution of normal velocity component for Q1–Q5 (rows, top to bottom) for topographic highs (marked as T. High) corresponding to the classes (+1)–(+4), topographic lows (marked as T. Lows) corresponding to the classes (-1)–(-4), and combined (columns, left to right). Horizontal and vertical axes correspond to normal velocity (m/s) and the percent values of topographic classes, respectively.

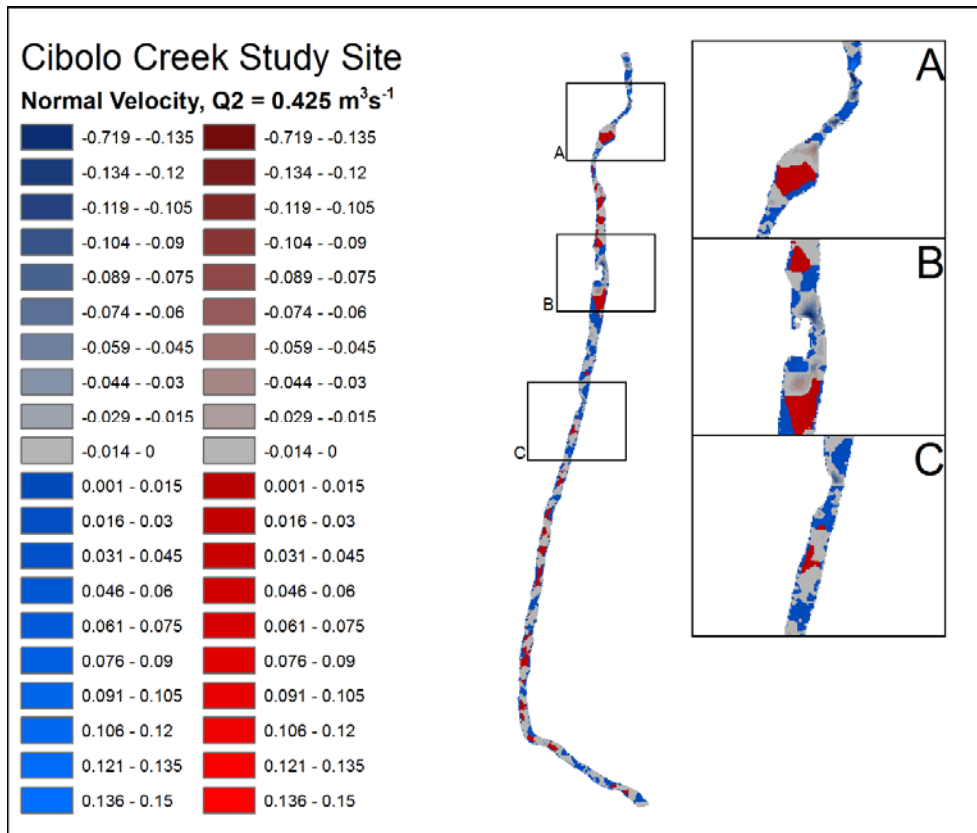
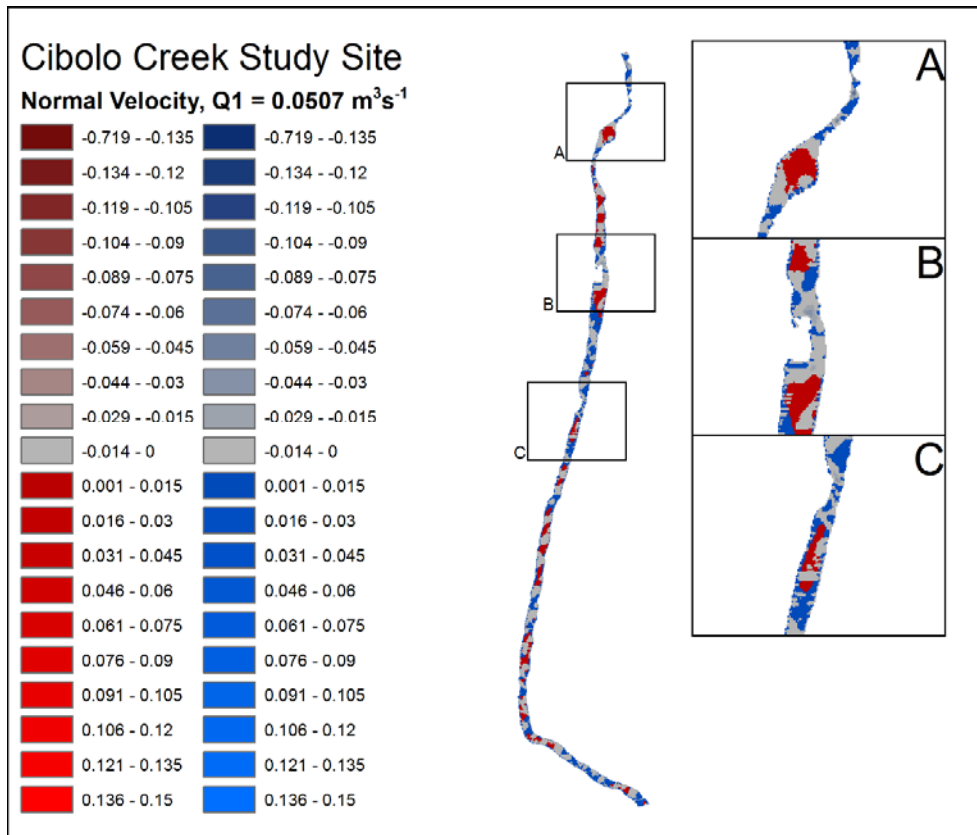


Figure 8.16. Spatial distribution of normal velocity (m/s) for Q1–Q5 for topographic highs (red colors) and lows (blue colors).

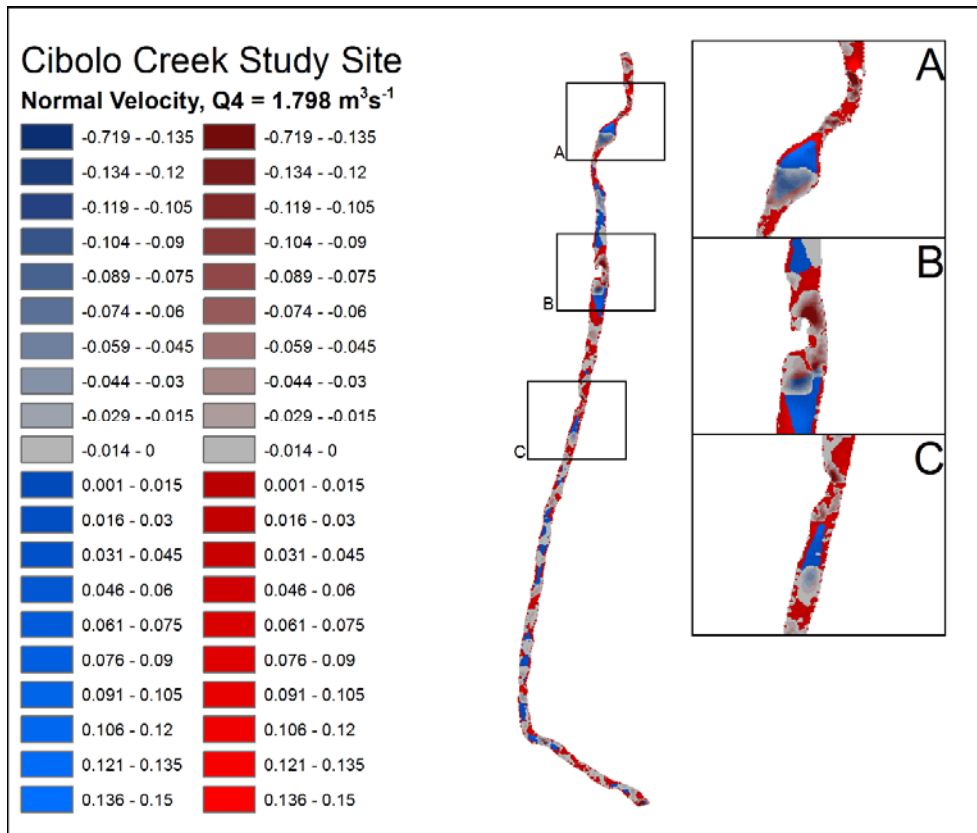
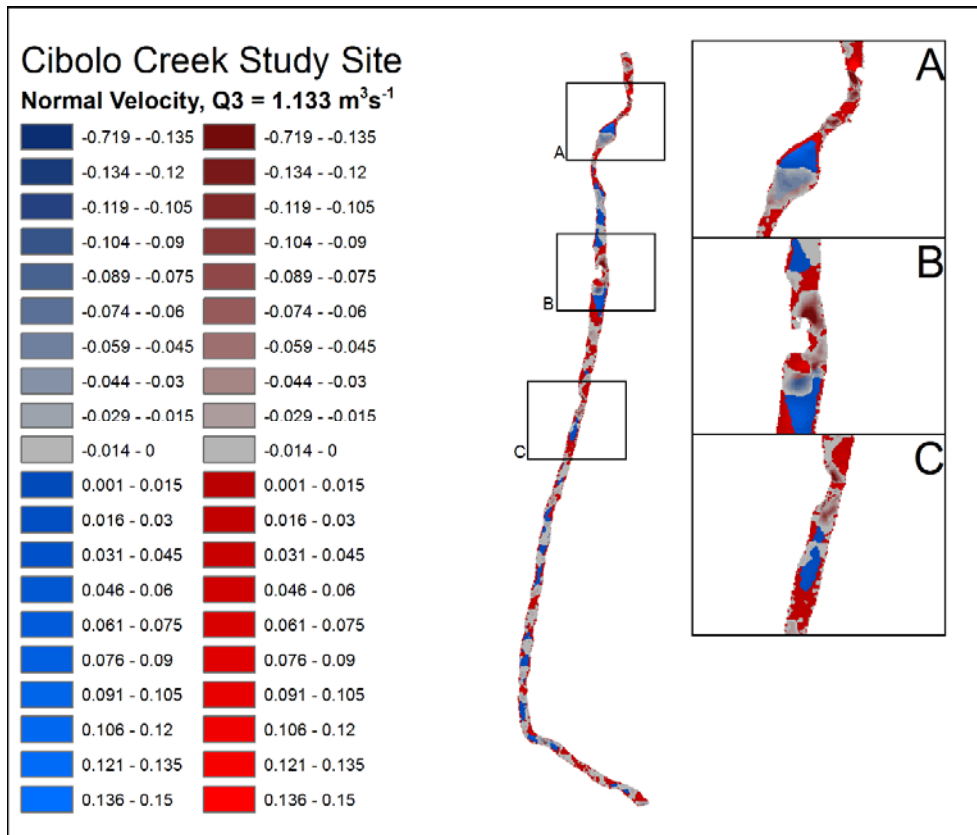


Figure 8.16 (cont'd). Spatial distribution of normal velocity (m/s) for Q1–Q5 for topographic highs (red colors) and lows (blue colors).

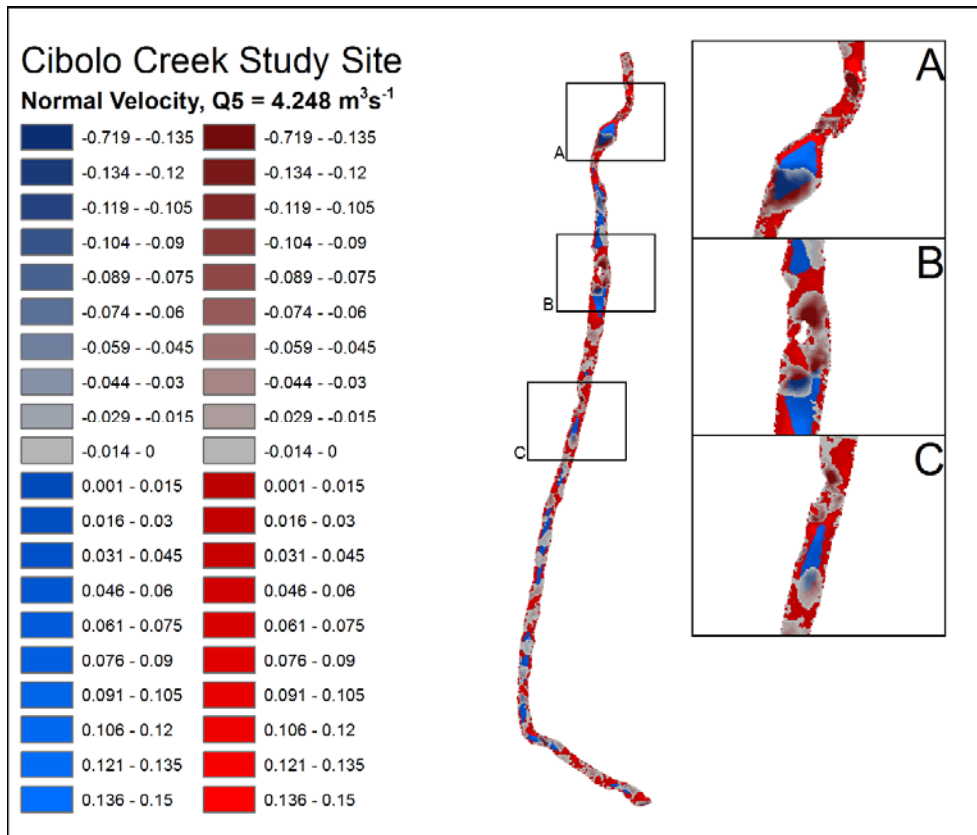


Figure 8.16 (cont'd). Spatial distribution of normal velocity (m/s) for Q1–Q5 for topographic highs (red colors) and lows (blue colors).

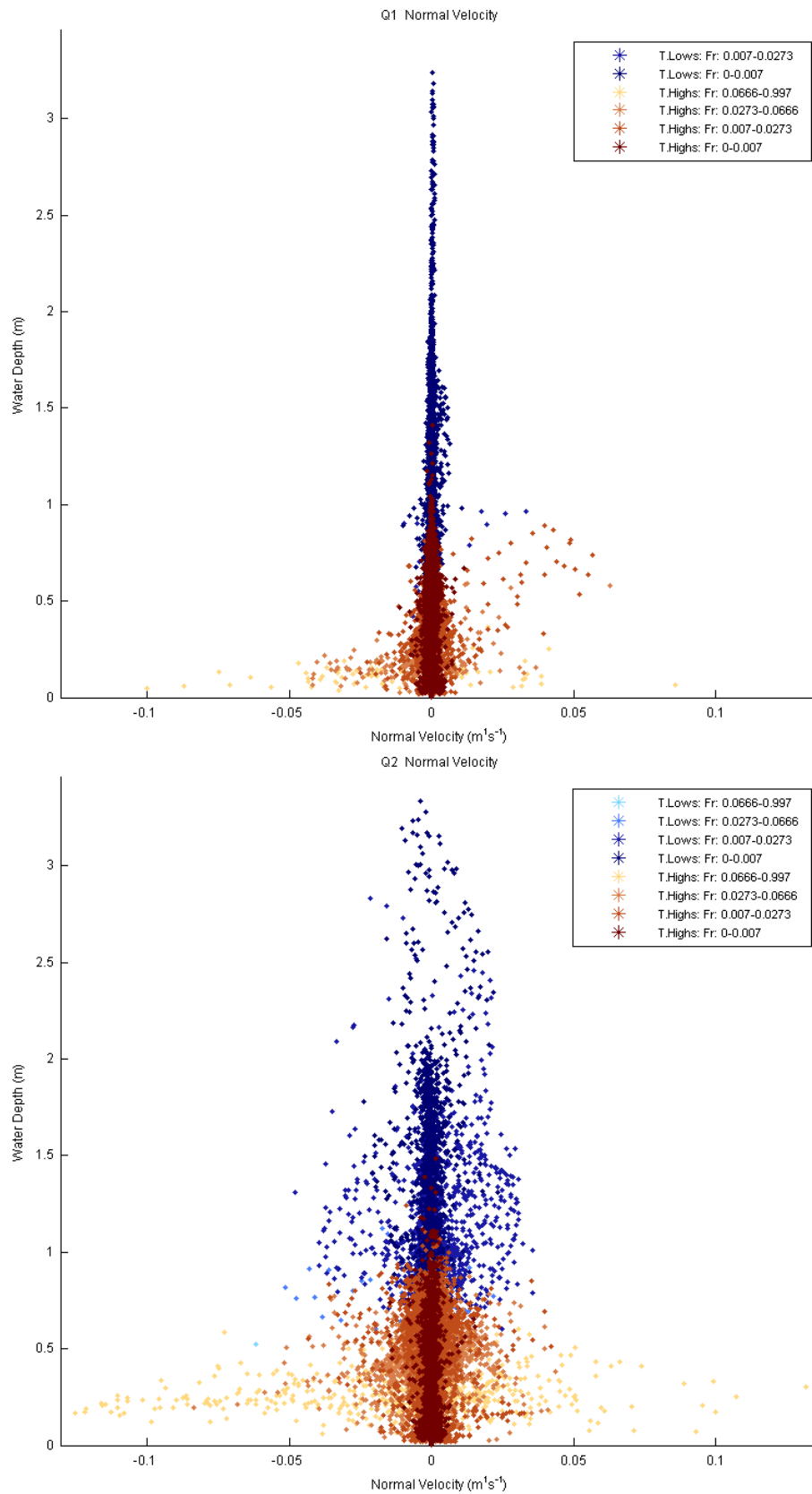


Figure 8.17. Distribution of normal velocity in relation to water depth for Q1–Q5 classified by topographic highs marked as T. Highs (brown colors), topographic lows marked as T. Lows (blue colors), and Froude number (Fr).

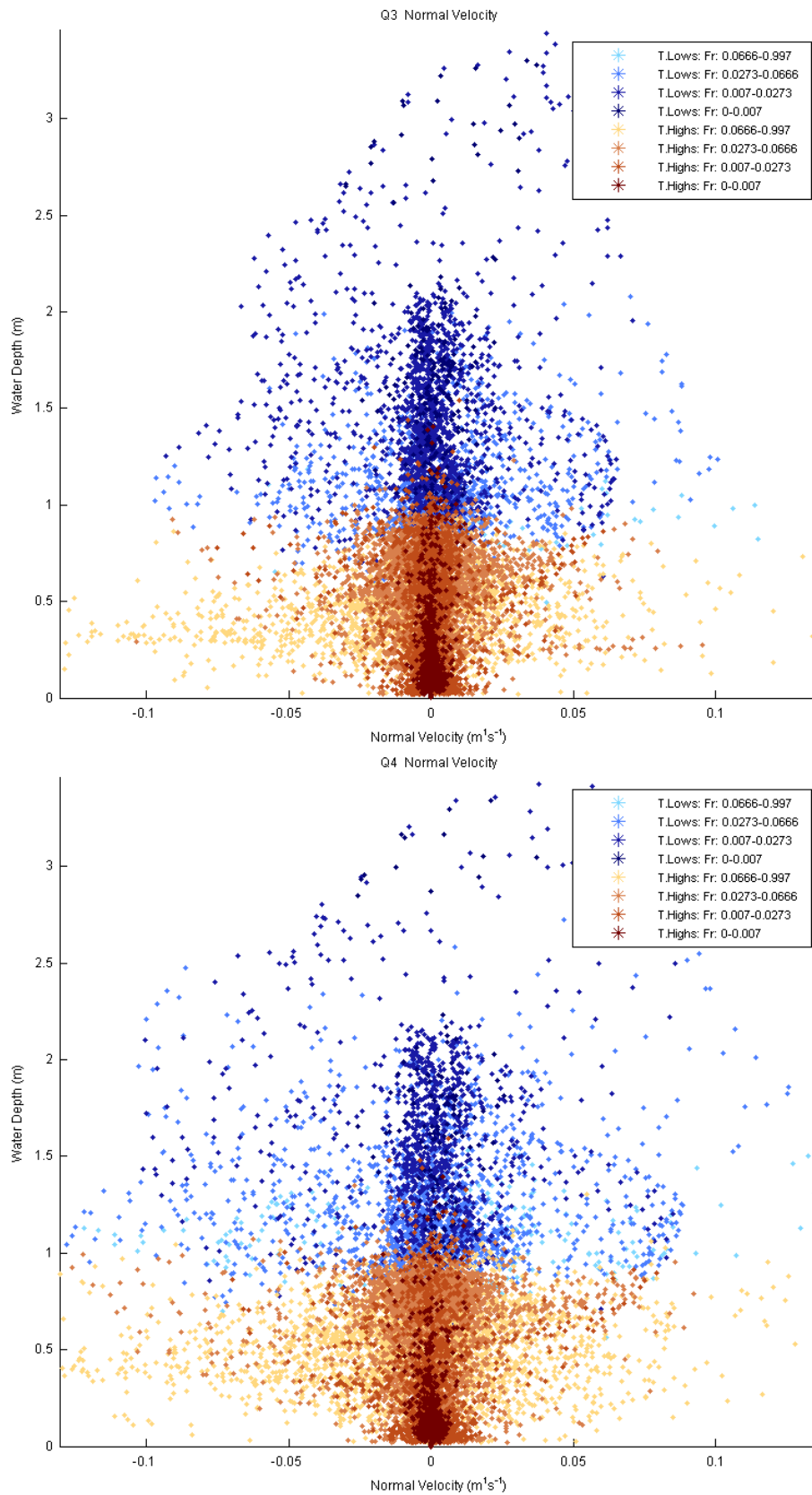


Figure 8.17 (con'td). Distribution of normal velocity in relation to water depth for Q1–Q5 classified by topographic highs marked as T. Highs (brown colors), topographic lows marked as T. Lows (blue colors), and Froude number (Fr).

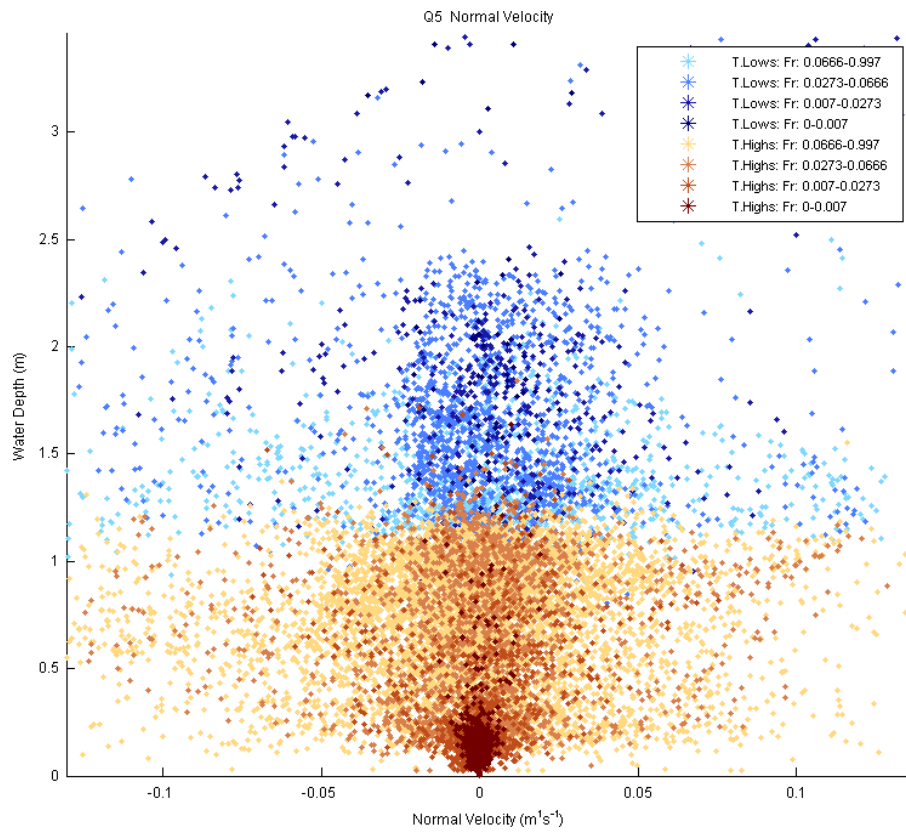


Figure 8.17 (cont'd). Distribution of normal velocity in relation to water depth for Q1–Q5 classified by topographic highs marked as T. Highs (brown colors), topographic lows marked as T. Lows (blue colors), and Froude number (Fr).

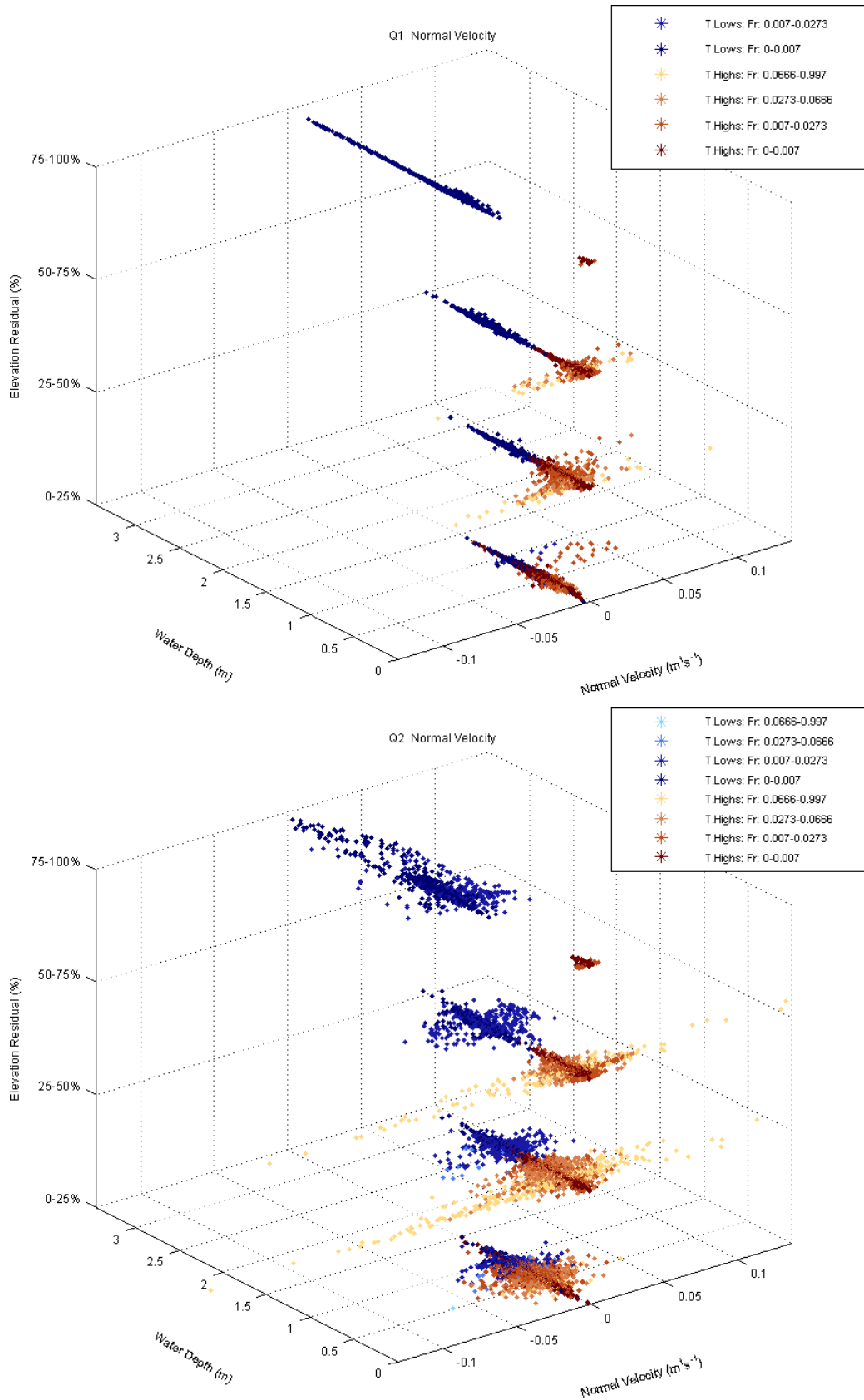


Figure 8.18. Distribution of normal velocity for topographic high (T. Highs)/low (T. Lows) subclasses (Figure 4.2) and Q1–Q5, classified by Froude number (Fr).

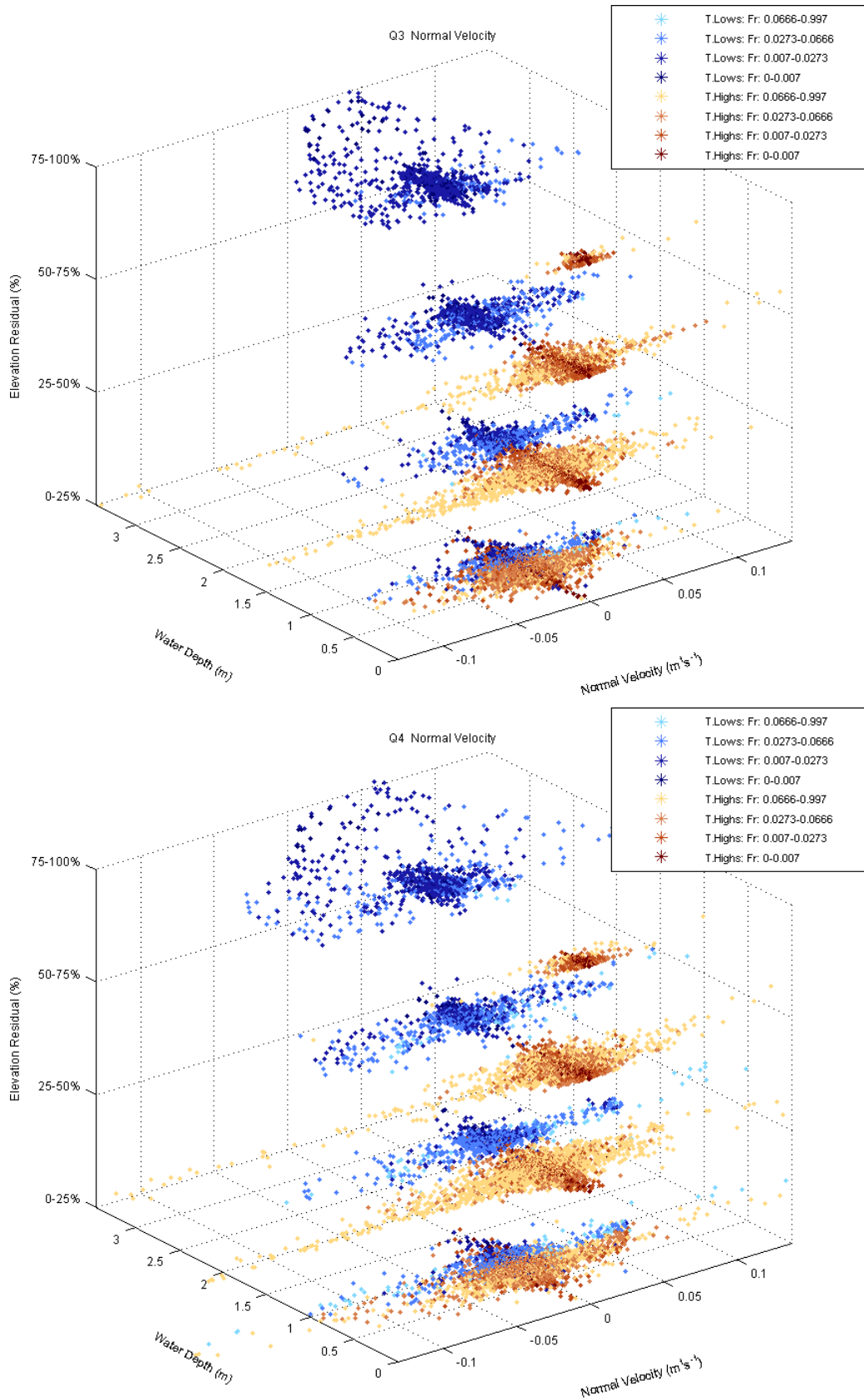


Figure 8.18 (cont'd). Distribution of normal velocity for topographic high (T. Highs)/low (T. Lows) subclasses (Figure 4.2) and Q1–Q5, classified by Froude number (Fr).

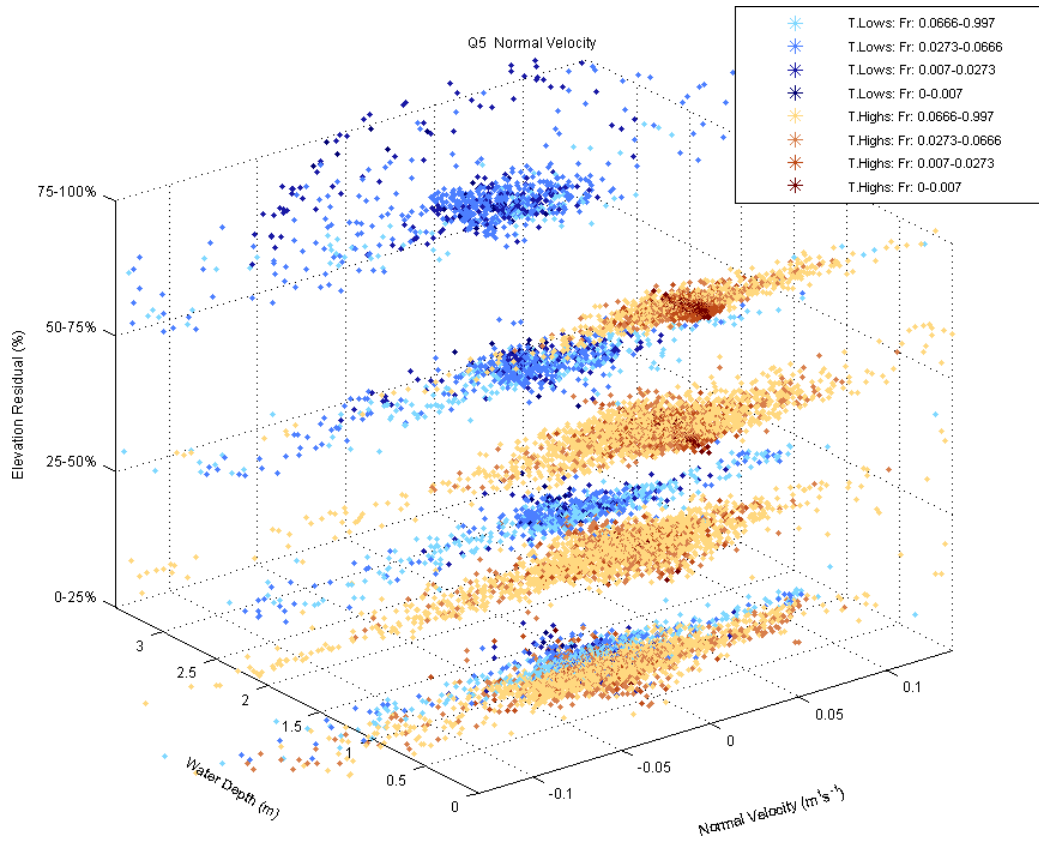


Figure 8.18 (cont'd). Distribution of normal velocity for topographic high (T. Highs)/low (T. Lows) subclasses (Figure 4.2) and Q1–Q5, classified by Froude number (Fr).

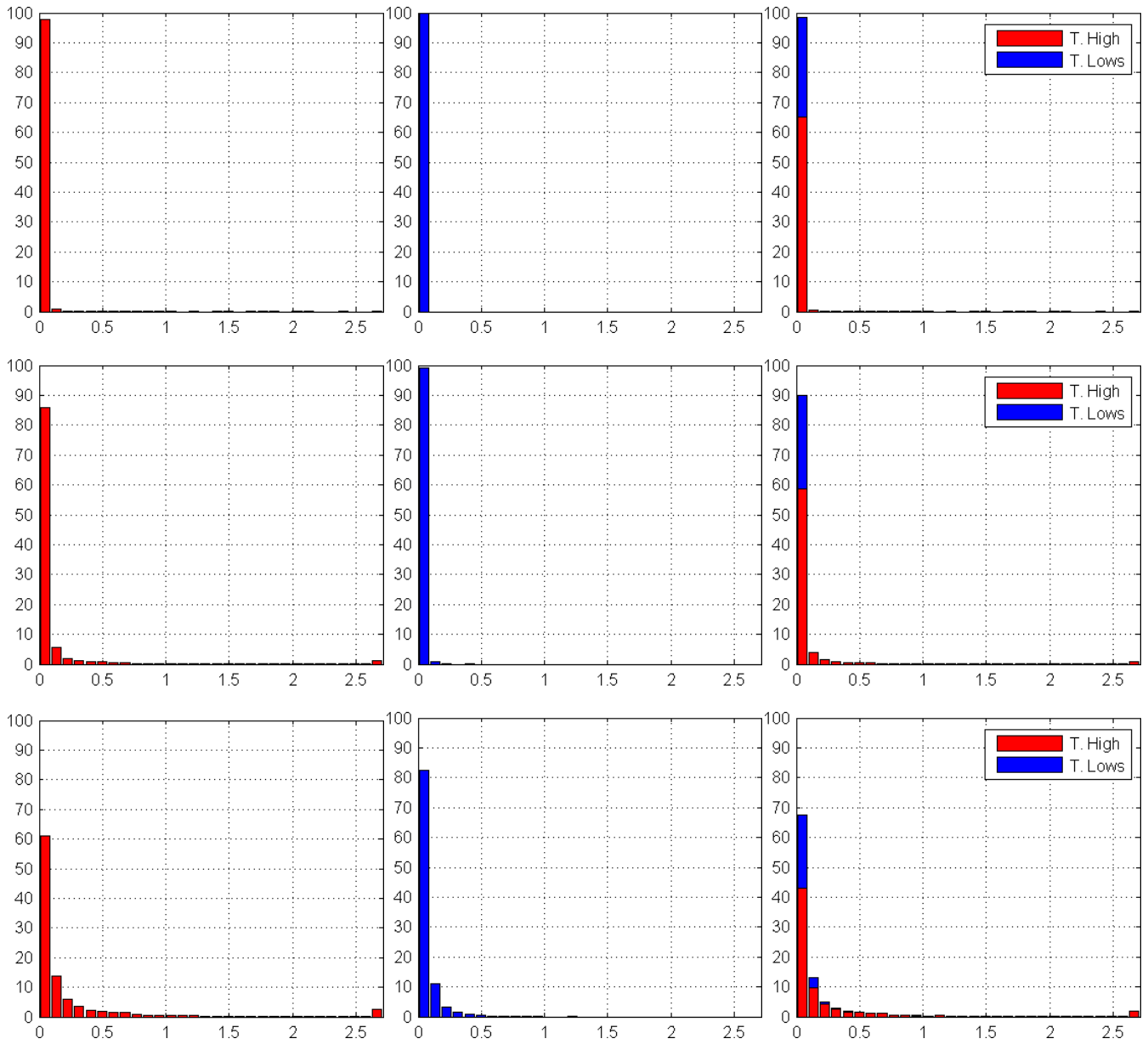


Figure 8.19. Distribution of shear stress for Q1–Q5 (rows, top to bottom) for topographic highs (marked as T. High) corresponding to the classes (+1)–(+4), topographic lows (marked as T. Lows) corresponding to the classes (-1)–(-4), and combined (columns, left to right). Horizontal and vertical axes correspond to shear stress ($\text{kg} \times \text{m/s}^2$) and the percent values of topographic classes, respectively..

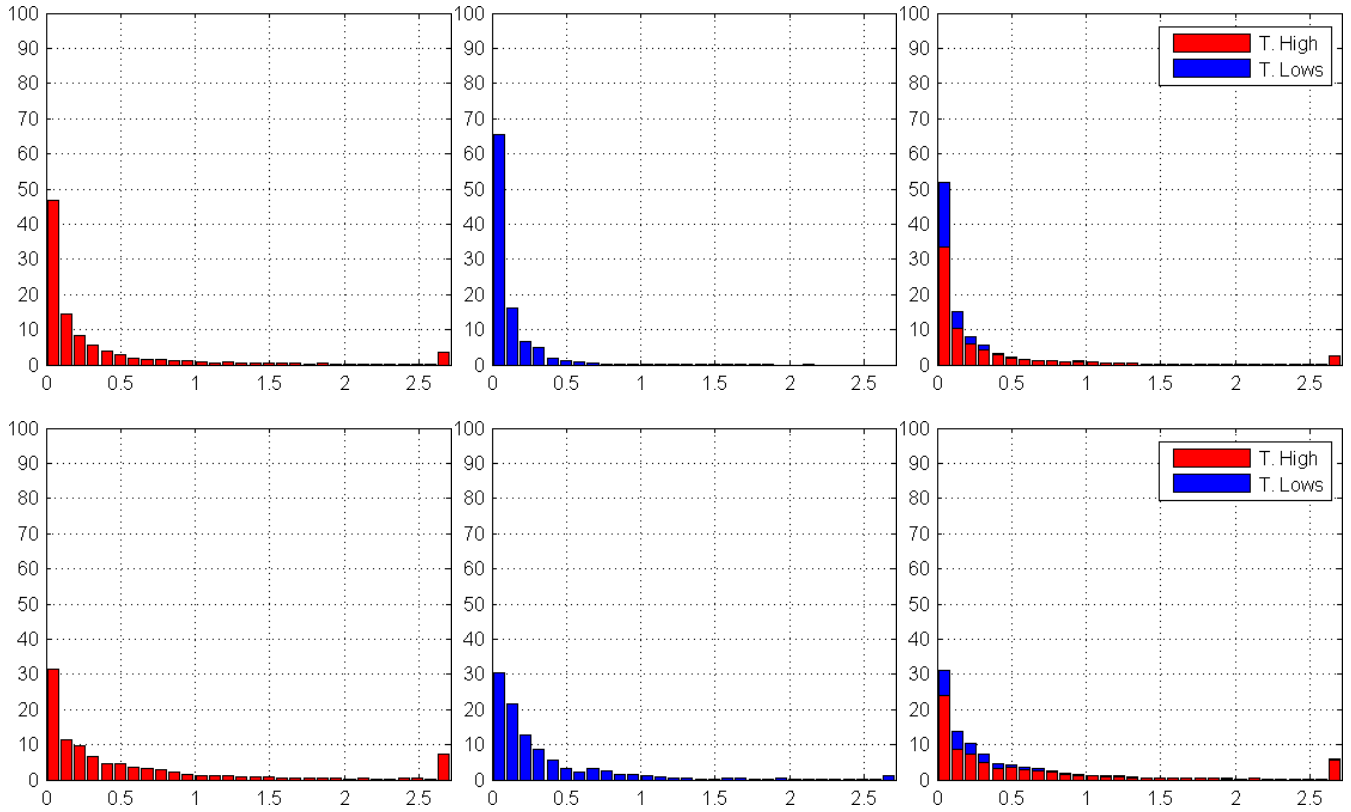


Figure 8.19 (cont'd). Distribution of shear stress for Q1–Q5 (rows, top to bottom) for topographic highs (marked as T. High) corresponding to the classes (+1)–(+4), topographic lows (marked as T. Lows) corresponding to the classes (-1)–(-4), and combined (columns, left to right). Horizontal and vertical axes correspond to shear stress ($\text{kg} \times \text{m/s}^2$) and the percent values of topographic classes, respectively.

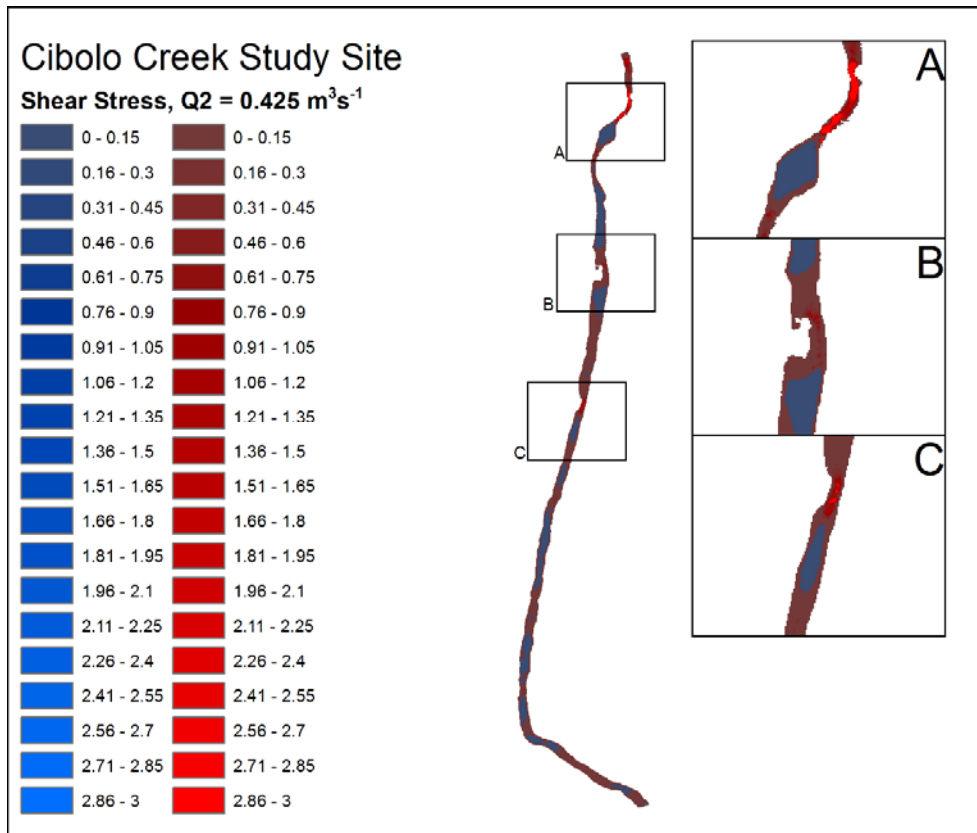
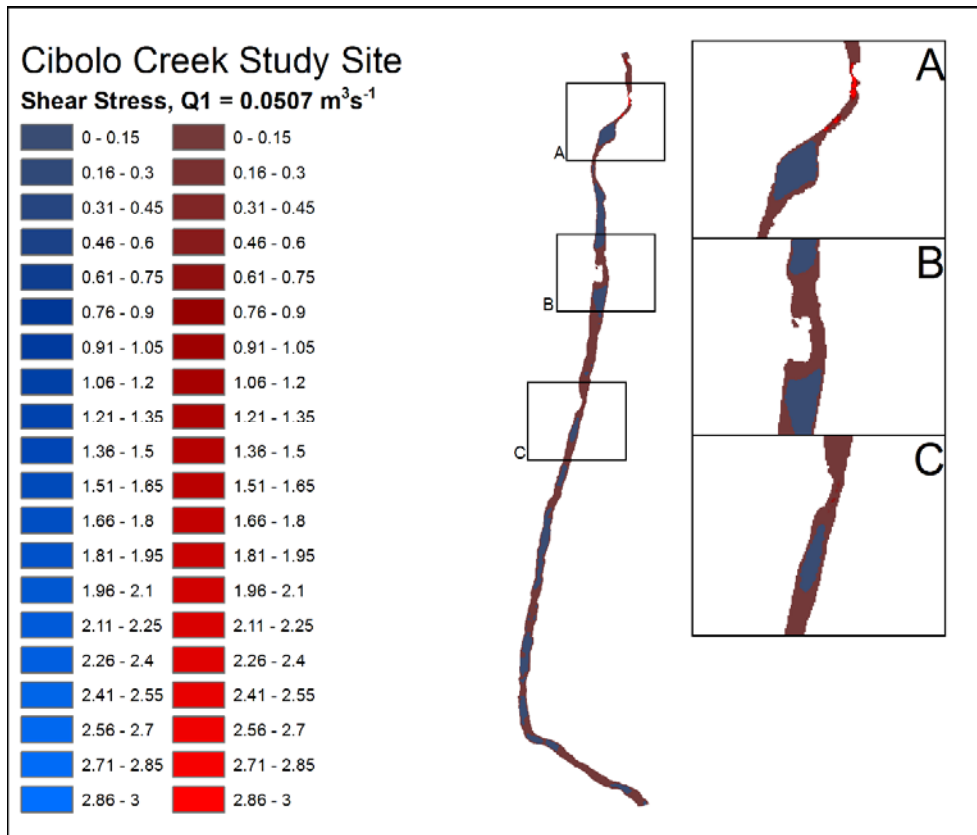


Figure 8.20. Spatial distribution of shear stress ($\text{kg} \times \text{m}^2/\text{s}^2$) for Q1–Q5 for topographic highs (red colors) and lows (blue colors).

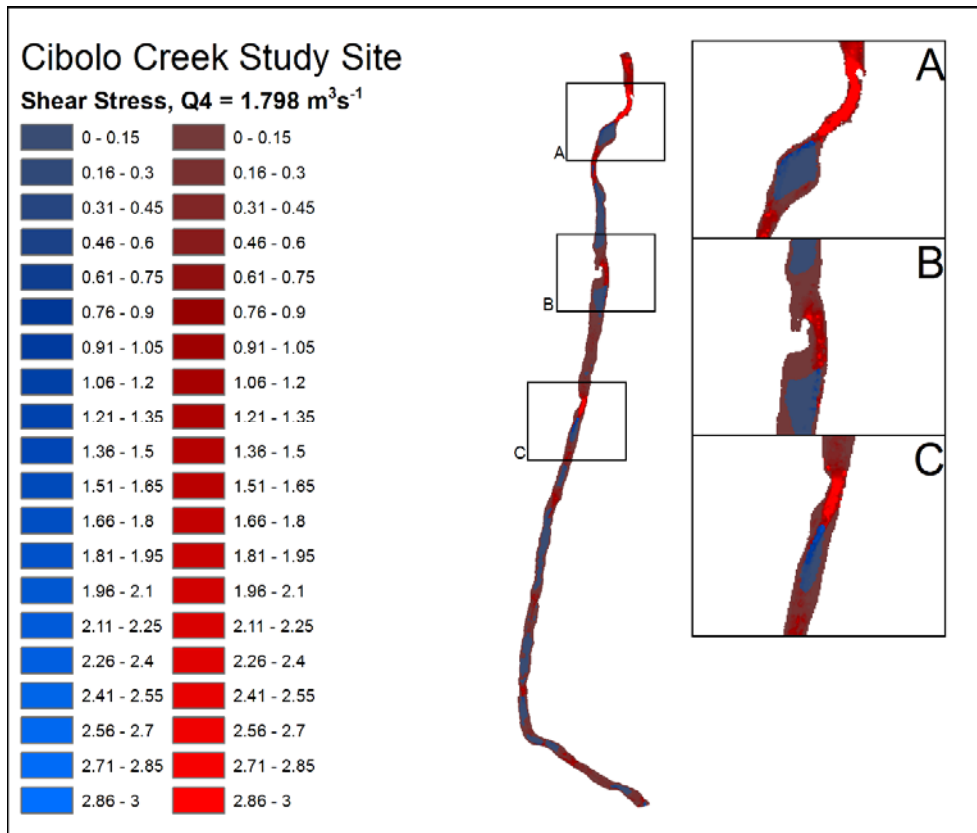
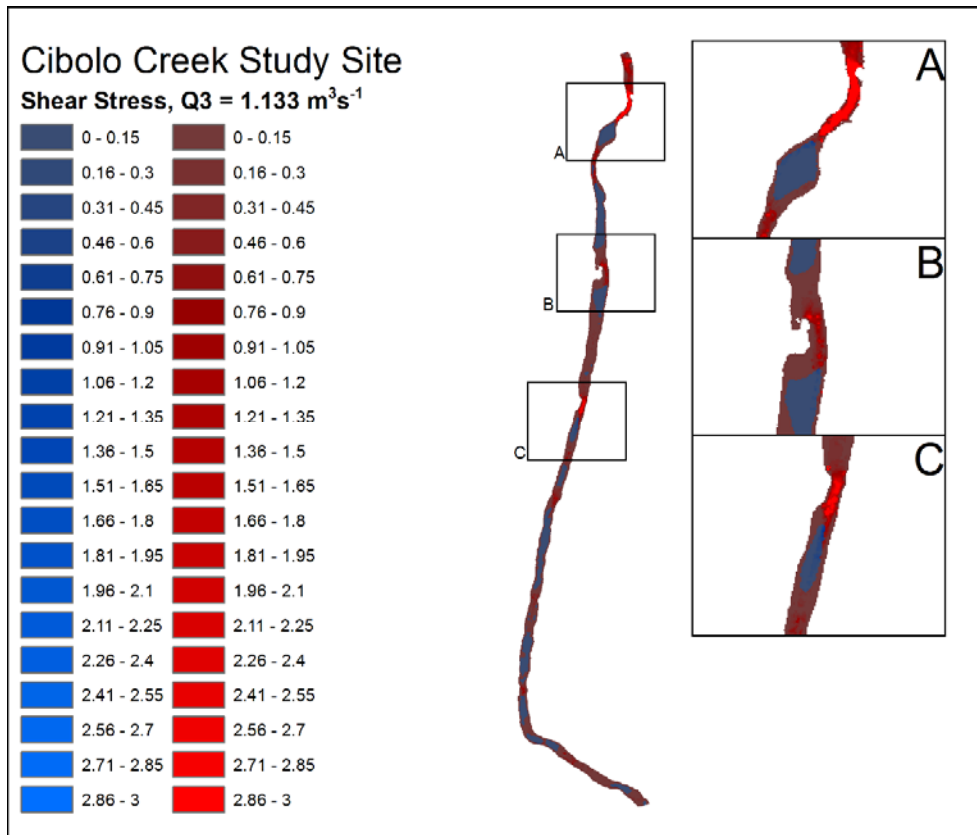


Figure 8.20 (cont'd). Spatial distribution of shear stress ($\text{kg} \times \text{m/s}^2$) for Q1–Q5 for topographic highs (red colors) and lows (blue colors).

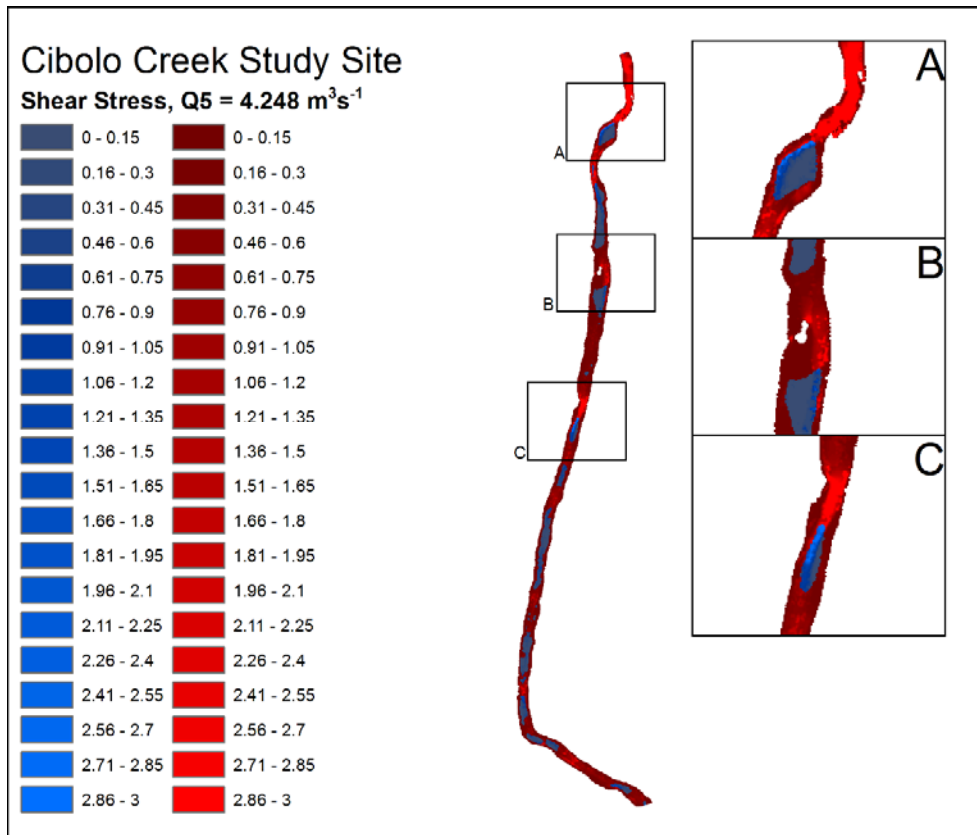


Figure 8.20 (cont'd). Spatial distribution of shear stress ($\text{kg} \times \text{m/s}^2$) for Q1–Q5 for topographic highs (red colors) and lows (blue colors).

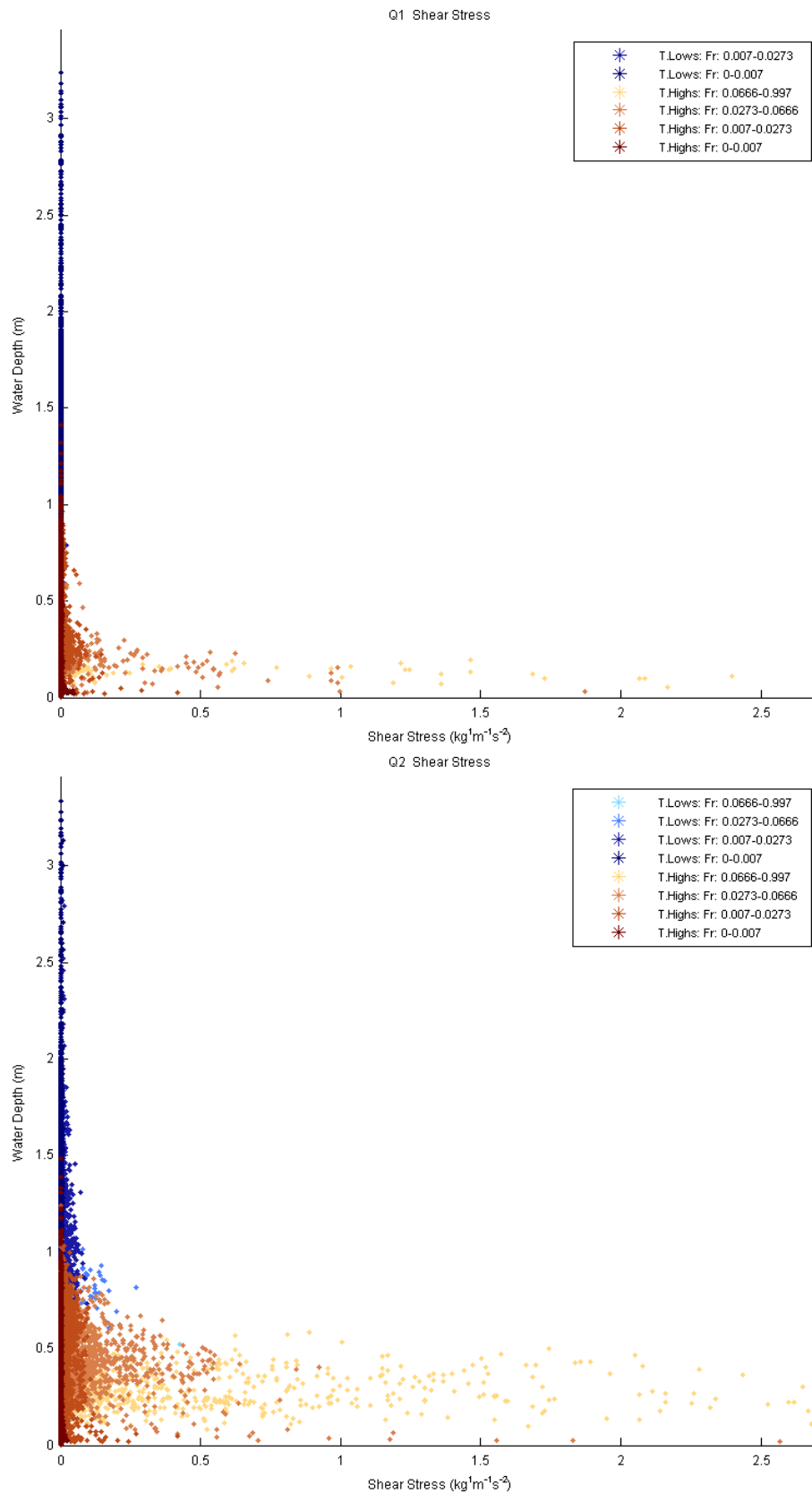


Figure 8.21. Distribution of shear stress in relation to water depth for Q1–Q5 classified by topographic highs marked as T. Highs (brown colors) and topographic lows marked as T. Lows (blue colors) and Froude number (Fr).

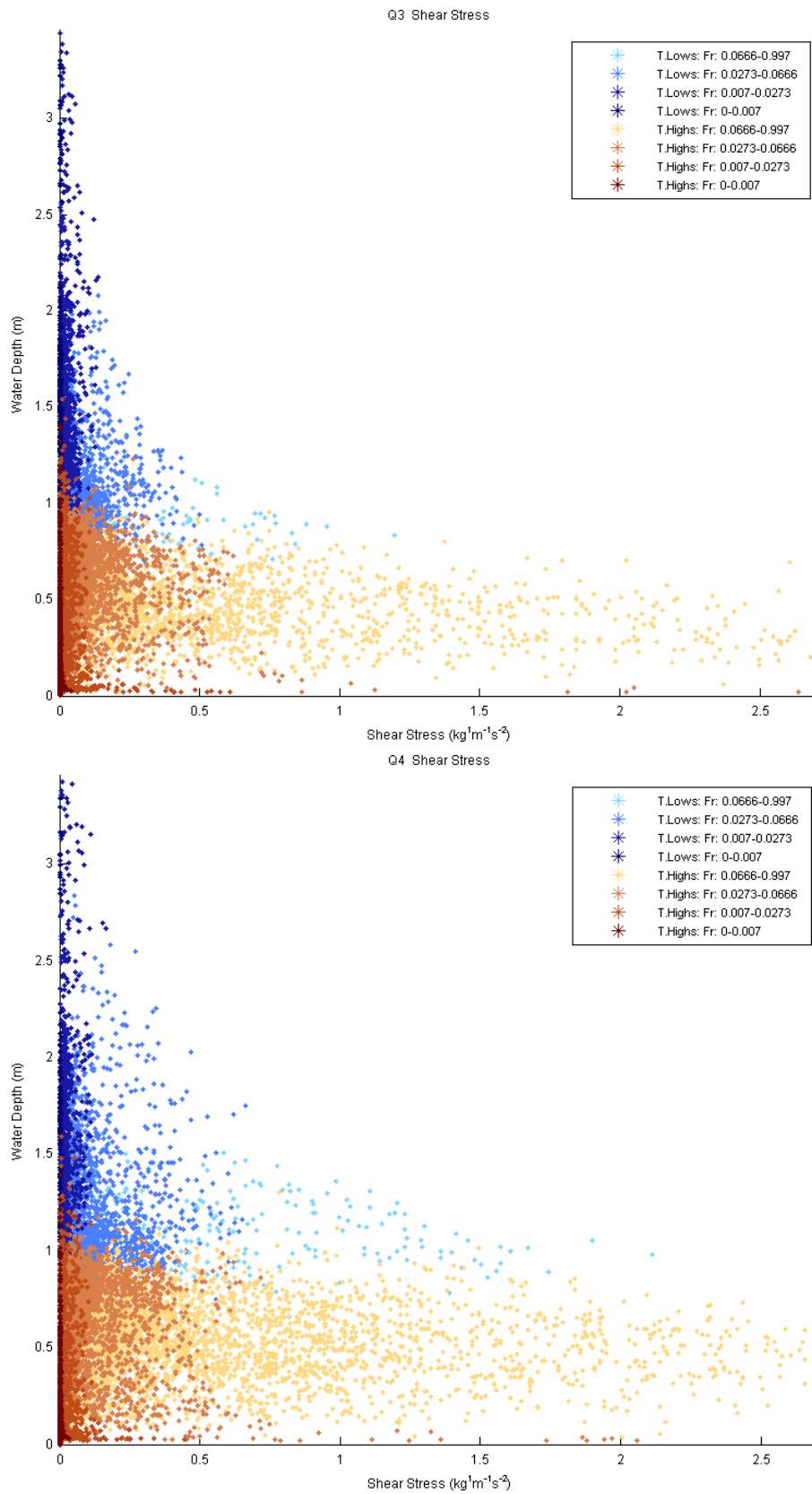


Figure 8.21 (cont'd). Distribution of shear stress in relation to water depth for Q1–Q5 classified by topographic highs marked as T. Highs (brown colors) and topographic lows marked as T. Lows (blue colors) and Froude number (Fr).

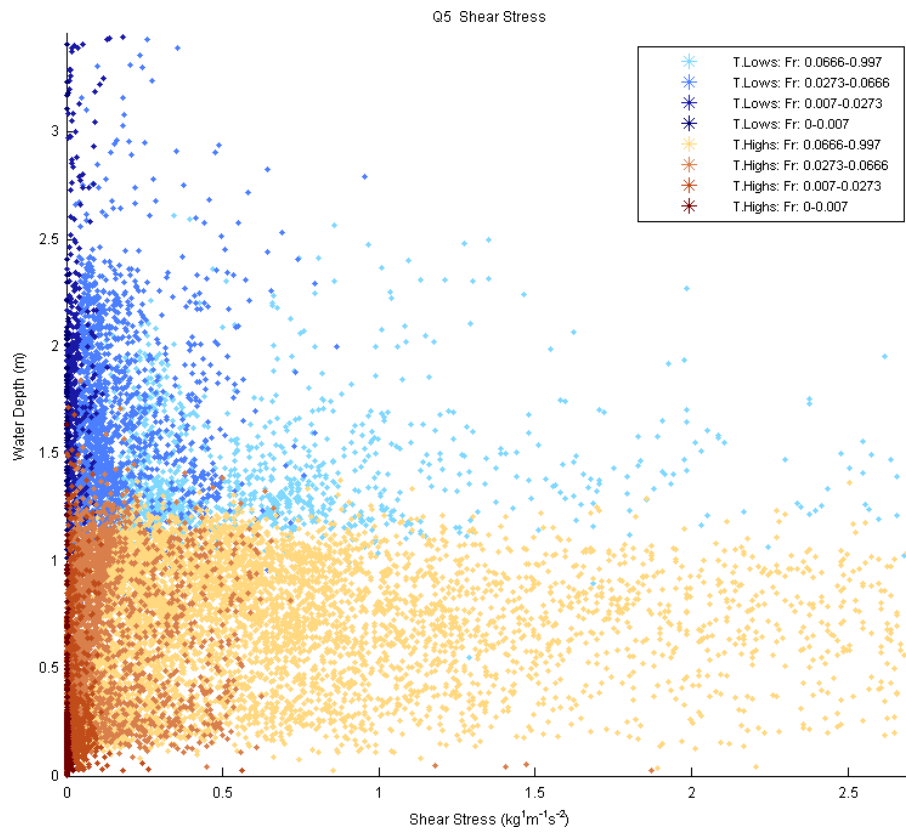


Figure 8.21 (cont'd). Distribution of shear stress in relation to water depth for Q1–Q5 classified by topographic highs marked as T. Highs (brown colors) and topographic lows marked as T. Lows (blue colors) and Froude number (Fr).

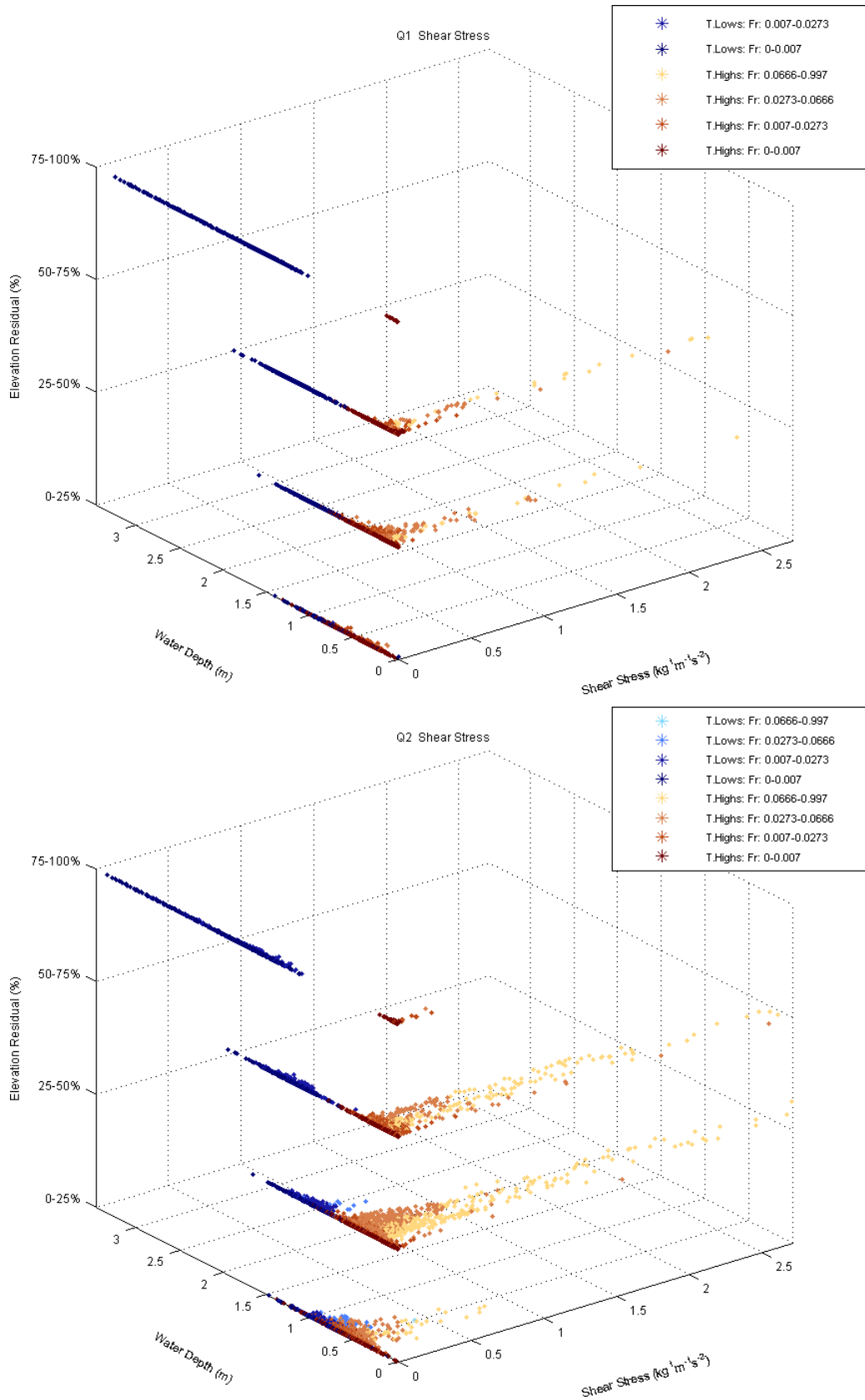


Figure 8.22. Distribution of shear stress for topographic high (T. Highs)/low (T. Lows) subclasses (Figure 4.2) and Q1–Q5, classified by Froude number (Fr).

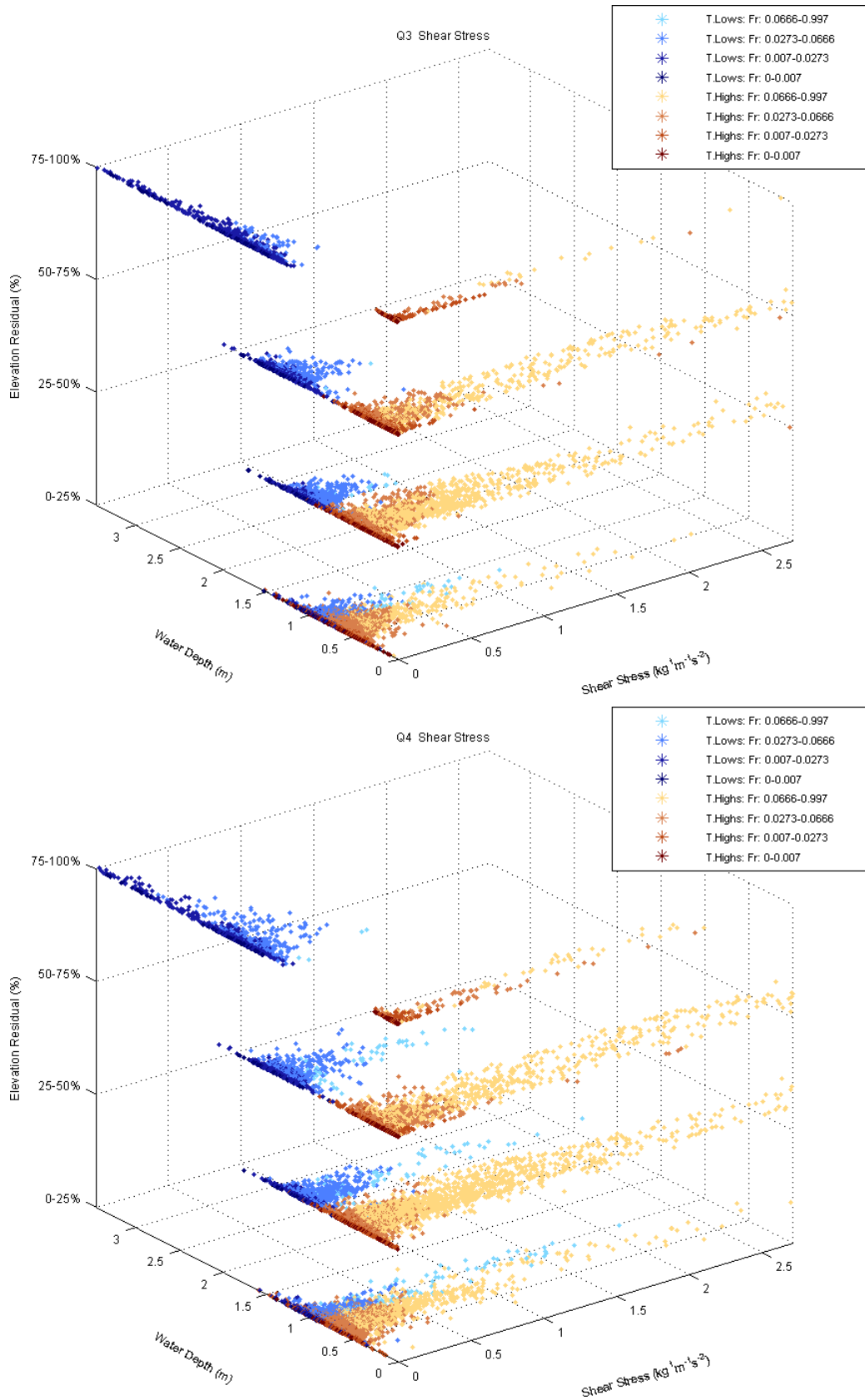


Figure 8.22 (cont'd). Distribution of shear stress for topographic high (T. Highs)/low (T. Lows) subclasses (Figure 4.2) and Q1–Q5, classified by Froude number (Fr).

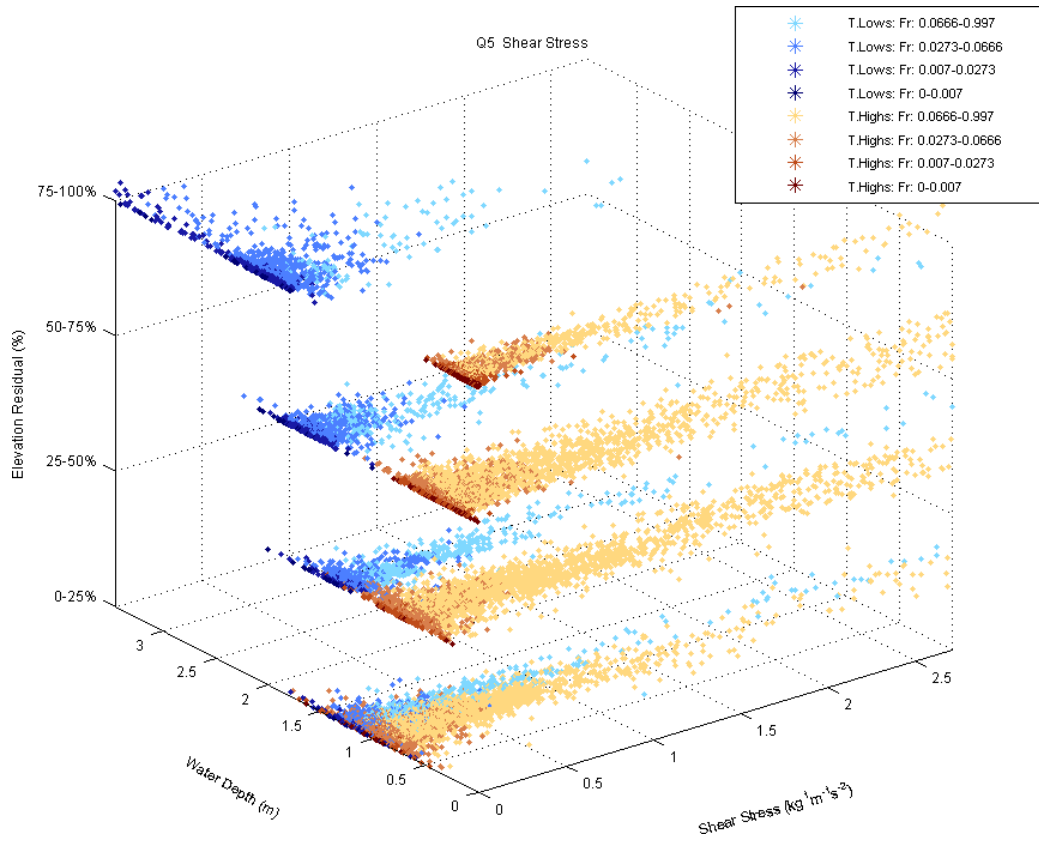


Figure 8.22 (cont'd). Distribution of shear stress for topographic high (T. Highs)/low (T. Lows) subclasses (Figure 4.2) and Q1–Q5, classified by Froude number (Fr).

9. DISCUSSION AND CONCLUSIONS

In this study, we characterized the channel morphology and flow hydraulics of select reaches on the lower San Antonio River (LSAR) and its tributary, the lower Cibolo Creek (LCC). The purpose was to refine geomorphic/hydraulic unit classification for use by the Texas Instream Flow Program (TIFP) in order to inform fish habitat mapping and assessment. The Goliad, the Falls City, and the Calaveras study reaches are located on the LSAR, the Cibolo reach is located on the LCC (Figure 4.3, Tables 3.1–3.2). In these reaches, we examined the spatial characteristic of channel morphology utilizing in-channel geomorphic units and of flow hydraulics in relation and under different discharge conditions.

We classified the geomorphic units based on topographic residuals obtained from detrended channel bathymetry. We utilized a detrending procedure similar to that of Clifford et al. (2006). Our classification defined negative residuals as topographic lows representing pool features and positive ones as topographic highs representing sediment bars/riffles and channel margins/edges. We further stratified the topographic lows (pools) and highs (bars/riffles/margins) by dividing each of them into four unique regions based on the quartiles of the minima and maxima of the lows and highs, respectively. These new classes correspond to the 0-25th, 25-50th, 50-75th, 75-100th percentiles of the detrended (+) and (-) elevations. We named them as (+1)–(+4) for topographic highs and (-1)–(-4) for topographic lows, respectively.

For each of these sites, we examined multiple modeled discharge conditions. The modeled discharge conditions consist of low, intermediate, and high flows that match discharge conditions related to habitat mapping (i.e., base flow levels of dry, normal, and wet, identified by aquatic modeling results by TIFP and SARA (2011), Table 3.2). Using these discharge levels, we examined a series of hydraulic variables, including water depth, Froude number (Fr), velocity magnitude, and shear stress and their spatial distributions within each reach.

Channel morphology and flow hydraulics in the study reaches. The findings show that, overall, channel geomorphology has a strong influence on the distribution of flow hydraulic. This influence changes within changing discharge. The Goliad and Calaveras reaches have very similar hydraulic properties, while the Cibolo reach is similar both the Goliad and the Calaveras reaches in terms of stream velocity. The Falls City reach has little in common with the other three reaches due to the presence of certain geologic controls (Barnes, 1976; Eargle and Snider, 1956).

As for the water depth, the Falls City reach displays the most platykurtic distribution among all reaches. This is expected as topographic lows (pools) and highs (sediment

bars/riffles/edges) essentially have different meaning in this reach as the geologic control creates two different regimes of topographic highs and lows (Figure 6.5). For other reaches, topographic lows feature a positive skewness, while topographic highs feature a negative skewness. Combined distributions for topographic highs and lows form a positively skewed distribution at all but highest water stages and varying levels of bimodality as stage increases with increasing discharge (Figures 5.5, 7.5, 8.5). Overall, the distributions of water depth for topographic highs for the Calaveras and the Goliad have very similar shape, with both becoming increasingly negatively skewed with increasing stage (Figures 5.5 and 7.5). In fact, the only reason why the Goliad reach is not negatively skewed at the highest stage is that the topographic lows are equally positively skewed. In addition, the Cibolo reach demonstrates the greatest bimodality at the highest stage with this being exclusively within the geomorphic class of topographic highs (Figure 8.5).

As for velocity magnitude, we observe particular inter-reach relationships (Figures 5.7–8.7). There is a great similarity between the distributions for the Goliad and the Calaveras reaches (Figures 5.7, 7.7). However, there is some dissimilarity as well; the Goliad reach has a larger proportion of low-valued velocity magnitudes than the Calaveras reach. This could suggest an influence from other upstream sources—such as the Falls City and the Cibolo reaches—on the Goliad. Further evidence is that both of these reaches feature a larger prevalence of low values for all hydraulic parameters. The spatial distribution of the velocity magnitudes demonstrates the effect of mid-channel bars and complex channel margin geometry (Figures 5.8–8.8). The Falls City and the Calaveras reaches feature constricted regions of planform resulting in local acceleration of flow downstream of these regions (Figure 6.8–7.8). The Falls City reach also has a unique section featuring high variability in water depth (a very low depth in this section and much deeper regions on both influent and effluent parts of the section) (Figure 6.8); resulting in a local acceleration of flow. In addition, what the Goliad, the Falls City, and the Calaveras to an extent have in common is the prevalence of local acceleration for topographic lows in regions of high curvature. The Cibolo reach has the lowest heterogeneity of velocity magnitude in relation to water depth, and the Goliad reach has the greatest. This fact coupled with similarity of flow attributes at the lesser extreme topographic levels (+/– 1 and 2) for the Goliad and the Calaveras reaches at the discharges of Q3 and Q4 show that these relationships depend on a position on the stream network (Figure 3.3) and on the particular discharges throughout these reaches.

As for the streamwise velocity, the Goliad has velocities associated with topographic lows that are similar to the Cibolo, but at a higher range (Figures 5.11, 8.11). The same is true for attributes associated with topographic highs for the Calaveras reach (Figure 7.11). Also, the Falls

City reach is unique in its stream velocity distribution—given that the Falls City contains the most leptokurtic distributions with modes centered on the lowest bin (Figure 6.11). This is not surprising, since most accelerations are associated with the two regions of topographic highs and little accelerations occur on the other lower level subclasses except for the highest discharge conditions. Spatially, stream velocity is very similar to velocity magnitude with the exception of backwaters (Figures 5.12–8.12). Some distinctions between the reaches can also be deduced by the regions where backwaters commonly form. In general, backwaters are observed at complex channel margins. However, all reaches—with the exception of Goliad—have backwaters that tend to form at the influent edge of pools. Another flow feature manifested in both streamwise and normal velocities is eddies. For the Falls City and the Cibolo reaches, there are very specific topographic lows at the influent portions of these reaches that feature flow reversal as water stage increases. At the highest water stages, the general shape of the relationship between stream velocity and water depth at the Falls City and the Cibolo reaches are quite similar although the Falls City has the much greater range in depth and the Cibolo has much lower range in stream velocity (Figures 6.13 and 8.13).

The distributions of normal velocity show that all four reaches display a sawtooth-like shape with some skewness and kurtosis. The Falls City reach features the greatest leptokurtic shape for nearly all stages except for the highest stage corresponding to Q5. Overall, the distributions for the Calaveras and the Goliad reaches are very similar. In the Calaveras reach, positive normal velocity is dominant—which moves toward the right bank in the downstream direction; in contrast, negative normal velocity is dominant in the Goliad reach. For the Cibolo, the leptokurtic nature of the distribution is similar to that of the Falls City at low water stages. After Q3, the shape is the most balanced of all four reaches—with proportions of negative and positive velocities being nearly equivalent. Much of the difference in normal velocity distribution are most likely attributable to planform shape of the particular reach. The distinction between positive and negative normal velocity is made based on the centerline that is derived at an equal distance from right and left banks at water extent corresponding to the highest water stage with respect to water levels at highest stages at Q5/Q6. However, the centerline cannot be the sole agent behind this distinction; local channel features such as mid-channel bars that emerge at high discharges as in the case of the Goliad reach, for example, can affect the distribution of normal velocity. As for the relationship between normal velocity and depth, in general, normal velocities have highest variety near the channel bed. The Calaveras reach has the highest ratio of water depth occupied by topographic

highs/low—with topographic highs being clustered at locations more than triple (~1 meter to 3.5 meters) the depth than that of topographic lows.

The distributions of shear stress are leptokurtic for the low water stages associated with Q1 and Q2 for all reaches (Figures 5.19–8.19). This may be attributable to the presence of roughness elements—particularly those in the same location as high velocity magnitude, which can amplify shear stress values. These amplified values manifest as outliers and represent tails on these distributions. In particular, the Falls City reach has very leptokurtic distribution with nearly all values within the first bin for all stages (Figure 6.19). In addition, all reaches demonstrate an inversely exponential distribution that only begins to take on a more platykurtic shape at highest stages. In particular, the Calaveras reach shows a distribution that begins to represent a Gaussian shape with a mode for both topographic highs and lows at highest water stage (Q5) that is in contrast to the inversely exponential shape of other reaches (Figure 7.19). In a spatial context, high shear stress values are present at locations where velocity magnitudes are high and there are roughness elements (Figures 5.20–8.20). This is particularly apparent in the Falls City reach—where the majority of the reach has no high shear stress values—but there is a large clustering of high values around the region B—one of the regions associated with topographic highs (Figure 6.20). Such clustering of high values explain the highly leptokurtic distribution of shear stress. However, this is also true to a lesser degree for other reaches—where topographic highs and lows are not as regional. In particular, the Calaveras reach has a nearly Gaussian distribution of shear stress for topographic lows due to the presence of roughness elements within the regions associated with topographic lows (Figure 7.20).

Geomorphic classification methodology. The findings of the study show the topographic residual and detrending approach adapted from Clifford et al. (2006) demonstrates utility in analyzing flow characteristics of reaches within the LSAR and the LCC utilizing a geomorphic context. The classification of the geomorphic units based on topographic residuals and their further stratification for geomorphic subclasses provides a useful quantitative approach that can be adopted in studies addressing fish habitat mapping and assessment.

Nevertheless, the analysis of the hydraulic properties associated with this classification scheme shows that a refined classification merits further investigation. One of these limitations of the approach is the failure in distinguishing between channel bed (sediment bar/riffle) and channel margin (edge) classes within the topographic highs. The results is the bimodal distributions observed in some hydraulic properties including velocity magnitude and shear stress at high

discharges. The bimodal tendencies of velocity magnitude for topographic highs could be due to the differing physical conditions that take place within in-channel (non-margin) and margin regions. There is some evidence that fish use margin habitats differently than other habitats (Osting et al. 2004), providing credence for a separate classification of these areas.

Although useful, the precise separation between non-margin bar/riffle and margin/edge habitats would be problematic with current methodology. Clifford et al. (2006) attempted to do this by considering the most extreme classes as channel margins. One complication will be that channel margins are contextual with the flow, in that it is not possible to create a single channel margin distinction for all flow conditions. Figures 5.5–8.5 demonstrate that bimodality is common only at high stage conditions—not all stage conditions. Another potential complication is the distinction between high-sloped channel margin habitats (such as at cutbanks) and low-sloped margin habitats (such as at point bars) since cut banks and point bars provide different habitat services to fish due to differing biotic and abiotic environmental factors (Osting et al., 2004). Therefore, a single distinction of channel-margin habitats will most likely demonstrate a bimodal or confounded behavior, and that distinction with respect to habitat will need to be informed by fisheries personnel or other informed stakeholders.

In addition, the similarity of results for the topographic high and low classes (+/-1) suggests that at least a subset of these two classes could be combined to form a single class of “near zero” topographical residuals that would be neither bar/riffle nor pool in nature. Also, the methodology allows for identifying “backwater” areas although they are not classified separately into a different class and such classification may be useful. Finally, further refinements of pool areas may be beneficial as well (e.g., head, body, and tail) in some locations with unusual hydraulic properties (for example, the region C at the Falls City reach).

Despite its limitations, the topographic residual and detrending approach provides an objective and quantitative classification of geomorphic units within riverine environments. Detailed analysis of the four reaches within the LSAR and LCC show that although there are overlap in hydraulic parameters between topographic highs and lows, there are distinct flow-centered characteristics that emerge from such classification. This opens up the possibility of further refining of this classification into flow-contextual margins. Thus, we believe that this study sets the stage for a detailed river habitat classification that is both in a geomorphic context and informed by flow-habitat studies to give margin distinction and fish habitat context.

10. REFERENCES

- Ambül, H. (1959). Die Bedeutung der Strömung als Ökologischer Faktor. *Schweiz. Z. Hydrol.* 21, 133–264.
- Braaten, P. J., Berry Jr. C. R. (1997). Fish associations with four habitat types in a South Dakota prairie stream. *Journal of Freshwater Ecology* 12(3), 477-489.
- Amsler, M. L., Bletter, M. C. M., Drago, L. D. (2009). Influence of hydraulic conditions over dunes on the distribution of the benthic macroinvertebrates in a large sand bed river. *Water Resources Research* 45, 15.
- Baras, E., Philippart, J. C. , Nindaba, J. (1996). Importance of gravel bars as spawning grounds and nurseries for European running water cyprinids. . In: M. Leclerc, H. Capra, S. Valentin, A. Boudreault and Y. Coté (Editors), *Ecohydraulics 2000. Proceedings of the 2nd International Symposium on Habitat Hydraulics*. INRS-Eau, Québec City, Canada, pp. 367-378.
- Barnes, V., 1976. Geologic Atlas of Texas: Crystal City-Eagle Pass Sheet. Bureau of Economic Geology, Austin, TX, Map. Available online [accessed 5-12-2017]: <http://begstore.beg.utexas.edu/store/geologic-atlas-of-texas/2096-ga0011.html>
- Braaten, P. J., Berry, C. R. (1997). Fish associations with four habitat types in a South Dakota prairie stream. *Journal of Freshwater Ecology*, 12(3), 477–489.
- Brooks, A.J.,Haeusler, T., Reinfelds, I., Williams, S. (2005). Hydraulic microhabitats and the distribution of macroinvertebrate assemblages in riffles. *Freshwater Biology* 50(2), 331-344.
- Brooks, N., Adger, W.N., Kelly, P.M. (2005). The determinants of vulnerability and adaptive capacity at the national level and the implications for adaptation. *Global Environmental Change* 15, 151–163.
- Brown, A. V., Brussock, P. P. (1991). Comparisons of benthic invertebrates between riffles and pools. *Hydrobiologia*, 220(2), 99–108.
- Clifford, N. J., Harmar, O. P., Harvey, G., Petts, G. E. (2006). Physical habitat, eco-hydraulics and river design: a review and re-evaluation of some popular concepts and methods. *Aquatic Conservation and Marine Freshwater Ecosystems* 16, 398–408.
- Davis, J. A., Barmuta, L. A. (1989). An ecologically useful classification of mean and near-bed flows in streams and rivers. *Freshwater Biology*, 21, 271-282.
- Dent, C. L., Grimm, N. B., Fisher, S. G. (2001). Multiscale effects of surface-subsurface exchange on stream water nutrient concentrations. *Journal of the North American Benthological Society*, 20(2), 162-181.
- Dingman, S.L., 2009. *Fluvial Hydraulics*. Oxford University Press: New York, New York, 559p.
- Eargle, D. H., Snider, J. L. (1956), Stratigraphy of Jackson Group (Eocene), South-Central Texas., *Bulletin of the American Association of Petroleum Geologists* 43(11).
- Fischer, H.,Sukhodolov, A.,Wilczek, S., Engelhardt, C. (2003). Effects of flow dynamics and sediment movement on microbial activity in a lowland River. *River Research and Applications* 19(5-6), 473-482.

- Frissell, C.A., Liss, W.J., Warren, C.E., Hurley, M.D. (1986). A hierarchical framework for stream habitat classification: viewing streams in a watershed context. *Environmental Management* 10(2), 199–214.
- Frothingham, K. M., Rhoads, B. L., Herricks, E. E. (2001). Stream geomorphology and fish community structure in channelized and meandering reaches of an agricultural stream. *Geomorphic Processes and Riverine Habitat* 4, 105–117.
- Frothingham, K. M., Rhoads, B. L., Herricks, E. E.. (2002). A multiscale conceptual framework for integrated ecogeomorphological research to support stream naturalization in the agricultural Midwest. *Environmental Management* 29(1), 16-33.
- Gessner, F. (1955). *Hydrobotanik. I. Energiehaushalt*. VEB Deutsch. Ver der Wiss., Berlin, 517 pp.
- Gorecki, V. I., Fryirs, K. A., Brierley, G.J. (2006) The relationship between geomorphic river structure and coarse particulate organic matter (CPOM) storage along the Kangaroo River, New South Wales, Australia. *Australian Geographer* 37: 285–311.
- Gregory, S. V., Swanson, F. J., Mckee, W. A., Cummins, K. W. (1991). An Ecosystem Perspective of Riparian Zones. *Bioscience* 41(8), 540–551.
- Güneralp, İ., Rhoads, B. L. (2008) Continuous characterization of the planform geometry and curvature of meandering rivers, *Geographical Analysis* 40(1), 1–25.
- Hart, D. D., Finelli, C. M. (1999). Physical-biological coupling in streams: the pervasive effects of flow on benthic organisms. *Annual Review of Ecological Systems* 30, 363–295.
- Hesse, R., Allee, W. C., Schmidt, K. P. (1937). Ecological animal geography; an authorized, rewritten edition based on Tiergeographie auf ockologischer grundlage by Richard Hesse. Prepared by W. C. Allee and Karl P. Schmidt. J. Wiley & Sons, Inc., New York. Available online [accessed 5-12-2017]: <http://www.biodiversitylibrary.org/item/27612>.
- Huet, M. (1949) Aperçu des relations entre la pente et les populations piscicoles des eaux courantes. *Schweizerische Zeitschrift für Hydrologie* 11(3-4), 332-351., 333–351.
- Kemp, J. L., Harper, D. M., Crosa, G. A. (1999). Use of 'functional habitats' to link ecology with morphology and hydrology in river rehabilitation. *Aquatic Conservation-Marine and Freshwater Ecosystems* 9, 159–178.
- Lake, P. S. (2000). Disturbance, patchiness, and diversity in streams. *Journal of North American Benthological Society* 19(4), 573–592.
- Lancaster, J., Hildrew, A. G. (1993). Flow Refugia and the Microdistribution of Lotic Macroinvertebrates. *Journal of the North American Benthological Society* 12(4), 385–393.
- Laurent, S., Michel, L., Michele, T., Celine, J., Anne, V., Pascal, B., et al. (2011). Using hydro-geomorphological typologies in functional ecology: Preliminary results in contrasted hydrosystems. *Physics and Chemistry of the Earth* 36(12), 539–548.

- Marchese, M. R., Wantzen, K. M., de Drago, E. I. (2005). Benthic invertebrate assemblages and species diversity patterns of the upper Paraguay river. *River Research and Applications* 21, 485–499.
- Moir, H. J., Gibbins, C. N., Soulsby, C., Webb, J. (2004). Linking channel geomorphic characteristics to spatial patterns of spawning activity and discharge use by Atlantic salmon (*Salmo salar* L.). *Geomorphology* 60(1-2), 21–35.
- Moir, H. J., Pasternack, G. B. (2008). Relationships between mesoscale morphological units, stream hydraulics and Chinook salmon (*Oncorhynchus tshawytscha*) spawning habitat on the Lower Yuba River, California. *Geomorphology* 100, 527–548.
- Ott, R.L., Longnecker, M. (2010). *An Introduction to Statistical Methods and Data Analysis*. Brooks/Cole, Belmont, California, 1273 pp.
- Osting, T., Mathews, R., Austin, B. (2004). Analysis of instream flows for the lower Brazos River – hydrology, hydraulics, and fish habitat utilization. Submitted to the US Army Corps of Engineers in fulfillment of TWDB Contract No. 2001-REC-015. Texas Water Development Board, Austin, TX. Available online [accessed 5-12-2017]: http://www.twdb.texas.gov/publications/reports/contracted_reports/doc/2001001015_BrazosInstreamFlows.pdf
- Python, 2010. *Mathematical Functions*. Available Online. Python Software Foundation. Available online [accessed 5-12-2017]: <https://www.python.org/doc/>
- Rabeni, C.F., Jackson, R.B. (1993). The Importance of Fluvial Hydraulics to Fish-habitat Restoration in Low-gradient Alluvial Streams. *Freshwater Biology* 29, 211–220.
- Rhoads, B. L., Schwartz, J. S., Porter, S. (2003). Stream geomorphology, bank vegetatin and three-dimensional habitat hydraulics for fish in midwestern agricultural streams. *Water Resources Research* 39(8).
- Richter, B.D., R. Matthews, D.L. Harrison, Wigington, R. (2003). Ecologically sustainable water management: managing river flows for ecological integrity. *Ecological Applications* 13(1), 206–224.
- Rivers-Moore, N. A., Jewitt, G. P. W. (2007). Adaptive management and water temperature variability within a South African river system: What are the management options? *Journal of Environmental Management* 82(1), 39-50.
- Saffel, P. D., Scarnecchia, K. L. (1995). Habitat use by juvenile Bull Trout in belt-series geology watersheds of Northern Idaho. *Northwest Science* 69(4), 304–316.
- Schmitt, L., Lafont, M., Trèmolieres, M., Jezequel, C., Vivier, A., Breil, P., Namour, P., Valin, K., Valette, L. (2011). Using hydro-geomorphological typologies in functional ecology: Preliminary results in contrasted hydrosystems. *Physics and Chemistry of the Earth* 36(12), 539-548.
- Schneider, K. N., Winemiller, K. O. (2008). Structural complexity of woody debris patches influences fish and macroinvertebrate species richness in a temperate floodplain-river system. *Hydrobiologia* 610, 235–244.

- Schwartz, J. S. (2002). *Stream Habitat Characterized by Stage-Specific Flows and Three-Dimensional Geomorphological Complexity: Development of Ecological Criteria for Stream Restoration Design*. Unpublished Dissertation, University of Illinois at Urbana-Champaign, Urbana-Champaign, IL.
- Schwartz, J. S., Herricks, E. E. (2005). Fish use of stage-specific fluvial habitats as refuge patches during a flood in a low-gradient Illinois stream. *Canadian Journal of Fisheries and Aquatic Sciences* 62, 1540–1552.
- Statzner, B., Higler, B. (1986). Stream hydraulics as a major determinant of benthic invertebrate zonation patterns. *Freshwater Biology* 16, 127–139.
- Statzner, B., Gore, J. A., Resh, V. H. (1988). Hydraulic stream ecology: observed patterns and potential applications. *Journal of the North American Benthological Society* 7(4), 307–360.
- Steffler, P., Blackburn, J. (2002). River2D: Two-Dimensional Depth Averaged Model of River Hydrodynamics and Fish Habitat. Introduction to Depth Averaged Modeling and User's Manual. University of Alberta. Available online [accessed 5-12-2017]:
<http://www.river2d.ualberta.ca/>
- Thomson, J. R., Taylor, M. P., Fryirs, K. A., Brierley, G. J. (2001). A geomorphological framework for river characterization and habitat assessment. *Aquatic Conservation: Marine and Freshwater Ecosystems*: 11(5), 373–389.
- (TIFP) Texas Instream Flow Program and (SARA) San Antonio River Authority (2011). Instream Flow Study of the Lower San Antonio River and Lower Cibolo Creek, Interim Progress Report and Instream Flow Recommendations. Prepared for Lower San Antonio River Sub-Basin Workgroup. Available online [accessed 5-12-2017]:
<https://www.sara-tx.org/wp-content/uploads/2015/04/Instream-View-Report.pdf>
- (TIFP) Texas Instream Flow Program and (SARA) San Antonio River Authority (2012). Instream Flow Study of the Lower San Antonio River and Lower Cibolo Creek, Study Design, Prepared for Lower San Antonio River Sub-Basin Study Design Workgroup, March 2012. Available online [accessed 5-12-2017]:
<https://www.sara-tx.org/wp-content/uploads/2015/04/Instream-Study-Design.pdf>
- (TPWD) Texas Parks and Wildlife Department, (TCEQ) Texas Commission on Environmental Quality, and (TWDB) Texas Water Development Board (2008). Texas Instream Flow Studies: Technical Overview. Texas Water Development Board Report 369, Austin, Texas. Available online [accessed 5-12-2017]:
http://www.twdb.texas.gov/publications/reports/numbered_reports/doc/R369_InstreamFlows.pdf
- Wadeson, R. A., & Rowntree, K. M. (1998). Application of the hydraulic biotope concept to the classification of instream habitats. *Aquatic Ecosystem Health and Management* 1(2), 143–157.